UCRL-17941
UC-28
Particle Accel. and High Volt. Mach.
TID-4500 (53rd Ed.)

UNIVERSITY OF CALIFORNIA

Lawrence Radiation Laboratory
Berkeley, California

AEC Contract No. W-7405-eng-48

1966 CERN–LRL–RHEL SHIELDING EXPERIMENT AT THE CERN PROTON SYNCHROTRON

William S. Gilbert, Denis Keefe, Joseph B. McCaslin
H. Wade Patterson, Alan R. Smith, and Lloyd D. Stephens
Lawrence Radiation Laboratory, Berkeley

Kenneth B. Shaw, Graham R. Stevenson, and Ralph H. Thomas
Rutherford High Energy Laboratory

Ronald D. Fortune and Klaus Geobel
CERN

September 1968

DISCLAIMER

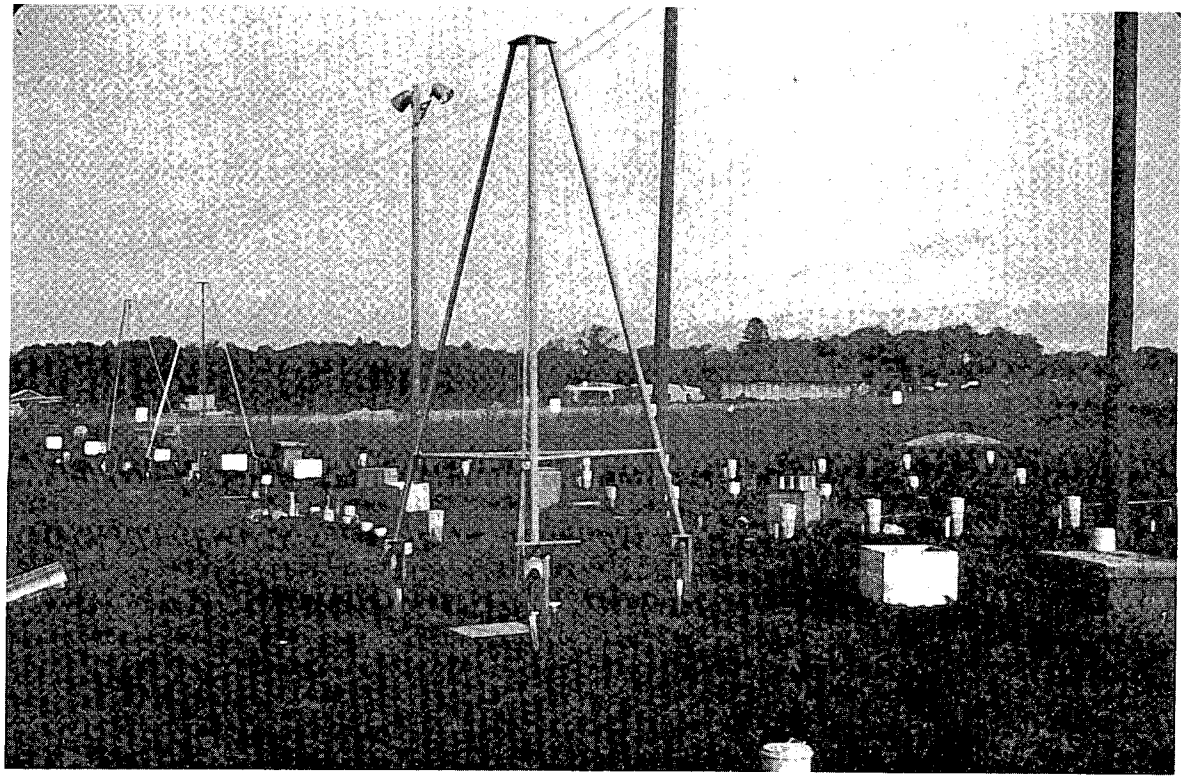

Frontispiece. Experimental area on the ring top above the CERN proton synchrotron at Geneva, Switzerland. The tripod devices were used to lower sets of detectors into vertical holes drilled into the earth above and around the accelerator. Tops of a number of casings of these holes are visible.

1966 CERN–LRL–RHEL SHIELDING EXPERIMENT AT THE CERN PROTON SYNCHROTRON

Contents

1966 CERN–LRL–RHEL SHIELDING EXPERIMENT AT THE CERN PROTON SYNCHROTRON

William S. Gilbert, Denis Keefe, Joseph B. McCaslin, H. Wade Patterson, Alan R. Smith, and Lloyd D. Stephens
Lawrence Radiation Laboratory, Berkeley

Kenneth B. Shaw, Graham R. Stevenson, and Ralph H. Thomas
Rutherford High Energy Laboratory

Ronald D. Fortune and Klaus Goebel
CERN

September 1968

ABSTRACT

The high cost of shielding of high-intensity accelerators in the 100-GeV energy range has stimulated keen interest in the radiation problems associated with these accelerators. As of 1966, available experimental data were perplexing and even conflicting. To resolve these difficulties, three laboratories--CERN, Lawrence Radiation Laboratory, and the Rutherford High Energy Laboratory combined their resources in the latter part of 1966 to carry out an extensive study of many of the major uncertainties in the radiation environment of the 28-GeV CERN proton synchrotron (CPS). Proton beam loss, neutron spectra, radiation levels in the accelerator room, and transmission of radiation through earth shielding and along tunnels were measured at 14.6 and 26.4 GeV/c. The volume of data obtained was so great that analysis and publication has required nearly two years. In the course of data reduction, computer programs for the evaluation of neutron spectra were developed and a study made of the conversion of neutron spectral information to dose equivalent. Useful information was obtained on the distribution of beam loss around the vacuum chamber of the CPS. The data obtained have been qualitatively explained by Monte Carlo calculations due to Ranft. The transmission of radiation through the earth shield was analyzed by a computer program FLUXFT through generalization of an empirical model first used by Moyer. Excellent agreement is obtained with the experimental data. The success of the model in explaining the observed radiation field at the CPS gives confidence in extrapolation to accelerators in the energy region around 200 GeV. The transmission of radiation along tunnels was studied and successfully interpreted in terms of a simple model. All data used in the analysis programs, as well as almost all other data, are presented in tables.

I. INTRODUCTION

The increases in beam energy and intensity of high-energy particle accelerators made possible in recent years have necessitated a closer study of general radiation problems. Although the shortage of basic data could be overcome for smaller accelerators by deliberate overdesign of radiation shields, this is economically unsound in accelerators as expensive as the 200- and 300-GeV proton synchrotrons proposed respectively by the Lawrence Radiation Laboratory, Berkeley[UCRL 65] and by CERN, Geneva.[CERN 64] Furthermore, accurate estimates of induced activity produced in the accelerator and radiation damage to it become extremely important. Hitherto, personnel radiation exposures from radioactive machine components have not required extensive use of remote-handling techniques. Errors in the estimated radiation levels of these proposed accelerators could seriously affect future operating efficiency. Similarly overestimates of radiation damage could lead to the unnecessary use of new and expensive radiation-resistant materials, involving time-consuming development programs. The 200-GeV Accelerator Design Study showed the importance of an accurate knowledge of the magnitude and distribution of beam loss from the vacuum chamber of the accelerator in assessing induced activity and radiation damage.

Comparison between the shield thicknesses calculated by the Berkeley group for a 200-GeV accelerator and by the CERN group for a similar 300-GeV synchrotron may easily lead one to false conclusions. Although the shield thickness around the bulk of the 200-GeV synchrotron, estimated at 1465 gm-cm^{-2}, agrees well with the CERN proposal of 1480 gm-cm^{-2} for the 300-GeV accelerator, this agreement is more apparent than real. Gilbert has appraised the internal differences between these calculations and compared measurements made at different laboratories, with the specific interest of the 200-GeV synchrotron in mind.[GilW 66] Of most significance for the proposed high-energy synchrotrons are those shielding measurements made at Brookhaven and CERN.

At these laboratories, different techniques and geometrical conditions were used for the shielding experiments, and the results obtained differ in the nature of the radiation field measured and its transmission through earth shielding. The experimental results are therefore, not, directly comparable. Thus for example, Casey et al.[CasR 67] reported that measurements in the sand shielding of the Brookhaven alternating-gradient synchrotron in a direction transverse to the circulating beam and close to an internal target indicate a high-energy neutron attenuation length of 83 g-cm^{-2}. Further details of these measurements are given in papers by Moore[MooW 66] and Distenfeld.[DisC 65] On the other hand, at CERN, nuclear-emulsion measurements in the forward direction in steel indicate an attenuation length of 120 g-cm^{-2},[ChiR 65] a value very roughly confirmed in the transverse direction by Capone et al.[CapT 65] and by the Monte Carlo calculations of Ranft.[RanJ 66] Shielding measurements made at Dubna by Aleinikov et al.[AleV 66] give a value for attenuation of about 150 g-cm^{-2}.

Similar discrepancies also arise in the measurements of dose composition at the surface of thick shields around high-energy accelerators. Brookhaven has reported a significant contribution (as high as ~ 80%) to the dose equivalent from neutrons of energy greater than 20 MeV.[DisC 67] Similar results were reported from CERN by Capone et al. for measurements on the surface of the earth shield, where values were obtained between 50 and 90% for the proportion of the dose equivalent due to high-energy neutrons. Previous results obtained at CERN above concrete indicate somewhat lower proportions.[BarJ 65] Experience at the Bevatron[PatH 65] and Nimrod[PerD 65, PerD 66] indicates results in general agreement with CERN data above a concrete shield. Thus Perry quotes the high-energy neutron dose equivalent contribution as ~ 10%, in agreement with estimates by Thomas based on the equilibrium spectrum expected in a nuclear cascade.

The proceedings of the Symposium on Accelerator Dosimetry and Experience held at Brookhaven in 1965 describes much of the most recent published data available to radiation physicists for the design of future accelerators. In a review article summarizing this conference, Thomas has set out some of the major areas where further data are needed:[ThoR 66]

(a) Definitive experiments of the effective attenuation length of the nuclear cascade need be made both for different materials and at a variety of angles to targets.

(b) Detailed measurements of the energy spectrum of particles emerging from a thick shield are required so that the importance of high-energy neutrons in the assessment of total dose equivalent may be estimated.

(c) Measurements are required on the transmission of each component of the incident radiation field as a function of penetration along tunnels. Very little experimental information exists on the transmission of ducts for high-energy neutrons. Consequently, at present the design of low-transmission ducts is necessarily conservative. A great deal of money may potentially be saved if adequate information on duct transmission is obtained.

The resolution of these and other problems is of more than academic interest. Both the Brookhaven alternating gradient synchrotron (AGS) and the CERN proton synchrotron (PS) have improvement programs underway involving an increase in circulating proton beam and, consequently, necessitating thicker shielding. Storage rings are under construction at CERN (ISR project), and confirmation of the shielding design for this facility is desirable, since it is both difficult and expensive to augment shields after the initial construction stage. At higher energies (200 to 300 GeV) the scale of the project becomes so vast that relatively modest changes in shield thickness represent significant changes in construction costs. For example, for the 200-GeV accelerator a reduction of 2 m in the thickness of the originally specified 7 m of earth cover would result in a saving of some $3,000,000 and would also bring additional advantages related to convenience of access, siting, etc.

Even if shielding data from existing accelerators were in agreement, there would be no reliable way to extrapolate data to 200 to 300 GeV. In order to do this successfully one must obtain a detailed knowledge and understanding of the loss mechanisms at existing and proposed accelerators, and the generation of the nuclear cascade within the shield. Such a series of experiments would involve a great deal of accelerator time, for which there is a great demand. However, the potential consequences of the uncertainties in this area led a European Committee for Future Accelerators Working Group concerned with machine utilization to make the following recommendation:[CERN 66]

"The calculation of shielding for the accelerator and experimental areas, and the design of access tunnels depends, among other things, on knowledge of both transverse and longitudinal attenuation lengths, build-up factors, dose spectrum outside thick shields, and radiation attenuation in the tunnels. Present information on these factors is generally unsatisfactory and inadequate. The Working Group felt strongly that more reliable information would help to avoid the need for a high degree of conservatism in shielding design, and could certainly lead to significant cost reductions. Therefore, it is recommended that experiments on an adequate scale be carried out in the near future, for example at CERN, to improve present information. The Working Group wished to emphasize the vital importance and urgency of these experiments. They should have at least as high a priority as normal physics experiments, with opportunity for data interpretation between runs to guide the course of the work. A concentrated effort on shielding studies could, and should, be obtained by a collaboration of experts from the various interested European Laboratories."

The economic motivation is then clear for a series of measurements designed to yield data on the shielding processes around existing accelelerators. Using these data, one could make reliable predictions of the radiation environment to be expected around the new generation of high-energy proton synchrotrons.

In the opinion of the many accelerator and radiation physicists consulted in planning this experiment, three separate areas required explanation:

1. The proton-beam loss distribution and its variation with machine energy, targetting, and other operating modes. Particular importance was attached to a study of so-called random losses and their absolute magnitude.

2. Particle flux and γ dose distribution inside the accelerator to study the shielding effects of the steel magnets. The angular distribution of particles around targets and dose rates on the vacuum chamber are important.

3. A study of the generation of the nuclear cascade through the earth shielding in three dimensions. Detailed measurements with several detectors would enable spectra to be estimated.

In view of these considerations, approximately 100 hours of primary user time on the CERN PS were made available for a systematic series of shielding experiments. The exposures were arranged in 8 shifts of about 12 hours duration, and some additional measurements were made during normal PS operation.

The shielding experiment described in this paper required the combined resources of the shielding and health-physics personnel from three laboratories: CERN, LRL, and Rutherford. Since the determination of the beam-loss distribution around the accelerator was considered to be an essential aspect of these investigations, a large fraction of the effort was expended to this end. Fortunately, we could use equipment and techniques already developed during related work done previously by CERN personnel. To control the proton-beam loss pattern, we required exclusive use of the PS during our exposures. We relied primarily on activation detectors, hundreds of which could be simultaneously exposed during a given machine run and subsequently counted. This technique was economical of machine beam time, but required that several electronic counting systems be used simultaneously, since all the detectors decayed in activity after being removed from the radiation field; this is one reason for the participation of personnel and equipment from more than one laboratory. By using detectors with different thresholds, information on the spectrum of particles in the radiation field was obtained.

This report covers four general topics:

1. *General Description of the Experiment.* This includes a brief description of the CERN PS, as well as the targetting and beam-monitoring techniques.
2. *Experimental Techniques.* Various techniques used to study the radiation field close to the accelerator and in the earth shielding are discussed along with instrument calibration.
3. *Experimental Data.* A comprehensive set of various data from the series of experiments is included. Such a procedure enables independent interpretation of the experiment from our fundamental data.
4. *Interpretation of Data.* A phenomenonological model is described which adequately reproduces the experimental determinations of flux inside the machine tunnel and earth shield in terms of a limited set of parameters. The computer programs used in the interpretation of the data are summarized. These include TELLY, which is used to determine the neutron spectra and dose from threshold-detector results, and FLUX, used to determine the best constants in our phenomenonological model. The FLUX program, together with the constants derived from this shielding experiment, enable one to specify shield contours for the improved CPS, the U.S. 200-GeV, and European 300-GeV accelerators.

The experimental program at the CPS extended from September to December, 1966. During this time preliminary analysis of the data was performed, and the general picture of the radiation field was available to the members of the experimental teams involved. Systematic reduction of the data, model building and computer program development, and report writing has taken over 18 months. During this time more experimental work was done to resolve some problems in instrument calibration; some nine computer programs were written and used to interpret various aspects of the behavior of the measured radiation field; and preliminary results were made available through the following written reports and talks at technical meetings:

William S. Gilbert, Radiation Problems with High Energy Proton Accelerators, in *Proceedings of the 1967 U.S. National Particle Accelerator Conference, Washington, D.C., March 1-3, 1967,* IEEE Trans. Nucl. Sci. *NS-14,* No. 3 (1967).

R. D. Fortune, W. S. Gilbert, and R. H. Thomas, Shielding at the CERN-PS; CERN/LRL/RHEL Collaboration 1966, UCID-10199, April 28, 1967.

J. Ranft, Monte Carlo Calculation of Particle Loss Distributions Along the Vacuum Chamber of the CPS Near Internal Targets and of the Transverse Attenuation of Strongly Interacting Particle Fluxes in the P.S. Magnet Units and Earth Shield, MPS/Int. MV/EP 67-5, June 20, 1967.

William S. Gilbert, Beam Loss and Shielding Experiments Relevant to High Energy Proton Synchrotrons, in *Proceedings of the Sixth International Conference on High Energy Accelerators, Cambridge, September 1967* (Cambridge Electron Accelerator, Cambridge, 1967).

William S. Gilbert, Health Physics Considerations in the Design of a High Energy Accelerator, talk presented at the AEC Contractors Health Protection Meeting, Augusta, Georgia, January 30-31, 1968.

W. S. Gilbert, H. W. Patterson, and A. R. Smith, Accelerator Neutron Spectra and Spectra-to-Dose Conversion, talk presented at Fourteenth Annual Meeting, American Nuclear Society, Toronto, Canada, June 9-13, 1968.

REFERENCES

AleV 66. V. E. Aleinikov, V. N. Lebedev, V. Mantseva, and M. I. Salatskoya, Attenuation in Concrete of a Neutron Flux Emitted at an Angle of 90° to the Primary Proton Beam of a 10-GeV Synchrophasotron, SLAC Trans.-57, 1966.

BarJ 65. J. Baarli and A. H. Sullivan, Radiation Dosimetry for Protection Purposes near High-Energy Particle Accelerators, Health Physics *11–5,* 353 (1965).

CapT 65. T. Capone et al., A Radiation Survey inside and outside the CPS Tunnel to estimate the Effectiveness of the Roof Shielding, CERN Report DI/HP/71, February 1965.

CasR 67. R. Casey, C. Distenfeld, G. S. Levine, W. H. Moore, and L. Smith, Nucl. Instr. Methods *55,* 253 (1967).

CERN 64. Report on the Design Study of a 300-GeV Proton Synchrotron by the CERN Study Group on New Accelerators, CERN/563 (2 vols.), November 1964.

CERN 66. Preliminary Conclusions of E.C.F.A. CERN/SPC/228/Rev. 2, June 17, 1966.

ChiR 65. R. L. Childers, C. D. Zerby, C. M. Fisher, and R. H. Thomas, Nucl. Instr. Methods *32,* 53 (1965).

DisC 65. C. Distenfeld, AGS Conversion Summary, CONF-651109, November 3, 1965.

DjsC 67. C. Distenfeld, private communication.

GilW 66. W. S. Gilbert, in "200-BeV Accelerator — Preliminary Project Report", UCRL-16606, January 1966.

MooW 66. W. H. Moore, Source of High-Energy Particles from an Internal Target in the AGS, AGSCD-6, January 24, 1966.

PatH 65. H. W. Patterson, Accelerator Radiation Monitoring and Shielding, paper presented at USAEC First Symposium on Accelerator Radiation Dosimetry and Experience, Brookhaven, N.Y., 1965, CONF-651109, November 1965.

PerD 65. D. R. Perry and K. B. Shaw, Radiation Levels in and around Nimrod, Rutherford Laboratory Report RPP/R1, November 1965; paper read at Brookhaven Symposium, CONF-651109.

PerD 66. D. R. Perry, Neutron Dosimetry Methods and Experience on the 7-GeV Proton Synchrotron, Nimrod, Rutherford Laboratory Report RPP/R2, 1966; paper read at IAEA Symposium on Neutron Monitoring for Radiological Protection, Vienna, Austria, August 1966.

RanJ 66. J. Ranft, Improved Monte-Carlo Calculation of the Nucleon-Meson Cascade in Shielding Materials, CERN Report MPS/Int. MU/EP 66-8, August 15, 1966.

ThoR 66. R. H. Thomas, Radiation Hazards of the New Generation of Accelerators, Nucleonics *24,* 64 (1966).

UCRL 65. 200-BeV Accelerator Design Study, UCRL-16000 (2 vols.), June 1965.

II. THE CERN PROTON SYNCHROTRON

A. General Description

The CERN proton synchrotron (CPS) is a strong-focusing machine that accelerates protons to a maximum energy of some 28 GeV. In this chapter we describe the physical layout of the machine and the operational details relevant to the shielding measurements.

B. Internal Beam Line

The general layout of the accelerator is shown in Fig. II-1. Under normal operation, the linac injects 50-MeV protons into the main ring, where they are accelerated in a clockwise direction (in plan view) and ejected, either directly as extracted beams or as secondary beams from internal targets, into one or more of the experimental halls labelled South, North, and East. Protons of the internal beam are retained in an equilibrium orbit of 100-m mean radius by 100 magnets of 4.26-m physical (iron) length and 4.4-m magnetic length. Figure II-2 shows the principal magnet dimensions. Field-free straight sections between the magnets house injection, ejection, focusing, radiofrequency acceleration, monitoring, targetting, and other equipment. The standard "short" straight sections are of 1.74-m physical (iron-to-iron) length and 1.6-m field-free length. "Long" straight sections are of 3.14-m physical length and 3.0-m field-free length. The beam is contained in an elliptic-section stainless steel vacuum tank of 2-mm wall thickness, 7-cm vertical internal diameter, and 14.5-cm horizontal internal diameter.

C. Ring Tunnel and Shield

Radiation protection requires that the main ring be shielded by at least several hundred grams of material. The ring is therefore enclosed in a concrete tunnel. Atop the tunnel roof is a 25-cm layer of drainage gravel over which is approximately 3 m of earth shielding. The corresponding gravel thickness on each side of the tunnel is 50 cm. The normal cross section of the ring tunnel and earth shield is shown in Fig. II-3. It should be noted that the radius of the beam line is 25 cm greater than the mean radius of the tunnel building. The trench originally excavated for the construction of the tunnel cuts into sandstone bedrock whose top level is about 3 m below original ground level, i.e., about 3 m above the beam plane.

Particular attention was given in this shielding experiment to a measurement of the density of the earth shield over the entire region of the experiment. The results of these measurements and of related measurements on grain-size distribution, compaction characteristics, chemical analyses, and earth-surface and rock-profile surveys are given in a separate report,[ForR 67b] where they have been used to derive shielding thicknesses in gm-cm^{-2} for each detector position used in the experiment.

Figure II-4 shows a plan of the hole positions where most of the measurements were made. The principal planes of interest in the shielding experiment, the radial and tangential vertical planes through target 32, are covered by special borings at B1, B2 and A1, A2, respectively. Comparison tests between different methods of measuring the density were made on samples taken from the test region P1...P6 and F.

Five methods were compared in the test region:

a. Measurement in the laboratory of undisturbed fragments from samples obtained by forcing a 5-cm-diam tube into the earth.

b. As for (a), except that the samples were obtained by dry drilling with a 15-cm-diam tubular bit.

c. Weighing all the loose earth removed from the 15-cm holes and calculating the volume from the measured length of hole and the effective diameter of the sample $=$ 1/3 o.d. + 2/3 i.d.

d. Weighing the loose earth removed from a large pit F, nominally 1.2 by 1.2 by 0.8 m deep, and calculating the volume from the measured linear dimensions.

e. Balloon method: This method is suitable only where horizontal surfaces are accessible and was used only in the pit F.

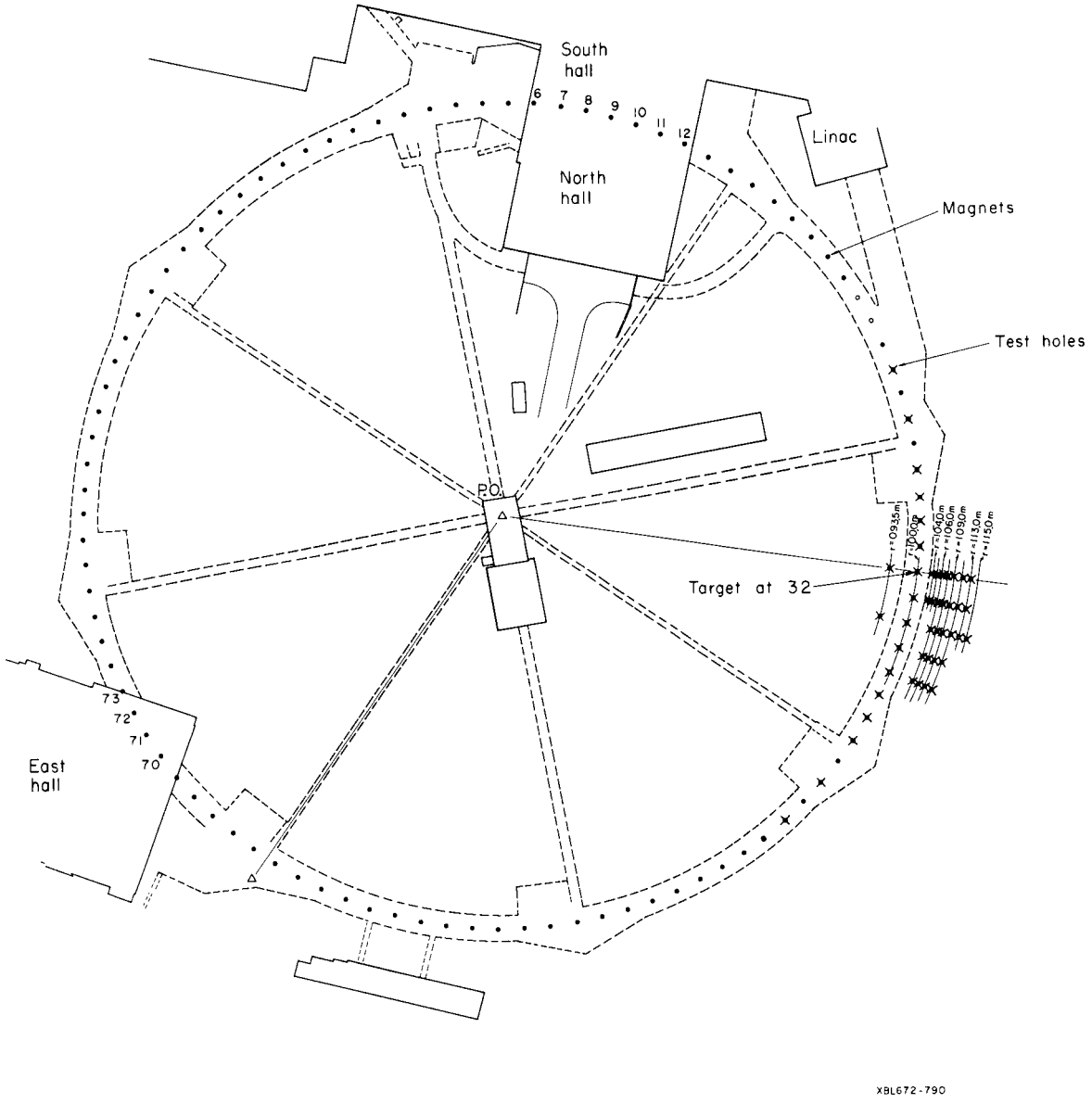

Fig. II-1. General layout of the CERN proton synchrotron.

Three sets of density measurements were made. Just before the shielding experiment and using mainly method (a), measurements were made along the ring top, above the beam orbit, of the humus or top soil density, the earth density, and the rock density. It was the unexpectedly high densities determined in this set of measurements (previous shielding experiments have used ρ = 1.7 gm-cm^{-3}) which led to the subsequent confirmatory measurements made in the test region P1...P6 and F, and in holes A1, A2, B1, and B2. A summary of the results of these three sets of measurements is given in Table II A.

Tables IIB, IIC, and IID give the location and shielding thicknesses in gm-cm^{-2} for various detector positions in the orbital and radial holes with reference to the beam orbit. The thickness of the concrete wall (density 2.40 gm-cm^{-3}) and gravel layer (density 1.40 gm-cm^{-3}), 36 cm and 50 cm respectively in the horizontal plane, and 40 cm plus variable gravel thickness vertically, were added to the earth (plus rock) thicknesses. These data are used to deduce the shielding thickness in gm-cm^{-2} corresponding to each detector position used in the experiment.

Although too few measurements were made to obtain a good estimate of the precision of the methods, a correlation diagram, Figure II-5, shows the variation in density as a function of depth below ground surface. It can be seen that in accordance with the summary given in Table II A, the densities in humus and rock are slightly less than and greater than the densities in earth respectively. However, no significant variation with depth can be seen. Figure II-6 shows the profile of the rock layer in the region of target 32.

The weight percent of water in the earth was also found to be surprisingly high, ranging as high as 24.2%, with most of the values lying between 10 and 20%. Later experimental evidence shows that this water content had an important effect on the neutron spectrum.

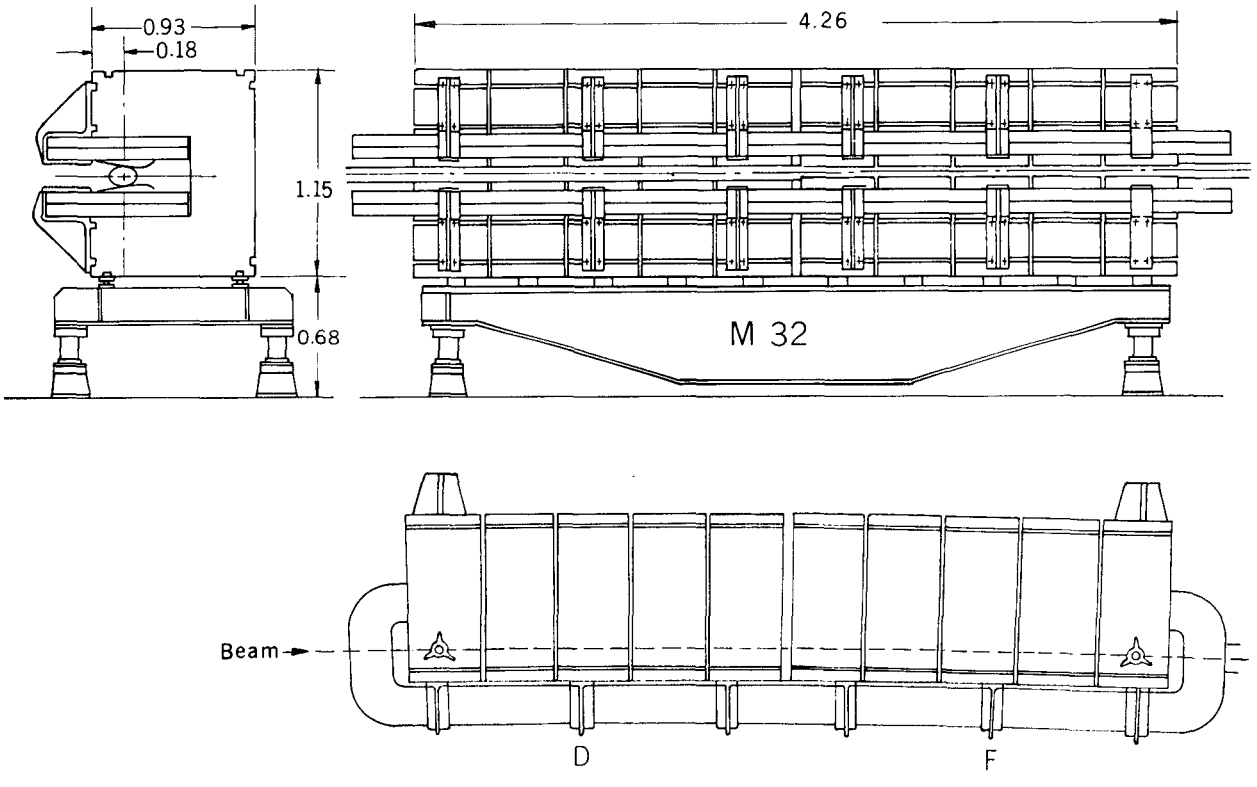

Fig. II-2. (top) Cross section and elevation views and (bottom) plan view of a typical main ring magnet of the CERN proton synchrotron. Dimensions are in meters.

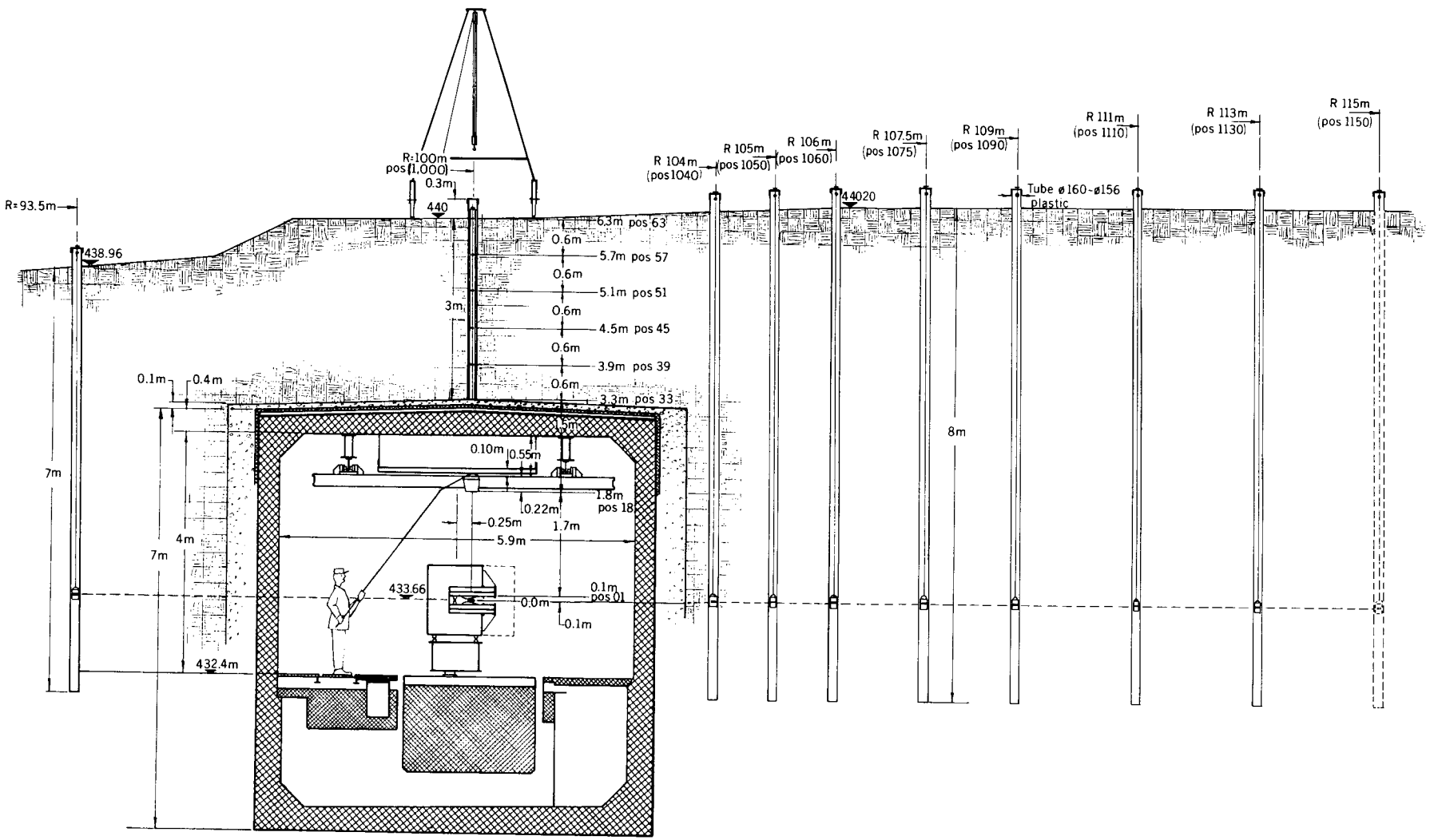

XBL 6712-2120

Fig. II-3. Normal cross section of the ring tunnel and earth shield in the area of the experimental measurements.

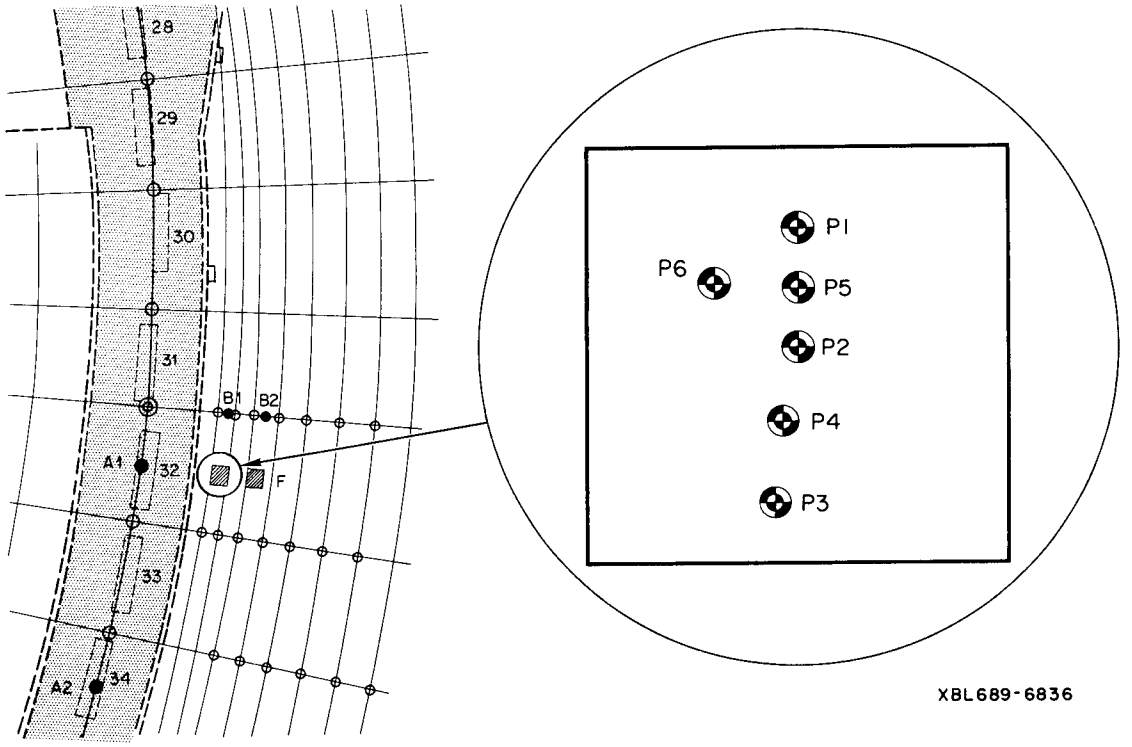

Fig. II-4. Positions of earth-density measurements.

Table II A. Summary of results of density measurements.

Measurement set	Test area	A1, A2 B1, B2	First set 15.9.66
Earth density ($gm\text{-}cm^{-3}$)	2.159 ± 0.016	2.159 ± 0.007	2.196 ± 0.023
	2.159 ± 0.006		
		2.161 ± 0.006	
Humus density ($gm\text{-}cm^{-3}$)	1.930 ± 0.030	1.895 ± 0.027	1.867 ± 0.057
		1.906 ± 0.019	
Rock density ($gm\text{-}cm^{-3}$)			2.352 ± 0.017

D. Main Experimental Area for the Shielding Measurements

The choice of a particular section of the synchrotron ring in which to install a target for the shielding experiment was governed by the following requirements:

(a) The target should be in the upstream part of one of the eight uniform-sectioned segments of the tunnel, to minimize complications in the flux pattern in the shield downstream of the target.

(b) The topography of the shielding earth above and downstream of the target should be amenable to hole-digging operations, i.e., it should be flat and firm over 60 m length of the ring and to a radial distance of 10 to 15 m outside the ring.

(c) The segment chosen should be in an established "quiet" area so that the hole complex can be used for the study of flux patterns both for target-region and quiet-region conditions.

These conditions are fulfilled for the target installed in straight section 32. The normal tunnel cross section, shown in Fig. II-3, extends from 18 m upstream to 40 m downstream of the target. From the linac intersection to the North Hall road which crosses the ring about 100 m downstream, the ground is flat to ± 0.4 m over and outside the ring. This road gave easy access for hole-drilling operations and for quick transfer of activation detectors between hole locations and counting rooms. In addition, previous measurements by the CERN Health Physics group show that with a target in straight section 81 there is relatively low beam loss in this segment.

The detailed layout of the hole region is shown in Fig. II-7. We used a cylindrical coordinate system with the vertical axis through the center of the accelerator, the vertical plane through the axis and the straight-section-32 target position as azimuthal reference, and the horizontal beam plane as vertical zero. Vertical planes radiating from the axis are numbered 1 through 100 according to the number of the straight sections through which they pass. Holes are identified on this coordinate system by a pair of numbers which denote the straight section and the radius in meters. Detector locations are indicated by a triplet which gives the straight section, radius, and height.

Thirty 16-cm-diameter detector holes were drilled in the earth shield up to a radius of 115 m (or 15 m outside the beam orbit) and to a depth of about 1.5 m below the beam plane. These holes, which permitted deep attenuation measurements in the horizontal (beam) plane, are referred to in the report as "radial" holes.

Table II B. Location and shielding of radial holes for detectors.

Hole No. (SS/r)[a]	Radial distance[b] (m)	Radial shielding		
		(in earth-m)	(in rock-m)	Total (in g-cm^{-2})
32/0935	6.5	2.44	0	684
32/1040	4.0	0.44	0	251
32/1050	5.0	1.44	0	468
32/1060	6.0	2.39	0.05	685
32/1075	7.5	2.39	1.55	1037
32/1090	9.0	2.39	3.05	1390
32/1110	11.0	2.39	5.05	1861
32/1130	13.0	2.39	7.05	2331
33/1040	4.0	0.44	0	251
33/1050	5.0	1.44	0	468
33/1060	6.0	2.29	0.15	687
33/1075	7.5	2.29	1.65	1039
33/1090	9.0	2.29	3.15	1392
33/1110	11.0	2.29	5.15	1863
33/1130	13.0	2.29	7.15	2333
34/0935	6.5	2.44	0	684
34/1060	6.0	1.99	0.45	692
34/1075	7.5	1.99	1.95	1045
34/1090	9.0	1.99	3.45	1398
34/1110	11.0	1.99	5.45	1868
34/1130	13.0	1.99	7.45	2339
34/1150	15.0	1.99	9.45	2809
35/1060	6.0	1.99	0.45	692
35/1075	7.5	1.99	1.95	1045
35/1090	9.0	1.99	3.45	1398
35/1110	11.0	1.99	5.45	1868
36/1060	6.0	2.44	0	684
36/1075	7.5	3.24	0.70	1021
36/1090	9.0	3.24	2.20	1374
36/1110	11.0	3.24	4.20	1844

a. Numbers 32 through 36 refer to the straight section; the other number is the radial distance from the center of the synchrotron orbit.

b. The radial distance from the beam line is given. Negative values indicate distance from the beam line inward, positive values outward.

Table II C. Height of detector positions in orbital holes in meters with reference to the beam height.

Detector position No.	Straight section hole No.															
	24	26	28	29	30	31	32	33	34	35	36	37	38	39	41	43
Ground level	6.35	6.38	6.38	6.35	6.42	6.40	6.42	6.39	6.29	6.30	6.26	6.26	6.27	6.32	6.39	6.40
63.0[a]	6.57	6.42	6.58	6.41	6.44	6.48	6.62	6.37	6.58	6.40	6.26	6.54	6.43	6.52	6.52	6.35
62.0	6.52	6.37	6.53	6.36	6.39	6.43	6.57	6.32	6.53	6.35	6.21	6.49	6.38	6.47	6.47	6.30
61.0	6.47	6.32	6.48	6.31	6.34	6.38	6.35	6.27	6.48	6.30	6.16	6.44	6.33	6.42	6.42	6.25
60.5	6.43	6.28	6.44	6.27	6.30	6.34	6.48	6.23	6.44	6.26	6.12	6.40	6.29	6.38	6.38	6.21
60.0	6.39	6.24	6.40	6.23	6.26	6.30	6.44	6.19	6.40	6.22	6.08	6.36	6.25	6.34	6.34	6.17
59.0	6.27	6.12	6.28	6.11	6.14	6.18	6.32	6.07	6.28	6.10	5.96	6.24	6.13	6.22	6.22	6.05
58.0	6.10	5.95	6.11	5.94	5.97	6.01	6.15	5.90	6.11	5.93	5.79	6.07	5.96	6.05	6.05	5.88
57.0[a]	5.98	5.83	5.99	5.82	5.85	5.89	6.03	5.78	5.99	5.81	5.67	5.95	5.84	5.93	5.93	5.76
56.0	5.93	5.78	5.94	5.77	5.80	5.84	5.99	5.73	5.94	5.76	5.62	5.90	5.79	5.88	5.88	5.71
55.0	5.88	5.73	5.89	5.72	5.75	5.79	5.93	5.68	5.89	5.71	5.57	5.85	5.74	5.83	5.83	5.66
54.5	5.84	5.69	5.84	5.68	5.71	5.75	5.89	5.64	5.84	5.67	5.53	5.80	5.70	5.78	5.78	5.64
54.0	5.80	5.65	5.81	5.64	5.67	5.71	5.85	5.60	5.81	5.63	5.49	5.77	5.66	5.75	5.75	5.58
53.0	5.68	5.53	5.69	5.52	5.55	5.59	5.73	5.48	5.69	5.51	5.37	5.65	5.54	5.63	5.63	5.46
52.0	5.49	5.34	5.50	5.33	5.36	5.40	5.54	5.29	5.50	5.32	5.18	5.46	5.35	5.44	5.44	5.27
51.0[a]	5.39	5.24	5.40	5.23	5.26	5.30	5.44	5.19	5.40	5.22	5.08	5.36	5.25	5.34	5.34	5.19
50.0	5.34	5.19	5.35	5.18	5.21	5.25	5.39	5.14	5.35	5.17	5.03	5.31	5.20	5.29	5.29	5.12
49.0	5.29	5.14	5.30	5.13	5.16	5.20	5.34	5.09	5.30	5.12	4.98	5.26	5.15	5.24	5.24	5.07
48.5	5.25	5.10	5.26	5.09	5.12	5.10	5.30	5.05	5.26	5.08	4.94	5.22	5.11	5.20	5.20	5.03
47.0	5.09	4.94	5.10	4.93	4.96	5.00	5.14	4.89	5.10	4.92	4.78	5.06	4.95	5.04	5.04	4.87
46.0	4.92	4.77	4.93	4.76	4.79	4.83	4.97	4.72	4.93	4.75	4.61	4.89	4.78	4.87	4.87	4.70
45.0[a]	4.80	4.65	4.81	4.67	4.67	4.71	4.85	4.60	4.81	4.63	4.49	4.77	4.66	4.75	4.75	4.58
44.0	4.76	4.61	4.77	4.60	4.63	4.67	4.81	4.56	4.77	4.59	4.45	4.73	4.62	4.71	4.71	4.54
43.0	4.70	4.55	4.71	4.54	4.57	4.61	4.75	4.50	4.71	4.53	4.39	4.67	4.56	4.65	4.65	4.48
42.5	4.66	4.51	4.67	4.50	4.53	4.57	4.71	4.46	4.67	4.49	4.35	4.63	4.52	4.61	4.61	4.44
42.0	4.62	4.47	4.63	4.46	4.49	4.53	4.67	4.42	4.63	4.45	4.31	4.59	4.48	4.57	4.57	4.40
41.0	4.50	4.35	4.51	4.34	4.37	4.41	4.55	4.30	4.51	4.33	4.19	4.47	4.36	4.45	4.45	4.28
40.0	4.33	4.18	4.34	4.17	4.20	4.24	4.37	4.13	4.34	4.16	4.02	4.30	4.19	4.28	4.28	4.11
39.0[a]	4.21	4.06	4.22	4.05	4.08	4.12	4.26	4.01	4.22	4.04	3.90	4.18	4.07	4.16	4.16	3.99
38.0	4.17	4.02	4.18	4.01	4.04	4.08	4.22	3.97	4.18	4.00	3.86	4.14	4.03	4.12	4.12	3.95
37.0	4.11	3.96	4.12	3.95	3.98	4.02	4.16	3.91	4.12	3.94	3.80	4.08	3.97	4.06	4.06	3.89
36.5	4.07	3.92	4.08	3.91	3.94	3.98	4.12	3.87	4.08	3.90	3.76	4.04	3.93	4.02	4.02	3.85
36.0	4.03	3.88	4.04	3.87	3.90	3.94	4.08	3.83	4.04	3.86	3.72	4.00	3.89	3.98	3.98	3.81
35.0	3.91	3.76	3.92	3.75	3.78	3.82	3.96	3.71	3.92	3.74	3.60	3.88	3.77	3.86	3.86	3.69
34.0	3.74	3.59	3.75	3.58	3.61	3.65	3.79	3.54	3.75	3.57	3.43	3.71	3.60	3.69	3.69	3.52
33.0[a]	3.62	3.47	3.63	3.46	3.49	3.53	3.67	3.42	3.63	3.45	3.31	3.59	3.48	3.57	3.57	3.40
Bottom of tube	3.58	3.43	3.59	3.42	3.45	3.49	3.63	3.38	3.59	3.41	3.27	3.55	3.44	3.53	3.53	3.36
48.0	5.21	5.06	5.21	5.05	5.08	5.12	5.25	5.01	5.21	5.04	4.90	5.17	5.07	5.15	5.15	4.99

a. These positions were most often used in the experiment.

Table II D. Thickness of shielding below detector positions in g-cm^{-2} in orbital holes.

Detector position No.	Straight section hole No.															
	24	26	28	29	30	31	32	33	34	35	36	37	38	39	41	43
Ground level	756	774	762	768	781	774	768	780	742	758	760	738	749	754	769	784
63.0[a]								796			760					793
62.0		772			774			785			749					782
61.0		761		759	763	769		754		758	738					751
60.5		753		751	755	761		746		750	730					743
60.0		744		742	746	752		737		741	721		745			734
59.0	739	718	739	716	720	726	746	711	739	715	695	733	719	731	731	708
58.0	702	681	703	679	683	689	709	674	703	678	658	697	682	695	695	671
57.0[a]	676	655	677	653	657	663	683	648	677	652	632	671	656	669	669	645
56.0	666	645	667	643	647	653	673	638	667	642	622	661	646	659	659	635
55.0	655	634	656	632	636	642	662	627	656	631	611	650	635	648	648	624
54.5	646	625	647	623	627	633	653	618	647	622	602	641	626	639	639	615
54.0	638	617	639	615	619	625	645	610	639	614	594	633	620	631	631	607
53.0	612	591	613	589	593	599	619	584	613	588	568	607	592	605	605	581
52.0	571	550	572	548	552	558	578	543	572	547	527	566	551	564	564	540
51.0[a]	549	528	550	526	530	536	556	521	550	525	505	544	529	542	542	518
50.0	538	517	539	515	519	525	545	510	539	514	494	533	518	531	531	507
49.0	527	506	528	504	508	514	534	499	528	503	483	522	507	520	520	496
48.5	519	498	520	496	500	506	526	491	520	495	475	514	499	512	512	488
48.0	510	489	511	487	491	497	517	482	511	486	466	505	490	503	503	479
47.0	484	463	485	461	465	471	491	456	485	460	440	479	464	477	477	453
46.0	447	426	448	424	429	434	454	419	448	423	403	442	427	440	440	416
45.0[a]	422	401	423	399	403	409	429	394	423	398	378	417	402	415	415	391
44.0	413	392	414	390	394	400	420	385	414	389	369	408	393	406	406	382
43.0	400	379	401	377	381	387	407	372	401	376	356	395	380	393	393	369
42.5	391	370	392	368	372	378	398	363	392	367	347	386	371	384	384	360
42.0	383	362	384	360	364	370	390	353	384	359	337	378	363	376	376	350
41.0	357	336	358	334	338	344	364	339	358	333	313	352	337	350	350	326
40.0	320	299	321	297	301	307	327	292	321	296	276	315	300	313	313	289
39.0[a]	294	273	295	271	275	281	301	266	295	270	250	289	274	287	287	263
38.0	285	264	286	262	266	272	292	257	286	261	241	280	265	278	278	254
37.0	272	251	273	249	253	259	279	244	273	248	228	267	252	265	265	241
36.5	264	243	265	241	245	251	271	236	265	240	220	259	244	257	257	233
36.0	255	234	256	232	236	242	262	227	256	231	211	250	235	248	248	224
35.0	229	208	230	206	210	216	236	201	230	205	185	224	209	222	222	198
34.0	193	172	194	170	174	180	200	165	194	169	149	188	173	186	186	162
33.0[a]	167	146	168	144	148	154	174	139	168	143	123	162	147	160	160	136
Bottom of tube	158	137	159	135	139	145	165	130	159	134	114	153	138	151	151	127

a. These positions were most often used in the experiment.

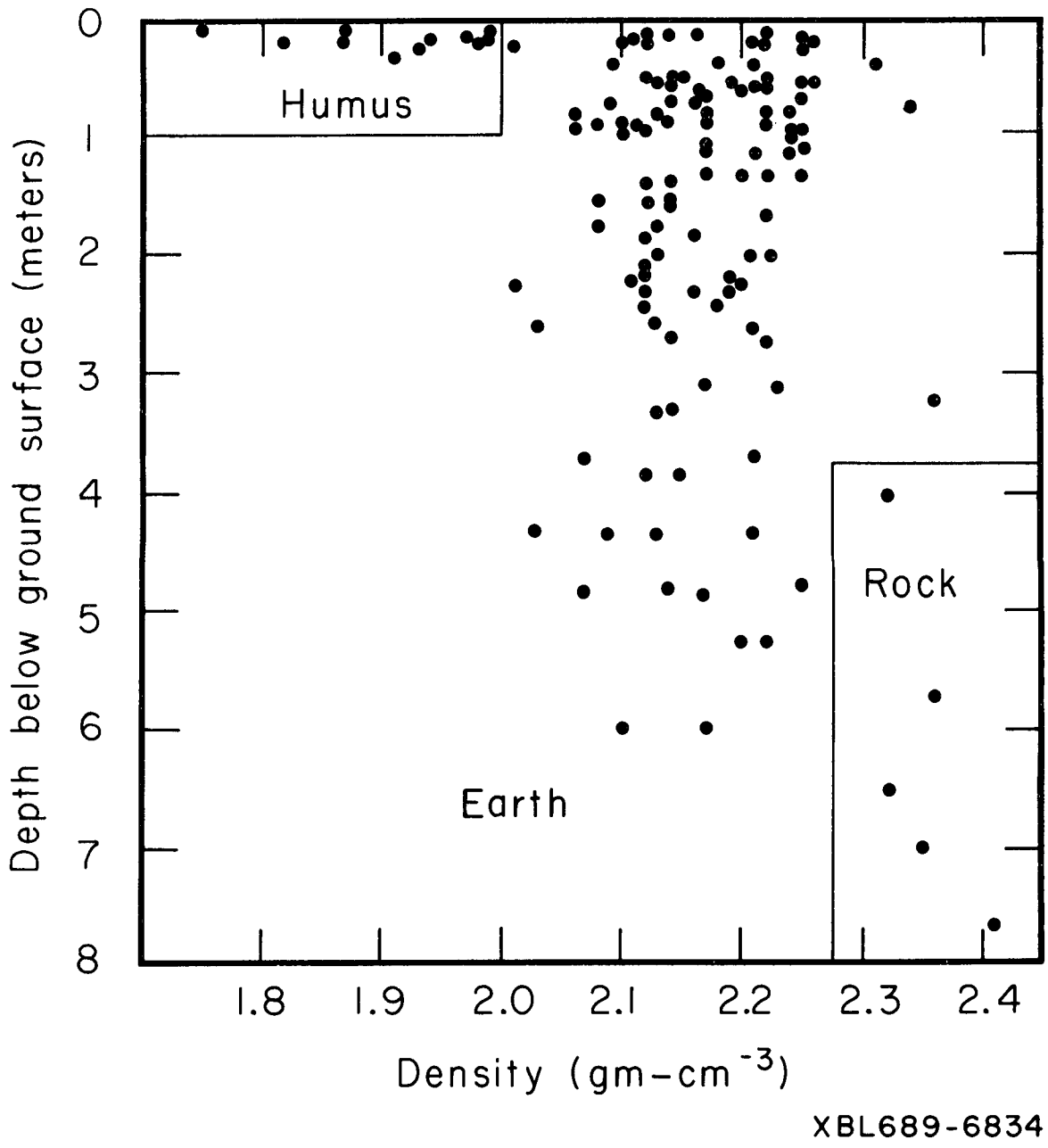

Fig. II-5. Plot showing correlation of earth density vs depth.

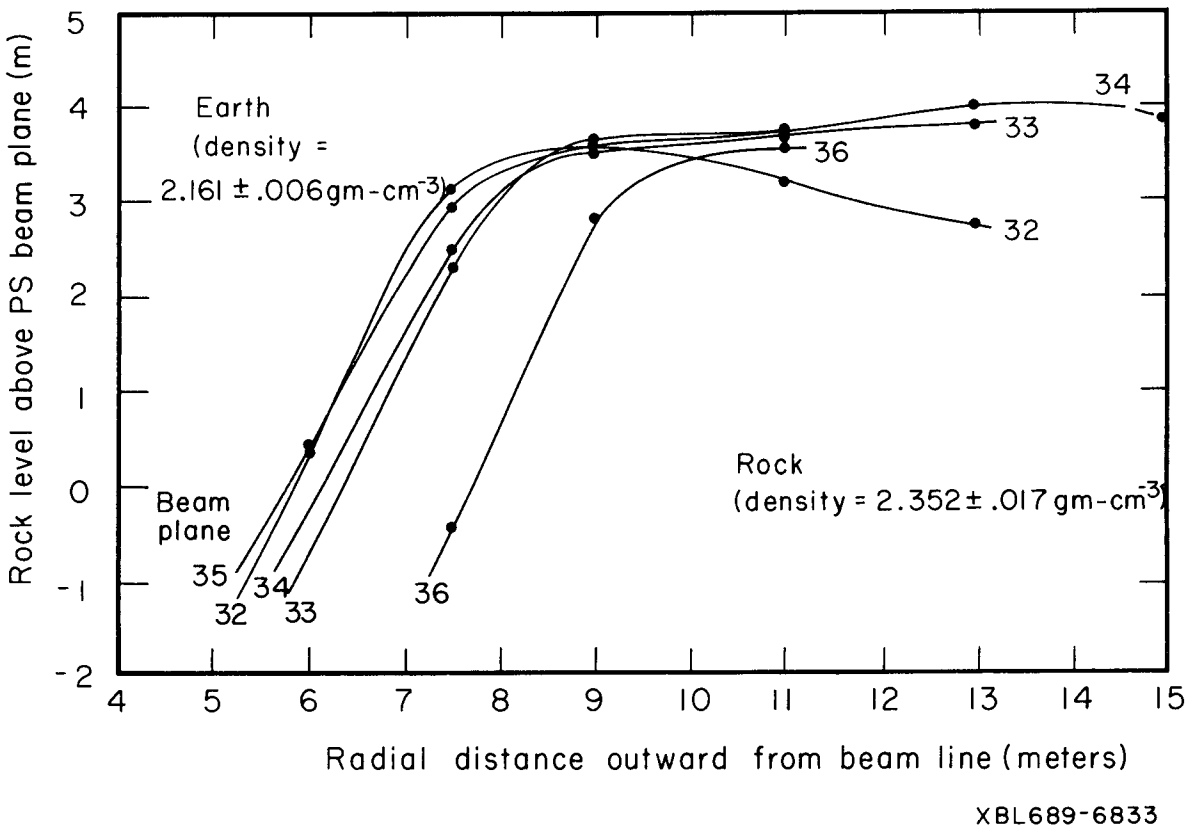

Fig. II-6. Rock profiles in the target 32 region.

Sixteen detector holes were drilled vertically over the beam line on the arc extending from straight section 24 to straight section 43 to a depth of about 3 m, limited by the depth at which gravel was encountered by the drill operators. These holes are referred to as "orbital" holes. Sample holders, consisting of a cylindrical steel frame holding activation detectors spaced by steel cans containing earth, were lowered into these orbital holes by means of the tripod lifting rigs shown in Figs. II-3 and II-8.

E. Target and Beam Clipper

Most straight sections have vacuum pumping manifolds carrying flanges on which target mechanisms can be mounted. Presence of other equipment as mentioned in Section II-B could exclude the use of a particular flange as a target mount, but we were fortunate in being able to find suitable positions for our main target in straight section 32, for our subsidiary target for radial tunnel illumination in straight section 52, and for the beam clipper in straight section 79. The straight-section target geometry is shown in Fig. II-8 and the clipper region in Fig. II-9.

The detail of our target head is shown in Fig. II-10. A semicircular sheet of 100 μ Be foil mounted on a 1 mm-thick frame was flipped into position after the acceleration cycle, so that the diameter of the semicircle coincided with the vertical axis of the elliptic vacuum pipe. The accelerated beam was then swept across the target by a suitable adjustment of the flat-top gradient so as to give a beam pulse of approximately 100 msec.

A monitoring sandwich of 10-30-10 μ aluminum foil was glued to the upstream face of the Be foil. This sandwich could be detached from the Be at the end of a run and the center foil measured for total proton flux during the run. This monitoring is discussed in Chapter V.

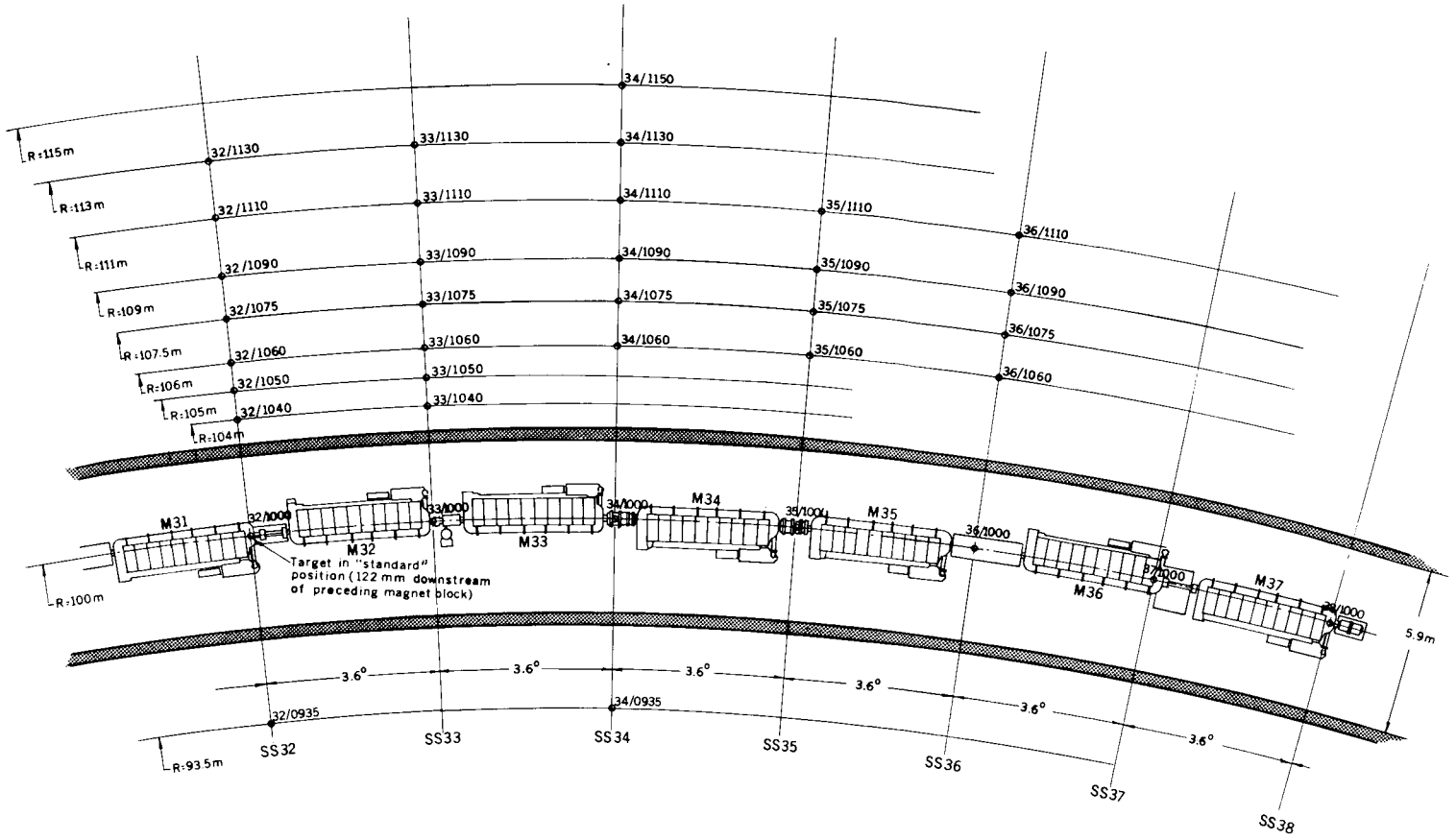

XBL 6712 2119

Fig. II-7. Detailed layout of the hole region.

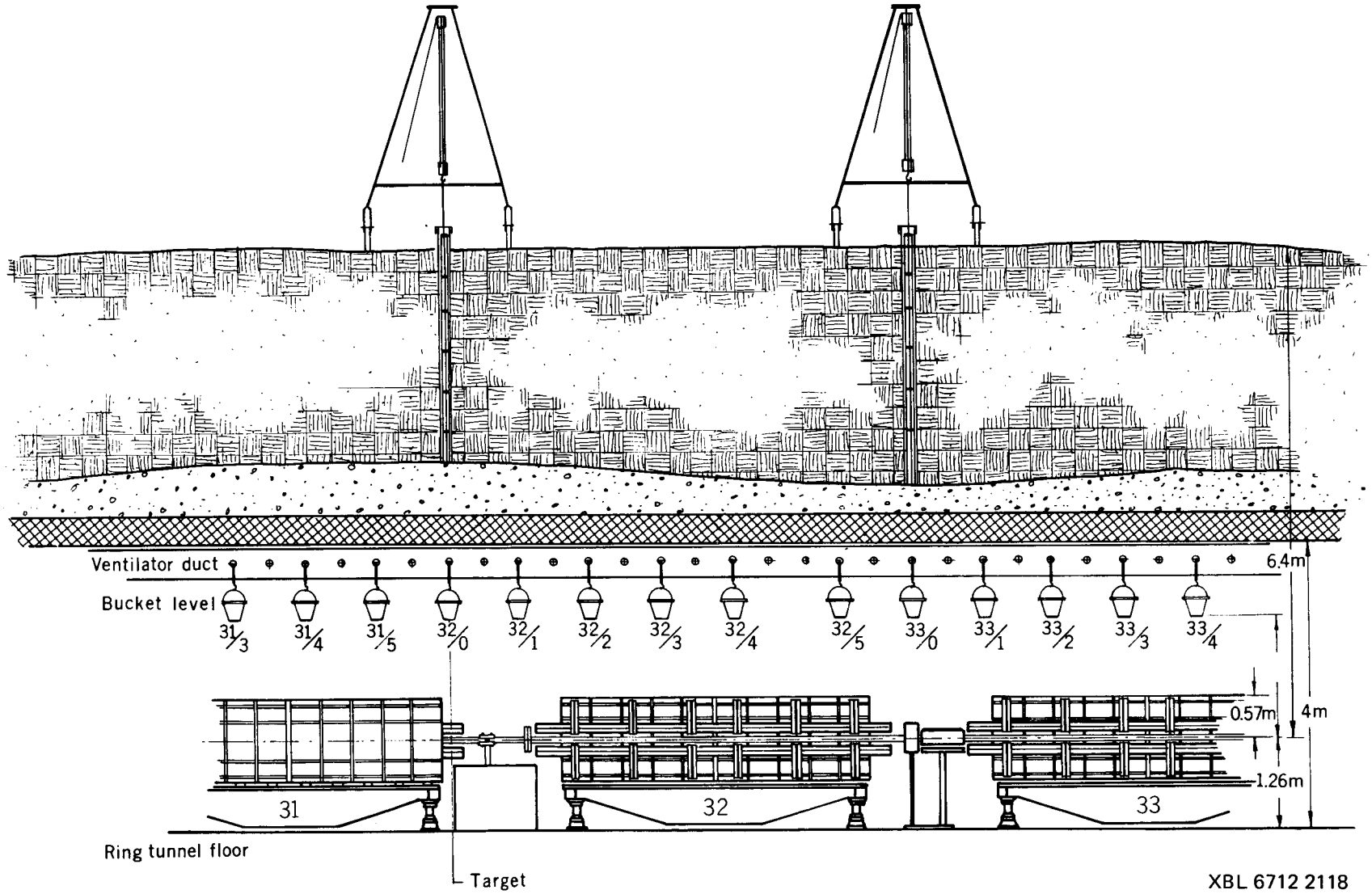

Fig. II-8. Target geometry at straight-section 32.

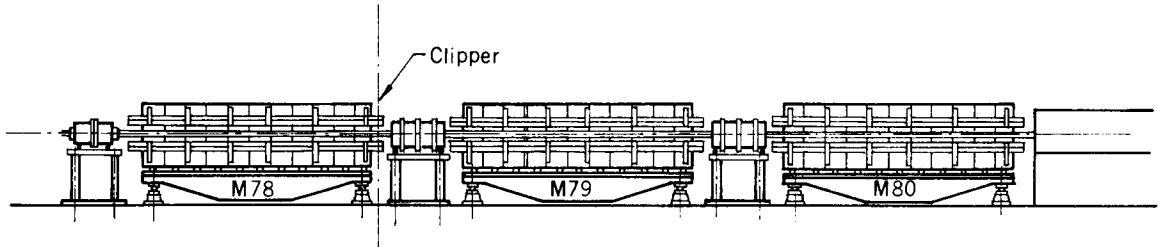

XBL 6712 2121

Fig. II-9. Clipper-region target geometry.

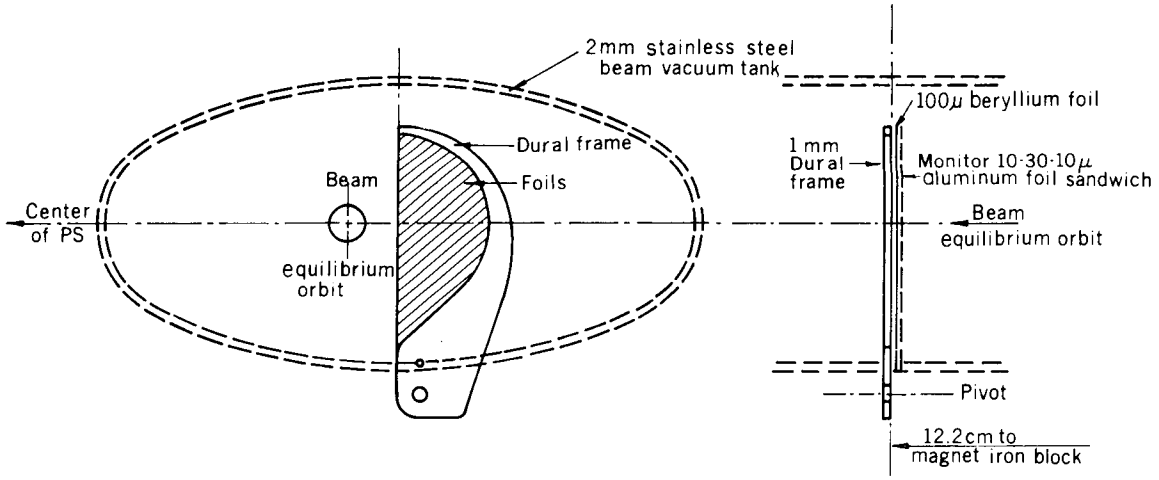

XBL 6712 2122

Fig. II-10. Detail of the target head.

The beam-spot size after acceleration but just before targetting is 8 mm at p = 26.4 GeV/c and 13.2 mm at p = 14.6 GeV/c, and the effective horizontal apertures are 83 mm and 79 mm respectively.

During the sweep across the target, the beam spirals outwards and the beam width increases rapidly due mainly to multiple scattering in the target. To reduce random beam loss around the ring resulting from this, we have used a solid copper beam clipper on a standard target mount in straight section 79. Detailed dimensions of the clipper are shown in Fig. II-11, and systematic investigation of the efficacy of the clipper in reducing background beam loss is reported in Chapter V.

F. Radial Tunnels

A plan view of the eight tunnels radiating from the center of the synchrotron is shown in Fig. I-1. These tunnels intersect the main ring at the ring tunnel enlargements where survey pillers are located. The central building houses the central survey pillar. Four of these eight tunnels have a rectangular cross section as shown in Fig. II-12, and four have an ovate cross section, also shown in Fig. 11-12. The plan view of the intersection of each type of tunnel with the main-ring tunnel are shown in Fig. II-13. Two of the large

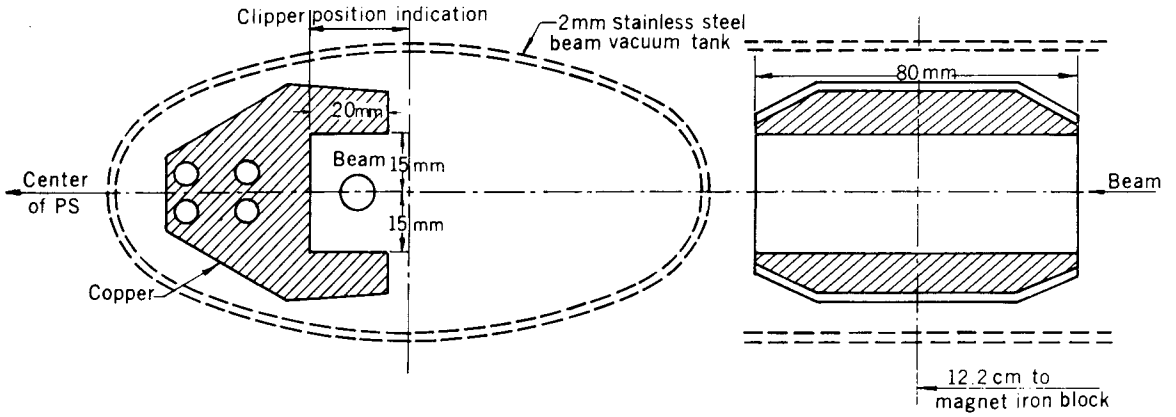

Fig. II-11. Detail of the beam clipper.

tunnels, leading to straight sections 52 and 77, and one of the small tunnels, leading to straight section 89, were used for tunnel attenuation measurements (see Chapter X1).

G. Monitoring

A capacitive pickup was used to monitor the total number of accelerated protons in the internal beam during each beam pulse. The integrated number of protons per minute was printed out on an 8-channel column printer along with the integrated total during the run. This was the principal beam monitor.

In addition, Cerenkov counters placed near the target and the beam clipper were used to monitor the relative reduction in target strength due to the insertion of the beam clipper in the beam. In an attempt to preserve some consistency in the beam-loss pattern, the radial position of the beam clipper was adjusted from time to time so that the target interactions were reduced to about 90% of the no-clipper rate. Numbers proportional to the integrated Cerenkov-counter output per unit time and the total Cerenkov output for the run were printed on the same 8-channel recorder for both the target and beam-clipper counters.

The absolute number of protons interacting in the target was measured for three of our eight runs by the CERN Nuclear Chemistry Group from the radioactivity of the aluminum foil glued directly to the Be target.

Reference

ForR 67. R. D. Fortune, CERN-LRL-RHEL Shielding Experiment. Transverse Shielding Thickness for Each Detector Position, Deduced from Measurement of Density and Profile of the P.S. Earth Shield, CERN report ISR 300/GS/67-4, January 19, 1967.

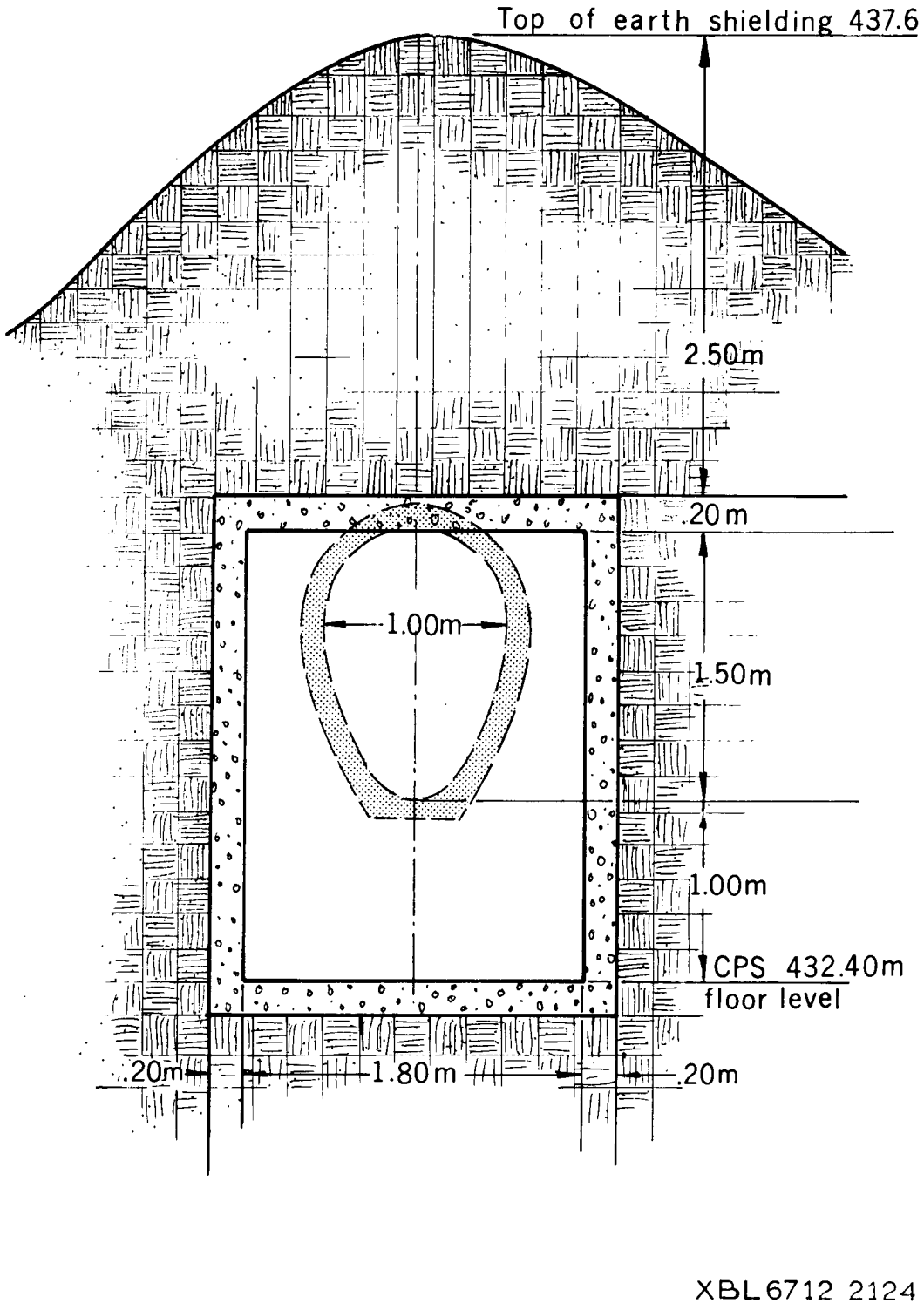

Fig. II-12. Comparison of the rectangular and ovate cross sections of the tunnels.

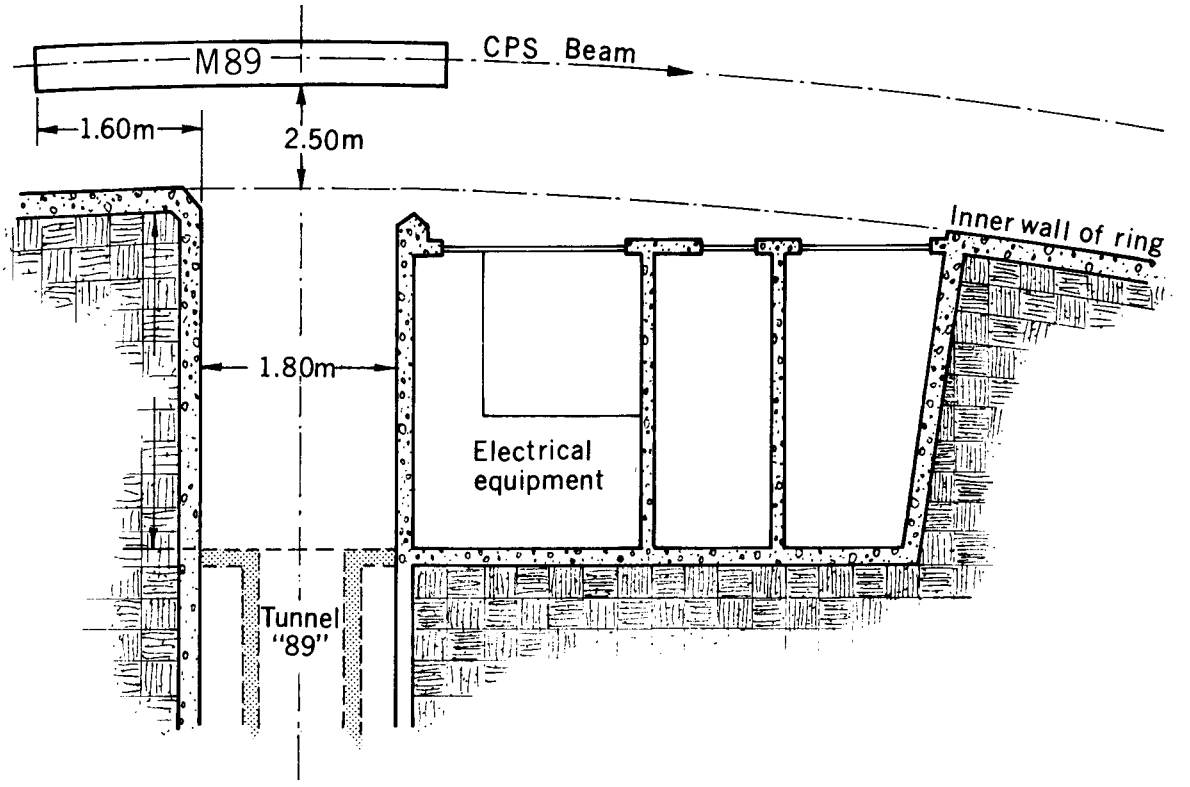

Fig. II-13. Plan view of the intersection of each type of tunnel with the main-ring tunnel.

III. EXPERIMENTAL TECHNIQUES

A. Introduction

Activation detectors, proportional counters, emulsions, thermoluminescent dosimeters, and an air ionization chamber were used to study the composition, intensity, and energy spectrum of the radiation field, and attenuation in the earth shield. Target angular-distribution studies were also undertaken with activation detectors, as were studies of tunnel transmission, and concrete and steel activation.

B. Detection Systems

Most measurements were made with activation detectors. Some detector systems and methods of utilization are relatively new and have been developed specifically to study radiation fields near high-energy accelerators.[MCaJ 67a] Great emphasis has been placed on the achievement of high sensitivity, because some measurements are made with many feet of shielding between the source of the radiation and the detector. To achieve the necessary sensitivity, the detector mass was sometimes rather large, for example 2700-g plastic scintillators and 6600-g aluminum detectors. Corresponding emphasis has been placed both on optimizing the energy interval for counting, and on considerations of background reduction and stabilization. Activation techniques provide an essentially nondirectional response and allow a large number of simultaneous measurements over a wide dynamic range of flux intensity. Construction of detailed spectral information from measurements made with a set of activation detectors requires detailed knowledge of the reaction cross sections. However, general spectral features can be inferred without such detailed knowledge; for example, changes in spectral shape can be discerned from changes in relative responses of the several detectors as different locations are studied. Attenuation measurements through the earth shield, assuming a depth-invariant spectrum, are even more easily interpreted. All of these considerations have been applied to data taken during this experimental program.

Gathering large quantities of data simultaneously by exclusive use of electronic counter techniques would be difficult at best. The quantity of electronic equipment necessary and the continuous effort required to assure proper performance precludes such an approach for an experiment of this size. In addition, severe restrictions would be imposed by the directional response of counters, susceptibility of counters to gamma-pileup interference and induced electrical interference, and finite resolving time of counters. Of course, there are also practical problems such as the difficulty involved in handling large numbers of counters, susceptibility of counters, cables, etc. to electrical breakdown when exposed to moisture and when operating in the high-humidity orbit and radial holes. Then too, the very size of most counters presents problems in defining their effective positions in a given hole. Streaming also is enhanced in a hole containing a number of counters.

Advantageous though limited use was made of several prompt detectors. The moderated BF_3 counter, polyethylene-lined proportional counter, thorium and bismuth fission counters, and the ion chamber were all used, although not necessarily simultaneously, under conditions that allowed careful attention to the problems outlined above.

A brief description is given of the major techniques used in this series of experiments. Table III A summarizes some of the important characteristics of each technique; the order and numbering of entries on this table are keyed to the descriptions of detectors that follow in the text.

On Table III A we mention sensitivity values for each detector. As regards activation detectors, these values have a special meaning that requires some clarification here. Each sensitivity value defines a detector response in terms of irradiation to saturation and an immediate counting analysis. If we also specify a long counting time, and take cognizance of appropriate background count rates, simple calculations show that several of the activation techniques can accurately measure fluxes considerably lower than 1 n/cm^2-sec. For example, a 2700-g plastic scintillator can measure a flux of 0.2 n/cm^2-sec, and a 6600-g

Table III A. Important characteristics of various detection techniques.

Detector	Reaction	Energy range (MeV)	Detector size	Response to unit flux	Background response
1. gold foils moderated	$^{197}Au(n,\gamma)^{198}Au$	0.02 to 20	2.54-cm-diam, 0.5-g foil in paraffin cylinder	2.1 cpm[b]	10 cpm
gold foils bare	$^{197}Au(n,\gamma)^{198}Au$	thermal	2.54-cm-diam, 0.5-g foil	1.8 cpm[b]	10 cpm
2. sulfur	$^{32}S(n,p)^{32}P$	>3	2.54-cm-diam, 4-g disk	0.049 cpm[a]	10 cpm
3. plastic scintillator	$^{12}C(n,2n)^{11}C$	>20	13 to 2700 g	88 cpm[a] at 85% efficiency 1700-g scint.	165 cpm 1700-g scint.
4. mercury	Hg( ) ^{149}Tb	>600	up to 500 g	0.03 cpm[b]	0.1 cpm
gold foils	^{197}Au( ) ^{149}Tb	>600	2.54-cm-diam 0.5 g	2.7×10^{-6} cpm[b]	0.1 cpm
5. BF_3 proportional counter moderator	$^{10}B(n,\alpha)^{7}Li$	0.02 to 20	400 cc at 20 cm Hg 96% enriched	400 cpm 6-cm-thick moderator	2 to 3 cpm
6. polyethylene-lined prop. counter	proton recoil	0.05 to 20	800-cm^2 PE radiator, Ar-CO_2 filled	1 count = 15 MeV/cm^2 at zero bias	<1 cpm
7. large bismuth fission counter	$^{209}Bi(n,f)$	>50	30-cm-diam parallel plates 60-g Bi	1.05 cpm at zero bias, E_n = 220 MeV	<1 cph
small bismuth fission counter	$^{209}Bi(n,f)$	>50	5-cm-diam parallel plates	0.02 cpm at zero bias	<1 cph
8. thorium fission counter	$^{232}Th(n,f)$	>2	5-cm-diam parallel plates	0.017 cpm at zero bias (PuBe spectrum)	<1 cpm
9.1 gold foil, moderated	$^{197}Au(n,\gamma)^{198}Au$	0.02 to 20	5.08-cm-diam, 2.0-g foil	10.1 cpm[a]	48 cpm NaI (Tl)
gold foil, bare	$^{197}Au(n,\gamma)^{198}Au$	thermal	5.08-cm-diam, 2.0-g foil	13.4 cpm[a]	48 cpm NaI (Tl)

9.2	large indium foil, bare	$^{115}In(n,\gamma)^{116m}In$	thermal	7.6-cm by 15.2-cm foils (four) 46 g total	300 cpm[a] (estimated)	75 cpm NaI (Tl)
9.3	aluminum	$^{27}Al(n,\alpha)^{24}Na$	> 6	16.9 to 6600 g	101 cpm[a] 6600 g E_n = 14 MeV	111 cpm, 16.9 g 118 cpm, 6600 g NaI (Tl)
9.4	aluminum	$^{27}Al(\ )^{22}Na$	> 25	16.9 g	0.21 cpm[a]	67 cpm NaI (Tl)
9.5	plastic scintillator	$^{12}C(\ )^{7}Be$	> 30	2.54-cm diam by 2.54-cm high	0.0114 cpm[a]	59 cpm NaI (Tl)
9.6	Na, Mg, Al, Si, Ca, aggregate	various	various	4.5-cm diam by 2 cm high 10 to 40 g	not measured	13.0 cpm NaI (Tl)
	FeO	various	various	4.5-cm diam by 2 cm high 25 to 30 g	not measured	various NaI (Tl)
	Na_2CO_3	$^{23}Na(n,\gamma)^{24}Na$	thermal	4.5-cm diam by 2 cm high 11 g Na	not measured	13.0 cpm NaI (Tl)
10.	emulsion Ilford	proton recoil	2 to 20	600 μ thick		
	emulsion Ilford	star production	> 20	600 μ thick		
11.	neutron film Kodak Type-B	proton recoil	0.5 to 25	~ 30 μ thick	0.00083 track per normally incident neutron	
12.	mica fission-track plates	fission in Bi, Pb, Au	> 50 in Bi	> 1 cm^2	1.79×10^{-6} tracks per neutron for Bi	
13.	ion chamber	charge collection	> 0.02	3.7 liter air-filled		
14.	LiF TLD-700			22 mg, enriched to 99.99% ^{7}Li		
15.	β-γ film	(See section II 14 b for response characteristics.)				

a. At saturation and zero time.
b. At saturation, zero time, and zero bias.

aluminum sample can measure a flux of 0.02 n/cm^2-sec. In both cases the flux values are close to the minimum measurable fluxes, and require counting times of at least one half-life of the measured isotope.

Since a particular counting system is unavailable for analysis of any other samples during a low-activity determination, it should be clear that such determinations can be made only on a one-at-a-time basis for each type detector; in practice, one cannot determine both the very low fluxes and many intermediate-value fluxes from the same irradiation. Our experimental program could only be accomplished if many points were measured during each accelerator run. Thus, we measured the many points and, for the above-mentioned plastic scintillator and aluminum detectors, rarely were able to measure less than unity flux intensity. Practical sensitivities of the other activation detectors were similarly affected.

1. Moderated Gold-Foil Techniques

The thermal-neutron-capture cross section of gold, the convenient half-life (2.7 d)[LedC 67], and beta-emission of the reaction product Au^{198} make this a useful and sensitive detector of fast neutrons when appropriate moderators are used.[SteL 58] (Reference[LedC 67] has been used throughout this report for values of nuclear decay parameters such as half-life, decay scheme, branching ratio, etc.). For fast-neutron detection, the gold foils are encased in cadmium-clad paraffin cylinders; these moderators are 15-cm-diam right circular cylinders of 15-cm height. Some neutrons that penetrate the cadmium jacket become thermalized near the centrally located foil and are captured by it; the thermal-neutron flux detected by the gold foil is (nearly) directly proportional to the incident fast-neutron flux in the energy range from about 0.02 to 20 MeV.

The beta activity in these 2.54-cm-diam, 0.5-g foils is conveniently measured with a thin-window methane-flow proportional counter. If a 0.50-g foil were irradiated to saturation in unit flux and counted immediately afterwards, we would observe 2.1 c/min at the zero-bias point of the electronic counting system. For typical counter operation, we observe about 90% of this zero-bias count rate, and maintain close check on the operating point through frequent use of the beta-activity from a Cs^{137} source. (See section 9.1 of this chapter for discussion of the gold-foil technique for low-intensity neutron flux measurements.)

2. Sulfur Technique

The S^{32} (n,p) P^{32} reaction is frequently used for the measurement of fast-neutron flux around high-energy particle accelerators. This technique has several advantages:

(a) The resultant P^{32} is a beta emitter and can easily be separated from most of the sulfur by a simple burning technique if necessary.[ReiP 58]

(b) The cross section for the reaction has been thoroughly investigated from 1 to 20 MeV.[LisH 62]

(c) P^{32} half-life is 14.3 d; samples can therefore be recounted when required.

(d) Samples are readily available commercially in disk form and are of low cost. The long half-life of P^{32} does have the disadvantage that the technique is insensitive for short irradiations. At the Rutherford Laboratory the technique is usually limited to the use of convenient 4-g samples (2.54-cm-diam, 0.64-cm-thick). The lowest detectable flux for such samples, determined by a count rate equal to the background of the detection equipment, is 10^3 n/cm^2-sec for a 12-h irradiation, and 10^2 n/cm^2-sec if the sample is irradiated to saturation.

Shaw has described the sulfur technique and calibration used at the Rutherford Laboratory.[ShaK 63] Calibrations using several monoenergetic neutron sources have been performed, and a calibration constant obtained relating sample count rate to neutron flux. For a typical high-energy-accelerator radiation environment, the effective value of the (n,p) reaction cross section is estimated to be 300 mb, with an effective threshold of 3 MeV.[ShaK 63] The count at saturation activity of our disks is given by

$$C_{sat}\ (\text{cpm}) = 0.049\ \phi,$$

where C_{sat} is the saturation count rate of the 4-g sample, and ϕ is the neutron flux in n/cm^2-sec. Counting is usually performed on either an end-window Geiger counter, a thin plastic scintillator, or a gas-flow proportional counter, the choice of counter depending on the activity of the sample.

If one assumes that the measured activity is due entirely to neutrons, the saturated activity is given by

$$C_{sat} = K \int_{E_{min}}^{E_{max}} \phi_n (E)\, \sigma_n (E)\, dE, \qquad (1)$$

where:

K is a constant,
$\phi_n (E)\, dE$ is the differential neutron spectrum,
$\sigma_n (E)$ is the cross section at energy E,
E_{min} is the threshold energy for the reaction, and
E_{max} is the upper energy limit of the spectrum.

The integral of Eq. (1) may be expressed as

$$\bar{\phi}_n (E,E_0)\, \bar{\sigma}_n (E,E_0), \qquad (2)$$

where:

$\bar{\phi}_n (E,E_0)$ is the number of neutrons greater than E_0, and
$\bar{\sigma}_n (E,E_0)$ is an appropriately chosen cross section.

Shaw[ShaK 63] shows that, provided E_0 is chosen greater than E_{min} (the reaction threshold, 2.3 MeV), then a corresponding value of $\bar{\sigma}_n (E,E_0)$ may be selected which gives the value of $\bar{\phi}_n (E,E_0)$ to better than 30% for spectra typically found outside thick accelerator shields. More precise values of (E,E_0) may of course be obtained from spectrum-unfolding programs, such as TELLY.

3. The C^{11} Technique

Carbon-11 is a positron emitter with $E_{max} = 0.98$ MeV and a half-life of 20.34 min. It can be produced from C^{12} by (p,pn), (n,2n), (γ,n) reactions, and by other charged particles. The excitation functions for these reactions have been studied experimentally; most information is available for the (p,pn) reaction. Cumming has summarized the proton data available up to the end of 1962.[CumJ 63] Measurements have been made between threshold (20.6 MeV) and 28 GeV. Beyond threshold the reaction cross section increases rapidly to a peak value of about 92 mb at 35 MeV, then falls to 61 mb at 100 MeV and 49 mb at 142 MeV, finally reaching a fairly constant value around 27 mb at higher energies.

Less information exists for the (n,2n) reaction. The (n,2n) cross section is lower than that for (p,pn) partly because (p,n) exchange collisions can produce C^{11} but (n,p) exchanges cannot. An effective (n,2n) cross section of 22 mb is used.[MCaJ 60]

The production of C^{11} from C^{12} may therefore be used as a practical means of measuring particle fluxes in the accelerator radiation environment with energies greater than about 20 MeV. In typical situations outside shielding, the radiation field is such that the only significant C^{11} activity is produced by neutrons. However, in regions close to the unshielded proton beam, both energetic photons and protons may be present, and careful assessment of the data is necessary.

A convenient technique is to irradiate plastic scintillators in the area to be monitored and then count the sample on top of a vertically mounted photomultiplier employing a mineral-oil optical coupling.[MCaJ 60, ShaK 62] The scintillator sizes varied from 2.54 cm long by 2.54 cm diam to 20.3 cm long by 12.7 cm diam. The entire positron energy is absorbed in the scintillator, and in the larger scintillators a portion of the annihilation gamma-ray energy is contained. Special care in selection of the energy interval for counting, the counting room location, and shielding materials around the photomultiplier repay with high sensitivity and reproducibility. Typically, at CERN the background rate observed in our 12.7-cm-long

by 12.7-cm-diam scintillators was 165 cpm (system 1 with 85% counting efficiency), equivalent to the irradiation to saturation in a flux of ~ 2 n/cm^2-sec^{-1}. The flux estimate is made from an absolute determination of the C^{11} produced within the scintillator, and is based on an assumed 22-mb reaction cross section.

All scintillators were contained in heavy-duty plastic bags during irradiation to guard against accidental radioactive contamination. Great care was taken to insure that radon-daughter contamination did not occur during any operations associated with the counting analysis. Note that a one-hour exposure to the radon daughter concentration in the ambient air of our counting room could easily *double* the apparent background (BKG) in an unirradiated scintillator. Such considerations are obviously important for obtaining valid data from low-activity scintillators.

4. Mercury and Gold-Foil (Tb^{149}) Techniques

In addition to the activation techniques with fairly low-energy thresholds ($E < 50$ MeV), a method has been developed for detection (in mercury) of small fluxes of nuclear particles of energy greater than about 600 MeV. The excitation function for Tb^{149} production from gold has been determined between threshold and 3 GeV by Duffield and Friedlander[DufR 54] and up to 6.2 GeV by Winsberg,[WinL 59] but with significant differences between these two sets of measurements. Franz and Friedlander[FraE 66] have more recently covered the entire region between 600 MeV and 30 GeV, and Brunnix[BruE 65] has reported measurements between 7 and 27 GeV. We adopt the more recent data, and consider that the excitation function for this reaction is well known up to proton energies of about 30 GeV.

Although the reaction on gold is of great use for monitoring intense proton beams, the technique using small gold foils is not adequately sensitive for the relatively small high-energy particle fluxes found in the general environment around proton accelerators. The range of Tb^{149} alpha particles in gold is only about 11 mg/cm^2, so greater sensitivity cannot be achieved by the use of greater thicknesses of material. The use of large areas of thin gold foil presents difficult geometry problems during both irradiation and counting, and still lacks sensitivity for any reasonable-size detector. Some technique for extracting the Tb^{149} produced in large quantities of target material is required so that the detection efficiency can be increased.[MCaJ 67]

It is observed that Tb^{149} produced in mercury diffuses slowly to the top surface of the liquid. Unfortunately the time taken for an appreciable fraction of this Tb^{149} to appear at the surface by natural gravity separation is extremely long compared with the 4.1-h half-life of the nuclide. The separation process may be enhanced by centrifuging the Hg samples; for example, it is found that a reproducible fraction ($\sim 60\%$) of the Tb^{149} produced within the entire volume of a 481-g mercury sample can be extracted from the liquid surface during a 1-h centrifuging time at approximately 1700 g force. Ordinary pressure-sensitive cellulose acetate adhesive tape may be used to remove the separated Tb^{149} and provides an adequate backing for a very thin alpha source, which may be counted on a methane gas-flow proportional counter.

The mercury detector was calibrated by irradiating a 481-g cylindrical sample (2.86-cm-diam and about 6.3-cm-long) of mercury in the 6.2-GeV external proton beam of the Bevatron. A thin gold foil was used to monitor the proton intensity, and thick gold foils placed in front and behind the sample determined beam loss through the mercury sample.

The amount of Tb^{149} activity produced in a gram of mercury is found to be approximately the same as that produced in a gram of gold, but because at least 50% of the Tb^{149} can easily be extracted from large volumes of mercury, use of the mercury-centrifuge system offers an enormous increase in sensitivity. In this experiment the increase (obtained by a 1-h centrifuging of 480-g samples) amounted to a factor of more than 10^4, compared to a 5 cm^2 area gold foil that was infinitely thick with respect to the range of Tb^{149} alphas.

A sensitivity of about 0.03 c/min per proton/cm^2 sec can be obtained with 500-g mercury samples, although an additional correction may be necessary for mercury self-shielding during the irradiation. A tape sample containing 60% of the Tb^{149} produced in a 500-g capsule of mercury that had been irradiated to saturation in a flux of about 3 protons/cm^2-sec would yield an initial counting rate of 0.1 c/min. This corresponds to the easily attainable background of 0.1 c/min for our methane-flow counter. As with the other activation detectors, we were unable to achieve this low-flux determination capability during the experimental program. The time-consuming sample preparation (centrifuging), and the very low count rates obtained from low-flux irradiations are particularly important problems here that prevent attainment of the indicated performance.

We assume that neutrons and protons are equally effective in producing Tb^{149} from mercury, so this method is directly applicable to neutron detection.

5. Moderated BF_3 Proportional Counter

BF_3 proportional counters are widely used as neutron detectors. The counter used in this experiment is 5.1 cm diam by 22.9 cm active length. It is filled with 96% enriched B^{10} to 20 cm Hg. A 6.4-cm-thick paraffin moderator surrounded by cadmium is used as the jacket for the BF_3 counter and provides a reasonably flat response to 0.02-to 20-MeV neutrons.

6. Polyethylene-Lined Proportional Counter

The counting rate of this detector has been shown to be proportional to the neutron-energy flux density.[MoyB 52] It is filled to a pressure of 1 atmosphere with a mixture of 96% Ar-4% CO_2 and lined with 0.32 cm of polyethylene. Calibration is obtained by extrapolation of the discriminator curve to the count rate at zero discriminator bias; the discriminator curve is derived from counting the proton recoil events under conditions of constant amplifier gain and high voltage. For the particular size counter used here the zero-bias intercept is found, both by calculation and by experiment, to be 15 MeV/cm^2 per count over the 0.1-to 20-MeV range of incident neutron energy. If simultaneous measurements are made with a flux detector, the average neutron energy can be obtained by dividing the energy in MeV/cm^2 by the flux in n/cm^2.

7. Bismuth Fission Counters

Bismuth fission (effective threshold about 50 MeV) is detected in an ion chamber with bismuth-coated parallel plates.[MCaJ 66, KelE 48, WieC 49, HesW 57, BeaJ 59] Operation of the chambers in the pulse mode discriminates strongly against gamma rays and low-energy reactions, since the ratio of fission pulse height to pulse height of other particles is on the order of their energy ratio. The chambers are equally sensitive to neutrons and protons above 50 MeV and to pions, but relatively few of these charged particles are present outside of a thick radiation shield. However, an anticoincidence blanket can be used to subtract their effect. The Bi fission cross section for protons is well known from threshold to about 30 GeV.[DeCH 63]

The large Bi fission counter has forty-two 30-cm-diam aluminum plates coated with Bi^{209} to a depth of 1 mg/cm^2. The sensitivity is about 1 cpm-n^{-1}-cm^{-2}-sec^{-1}. A smaller version of this chamber has a sensitivity of 2×10^{-2} cpm-n^{-1}-cm^{-2}-sec^{-1}.

8. Thorium Fission Counter

The thorium fission counter, similar in construction to the small bismuth fission counter, is a pulsed parallel-plate ion chamber which has a sensitivity of about 1 count per 3.5×10^3 n/cm^2 from a PuBe neutron-source spectrum; the threshold energy for fission is about 2 MeV. The counter is most frequently used as a monitor to indicate changes in the intensity of the radiation field during exposure of passive activation detectors, and was so used during this experiment.

9. Gamma-Ray Spectrometric Technique

All gamma-ray counting was performed with a NaI (Tl) scintillation crystal gamma-ray spectrometer. The detector for this system was a 20.3-cm-diam by 10.2-cm-thick NaI(Tl) crystal, and data were acquired with a Victoreen 1600-channel (SCIPP-1600) pulse-height analyzer (PHA). We have given particular attention to providing a system with high sensitivity, low background (BKG), and high stability.

High sensitivity is an intrinsic property of a large NaI (Tl) crystal; however, the BKG response may be correspondingly high. By careful choice of detector components and shield materials, we have been able to reduce the BKG to a very low level, and thereby can take full advantage of the high intrinsic sensitivity even when sample activities are extremely weak.

The crystal has a stainless steel case and a 17.8-cm-diam optical window of fused quartz. A single 12.7-cm-diam EMI type 9530-Q phototube (faceplate and part of the envelope are fused quartz) is optically coupled to the window with a Dow-Corning silicone grease. The phototube is without a base, and the mating socket is made of Teflon. The crystal, phototube, and voltage divider were incorporated into a single unit at LRL.

The detector assembly is mounted in a vertical position inside a 10.2-cm-thick Pb brick shield. The crystal faces upward, and the entire assembly is supported on a low-mass styrofoam structure. Samples are usually placed on a thin steel plate that rests directly on the crystal case and serves to protect the crystal as well as to provide centering marks for sample placement. Styrofoam spacers are used to provide counting distances other than against the crystal. The preamplifier is located outside the Pb shield; thus, only the

detector assembly and the two connecting cables are inside the shield. The shield interior volume has a 25-cm-square horizontal cross section with about 25 cm of vertical clearance above the crystal for sample placement. The shield opens at the top by means of a rolling door, also 10.2-cm-thick Pb.

Bricks for the inner 5 cm thickness were obtained from the St. Joseph Mine in Missouri, selected because of the known low activity of Pb from this source. The outer 5 cm thickness is also of low-activity Pb obtained from Sala Silver Gruva in Sweden, another recognized source of low-activity Pb.

Background characteristics of this detector-shield combination are shown on Table III B. Here we list the isotopes measured, the selected channel intervals, the spectral features included in these intervals, and the corresponding BKG rates. We observe the gamma-ray energy interval 0.1 to 4 MeV, at energy calibration of ~ 10 keV/channel for 400-channel spectra and ~ 40 keV/channel for 100-channel spectra. On Figs. III-1 and III-2, we show typical spectra of the measured isotopes as observed in our activation elements, along with a BKG spectrum; vertical bars on sample spectra indicate the selected analysis intervals.

Data were acquired on the pulse-height analyzer (PHA) in the format of either 400-or 100-channel spectra. Digital information in each spectrum was permanently recorded with a Monroe Datalog printer. Counts in a selected energy interval were obtained in two ways. The peak-area integration feature of the PHA allowed us to perform this summation electronically in a few seconds at the end of each data run. A special kind of single-channel pulse-height analyser (SCA) provided a second method to obtain the total. The SCA had digitally selected lower and upper bounds for the window, and operated on channel address information supplied from the PHA. By proper selection of SCA window boundaries, we could match exactly to the selected PHA interval, in order to observe a running summation in this interval throughout PHA analysis time. SCA information was used to determine the length of PHA analysis time to achieve the desired statistical quality of the data. SCA information was also used as a check on PHA data, to minimize operator errors that tend to occur with long hours of counting.

We maintained the correct energy calibration of the spectrometer by frequent checks with a Cs^{137} source. The 0.662-MeV Cs^{137} peak was required to be centered exactly in channel 66 of the 400-channel spectra, or divided equally between channels 16 and 17 of the 100-channel spectra. The Cs^{137} source was also used to check both energy resolution and absolute detection efficiency of the spectrometer; neither parameter was observed to change during the experimental program.

a. Moderated and Unmoderated Gold-Foil Techniques. Large increases in sensitivity are possible with the gold-foil techniques if both foil diameter and thickness are increased, and the foils are then counted with the NaI (Tl) scintillation crystal gamma-ray spectrometer. For example, a single 5.08-cm-diam foil weighing 2.0 g gives 10.1 c/min if exposed to saturation in unit flux in a moderator and counted immediately afterwards; five such foils exposed together and counted together give 31.3 c/min. We used the same 20.3-cm-diam by 10.2-cm-thick NaI (Tl) crystal spectrometer system as is used for all other gamma-ray activation analysis, and accepted only those channels in the spectrum falling within the 0.412-MeV peak that accompanies Au^{198} decay. The low spectrometer background—48.0 c/min in this channel-37 to-46 interval of the 400-channel spectrum—permits us to take practical advantage of the absolute sensitivity increase indicated here. All low-intensity fluxes were determined from exposures of moderated 5.08-cm-diam Au foils.

Bare Au foils were used to determine slow-neutron fluxes. The same 2.54- and 5.09-cm-diam foils were used and were counted as described above. Sensitivity values for foil count rates resulting from saturation exposure to unit flux are:

Foil diameter (cm)	Sensitivity (c/min)
2.54	3.5
5.08	13.4

b. Indium Foil Technique. Large-area indium foils were used to extend radial hole measurements to the greatest possible shield thickness. These foils were intended to give only relative values for slow-neutron fluxes existing in radial holes, to show the slope of the attenuation profile at such shield positions. Therefore, an absolute calibration was not attempted. Each detector was in the form of a cylindrical shell 30.5 cm in circumference and 7.6 cm high with a 0.025-cm wall thickness. The detector was constructed from four individual foils, each of which measured 7.7 by 15 by 0.0127 cm and weighed 11.5 g.

Table III B. Characteristics of scintillation spectrometer.

Isotope	Channel interval	Channels in spectrum	Spectral features included	BKG at CERN (cpm)
Be^{7}	43-54	400	0.477-MeV peak	59.0
Na^{22}	45-59	400	0.511-MeV peak	54.4
	160-190	400	Sum peak (0.511 plus 1.27 MeV)	12.6
Na^{24}	30-75	100	1.37-MeV peak through 2.75-MeV peak	111
	63-75	100	2.75-MeV peak	13.0
In^{116m}	100-144	400	1.10-MeV peak through 1.29-MeV peak	75.0
Au^{198}	37-46	400	0.412-MeV peak	48.0

Decay of the induced In^{116m} activity was measured with the low-background NaI (Tl) scintillation crystal gamma-ray spectrometer. We accept the interval from channel 100 through 144 of the 400-channel spectrum as valid In^{116m} decay information. This interval includes two strong gamma-ray peaks at energies of 1.09 and 1.29 MeV and provides the most favorable signal-to-background ratio in any portion of the spectrum for our spectrometer system. Background in the selected interval is 75 c/min, compared with an estimated sensitivity of 300 to 400 c/min per four-foil detector as a result of irradiation to saturation for the 54-min activity in unit flux. Great care was taken to insure that radon-daughter contamination did not affect counting results from these large-surface-area detectors. Using this technique, we could obtain relative data to include the 1090-series radial holes. Typically, detectors were exposed simultaneously in three successive radial holes at a single azimuthal position, thus providing a three-point attenuation profile. Such profiles could be joined to data taken at shallower depths through use of suitable normalizing positions.

c. Aluminum Technique. Al^{27} (n,α) Na^{24}. The reaction Al^{27} (n,α) Na^{24} is often used as a threshold detector to measure neutrons with energies greater than about 6.5 MeV.[SmiA 65] We have developed this aluminum detector as a low-flux measuring technique, and employ it as one of the primary measurement techniques in this experiment. The reaction product, Na^{24}, decays with a 15.0-h half life and emits two gamma rays in cascade during this process. The high energies of the gamma rays, 1.37 and 2.75 MeV, and the relative transparency of aluminum to these radiations, makes possible the use of detectors containing large amounts of material. The largest samples used here contain 6600 g.

Analysis of Na^{24} activity is performed with the NaI (Tl) scintillation crystal gamma-ray spectrometer, which uses a 20.3-cm-diam by 10.2-cm-thick crystal as the gamma-ray detector. Events in the gamma-ray energy interval 0 through 4 MeV are recorded as a 100-channel spectrum in the pulse-height analyzer, and the interval including channels 30 through 75 is selected to measure the Na^{24} activity. This interval includes the two gamma-ray peaks and the intervening continuum; it provides the optimum signal-to-background ratio in our spectrometer system because of the very low background we have been able to achieve. It also provides the high sensitivity necessary for successful low-flux measurement. No long-lived competing activities interfered with these measurements at the relatively short decay times allowed before sample analysis, nor did short-lived activities interfere in Na^{24} assay.

The aluminum detector was calibrated using a 14-MeV (d,t) neutron source of known yield. We express *measured* aluminum fluxes in terms of this 14-MeV calibration, unless explicitly noted to the contrary. Thus, an aluminum-measured flux quoted to be 100 n-cm^{-2}-sec^{-1} is just the flux of 14-MeV neutrons that would have produced the activity observed in the detector. The flux to which the detector was actually exposed is usually different from this quoted value because of neutron-energy spectral differences and the variation of reaction cross section with neutron energy. Such effects are discussed in detail in Chapter IX, "Flux-to-Dose Conversion"; we will simply state here that aluminum-detector data satisfy the requirement of this experiment, and are the main source of attenuation-profile information.

Sample weights varied from 16.9 to 6600 g, in order to span the dynamic range of flux intensities encountered. Spectrometer background from channels 30 through 75 was 111 c/min in the absence of any

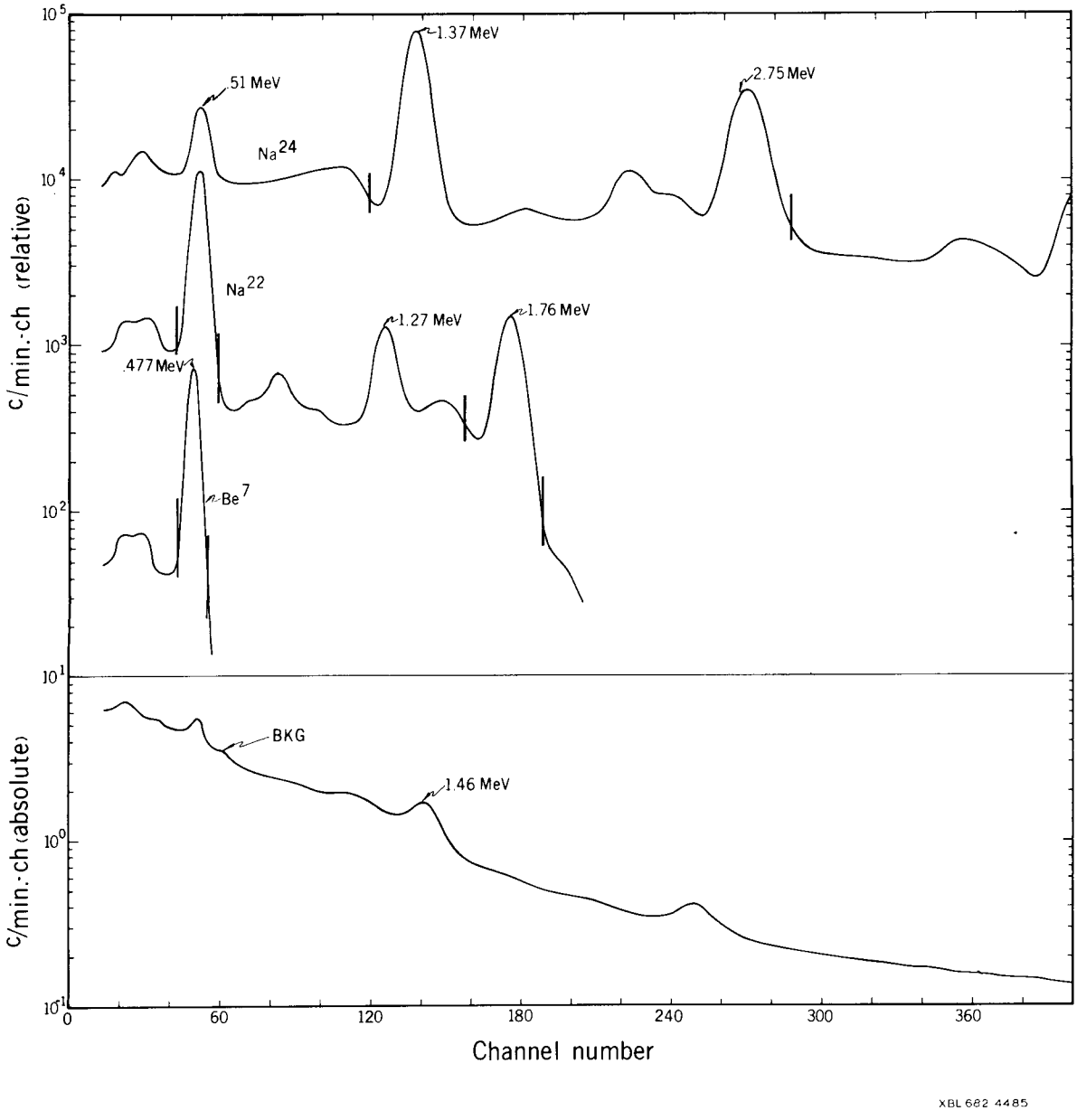

Fig. III-1. Typical spectral shapes recorded by our scintillation spectrometer from gamma emitters of interest.

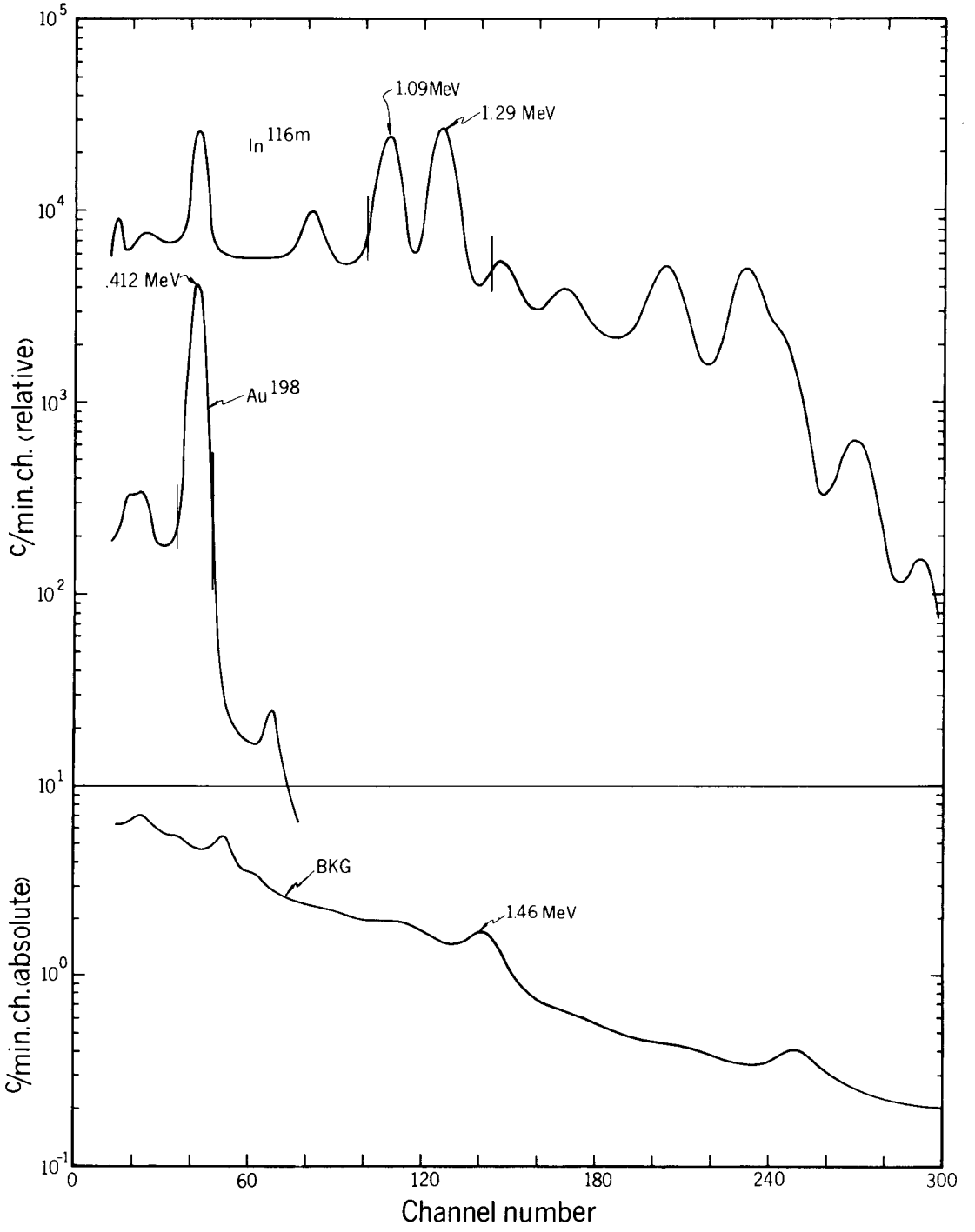

Fig. III-2. Typical spectral shapes recorded by our scintillation spectrometer from gamma emitters of interest.

sample, and increased to 118 c/min when an unirradiated 6600-g sample was counted. The increase was found to be caused by slight thorium contamination in our aluminum, and was taken into account during data analysis. In comparison, the count rate observed from a 6600-g sample exposed to saturation in unit flux at 14-MeV neutron energy and counted immediately afterwards is 101 c/min. Measurement of unit flux is not difficult in such circumstances.

Most samples were composed of pea-size pellets, chosen for the ease with which both sample shape and weight could be changed; some solid metal disks were also used. All samples were contained in plastic bags or boxes during irradiation to guard against accidental radioactive contamination. In addition, great care was taken to insure that radon-daughter contamination did not occur during any operations associated with counting. Both these considerations are important for obtaining valid data from low-activity samples.

i. Detector calibration. In our initial work we used 10.2-cm-diam by 2.54-cm-thick aluminum disks counted with a 10.2-cm-diam by 5.1-cm-thick NaI (Tl) scintillation crystal gamma-ray spectrometer. This disk-crystal system was calibrated with a known flux of 14-MeV neutrons generated by the (d,t) reaction. During calibration, yield of the neutron generator was measured by an associated particle detector whose output information was presented on a multichannel PHA, to verify that all accepted counter pulses were associated with the (d,t) reaction. The absolute yield of 14-MeV neutrons from the target was estimated to be known to an accuracy of ±2% absolute.[RubL 62]

Aluminum-detector calibrations are always expressed in the following terms: A detector is assumed to be irradiated to saturation (with respect to Na^{24} activity), in unit flux at 14-MeV neutron energy. The count rate from the irradiated detector is measured in the selected Na^{24} interval of the gamma-ray spectrum. The rate is corrected for decay during the time between exposure end and analysis start; this decay-corrected count rate then becomes the calibration constant for that particular disk-crystal system. For the combination just described, the calibration constant was found to be 3.16 c/min, and represents the counting rate observed in the disk immediately after irradiation to saturation in unit flux at 14-MeV neutron energy. The gamma-ray spectral interval appropriate to this calibration constant includes only the area under the 1.37-MeV peak of the Na^{24} spectrum.

A number of different size disks and different size NaI (Tl) crystals have been used since the 1962 calibration; in addition, the interval of the gamma-ray spectrum accepted as a measure of Na^{24} activity has also varied. In all cases, generation of new calibration constants has been based on the 1962 calibration in combination with appropriate sets of relative measurements. For example, if we wish to obtain the calibration constant for a different size crystal and a 10.2-cm-diam by 2.54-cm-thick disk, this disk would be irradiated to convenient activity and then analyzed with both the 10.2-cm-diam by 5.1-cm-thick crystal and the crystal in question. To calibrate a different size aluminum disk, we would expose both the 10.2-cm-diam by 2.54-cm-thick disk and the disk in question to simultaneous equal irradiations, and then analyze their Na^{24} activities with the same crystal. Such procedures have been used to generate calibration constants for a wide variety of disk sizes, ranging from a 5.1-cm-diam by 0.32-cm-thick disk (weight 16.9 g), to a five-member array of 20.3-cm-diam by 2.54-cm-thick disks (total weight 11 250 g). Among the NaI (Tl) crystals so calibrated, the most frequently used sizes are 10.2 cm diam by 5.1 cm thick, and 20.2 cm diam by 10.2 cm thick. The accepted gamma-ray spectral interval has included only the 1.37-MeV peak, only the 2.75-MeV peak, both peaks, and both peaks plus the intervening continuum. Selection of the counting interval may be determined by any of a number of factors, including desired counting statistics, background count rate, number of samples to be counted, and interfering activities. In all relative measurements, the errors due to counting statistics were kept well below ±1%, so that these errors would not contribute significantly to the total errors associated with derived calibration constants.

Most aluminum detectors used in the experiment consisted of carefully weighed quantities of pea-sized pellets; this form was chosen for the ease with which both sample shape and size could be changed to meet the wide latitude of conditions encountered at various measurement sites. A number of solid disks were also used. In Table III C we list all sample sizes used, along with their calibration constants, appropriate spectrometer BKG rates, and typical regions of use. Some loss of sensitivity resulted from the use of pellets instead of solid disks; for example, Table III C shows that a 2250-g disk has a somewhat higher calibration constant than a 2200-g pellet sample of the same diameter.

Table III C. Aluminum threshold detectors: CERN experiment sample parameters.

Pellet samples	Calibration constant (c/min)	BKG (c/min)	Typical exposure sites with target 32
100 g	4.4	111	Roof buckets
500 g	16.4	112	Orbit holes 31-36
1100 g	32.8	113	Orbit holes 24-30, 37-43
2200 g	57.2	115	Orbit holes 24-30, 34-43 Radial holes > 1060
3300 g	74.2	116	Surface 28-37
6600 g	101	118	Radial holes 1075, 1090
Disk samples			
5.1 cm diam by 0.32 cm thick 16.9 g	0.842	111	Target distribution studies near magnets 32 and 33
10.2 cm diam by 2.54 cm thick 555 g	21.2	112	Orbit holes; streaming studies
20.3 cm diam by 2.54 cm thick 2250 g	65.0	115	Surface 28-37

ii. Interfering activities. Among the nuclides that can be produced from neutron bombardment of Al^{27}, those listed on Table III D might be expected to interfere with certain methods of Na^{24} assay by gamma-ray analysis. The last column of Table III D explains briefly how we avoid any interference from these activities. Of the listed isotopes, Na^{22} is potentially the most troublesome; a several-week irradiation would produce enough Na^{22} activity to interfere with our normal Na^{24}-assay procedure much sooner than the 200-hour decay-time limit quoted in Table III D. In such cases, Na^{24} assay could be done by recognizing only the 2.75-MeV peak to be valid Na^{24} data. However, all irradiations of aluminum detectors during the experiment were sufficiently brief and all decay times short enough so this special analysis method was not required for any aluminum detector; the full interval could be used in all cases.

Interfering activities can also be produced from small quantities of other elements present in aluminum samples. All pellet samples and the 5.1-cm-diam by 0.32-cm-thick disks were of type 1100 aluminum, a material that is typically 99% aluminum by weight. The 10.2-cm-diam and 20.3-cm-diam disks were of type 6061 aluminum, the standard machinable alloy in use at LRL Berkeley; it is typically about 98% aluminum by weight. Compositions of these two materials are given in Table III E.

A variety of interfering activities might be expected from the minor components listed in Table III E; however, the low abundance of the elements eliminates from consideration all possible isotopes except those resulting from slow-neutron capture, *i.e.*, reactions with high cross sections. In fact, the only isotope ever observed to cause interference is Mn^{56}, the result of slow neutron capture in the fractional percentage of manganese present in both materials. This problem has been encountered in both materials, but only at the Berkeley 88-Inch Cyclotron, in situations where the spectrum is particularly rich in slow neutrons. No problem of Mn^{56} interference was observed during the CERN 1966 experiment, although a close watch was kept throughout all Na^{24} spectral determinations.

d. Aluminum Technique: $Al^{27} \rightarrow Na^{22}$. The transformation $Al^{27} \rightarrow Na^{22}$ can also be used as a threshold detector for neutrons. The threshold is in the vicinity of 30 MeV for the neutron-induced reaction; for the purpose of flux computation, the reaction cross section is here taken to be approximately constant at 10 mb beyond about 60 MeV.

The Na^{22} content of an aluminum sample can thus provide information related primarily to the high-energy portion of the neutron spectral distribution. When these data are combined with Al^{27} (n,α) Na^{24}

Table III D. Gamma emitters produced in aluminum: interference with Na^{24} assay.

Nuclide	Half-life	Gamma-ray energy and abundance	Methods of eliminating interference with Na^{24} assay
Be^{7}	53.6 day	0.477 (10%)	Energy below selected interval.
C^{11}	20.4 min	β^+, 0.511 (200%)	Energy below selected interval.
F^{18}	110 min	β^+, 0.511 (194%)	Energy below selected interval.
Na^{22}	2.62 yr	β^+, 0.511 (180%) 1.275 (100%)	Energy below selected interval. Assay before > 200-hr decay of Na^{24}.
Mg^{27}	9.46 min	0.84 (70%) 1.013 (30%)	Energy below selected interval. Energy below selected interval; noncoincident γ rays; no sum peak.
Al^{26}	7.4×10^5 yr	β^+, 0.511 (170%) 1.12 (4%) 1.81 (100%)	Undetectable from these short irradiations.
Al^{28}	2.31 min	1.780 (100%)	Allow 1-h decay before Na^{24} assay.

Table III E. Chemical compositions of aluminum threshold detector material.

	Disks: type 6061		Pellets: type 1100	
Element	% of total		Element	% of total
Mg	0.80 min	1.20 max		
Si	0.40 min	0.80 max		
Fe		0.7 max	Si and Fe	1.0 max
Cu	0.15 min	0.40 max	Cu	0.20 max
Mn		0.15 max	Mn	0.05 max
Zn		0.25 max	Zn	0.10 max
Cr	0.15 min	0.35 max		
Ti		0.15 max		
others total		0.15 max	others total	0.15 max
Al		balance	Al	balance
	~ 98%-typical			99+%-typical

data and data from other threshold detectors, we gain insight into the shape of the incident-neutron spectrum. Our use of this reaction was restricted to locations inside the accelerator ring tunnel, where we undertook detailed investigations of the angular and energy spectral distributions of secondary particles coming from the vicinity of the primary target.

We again use the NaI (Tl) scintillation-crystal-gamma-ray spectrometer to measure Na^{22} content of aluminum samples. Because of the mode of Na^{22} decay and the response characteristics of the spectrometer system, the optimum counting interval included two bands: channels 45 through 59 centered on the 0.511-MeV positron annihilation gamma-ray peak, and channels 160 through 190 centered on the sum peak resulting from coincident emission (90% of the time) of the positron and a 1.27-MeV gamma ray.

The 2.60-year half life of Na^{22} is not well matched to the few-hour irradiations scheduled during our experiment; practical sensitivity is greatly reduced for this reason. Even so, we were able to obtain detailed flux profiles in the high-flux regions near the primary target by using only the 16.9-g aluminum-disk samples. We made no attempt to measure Na^{22} in any aluminum samples that were exposed inside the earth and concrete shielding.

e. Plastic Scintillator (Be^7) Technique. The transformation $C^{12} \rightarrow Be^7$ can also be used as a threshold detector for neutrons. The threshold is in the vicinity of 30 MeV (but somewhat higher than the $Al^{27} \rightarrow Na^{22}$ threshold); for flux computation we assume that the reaction cross section is approximately constant at 10 mb beyond about 60 MeV. The Be^7 content of a plastic scintillator can thus provide information related primarily to the high-energy portion of the neutron spectral distribution. When these data are combined with data from other threshold detectors, we gain insight into the shape of the incident neutron spectrum. Our use of this reaction was restricted to locations inside the accelerator ring tunnel, where we investigated in detail the angular distribution of secondary particles coming from the vicinity of the primary target.

We again use the NaI (Tl) scintillation-crystal gamma-ray spectrometer to measure Be^7 content of the samples. Beryllium-7 decays with emission of a 0.477-MeV gamma ray 10% of the time; our counting interval, channels 43 through 54, is centered on this peak, and the appropriate background rate is 59 c/min. Referred to the totality of Be^7 decays, the absolute detection efficiency of the spectrometer for a 2.54-cm-diam by 2.54-cm-high plastic scintillator was determined experimentally and found to be 3.0%. (This value is based on the assumption that the plastic-scintillator counting system is 100% efficient for C^{11}-decay events at the zero-bias point.)

In addition to the unfavorable gamma-ray branching of Be^7 decay, the relatively long (53.6-d) half life of this isotope prevented attainment of a significant fraction of saturation activity in any of our samples — values of 1% were typical. The result was low sensitivity in practice, and the detector could only be used in the highest flux regions inside the tunnel. However, we were able to obtain detailed flux profiles for angular-distribution studies near the primary target by using the small 2.54-cm-diam by 2.54-cm-high plastic scintillators. We made no attempt to measure Be^7 in any scintillators that were exposed inside the earth and concrete shielding.

f. Concrete and Steel Activation-Study Techniques

i. Concrete activation. Production of Na^{24} in concrete was studied by exposing small samples of the major elements that make up concrete (sodium, calcium, magnesium, silicon, and aluminum) simultaneously with a similar sample of chemically analyzed powdered concrete. Ten to 40-g samples were exposed in 45-mm-diam by 20-mm plastic vials on the surface of the proton-synchrotron tunnel walls or buried at various depths between concrete blocks. After exposure a gamma spectrometric measurement was made of the Na^{24} content. We were able to account for the measured Na^{24} in concrete by measuring the Na^{24} produced in the major constituents of the concrete, as can be seen in Table III F.

Analysis of the Na^{24} activities produced in ordinary concrete shielding and boron-loaded shielding at the Bevatron indicates that an economical reduction in Na^{24} activity in concrete may be made by adding a few tenths of a percent of weight of boron to the aggregate in the first 50 cm of shielding around a high-energy accelerator such as the 200-GeV proton synchrotron.[GilW]

II. Steel activation. Production of radioactivity in steel of the CERN PS magnets was studied by exposing 23-g samples of iron oxide (red rouge) in 45-mm-diam by 20-mm plastic vials on all surfaces of the magnet and in an array in space around the magnet. The beam was monitored, and the radionuclides produced were studied with gamma-ray spectrometry techniques.

Table III F. Na^{24} production in concrete constituents.

Sample	Weight (grams)	A_s^* (c $min^{-1}g^{-1}$)	W_i^{**} (grams)	W_iA_s	$\frac{W_iA_s}{A_{s_{concrete}}}$
Concrete aggregate	30.46	5410	1.000	5410	1.000
Na	11.13	244,000	0.0200	4880	0.902
Mg	11.97	5,880	0.0149	87.6	0.016
Al	36.87	3,610	0.068	245.5	0.045
Si	31.76	870	0.336	292.3	0.054
Ca	30.21	62	0.021	1.30	0.0002
				Σ = 5506.7	Σ = 1.017

*A_s is the activity in counts per minute per gram.

**W_i is the fractional weight in concrete in grams.

iii. Thermal-neutron flux pattern near target 32. As an adjunct to the concrete-activation and magnet-activation studies, we measured the thermal-neutron flux pattern in the accelerator tunnel at and around magnet 32. Thermal-neutron detectors were the same sodium carbonate samples as used in the concrete-activation study; 22 such detectors were arranged in a three-dimensional array in the tunnel around magnet 32 and irradiated during run V. Gamma-ray spectrometric analysis for Na^{24} activity was carried out as for the concrete activation samples, that is, accepting only the data from channels 63 through 75 as Na^{24} information.

10. Ilford-Emulsion Techniques

a. Proton Recoil Tracks in Emulsions. Another basic way of measuring a neutron-energy spectrum is to measure the track-length distribution of proton recoils in a nuclear emulsion.[PatH 65, LehR 64] We use Ilford L.4 600-μ emulsions. Our scanning microscope has been adapted to function with a card punch, so that the x, y, and z coordinates for the end points of each track can be stored on demand. When the end points of 1000 or more tracks have been stored, a computer generates a proton recoil spectrum, taking into account emulsion shrinkage and the decreasing probability with increasing track length that a track will start and stop in the emulsion. A smooth curve is drawn by hand through the individual points in the proton recoil spectrum and this curve is then differentiated to produce a neutron spectrum. An integrated exposure between 5×10^6 and 10^8 n/cm^2 is ideal for usual spectra from isotopic sources and accelerators. The useful neutron-energy interval is from 1 or 2 to about 20 MeV. Below this energy the recoil tracks are too short to measure accurately, and background due to α tracks and protons from N^{14} (n,p) C^{14} in the emulsion is troublesome. Above this energy the number of tracks is too small for meaningful statistics, and allowance may be needed for background due to cosmic-ray neutrons.

b. Neutron Spectroscopy Using Stars in Emulsions. The average number of gray prongs per star in nuclear emulsion is found to be proportional to the average incident neutron energy.[RemR 65] This has been investigated for neutron energies from 20 to 300 MeV. Two advantages to this system over measurement of proton-recoil track length are clearly seen. Because the kinetic energy of a proton from a nuclear star is less than that of a recoil proton, the range in the emulsion is considerably less. Recoil-proton tracks, on the other hand, seldom both begin and end in the same emulsion. Also, the direction of the incident neutron need not be known for counting prongs from nuclear stars.

Neutrons of 20 to 260 MeV from stripped deuterons were used to irradiate six Ilford K.5 emulsions (7.6-by 2.54-cm, 600-μ). The neutrons were considered to be monoenergetic, with a peak energy of one-half the deuteron energy. There is, of course, a symmetrical spectrum of energies about the peak with

a full-width-at-half-maximum (FWHM) intensity given by

$$FWHM = 2(B_d \times E_d)^{1/2},$$

where B_d is the deuteron binding energy (2.18 MeV), and E_d is the energy of the incident deuteron (MeV). Neutrons of 300-MeV peak energy were obtained by bombarding Be with 360-MeV protons.

From 20 to 300 MeV the ratio of gray prongs per star increased by a factor of 50 from ≈ 0.01 at 20 MeV to ≈ 0.5 at 300 MeV. Between 500 and 1400 stars were scanned for each energy region. In comparison of the gray-prong method and an independent determination using threshold detector methods, Patterson and Omberg found substantial agreement for flux shapes derived from cosmic rays and for radiation fields at the Bevatron. [OmbR 67]

11. Fast-Neutron Films

The response of the Kodak Personnel Neutron Film has been shown to be essentially independent of energy for neutrons incident normally and having energies between 500 keV and 25 MeV.[ThoW 61, SteG 65a] Such films were exposed together with neutron activation detectors to obtain information on the energy spectrum of neutrons in the PS ring tunnel and in the radial-tunnel attenuation measurements. After development the films were scanned with a Cooke M4000 microscope (total magnification 675X), the scanning field being defined by a square eyepiece graticule giving an effective field size of 100 by 100 μ. Tracks were counted if they had five or more developed grains, and appropriate corrections were made for edge effects due to the finite size of the scanned area (Marshall and Stevenson 1967).[MarT 67] Whenever possible about 500 tracks were counted on each film, except where the track density was so low as to make this impracticable. Control films were developed with each batch of films and examined to determine the background track density.

Stevenson has reported the calibration factors appropriate to normally incident neutrons in the energy range 500 keV through 25 MeV to be[SteG 65b]

$$1 \text{ proton cm}^{-2} = 1.2 \times 10^3 \text{ neutrons cm}^{-2} = 4.5 \times 10^{-5} \text{ rem}.$$

The effect of the angle of incidence on the above calibration is most marked between 1 and 6 MeV, where the maximum range of the recoil proton is less than the thickness of the wrapper around the film. However, this effect should be small at low energies, where most tracks are produced in the emulsion itself, and at energies greater than 10 MeV where the wrapper is thin compared to the maximum range of the recoil protons. At grazing incidence the response of the film to Am-Be neutrons (mean energy 4 MeV) is a factor of two lower than that at normal incidence. However, for 14-MeV neutrons the response is approximately independent of angle of incidence.[SteG 65c] Therefore, use of the above calibration should not result in large errors in these experiments.

12. Production of Fission Tracks in Mica

Transmission-microscope studies have shown that heavy charged particles impinging on some dielectric solids produce linear chains of radiation-damage material.[SilE 59, PriP 62a] These damage sites can be chemically etched and viewed with an optical microscope.[PriP 62a, PriP 62b]

A critical rate of energy loss in the solid has been assumed such that only particles of mass number $\geqslant 30$ could produce observable tracks.[FleR 64] However, a recently improved criterion applicable over a wider energy range has been formulated which predicts track formation if the rate of primary ionization exceeds a critical rate for that solid.[FleR 65]

We have used mica strips in contact with bismuth, lead, and gold. Tracks formed in the mica by the fissioning of these elements are visible, after suitable chemical etching, under an optical microscope. Track density is converted to incident flux density; a 130-mb cross section for bismuth fission is assumed. Fission cross section of ≈ 80 mb for lead and ≈ 40 mb for gold were estimated by noting the ratios between the track densities from the bismuth, lead, and gold foils.

13. Ionization Chamber

A 3.7-liter, 1-atmos air ionization chamber with a 3-mm Lucite wall was used for measurements on top of the earth shield above both the target and clipper.[MCaJ 64] The silicon planar diffused p-channel

metal oxide semiconductor used as the electrometer element exhibits a leakage current of $< 10^{-16}$ A. Ionization current is measured by either of two methods: IR drop (rate-meter function) or by time rate of change of charge (integration function). Ratemeter ranges are in decade steps from 0.001 to 10 R/h and are best used for measuring radiation from nonpulsed sources. Integration ranges of 1 and 10 μR per full scale provide a sensitive, low-background-measurement method that is not adversely affected by the pulsed nature of the accelerator radiation field. The instrument is hand-held, portable, and capable of continuous operation for several months from a single set of batteries. Calibration of all ranges was done with Ra sources previously compared with NBS standard sources.

14. Gamma Dosimetry

In regions close to the accelerator, particularly in the accelerator tunnel itself, there is a significant photon contribution to the dose equivalent. Shaw et al. report that, close to the extracted proton beam of Nimrod, the dose equivalent due to low-energy gamma rays is roughly ten times that due to neutrons.[ShaK 66] Two independent techniques were used in the present series of experiments to assess photon dose rates--thermoluminescent dosimeters and film badges. The response of these dosimeters to neutral and charged particles is shown to be insignificant compared with their photon response in many regions explored.

a. Thermoluminescent Dosimeters. The use of lithium fluoride as a thermoluminescent dosimeter (TLD) is common for measuring the rad dose from γ rays, β particles, and other charged-particle radiations.[WinC 65] For our experiments, samples of annealed TLD-700 powder (enriched to 99.997% in Li^7), graded to a particle size between 75 and 150 μ, were volumetrically dispensed into cylindrical 3.5-mm-i.d. by 15-mm-long Teflon capsules. The mean sample weight thus dispensed was 22 mg, with a standard deviation of 1 mg and an extreme range of 5 mg.

The irradiated samples were measured by the Radiological Safety Division of A. E. E. Winfrith, who used the readout system described by Perry and George.[PerK 65] The powder is emptied onto a planchette and then heated in an atmosphere of nitrogen. A photomultiplier tube is used to measure the light output as the lithium fluoride powder is heated. The dc photomultiplier output is then converted into a pulse train, the repetition rate of which is proportional to the dc input. Thus by counting the number of pulses in a precise temperature interval as the powder is heated, one obtains a measure of the energy absorbed by the lithium fluoride. Calibration of TLD-700 with Co^{60} γ rays and 4-MeV electrons has shown the response to be proportional to the dose from 3×10^{-3} to 3×10^{3} rads.[PreH 66] The light output is calibrated in units of the equivalent Ra-γ rad dose (i.e., the amount of light from a sample of the powder exposed to a Ra^{226} source under conditions in which the dose measured by the appropriate air-ionization chamber would be one rad).

b. β-γ Films. Estimates of the photon and charge-particle dose rates in these experiments were also obtained from the blackening of Kodak Radiation Monitoring films. These are double-emulsion films with a slow emulsion on one surface of a cellulose acetate base and a faster emulsion, 150 times more sensitive, on the other surface. By photometric measurement of the optical density of the combined emulsion, doses from 0.020 to 20 rad can be estimated; for higher doses the more sensitive emulsion is stripped from the base and the optical density of the slow emulsion only measured. Thus the upper dose limit of the technique can be extended to 1500 rad.

In order to obtain crude information on the energy spectrum of the photons, some of the films were exposed in the A.E.R.E./RPS holder,[HeaM 63] which has an array of metal and plastic filters designed to modify the response of the film to photons of different energies. Details of the filter areas are given in Table III G.

Standard calibration curves were obtained for both the slow and the combined emulsions by exposing at normal incidence films of the same emulsion batch as that used in the experiment, to different doses of radium γ rays. These films were developed in the usual manner, and the optical density under any filter area is expressed as an "apparent radium dose". From these apparent doses, after subtraction of background "fog" on the films, the $(x + \gamma)$ and thermal-neutron doses were calculated, using the dose-evaluation method developed for personnel dosimetry described by Heard and Jones.[HeaM 63] In this method, the apparent dose under a given filter area is designated by the name of that filter area. Thus the $x + \gamma$ dose may be calculated by using

$$x + \gamma \text{ dose} = \text{Tin} + \frac{\text{Dural}}{50} + \frac{300 - \text{Dural}}{10} - \frac{\text{s.n.}}{3} ,$$

where s.n. is the thermal-neutron dose, calculated by using

$$\text{s.n.} = \frac{\text{Cd} - \text{Tin}}{2.1}$$

Table III G. Filter areas of the AERE/RPS film holder.

Name	Description	Use
50	50-mg/cm^2 plastic filter (polypropylene)	dose assessment
300	300-mg/cm^2 plastic filter	dose assessment
W	open window (no filtration)	x-ray and γ dose assessment
Tin	0.071-cm tin + 0.030-cm lead filter	
Dural	0.102-cm duralumin	
Cd	0.071-cm cadmium + 0.030-cm lead filter	thermal-neutron dose assessment

c. Response of Film Badges and TLD to Neutrons, Protons, and Charged Particles. In mixed fields of radiation it is important that the response of each detector to all components of the radiation field be understood. This paragraph discusses the response of threshold detectors, film badges, and thermoluminescent dosimeters to neutrons, protons, and other charged particles and x rays.

i. Response to protons. Typically, above the target in straight section 32 the dose rate measured by both TLD and film badges was 2 X 10^3 rads-h^{-1}, and the corresponding fast-particle flux (E > 20 MeV) was 5 X 10^6 particles-cm^{-2}-sec^{-1}. It is unlikely that more than a third of this particle flux is high-energy protons. Therefore an upper limit to the apparent γ dose due to protons is

$$\left(\frac{1}{3} \text{ proton-particle}^{-1}\right) \times \left(5 \times 10^6 \text{ particles-cm}^{-2}\text{-sec.}^{-1}\right) \times \left(2 \times 10^{-4} \text{ rads-h-proton-cm}^{-2}\text{-sec}^{-1}\right)$$

$$= 3.3 \times 10^2 \text{ rad h}^{-1}$$

or $\leqslant$ 16% of the total dose.

In situations where the nuclear cascade is well developed, as for example in the earth shield or above the magnets, the fraction of the apparent gamma dose due to protons will be somewhat smaller.

ii. Response to neutrons. Wingate et al.[WinC 65] report measured values of the response to LiF thermoluminescent powder in terms of the equivalent rad dose from Co^{60} γ rays. These results are expressed in Table III H.

Table III H. Response of LiF thermoluminescent powder to neutrons.

Neutron energy (MeV)	Neutron-cm^{-2} equivalent to 1 rad Co^{60}
2	1.25 X 10^{10}
5	5.87 X 10^9
14	9.1 X 10^8

If we arbitrarily take 1 n-cm^{-2} = 2 X 10^{-10} Co^{60} rad, then a particle flux of 5 X 10^{6} n-cm^{2} sec^{-1}, two thirds of which is neutrons, will produce an apparent Co^{60} dose rate of (2/3)(5 X 10^{6})(2 X 10^{-10})(3.6 X 10^{3})= 2.4 Co^{60} rads-h^{-1} or approximately 0.1% of the total dose.

iii. Summary. At present detailed knowledge of the charged-particle component of the radiation is inadequate to enable us to draw quantitative conclusions. However, in situations where the radiation field is relatively rich in charged particles, the apparent γ reading due to protons is not likely to exceed 15% and may be much less. In situations where the nuclear cascade is well developed and neutrons predominate, the apparent γ reading due to charged particles is certainly less than 5%. The apparent reading due to neutrons is always less than 0.1%.

References

BeaJ 59. J. W. Beasley, The Mean Fission-Fragment Range in Bismuth As Applied to Pulse-Type Ion Chambers, UCRL-8760, May 15, 1959.

BruE 65. E. Bruninx, Nucl. Phys. *64*, 81 (1965).

DeCH 63. H. G. De Carvalho, G. Cortini, M. Muchnik, G. G. Potenza, R. Rinzivillo, and W. O. Lock, Fission of Uranium, Thorium, and Bismuth by 20-GeV Protons, Nuovo Cimento *27* (2), 468 (1963).

CumJ 63. J. B. Cumming, Monitor Reactions for High-Energy Proton Beams, Ann. Rev. Nucl. Sci. *131,* 261 (1963).

DufR 54. R. B. Duffield and G. Friedlander, in Brookhaven National Laboratory Annual Report, 1954 BNL-303, 1954, p. 27.

FleR 64. R. L. Fleischer, P. B. Price, R. M. Walker, and E. L. Hubbard, Phys. Rev. *113A,* 1443 (1964).

FleR 65. R. L. Fleischer, P. B. Price, and R. M. Walker, J. Appl. Phys. *36,* 3645 (1965).

FraE 66. E. M. Franz and G. Friedlander, Nucl. Phys. *76,* 123 (1966).

GilW. W. S. Gilbert, H. W. Patterson, and A. R. Smith, Accelerator-Produced Na^{24} in Concrete; to be published, 1969.

HeaM 63. M. J. Heard and B. E. Jones, "A New Film Holder for Personnel Dosimetry," in *Personnel Dosimetry Techniques for External Radiation; Their Applications in Nuclear Installations,* Madrid Symposium, 1963 (ENEA, Paris, 1963), pp. 89-109.

HesW 57. W. N. Hess, H. W. Patterson, and R. Wallace, Nucleonics *15,* 74 (1957).

KelE 48. E. L. Kelly and C. Wiegand, Phys. Rev. *73,* 1135 (1948).

LedC 67. C. M. Lederer, J. M. Hollander, and I. Perlman, *Table of Isotopes,* Sixth Edition (John Wiley and Sons, New York, 1967).

LehR 64. R. L. Lehman, Energy Spectra of Stray Neutrons from the Bevatron, Nucleonics *22,* No. 11, 35 (1964).

LisH 62. H. Liskien and A. Paulsen, Compilation of Cross Sections for Some Neutron-Induced Threshold Reactions, Euratom report EUR-119e, July 1962.

MarT 67. T. O. Marshall and G. R. Stevenson, in *Symposium on Solid-State Chemical Radiation Dosimetry,* STI/PUB-136 (IAEA, Vienna, 1967).

MCaJ 60. J. B. McCaslin, A High-Energy Neutron-Flux Detector, Health Phys. *2,* 399 (1960).

MCaJ 64. J. B. McCaslin, Rev. Sci. Instr. *35,* 1587 (1964).

MCaJ 67a J. B. McCaslin, H. W. Patterson, A. R. Smith, and L. D. Stephens, Some Recent Developments in Technique for Monitoring High-Energy Accelerator Radiation, in *Proceedings of First International Radiation Protection Association, Rome, Italy, September 5-10, 1966* (Pergamon Press, New York, 1967),

MCaJ 67. J. B. McCaslin and L. D. Stephens, High-Sensitivity Neutron and Proton Flux Detector with a Practical Threshold Near 600 MeV, Using Hg (spallation) ^{149}Tb, UCRL-17505, April 1967.

MoyB 52. Burton J. Moyer, Survey Methods for Fast and High-Energy Neutrons, Nucleonics *10,* No. 5, 14 (1952).

OmbR 67. R. P. Omberg and H. W. Patterson, Application of the Stars Produced in a Nuclear Emulsion to the Determination of a High Neutron Energy Spectrum, UCRL-17063, February 1967.

PatH 65. H. W. Patterson, Accelerator Radiation Monitoring and Shielding, in *Proceedings of the First AEC Symposium on Accelerator Radiation Dosimetry and Experience, Brookhaven National Laboratory, November 3-5, 1965* (Brookhaven, Upton, L. I., 1965).

PerK 65. K. E. G. Perry and E. George, UKAEA report AEEW-R-411, 1965.

PreH 66. H. E. Preston, Rutherford High Energy Laboratory, private communication, 1966.

PriP 62a. P. B. Price and R. M. Walker, J. Appl. Phys. *33,* 3407 (1962).

PriP 62b. P. B. Price and R. M. Walker, Phys. Rev. Letters *8,* 217 (1962).

ReiP 58. P. W. Reinhardt and F. J. Davis, Health Phys. *1-2,* 169 (1958).

RemR 65. R. Remy, Neutron Spectroscopy by the Use of Nuclear Stars From 20 to 300 MeV (M.S. thesis), UCRL-16325, August 17, 1965.

RubL 62. L. Ruby, Lawrence Radiation Laboratory, private communication.

ShaK 62. K. Shaw, High-Energy Flux Measurement Using Plastic Scintillators, DI/HP/6, 1962.

ShaK 63. K. B. Shaw, The Measurement of Accelerator Produced Neutron Flux Using the S^{32} (n,p) P^{32} Reaction, NIRL/R/31, March 1963.

ShaK 66. K. B. Shaw et al., Radiation Measurements Around the Nimrod 7-GeV External Proton Beam, RHEL/M/112, September 1966.

SilE 59. E. C. H. Silk and R. S. Barnes, Phil. Mag. *4,* 970 (1959).

SmiA 65. A. R. Smith, Threshold Detector Application to Neutron Spectroscopy at the Berkeley Accelerators, in *Proceedings of the USAEC First Symposium on Accelerator Radiation Dosimetry and Experience, Brookhaven National Laboratory, November 3-5, 1965* (Brookhaven, Upton, L.I., 1965); pp 365-409.

SteL 58. L. D. Stephens and A. R. Smith, Fast-Neutron Surveys Using Indium-Foil Activation, UCRL-8418, August 13, 1958.

SteG 65a. G. R. Stevenson, Rutherford High Energy Laboratory Report R.P.S./1/5, 1965.

SteG 65b. G. R. Stevenson, unpublished experimental data, 1965.

SteG 65c. G. R. Stevenson, Rutherford High Energy Laboratory Report R.P.S./1/13, 1965.

ThoW 61. W. T. Thornton, D. M. Davis, and E. D. Gupton, The ORNL Badge Dosimeter Personnel Monitoring Application, ORNL-3126, December 21, 1961.

WieC 49. C. Wiegand, Rev. Sci. Instr. *19,* 790 (1949).

WinC 65. C. L. Wingate, E. Tochlin, and N. Goldstein, Response of Lithium Fluoride to Neutrons and Charged Particles, in *Proceedings of the International Conference on Luminescence Dosimetry, Stanford University, Stanford, California, July 21-23, 1965; in Luminescence Dosimetry,* USAEC Rept. CONF-650637 (1965).

WinL 59. L. Winsberg, in Chemistry Division Semiannual Report UCRL-8618, 1959, p. 52.

IV. EXPERIMENTAL RESULTS

A. Introduction

The shielding experiment can be conceived of as a series of particle flux measurements moving from the primary-proton-beam vacuum pipe progressively outward through the synchrotron magnets, machine tunnel, and earth shielding. The use of activation detectors with different threshold energies enables one to determine the radiation field's energy spectrum and hence biological dose at a given location, as discussed in Chapters III and IX.

Eight CPS machine running periods, each approximately 12 hours long, were allocated to this shielding experiment. In each run, samples were changed so that a given run contained a number of shorter subruns, called exposures. Details of this running pattern are given in the run summaries that are included with the detector counting data in the appendicies. In five of the runs, the momentum of the primary proton beam was near the accelerator maximum, 26.4 GeV/c, and close to half the maximum, 14.6 GeV/c, in the other three runs. We were thus able to examine some shielding data as a function of primary proton momenta.

B. Conversion of Detector Counts to Particle Fluxes

Our aim during the experiment was to reduce all the data from each run before preparations for the next began. By so doing we could check for irregularities and inaccuracies in the data, and meaningfully compare data from different detectors. Because there was approximately one run per week, each involving the analysis of as many as 200 activation detectors, we very much needed to reduce our raw data to normalized counting rate or flux immediately. For this purpose we used a LOCI computer* to find the incident flux density ϕ in n/cm^2-sec:

$$\phi = \frac{[Nd - B(tc)]\ C1\ C2}{T\ [e^{-td/\tau} - e^{-(td+tc)/\tau}]\ [1 - e^{-ti/\tau}]\ C_3}$$

where Nd is the number of counts during the counting period, B is the background in cpm, tc is the counting period, C_1 is the zero-bias correction factor, C_2 is the weight correction factor, C_3 is the conversion factor in counts/minute-unit flux, T and τ are the mean life, td is the decay time, and ti is the irradiation time.

We required the LOCI to solve this equation or modifications of this equation for the following four quantities:

1. flux density, as shown
2. percent statistical error in Nd $= \dfrac{100[Nd^{1/2}]}{Nd - B(tc)}$
3. detector count rate at end of exposure $= \dfrac{[Nd - B(tc)]\ C1\ C2}{T\left[e^{-td/\tau} - e^{-(td+tc)/\tau}\right]}$

*Manufactured by the Wang Corporation, Natick, Massachusetts. This is a desk-top calculator that performs its operations using natural logs and is therefore particularly well suited to exponential decay problems. Two card readers enable one to use a program of up to 160 instructions.

4. detector count rate at end of exposure corresponding to infinite exposure time $= \dfrac{[Nd - B(tc)]\ C1\ C2}{T\left[e^{-td/\tau} - e^{-(td+tc)/\tau}\right]\left[e^{-ti/\tau}\right]}$.

The expression $T\left[e^{-td/\tau} - e^{-(td+tc)/\tau}\right]$ in these equations corrects the observed count rate for decay time, td. It also corrects for decay during the counting interval, tc, which in the case of some measurements with carbon detectors was a large fraction of the half life.

Calculations of count rates at infinite exposure time (saturation), for short half-lived detectors, based on the actual exposure time, were not always sufficiently accurate if there were significant beam-current intensity variations. The decay-corrected unsaturated counting rates were often used for preliminary comparison purposes and saturation factors corrected for beam intensity variations were applied later.

Because some assumptions or simplifications are introduced when counting rates are converted to flux densities [e.g., reaction cross sections assumed to be energy-independent above the reaction threshold, C^{11} production via (n,2n) rather than (p,pn) reaction, etc.] it has been useful during the experiment to compare data in terms of saturated count rates.

Clearly, the feedback provided by nearly concurrent data reduction aided immeasurably in planning subsequent runs and in the early detection of difficulties and irregularities. Only with a prohibitive extension of time, manpower and effort could one hope to complete such an experiment without concomitant computer assistance.

Sometimes, as was previously mentioned, it was necessary to take cognizance of variations in the intensity of the beam current. Such variations become increasingly important as the half-life of the radionuclide of interest becomes shorter. Thus, we made corrections of this sort to the carbon and mercury data, but it was not necessary to apply these corrections to the longer-lived Na^{24} and Na^{22} from aluminum for the beam-current variations encountered. It is assumed for this purpose that variations indicated by the graphical and tabular records of the circulating beam intensity accurately reflect changes in the intensity of the radiation field.

Consider, for example, Run IV and the corrections applied to Hg data to normalize this data to saturation in the beam of 10^{12} protons per second (p/sec). The graph of circulating beam vs time is divided into a number of rectangular segments. The fraction F_k of the observed detector activity due to any one segment depends on three factors:

1. the beam intensity, I_k
2. the degree of saturation, S_k, where

   $S_k = 1 - e^{-ti\,(k)/\tau}$

   $t_i\,(k)$ = irradiation time for segment k

   τ = mean life of Tb^{149}

3. the decay time from the end of the segment to the end of the irradiation,

   $D_k = e^{-td/\tau}$.

The fractional activity due to segment F_k is then given by

$$\frac{(I_k)\,(S_k)\,(D_k)}{\Sigma_{F_1}^{F_n}\,(I)\,(S)\,(D)}\ .$$

Normalizing to a beam intensity of $I = 10^{12}$ p/sec and correcting for saturation and decay of segment F_k yields

$$\frac{(I_k)\,(S_k)\,(D_k)}{\Sigma_{F_1}^{F_n}\,(I)\,(S)\,(D)} \times \frac{10^{12}\ \text{p/sec}}{(I_k)\,(S_k)\,(D_k)} = \frac{10^{12}\ \text{p/sec}}{\Sigma_{F_1}^{F_n}\,(I)\,(S)\,(D)}\ .$$

Parameters I, S, and D for segments 1 through 7 are given in Table IVA.

Table IVA. Parameters I, S, and D for segments 1 through 7.

Segment	I(p/sec)	S	D	(I) (S) (D)
1	1.249×10^{11}	0.080002	0.490309	0.048992×10^{11}
2	1.332×10^{11}	0.139662	0.569252	0.105898×10^{11}
3	1.306×10^{11}	0.201776	0.733537	0.193012×10^{11}
4	1.344×10^{11}	0.0494431	0.789280	0.052449×10^{11}
5	1.344×10^{11}	0.0841402	0.875988	0.099061×10^{11}
6	1.146×10^{11}	0.0763673	0.94788	0.082956×10^{11}
7	1.078×10^{11}	0.0510477	1.0000	0.055029×10^{11}
				$\Sigma_{F_1}^{F_7}$ (I) (S) (D) $= 0.637397 \times 10^{11}$

The observed detector count rate corrected to the time at the end of the irradiation (zero time) is then multiplied by

$$\frac{10^{12}}{0.637 \times 10^{11}}$$

to yield counts per minute at zero time and saturation normalized to a circulating beam intensity of 10^{12} p/sec.

A computer program (PULSAC) in FORTRAN IV language for the CDC-6600 has been written (Routti) which performs these segmented beam calculations. In addition, given the necessary detector and irradiation parameters, it computes flux normalized to a circulating beam of 10^{12} p/sec.

C. Beam Pipe (Vacuum Tank) Data

The closest that detectors can be placed to the circulating primary proton beam is on the outside of the beam vacuum tank. Detectors at these locations are exposed to the highest particle fluxes. These fluxes are related to beam loss, as treated in detail in Chapter V.

D. Buckets

Plastic buckets were suspended below the ceiling of the accelerator tunnel but above the main ring magnets; the samples in these buckets were 1.74 meters above the circulating beam. The nuclear cascade at the buckets has already been well developed in passing through the iron of the magnets. The Z coordinates and location nomenclature are similar to those for the vacuum tank detectors, and are listed in the data tables that appear in the appendices.

E. Orbit Holes

The outward and upward traveling particles are exponentially attenuated through the shielding through nuclear interactions. These attenuated neutron fluxes are detected with activation detectors placed in the 15.2-cm-diam orbit holes drilled vertically above the beam orbit. The streaming corrections that are applied to fluxes measured in these orbit holes are discussed in Chapter VII.

Figure IV-1 shows the attenuation of neutron flux as measured with aluminum activation detectors at orbit holes 31, 32, and 33. The target is located directly beneath hole 32. Although the experimental points are well fitted by straight lines, it is incorrect to assume that the slopes of these lines yield the attenuation mean free path in the earth. This is because geometrical effects and integrations over source distributions must be taken into account; the fitting procedure is treated in Chapter VIII.

F. Radial Holes

Drilled vertical 15.2-cm-diam holes were located on radial lines through some of the orbit holes but at several radii greater than that of the beam orbit. Data were taken at a height equal to that of the beam, i.e., the cascade particles were traveling in the horizontal plane. Shield thicknesses greater than the vertical earth shielding of the orbit holes could be investigated with these radial holes.

Figure IV-2 shows aluminum detector activity vs shield thickness for three sets of these radial holes. The geometry is more complex than in the orbit-hole case above. Streaming was looked for and found to be unimportant.

G. Surface

Various detectors were placed on the top of the earth shielding, at the shielding-air interface. Data from these detectors are referred to as surface or ring-top data. These locations were the most accessible, but the neutron fluxes were low since the full shield thickness lay between the accelerator source and detectors. Measurements were generally made directly above the beam orbit, but some data were taken at other radii.

An extremely sensitive detector, the integrating ion chamber, was used in run VII to map the radiation field at the surface while the accelerator was running. Not only was the radiation measured along the beam orbit line, but also at smaller and larger radii. Some secondary production products, neutrons and negatively charged particles, will tend to travel toward larger radii as they move forward (the centrifugal effect), and positively charged particles of momenta lower than that of the primary beam will be bent to smaller radii as they move forward in the accelerator's magnetic field. The data are presented in Figs. IV-3 and IV-4. As can be seen from Fig. IV-4, the maximum radiation downstream from the target and clipper is found on the inside of the beam orbit and so the anti-centrifugal effect predominates.

H. Miscellaneous

1. Neutron attenuation through straight hollow ducts

Measurements and theories of neutron streaming through the radial tunnels are covered in Chapter XI.

2. Magnet activations

Pure rouge (ferric oxide) samples were exposed in various locations of the main ring magnet in order to determine the relevant cross sections for production of radioactive products from the magnet iron. These data are not included in this report.

3. Concrete activation

The production of radioactive Na^{24} in the concrete of the tunnel walls through fast-neutron processes and thermal-neutron capture was investigated through the use of samples on the tunnel walls and magnet faces. Most of these data are not included in this report.

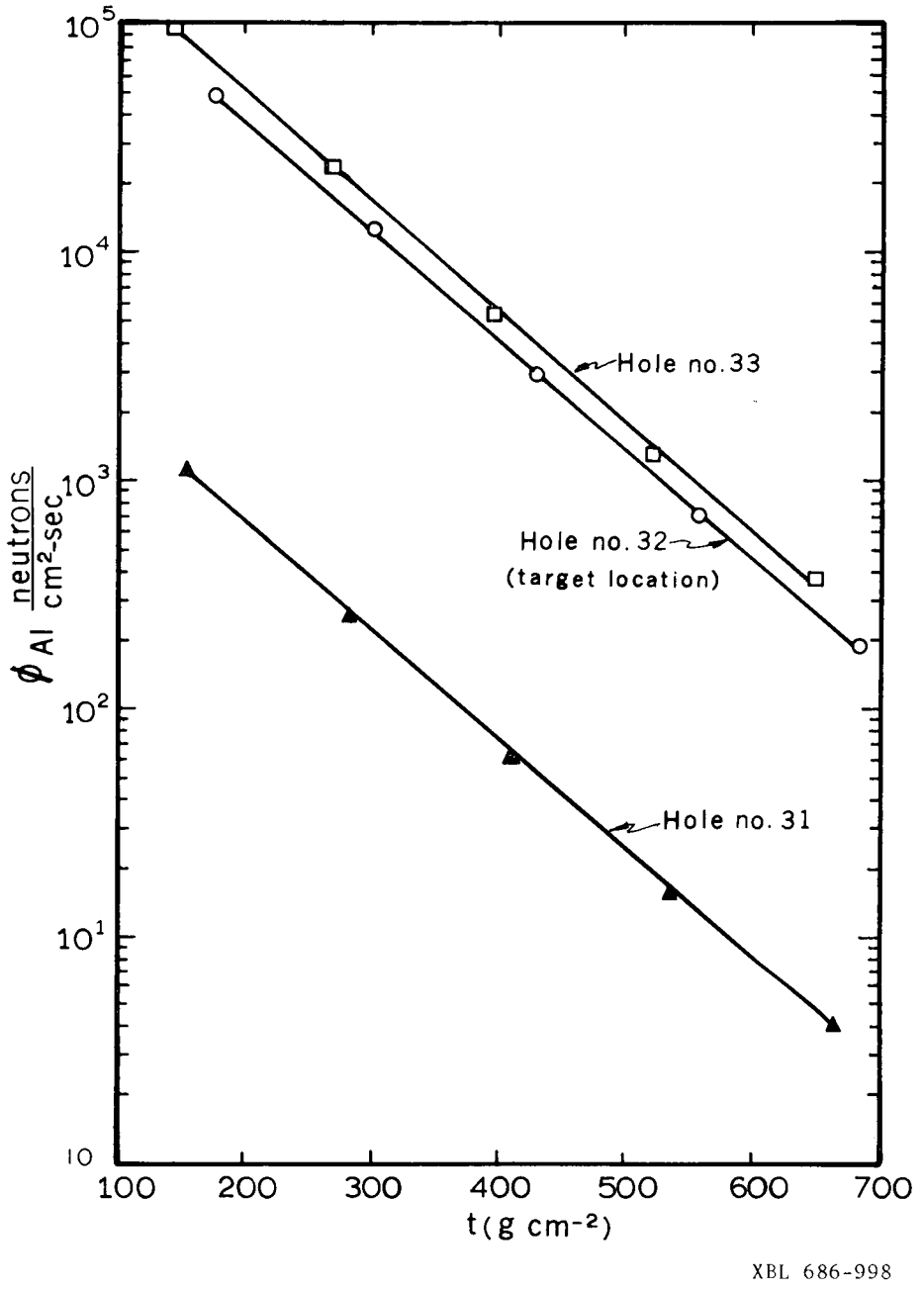

Fig. IV-1. Orbit-hole data for aluminum activation detectors, Run VII.

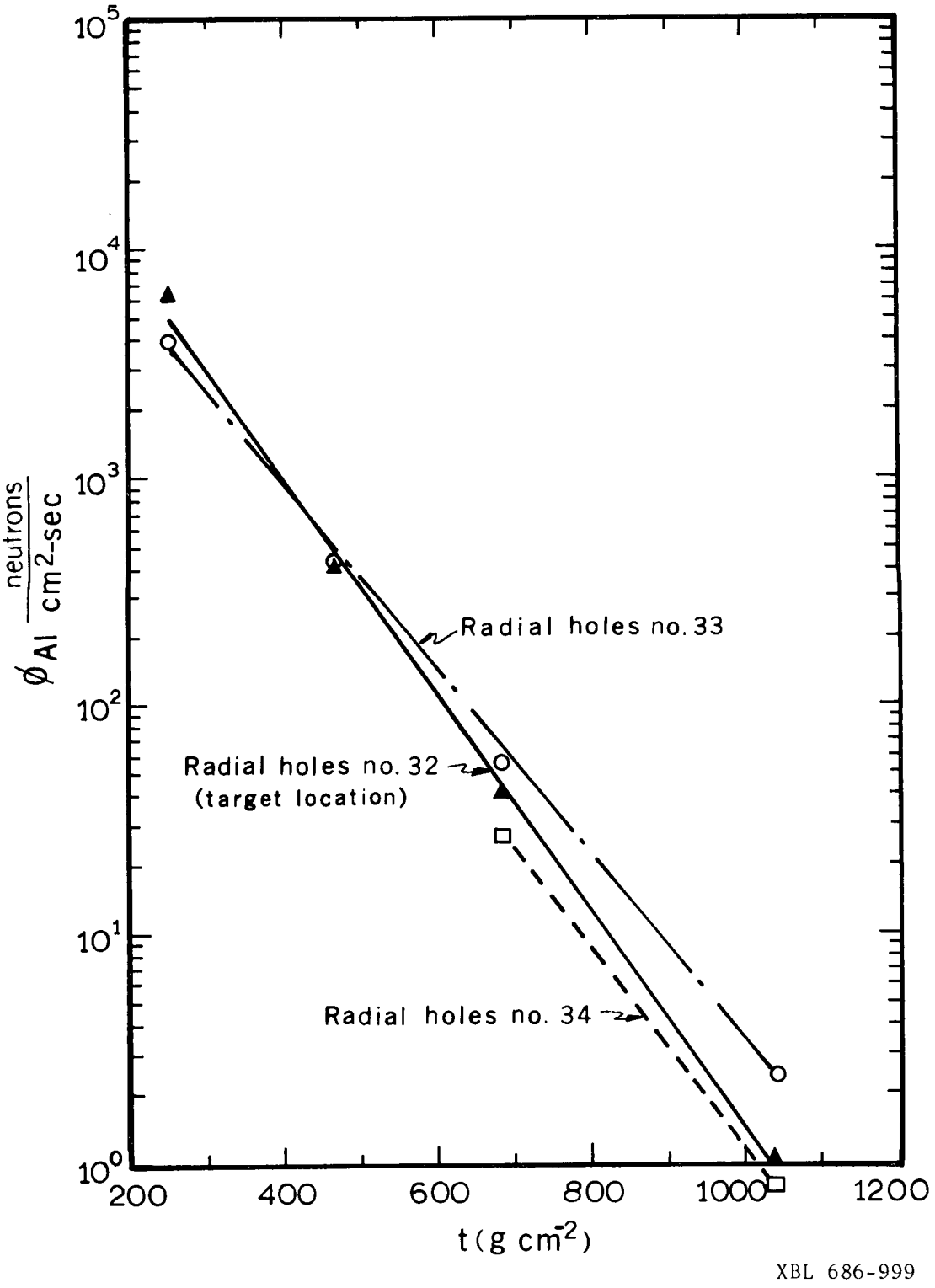

Fig. IV-2. Radial-hole data for aluminum activation detectors, Run III.

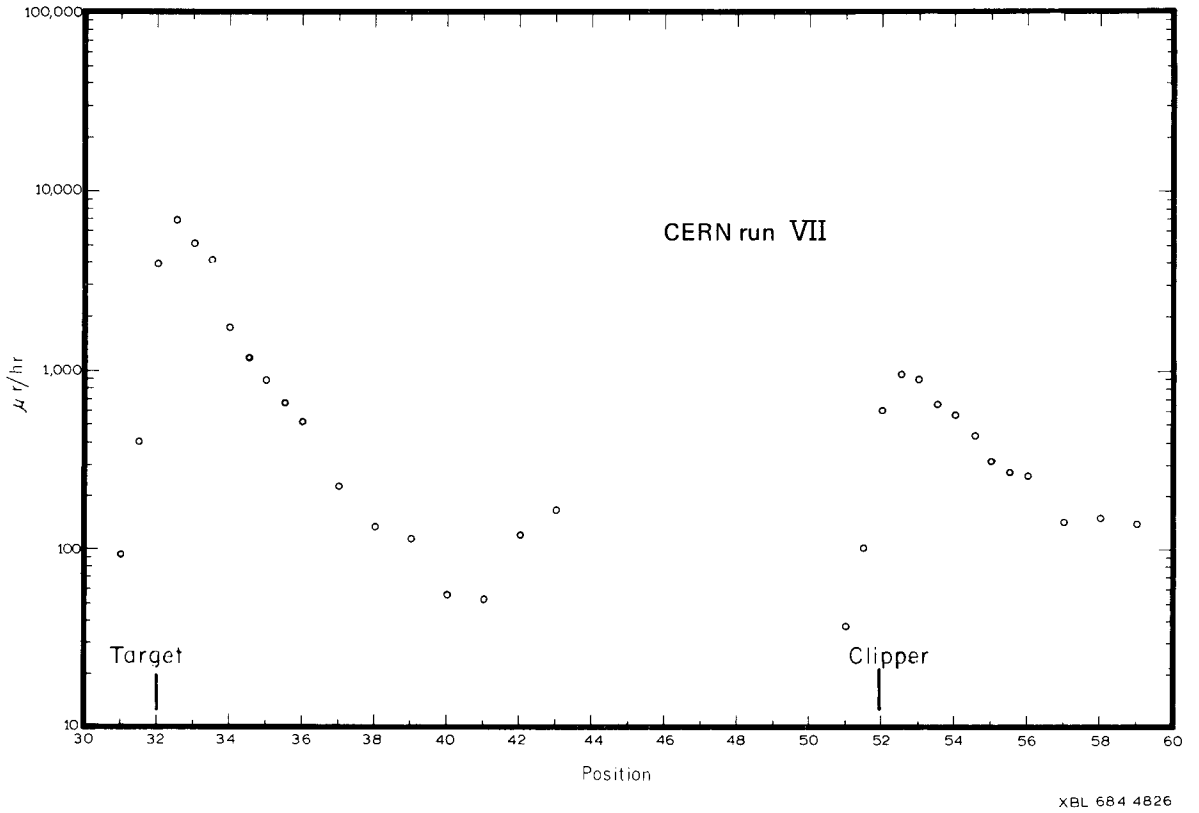

Fig. IV-3. Ring-top ionization-chamber data for positions directly above beam orbit for Run VII.

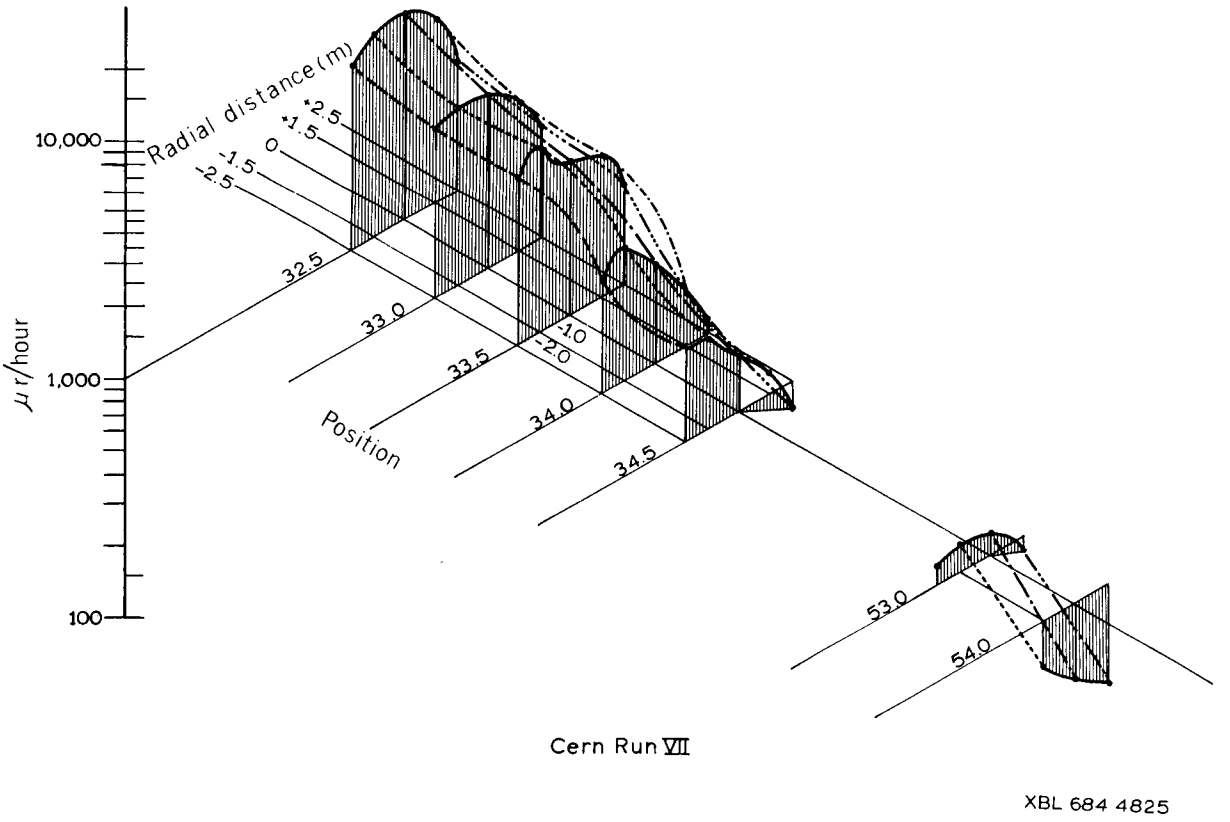

Fig. IV-4. Isometric view of ring-top ionization-chamber data for Run VII.

V. BEAM-LOSS DISTRIBUTION

A. Introduction

The loss of the multi-GeV primary proton beam circulating around the accelerator begins the cascade process through which the radiation field is established in the accelerator, its enclosure, and the shielding, and through skyshine, at a considerable distance from the accelerator ring. The nature of the cascade process is such that the primary protons comprise but a small portion of the radiation field that results; lower-energy radiation carries away most of the energy. The primary beam can be lost on a target or beam clipper that is flipped into the beam after the acceleration cycle, and it can also be lost on the vacuum chamber walls. Beam can also be extracted from the accelerator, but a portion may strike an extraction septum. From a beam-loss standpoint, a septum then plays the roll of an internal target, and we shall define the beam loss as all beam lost around the accelerator, whether on an object inside the vacuum chamber or on the chamber walls.

One could, in principle, experimentally measure the primary beam loss if he could cover the surface of the vacuum chamber and the surfaces of the internal targets with detectors that only responded to protons of the primary energy. The entire surface integral would then correspond to the entire circulating beam (all of which has to be eventually lost somewhere), and the distribution of detector activity would correspond to the distribution of beam loss. The first difficulty in this procedure is that the large physical scale of a major accelerator requires that the number of detectors range from hundreds to thousands if both detail and accuracy are desired. The second difficulty is more fundamental in that there is no suitable detector that responds only to the primary proton energy.

Figure V-1 is a schematic representation of the beam-loss-detector-activation process. A thin target is shown in the vacuum chamber with the beam passing through it, the target being located in the straight section between two main ring magnets. Two detectors are shown on the vacuum chamber, one between the vacuum pipe and a magnet, and the other above the straight section. For each detector three categories of radiation can be incident:

1. primary protons of full energy, almost parallel to the chamber walls.
2. secondary particles from the target (or chamber walls), neutrons, protons, and pions of relatively high energies.
3. cascade products of all types, with most of the particles of low energies down to the MeV region.

These cascade products are directed to the detectors from the magnets in which the cascade was developed. The detector activation depends not only on the incident radiation spectrum, but also on the detector response function, as discussed below.

Figures V-2 and V-3 show the response functions for several activation detectors that are used to monitor accelerator radiation. Figure V-4 shows the neutron spectra found at several accelerator locations and in cosmic radiation. Considering these figures together, one can see that the sensitivity of activation detectors increases as the threshold energy is reduced, as discussed in chapter III. Hence in a given irradiation, it is technically difficult to measure more than a few Hg → Tb detectors, which have a threshold energy of some 600 MeV, and even then only high flux levels can be measured. Although this is the highest threshold detector presently available, the energy is far below the primary proton energy, and many secondary products are detected. Finally, one does not have much information on the response function of the various detectors for mesons; yet it is known that these high-energy cascades contain mesons in large numbers.

From the above, it is clear that there is no straightforward way to measure the beam-loss distribution with the detectors available. However, there are several methods of indirectly measuring this loss, and one can then check them against each other. If one assumes that the cascade is well developed in the magnets and the radiation spectrum is about the same all around the accelerator, then the beam loss around the ring will be proportional to the activity distribution of any detector. These detectors can be placed on the outside of the vacuum chamber, one's closest approach to the region of primary beam loss. One also can

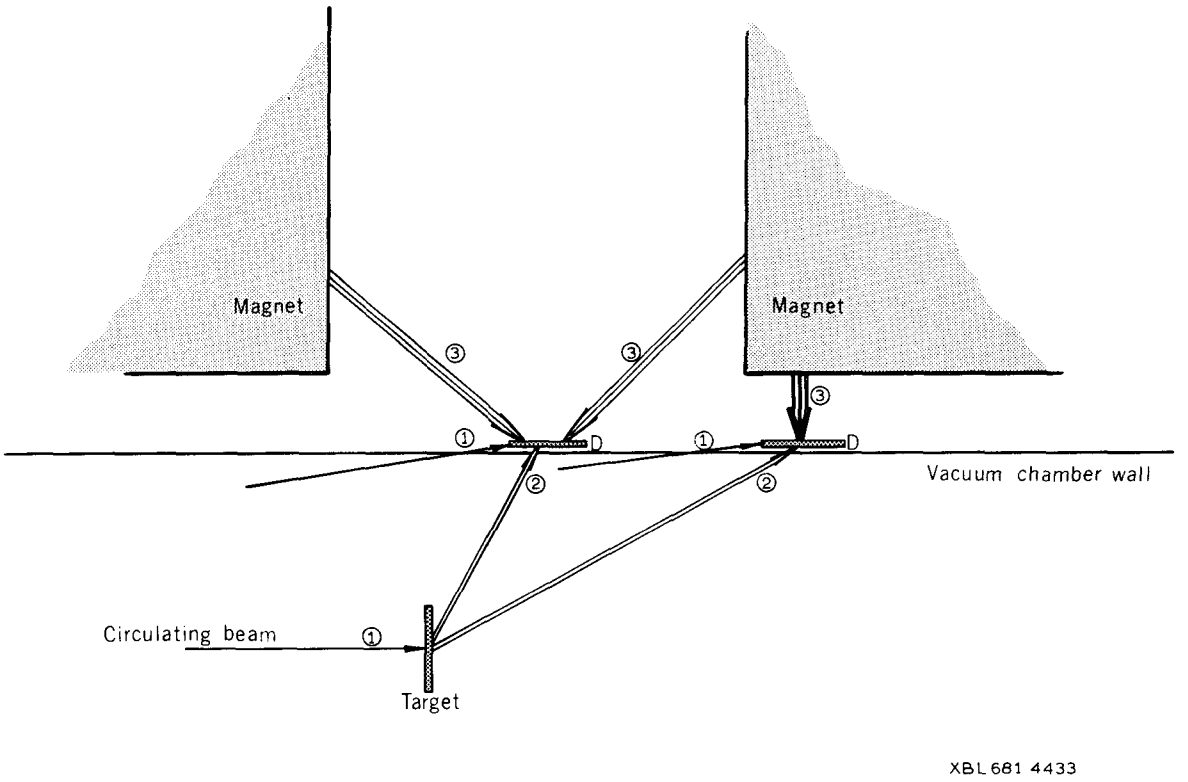

Fig. V-1. Schematic representations of beam-loss and detector-activation processes.

place detectors above the magnets, which reduces the ratio of primary protons in the radiation field. One can also examine detectors in and above the earth shield, in which case on knows that an equilibrium spectrum has been established. Each of these methods will be discussed in turn.

B. Activation Detectors on the Vacuum Chamber

The CERN Health Physics Group routinely measures the radiation field around the PS with aluminum activation detectors placed on the vacuum chamber near each of the 100 main ring magnets. Normally these detectors are changed and counted every two weeks, which corresponds to the period between the shutdowns for routine maintenance. A minimum of 100 such Al measurements for each of the run periods was carried out in a manner similar to that of the CHP routine, and for most of the runs extra detectors were used to yield increased spatial resolution. Figure V-5 shows the distribution of this activity around the accelerator. Two features are apparent: the losses immediately following the internal target and clipper are large compared with the losses elsewhere, and the smaller random losses far from the targets are quite variable and by no means uniform.

In three of our runs, two at 26.4 GeV/c and the other at 14.6 GeV/c, in addition to the aluminum detectors, sulfur and TLD (thermoluminescent detectors) were placed on the vacuum chamber. The TLD responds principally to gamma rays and charged particles while the sulfur ($E_T \sim 3$ MeV) responds to neutrons of a lower energy than aluminum ($E_T \sim 6$ MeV).

Table VA lists representative fluxes measured at 26.4 (Run I) and 14.6 GeV/c (Run VI) normalized to a circulating proton current of 10^{12} p sec^{-1} in the vicinity of target 32. Refer to the Appendix for a complete list of fluxes at the 100 standard location. Comparison of the sulfur fluxes (Φ_s) with the aluminum data indicates proportionality between the two. For ease of comparison the quoted Na^{24} specific activities

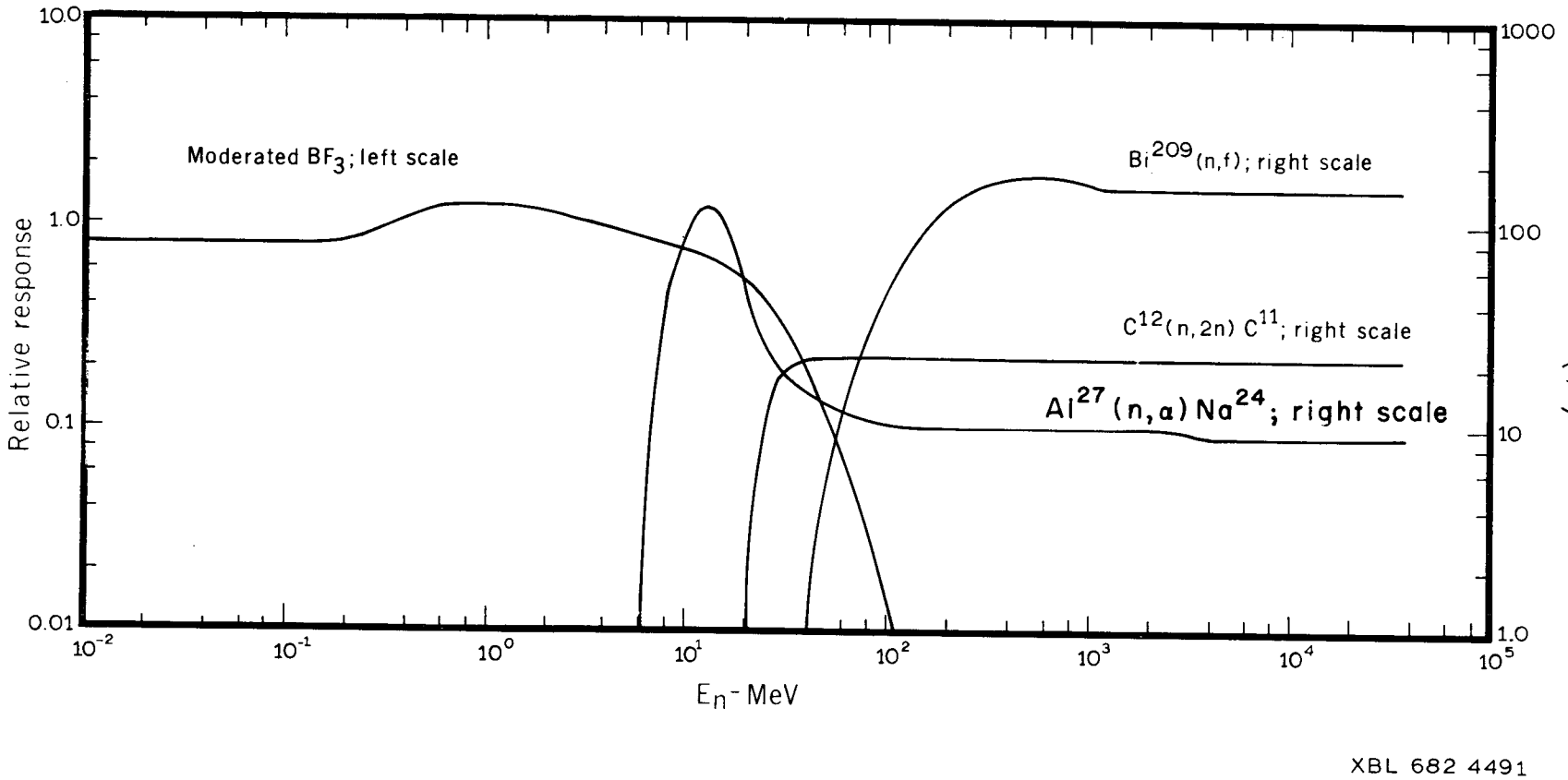

Fig. V-2. Response functions of several detectors used in this experiment.

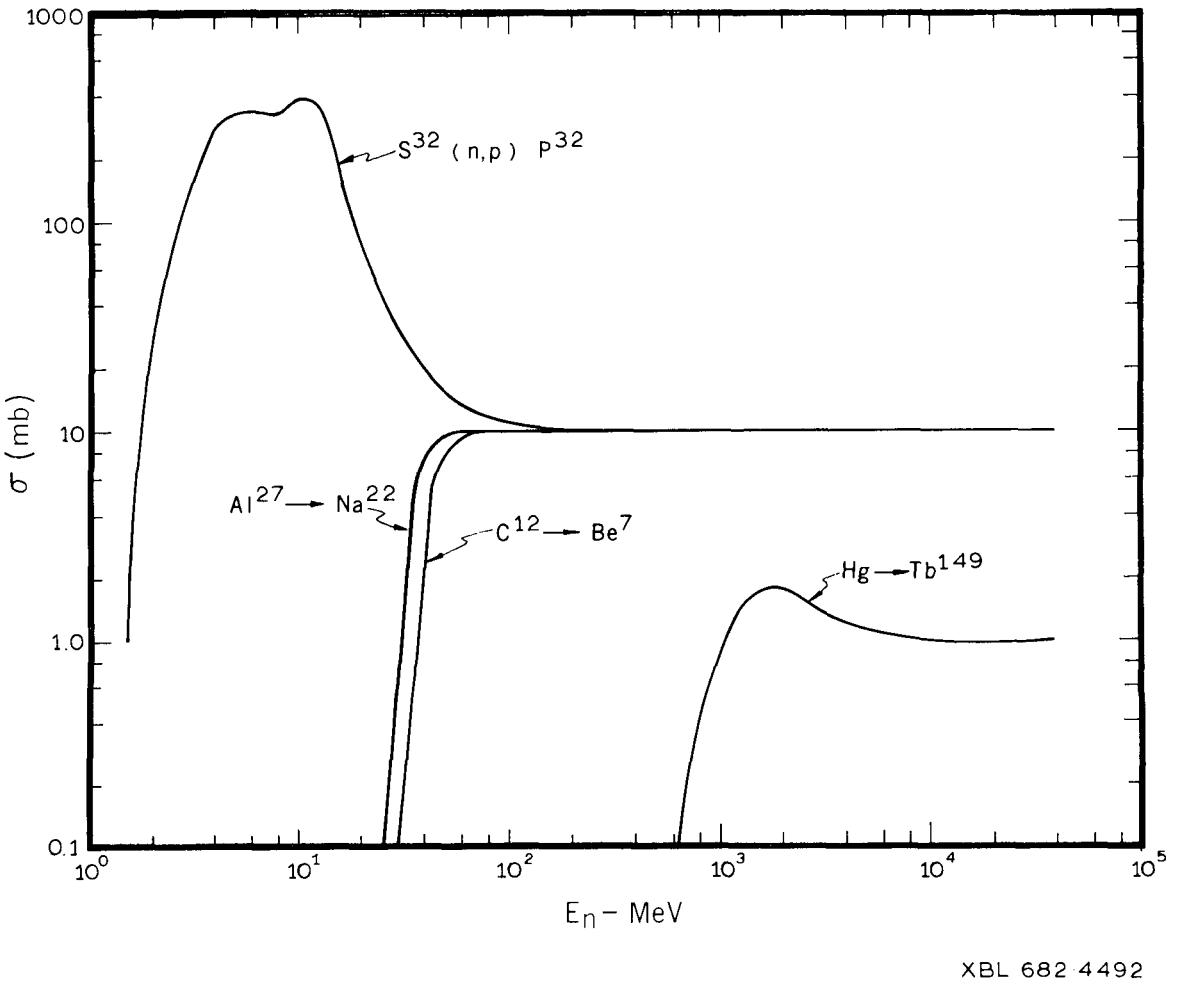

Fig. V-3. Response functions of several detectors used in this experiment.

in the aluminum foils may be converted to an equivalent particle flux by assuming an appropriate production cross section (Chapter III). We have used an activation cross section of 120 mb here, but of course the resultant particle "flux" quoted is physically meaningful only in the sense that an equivalent monoenergetic flux of 14-MeV neutrons would be necessary to produce the observed Na^{24} specific activity in our samples. The relationship between 14-MeV equivalent flux and saturated specific activity is given by

$$\Phi_{Al} = 13.8\, S_{sat},$$

where S_{sat} is measured in $pCi\text{-}gm^{-1}$. Calculated values of the ratio Φ_s/Φ_{Al} (equivalent 3-MeV sulfur flux divided by equivalent 14-MeV aluminum flux) were independent of proton energy within the accuracy of the data.

Thermoluminescent detectors were placed at approximately one third of the straight section positions at both high and low energy. This technique is of additional value in that the gamma dose at the vacuum chamber provides useful information for the design of magnet-coil insulation. Similar results were obtained in comparing the ratio of TLD dose to Φ_{Al}. The ratio TLD/Φ_{Al} was insensitive to proton energy and again distributed normally about a mean value of $6.65 \times 10^{-4} \pm 5\%$ rads $h^{-1}/n\text{-}cm^{-2}\text{-}sec^{-1}$. In this case the mean value is determined with somewhat less precision due to the higher standard error of ± 40% on individual points. The total range of fluctuations about the mean was again about a factor of two. It was our experience in using thermoluminescent detectors in this series of experiments that particular care had to be taken to avoid spurious readings. The danger of potential contamination of the LiF powder or errors

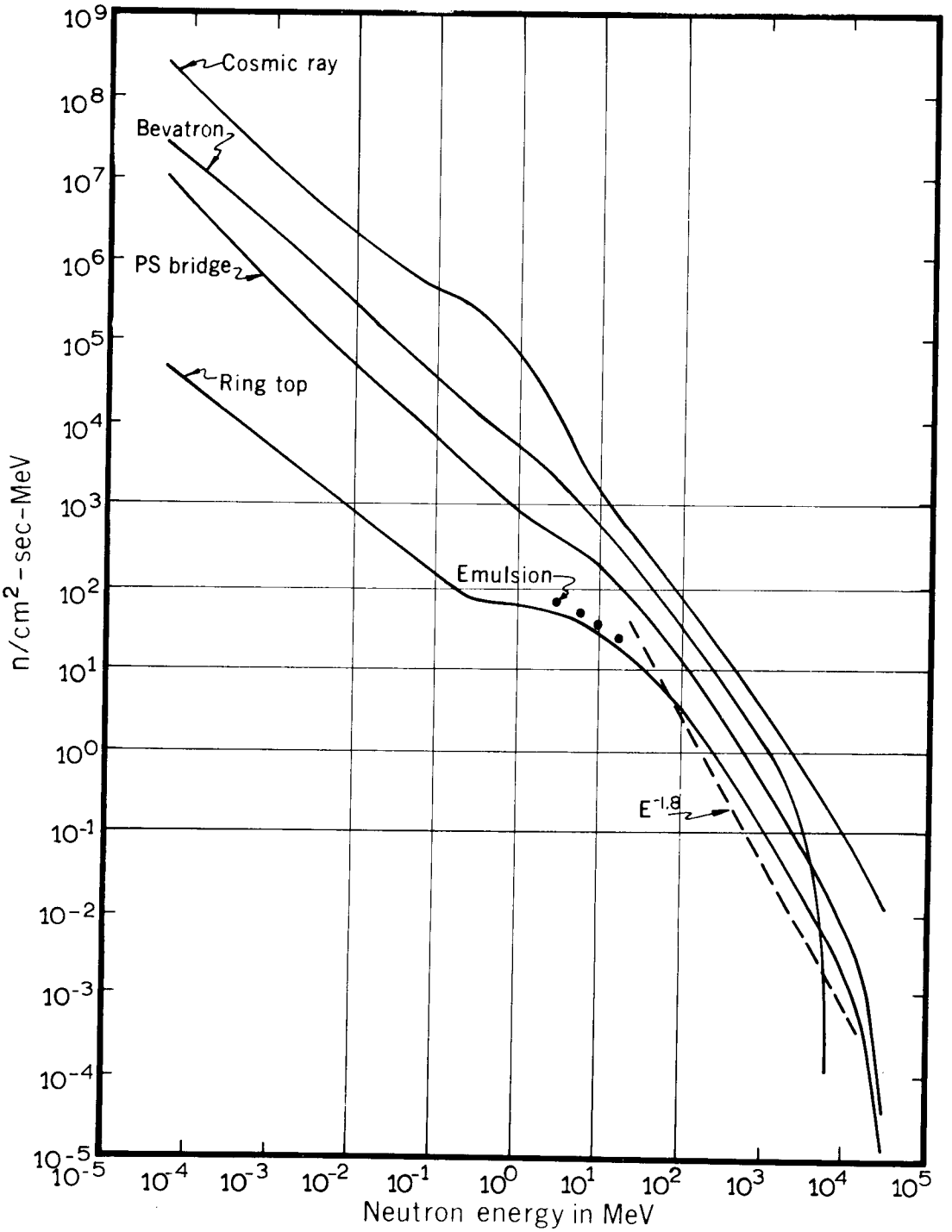

Fig. V-4. Neutron spectra deduced from detectors used in this experiment; relative intensities of spectra are not meaningful.

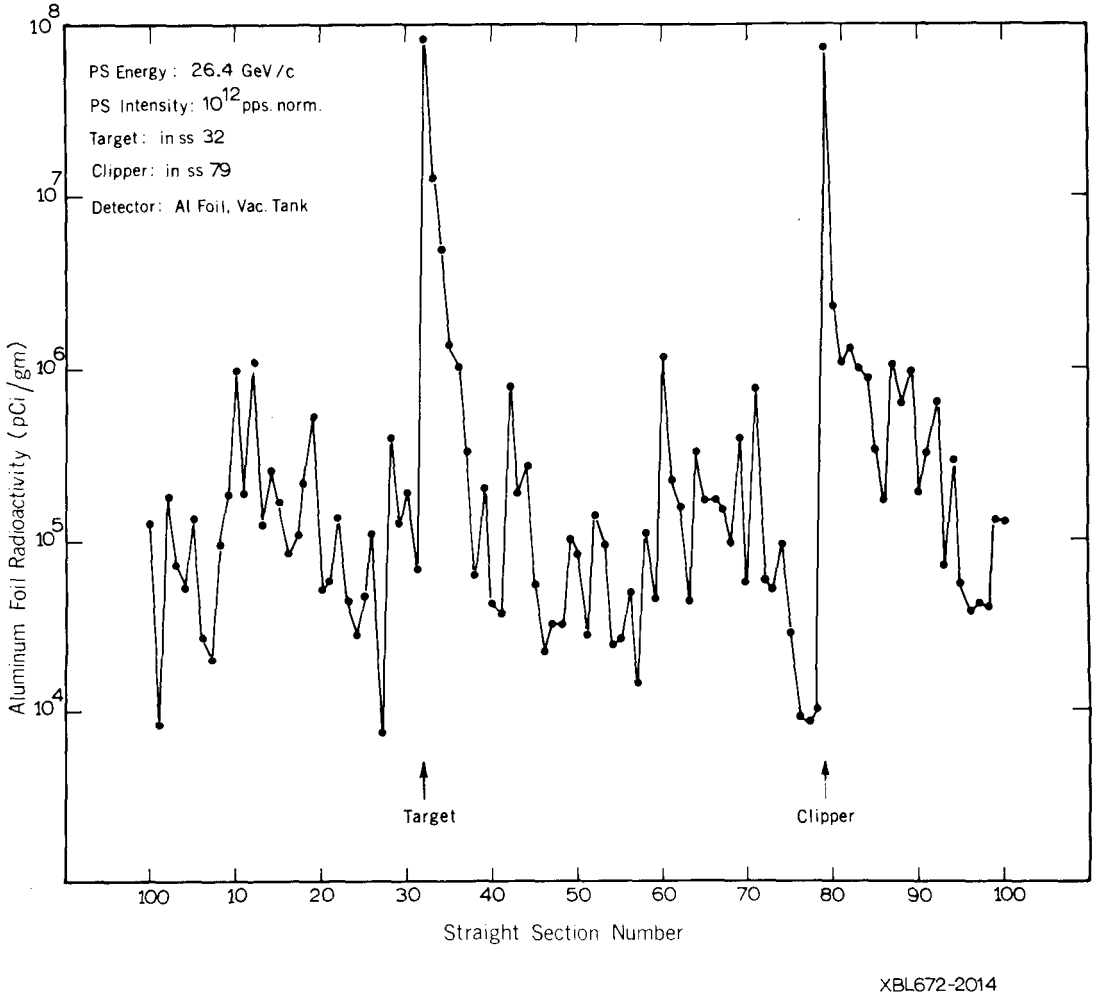

Fig. V-5. Activities in aluminum foils at the 100 standard locations on the vacuum chamber.

in the quantity of powder dispensed makes it essential to make two or more independent exposures if good accuracy is required. Particular care had to be taken at high exposures to avoid saturation of the reader. Such potential errors satisfactorily account for the somewhat broader distribution observed in the values of TLD/Φ_{Al}. One final point is worth mentioning; we have noted substantial discrepancies in the calibrations of different laboratories making TLD measurements. This may partly be explained by uncertainties in the calibrations at high exposures (not normally encountered in routine health-physics procedures). The absolute values of TLD dose quoted here are our best estimates based on calibrations at A. E. W. (Winfrith) and A. E. R. E. (Harwell), and are quoted as rads deposited in water (or soft tissue).

It may be seen from these measurements that any one detector may be used to predict the results of either or both the other two to about 30% accuracy on the average, and to a factor of two in the worst cases. No plausible explanation has been found for the occasional fluctuations observed, but they are perhaps not unreasonable in view of differences in detector response, radiation field, and flux gradients found at the vacuum chamber. Rather, we feel encouraged that these three independent techniques agree so closely.

The spacing of the average magnet and standard aluminum detector is 6.3 meters, and one would desire to use the 100 activities in performing a line integral around the accelerator, the integral presumably being proportional to the total circulating beam lost within the accelerator. One observes that the measured activity often varies by a large factor from one magnet to the next, even far from the target position, so one

Table VA. Representative fluxes measured at standard locations on vacuum chamber, normalized to beam intensity of 10^{12} sec^{-1}.

Location	Flux			
	Run I, 26.4 GeV/c		Run VI, 14.6 GeV/c	
	Aluminum foils ($pCi\text{-}g^{-1}$)	Sulfur ($n\text{-}cm^{-2}\text{-}sec^{-1}$)	Aluminum foils ($pCi\text{-}g^{-1}$)	Sulfur ($n\text{-}cm^{-2}\text{-}sec^{-1}$)
24	1.97E + 4	4.43E + 5	4.80E + 4	7.24E + 5
25	3.40E + 4	5.20E + 5	3.72E + 4	5.78E + 5
26	7.75E + 4	1.56E + 6	1.31E + 5	3.49E + 6
27	5.86E + 3	7.44E + 4	2.97E + 3	8.83E + 4
28	2.79E + 5	4.48E + 5	3.35E + 5	6.76E + 6
29	8.66E + 4	1.83E + 6	2.08E + 5	4.19E + 6
30	1.38E + 5	3.79E + 6	2.00E + 5	3.63E + 6
31	4.72E + 4	9.41E + 5	7.27E + 4	9.56E + 6
32	5.68E + 7	6.61E + 8	4.11E + 7	4.79E + 8
33	8.96E + 6	1.09E + 8	4.65E + 6	6.27E + 7
34	3.34E + 6	4.57E + 7	1.35E + 6	2.07E + 7
35	9.82E + 5	1.57E + 7	4.40E + 5	7.93E + 6
36	7.16E + 5	8.92E + 6	3.61E + 5	4.64E + 6
37	2.31E + 5	2.71E + 6	1.44E + 5	2.12E + 6
38	4.29E + 4	5.94E + 5	3.81E + 4	5.33E + 5
39	1.42E + 5	1.71E + 6	1.24E + 5	2.28E + 6
40	3.05E + 4	5.60E + 5	3.31E + 4	3.49E + 5
41	2.68E + 4	2.98E + 5	7.30E + 4	9.97E + 5
42	5.58E + 5	6.90E + 6	4.43E + 5	6.74E + 6
43	1.36E + 5	2.42E + 6	1.33E + 5	1.69E + 6
44	1.87E + 5	3.05E + 6	1.76E + 5	2.89E + 6
45	3.73E + 4	5.44E + 5	3.52E + 4	9.48E + 5
46	1.61E + 4	1.68E + 5	1.25E + 4	3.36E + 5
47	2.26E + 4	3.54E + 5	9.47E + 3	1.62E + 5
48	2.40E + 4	3.79E + 5	1.39E + 4	2.73E + 5

does not know what to assume for the activity between measured points. The simplest assumption is that the activity is constant for the entire magnet length, and so the total loss is proportional to the sum of the 100 standard foils, and the loss following the target is equal to the sum of seven or eight standard foils at and downstream from the target. It actually turns out that more than half of the summed activity of the 100 foils is accounted for by just two foils, the one nearest the target at magnet 32 and the one nearest the clipper, which for all but one run was at magnet 79. We summed the activities in groups of ten, so the target group was from magnets 31 through 40. However, for the clipper at magnet 79 the sums were from 71 through 90, the extra magnets changing the sum very little. Inspection of Fig. V-4 shows that these sums include all the detectors downstream from the target and clipper whose activity was raised above background by the target and clipper.

For run I we had only the standard positions, but had sulfur on the vacuum tank, and sulfur and aluminum detectors in buckets 1.74 m above the beam line and spaced at the standard intervals of one location per magnet. Table VB lists the fraction of the summed activities for these detectors. The proton momentum was 26.4 GeV/c.

Table VB. Run I, 100 standard positions.

Detector	Target loss $\frac{\Sigma_{31\text{-}40}}{\Sigma_{1\text{-}100}}$	Clipper loss $\frac{\Sigma_{71\text{-}90}}{\Sigma_{1\text{-}100}}$	Target and clipper loss	Quiet-area loss
Al, vacuum chamber	0.513	0.420	0.933	0.067
S, vacuum chamber	0.477	0.448	0.925	0.075
Al, bucket	0.560	0.299	0.859	0.141
S, bucket	0.515	0.308	0.823	0.177

Inspection of the table shows that, at each location, the sulfur and the aluminum detectors yielded similar sums, which they should, since their response functions are similar. The loss pattern was different as observed from the bucket-position values as compared with the vacuum-pipe values; in fact the loss in the quiet region was about double. This might be a consequence of some combination of angular distribution of cascade particles with their attenuation in going from the beam pipe to the buckets, but the reason was not clear. Using either set of data, one would be gratified at how effective the clipper was in reducing the losses in the quiet or nontarget areas.

Actually the results above were all in error, because the detectors were too widely spaced. The spacing in the high-loss regions near the target and clipper was reduced from 6.3 m to some 1 m, and the activity between detectors was assumed to be given by a linear interpolation between the measured points.

The losses for run II as deduced from the 100 standard aluminum foils on the vacuum tank were:

$$\text{target loss} = \Sigma_{31\text{-}40}/\Sigma_{1\text{-}100} = 0.407$$

$$\text{dump loss} = \Sigma_{71\text{-}90}/\Sigma_{1\text{-}100} = 0.460$$

$$\text{target and dump loss} = 0.867$$

$$\text{quiet-area loss} = 0.133.$$

In this run we deduced from the vacuum-pipe fine-structure foils in the target and clipper areas that the sums above had to be multiplied by 0.772 for the target loss, 0.293 for the dump loss, and 1.0 for the quiet-region loss. This last factor was established in later runs when more fine-spacing foils were distributed about the quiet region. Thus we obtain the total loss:

target loss	$\propto$ 0.407 X 0.772	= 0.314 → 0.539 total loss
dump loss	$\propto$ 0.460 X 0.293	= 0.135 → 0.232 total loss
quiet-area loss	$\propto$ 0.133 X 1	= 0.133 → 0.229 total loss
total loss	$\propto$	0.582 → 1.000

Therefore, for run II and vacuum-pipe detectors the total loss in the target and dump regions is 77% and in the quiet areas is 23%.

We also placed buckets in the target and dump areas with close spacing in run II and later runs. However, we could not have the close spacing for the buckets in addition to the 100 standard bucket positions, and in later runs the buckets were placed with close spacing over the target and clipper regions with some 10 to 20 additional standard spacings.

In run II, for sulfur in buckets, we deduced that the target loss as calculated from the standard positions had to be multiplied by 0.831, and the clipper area loss by 0.623. If we apply these correction factors to the data from run I (the running conditions were made as similar as possible), we get the following loss-distribution picture for run I:

target loss	$\propto$ 0.515 X 0.831	= 0.428 → 0.537 total loss
dump loss	$\propto$ 0.308 X 0.623	= 0.192 → 0.241 total loss
quiet-area loss	$\propto$ 0.177 X 1	= 0.177 → 0.222 total loss
total loss	$\propto$	0.797 → 1.000

The total loss for run I and with detectors placed in buckets near the ceiling and above the magnets is 78% in the target and dump regions and 22% in the quiet area. Agreement between these loss patterns and those deduced in run II above show that when the detectors are placed close enough together, one obtains the same general picture from detectors on the vacuum pipe as above the magnets.

Since the flux is greater at the vacuum chamber and one can more easily place a large number of samples there, the beam-pipe detectors were used in each run as beam-loss monitors. (The CERN Health Physics Group increased the number of aluminum detectors they could process from run to run until, at the end of the program, they counted 300 such foils.)

Using the aluminum detectors on the vacuum chamber with standard spacing in the quiet areas and fine spacing in the target and clipper areas, we obtain the beam-loss distributions listed in Table VC.

Table VC. Beam-loss distribution on the vacuum chamber.

Run	p (GeV/c)	Target loss	Clipper loss	Quiet-area loss
II	26.4	0.54	0.23	0.23
III	26.4	0.66	0.22	0.12
IV	26.4	0.70	0.19	0.11
V	26.4	0.62	0.25	0.13
VI	14.6	0.52	0.19	0.29
VI 1/2	14.6	0.53	0.26	0.21
VII	14.6	0.50	0.22	0.28
VIII	14.6	0.40	0.31	0.29

For the later runs we were able to obtain fine-spacing data for some 20 to 30 magnets in the quiet, or low-loss, areas.

C. Fine-Structure Details

Figure V-6 shows the aluminum detector data in the target area in which the effect of the gap between the magnet ends can be seen. The line representing the exponential decrease in source strength is the analytic representation used in our calculation model and is discussed in Chapter VIII.

Figure V-7 shows the distribution of standard foil activity through the quiet and target areas, together with the activity distributions per magnet as deduced from the fine-spacing foils which were used in this run, run VII. One concludes that the loss distribution in the quiet area does not fluctuate as widely from magnet to magnet as the standard foils would indicate, but the loss is by no means uniform around the ring.

To achieve even greater spatial resolution than that discussed above, spacings of 10 cm for sulfur detectors and of 20 cm for 600-MeV-threshold Au → Tb detectors were used immediately downstream of the target for approximately 1 m. Figure V-8 shows neutron fluxes determined from the S activity and the Au → Tb activity.

D. Loss as a Function of Polar Angle

Figure V-9 represents a cross section of the CPS vacuum chamber with four aluminum monitor foils placed around the chamber. The polar angle is measured between a horizontal line from the beam orbit toward the center of the ring and a line from the beam orbit toward the point of interest on the vacuum chamber. The top position a, for which $\Phi = 90$ deg, is the standard vacuum-chamber monitor position. The question to be answered is, is the loss at the top of the chamber representative of the loss at other places around the chamber, or can the loss be many times greater elsewhere? Since the aluminum detectors respond to relatively low-energy neutrons, greater than some 6 MeV, it was felt that the losses around the chamber would be relatively uniform, and that the standard monitors would be representative of the losses around the chamber.

In four separate runs we exposed aluminum monitor foils as illustrated in the diagram above. The activation data in units of $pCi\text{-}g^{-1}$ and these activities relative to that at the standard position, a, are listed in Tables VD through VG. When hundreds of foils are simultaneously exposed and counted, there is always the possibility that one or two foils can be miscounted, mislabeled, or misplaced. In Table VD, location 32d, the data point seems suspect. In Tables VF and G, the points 19d are in excellent agreement with one another and indicate that, in this location, the loss to the inside of the ring is much larger than in the other directions. For all the other locations, the aluminum activation varies little with polar angle, less than a factor of 2. There seems to be more activity toward the inside of the ring position d, as compared with position b, but the standard position a generally lies between these values. On the basis of the tabulated data, we conclude that foils on top of the vacuum chamber yield activities proportional to neutron flux around the vacuum chamber.

E. Beam-Loss Distribution from FLUX Program

The experimental data points have been fitted by an analytic model through the FLUX program, as discussed in Chapter VIII. In this model the source term is taken to be a constant around the ring plus an exponential starting at the target and decreasing with distance downstream. The height and relaxation length of this exponential, together with other variables, are allowed to change until a best fit is achieved. The results are not especially sensitive to the values involved with the exponential source term. If few data points are available, this source term evaluation is especially uncertain. Keeping these caveats in mind, one does get some information on beam loss through this procedure.

To compare the FLUX results with the aluminum monitor foil results of Table VC we must subtract the clipper-loss portion of the loss distribution. For example, in run II the sum of the target, clipper, and quiet-area losses is 0.54 + 0.23 + 0.23 = 1.00. From this we have

$$\eta_{\text{target}} = \frac{\text{target loss}}{\text{target + quiet-area loss}} = \frac{0.54}{0.77} = 0.70.$$

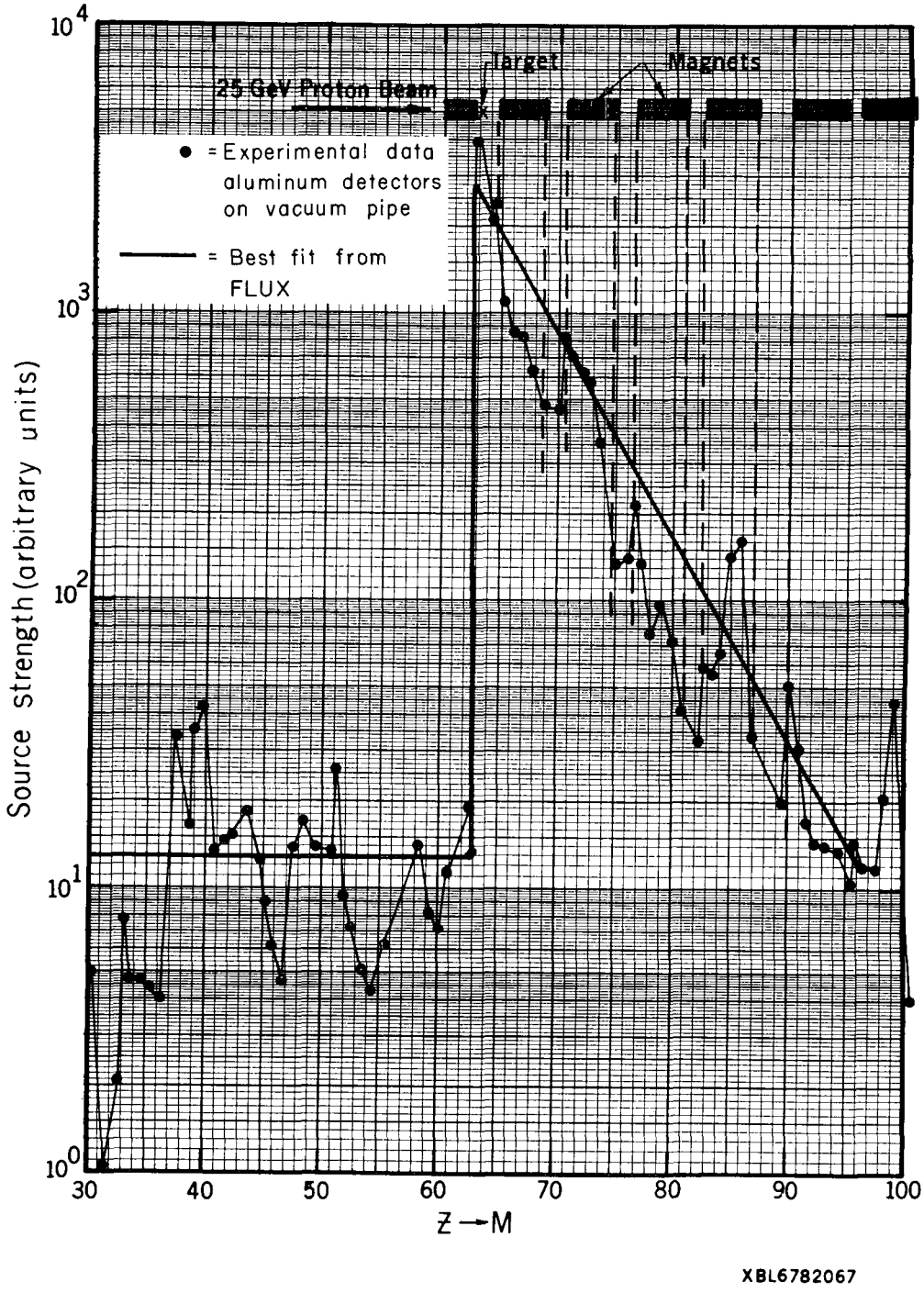

Fig. V-6. Fine-structure details in target vicinity, comparing measured aluminum-foil activities with beam-loss model used in FLUX program.

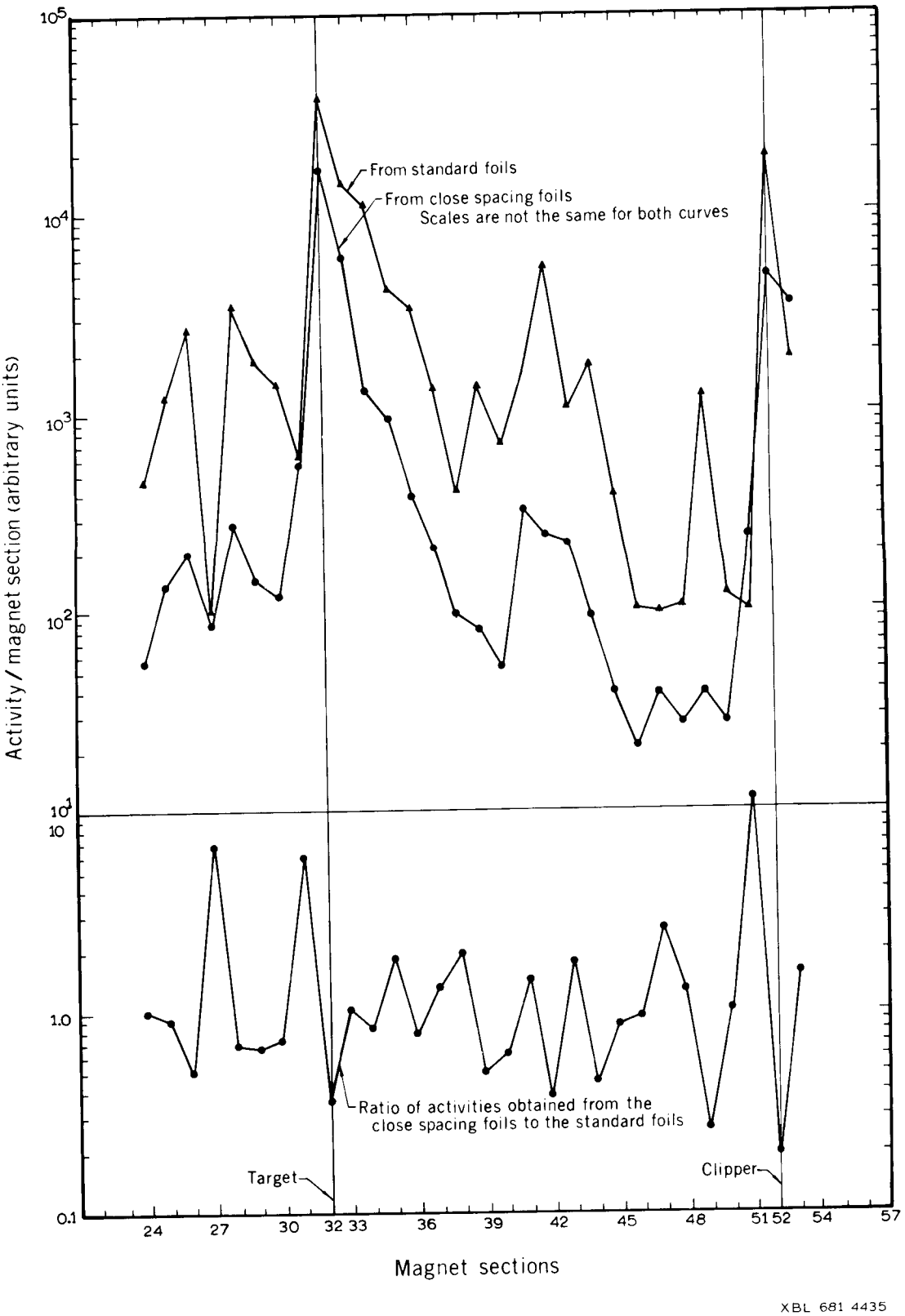

Fig. V-7. Comparison of standard foil activities with close-spacing foil activities at both target and quiet areas.

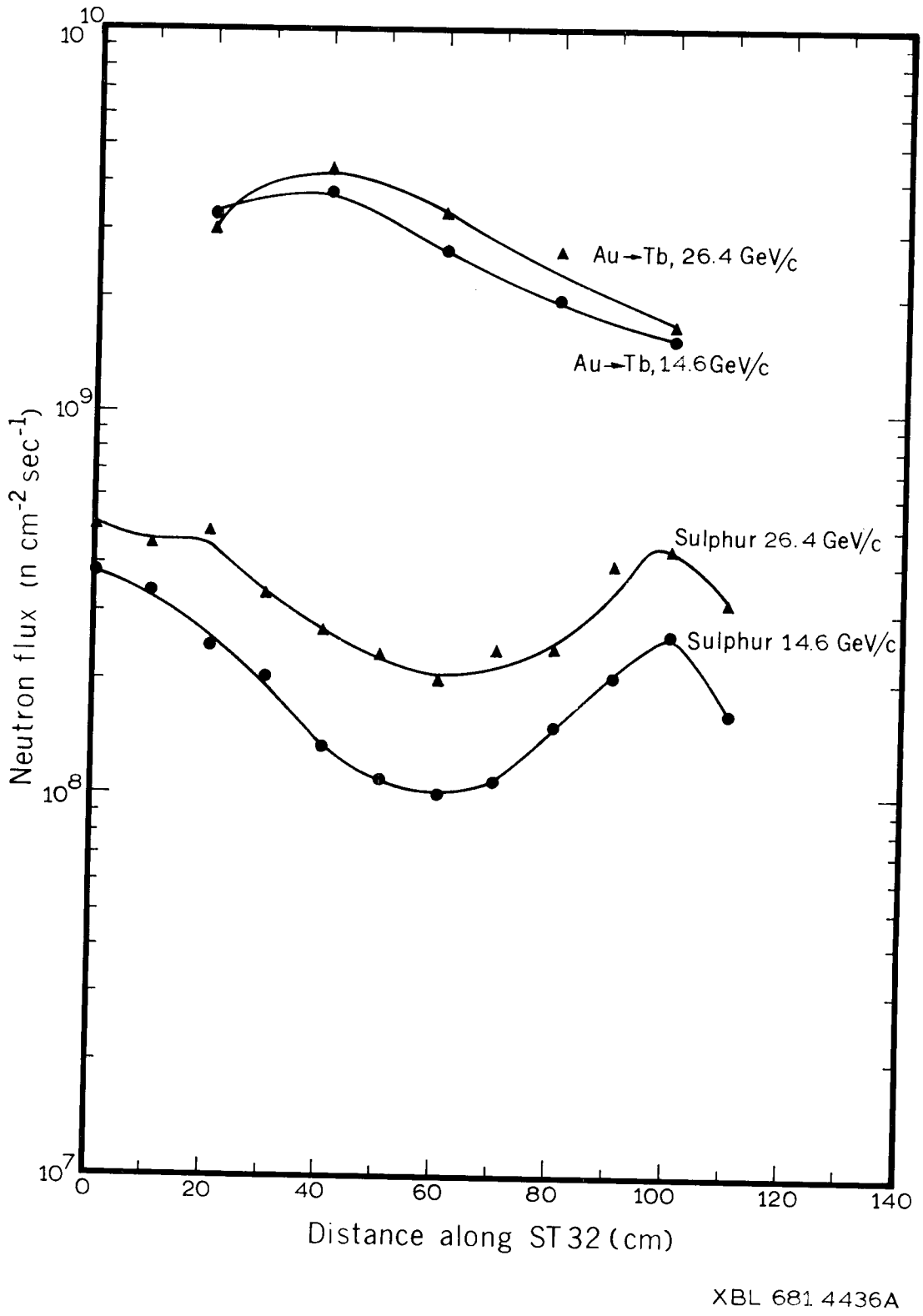

Fig. V-8. Neutron fluxes measured with sulfur and Au → Tb^{149} detectors on vacuum chamber immediately downstream from target 32.

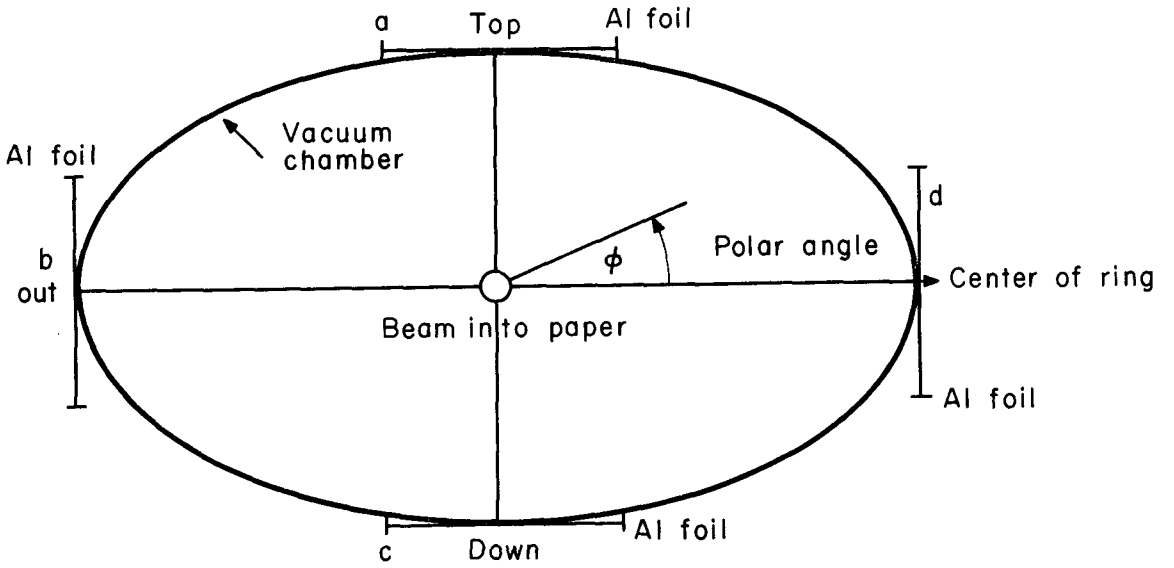

XBL 689-6835

Fig. V-9. Cross-section diagram of CPS vacuum chamber, showing placement of aluminum foil detectors around the chamber.

Table VD. Measured activities in aluminum foils exposed around the vacuum chamber, run IV, October 18, 1966; 26.4 GeV/c; target at 32.

Location	Activity (10^4pCi-g^{-1})	Relative activity
32 a	6673	1.00
32 b	3728	0.56
32 c	4603	0.69
32 d	533	0.08
33 a	613	1.00
33 b	680	1.11
33 c	433	0.71
33 d	914	1.49
33^{B}_{a}	852	1.00
33 b	721	0.85
33 c	912	1.07
33 d	879	1.03
34^{B}_{a}	256	1.00
34 b	206	0.80
34 c	250	0.98
34 d	280	1.10
35^{B}_{a}	76.1	1.00
35 b	96.3	1.27
35 c	71.0	0.93
35 d	115.4	1.52

Table VE. Measured activities in aluminum foils exposed around the vacuum chamber, run IV-1/2, October 31, 1966; 19.2 GeV/c; Targets not near M32.

Location	Activity (10^4 pCi-g^{-1})	Relative activity
32 a	5.85	1.00
32 b	5.99	1.02
32 c	4.95	0.85
32 d	7.49	1.28
33 a	32.2	1.00
33 b	14.2	0.44
33 c	31.0	0.96
33 d	42.0	1.30
34^B_a	6.20	1.00
34^B_b	4.06	0.65
34^B_c	5.01	0.81
34^B_d	5.66	0.91

Table VF. Measured activities in aluminum foils exposed around the vacuum chamber, run VI, November 16, 1966; 14.6 GeV/c; target at M32.

Location	Activity (10^4 pCi-g^{-1})	Relative activity
19^B_a	41.4	1.00
19^B_b	21.3	0.51
19^B_c	30.6	0.74
19^B_d	214.3	5.18
32 a	2330	1.00
32 b	1761	0.76
32 c	2634	1.13
32 d	1880	0.81
36^B_a	22.5	1.00
36^B_b	14.2	0.63
36^B_c	20.8	0.92
36^B_d	16.7	0.74
60 a	144.2	1.00
60 b	72.1	0.50
60 c	75.1	0.52
60 d	81.5	0.57

Table VG. Measured activities in aluminum foils exposed around the vacuum chamber, run VI-1/2, November 18, 1966; 14.6 GeV/c; target at M32.

Location	Activity (10^4 pCi-g^{-1})	Relative activity
19^B_a	54.1	1.00
19^B_b	30.3	0.56
19^B_c	43.7	0.81
19^B_d	303.5	5.61
32 a	2486	1.00
32 b	1822	0.73
32 c	2416	0.97
32 d	1789	0.72
36^B_a	25.0	1.00
36^B_b	21.3	0.85
36^B_c	19.1	0.76
36^B_d	19.6	0.78
60 a	144.3	1.00
60 b	65.8	0.46
60 c	68.2	0.47
60 d	69.3	0.48

The FLUX results are shown in Table VH. The target efficiencies deduced from the vacuum-pipe foil monitors and from the other detectors as fitted through the FLUX program seem to be in reasonable agreement. For the reasons stated above this agreement cannot be expected to be truly quantitative.

F. Radiochemical Determination of Target Efficiency

The target configuration used in all runs is shown in Fig. V-10. The primary beam passed through a 100-μ thick beryllium foil and three aluminum monitor foils of 50-μ total thicknesses. The central 30-μ foil was γ-counted with a NaI-crystal spectrometer and the Na^{22} and Na^{24} activity produced from the aluminum was measured. From the measured activity, the thickness of the target, and the cross section for this reaction, one can calculate the number of primary protons that passed through the target. From the PS beam monitoring, one can determine the total number of protons that were accelerated in a given run. The ratio of these two numbers is the equivalent number of times each proton passed through the target before being lost, the number of multiple traversals. From the number of multiple traversals and the total cross sections of the target materials, one can calculate the number of interactions in the target and presumably the number of protons lost in the vicinity of the target. This leads to a determination of the target efficiency that can be compared with the efficiencies calculated earlier in this chapter.

In Table VI the fractional losses downstream from the target, or target efficiencies, as determined from this technique are compared with those from the aluminum vacuum-tank foils.

Table VH. FLUX results on beam-loss distribution

Run No.	$\eta_{Vac.\ pipe}$	η_{FLUX}	Detector Location	Detector Type	Comments
I	0.69	0.47	surface	C	Coarse spacing, 6.3 meters, was used for all detectors
		0.74	surface	Al	
		0.85	bucket	C	
		0.78	bucket	Au	
		0.95	bucket	Al	
		0.98	bucket	S	
		0.94	bucket	TLD	
II	0.70	0.67	orbit holes	C	
		0.71	orbit holes	Al	
		0.62	bucket	C	
		0.71	bucket	Al	
		0.75	bucket	S	
III	0.85	0.28	surface	Au	Very few detectors were exposed
IV	0.86	0.52	orbit holes	Al	Few detectors were exposed
V	0.83	0.75	surface	C	
		0.70	orbit holes	Al	
		0.50	bucket	Al	
VI	0.64	0.59	orbit holes	Al	
		0.47	bucket	Al	
VII	0.64	0.20	surface	Au	Very few detectors
		0.76	orbit holes	C	
		0.68	orbit holes	Al	
		0.71	bucket	C	
		0.44	bucket	Au Mod	Very few detectors
		0.47	bucket	Au	Very few detectors
		0.52	bucket	Al	
		0.51	bucket	S	
VIII	0.58	0.74	bucket	Al	
		0.33	bucket	S	

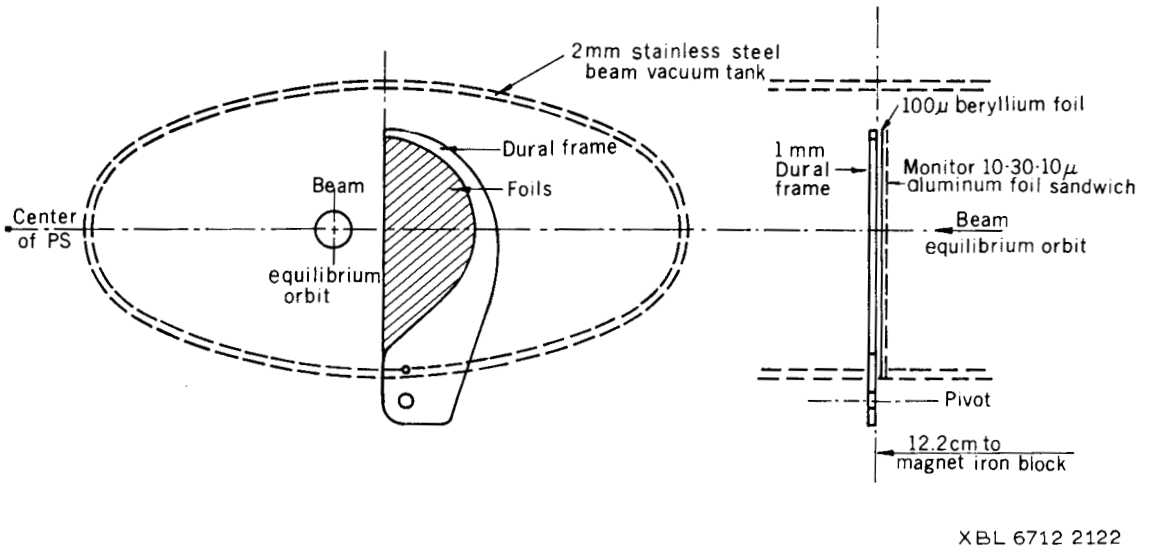

Fig. V-10. Detail of the target head.

Table VI. Beam loss near the target.

Run	p (GeV/c)	Target loss, Al chamber foils	Target loss, radiochemical
II	26.4	0.54	0.34
IV	26.4	0.70	0.53
VIII	14.6	0.40	0.54

At the higher beam momentum, the two methods of determining target efficiency are not in good agreement. At the lower beam momentum, the numbers are in good agreement. We have not attempted to assign errors to these calculated efficiencies, since a fairly long chain of reasoning is involved in deducing target efficiencies from the radiochemical technique, as shown below.

We define P_A as the probability of a proton's activating the monitor foil; P_T as the probability of a proton's interacting in the target (removal); P_L as the probability of a proton's being removed in going around the accelerator once. From known cross section, we can calculate P_A, as well as P_T, which includes P_A. However, P_L, which includes P_T, is not calculable and must be measured in some manner.

On the first proton trip around the accelerator (shown diagramatically below), we have activation$_1$ = P_A and target interaction$_1$ = P_T.

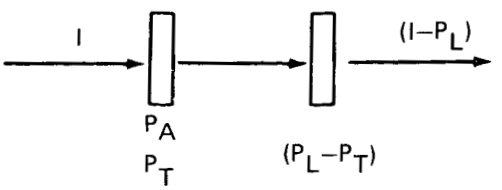

On the second circuit, we have activation$_2$ = P_A $(1-P_L)$ and interaction$_2$ = P_T $(1-P_L)$.
Therefore, total activations = P_A $[1 + (1-P_L) + (1-P_L)^2 + \cdots] = P_A/P_L$
and total target interactions = P_T $[1 + (1-P_L) + (1-P_L)^2 + \cdots] = P_T/P_L$.

From the beam monitor one obtains the number of protons accelerated = N_{beam}. From the radiochemical analysis of the monitor foil (which determines P_A) one obtains N_{target}, the number of protons that have passed through the target. Using N_{target} and N_{beam}, we have

M = number of multiple traversals = $\frac{N_{target}}{N_{beam}} = \frac{1}{P_L}$. The target efficiency, η, is the probability that the circulating proton interacts or is removed at the target in one complete revolution, i.e.,

$$\eta = \frac{P_T}{P_L}.$$

G. Cerenkov Counters and Operation of a Beam Clipper

The control of beam losses far from the target through the use of a beam clipper, or collimator, located more than a betatron wave length from the target has been discussed by Hereward et al.[HerH 65] The clipper we used is shown in Fig. V-11 and was placed at straight section 79 in all but one of our runs. Two Cerenkov counters ($\hat{C}$) were placed downstream of the target at straight section 32 and of the clipper at straight section 79 and were adjusted to count relativistic secondaries from these sources, the counting rates being proportional to the primary beam interacting in the target and clipper. The clipper was moved into the beam until the target $\hat{C}$ counter had its counting rate reduced about 10%. This condition was supposed to yield the greatest reduction in the random beam losses away from the target and clipper, as calculated by Richter.[RicW 66] Because the $\hat{C}$ counting rates were only modest, and the beam orbit was not perfectly constant in time, the fraction of the beam intercepted by the clipper varied somewhat.

An idea of how effective the clipper was can be obtained as follows: From Table VC, run IV, we have:

target loss = 0.70

clipper loss = 0.19

quiet area loss = 0.11.

When the clipper was not used, for the same circulating beam, the target $\hat{C}$ counter increased its counting rate by 10%. Then:

target loss = 1.1 (0.70) = 0.77

clipper loss = 0

quiet-area loss = 0.23.

This quiet-area loss of 0.23 is approximately double the quiet-area loss of 0.11 when the clipper was used. Likewise, for the other runs, the use of the clipper reduced the random losses in the quiet areas to about half that without the clipper. This is a useful reduction but considerably less than that expected from theory for an idealized accelerator.[HerH 65]

J. Ranft performed a beam loss Monte-Carlo calculation for the target, clipper, and beam conditions that we actually used in our runs.[RanW 67] The results of his calculation together with the measured vacuum tank aluminum monitor foils are shown in Figs. V-12 and V-13. Although there is encouraging agreement in the qualitative behavior, or shape, of the calculated and experimental results, agreement is by no means quantitative. Considerably more effort is required, both theoretical and experimental, before one can design collimators that will reduce the random quiet-area loss to truly low values, say 5% or less of the interacting primary beam.

H. Conclusions

From the information developed in the preceding sections we have been lead to the following conclusions concerning the distribution of beam loss around the CPS:

1. One obtains approximately the same loss distribution around the accelerator for different activation detectors and for different placement of these detectors, viz., on the vacuum chamber, at the ceiling of the enclosure, in the earth shield, and on top of the earth shield. For convenience, aluminum detectors on the vacuum chamber were most extensively used to monitor beam loss.

2. Close spacing, of the order of 1 meter, is required in the high-loss regions in order to obtain sufficient spatial resolution to make a quantitative estimate of beam loss.

3. Although the accelerator operating conditions and beam-orbit dynamics changed somewhat from run to run, we found the beam-loss distributions quite constant from run to run, especially in the location of isolated high-loss regions far from the target and clipper.

4. Loss distributions as determined from performing line integrals of the detector activities around the ring did not agree with target-efficiency calculations using radiochemical analysis of the target. Theoretical, and perhaps more experimental, effort seems to be required in this area.

5. Clipper performance seemed promising in that it decreased the random losses by about a factor of two. However the control of these losses was not as effective as had been hoped for. More theoretical and experimental effort might result in even smaller random losses in the quiet areas.

6. With the target and clipper that were used in our series of experiments, the quiet-area loss at approximately maximum energy was $\approx$ 15%, and at half energy the loss was $\approx$ 25%. Without detailed orbit calculations one might then assume for a first approximation, that a new accelerator using a clipper in addition to a primary loss point (such as an extraction septum) would have some 15% of the interacting beam distributed fairly uniformly over the quiet areas of the machine.

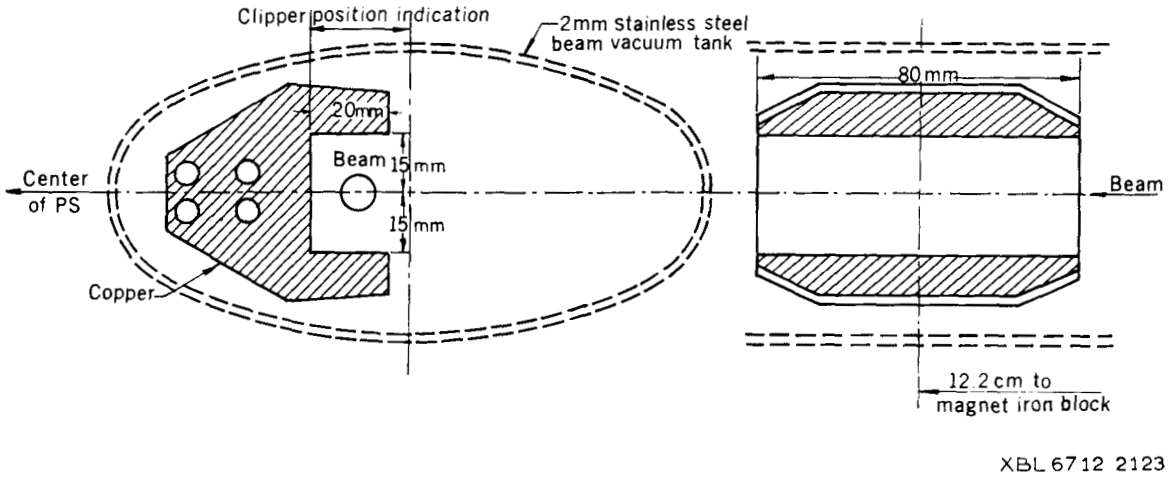

Fig. V-11. Detail of the beam clipper.

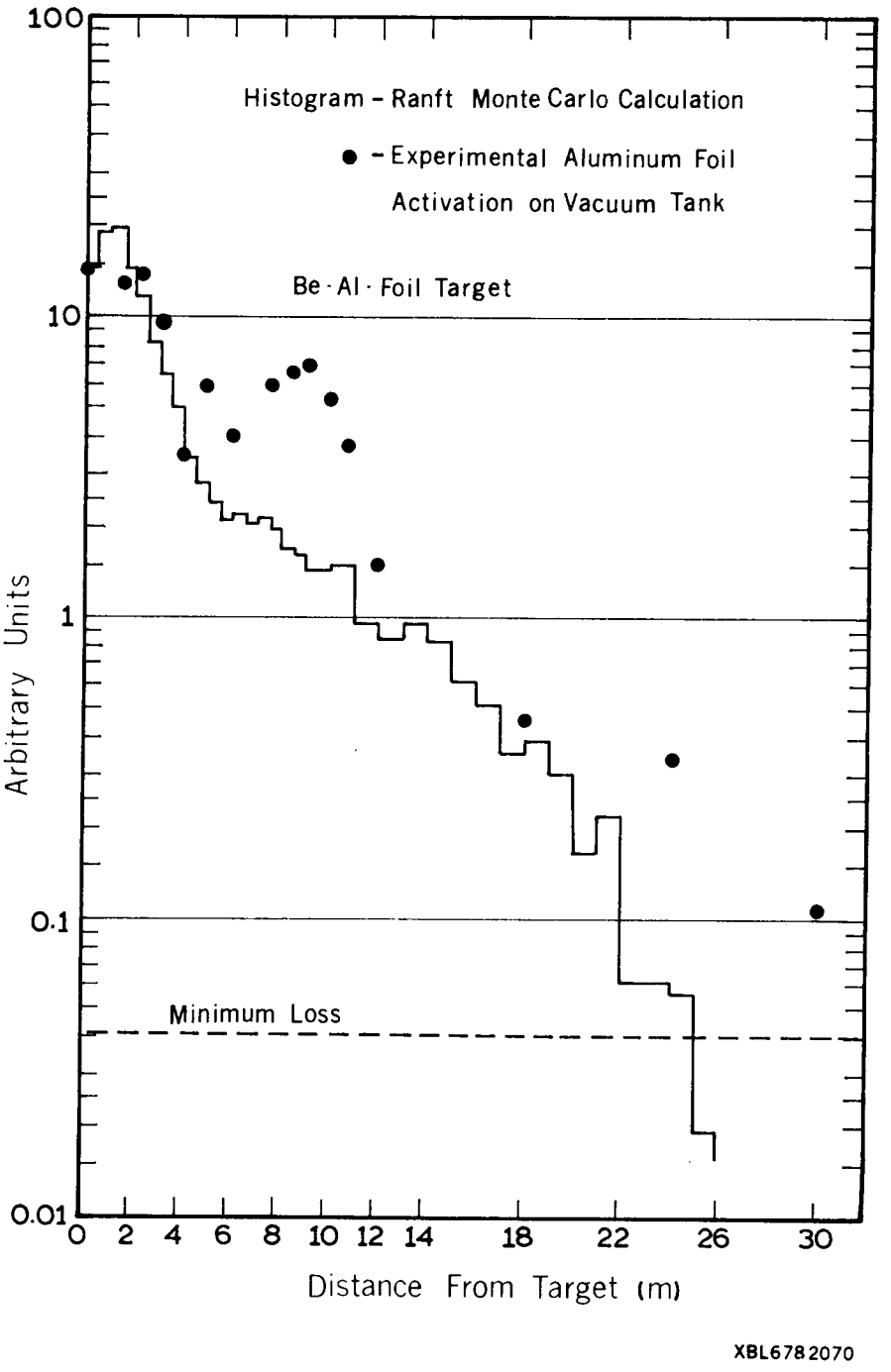

Fig. V-12. Comparison of measured vacuum-chamber aluminum-foil activities with Ranft's beam-loss calculation for target area.

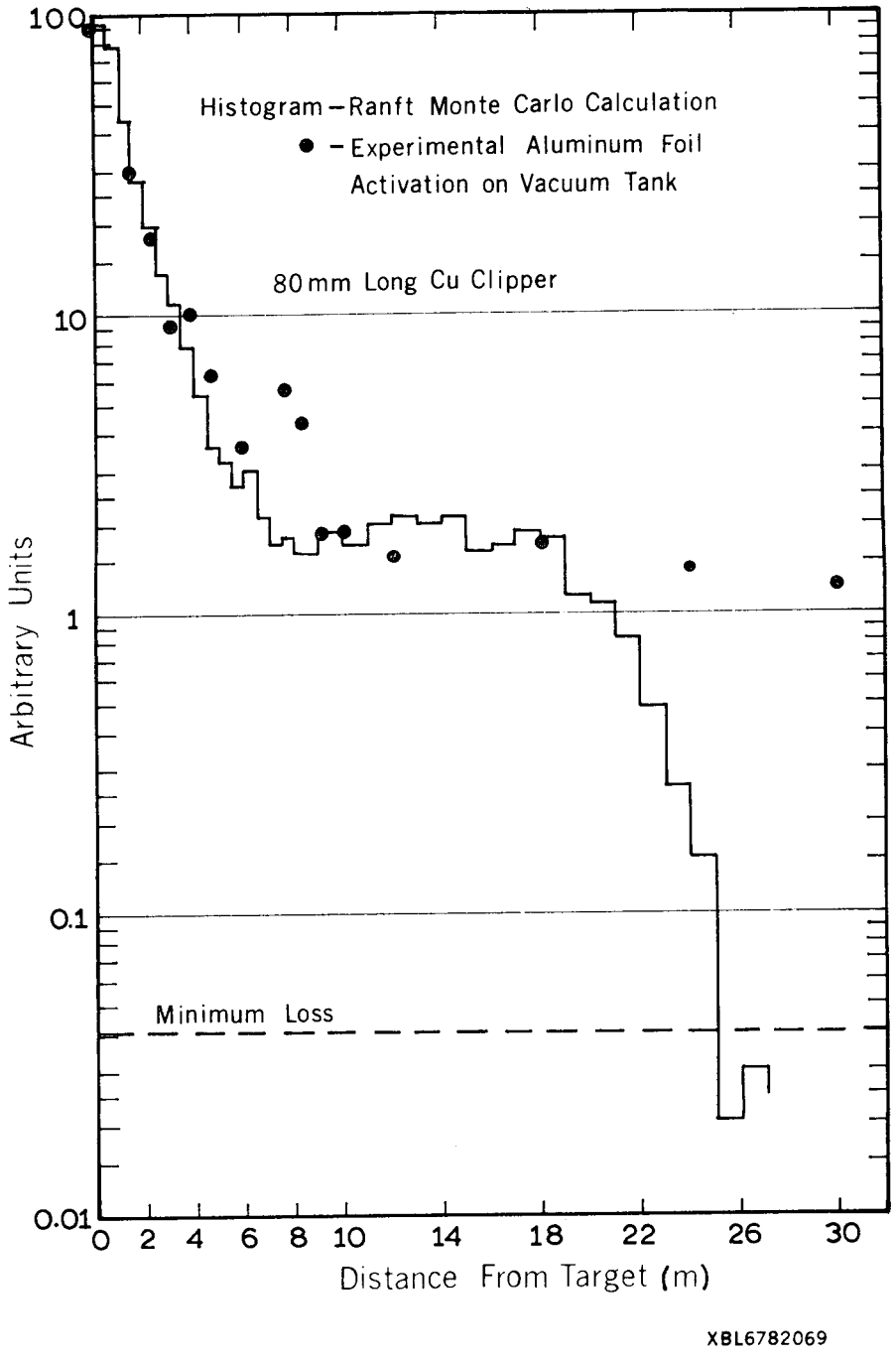

Fig. V-13. Comparison of measured vacuum-chamber aluminum-foil activities with Ranft's beam-loss calculation for clipper area.

References

HerH 65. H. G. Hereward, J. Ranft, and W. Richter, Efficiency of Multitraversal Targets, CERN 65-1, January 6, 1965.

RicW 66. W. Richter, CERN, private communication.

RanJ 67. J. Ranft, Monte-Carlo Calculation of Particle Loss Distributions Along the Vacuum Chamber of the CPS Near Internal Targets and of the Transverse Attenuation of Strongly Interacting Particle Fluxes in the P.S. Magnet Units and Earth Shield, CERN Internal Report MPS/Int. MU/EP 67-5, June 20, 1967.

VI. ANGULAR DISTRIBUTION OF RADIATION NEAR INTERNAL TARGETS

A. Relative Detector Activation

We attempted to measure the angular distribution of radiation produced in the thin Be-Al target by placing various activation detectors at a constant radius from the target, at various angles from the beam direction. A lightweight detector holder of foamed plastic was used, as can be seen in Fig. VI-1. It was assumed that virtually all the radiation would issue from the internal target, and the relative fluxes in a given type of detector would be a measure of the angular distribution for the component of the radiation field to which that detector responds. For run V the primary proton momentum was 26.4 GeV/c, and the various angular detector data are shown in Fig. VI-2, with the detectors 100 cm from the target. Qualitatively, the curves have the correct behavior in that the higher-energy-threshold detectors display the most forward-peaking distributions and the lowest-energy-threshold, sulfur, has the flattest distribution. As can be seen from Fig. VI-1, magnet 31 is immediately upstream of the target, restricting the angular range covered to 3 to 90 deg.

Data were also taken 25 cm from the target; these are shown on Fig. VI-3. If all the radiation came from the target, the fluxes at a given angle would have an inverse-square distance relationship, or the fluxes at 25 cm should be 16 times those at a 100-cm radius at the same angles. The ratios of the fluxes at 25 cm and 100 cm are shown in Fig. VI-4. One sees that much of the radiation is not from the target, with the possible exception of the 600-MeV threshold Hg → Tb. Therefore the angular distribution of Figs. VI-2 and VI-3 are not those from a point source. What is actually measured is a folding of an extended-source distribution and a point-source angular distribution. For a uniform line source with any given angular distribution, the ratio of the fluxes at two radii is the inverse first power of the radii, and this is about what is seen by the sulfur. For run VI the primary proton momentum was reduced to 14.6 GeV/c. Similar data were obtained; the ratios of the fluxes at 25 to 100 cm are shown in Fig. VI-5. The distributed source distribution is primarily due to the background contributed by beam interactions in the vacuum vessel and gradient magnet downstream of the target.

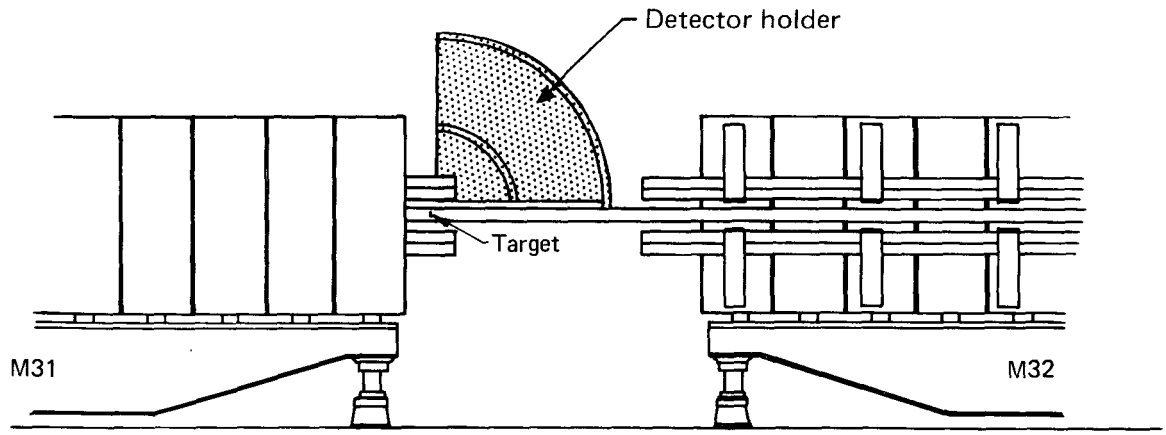

XBL682 4453

Fig. VI-1. Target 32 region, showing lightweight detector holder in position.

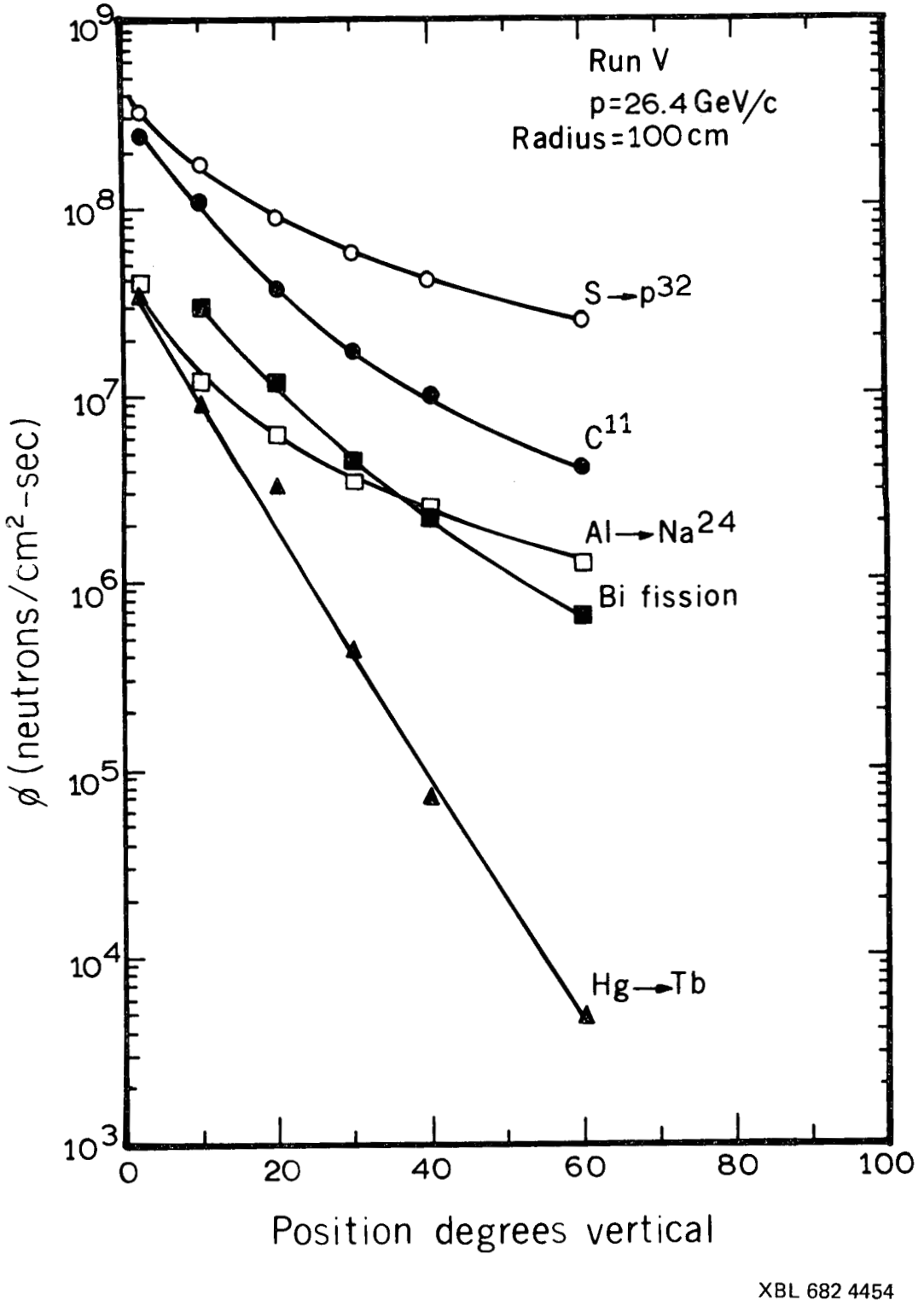

Fig. VI-2. Response of detectors on 100-cm arc at 26.4 GeV/c, Run V.

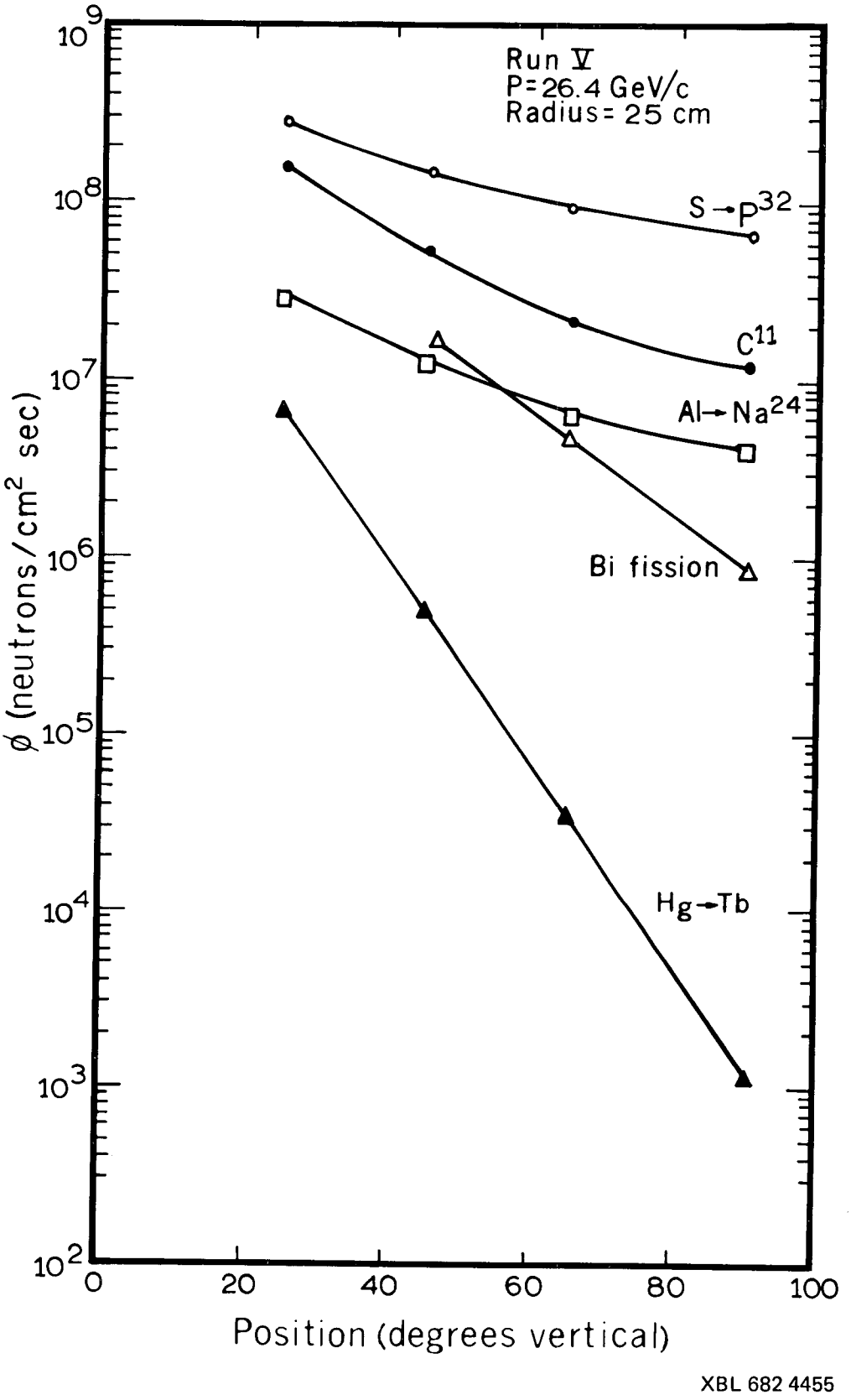

XBL 682 4455

Fig. VI-3. Response of detectors on 25-cm arc at 26.4 GeV/c Run V.

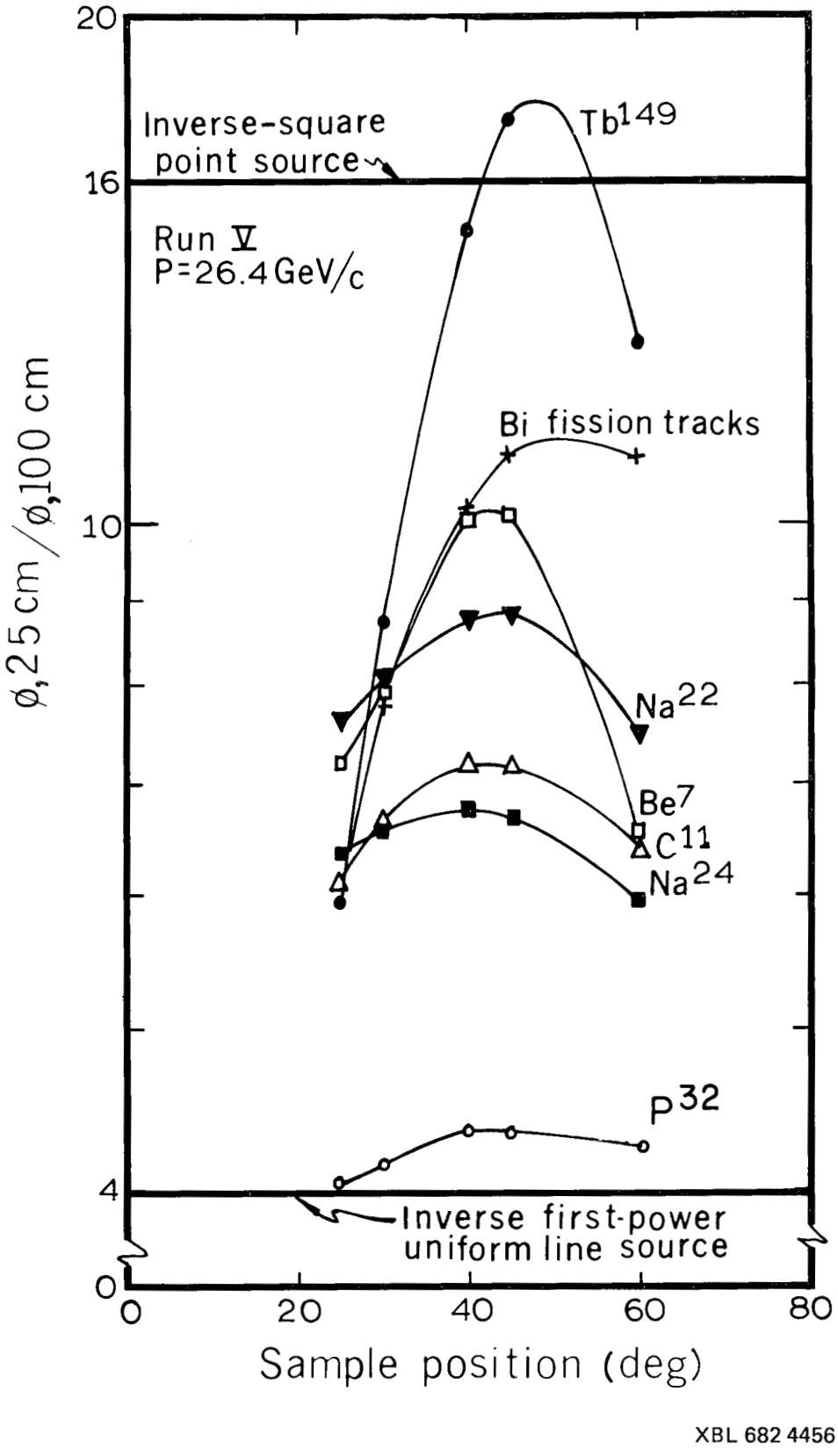

Fig. VI-4. Ratios of fluxes at 25-cm arc to fluxes at 100-cm arc, 26.4 GeV/c, Run V.

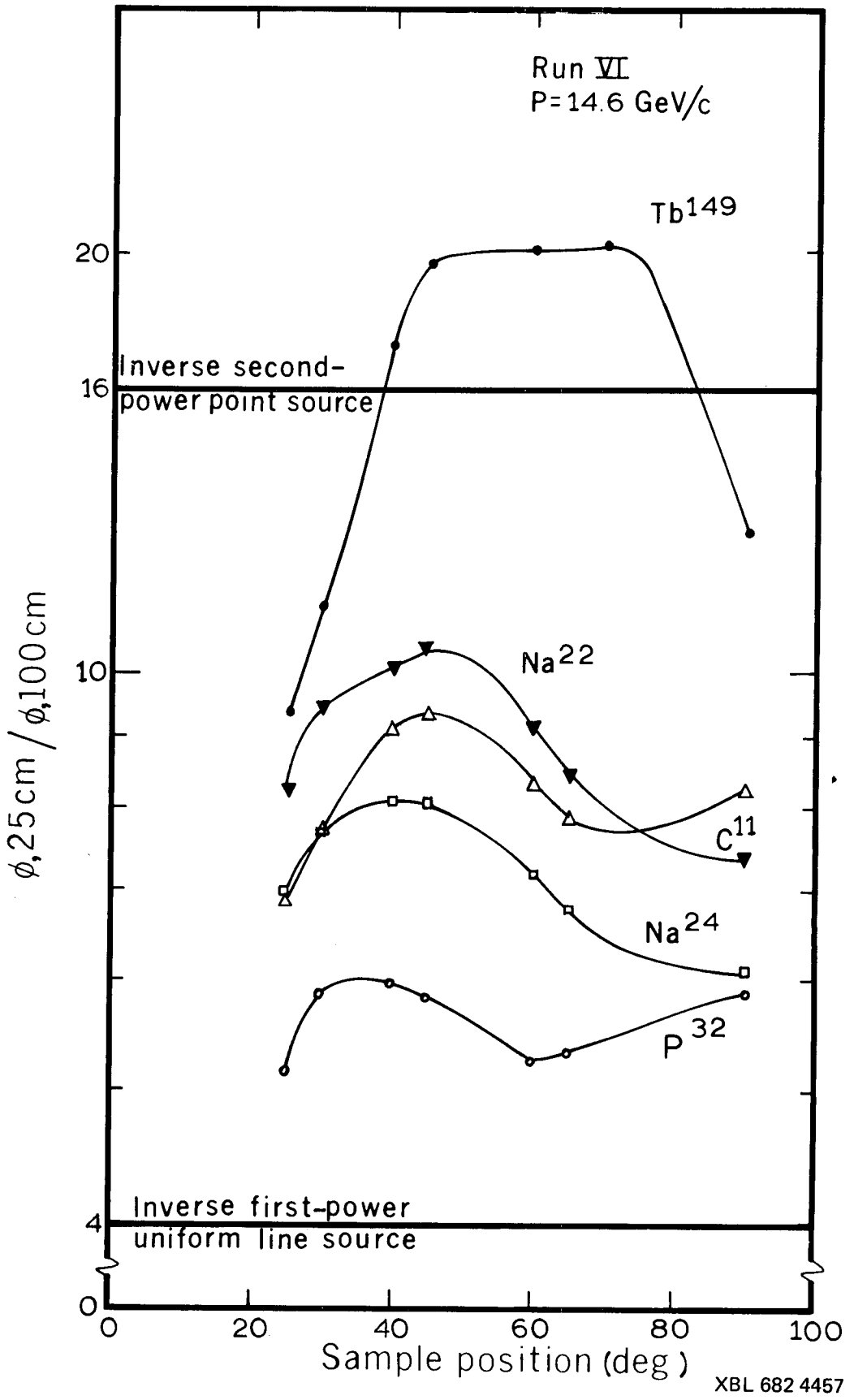

Fig. VI-5. Ratios of fluxes at 25-cm arc to fluxes at 100-cm arc, 14.6 GeV/c, Run VI.

B. Source Distribution

Our usual beam-loss monitor foils on the vacuum pipe (See Chap. IV) are spaced some 1 m apart. This resolution is too poor to yield details on beam loss immediately downstream of the target. In these angular-distribution experiments, runs V and VI, detectors were placed on the vacuum chamber immediately downstream of the target; low-threshold-energy sulfur detectors were placed every 10 cm, and the 600-MeV-threshold Au → Tb detectors every 20 cm downstream from the target for a distance of 1 m. The relative activities of the sulfur and the Au → Tb detectors are shown in Fig. VI-6. As discussed in Chap. V, one can not assume that the primary beam loss, or source, is simply proportional to the fluxes measured on the beam pipe. In this case particularly, these detectors receive secondaries from the target in addition to those from the beam pipe. There is no unique way to subtract out the contribution from the target, since the angular distribution we seek is required in order to make the subtraction. Rather, one must search for a self-consistent combination of source and angular distributions, that will agree with the measured data. Practically speaking, the data on the beam pipe serve to suggest a trial source function for fitting the other data. It is overly complex to compute the fluxes that would be produced by the physical vacuum chamber, which is an elliptical shell in cross section, and so we simplify the geometry to make all the beam loss occur in the center of the vacuum chamber, where none actually will occur except at the target. At distances from the vacuum chamber greater than the dimensions of the chamber, this approximation should not lead to appreciable error, but can not be expected to yield accurate results on the vacuum chamber itself.

C. Folding of Source and Angular Distributions

The geometry of both the experimental measurements is shown in Fig. VI-7. Referring to this figure we can calculate the folding as follows: The flux at any point (R,α) is

$$\Phi(R,\alpha) = \int_{Z_{min}}^{Z_{max}} \frac{S(Z)\,\Theta(\theta)}{\ell^2}\, dZ, \tag{1}$$

where S(Z) is the source distribution, and $\Theta(\theta)$ is the angular distribution. From Fig. VI-7 we see that

$$R\cos\alpha = Z + a, \tag{2}$$

$$R\sin\alpha = b, \tag{3}$$

$$\tan\theta = \frac{b}{a} = \frac{R\sin\alpha}{R\cos\alpha - Z}, \tag{4}$$

and

$$\ell^2 = a^2 + b^2 = R^2 + Z^2 - 2ZR\cos\alpha\,. \tag{5}$$

The integral in Eq. (1) must generally be evaluated by numerical methods.

Some simple examples are given below to illustrate the results of folding different source and angular distributions.

1. Case 1 -- Sulfur Neutrons

In this case the radiation from source S(z) is constant from Z = zero to Z = R, and is zero elsewhere. This corresponds to the sulfur and Au vacuum-pipe data. The angular distribution corresponds to isotropic emission, or $\Theta(\theta)$ = constant. The integral in Eq. (1) is numerically evaluated for several angles, and the result is plotted in Fig. VI-8 together with the measured activations of the low-threshold-energy sulfur detectors of run V. Agreement is quite good, and since an isotropic angular distribution was assumed in the calculation, one sees how large an error is made by assuming that the counting rate of such an experiment represents the angular distribution.

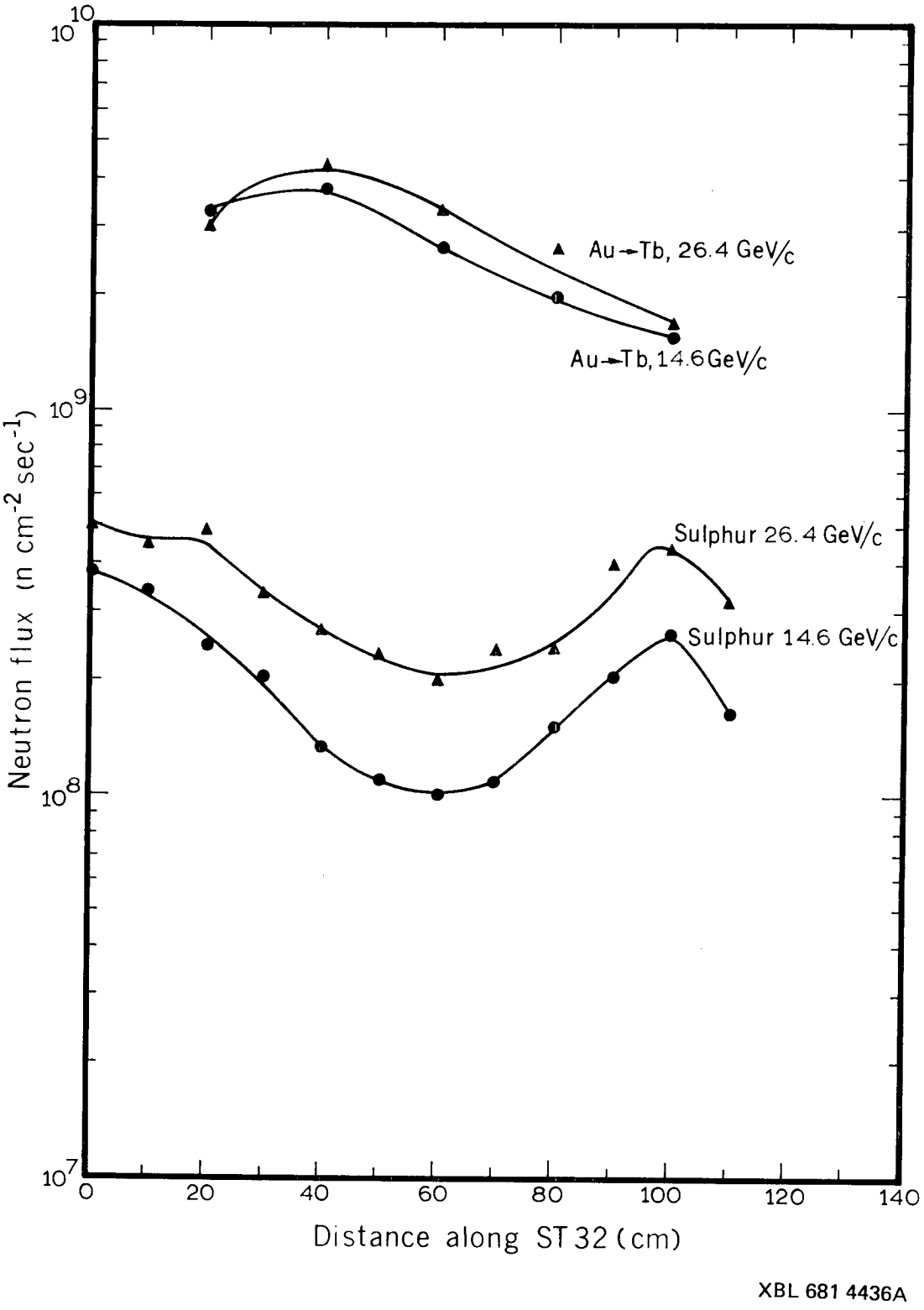

Fig. VI-6. Response of sulfur and Au → Tb^{149} detectors for positions on vacuum chamber immediately downstream from target 32.

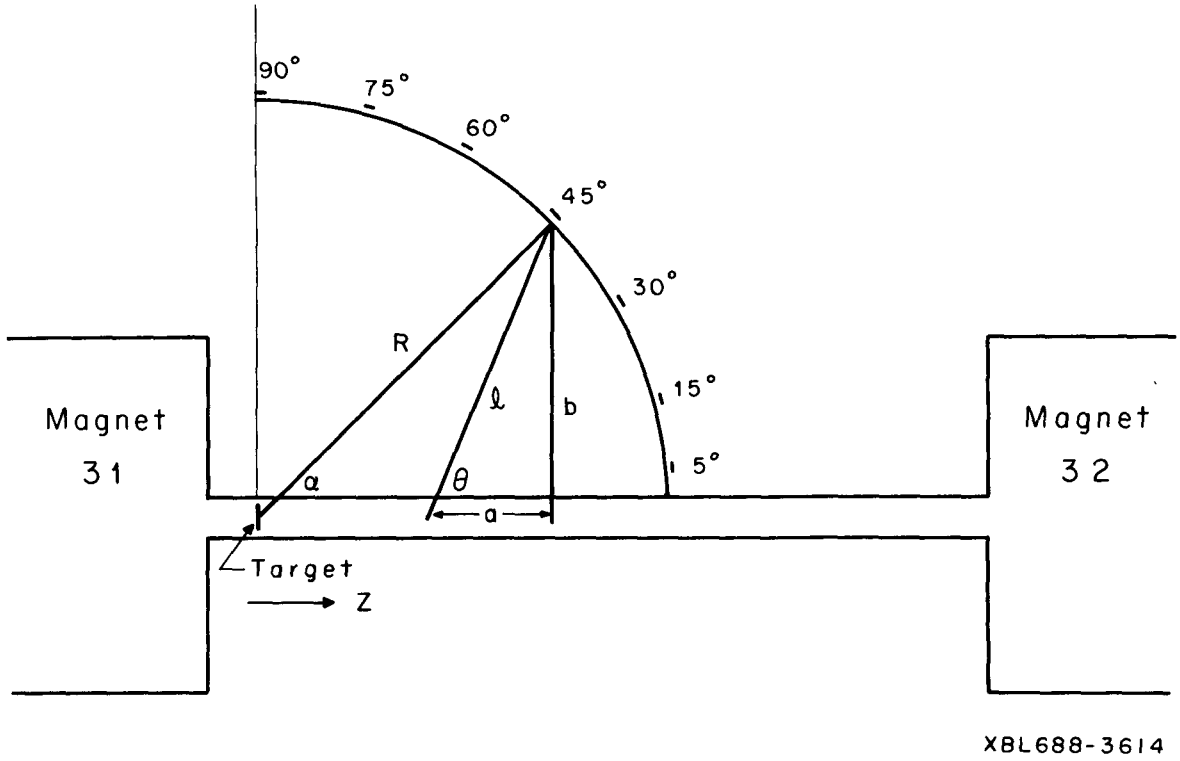

Fig. VI-7. Sketch of experimental layout, showing geometrical relationships used in derivation of angular distribution functions.

2. Case 2

Alternatively, we can assume that the relative activation vs angle data for sulfur (run V) is the correct angular distribution. Then, as in case 1, radiation from S(Z) is constant from Z = zero to Z = R, as measured. In Fig. VI-9 the result of this calculation is shown together with the experimental relative activation. The difference in shape of the two curves shows that the assumed angular distribution is not self-consistent, i.e., it does not yield the experimental results when folded with the constant source. This is not surprising, since we obtained good agreement in Case 1, using an isotropic angular distribution.

3. Case 3 -- Carbon Detector; "Measured" Angular Distribution

This example is similar to Case 2 above except that the higher-threshold-energy detector, carbon, is used. The results are displayed in Fig. VI-10. Again we see that the measured relative detector activation is not the correct emitted neutron angular distribution.

D. Fitting with the FLUX Computer Program

The numerical integrations of the previous section can be performed more easily and accurately with our CDC-6600 machine program, FLUX, provided the angular distributions can be expressed in certain analytic forms. The machine program and the fitting of the experimental data of the whole of the experimental program are treated in Chapter VIII. Here we briefly discuss those portions of the program that involve the angular-distribution aspect of the entire problem, so that we may interpret the angular-distribution experiments through this calculational procedure.

Analytic functions are used to represent source distribution, emergent radiation angular distribution from each source element, attenuation of radiation through iron and earth, and buildup of radiation on

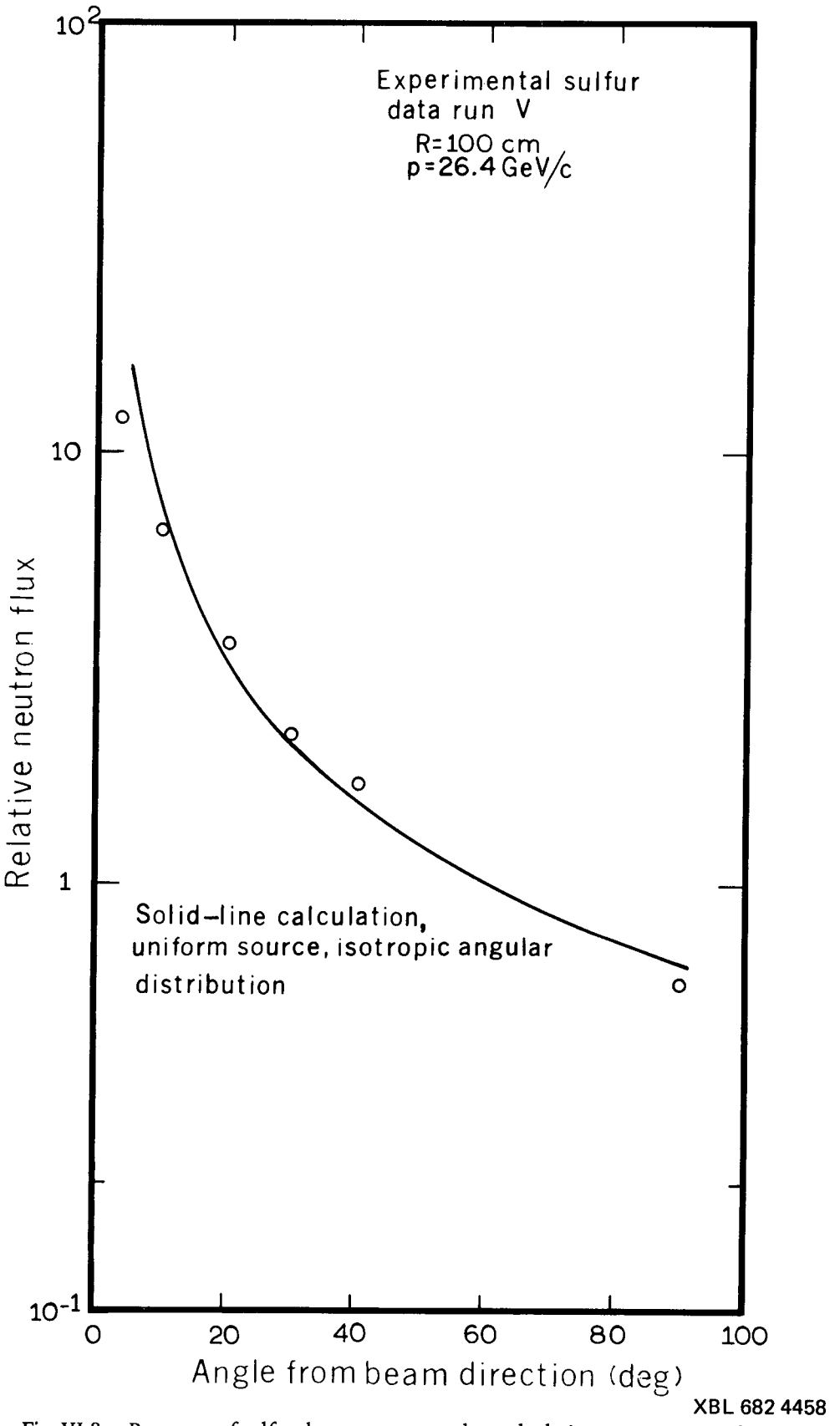

Fig. VI-8. Response of sulfur detector compared to calculation assuming a uniform line source with isotropic angular distribution, 26.4 GeV/c, Run V.

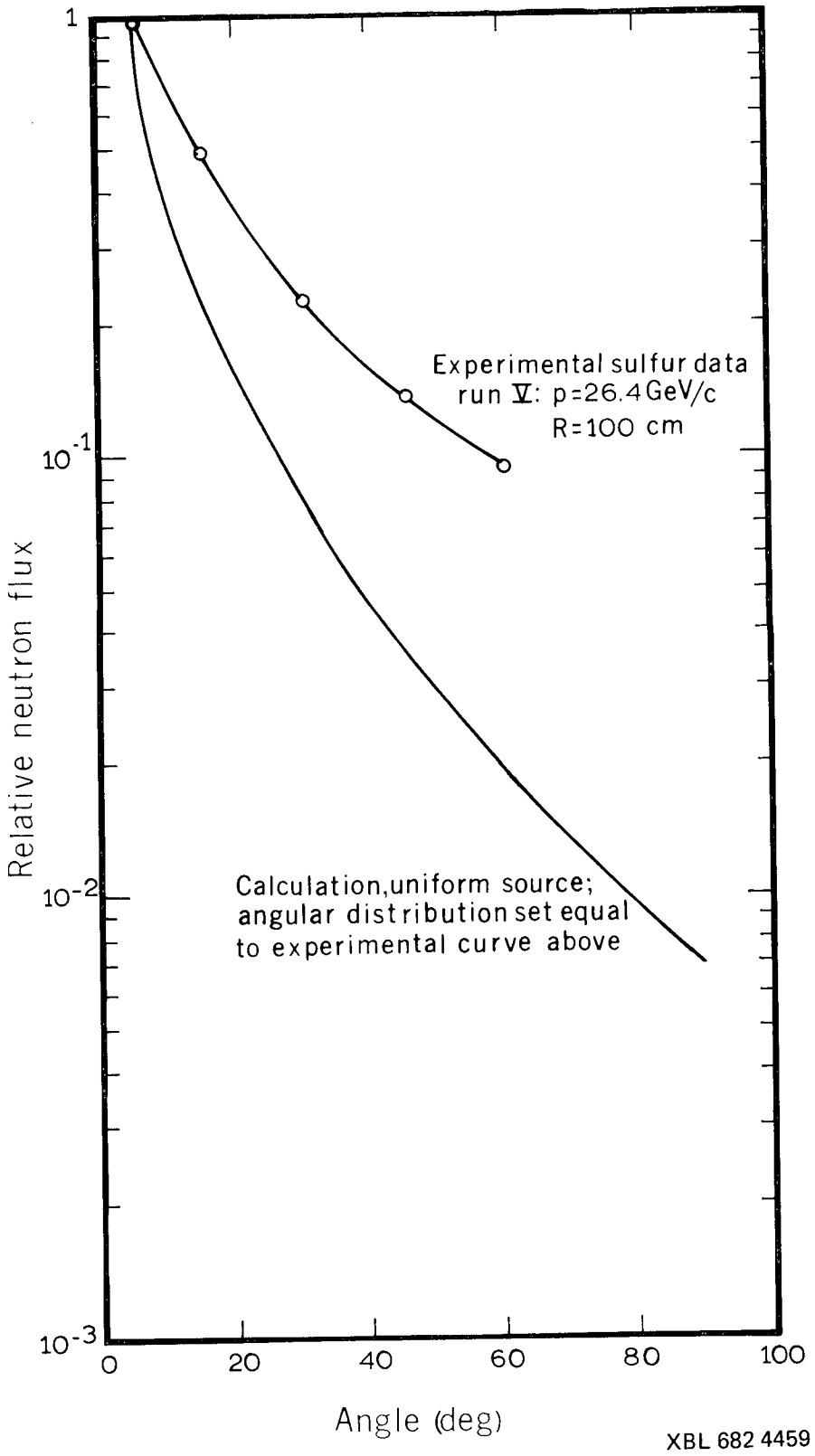

Fig. VI-9. Response of sulfur detector compared to calculation assuming a uniform line source with angular distribution identical to measured sulfur response, 26.4 GeV/c, Run V.

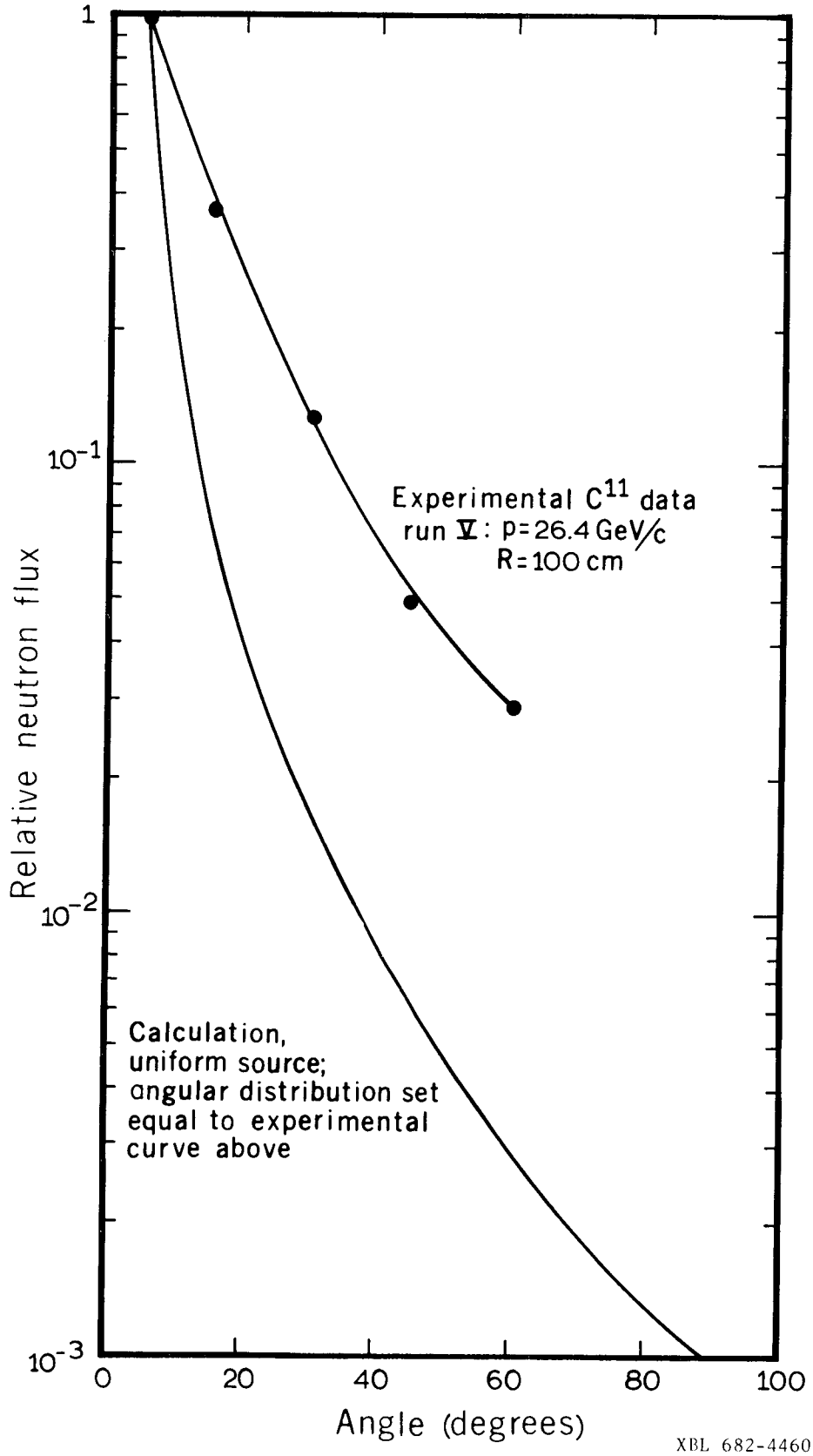

Fig. VI-10. Response of carbon detector compared to calculation assuming a uniform line source with angular distribution identical to measured carbon response, 26.4 GeV/c, Run V.

traversing the attenuating materials. These functions contain eight free parameters that form the starting conditions for the calculations, together with the known geometry and measured experimental neutron fluxes. Fluxes are calculated by numerical integration for each point at which experimental fluxes have been measured.

If, for the i th point, Φ_i is the calculated flux and Φ_i is the measured flux, then we can use the expression

$$V = \sum_i \left(\frac{\Phi_i - \phi_i}{\phi_i} \right)^2$$

as a measure of the quality of the fit. The free parameters are then allowed to vary from their initial values so that V is reduced, eventually to some minimum.

The two simple analytic forms that best fit the experimental angular distribution data are:

$$\text{(i)} \quad \Theta(\theta) = a_2 e^{-a_4 \theta}$$

$$\text{(ii)} \quad \Theta(\theta) = (1 + a_2\theta)^{-a_4} .$$

The program can adjust the constants a_2 and a_4 until the experimental results are most closely reproduced. Different source distributions can be used, and data taken at various distances from the target can be simultaneously fitted. Form (i) above yields a slightly better fit to the data than does form (ii), and in less computer running time. Therefore the exponential form, (i), was used to fit the experimental data. As will be seen, the fit is not extremely sensitive to the value of the angular-distribution parameter, a_4, so a_4 is not well-constrained by this procedure.

1. Hg → Tb Detectors

This is the highest-neutron-energy detector we used; the threshold is approximately 600 MeV (see chapter III). In section VIA it was shown that the source distribution had to include radiation from the beam pipe in addition to radiation from the thin beryllium target. We found that the experimental data could be well fitted by a constant-strength line source along the beam pipe, starting at the target and extending some 10 meters downstream, plus a point-like source at the target. The ratio of the intensities of the point-like source and the constant line source was a problem variable. Data from the two arcs of radii 25 cm and 100 cm were used, as were data from the buckets below the tunnel ceiling. Data were taken and fitted at both p = 26.4 GeV/c and p = 14.6 GeV/c.

The FLUX results are a_4 = 7.2 to 7.4 with no apparent difference for the two initial momenta. If we take a_4 = 7.3, then the exponential-form fit is $\Theta(\theta) = e^{-7.3\theta}$. Accordingly, the normalized fluxes for zero and 90 deg are:

$$\phi \text{ (0 deg)} = 1$$

$$\phi \text{ (90 deg)} = 10^{-5}.$$

2. $S^{32} \rightarrow P^{32}$ Detectors

This was the lowest-threshold-energy detector we used in the angular-distribution experiments. The procedure, location of the data points, and the use of two initial proton momenta, were the same as with the Hg → Tb reaction discussed above.

The FLUX results are a_4 = 0 to 0.8, a very flat distribution.

3. Intermediate Threshold Energies for Al → Na^{24}, C^{11} and Bi Fission

Results with the Al → Na^{24}, $C^{12} \rightarrow C^{11}$, and Bi fission detectors are:

a.	Al → Na^{24}	for p = 26.4 GeV/c, a_4 = 2.3
		for p = 14.6 GeV/c, a_4 = 1.1
b.	$C^{12} \rightarrow C^{11}$	for p = 14.6 GeV/c, a_4 = 4.1
c.	Bi fission track plates	for p = 26.4 GeV/c, a_4 = 3.4.

As mentioned above, the value of a_4 is not uniquely determined by this fitting method, since a change in source distribution function influences the best value of a_4. Therefore relatively few computer runs were made for the detectors in this section, and not all the experimental data were processed. What is generally clear is that the exponential slopes increase with increasing energy of the emitted secondaries.

4. Mica-Track Plates

Mica-track (fission-product) plates were used in buckets with Bi, Pb, and Au as the fissionable materials. There were insufficient points to use the FLUX fitting program, but the observed relative activities are shown in Fig. VI-11. If one weights these activities by the square of the distances from the target to the respective buckets, one gets exponential angular dependences for the three materials between 20 and 60 deg. The thresholds range from 50 to about 120 MeV. From the data with other detectors, we do not expect all the radiation to issue from the target, so the significance of the exponential angular dependence is not clear.

The constants a_4 for bismuth, lead, and gold are

$$\text{Bi: } a_4 \approx 3.6$$

$$\text{Pb: } a_4 \approx 3.6$$

$$\text{Au: } a_4 \approx 3.9.$$

5. Detectors in Earth Shield, Orbit Holes

Aluminum and carbon detectors in orbit-hole locations are exposed to neutron fluxes that have passed through the iron magnets and various thicknesses of concrete and earth shielding. Cascade development and preferential removal of low-energy products serve to establish an equilibrium particle spectrum for these detectors in the shield. The analysis model used in Chapter VIII is equivalent to following the production and absorption of the most penetrating high-energy component of the secondary radiation. Fitting with the FLUX program we find that an $a_4 = 2.1$ to 2.4 is indicated. Comparison with the a_4 derived from the angular-distribution experiments near the target leads to a fairly low energy for the penetrating component, i.e., the Al → Na^{24} detector threshold.

The reason the above evaluation is not valid is that the geometry of the detectors in the earth effectively restricts the angular range of secondary particles to 90±30 deg, other directions leading to such long path lengths in absorbers that such contributions become negligible. The angular distribution experiments, on the other hand, utilized data from 3 to 90 deg. Therefore no quantitative information on the energy of the penetrating secondaries is obtained by this type analysis of the orbit-hole data. Measurements in the 60-to 120-deg angular range and with Bi, Pb, and Au fission-track plates (thresholds 50- to 120-MeV) would be useful in making the type analysis discussed above.

6. Comparison with Other Data

An independent experiment has been performed using activation detectors to measure the angular distribution of secondary particles at the CERN PS.[ChaS 67] The target location was at the middle of straight section 82, the detectors were placed at a radial distance of 50 cm from the target, and the angular range 10 to 170 deg was investigated. The primary proton momentum was 19.2 GeV/c, and thin targets of Be, Al, Cu, and U were used. The detector reactions used were Au → Tb^{149} $C^{12} \rightarrow C^{11}$, Al → Na^{24}, $S^{32} \rightarrow P^{32}$, $Au^{197} + n \rightarrow Au^{198}$, TLD, and ferrous-ferric dosimetry. Comparison with our results is made below.

a. $S^{32} \rightarrow P^{32}$

The experimental data have been normalized to the activation measured at an angle of 60 deg to the beam so that comparison can be made with our data at radii equal to 25 and 100 cm. The data appear in Fig. VI-12, and one can see that the general shapes of the relative activations agree.

The best fit from the FLUX program yields $a_4 = 1.9$, compared with the range 0 to 0.8 when fitting our data. There was little difference in the variance for the CERN Health Physics when $a_4 = 1$ was used. There are 13 data points, and with $a_4 = 1$, V is 0.30, and the maximum difference between a calculated and

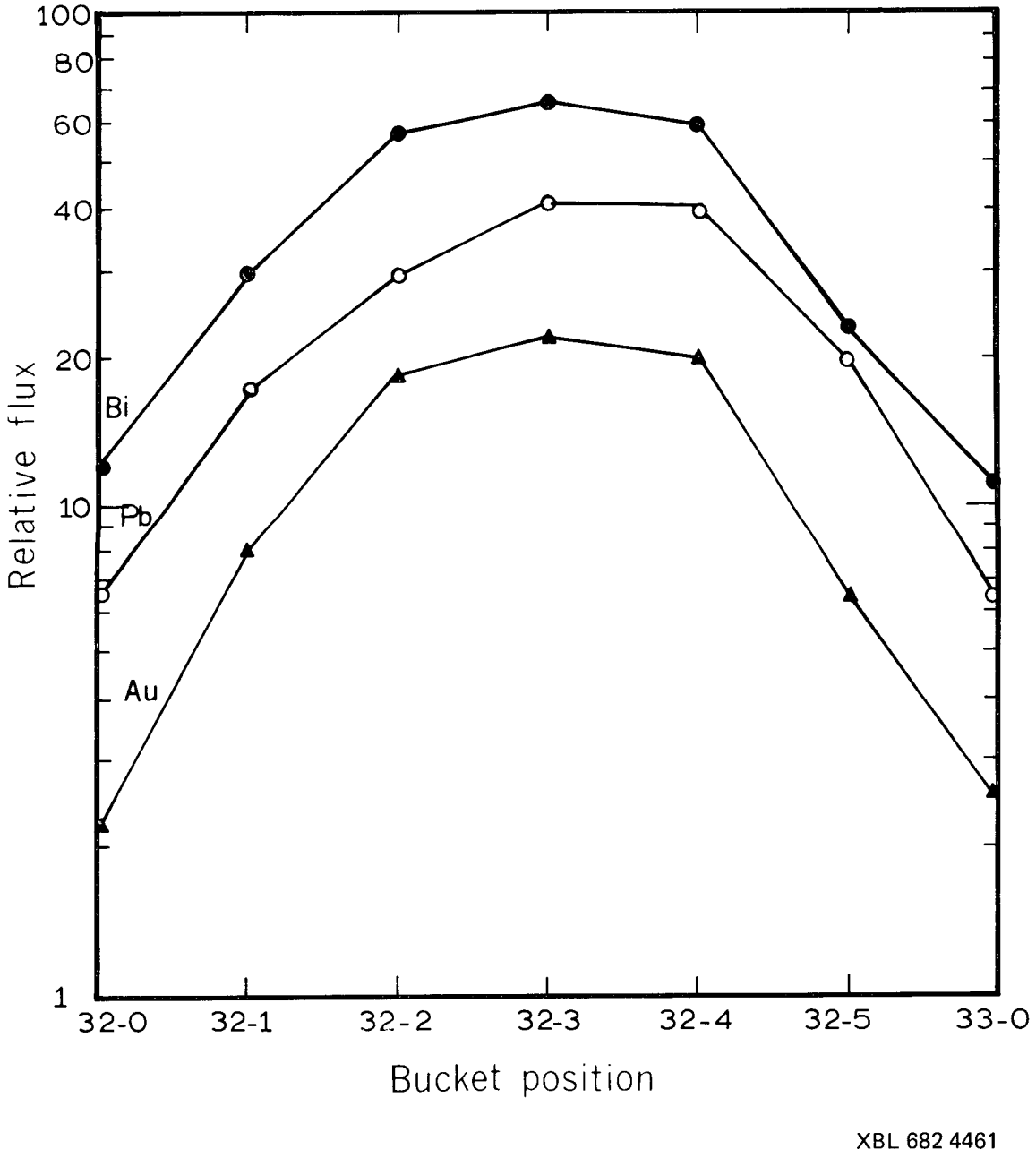

Fig. VI-11. Relative fluxes from Bi, Pb, and Au fission track detectors (mica) at bucket positions near target 32, 26.4 GeV/c, Run V.

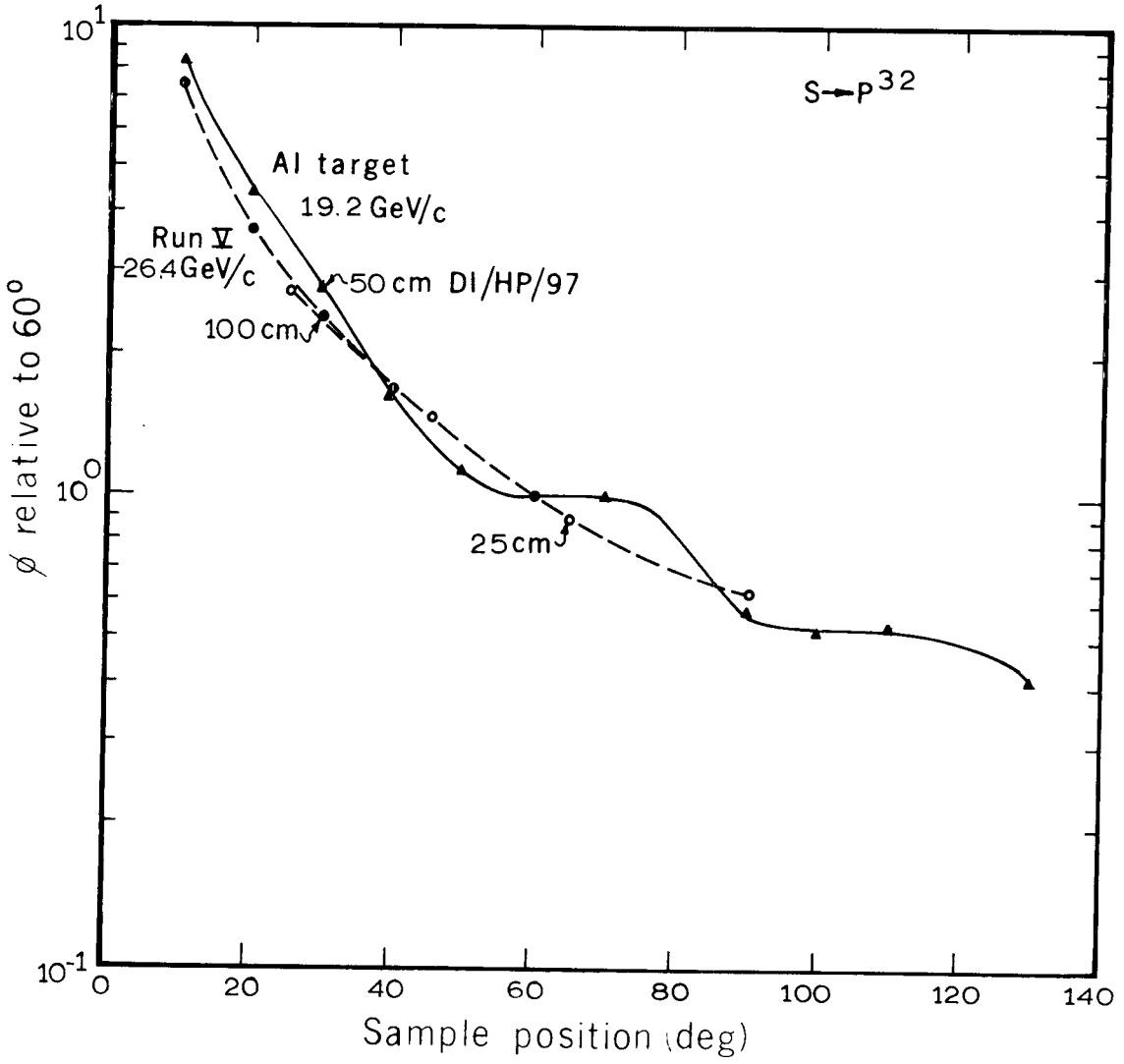

XBL 682 4462

Fig. VI-12. Comparison of sulfur detector results of this experiment to results of Charalambus et al.

measured point is 39%. For $a_4 = 1.9$, V is 0.16 and the maximum difference is reduced to 17%. Both variances are small; therefore the dependence on a_4 is weak. Since the target was at a different location in the accelerator, the source distribution could have differed from that in our experiment.

b. $Al \rightarrow Na^{24}$

The data are presented in Fig. VI-13. The FLUX fitting program yields best fits for the data as follows: $a_4 = 3.0$ for the Be target, $a_4 = 2.8$ for the Al target. For our runs, we have $a_4 = 1.1$ to 2.3.

c. $C^{12} \rightarrow C^{11}$

The data are presented in Fig. VI-14. The FLUX program yields best fits as follows: $a_4 = 4.7$ for the Be target, $a_4 = 3.6$ for the Al target. For our run, we have $a_4 = 4.1$.

d. $Au \rightarrow Tb^{149}$

The data normalized at an angle of 30 deg are shown in Fig. VI-15. The reduced sensitivity of the $Au \rightarrow Tb^{149}$ detectors restricted the CERN Health Physics data to the 30-deg and forward region. There are too few points to use the FLUX fitting program on these data. Inspection of the superposed data show reasonable agreement between the two independent experiments.

Reference

ChaS 67. S. Charalambus, K. Goebel, D. Nachtigall, Angular Distribution of Secondary Particles and Dose-rates Produced by 19.2 GeV/c Protons Bombarding Thin Be, Al, Cu, and U Targets, CERN DI/HP/97, March 14, 1967.

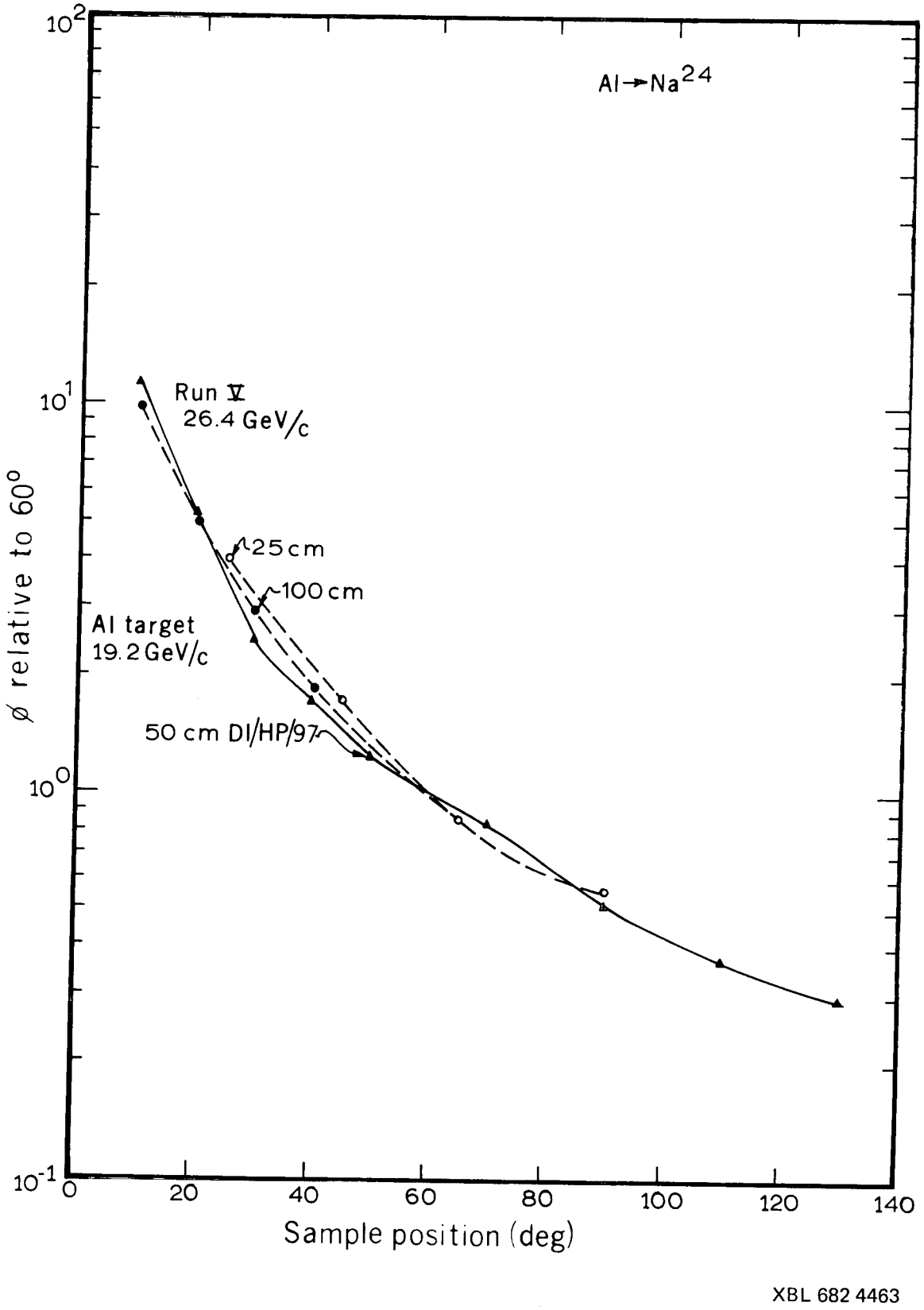

Fig. VI-13. Comparison of aluminum detector results of this experiment to results of Charalambus et al.

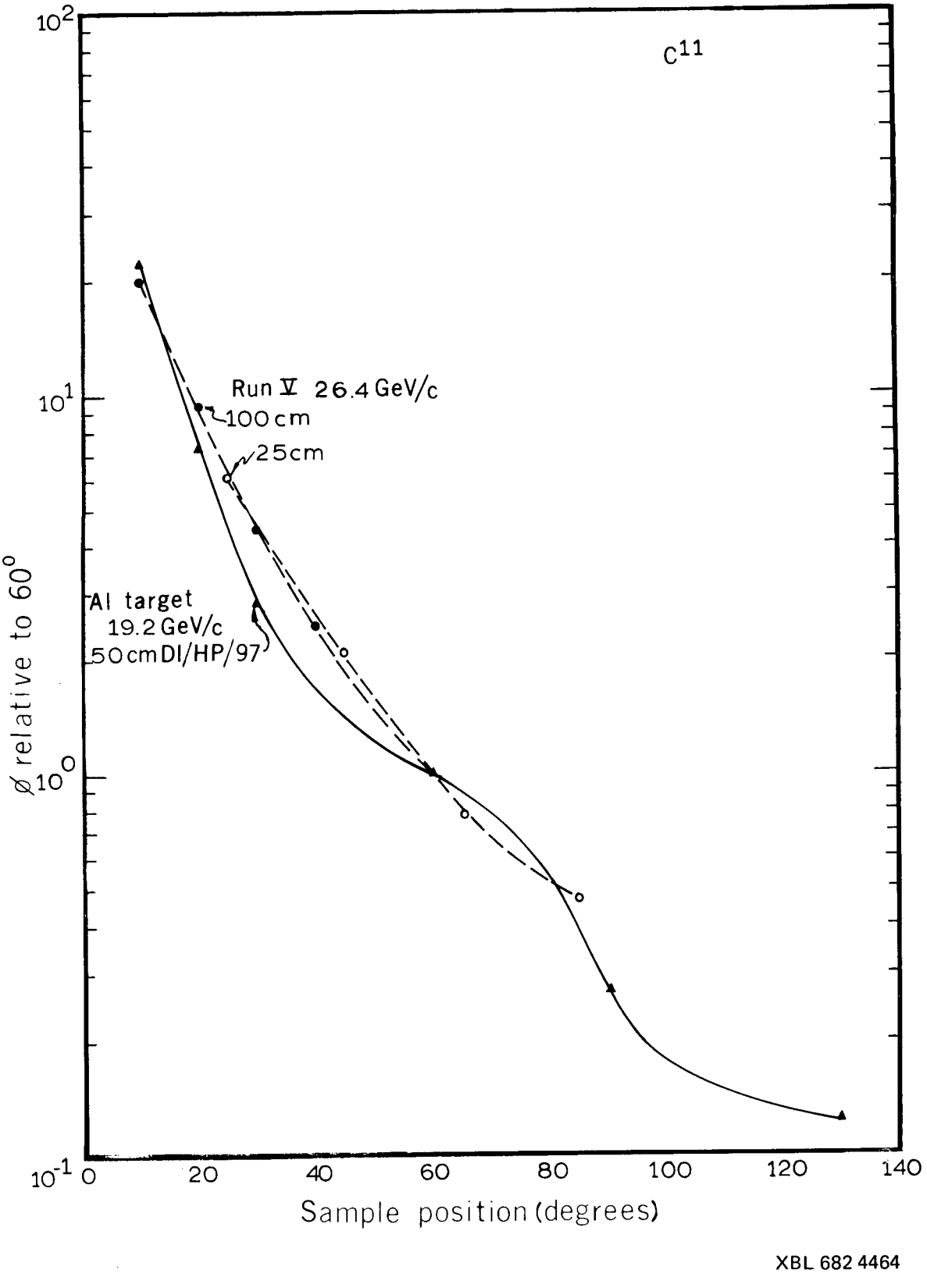

Fig. VI-14. Comparison of carbon detector results of this experiment to results of Charalambus et al.

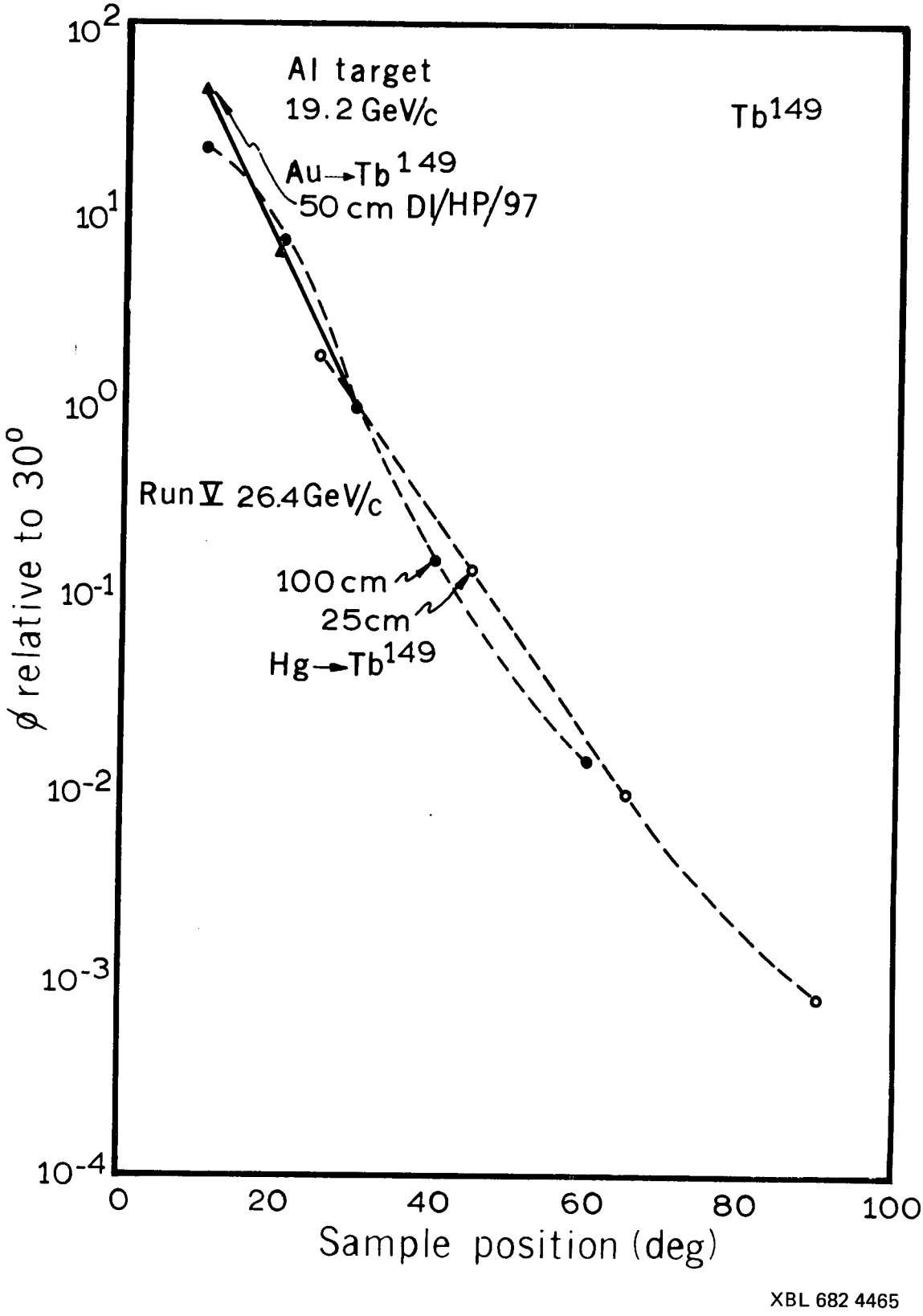

Fig. VI-15. Comparison of Hg → Tb^{149} detector results of this experiment to Au → Tb^{149} results of Charalambus et al.

VII. NEUTRON STREAMING IN THE VERTICAL ORBIT HOLES

As described in Chapter IV, activation detectors were placed in the earth shield in light steel-frame sample holders at standard positions above the beam orbit. These holders were some 3 m long and allowed six sets of samples to be used, with a spacing of approximately 0.6 m (see Fig. VII-1). For adequate sensitivity we required 10-cm-diam samples; a thickness of up to 5 cm could be accommodated in the sample slot. The space between the samples was occupied by steel cans filled with earth, to prevent neutrons from streaming up the vertical holes in the earth shielding. These cans were some 12.7 cm diam, the steel frames were 13.7 cm diam, and the internal diameter of the plastic hole liner was 15.6 cm.

The average density in the orbit hole with sample holder in place was considerably smaller than in the earth shield for two reasons: The air gaps resulting from the radial spacing required for mechanical clearance was equivalent to 40% of the total volume of the hole, and the earth that was put into the cans was not compacted to as high a density as existed in the shield. We decided that attenuation measurements should be made with different average densities in the orbit holes, so that one might estimate how different the flux might be in the full-density undisturbed earth shield from that in our standard sample holes.

During one machine run, we wished to make several sets of attenuation measurements, each set corresponding to a different average density in the orbit hole, so that the targetting might be as constant as possible. Carbon-11 activation detectors were chosen because the short half-life permitted several sets of samples to be activated and counted during our normal 12-hour running period. From previous runs we knew that the sensitivity and reproducibility of the carbon was equivalent to the longer-lived aluminum in the region in which the streaming experiment was performed. Two orbit holes were used, No. 32 directly above the target, and No. 33 one magnet downstream from the target. Since the target was in line with hole 32, it was thought that more streaming might be observed in this hole than in hole 33, which is assumed to be more typical of the other orbit holes. In Fig. VII-2 one can see the geometry of these holes and note that there is approximately 0.6 m of concrete and gravel below the drilled holes.

In each of the two holes, the plastic scintillators within which the C^{11} was produced were placed at five vertical locations. Four different densities were used in each hole. Table VIIA lists the contents of the holes and the resultant average density. The undisturbed-earth density is $\rho = 2.16$ g-cm^{-3}.

Table VIIA. Average density $\bar{\rho}$ in holes 32 and 33.

Identification	Description	$\bar{\rho}$ (g-cm^{-3})
Empty	Sample holder, detectors	0.12
Earth or standard	Sample holder, detectors, cans with earth	0.96
Earth plus water	Sample holder, detectors, cans with earth and water	1.37
Aluminum plus water	Sample holder, detectors, Al cylinders and water	1.93

The positions are designated by the nominal heights above the beam line in tenths of meters, but the actual positions are somewhat different (see Table II-C). Position 33, which corresponds to our lowest position, is directly above the concrete and gravel, and nominally is 330 cm above the beam. Position 39 corresponds to 390 cm, and the other three sample positions are 45, 51, and 57.

In each run the circulating proton current was monitored, and the neutron fluxes were obtained from the C^{11} counting data. Since the loss distribution does not stay constant throughout a run, we normalized each set of data to the flux at the bottom of the hole, position 33, since the density of the concrete and gravel remain constant. There might be some question as to whether changing the density of the material

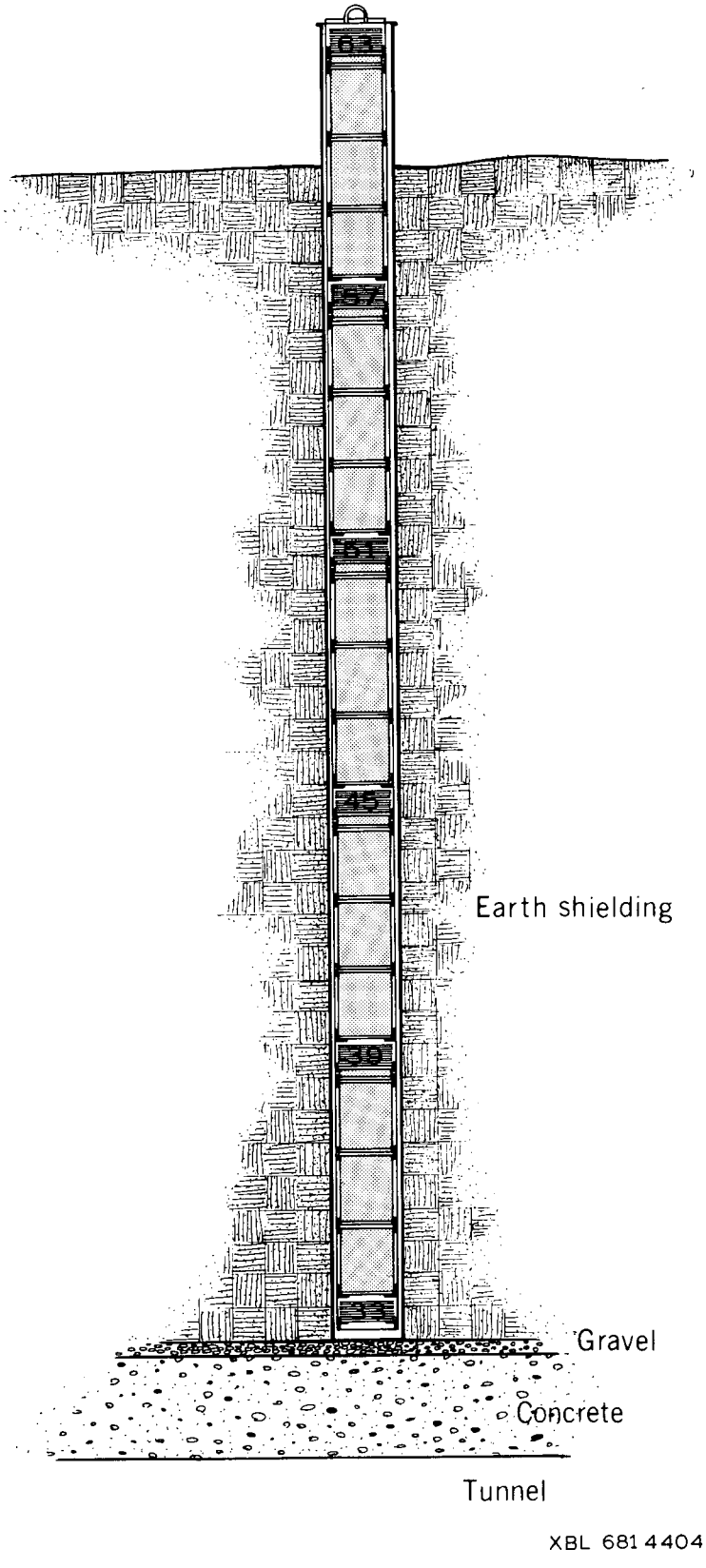

Fig. VII-1. Sample holder positioned in orbit hole.

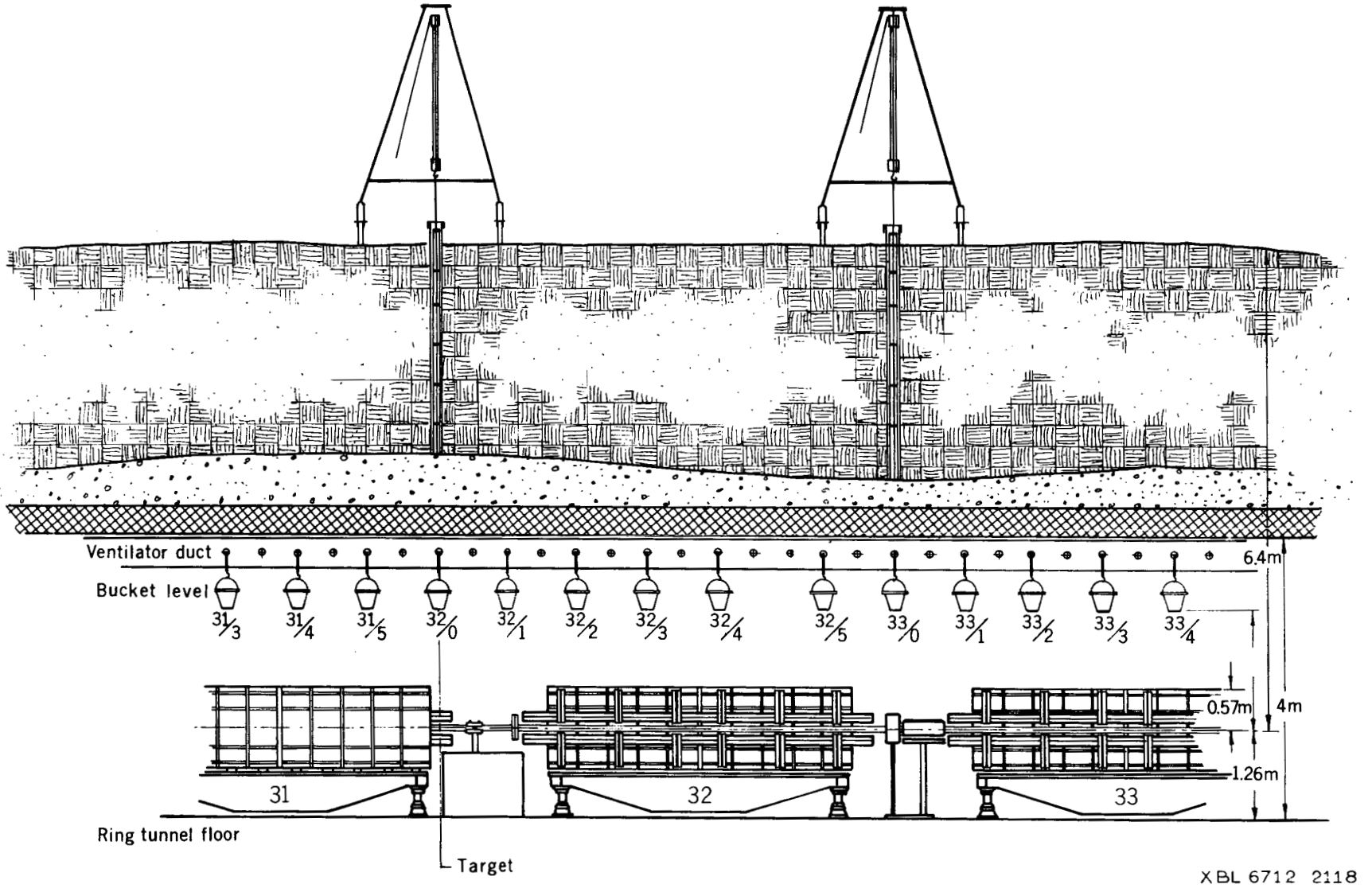

Fig. VII-2. Vertical cross section of the accelerator tunnel surmounted by the earth shielding which is pierced by the vertical orbit holes.

UCRL-17941

above the bottom sample might change the apparent flux through backscattering. Table VIIB lists the measured fluxes at the bottom of holes 32 and 33, normalized to the same circulating beam. Although there is scatter in the data, there does not seem to be a recognizable density effect.

Table VIIB. Average density and flux values at position 33 in holes 32 and 33.

Shielding in hole	$\bar{\rho}$ (g-cm^{-3})	Φ_{C11} at position 33 $\left(\frac{\text{neutrons-cm}^{-2}}{10^{12}\text{ protons}}\right)$	
		Hole 32	Hole 33
Empty	0.12	1.42×10^5	3.50×10^5
Earth, standard	0.96	1.46×10^5	2.97×10^5
Earth and water	1.37	1.25×10^5	3.04×10^5
Aluminum and water	1.93	1.28×10^5	3.17×10^5

The experimental data, normalized to the bottom positions, are shown in Fig. VII-3 for hole 32 and in Fig. VII-4 for hole 33. A cross-plot of flux vs density is shown in Fig. VII-5, and an extrapolated value at earth density $\rho = 2.16$ is obtained. The smooth curve connecting the points is not based on a theoretical model. It seems that there is a large streaming effect if the average density in the holes is less than the standard earth-filled arrangement. When the density is increased, there seems to be a relatively small change. The ratios R of the fluxes at $\rho = 2.16$ g-cm^{-2} vs the corresponding fluxes at the standard $\rho = 0.96$ g-cm^{-3} are shown in Table VIIC:

Table VIIC. Average ratios of flux at $\rho = 2.16$ g-cm^{-2} to flux at $\rho = 0.96$ g-cm^{-2} for various positions.

Position No.	R for hole 32	R for hole 33	$(R_{32} + R_{33})/2$
39	0.89	0.86	0.87
45	0.81	0.73	0.77
51	0.78	0.71	0.74
57	0.74	0.71	0.73

Qualitatively the entries in the table for the two holes are similar and, in the direction one would expect, the streaming correction increases with greater thickness. The uncertainties implicit in the normalization and curve-fitting procedures persuade us that the ratios must be uncertain by several percent, and one can use for all holes the combined ratios for holes 32 and 33. Fortunately the corrections are small and change the apparent mean-free-path even less.

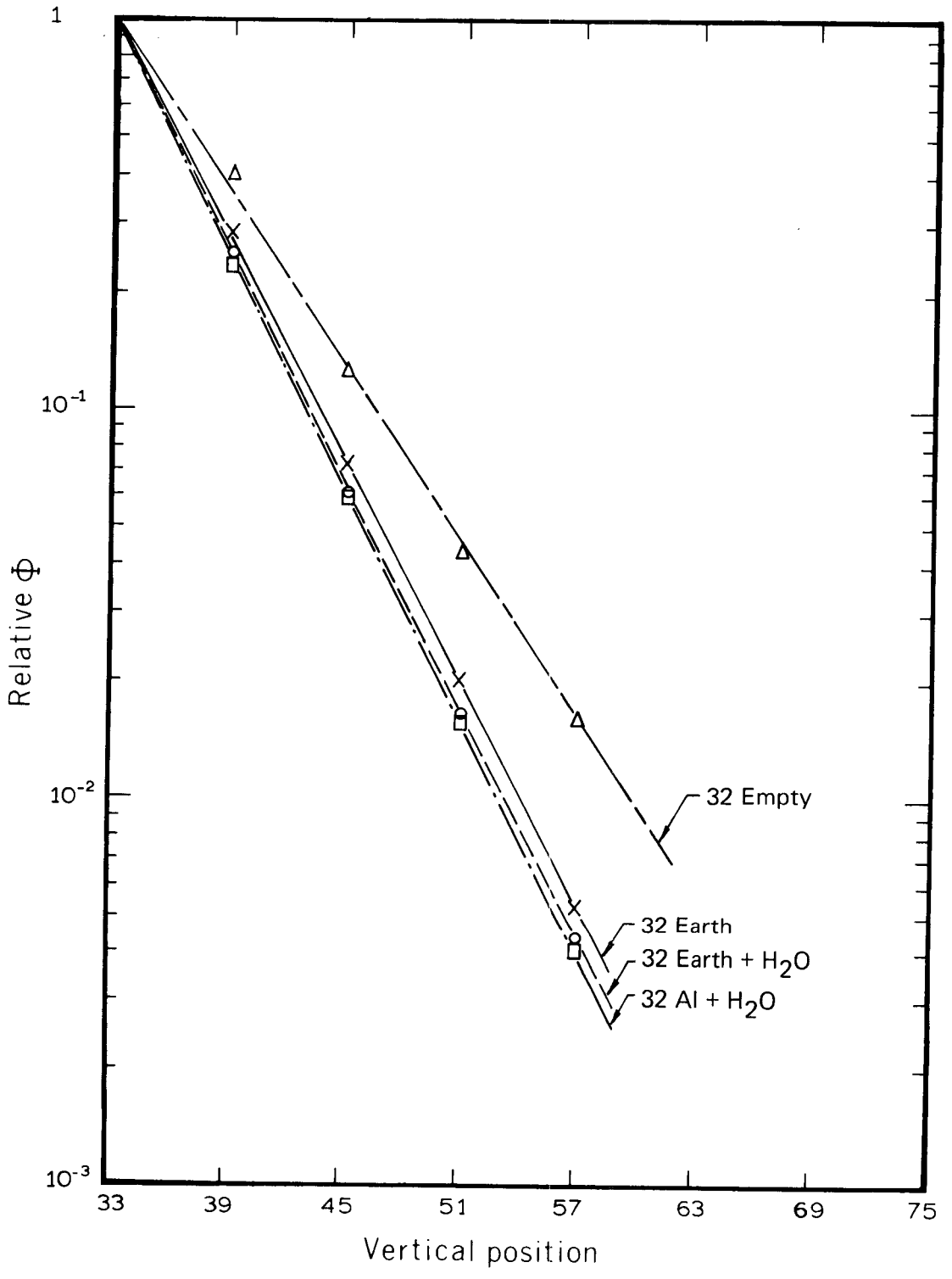

Fig. VII-3. Relative flux vs vertical position at hole 32, normalized to the bottom positions.

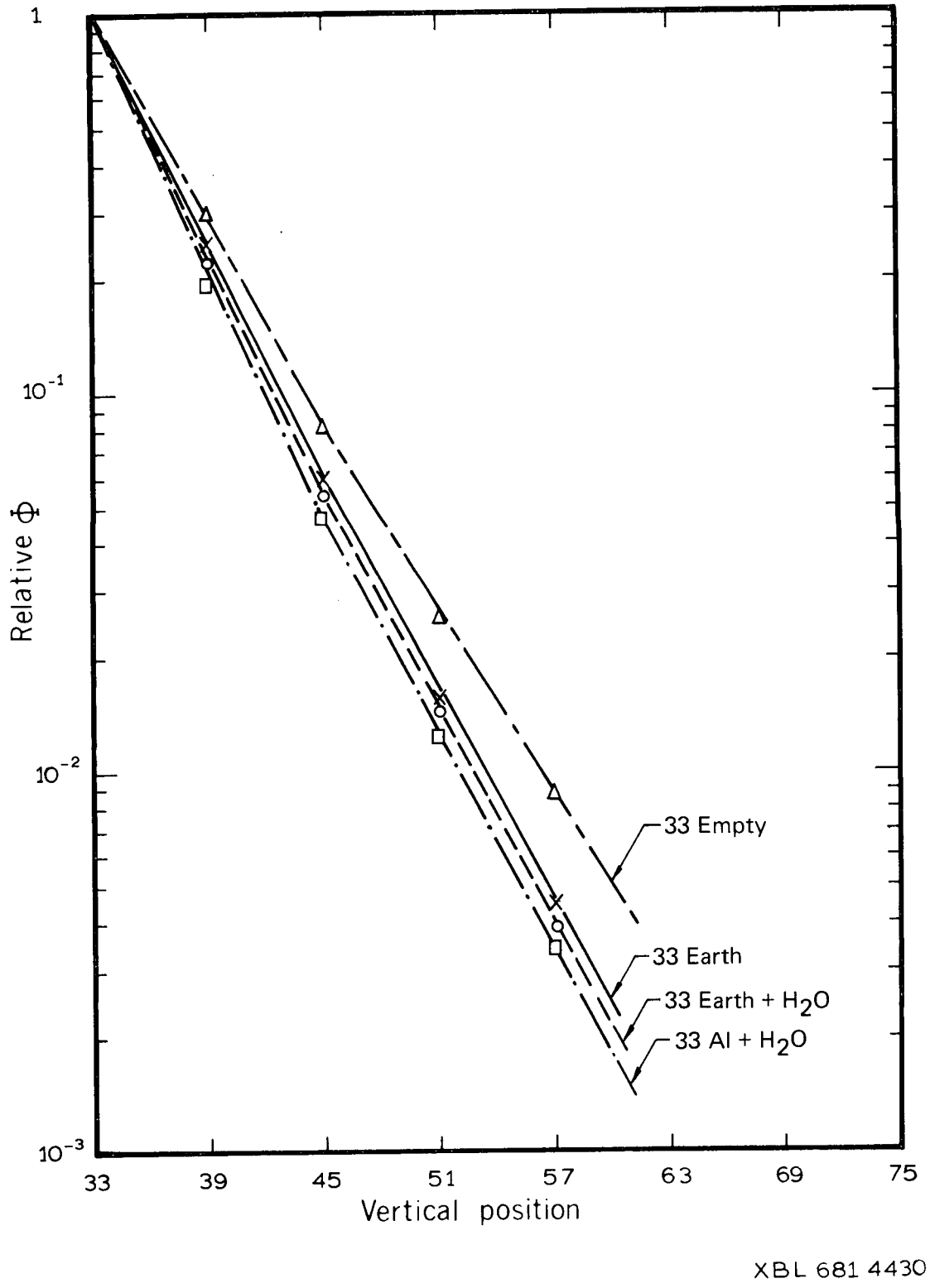

Fig. VII-4. Relative flux vs vertical position at hole 33, normalized to the bottom positions.

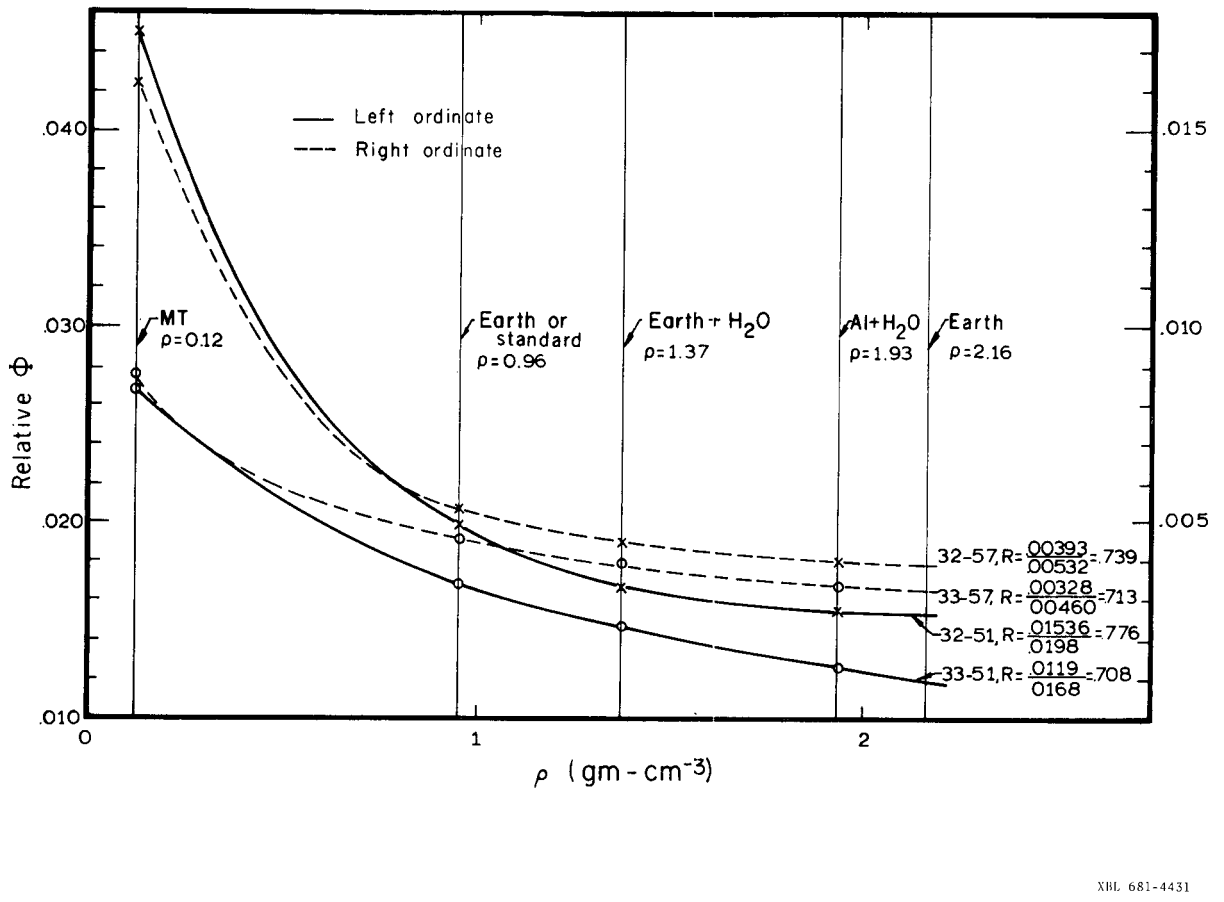

Fig. VII-5. Relative flux vs density of material in hole at positions in holes 32 and 33.

For completeness, the actual flux values, not normalized to the bottom position, are given in Table VIID.

Table VIID. Measured C^{11} neutron flux in neutron-cm^{2}-sec^{-1}.

Location	Empty hole	Standard earth	Earth and water	Aluminum and water
	$*4.49X10^{11}$ p-sec^{-1}	$*2.34X10^{11}$ p-sec^{-1}	$*4.47X10^{11}$ p-sec^{-1}	$*4.00X10^{11}$ p-sec^{-1}
32-33	6.36×10^{4}	3.41×10^{4}	5.62×10^{4}	5.14×10^{4}
32-39	2.51×10^{4}	9.61×10^{3}	1.39×10^{4}	1.20×10^{4}
32-45	7.77×10^{3}	2.44×10^{3}	3.43×10^{3}	3.06×10^{3}
32-51	2.71×10^{3}	6.89×10^{2}	9.29×10^{2}	8.00×10^{2}
32-57	1.06×10^{3}	1.81×10^{2}	2.45×10^{2}	2.05×10^{2}
	$*2.34X10^{11}$ p-sec^{-1}	$*4.49X10^{11}$ p-sec^{-1}	$*4.00X10^{11}$ p-sec^{-1}	$*4.47X10^{11}$ p-sec^{-1}
33-33	8.02×10^{4}	1.33×10^{5}	1.21×10^{5}	1.42×10^{5}
33-39	2.39×10^{4}	3.30×10^{4}	2.76×10^{4}	2.73×10^{4}
33-45	6.60×10^{3}	8.04×10^{3}	6.58×10^{3}	6.68×10^{3}
33-51	2.03×10^{3}	2.07×10^{3}	1.75×10^{3}	1.72×10^{3}
33-57	7.01×10^{2}	6.00×10^{2}	4.78×10^{2}	4.80×10^{2}

* Average value of the intensity of the circulating proton beam.

VIII. PHYSICAL MODEL, COMPUTER PROGRAMS, RESULTS, AND BEST FITS

A. Introduction

The data described in previous chapters represent the most comprehensive and systematic study to date of the radiation field around a high-energy accelerator. The compilation of these data has, of itself, clarified many of the obscurities which have hitherto bedeviled the accelerator radiation physics field.

Before considering the quantitative analysis of our experimental data, it is worth stating some of the qualitative conclusions we draw from this experiment. Some of these conclusions may seem obvious, but a systematic study of the literature will show the necessity to state them. Thus, for example, we are able to make the following categorical statements as a result of this experiment:

1. The "attenuation length" defined in the literature is a hybrid construct susceptible to grave misinterpretation. As has been shown in previous publications,[ForR 67] the value derived from our data may vary between 95 and 125 gm-cm^{-2}, depending upon the particular geometrical factors assumed. However, whether plane-wave, cylindrical, or spherical geometry is chosen, our measurements confirm the existence of a constant attenuation length over at least four orders of magnitude (of neutron flux).
2. In quoting values of attenuation length, particular care must be taken to obtain an accurate value of density of the shielding material. We were assured, in good faith, by many competent authorities that the density of the earth shielding above the CPS was 1.7 gm-cm^{-3}. As we have shown in Chapter II, careful measurements gave a value of 2.2 gm-cm^{-3}. Such errors (~30 percent) are much more likely to explain discrepancies in the literature than the relatively small experimental errors involved in transmission measurements. Furthermore, such errors are also possible in the estimates of density of other common shielding materials of irregular composition such as wood, concrete and laminated iron.
3. The measured transmission of radiation through the CPS earth shield is largely independent of the detectors used in this series of measurements. The ratios of detector responses remain constant within the earth shielding. Thus for practical purposes the assumption of an "equilibrium spectrum" is a valid concept. We found no evidence that the neutron spectrum in the earth shield differed either with or without a nearby operating target. Significant changes in the neutron spectrum were found, however, if the shielding material was changed (e.g. earth vs concrete).
4. Dose equivalent per unit fluence may accurately be evaluated from a set of measurements using threshold detectors. Given the appropriate set of conversion factors, measurements with only four of our threshold detectors can assess the neutron component of the dose equivalent to better than 20%. Furthermore, for all the neutron spectra we have examined, both at the CPS and at other high-energy accelerators, the dose equivalent per unit fluence is an insensitive function of spectrum (Chapter IX).
5. Beam-loss distribution was essentially stable at a given acceleration energy and changed only slightly with energy. Certainly, for the duration of our experiments the CPS was not as unpredictable as many pessimists had led us to believe. As expected, most beam loss occurred in the region of the target and beam clipper. The gross features of the beam-loss pattern downstream of a target are given by Monte Carlo calculations; however, at present the accuracy of the calculations does not permit direct comparison with the experimental data. Furthermore, such estimates of the efficiency of the clipper in reducing general beam loss are in error by a factor of two or more. We can not now explain in detail the generally distributed beam loss, but on the CPS at least, these local losses far from the target may be as high as 1% of those observed at targets. Until the reason for the existence of these distributed losses is explained, there is little hope of reducing them (Chapter V).

B. The Moyer Model

1. General

The mere accumulation of extensive data on one particular accelerator is, however, of only limited value. We have attempted to interpret our results in terms of a simple phenomenological model which permits extrapolation to other proton accelerators.

In setting up this model we have been largely influenced by the work of Moyer[MoyB 61] and its subsequent development by DeStaebler[DeSH 62] and by Gilbert and Thomas.[GilW 65]

The physical features of this model are now described briefly. Consider the typical accelerator geometrical configuration shown in Fig. VIII-1. Here a high-energy proton beam interacts with a target in the accelerator vacuum chamber. Secondary particles are emitted from the target as a result of nuclear interactions. The basic problem is to estimate the total number and energy spectrum of those neutrons that penetrate the accelerator shielding. Let us assume that we know

$$\left(\frac{d^2n}{dT d\Omega}\right)$$

which is the number of neutrons emitted from the target with energy between T and $T + dT$ into a solid angle $d\Omega$ per incident proton as a function of angle θ to the incident proton beam. For any angle θ the number of particles emitted into solid angle $d\Omega$ from N particles-sec^{-1} interacting is

$$N\left(\frac{d^2n}{dT d\Omega}\right)$$

The path length through the overhead shielding is given by $d\csc\theta$. Thus if the removal mean free path of neutrons of energy T is $\lambda(T)$, an attenuation factor of $\exp[-d\csc\theta/\lambda(T)]$ must be applied. In addition, a buildup factor should be applied which takes account of "scattering in" and, in a gross way, of particles that are produced by interactions of higher-energy particles and which arrive at the shield surface in the energy interval $T + dT$. The flux of particles of energy between T and $T + dT$ leaving the shield surface at angle θ to the target is then given by

$$\frac{dn}{dT} = N\left(\frac{d^2n}{dT\,d\Omega}\right)d\Omega \cdot B(T)\exp[-d\csc\theta/\lambda(T)]\ , \tag{1}$$

where the solid angle $d\Omega$ is given by

$$4\pi d\Omega = \frac{1}{r^2} = \frac{1}{(a+d)^2\csc^2\theta}\ . \tag{2}$$

The integral flux at point p is

$$\Phi_p = \int_{T_{min}}^{T_{max}} \frac{dn}{dT}\cdot dT = \int_{T_{min}}^{T_{max}} N\left(\frac{d^2n}{dT d\Omega}\right)d\Omega\, B(T)\exp[-d\csc\theta/\lambda(T)]\,dT \tag{3}$$

where T_{min} and T_{max} represent reasonable energy limits for the integral.

2. Empirical Use of Moyer Model to Estimate Bevatron Shielding

Moyer[MoyB 61] has used a version of Eq. (3) to satisfactorily predict additional shielding for the Bevatron.[SmiA 65] Because at the time of his calculations experimental data was limited, he proceeded by making several reasonable physical assumptions:

a. Because the neutron inelastic cross section is essentially constant above 150 MeV, Moyer wrote

$$\lambda(T) = \lambda\ (\text{const}) \text{ for } T > 150 \text{ MeV}$$

and

$$\lambda(T) = 0 \qquad \text{for } T < 150 \text{ MeV}.$$

This is equivalent to ignoring the lower-energy neutrons produced, i.e., to setting $T_{min} = 150$ MeV in the integral of Eq. (3). Thus Φ_p now becomes $\Phi_p\,(E > 150\text{ MeV})$. However, for the typical shield thickness around high-energy accelerators, the larger intensity of low-energy neutrons produced at the source

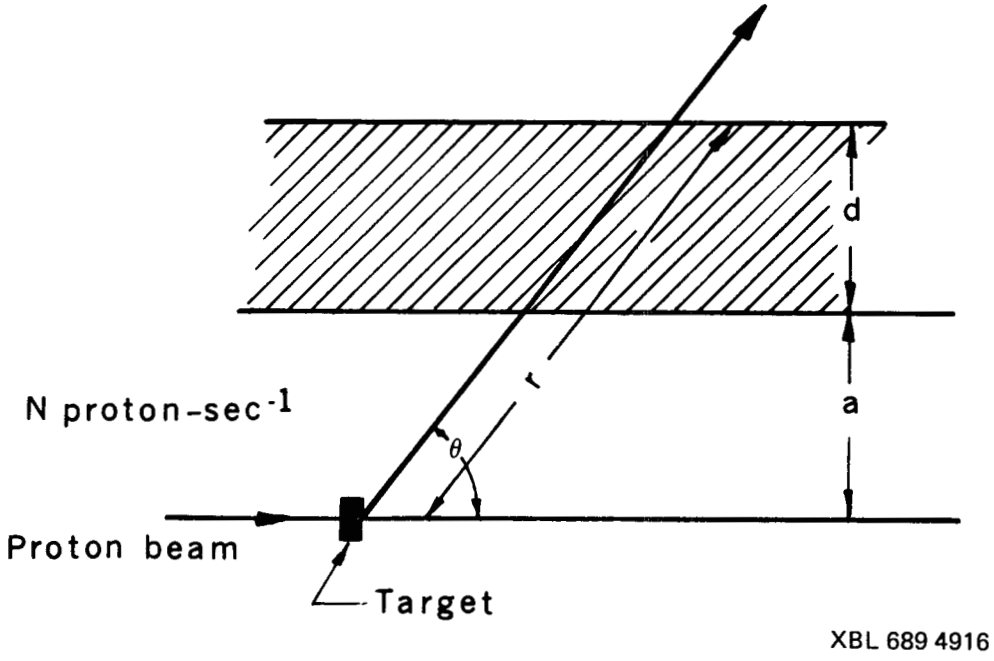

Fig. VIII-1. Schematic representation of typical accelerator geometry.

inside the shield is more than compensated for by the considerably larger attenuation cross sections appropriate to these energies. Thus the flux at point p can be written as

$$\Phi_p\,(E > 150\ \text{MeV}) = N \exp\left(\frac{-d\csc\theta}{\lambda}\right) d\Omega \int_{150\ \text{MeV}}^{T_{max}} B(T)\left(\frac{d^2n}{dT\,d\Omega}\right) dT. \qquad (4)$$

b. The integral in Eq. (4) is simplified by writing it as the product of a multiplicity factor, $m(T_{max})$, which is the number of neutrons emitted at all angles from the target with energy greater than 150 MeV with a relative angular distribution $f(\theta)$. Thus we can write

$$\int_{150\ \text{MeV}}^{T_{max}} B(T)\left(\frac{d^2n}{dT\,d\Omega}\right) dT = m(T_{max})\ f(\theta)\,. \qquad (5)$$

(It should be noted that $m(T_{max})$ is a constant for given T_{max} and a given target.)
Equation (4) is further simplified to

$$\Phi_p\,(E) = \frac{N\, m(T_{max})\ f(\theta)}{(a+d)^2 \csc^2\theta} \exp\left(\frac{-d\csc\theta}{\lambda}\right)\,. \qquad (6)$$

Moyer estimated $m(T_{max})$ and $f(\theta)$ in the particular case for 6-GeV protons incident upon a thick (~ 100 g-cm^{-2}) copper target.[MoyB 61] In obtaining suitable values he utilized cosmic-ray data, the Monte Carlo calculations of Metropolis et al.,[MetN 58] and experimental data taken at the Bevatron.[SmiA 65]

c. The dose equivalent DE_p produced by neutrons with energies greater than 150 MeV was then estimated by assuming a constant dose equivalent per unit fluence, F:

$$DE_p\ (E > 150\ \text{MeV}) = F\ \Phi_p\ (E > 150\ \text{MeV}), \tag{7}$$

and the total DE evaluated by writing

$$DE\ (\text{total}) = k\ DE_p\ (E > 150\ \text{MeV}), \tag{8}$$

where k is a constant greater than 1. This last approximation is made plausible by considering that the low-energy neutrons are in equilibrium with neutrons greater than 150 MeV at shielding depths greater than a few mean free paths.

Thus Moyer's final simplification of Eq. (1) becomes:

$$DE_p\ (\text{total}) = \frac{kF \cdot N\, m(T_{max})\, f(\theta)}{(a+d)^2 \cdot \csc^2\theta} \cdot \exp\left(\frac{-d\ \csc\theta}{\lambda}\right) \tag{9}$$

Solution of Eq. (9) was obtained by calculating $(DE)_p$ as a function of d and then fixing d at the required $(DE)_p$.

Moyer's shield calculation was predicated on an increase by a factor of 50 in proton intensity of the Bevatron beam and a removal of temporary wooden shielding that afforded a neutron-flux attenuation factor of 2. The effective design neutron attenuation (or reduction in transmission) was therefore a factor of 100. Extensive neutron-flux measurements were made before and after the improvement program. The overall effect of the recommended shield was to reduce the neutron flux levels by 90 to 100, the exact value depending on the neutron detector and detector location.

3. Generalization of the Moyer Model

While the approximations used by Moyer produce satisfactory results at the Bevatron, the model needs to be generalized to enable its wider use. For an accelerator which may be considered as a line source of neutrons, Eq. (3) may be rewritten as

$$\Phi_p = \iint S(Z)\left(\frac{d^2n}{dT\,d\Omega}\right) d\Omega\ B(T) \exp\left(\frac{-d\ \csc\theta}{\lambda(T)}\right) dZ\,dT, \tag{10}$$

where S(Z) is the number of protons interacting in a line element dZ, and the other symbols have previously been explained. The integrals are carried out over the appropriate limits of Z and T. For general use the geometrical configurations of different accelerators need to be considered, together with the variation of buildup factors and angular distributions with proton energy.

Our experiment enabled us to check whether an expression of the type in Eq. (10) can successfully explain our measurements. Figure VIII-2 shows a section of the CPS tunnel. In our experiment we obtained values of $\Phi(E > E_0)$ with several threshold detectors, threshold E_0, over a matrix of points within the shielding and inside the accelerator tunnel. Thus the practical problem is to seek a solution of Eq. (10) from the given measured values of $\Phi(E > E_0)$ in terms of parameters of the quantities within the integral. To facilitate this we rewrite Eq. (10) in the form:

$$\Phi_p\ (E > E_0) = \int S(Z) \cdot \Theta(\theta) \cdot B(X) \cdot e^{-X}\, d\Omega\, dZ\,. \tag{11}$$

Here $\Theta(\theta)$ is the angular distribution, B(X) is the buildup factor appropriate to the proton primary energy and threshold detector, and $X = \ell_{Fe}/\lambda_{Fe} + \ell_E/\lambda_E$, where ℓ_{Fe} and ℓ_E are respectively the path lengths through the iron and earth at angle θ, and λ_{Fe} and λ_E are the attenuation lengths in the iron and earth.

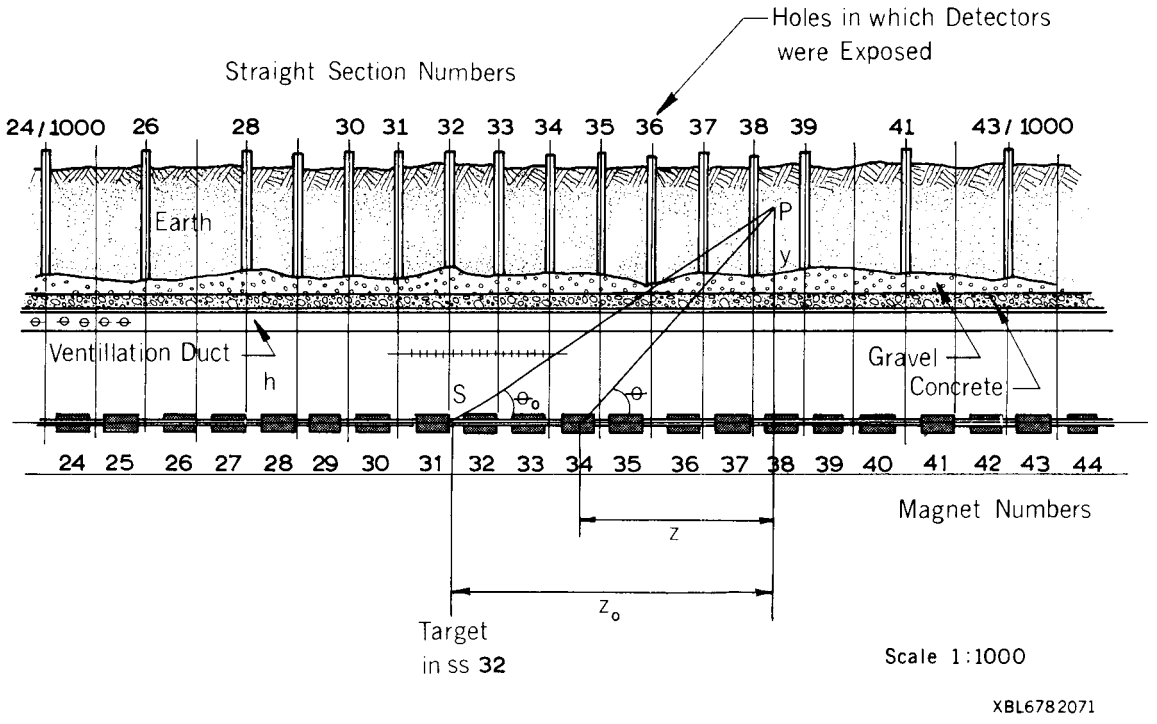

Fig. VIII-2. Elevation view of CPS in vicinity of target 32.

C. Computer Programs Based on Moyer Model

1. Simple Program -- LOCI Desk Computer

In order to obtain preliminary fits to our experimental data and to assess the complexity of so doing, a set of 44 data points obtained with aluminum detectors placed in the earth shield in the target region was used. The data points were at distances up to 25 m upstream and 70 m downstream of the target and at shield thicknesses of 0.76 m, 1.35 m, 1.92 m, and 2.53 m.

To facilitate solution of Eq. (11) analytic expressions for S(Z) and $\Theta(\theta)$ were assumed, while no buildup factor was explicitly used.

The experimental data taken on the beam vacuum chamber suggests the functional form

$$S(Z) = 1 + a_1 \exp(-a_3 Z), \tag{12}$$

with a_3 corresponding to a relaxation length of about 6 m. This expression grossly describes the function, S(Z) for distances up to 40 m from the targets.

For the angular distribution an expression was used of the form

$$\Theta(\theta) = (1 + a_2\theta)^{-a_4}. \tag{13}$$

No account of absorption in the iron was made and B(X) was set equal to unity.

Using the empirically determined values,

$$a_3 = 0.154\ \text{m}^{-1} \text{ and } a_2 = 5.74\ \text{rad}^{-1},$$

and fitting parameters a_4 and a_6 (mean free path of earth), we first evaluated the integrals of Eq. (11) on a LOCI electronic desk computer.* Values of $a_4 = 1.86$ and $a_6 = 123\ \text{gm-cm}^{-2}$ gave a good fit to the data points.

Although this preliminary analysis was useful, it had severe limitations in flexibility, scope, and speed. The limited application here took several man weeks of labor, and even then only two parameters were allowed to vary. Furthermore, no good idea was obtained of the constraints placed on the free parameters by the data. It was clear that the numerical integrations and minimization procedures necessary to obtain the best values of the Moyer model parameters fitting our data could only be conveniently carried out with a digital computer.

2. Variation-of-Parameters Program, FLUXFT

FLUXFT is a CDC 6600 program constructed to aid in the determination of a suitable analytic description of radiation flux measurements taken at the CERN proton synchrotron. Basically we desire to construct and evaluate a function

$$\Phi(p,a) = \int_{-\infty}^{\infty} f(p,a,z)dz,$$

where p is the point (z_p,y_p) and [a] is a parameter vector $a_1....a_n$ such that the quantity

$$V(a) = \sum_{i=1}^{S} \left[\frac{\Phi(p_i,a) - \phi(p_i)}{\phi(p_i)} \right]^2$$

is minimized. The values $\phi(p_i)$ are the measured fluxes, and S is the number of data points.

The problem, as considered here, is a two-dimensional one. That is, we assume that the circular machine in the region of interest is suitably represented by a straight line. With this assumption, the problem can be defined by using a two-dimensional coordinate system in which z represents the linear distance along the beam line, and y the vertical height above the beam-line center. The origin is assumed to be to the left of minus infinity [this is physically meaningful since f(p,a,z) approaches 0 quickly] and all magnets and data points are assumed to be to the right of the origin. That is, we assume that $z > 0$ is true and that the integral converges in this region. The problem is defined by specifying all magnet edges, the magnet height, the earth-shielding height, the heights of the layers with different densities in the earth shielding, the measured flux $\phi(z_p,y_p)$ over the set of data points, and suitable starting values of the parameter vector components a_i. Standard library integration and minimization routines are used in the program to evaluate the integral and obtain the value of the parameter vector [a] that minimizes the quantity V(a). The program has been constructed as a set of subroutines and function subroutines to allow the analytic form of f(p,a,z) to be easily changed.

The FLUXFT program has been in routine use on the LRL Berkeley CDC-6600 for over a year. In addition, it has been used on the IBM-360 at the Rutherford High Energy Laboratory. The problem parameters and optional functional forms are enumerated below:

a. Source Distribution Function, S(Z).

In addition to the analytic expression for S(Z) used in section C1 above, it is possible to input a tabular set of source values which are linearly interpolated by a program subroutine:

(1) $S(Z) = 1 + a_1 \exp(-a_3 Z)$ (14)

(2) Tabular set of source values $S_i(Z)$.

b. Angular Distribution Function, $\Theta(\theta)$

The angular distribution of emitted neutrons is assumed to be the same for every source element, S(Z). Two options are available:

(1) $\Theta(\theta) = (1 + a_2\theta)^{-a_4}$ (15)

(2) $\Theta(\theta) = a_2 e^{-a_4\theta}$ (16)

c. Attenuation Lengths, $a_5 = \lambda_{Fe}$, $a_6 = \lambda_E$

The neutron transmission in iron is $e^{-\ell_{Fe}/a_5}$ in units of meters of Fe, and in earth it is $e^{-\ell_E/a_6}$ in units of g-cm^{-2}. In the general case, one allows both a_5 and a_6 to be free parameters. However it is plausible that

$$\frac{\lambda_{Fe}}{\lambda_E} = \left(\frac{A_{Fe}}{A_E}\right)^{1/3} \tag{17}$$

so that

$$\lambda_{Fe} \simeq 1.26\,\lambda_E\,. \tag{18}$$

d. Buildup Factor, B(x)

The buildup factor may be written as a polynomial in x, the number of neutron attenuation mean free paths traversed: $x = \ell_{Fe}/a_5$ or $x = \ell_{Fe}/a_5 + \ell_E/a_6$. We have limited this polynomial to a quadratic expression

$$B(x) = 1 + a_7 x + a_8 x^2. \tag{19}$$

e. Total Independent Parameters

Equation (11) for the calculated neutron flux above a given threshold E_0 can be written

$$\Phi(z_i,y_i,a) = a_9 \int_{-\infty}^{+\infty} \frac{(1 + a_1 e^{-a_3 z})a_2 e^{-a_4\theta}\, e^{-\ell_{Fe}/a_5}\, e^{-\ell_E/a_6}\,(1 + a_7 x + a_8 x^2)dZ}{(Z-Z_i)^2 + y_i^2}\,. \tag{20}$$

If a_2 is a fixed parameter, a_9 is a normalizing factor and is not an independent, or free, parameter. Usually a_2 is taken outside the integral and $(a_2 \cdot a_9)$ is a composite normalizing factor. Therefore with the simpler exponential version of the angular distribution, the maximum number of free, or computer-adjustable, parameters is seven $(a_1,a_3,a_4,a_5,a_6,a_7,a_8)$.

Simplification to only four free parameters is possible if the buildup factor is assumed constant and a_5 is set proportional to a_6 or set equal to a constant (a_1,a_3,a_4,a_6). Thus, by the use of a physically plausible model, it should be possible to reduce to as few as four the parameters necessary to describe experimental data involving 20 to 100 separate measurements. Two of these parameters, a_1 and a_3, refer to the distribution of primary beam loss and are therefore part of the accelerator beam-dynamics problem. The other two parameters, a_4 and a_6, refer to the equivalent angular distribution of those neutrons that dominate the shielding problem and the attenuation of these neutrons, and are therefore fundamentally related to the physical cross sections involved and not to the details of the accelerator in question. How well the data are fitted by the method discussed above and the values of the parameters to use for various accelerators are discussed in the following section D.

f. Minimization of the Quantity V(a)

Define

$$V_i(a) = \left[\frac{\Phi(p_i,a) - \phi(p_i)}{\phi(p_i)}\right]^2, \quad V(a) = \sum_i V_i(a). \tag{21}$$

The computer program FLUXFT minimizes the quantity V(a) through a variation of the parameter vector [a] ($a_1,\ldots a_8$ for those components of [a] that are allowed to be free variables). The quantity V(a) has sometimes been referred to as the problem variance, which is an extremely loose use of the term. Since no statistical conclusions are drawn from the final numerical values of V(a), the exact nomenclature is not important. Inspection of Eq. (21) shows that we are summing the squares of the relative errors for each measured flux, and giving each point an equal weighting factor. In certain counting experiments one gives higher weight to points measured with better statistical precision, and in certain types of error analysis one gives greater weight to points with the smaller relative or absolute errors; our giving all points equal weight calls for an explanation.

The dynamic range of neutron flux that exists around the CPS and that we measured is nine orders of magnitude. Within the earth shield, the fluxes vary by five orders of magnitude. Weighting on the basis of absolute error would make the low flux points dominate, which is unphysical since the total volume of the shield contains detector points. The counting statistics for all detectors are better than 5%, with most better than 1%; which is negligible compared with the differences between measured and calculated fluxes.

Two classes of systematic errors arise in using the model discussed above: one of these involves the departures of the actual accelerator and detector geometry from the model assumed for the calculations, the other class of errors involves not taking into account the spatial fluctuations in the primary beam loss. We feel that differences of 30% between calculated and measured fluxes (see D.2) are quite reasonable in the light of these sources of systematic error and that, since agreement is found over five orders of magnitude, the use of a more detailed computational model is not justified.

An extremely large V(a) means that there are gross differences between the calculated and measured fluxes, either due to initially poor choices for the free parameters (a variables) or incorrect input data. A correctly input problem will typically have V(a) $\approx$ 0.25 per point. The minimizing routine will then vary the parameter vector [a] until the V(a) reaches a minimum, typically V(a) $\approx$ 0.05 per point. The endpoint parameter vector [a] does not depend on the starting vector [a]. As discussed above, systematic errors could easily explain errors of 20 to 30% per point between measured and calculated fluxes. For this reason the smallest V(a) we expect is about 0.05 per point. Smaller V(a)'s are taken to be fortuitous rather than necessarily representing a better fit.

D. Results and Best Fits

1. General

In each of our eight accelerator runs, several sets of data were obtained simultaneously, a given set corresponding to one type of detector in one class of location, viz., aluminum detectors in orbit hole locations. The entire experimental program used several thousand data points. Data sets used in FLUXFT computer analyses ranged from 8 to 72 points. The larger the number of input data points, the longer the machine running time, and generally, the more constrained the fitting parameters. As explained in Section C-2e above, the FLUXFT program has a total of eight parameters (a's) that describe the physics involved, and one can choose how many of these parameters the program can vary to obtain the best fit to the data. Not only can one specify how many adjustable parameters there will be, but also in what groups and order these variations will be made. For a medium-size problem, say 40 locations or data points, the running time on the CDC-6600 can range from less than a minute if one fixes all the parameters and only has the program evaluate the various integrals, to some 20 minutes if one allows all eight parameters to be free or adjustable. Over 500 computer runs were made in the course of analyzing the data, the conclusions of which are summarized in the following discussions.

2. Example of Radiation Pattern from FLUXFT

In run II, the primary proton momentum is 26.4 GeV/c. Aluminum detector data from orbit-hole locations (52 fluxes) were input to the FLUXFT program with the following results:

a. Agreement between Calculated and Measured Fluxes.

$$\text{We have } V(a) = 1.47 \text{ or } \frac{V(a)}{52} = \overline{V_i(a)} = \left[\frac{\Phi(p_i,a) - \phi(p_i)}{\phi(p_i)}\right]^2 = 0.029/\text{point.}$$

Therefore the average difference between the calculated and measured neutron flux $= 0.17 = (0.029)^{1/2}$, over a flux range of 10^5. The largest difference is 33%.

b. Beam-loss Parameters.

The primary beam-loss distribution in the target region is $S(Z) = 1 + 220\, e^{-0.144\,(Z)}$ with

$a_1 = 220$

and

$a_3 = 0.144\ m^{-1}$.

c. Angular-Distribution Parameters.

The angular distribution of penetrating neutrons from each source element is $\Theta(\theta) = e^{-2.06\,\theta}$, with

$a_2 = 1$ (fixed)

and

$a_4 = 2.06\ rad^{-1}$.

d. Mean Free Path in Iron.

Parameter a_5 was set equal to 0.2 m of Fe (not allowed to vary).

e. Mean Free Path in Earth

The neutron mean free path in earth shield is $a_6 = 116.6$ g-cm^{-2}.

f. Buildup Factor.

The buildup factor is set equal to 1, meaning $a_7 = a_8 = 0$.

g. Normalization Constant

The normalizing factor is $a_9 = 5.00 \times 10^5$. Fluxes have units of n-cm^{-2}-sec^{-1} and were normalized to a circulating primary proton current of 10^{12} p-sec^{-1}.

3. Results and Best Fits, Specific Parameters

a. Beam-Loss Parameters.

The beam-loss parameters are $S(Z) = 1 + a_1 e^{-a_3 z}$. The circumference of the accelerator = 628 m, so the constant loss term is proportional to 628. The area-under-target loss term is proportional to a_1/a_3. These calculated loss terms can be compared with the line integral obtained from the aluminum detectors on the beam vacuum chamber, and agree quite well for orbit-hole data:

a_1 = 200 to 300 from the orbit-hole data

a_1 = 100 to 250 from the bucket data (inside accelerator tunnel)

a_3 = 0.13 to 0.17 m^{-1} from both orbit-hole and bucket data.

b. Angular Distribution a_4.

The angular distribution a_4 can be obtained from $\Theta(\theta) = a_2 e^{-a_4 \theta}$, $a_2 = 1$ (fixed). For Al and C^{11} detectors in orbit-hole locations, a_4 is 2.1 and 2.4 respectively. In bucket locations, a_4 is zero for S, ≈ 1 for Al, and ≈ 2 for C^{11}. The dependence of V(a) on the actual values of a_4 is fairly weak, so a_4 is not well-constrained.

c. Mean Free Path in Iron and Buildup Factor, a_5,a_7,a_8.

The transmission in iron is $e^{(-\ell_{Fe}/a_5)}$. The buildup factor in iron is $1 + a_7 (\ell_{Fe}/a_5) + a_8 (\ell_{Fe}/a_5)^2$.

The complexity of the beam-loss pattern together with the relatively few bucket detector locations results in a weak dependence of V(a) on a_5. We also found no improvement in fit when the buildup parameters a_7 and a_8 were allowed to vary. Therefore in most problems we set B(x) = 1 and a_5 = 0.2 m.

d. Mean Free Path in Earth Shield, a_6.

The transmission in earth is $e^{-\ell_E/a_6}$. We find extremely strong dependence of V(a) on the value of a_6, which equals 117 ± 2 g-cm^2. Aluminum and C^{11} detector data were fitted at both p = 26.4 and 14.6 GeV/c. In Fig. VIII-3, $V_i(a)$ vs a_6 is plotted for Al detectors with p = 26.4 GeV/c and C^{11} detectors with p = 14.6 GeV/c, all other components of the [a] vector being held fixed.

e. Normalization Factor, a_9.

Equation (11) for the calculated neutron flux above a given threshold E_0 can be written

$$\Phi(Z_i,y_i,a) = a_9 a_2 \int_{-\infty}^{+\infty} \left[\frac{\left(1 + a_1 e^{-a_3 z}\right) e^{-a_4 \theta} e^{-\ell_{Fe}/a_5} e^{-\ell_E/a_6}}{(Z-Z_i)^2 + y_i^2} \right] dZ. \qquad (22)$$

The units of Φ are n-cm^{-2}-sec^{-1} and, in our case, these were normalized to a circulating beam current of 10^{12} p-sec^{-1}. The normalizing constant a_9 (or $a_9 a_2$) is not only required for dimensional analysis (the circumference of the accelerator is implicitly included, and accelerator dimensions are given in meters and the fluxes in cm^{-2}) but also relates the kinetic energy of the primary protons in GeV to an equivalent number of neutrons above a given threshold as determined by an activation detector, such as aluminum or carbon. The actual value of a_9, for a given set of measured fluxes,

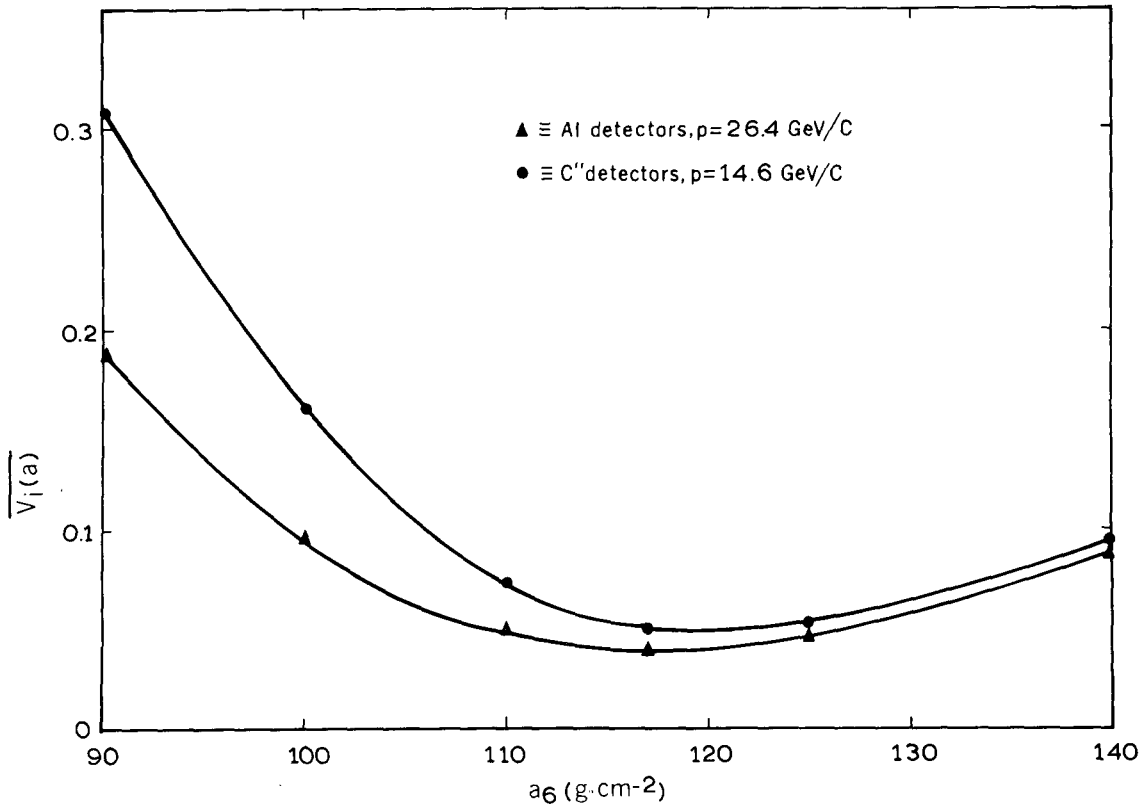

Fig. VIII-3. Dependence of V(a) on the value of a_6.

depends upon the values of a_1,a_3,a_4, and a_6. For example, the neutron fluxes in the earth shield are produced by neutrons emitted almost 90 deg to the beam direction (70 to 110 deg). The fit is not strongly influenced by the angular-distribution parameter a_4, since $\Delta\theta$ is relatively small; however, the actual value of $e^{-a_4\theta}$ for $\theta \approx 90$ deg is a strong function of a_4. Therefore a larger a_4 requires a large a_9 to match the calculated Φ_i to the measured ϕ_i. For the CPS run at two different primary proton momenta, we would expect the a_9's to be in the ratio of the relative beam proton kinetic energies if all the other a's were the same in the two cases.

f. Radial-hole data

Detectors were placed in vertical holes at great shielding thicknesses from the circulating beam. Since there were fewer of these positions than orbit-hole locations, the generalized analysis discussed above could not be performed. There were also some special geometrical difficulties. Calculations were carried out for a virtual shield located above the actual shield, and fluxes at an equivalent thickness in this virtual shield are compared with measured fluxes in the radial-hole locations in Table VIII-3, where the quantity R is the ratio between the measured flux in a given radial hole and the calculated flux in the virtual shield for the same position.

The greatest shielding thickness at which data were obtained corresponds to the 107.5-m radius holes, for which the earth shielding was 4.6 m. The neutron flux at this depth is approximately 0.01 that at the corresponding topmost orbit-hole location. As can be seen from the table, there is reasonable agreement between the fluxes measured in the radial holes and those extrapolated from the orbit holes by means of the FLUXFT program.

Magnets 34 and 35 have their open C-sides toward the outside radii. Now radial holes are immediately upstream from the corresponding magnet numbers, and we would expect radial holes 35 and 36 to have enhanced neutron fluxes, as is borne out by inspection of the Table.

Table VIII-3. Comparison of calculated and measured fluxes in radial holes for carbon and aluminum detectors at 26.4 and 14.6 GeV/c beam momenta.

	p = 26.4 GeV/c		p = 14.6 GeV/c	
Radial-hole location	R_C	R_A	R_C	R_A
32-104	1.5	1.4	1.3	1.1
32-105	0.9	0.8	0.7	0.6
32-106	0.8	0.7	0.4	0.5
32-1075	0.8	0.6	0.6	0.7
33-104	1.1	0.7	0.8	0.7
33-105	1.3	0.8	0.9	0.9
33-106	1.7	1.0	0.5	0.4
33-1075	1.4	1.4	0.8	1.6
34-106	1.8	1.1	0.7	0.8
34-1075	1.5	1.0	0.4	1.0
35-106	4.2	1.8	2.2	2.0
35-1075	4.0	1.5	2.1	2.7
36-106	5.1	2.4	4.4	3.4
36-1075	8.2	5.6	2.7	2.1

E. Summary

The major features of the radiation field around the CERN proton synchrotron are described well by our physical model that incorporates the shielding physics implicit in the Moyer model. The entire problem is separable into two parts: one involves the accelerator beam dynamics through the loss pattern of the primary protons; the other involves particle physics through secondary particle production in terms of both neutron energy and angular production as well as attenuation of these neutrons. In summary, the results of our study are as follows:

1. Beam-loss distribution is discussed in Chapter V. The general features can be explained through calculations of the type made by Ranft. Presumably such calculations can be made on machines still in the design stage and even more detailed theory is required to explain more detailed beam-loss features.
2. The angular distribution of emitted neutrons is discussed in Chapter VI, primarily from the standpoint of measurements made near the target. Theoretical aspects of this problem, based on a model by Ranft, are discussed in Chapter X.
3. The removal cross section, a factor which enters through the neutron-attenuation mean free path in earth, is well determined, and constant, for different detectors, different primary proton momenta, and different thicknesses of shield.
4. The neutron energy spectrum for transverse shielding reaches an effective equilibrium after only a few mean free paths. Hence the dose equivalent for unit fluence is constant throughout most of the shield volume, so long as the shield material is of uniform chemical composition.

References

DesH 62 H. S. De Staebler, Jr., Transverse Radiation Shielding for the Stanford Two-Mile Accelerator, SLAC-9, 1962.

ForR 67. R. D. Fortune, W. S. Gilbert, and R. H. Thomas, Shielding at the CERN–PS; CERN/LRL/RHEL Collaboration 1966, UCID-10199, April 28, 1967.

GilW 65 W. S. Gilbert and R. H. Thomas, in 200-BeV Accelerator Design Study, UCRL-16000, June 1965.

MetN 58 N. Metropolis, R. Bivins, M. Storm, A. Turkevich, J. M. Miller, and G. Friedlander, Monte Carlo Calculations on Intranuclear Cascades, Phys. Rev. *110,* 185 (1958); Phys. Rev. *110,* 204 (1958).

MoyB 61 Burton J. Moyer, Evaluation of Shielding Required for the Improved Bevatron, UCRL-9769, June 27, 1961; also in *First International Conference on Shielding around High-Energy Accelerators at Saclay, January 1962* (Presses Universitaires De France, Paris, 1962).

SmiA 65 A. R. Smith, Some Experimental Shielding Studies at the 6.2-BeV Berkeley Bevatron, in *Proceedings of the USAEC First Symposium on Accelerator Radiation Dosimetry and Experience, held at Brookhaven National Laboratory, November 3-5, 1965,* CONF-651109, 1965.

IX. FLUX-TO-DOSE CONVERSION

A. Introduction

All of our techniques (except use of ion chambers, TLD, and beta-gamma film) are basically those that measure particle fluxes; results of such measurements, when suitably grouped and analyzed, can yield particle-energy spectral information. Once particle fluxes and spectra are known, these quantities can be transformed into biological-dose terms through use of the current "best values" for conversion of particle type and energy into dose. The measurements are always in physical terms that can be easily reinterpreted if changes are made in flux-to-dose conversion factors.

The detectors used for spectral determination are primarily neutron detectors, although in some energy ranges they also respond to protons, pions, and gamma rays. When there are several mean free paths of shielding between the radiation source (target) and the measurement site, as in our case, we would expect little interference from these nonneutron components, with the possible exception of protons that have energies of at least a few hundred MeV. Protons and neutrons of such high energies produce similar responses in our detectors; furthermore, they are thought to be equivalent in terms of biological dose. "Equivalent" in this regard takes into account that the actual biological effect of such radiation, particularly the neutrons, has not been thoroughly studied. Typical calculations for 400-MeV nucleons normally incident on a slab of tissue-like material give, at 5 cm depth, values of 1.3×10^{-7} rem/proton and 4.5×10^{-8} rem/neutron. This difference is not an important error in our assumption, in view of the uncertainties in both the calculation and the actual biological effect, and because the dose delivered above 400 MeV in an equilibrium spectrum is small. Thus we feel justified in referring to measured particle fluxes and spectra as "neutron" fluxes and spectra, keeping in mind that we are including some proton component. We believe this proton component to be small.

B. Detectors

At well-shielded locations the spectral determination system consists of four detectors: a moderated foil (or moderated BF_3 counter), an aluminum disk, a plastic scintillator, and a bismuth fission (Bi-Fiss.) counter. The response functions we use here for these detectors are shown on Fig. IX-1; they are based on recent compilations by Bruninx[BruE 61-64] and Cumming [CumJ 63] and recent work of De Carvalho et al.[DeCH 63] Values of these functions are for neutron-induced reactions wherever such experimental data are available; neutron data exist mainly for energies below 20 MeV. The BF_3 response curve represents neutron data only, with the high-energy tail drawn at a reasonable slope. Aluminum, carbon, and bismuth-fission response functions are a blend of neutron data at lower energies with proton data at higher energies. Neutron and proton data have been joined smoothly in all cases, in a manner such that no significant proton reaction peaks are retained in the synthesized functions. It follows that if our spectra are in error in regard to intensity, the error will be in the direction of overestimating the intensity.

We call attention to the following general characteristics of the response functions. The BF_3 counter is sensitive mainly to neutrons below about 50 MeV; aluminum is sensitive to all neutrons above about 6 MeV. Carbon is sensitive above 20 MeV, and bismuth above about 50 MeV. As a result, our estimates of spectral shape above several MeV are rather closely limited, because at least two of the four detectors contribute information throughout this energy range. Below about 1 MeV the shape cannot be closely defined, because only the moderated foil gives spectral information in this energy region. For descriptions of the detectors, see Chapter III.

At locations inside the accelerator ring tunnel close to target 32 several other detectors were added to the four already described. These sites included several bucket positions above magnet 32 and a number of the angular-distribution measurement points discussed in Chapter VI. The reaction $S^{32}(n,p)P^{32}$ was used to improve spectral definition in the energy range from 1 to 10 MeV; $C^{12} \rightarrow Be^{7}$ and $Al^{27} \rightarrow Na^{22}$ were used to improve definition from 20 to 200 MeV; and $Hg \rightarrow Tb^{149}$, to improve definition above

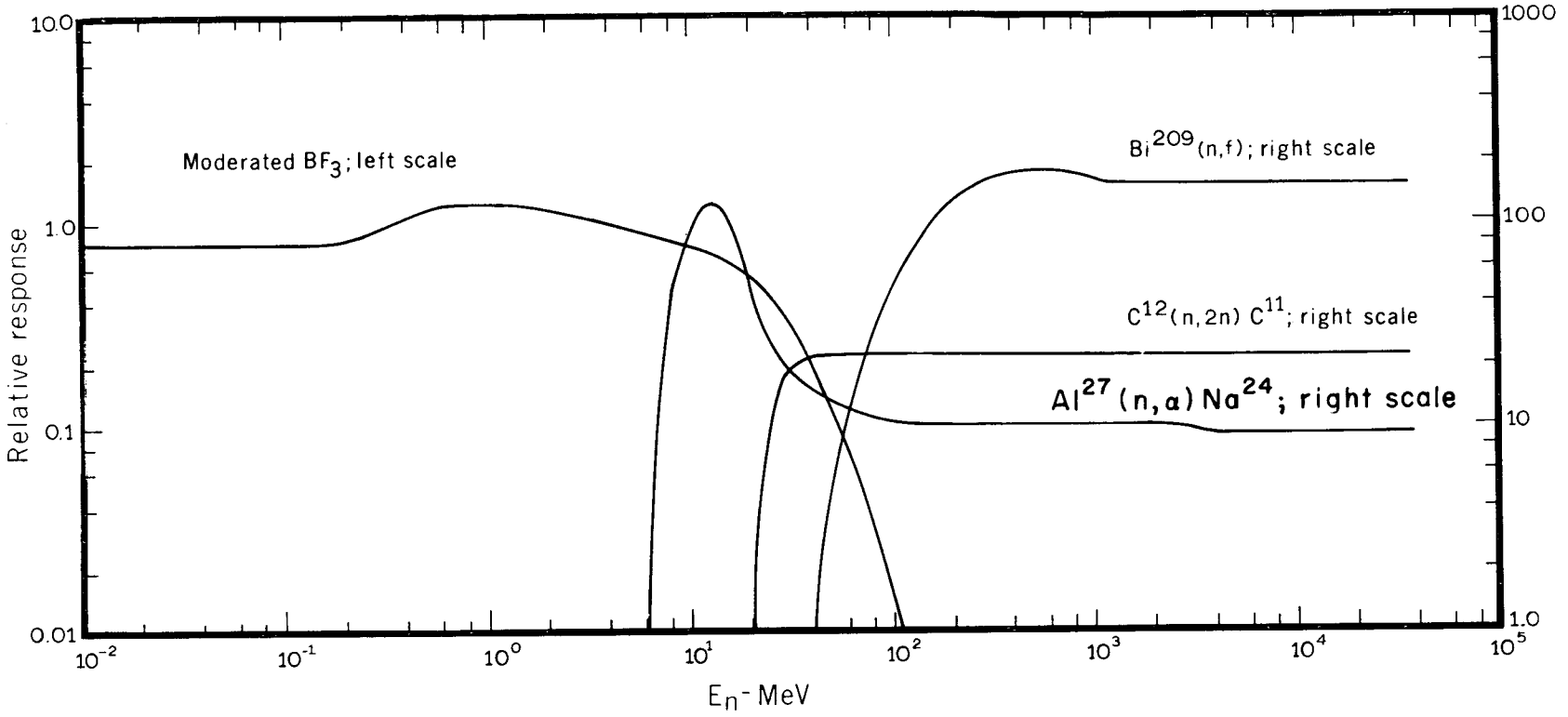

XBL 682 4491

Fig. IX-1. Response functions for the four detectors used to determine neutron spectra at well-shielded locations.

500 MeV. Response functions for these reactions are shown on Fig. IX-2; the curves were synthesized as described above, using the same data sources. The bismuth-fission detector used here was of the solid-state damage-track type (a slab of metallic bismuth against a thin sheet of mica) rather than a pulse counter. As before, we consider all particles to be neutrons, although we realize that there *may* be significant proton, pion, and photon contributions to the observed activities at these unshielded sites.

C. Computer Program TELLY

The experimental data from threshold detectors are usually defined in terms of the count rate observed in a particular field; those from counters such as the moderated BF_3 tube and bismuth-fission chamber are simply the observed count rates. The output y_i of any detector i is given by

$$y_i = k_i \int_{E_{min}}^{E_{max}} \sigma_i (E)\, \phi (E)\, dE,$$

where ϕ (E) is the neutron energy spectrum (particles/cm^2-sec-MeV), σ_i (E) is the cross-section curve for the particular detector, and k_i is a constant which converts the integral to the observed count rate. The problem is therefore one of determining the spectrum ϕ (E) from a knowledge of a set of y_i's with their

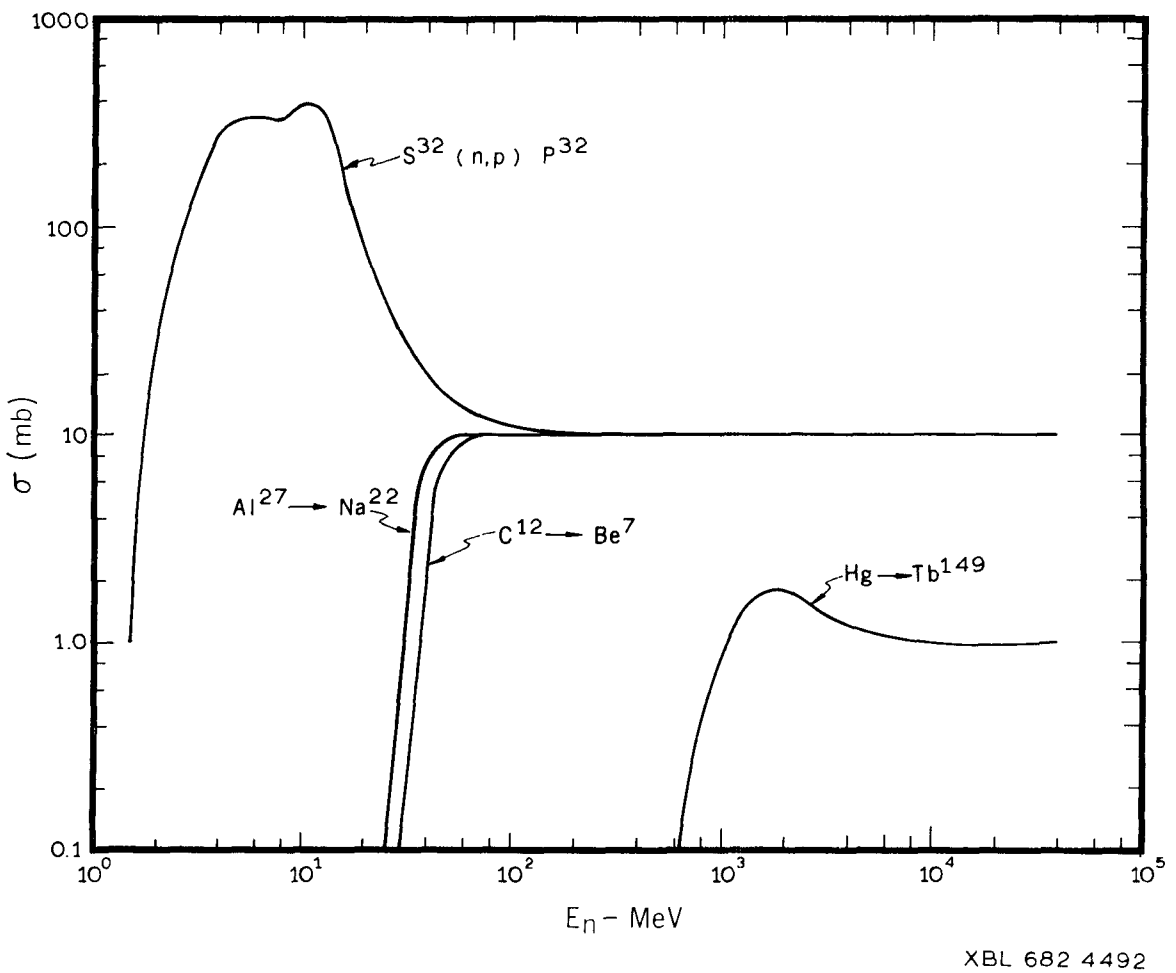

Fig. IX-2. Response functions for additional detectors used to determine neutron spectra inside the CPS tunnel near target 32.

corresponding σ_i's and k_i's. The digital computer programs written to solve such problems can be considered to be of two types, namely, open loop and closed loop. In an open-loop program, the operator must intervene to decide the nature of successive trial solutions (spectra). In a closed-loop program, the computer automatically selects successive trial solutions according to some specified internal scheme.

Both program types have been used with CERN data. An open-loop program TELLY was first developed and used for the analysis of most of the data. The procedures employed are described below in detail. To avoid the subjective judgments by the operator and to overcome the difficulty in finding a solution when more than a few measured responses are used, we have more recently developed closed-loop methods.[RouJ 68, HarD 68] These techniques may use as much physical *a priori* knowledge as is available, such as nonnegativity, nonoscillatory behavior, and cutoff energy of the neutron spectrum. The solution spectrum that matches the measured responses under these conditions is then computed automatically. In all cases investigated the solutions thus found were essentially identical with those obtained using TELLY. In either technique of course it is essential to be able to match the responses within reasonable experimental accuracy. This has been found to be the case both with the measured data and calculated responses corresponding to a wide variety of test spectra.

The computer program TELLY enables the user to construct a neutron-energy spectrum that matches experimentally observed responses from a set of energy-sensitive neutron detectors. The program computes counting rates that would be observed from a given neutron spectral distribution. TELLY employs an open-loop technique to solve the problem, in the sense that the user must supply modifications to an input neutron spectrum in order to achieve the match with a set of observed count rates. The spectral shapes are modified by using a light pen. One simply draws a desired modification on the cathode-ray tube (CRT) display, and almost instantly can observe the changes in calculated detector count rates brought about by this spectral alteration.

The program works as follows: The energy region from 48 eV to 36 GeV is divided into 72 intervals of nearly equal width on a logarithmic energy scale. Response functions for each detector are explicitly specified for the 72 intervals. An input spectrum is also specified for the same intervals. The program first displays this spectrum on the CRT. It then combines the spectrum, interval by interval, with each function in turn, to produce the counting rates that would be observed if the detectors were exposed to this flux distribution. The counting rates are also displayed on the CRT. The light pen can now be used to modify the CRT spectral shape, which generates a new set of detector count rates. Comparison of such trial count rates with a set of experimental count rates indicates the direction to be taken in successive spectral modifications. The process is continued until we have obtained the desired degree of match between observed and calculated count rates. That spectral distribution which produces the best match is then assumed to represent the experimental spectral distribution.

TELLY also computes the biological dose delivered by the trial spectra in each of the 72 energy intervals. Printed output includes a 72-point listing of differential flux spectrum, integral flux spectrum, dose integral, and a log-log plot of the differential flux spectrum. We have adopted these analytic expressions relating neutron energy to dose equivalent suggested by Thomas,[ThoR 65] as shown in Table IXA.

Table IXA. Analytic expressions for dose equivalent vs neutron energy.

Energy range (MeV)	$n\text{-}cm^{-2}\text{-}sec^{-1}$ equivalent to 1 $mrem\text{-}h^{-1}$
$< 10^{-2}$	232
$10^{-2} \cdot 10^{0}$	$7.20\ E^{-3/4}$
$10^{0} \cdot 10^{1}$	7.20
$> 10^{1}$	$12.8\ E^{-1/4}$

D. Experimental Conditions

The four-detector system was used to determine neutron-energy spectral distributions at two sites. These sites were chosen to represent shielding conditions often encountered near the PS machine, as well as to be pertinent to the main purpose of our experiment. The first of these, at station 33 on the ring top, is shielded by about 3.7 m of (mainly) earth from the accelerator ring tunnel. The location is one magnet unit downstream from the primary target position at station 32, and is just downstream from the peak in neutron flux profiles observed along the earth surface above the circulating beam orbit. Data were taken during periods of our control of the beam, so that only the station 32 target and a beam clipper at station 79 were active in the accelerator; thus some 70 to 80% of the beam was shared between target 32 and the clipper. The second site, on the PS bridge above station 11, is shielded by 1.8-m-thick concrete and is five magnet units downstream from a primary target at station 6. Data were taken while other experimental groups controlled the beam and several other targets were active; as a result, only about 15% of the total beam was directed onto target 6. However, there were no other nearby active targets that could be expected to contribute significantly to the radiation field at our measurement site.

The augmented system (six to eight detectors instead of four) was used at a number of locations near target 32, in conjunction with the angular-distribution studies described in Chapter VI. Sets of detectors were exposed at several bucket positions above magnet 32, and at positions along the two arcs centered on target 32.

E. Results

Typical spectral results from the ring-top and the PS bridge sites are shown on Fig. IX-3, along with the results obtained previously at the Berkeley Bevatron, and from cosmic radiation. For the ring-top site we also show results obtained from the proton-recoil distribution in a nuclear emulsion (for the energy range 2 through 20 MeV) and the slope of the spectrum above about 100 MeV inferred from star-prong analysis of the same emulsion. This line has a slope of $1/E^{1.8}$, a value similar to those obtained from the Bevatron and cosmic-radiation neutron spectra.

We believe these spectra to be closely restricted in general shape for energies above 2 to 3 MeV, where two or more of the detectors provide information. The good agreement between the TELLY spectrum and the emulsion spectrum obtained at the same ring-top location lends strong support to this statement. At lower energies, where only the moderated foil is sensitive, the spectral shape cannot be closely defined, and we have selected only simple shapes that satisfy the experimental counting rates. If we allow *no* sharp spectral structure (a sensible constraint in view of the physical principals and geometries involved), then the spectral shape can be considered to be reasonably well determined by the four-detector system down to about 0.1 MeV. Thus, we have good experimental information throughout the region of the neutron spectrum from which most of the biological dose results.

We call attention to the strong similarities among all the spectra shown on Fig. IX-3 for energies above 2 to 3 MeV; conversely, the major differences lie in the relative abundance (or depletion) of the low-energy population. Near the shield-air interface, the low-energy population is sensitive to the hydrogen content (mainly water) of the shield material. Our analysis of the earth cover above the tunnel showed a water content of 10 to 30% by weight—several times as much as is contained in typical concrete. On the assumption that CERN concrete is typical concrete, it is reasonable to assume this effect to be a major cause of the low-energy spectral differences noted here.

When we apply the flux-to-dose conversion factors (the analytic expressions by Thomas[ThoR 65]) to these spectral distributions, the following results are obtained from the TELLY program. Table IXB shows dose integrals at the ring top and PS bridge sites for actual experimental conditions. Dose values entered for each neutron energy are those doses delivered by all neutrons up to the listed energy. From the more detailed TELLY printout given in Table IXC, we can show that for the ring top, the aluminum detector responds in the energy range that contributes about 85% of this dose, and the carbon scintillator responds to the range that contributes about 70% of this dose. For the PS bridge site, corresponding values are about

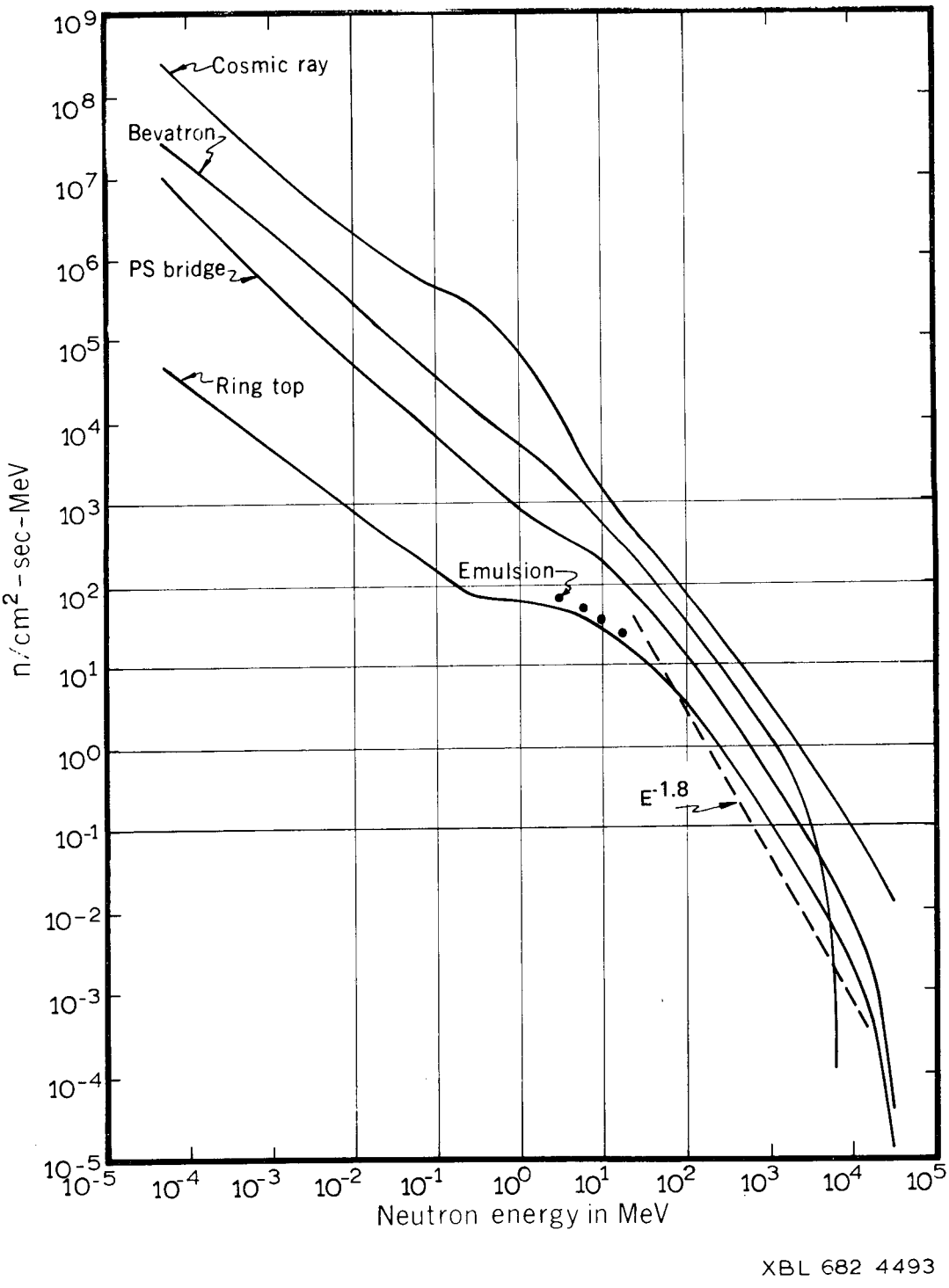

Fig. IX-3. Typical neutron spectra obtained from this experiment and from previous work. Relative intensities of spectra in this figure are arbitrary.

55% of the dose for aluminum and about 45% of the dose for carbon. Both detectors are seen to be well suited for these determinations.

The ring-top and PS bridge dose distributions are presented in a different format in Table IXD, along with results from the Bevatron, cosmic radiation, and the hypothetical 1/E spectrum. We use the same neutron-energy points as before, and now show the percentage of total dose delivered by all neutrons up to the listed energy. The last row on Table IXD lists values for the dose in rem/neutron delivered by each spectral distribution. The range of these values is less than a factor of 3, even though the actual distributions have large differences in certain energy regions.

Table IXB. Integral neutron dose values; TELLY program results.

Neutron energy (MeV)	Integral neutron dose (mrem/h)		
	Ring top	PS bridge	Bucket 32-2
6.0 E-05	2.04 E-04	3.06 E-02	5.68 E-04
6.0 E-04	2.14 E-03	1.88 E-01	4.24 E-03
6.0 E-03	5.38 E-03	3.50 E-01	9.03 E-03
6.0 E-02	1.84 E-02	7.68 E-01	2.36 E-02
6.0 E-01	1.94 E-01	3.48 E+00	1.32 E-01
6.0 E+00	2.37 E+00	1.42 E+01	4.87 E+01
6.0 E+01	9.22 E+00	3.20 E+01	3.74 E+02
6.0 E+02	1.81 E+01	4.93 E+01	6.21 E+02
6.0 E+03	2.25 E+01	5.79 E+01	6.32 E+02
3.4 E+03	2.38 E+01	5.92 E+01	6.32 E+02

It is of interest to determine whether reliable estimates of dose equivalent can be made with less then four detectors, and without the need to use a computer program such as TELLY. When only one detector is used its response must be related to the total neutron dose, even if the detector responds to neutrons in only a limited energy region. The flux equivalent to 1 mrem/h for each detector from each spectral distribution is listed in Table IXE; the flux measured by a detector is defined in the same way as in chapter III; e.g., for the aluminum detector the flux is the equivalent 14-MeV neutron flux. Inspection shows that a single detector can determine the dose equivalent in any of these spectra to within a factor of two.

Since each detector responds only to neutrons in a limited energy region, it is logical to relate this measurement to the dose equivalent from neutrons in the same energy region. By using two or more detectors which respond to neutrons from different parts of the spectrum, it should be possible to estimate the dose equivalent to greater precision than by using a single detector. Table IXF gives the flux-to-dose conversion factors that belong with each detector for one specified set of energy regions. These factors are much less dependent on neutron spectral shape than those listed in Table IXE. For two detectors the dose equivalent (DE) can be expressed as

$$DE = K_{AB}\left(\frac{\phi_A}{C_A} + \frac{\phi_B}{C_B}\right)$$

where ϕ_A and ϕ_B are the neutron fluxes determined by detectors A and B; K_{AB} is a factor which expresses either the lack of continuity or degree of overlap in the specified energy bounds of detectors A and B, and C_A and C_B are the appropriate dose-equivalent conversion factors from Table IXE.

The optimum combination of detectors is that which spans the largest fraction of the spectrum. Table IXG shows that a good estimate of dose equivalent is obtained by using a moderated BF_3 counter and

Table IXC. TELLY output for ring-top spectrum

Center points of energy intervals (MeV)	Differential flux (n/cm^2-sec-MeV)	Integral flux (n/cm^2-sec)	Integral dose (mrem)
5.20 E−05	7.25 E+04	5.80 E−01	2.50 E−03
6.52 E−05	6.35 E+04	1.76 E+00	7.57 E−03
8.62 E−05	5.71 E+04	3.10 E+00	1.33 E−02
1.14 E−04	4.63 E+04	4.58 E+00	1.97 E−02
1.52 E−04	3.67 E+04	6.23 E+00	2.69 E−02
2.05 E−04	2.93 E+04	7.99 E+00	3.44 E−02
2.72 E−04	2.34 E+04	9.74 E+00	4.20 E−02
3.68 E−04	1.86 E+04	1.19 E+01	5.12 E−02
4.98 E−04	1.48 E+04	1.40 E+01	6.04 E−02
6.62 E−04	1.18 E+04	1.62 E+01	6.98 E−02
8.72 E−04	9.52 E+03	1.84 E+01	7.94 E−02
1.15 E−03	7.72 E+03	2.09 E+01	9.01 E−02
1.54 E−03	6.14 E+03	2.37 E+01	1.02 E−01
2.06 E−03	4.89 E+03	2.66 E+01	1.15 E−01
2.74 E−03	3.91 E+03	2.95 E+01	1.27 E−01
3.68 E−03	3.11 E+03	3.31 E+01	1.43 E−01
4.98 E−03	2.47 E+03	3.67 E+01	1.58 E−01
6.64 E−03	1.97 E+03	4.03 E+01	1.74 E−01
8.74 E−03	1.59 E+03	4.41 E+01	1.90 E−01
1.15 E−02	1.29 E+03	4.82 E+01	2.10 E−01
1.54 E−02	1.03 E+03	5.28 E+01	2.38 E−01
2.06 E−02	8.20 E+02	5.78 E+01	2.75 E−01
2.74 E−02	6.54 E+02	6.27 E+01	3.21 E−01
3.69 E−02	5.21 E+02	6.87 E+01	3.91 E−01
4.99 E−02	4.14 E+02	7.46 E+01	4.79 E−01
6.64 E−02	3.30 E+02	8.08 E+01	5.90 E−01
8.74 E−02	2.67 E+02	8.71 E+01	7.30 E−01
1.15 E−01	2.17 E+02	9.40 E+01	9.21 E−01
1.54 E−01	1.72 E+02	1.02 E+02	1.18 E+00
2.06 E−01	1.38 E+02	1.10 E+02	1.54 E+00
2.74 E−01	1.20 E+02	1.19 E+02	2.01 E+00
3.69 E−01	1.15 E+02	1.32 E+02	2.88 E+00
4.99 E−01	1.11 E+02	1.48 E+02	4.20 E+00
6.64 E−01	1.07 E+02	1.68 E+02	6.23 E+00
8.74 E−01	1.04 E+02	1.92 E+02	9.30 E+00
1.15 E+00	1.01 E+02	2.25 E+02	1.38 E+01
1.54 E+00	9.57 E+01	2.68 E+02	1.98 E+01
2.06 E+00	8.74 E+01	3.20 E+02	2.71 E+01
2.74 E+00	8.07 E+01	3.81 E+02	3.55 E+01
3.69 E+00	7.62 E+01	4.69 E+02	4.76 E+01
4.99 E+00	6.61 E+01	5.65 E+02	6.09 E+01
6.64 E+00	5.95 E+01	6.75 E+02	7.62 E+01
8.74 E+00	4.98 E+01	7.92 E+02	9.25 E+01
1.15 E+01	4.05 E+01	9.21 E+02	1.11 E+02
1.54 E+01	3.22 E+01	1.07 E+03	1.34 E+02
2.06 E+01	2.57 E+01	1.22 E+03	1.59 E+02
2.74 E+01	2.05 E+01	1.37 E+03	1.87 E+02
3.69 E+01	1.63 E+01	1.56 E+03	2.23 E+02
4.99 E+01	1.23 E+01	1.74 E+03	2.60 E+02
6.64 R+01	8.85 E+00	1.90 E+03	2.96 E+02
8.74 E+01	6.49 E+00	2.06 E+03	3.33 E+02
1.15 E+02	4.92 E+00	2.21 E+03	3.73 E+02
1.54 E+02	3.34 E+00	2.36 E+03	4.14 E+02
2.06 E+02	2.23 E+00	2.50 E+03	4.54 E+02
2.74 E+02	1.42 E+00	2.60 E+03	4.88 E+02
3.69 E+02	9.04 E−01	2.71 E+03	5.23 E+02

Table IXC. (continued)

Center points of energy intervals (MeV)	Differential flux (n/cm^2-sec-MeV)	Integral flux (n/cm^2-sec)	Integral dose (mrem)
4.99 E+02	5.73 E−01	2.79 E+03	5.54 E+02
6.64 E+02	3.61 E−01	2.86 E+03	5.80 E+02
8.74 E+02	2.37 E−01	2.91 E+03	6.04 E+02
1.15 E+03	1.57 E−01	2.96 E+03	6.27 E+02
1.54 E+03	9.83 E−02	3.01 E+03	6.48 E+02
2.06 E+03	6.25 E−02	3.04 E+03	6.68 E+02
2.74 E+03	3.83 E−02	3.07 E+03	6.84 E+02
3.69 E+03	2.23 E−02	3.10 E+03	7.00 E+02
4.99 E+03	1.29 E−02	3.12 E+03	7.12 E+02
6.64 E+03	7.34 E−03	3.13 E+03	7.22 E+02
8.74 E+03	4.37 E−03	3.14 E+03	7.30 E+02
1.15 E+04	2.20 E−03	3.15 E+03	7.35 E+02
1.54 E+04	1.03 E−03	3.15 E+03	7.39 E+02
2.06 E+04	3.19 E−04	3.16 E+03	7.41 E+02
2.74 E+04	3.01 E−05	3.16 E+03	7.41 E+02
3.36 E+04	1.90 E−05	3.16 E+03	7.41 E+02

Rem per neutron = 6.53 E−08

Detector	Observed (proportional) c/min	TELLY computation c/min
Mod. BF_3	4.61 E+05	4.67 E+05
Aluminum	3.54 E+04	3.61 E+04
Carbon	2.00 E+05	1.97 E+05
Bismuth fission	1.11 E+03	1.17 E+03

Note: The *experimentally* observed detector count rate values were 1/30 the *proportional* observed values listed above. (Conversion of experimental to proportional quantities was done solely for convenience in the TELLY computer program.) The experimentally observed values were obtained with a circulating proton beam intensity of 1×10^{11} per sec, corresponding to a dose-equivalent rate of 24 mrem/h from this neutron spectrum. The nonneutron contribution (measured with the ionization chamber described in Chapter III, section 13) to the total dose-equivalent was observed to be 2.3 mrem/h.

Table IXD. Percentage distribution of neutron dose; TELLY program results

Neutron energy (MeV)	Percentage of dose from neutrons below listed energy					
	CERN proton synchrotron					
	Ring top	P S bridge	Bucket 32-2	Bevatron	Cosmic rays	1/E
6×10^{-5}		6.2 E−02		4.5 E−02	7.7 E−02	5.1 E−02
6×10^{-4}		3.6 E−01		3.0 E−01	4.8 E−01	3.0 E−01
6×10^{-3}	2.9 E−03	6.7 E−01		6.2 E−01	9.4 E−01	5.6 E−01
6×10^{-2}	2.1 E−02	1.35 E+00		1.7 E+00	2.85 E+00	1.18 E+00
6×10^{-1}	2.7 E−01	4.4 E+00	2.1 E−02	9.1 E+00	2.28 E+01	4.12 E+00
6×10^{0}	9.8 E+00	1.83 E+01	7.7 E+00	3.41 E+01	6.57 E+01	1.20 E+01
6×10^{1}	4.0 E+01	5.0 E+01	5.92 E+01	6.11 E+01	7.88 E+01	2.20 E+01
6×10^{2}	8.1 E+01	8.4 E+01	9.83 E+01	8.78 E+01	9.20 E+01	3.93 E+01
6×10^{3}	9.9 E+01	9.6 E+01	1.00 E+02	1.00 E+02	9.78 E+01	7.40 E+01
3.4×10^{4}	1.00 E+02	1.00 E+02	1.00 E+02	1.00 E+02	1.00 E+02	1.00 E+02
rem/neutron	6.53 E−08	3.83 E−08	5.98 E−08	3.17 E−08	2.30 E−08	5.85 E−08

Table IXE. Flux-to-dose conversion factors for single detectors.

Detector	Flux equivalent to 1 mrem/h				
	Ring top spectrum	PS bridge spectrum	Bevatron spectrum	Cosmic-ray spectrum	1/E spectrum
BF_3	1.66	4.33	6.2	10.7	3.0
Al	0.80	0.79	0.73	0.36	0.35
C	2.60	2.31	1.77	0.83	1.8
BIF	1.47	1.16	0.96	0.49	1.6

Table IXF. Flux-to-dose conversion factors in restricted energy regions.

Detector	Energy region	Flux equivalent to 1 mrem/h				
		Ring top spectrum	PS bridge spectrum	Bevatron spectrum	Cosmic-ray spectrum	1/E spectrum
BF_3	$<$ 10 MeV	12	19	16	16	22
Al	6 to 50 MeV	2.6	2.5	2.7	2.8	3.5
C	$>$ 20 MeV	3.2	3.2	3.2	2.9	2.1
BIF	$>$ 50 MeV	2.2	2.0	2.2	2.1	1.9

Table IXG. Accuracy of dose-equivalent estimation, in percent.

Flux-to-dose equations	$1.74\left(\frac{\phi(BF_3)}{8.0}+\frac{\phi(Al)}{3.3}\right)$	$1.13\left(\frac{\phi(BF_3)}{8.0}+\frac{\phi(C)}{3.0}\right)$	$1.05\left(\frac{\phi(BF_3)}{8.0}+\frac{\phi(Al)}{3.3}+\frac{\phi(BiF)}{2.4}\right)$
	(%)	(%)	(%)
Ring top spectrum	-20	+ 15	+10
PS bridge spectrum	+5	+ 5	+ 2
Bevatron spectrum	+25	+ 5	+ 1
Cosmic-ray spectrum	+35	- 2	
1/E spectrum	-25	- 10	-15

and a carbon detector; accuracies of about 20% are possible. There is some improvement in accuracy if three detectors are used with these conversion factors, as shown in the last column of Table IXG. Although the TELLY results are the basis for this comparison, we believe the use of all four detectors in conjunction with TELLY does provide the most accurate estimate of dose equivalent.

On Fig. IX-4 we show a TELLY-derived neutron spectrum for roof bucket position 32-2, obtained from detectors exposed during a full-energy experiment, Run V. All reactions except $Al^{27} \rightarrow Na^{22}$ were used to construct this spectrum. As measured from target 32, this bucket position lies at about 40 deg to the forward direction of the proton beam. The spectrum observed here is considered to be representative of that radiation which must be dealt with in providing transverse shielding for such accelerators. The lower curve on Fig. IX-4 is the ring top spectrum shown previously, repeated here for purposes of comparison; relative intensities of the two spectra are not meaningful.

At such an unshielded site, there may be significant activation in some detectors caused by charged particles and high-energy photons; thus the true neutron spectrum may look somewhat different from this representation. (In its present form, our spectral-analysis technique cannot distinguish among these choices of activating-particle fluxes.) It is instructive to assume that we have constructed a reasonable approximation to the true spectral shape; then, to inquire what dose distribution results from this particle distribution. The last column on Table IXB and the fourth column on Table IXD list some of the important dose-distribution characteristics. Of particular interest is the value for rem/neutron: 5.97×10^{-8} in this case, a value quite similar to values found for all other spectral shapes studied.

The CERN Health Physics (CHP) group performed many related sets of measurements during this series of experiments; some of these are discussed now. Complete records of such measurements are kept on file by CHP, and inquiries concerning detailed analysis of their data should properly be referred to that group.

Some of the detectors used by the CHP group are nearly identical to those used by LRL, and so it should be possible to compare results obtained by the two groups. Such comparisons can be made on two distinct levels: (1) measurement of particle fluxes; and, (2) estimation of dose delivered by the measured fluxes. Two flux-measurement techniques in common use by both groups (that were also used extensively in this work) are the moderated foil technique for fast-neutron flux measurement, and the plastic-scintillator technique for high-energy particle-flux measurement. Note that these techniques give information mainly from different regions of the neutron-energy spectrum, and so will indicate changes in the spectrum important enough to have a significant effect on the flux-to-dose conversion. (Spectral change is indicated when we observe a change in the ratio between responses of the two detectors.)

CHP and LRL groups were rarely able to make simultaneous flux determinations at a given location, partly because of the physical size of detectors, and partly because of space limitations at many measurement sites (particularly in orbit and radial holes). Comparisons must then be made via some normalization procedure that is based on monitor data. We use the measurement of circulating proton-beam intensity as the monitor quantity, and normalize flux values to constant intensity conditions: 10^{12} p/sec in this case. There is some uncertainty introduced by this kind of normalization, because to make use of it, we must assume that beam-target interactions remain constant from run to run--a relationship known to be somewhat inexact. Data from various monitor detectors suggest that the magnitude of this uncertainty is unlikely to be greater than 15%. If we can also assume that variations in irradiation *rate* during each exposure have been properly taken into account--an important item with these relatively short-lived activities--then the flux comparisons should be valid to the same precision, about 15%.

We show two sets of flux profiles from the experimental runs. The first, Fig. IX-5, shows fast-neutron flux profiles along the ground surface on the ring top directly above the circulating beam orbit, in the vicinity of Target 32. Open circles represent CHP data taken during Run VIII with moderated indium foils; crosses represent LRL data taken during Run VII with moderated gold foils. Flux values are normalized to a circulating proton-beam intensity of 10^{12} p/sec. In both cases, conversion of foil count rates to neutron flux intensity is based on calibration with Pu^{239}-Be neutron sources.

During our stay at CERN, the CHP reference Pu^{239}-Be source and the LRL standard Pu^{239}-Be source were compared directly. Measured emissions from the two sources were found to differ by 15% compared to the listed values, in the sense that the CHP source is 15% larger than listed if the LRL source

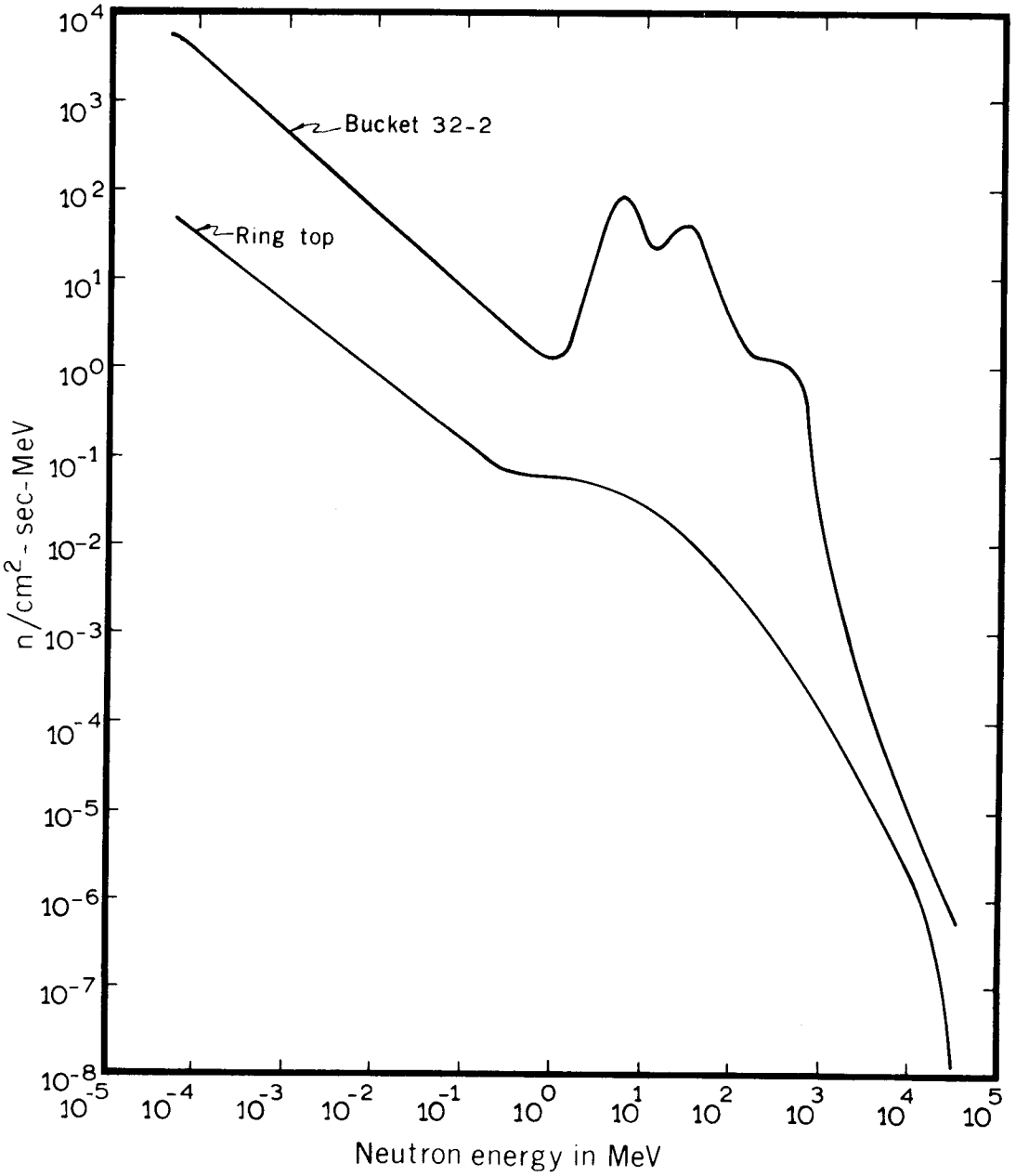

Fig. IX-4. Comparison of neutron spectra obtained at well-shielded and unshielded locations. Relative intensities of spectra in this figure are arbitrary.

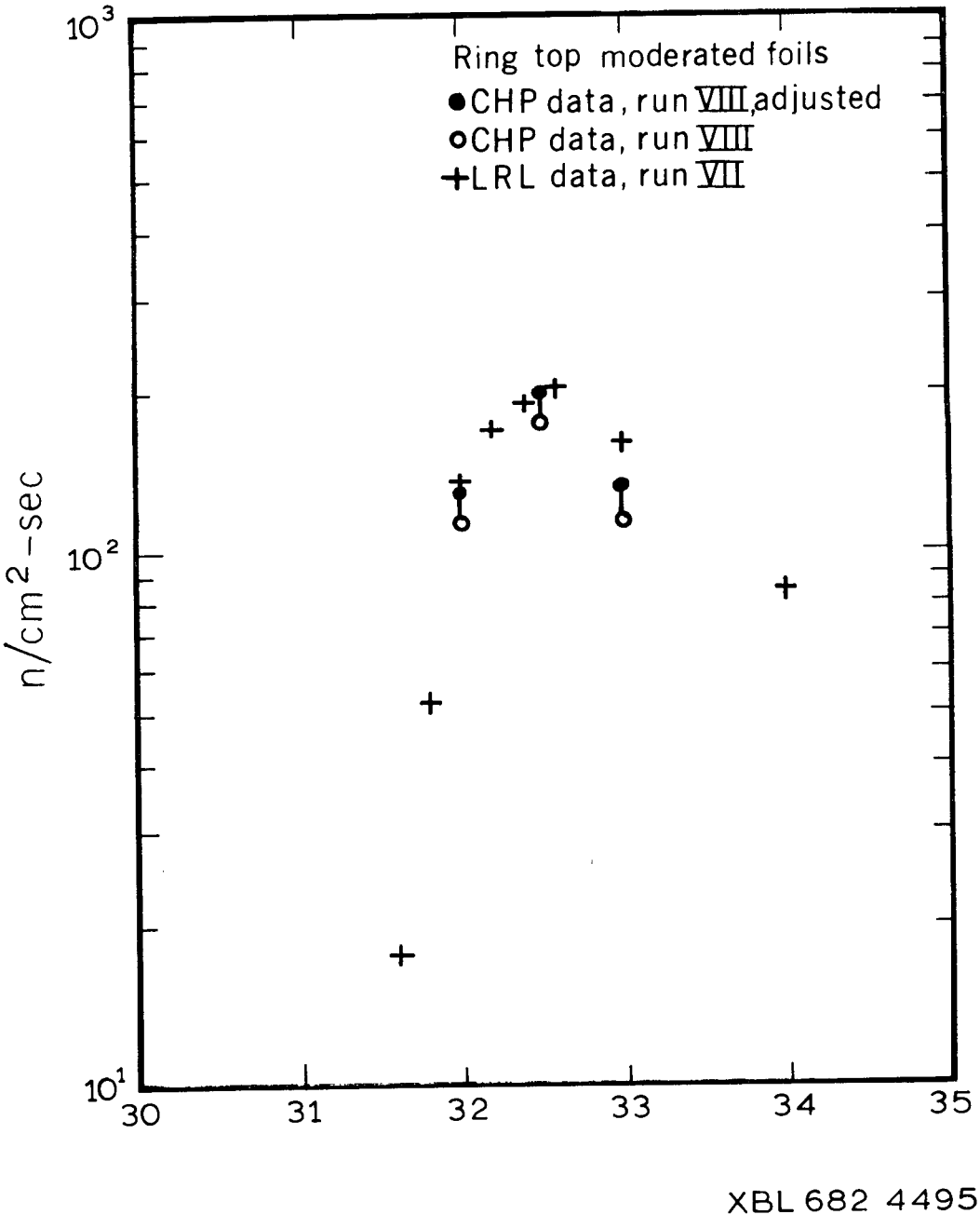

Fig. IX-5. Comparison of CHP and LRL moderated-foil results at ring top locations.

is correct. The LRL source has been calibrated twice by the U. S. National Bureau of Standards and twice by the manufacturer; all values so obtained fall within the ±3% error assigned to the absolute emission rate of the source. The CHP source was calibrated by the manufacturer and compared to Amersham Po-Be sources; these two values also agreed within ±3%; but differ from the LRL source value, as noted above. For the present flux-profile comparison, we assume the LRL source to be correct (although such may not be the case); therefore, the CHP profile must be raised by 15%, as shown by the solid circles on Fig. IX-5. (Subsequent recalibration of the CHP source confirmed validity of the corrections applied here to CHP data.)

The second comparison shows high-energy flux profiles, again from data taken along the ground surface on the ring top. On Fig. IX-6, the open circles represent CHP data taken during Run I, and open triangles represent CHP data taken during Run III; crosses represent LRL data taken during Run II. Flux values are normalized to a circulating proton-beam intensity of 10^{12} p/sec. Both groups use calibration values based on a 22-mb reaction cross section and 100% counting efficiency at the extrapolated zero-bias point on the discriminator curve. Some differences in calibration constants may arise from the zero-bias extrapolation procedure, which must be carefully done; however, these differences should not be greater than 5% when proper care is taken.

Comparisons of both sets of profiles indicate that CHP and LRL techniques for flux measurement are in good agreement, although normalization uncertainties obscure the true quantitative measure of agreement. Even in the presence of normalizing problems, the profiles are seen to agree within about 10%, except for the discrepancies between neutron-source calibrations. When source calibration is adjusted, the fast-neutron flux values are brought within the 10% limit.

The source-calibration discrepancies noted here between CERN and LRL may exist among other laboratories. These differences could be determined through exchange of neutron sources, but it is an inconvenient, cumbersome, and time-consuming effort to do so. Rather, an exchange of integrating neutron detectors can accomplish the same purpose. To this end, LRL has begun a program of source intercomparisons through use of moderated cobalt disks and nuclear emulsions.

We can directly compare these flux-measurement techniques from simultaneous irradiations performed at one location on the PS bridge. Table IXH lists the results, shown as values obtained under actual operating conditions; no normalizations enter into the calculations.

Results from both techniques show very good agreement; in fact, differences are less than 5% from the average values. Furthermore, if either value is correct, the other is less than 10% in error. We conclude that these two techniques, used by CHP and LRL either independently or jointly, will report the same flux intensities in a given radiation field. It follows that any differences in assignment of biological dose equivalent, when such dose equivalent is based on these flux measurements, must be due to differences in interpretation of flux-to-dose equivalent conversion.

Table IXH. Flux measurement technique comparison, PS bridge site.

	Flux (n/cm^2-sec)	
	LRL	CHP
Moderated foil	246	235[a]
C^{11}	132	124

a. This value is 15% greater than reported value, for reasons discussed in the text.

The flux-measurement comparisons were part of the larger purpose: to compare estimations of dose equivalent. At this PS bridge site, the CHP group used a number of additional radiation detectors including: a TE ionization chamber, an AIR ionization chamber, and a boron ionization chamber. The LRL group also employed aluminum and bismuth-fission threshold detectors, neutron track plates, and

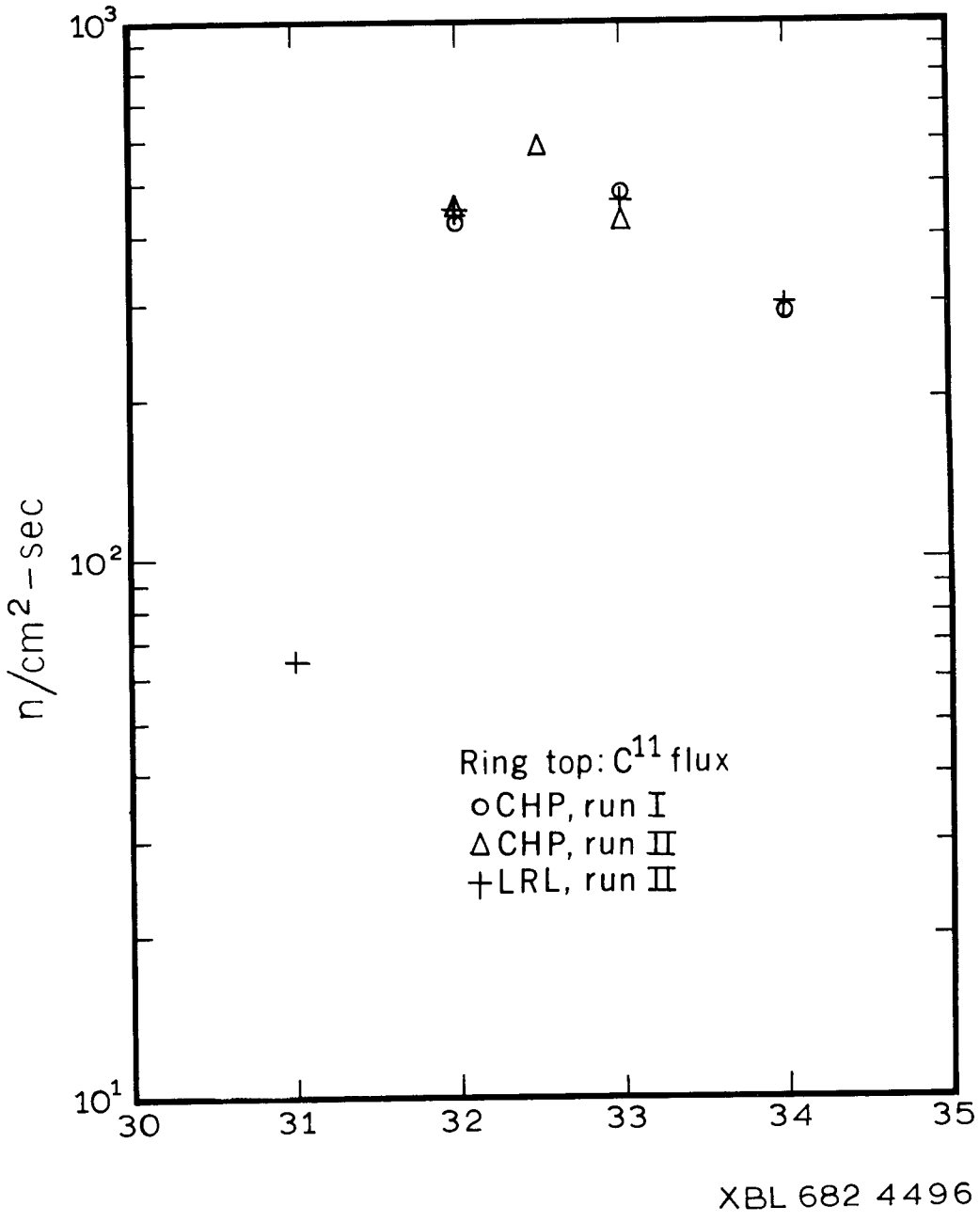

Fig. IX-6. Comparison of CHP and LRL carbon-scintillator results at ring top locations.

(ultimately) neutron spectral analysis through use of the TELLY computer program. Results of this comparison are shown on Table IXJ, where we are concerned only with the neutron contribution to the total dose. We note that CHP determined the "gamma-ray and charged particle" dose to be 4 mrem/h, an amount small relative to the neutron dose.

Table IXJ. Comparison of dose estimations at PS bridge site.

Neutron energy interval	LRL TELLY spectrum (mrem/h)	CHP survey (mrem/h)
< 1 eV		< 1
< 0.1 MeV	1	——
0.1 to 15 MeV	19	33
15 to 20 MeV	2	——
> 20 MeV	37	12
Total neutrons	59	45

LRL flux-to-dose conversion is accomplished as listed on Table IXA; CHP flux-to-dose conversion is accomplished as described in detail by Goebel,[GoeK 67] and is summarized briefly here. This interpretation is based on the concept of estimating separately the contribution to the dose equivalent (DE) of the most important reactions initiated by the mixed radiation field. The following reactions are considered separately:

1. High-energy particle (HEP) reactions with tissue: DE estimated from the integral strong-interacting particle flux above 20 MeV with a unique constant conversion factor of 10 HEP/cm^2-sec = 1 mrem/h;
2. Proton recoil reactions of fast neutron: DE estimated from the fast-neutron flux measured with a moderated BF_3 counter or a moderated indium foil, with a constant conversion factor of 7 n/cm^2-sec= 1 mrem/h;
3. Neutron absorption reaction of thermal (or greater than thermal) neutrons in tissue: DE estimated from the thermal-neutron flux measured with a BF_3 chamber or with Cd-shielded indium foils with a conversion factor of ~ 280 n_{th}/cm^2-sec = 1 mrem/h;
4. Electromagnetic interaction of the mixed radiation field: DE estimated from the response of an air-filled ionization chamber calibrated against a 10 mg Ra source.

By taking simultaneous measurements with a TE chamber, it is also possible to estimate the quality factor (QF) of the radiation field.

The CHP measurement shows the dose contribution from slow neutrons (< 1 eV) to be insignificant. The moderated foil response, as defined by CHP, lies in the neutron energy region 0.1 to 15 MeV; thus, all dose attributed to moderated foil response must result from this energy interval. In reality, the moderated foil responds in both the intervals below and above the 0.1- to 15-MeV band; therefore some of the assigned dose must also lie in these two adjacent bands. Thus the CHP value of 33 mrem/h should be compared to an LRL value that is 20 to 22 mrem/h. There does not seem to be serious disagreement here.

Above 20 MeV, a CHP value of 12 mrem/h is to be compared to an LRL value of 37 mrem/h; these values are considerably different. CHP dose assignment in this energy region is based only on C^{11} flux values; LRL dose assignment is also based on C^{11} flux, but with additional information from aluminum and bismuth fission detectors, via the TELLY program. We have seen that both C^{11} flux-determination methods are in good agreement, and so physical measurement is ruled out as an explanation for the difference in dose-equivalent estimation. A small part of the difference can be due to minor differences in the LRL interpretation of the neutron spectrum (TELLY program results). The remaining difference, which is by far

the most important part, is clearly related to a difference of interpretation of the dose equivalent associated with neutrons that are above 20 MeV energy. From the expression listed on Table IXA, the LRL flux-to-dose conversion at 20 MeV is 6 n/cm^2-sec per mrem/h, and is a monotonically decreasing function of energy for all energies above 10 MeV. In contrast, the CHP flux-to-dose conversion at 20 MeV is 10 n/cm^2-sec per mrem/h, and is taken to be constant for all higher energies. Thus we conclude that the differences in dose-equivalent estimation are due largely to administrative decisions, and are not related to any disagreement between physical-measurement techniques employed by the two groups.

References

BruE 61-64. E. Bruninx, High-Energy Nuclear Reaction Cross-Sections, CERN Reports CERN 61-1, January 16, 1961; CERN 62-9, February 15, 1962; CERN 64-17, March 18, 1964.

CumJ 63. J. B. Cumming, Monitor Reactions for High-Energy Proton Beams, Ann. Rev. Nucl. Sci. *13,* 261 (1963).

DeCH 63. H. G. De Carvalho, G. Cortini, M. Muchnik, G. G. Potenza, R. Rinzivillo, and W. O. Lock, Fission of Uranium, Thorium, and Bismuth by 20-GeV Protons, Nuovo Cimento *27,* (2), 468 (1963).

GoeK 67. K. Goebel, A. Rindi, A. H. Sullivan, J. Baarli; The Purpose, Interpretation and Utilization of Area Monitoring Measurements near the CERN Accelerators; in *Radiation Dose Measurements, Their Purpose, Interpretation and Required Accuracy in Radiological Protection, Stockholm Symposium, 1967, (*European Nuclear Energy Agency, Paris, 1967) pp. 435-458.

HarD 68. D. N. Hargreaves, Unfolding Neutron Energy Spectra Using the "Alfie" Routine, RHEL/M 147, July 1968.

RouJ 68. Jorma T. Routti, private communication, 1968.

ThorR 65. R. H. Thomas, The Radiation Field Observed Around High-Energy Nuclear Accelerators, in Proceedings of XI International Congress of Radiology, Rome, September 22-28, 1965.

X. DESIGN OF SHIELDING FOR HIGHER-INTENSITY AND HIGHER-ENERGY PROTON SYNCHROTRONS

A. General

At the time of our measurements in late 1966, the CERN proton synchrotron accelerated a beam of approximately 2×10^{11} protons per second at a maximum proton momentum of 26.4 GeV/c. The Brookhaven AGS at a maximum proton energy of some 30 GeV also has an average beam current of several times 10^{11} protons per second. Both of these accelerators have improvement programs underway that will increase the average beam current to more than 10^{13} protons per second. Proposed new accelerators of 200 GeV in the U. S. and 300 GeV in Europe also plan for beam currents greater than 10^{13} protons per second. In this chapter we consider the design of the shielding for these new and improved accelerators and the evaluation of relevant shielding constants from the CPS shielding experiment.

Our analysis of the measured CPS neutron fluxes enables us to predict the fluxes that would exist at shielding depths greater than those actually measured in our experiment. This is equivalent to designing shielding for the CPS (and with some modifications, for the Brookhaven AGS) with greater beam loss than is currently possible. We explain this procedure in detail in section B.

For new accelerators operating at different energies, and having different assumed beam losses and design parameters, the shield design problem requires more steps than those involved in increasing the beam loss in the CPS. In chapter VIII we demonstrated that the measured neutron fluxes were satisfactorily calculated using the Moyer shielding model as expressed through our FLUXFT computer program. In this procedure the problem is separable into the beam-loss distribution, which is a property of a given accelerator, and the physical processes that determine the multiplicity, angular distribution, and removal mean free path of the produced penetrating neutrons. These physical processes are either not energy-dependent above a certain primary proton energy, or can be scaled with energy with confidence; for these reasons the results of the CPS experiments can be used directly to specify shielding for higher-energy accelerators, as is covered in section C. The beam loss distribution problem, on the other hand, is a function of machine design and resultant beam dynamics.

The calculation of new shielding can be approached through three stages of increasing effort and correspondingly increasing detail and accuracy. For any new situation, the machine designer must specify the beam loss parameters, which in turn can be converted to primary beam loss around the accelerator in units of GeV-cm^{-1}-sec^{-1}. The FLUXFT constants and program and dose-depth curves developed for the CPS are then used in the following alternative ways:

1. Use dose-depth curves for CPS for the new problem, scaling for primary beam loss differences.
2. Run the FLUXFT program with the new accelerator beam-loss distribution expressed in program constants, and with the magnet and tunnel geometry assumed to be the same as for the CPS.
3. Run the FLUXFT program with magnet and tunnel geometry appropriate to the new accelerator, and with calculated beam loss distribution.

B. Higher Intensity CPS

1. Dose-Depth Curves for CPS at I = 10^{12} protons-sec^{-1}

The neutron fluxes measured around the CPS are satisfactorily calculated with the analytic procedures discussed in chapter VIII. Higher beam intensity and loss in the CPS will therefore require a thicker shield, and the expected fluxes can be calculated with our computer programs. The dose equivalent of these neutron fluxes then requires the use of the equivalence factors developed in chapter IX.

For example, we have used the neutron fluxes measured with 52 aluminum detectors in run II, in which the proton momentum was 26.4 GeV/c, or the energy was 25.5 GeV. These fluxes were then input to the FLUXFT program, and a best fit was obtained. New fluxes were then calculated at great depths.

Dose-depth curves for the quiet, or low-loss, region and for the maximum-target-loss region appear in Fig. X-1. These curves apply for the actual target and clipper used in our experiment, and are normalized to a circulating proton current of 10^{12} proton-sec^{-1}, *all of which is lost inside the accelerator.* These curves can be used to calculate shielding for new accelerators when the beam loss is expressed in units of GeV-cm^{-1}-sec^{-1}, as well as additional shielding for the improved CPS. Relevant features of the CPS are:

a. The magnet thickness above the beam line is H = 58 cm, the average density of laminated magnet ρ_{Fe} is approximately 7, and T_{Fe} is approximately 400 g-cm^{-2}. If the actual magnet is thicker or thinner, subtract or add the difference to the required earth shielding.

b. The ceiling or roof height is 2.74 m above beam line.

c. The shield is the concrete roof plus the gravel and earth:

(i) $\rho_{earth} = 2.16$ g-cm^{-3}.

(ii) $\rho_{(concrete + gravel)} = 2.00$ g-cm^{-3}.

d. The spectrum to dose-equivalent conversion of chapter IX shows that the greater water content of soil compared with concrete causes the dose equivalents for the same flux to be somewhat different in the two materials. The curves are for earth.

e. The beam loss in units of GeV-cm^{-1}-sec^{-1} can be evaluated in the following way:

(i) From chapter VIII, the beam-loss distribution is expressed as

$$S(Z) = 1 + a_1 \exp(-a_3 Z). \tag{1}$$

Here we use $a_1 = 220.4$ and $a_3 = 0.1453$ m^{-1}, which are the best-fit values determined using the FLUXFT program.

(ii) The CPS radius is 100 m; the circumference is 628 m.

(iii) The clipper loss is 0.426 target loss (from chapter V).

(iv) The loss around the entire accelerator due to the target can be expressed as

$$L = c \int_0^{628\ m} S(z)\, dz = C\left(628\ m + \frac{a_1}{a_3}\right). \tag{2}$$

Adding the clipper loss (iii) to Eq. (2) gives for the total loss

$$L_{total} = C\left(628\ m + 1.426\ \frac{a_1}{a_3}\right) = C\,(628\ m + 2163\ m)$$
$$= C\,(2791\ m). \tag{3}$$

The total loss expressed in terms of energy is

$$L_{total} = 10^{12}\ \text{protons-sec}^{-1} \times 25.5\ \text{GeV-proton}^{-1} = 2.55 \times 10^{13}\ \text{GeV-sec}^{-1}.$$

The quiet-region loss is then

$$L_{quiet\ region} = \left(\frac{1}{6.28 \times 10^4\ cm}\ \frac{628\ m}{2791\ m}\right) \times 2.55 \times 10^{13}\ \text{GeV-sec}^{-1}$$
$$= 9.14 \times 10^7\ \text{GeV-cm}^{-1}\text{-sec}^{-1},$$

and the maximum target loss is

$$L_{\substack{max. \\ target}} = a_1 L_{quiet} = 220.4 \times 9.14 \times 10^7\ \text{GeV-cm}^{-1}\text{-sec}^{-1}$$
$$= 2.01 \times 10^{10}\ \text{GeV cm}^{-1}\text{-sec}^{-1}.$$

2. Use of Dose-Depth Curves to Estimate Required Shielding

Figure X-1 gives dose rate as a function of shield thickness for two conditions of beam loss typical to the CPS. If we assume a circulating proton beam intensity of 10^{12} protons-sec^{-1} and the target and clipper operation which obtained throughout the experiment, the dose rate may be directly read from these curves.

These curves may also be used to estimate approximate shield thicknesses for other accelerators where beam loss and required dose rate lie in the same range as those given in the figure. These shield

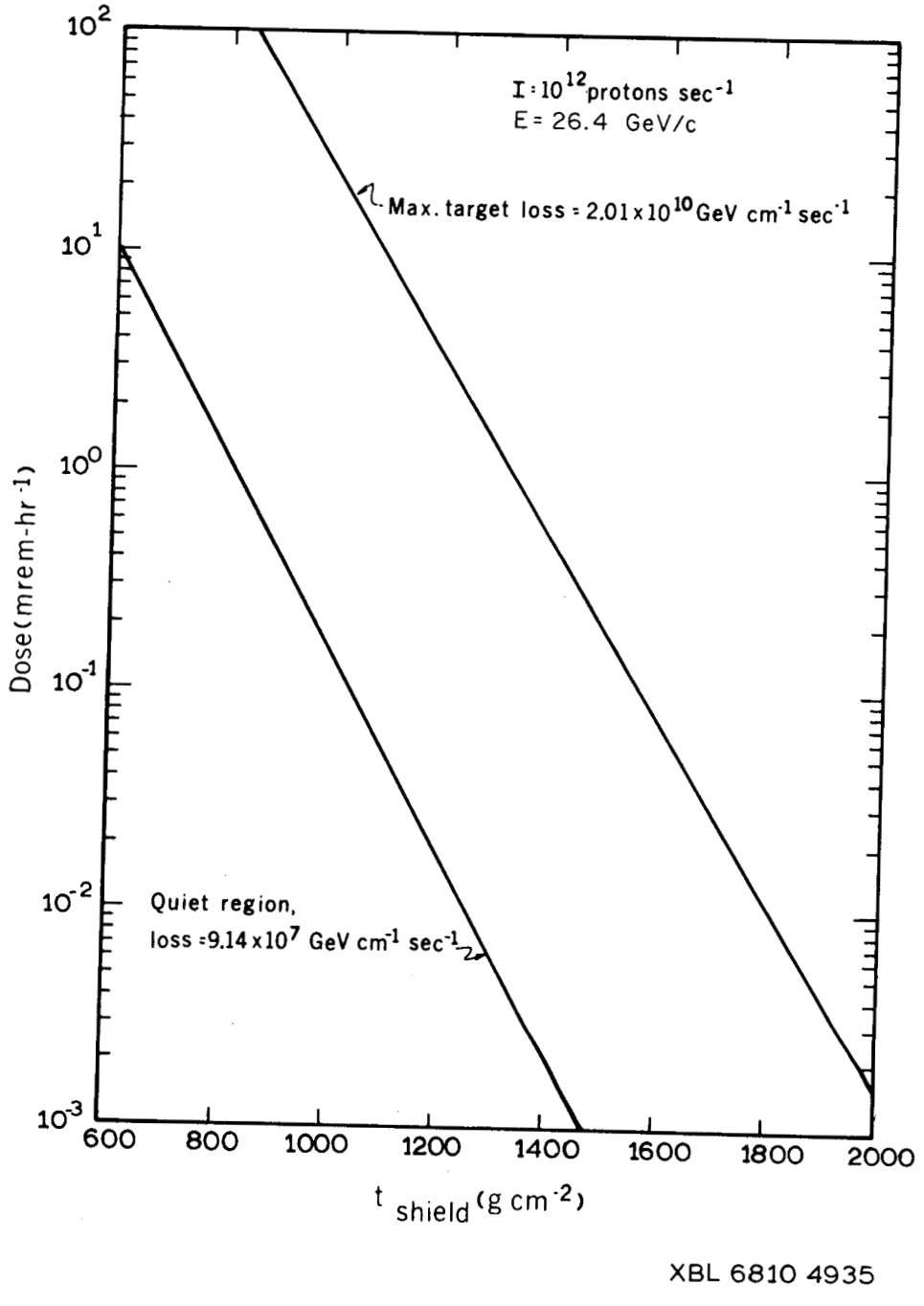

Fig. X-1. Variation of dose rate with shield thickness.

thicknesses can be obtained by a linear scaling of the two quantities, dose rate and beam loss. However, since these curves represent approximations from FLUXFT calculations, the further dose rate and beam loss are extrapolated from the values plotted here, the less accurate the approximations.

Specific examples of shield thickness estimates using this thickness are given in Table XA.

Table XA. Shielding required above CPS main ring for 0.8 mrem-h^{-1} at the surface.

Accelerator energy	(GeV)	Beam-current loss* ($psec^{-1}$)	Shielding required (g-cm^{-2}) Quiet region	Target region
Present PS	25.5	2×10^{11}	685	1175
Improved PS I	25.5	1×10^{12}	840	1345
Improved PS II	25.5	1×10^{13}	1055	1590

*These currents represent the total beam lost in the accelerator, not necessarily the total circulating beam.

C. FLUXFT Constants for Higher-Energy Synchrotrons

1. Dependence of a_9 on E for CERN Shielding Experiment

Neutron-flux measurements were made with carbon and aluminum activation detectors for two primary proton momenta; for example in run II, p = 26.4 GeV/c, and in run VII, p = 14.6 GeV/c. Table XB lists the FLUXFT program minimization-of-error parameters. For these four cases the parameters in the table were allowed to vary, while a_2 was fixed at 1, a_5 at 0.2, and a_7 and a_8 at zero.

Table XB. FLUXFT results

Detector	No. of points	Run	V(a)	a_1	a_3	a_4	a_6	a_9	$\frac{\Phi \cdot \phi}{\phi}$* Average	Maximum
C^{11}	16	II	1.35	236	0.157	1.75	114.1	7.44×10^5	0.29	0.56
Al	52	II	1.48	220	0.145	2.13	117.4	5.30×10^5	0.17	0.31
C^{11}	37	VII	0.76	339	0.174	2.46	118.6	1.02×10^6	0.14	0.32
Al	40	VII	0.46	221	0.167	2.13	116.1	4.02×10^5	0.11	0.31

*Φ is the measured flux; ϕ is the flux calculated by FLUXFT.

Since corresponding a's at the two proton energies are not the same (e.g., the angular distribution changes), a direct comparison of a_9 with beam kinetic energy is not possible. The measured fluxes at the higher beam energy are higher by a factor which varies between 1.2 and 2.0 than those at the lower energy as compared with the ratio of the proton kinetic energies of 1.86. By allowing a_9 to be a free parameter, its variation with proton kinetic energy may be studied in these two cases. The results of this procedure are given in Table XC. All eight of the other problem parameters are fixed:

$a_1 = 220$ $a_5 = 0.2$

$a_2 = 1$ $a_6 = 117$

$a_3 = 0.15$ $a_7 = 0$

$a_4 = 2.2$ $a_8 = 0.$

Table XC. FLUXFT results

Detector	No. of points	Run	V(a)	a_9	Maximum $\frac{\Phi-\phi}{\phi}$
C^{11}	16	II	1.52	1.29×10^6	0.55
Al	52	II	1.56	6.15×10^5	0.34
C^{11}	37	VII	1.73	9.16×10^5	0.46
Al	40	VII	1.09	3.47×10^5	0.35

From Table XC, the ratio of a_9 at the two energies for C^{11} is 1.41, that for aluminum is 1.78, and the ratio of kinetic energies is 1.86.

It is difficult to draw quantitative conclusions from these ratios, since from Table XB above, we can see that the best fits yield different beam-loss distributions at different primary proton energies, whereas, to obtain the a_9 ratios, we have to force all the problem constants to be the same. The high-energy carbon detectors were used less frequently in runs II and VII, so that here the constraint on the solution is weaker than in the other cases. Therefore we do not necessarily assume that the difference between the carbon and aluminum ratios are real, or that it depends on their different response functions. Rather we conclude that there is more flux at higher energy (for the same lost beam current) and the fits are not inconsistent with the linear dependence of the flux on proton energy.

2. Dependence of FLUXFT Results on a_4

a. Fitting of CPS shielding data.

Parameter a_4 is not as tightly constrained by the FLUXFT minimization-of-errors technique as are some other parameters. In Table XD, we list the values of V(a) for various values of a_4 for a typical problem, in this case 52 aluminum detectors in the earth shield in run II. The fixed parameters are:

$a_1 = 220$ $\quad$ $a_5 = 0.2$

$a_2 = 1$ $\quad$ $a_6 = 117$

$a_3 = 0.17$ $\quad$ $a_7 = a_8 = 0$

Table XD. Dependence of V(a) on a_4.

a_4	V(a)	Maximum $\frac{\Phi-\phi}{\phi}$
1.0	7.44	0.86
1.5	5.12	0.71
2.2	3.09	0.50
3.0	3.18	0.54
4.5	10.25	0.84

b. Moyer Integrals and Values of a_4

The influence of the angular distribution on the effective transmission has been studied by Routti and Thomas.[RouJ 69] The flux of high-energy particles of energy greater than 150 MeV has been shown (Chap. VIII) to be given by

$$\phi\ (E > 150\ \text{MeV}) \propto \int_0^{\pi} g(\theta)\ \exp\ (-d \csc \theta/\lambda)\ d\theta .$$

for a uniform source strength.

Assuming that the angular distribution $g(\theta)$ could be approximated by an exponential $e^{-a_4\theta}$ at angles close to 90 deg, Routti and Thomas evaluated integrals of this general form known as "Moyer" integrals. These integrals have been evaluated in the region of interest, i.e., values of a_4 between 0 and 13 for shield thicknesses up to 40 mean free paths.

For angular distributions typified by $a_4 \approx 2$, the transmission of high-energy particles is closely exponential at penetrations greater than about five mean paths. The effective slope of this exponential is fairly insensitive to the angular distribution coefficient (e.g., 2.4% change in effective mean path with a_4 changing from zero to 4).

3. Ranft Theory; a_4 and (a_2 a_9) Dependence

Ranft has given a semiempirical formula for the proton (neutron) yield in high-energy proton interactions.[RanJ 67] The double differential cross section is given by

$$\frac{d^2N}{d\Omega} = \left[\frac{A}{p_0} + \frac{Bp}{p_0^2}\left\{1 + a\ (1 - p_0/p)\right\}\right] X \left[1 + a\ \ (1 - \frac{pp_0}{m^2})\right] p^2 \exp\ (-cp^2\theta^2) \qquad (4)$$

in units of protons-GeV per steradian per interacting proton where A, B, and C are constants depending upon the target material; p is the secondary momentum in GeV/c; p_0 is the primary proton momentum in GeV/c; $a = [1 + (\frac{p_0}{m})^2]^{1/2}$; and m is the proton mass in GeV/c^2.

This formula agrees fairly well with experimental data for proton production from H_2, Be, and Pb targets for the following conditions:

(a) Secondary momenta in the range

$$0.5 \leqslant p \leqslant p_0$$

(b) Laboratory angle in the range

$$0 \leqslant \theta \leqslant 20 \text{ deg}$$

(c) Primary proton momenta in the range

$$10 \leqslant p_0 \leqslant 20 \text{ GeV/c}.$$

Extrapolation of this formula to higher energies is probably reasonable, and it is a fair assumption that neutron and proton spectra are similar from targets other than hydrogen in this region of energy and angle.[RanJ]

The angular distribution predicted by the formula is nearly isotropic for low-energy secondaries, in agreement with observation. No account is taken in the formula for evaporation particles, however, and extrapolation to these very low (evaporation) energies is not reliable.

At large angles the simplifying assumption $p \sin\theta \approx p\theta$ breaks down. The exact behavior of the angular distribution is not known, and additional experimental data is needed to establish it precisely.

Equation (4) may be integrated to give the angular distribution of protons produced with momenta greater than some threshold p_{min}.

$$\Theta(\theta)_{p > p_{min}} = \int_{p_{min}}^{p_0} \left(\frac{d^2N}{dpd\Omega}\right) dp. \qquad (5)$$

Values of $\Theta(\theta)$ have been obtained by numerical integration of Eq. (5) for values of p_0 between 1.7 and 300 GeV/c, with different values of p_{min} corresponding to proton energies of 0.1, 20, 150, and 600 MeV. This work is described fully elsewhere,[RouJ] but a brief description of the results will be given here for completeness.

At each threshold energy the family of curves for $\Theta(\theta)$ at different incident proton energies is exponentially decreasing about 90 deg. (Fig. X-2). The slope of this exponential is insensitive to primary proton energy and target material, but is a strong function of threshold energy for thresholds above about

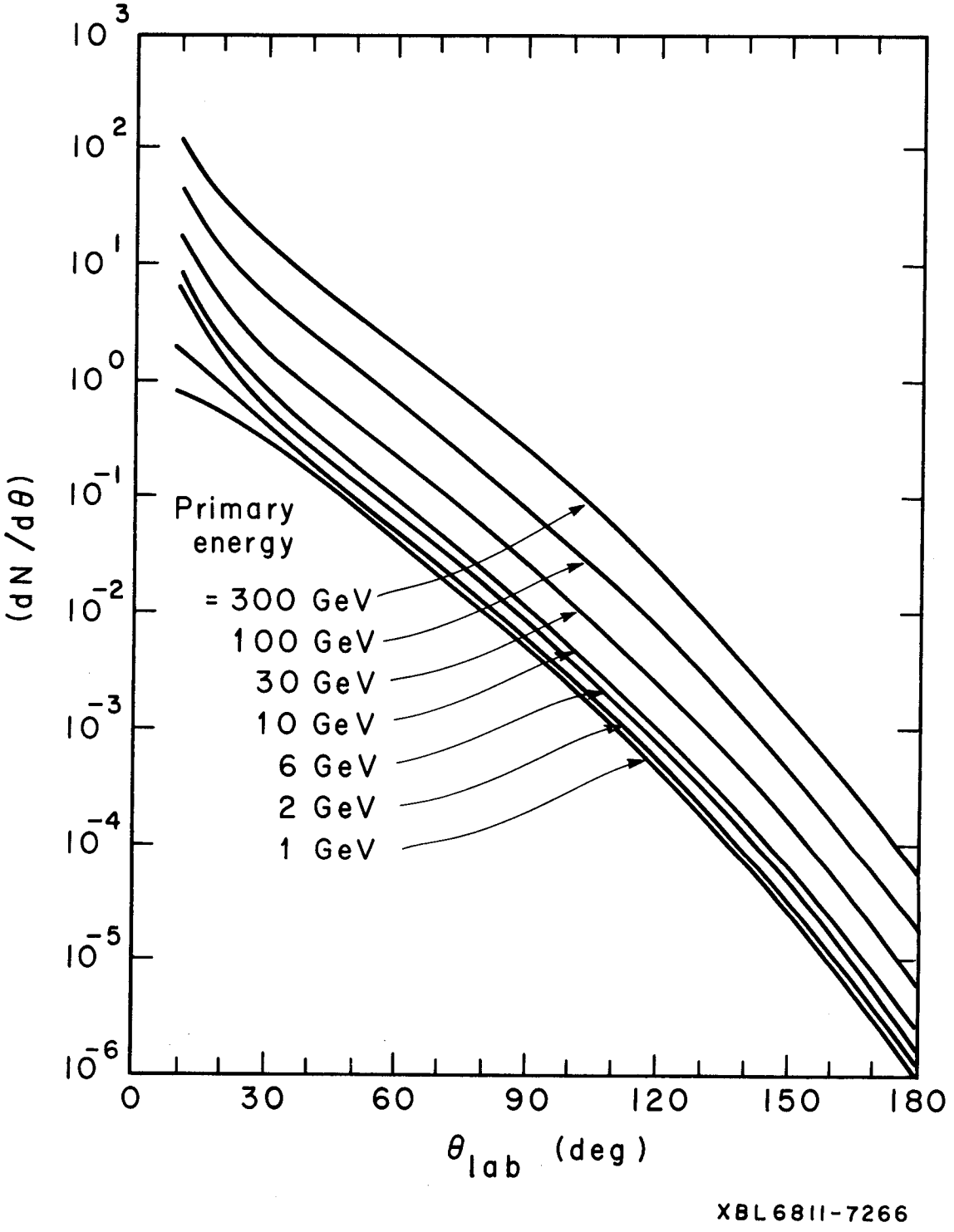

Fig. X-2. Angular distribution of protons of energy greater than 150 MeV from a thin beryllium target, calculated from Eq. (4).

50 MeV. The region over which the angular distributions are exponential depends somewhat upon threshold and primary proton energy, but is always valid from 60 to 120 deg, the angular range which is important in determining the transverse shield thickness of a high-energy accelerator. In this energy range, and for 60 deg $\leqslant \Theta \leqslant 120^{\circ}$, the angular distribution may therefore be written

$$\Phi(\theta) \approx c\, e^{-a_4\theta}. \tag{6}$$

At incident proton energies greater than about 10 GeV, the constant c is proportional to incident proton energy. This may be seen from Fig. X-3 where $(dn/d\theta)_{90\ deg}$ is plotted as a function of primary proton energy for thresholds of 0, 20, 150, and 600 MeV. The family of curves shown are all asymptotic to unit slope at high incident energies. The lower the threshold energy, the sooner is unit slope achieved. Therefore, in extrapolations to higher energies it is a fairly good approximation, to assume that, for energies greater than 10 to 20 GeV, the constant c of Eq. (6) is linearly proportional to incident proton energy. This may result in some small overestimate of particle fluxes at higher energies if the experimental values of $\Theta(\theta)$ at 10 and 20 GeV are used to obtain value of the normalizing constant in

$$\Theta(\theta) \approx a_2 E\, e^{-a_4\theta}. \tag{7}$$

To increase accuracy in the theoretical formula, evaporation particle production should be considered, and at present, no sound theoretical basis exists for any assumptions as to the form of the cross sections at laboratory angles as large as 90 deg. Also a highly accurate interpretation of the experimental data is difficult because of the interference from scattered particles and the finite source extension. A detailed interpretation of the available angular-distribution data will be given elsewhere.[RouJ] Here it is sufficient to say, however, that the calculated and measured angular distributions for both the C^{11} and Tb^{149} reactions are in fair agreement. Further, the exponent of angular distribution for the Tb^{149} reaction, was measured to be ~7.3 compared with a calculated value of ~ 14 for a threshold of 600 MeV.

The formula of Ranft predicts no change in angular distributions with increasing initial proton energy. Therefore, in extrapolating our experimental data to higher energies in order to estimate transverse shield thicknesses, it would seem plausible to assume constant a_4. In calculations in this chapter, we have assumed $a_4 \approx 2.1$ (see chap. VIII).

4. Extrapolation of Moyer Model Coefficients to Higher Energies

It is of interest here to summarize the Moyer model coefficients and discuss how they should change with increasing primary proton energy.

Beam-loss parameters: a_1, a_3

Complex variation with primary proton energy.

Angular-distribution parameters: a_2, a_4.

a_2 directly proportional to primary proton energy.

a_4 invariant with proton energy.

Mean free path in earth and iron: a_5, a_6

Invariant with proton energy.

Normalization constant, a_9:

As we have discussed in Chap. VIII, (Secs. C and D), the flux at any point in the shield is proportional to the product $a_2 \times a_9$. To a first approximation this product should vary linearly with primary proton energy. It follows that a_9 should be constant with primary proton energy.

5. Accelerator Beam Loss Parameters, a_1 and a_3

a. Measured Loss Pattern around the CPS

We have seen (chapters V and VIII) that with a target and clipper system designed to maximize the beam interactions in the vicinity of the target, the losses in the quiet regions were still some 15% of the circulating beam. We estimate that with only a target (no clipper) this quiet-region loss would be about 30%. Some of the reasons for this quiet-region loss are gas interactions, permanent and transient errors in the magnetic-field, radiofrequency phase errors, small-angle scattering and ionization loss in multiple passages through the target, and tune-up losses. The loss downstream from the target decreases almost exponentially with distance, the quiet-region loss rate being reached somewhere between 1/4 and 1/2 of a betatron wavelength.

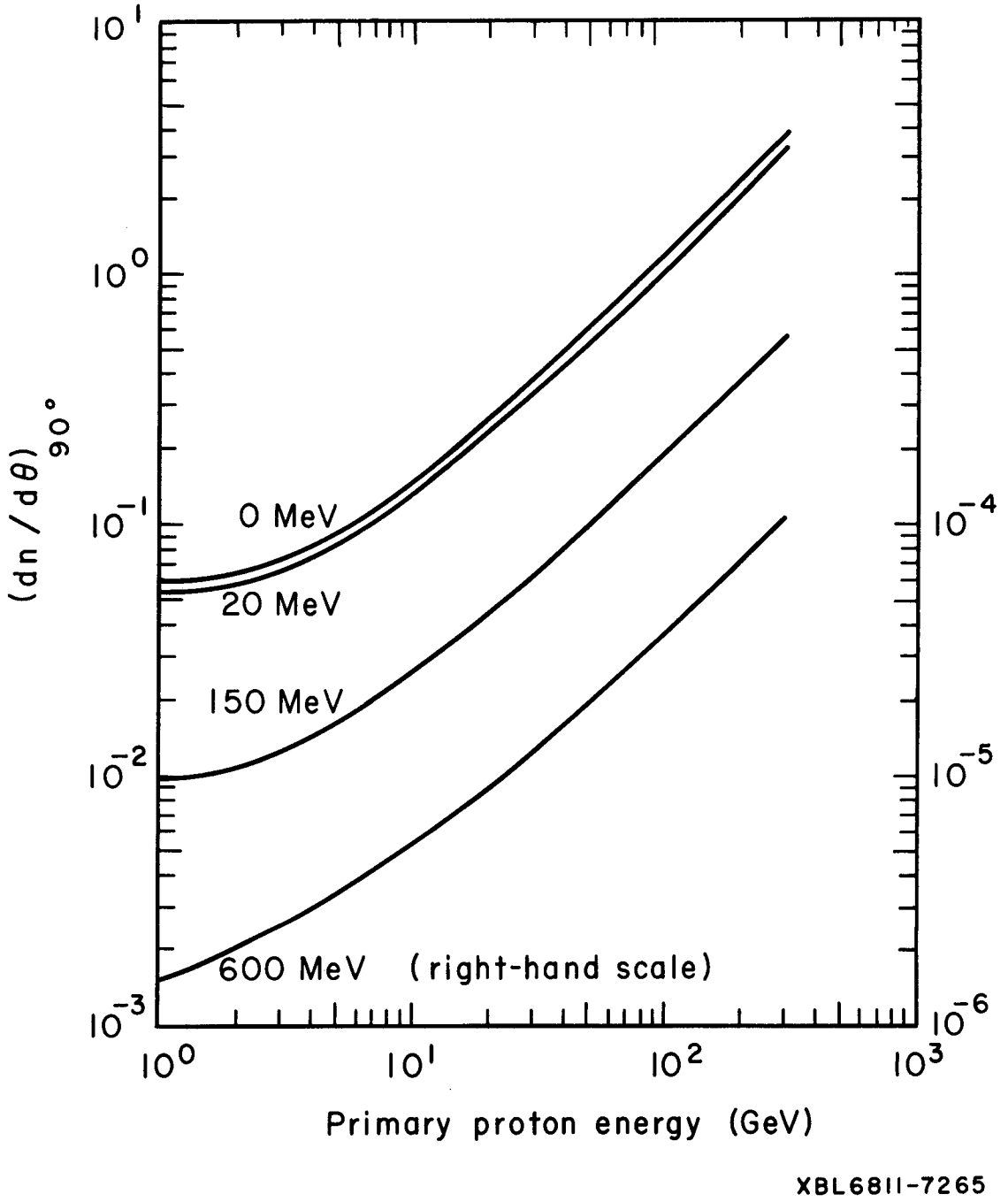

Fig. X-3. $(dn/d\theta)_{90°}$ as a function of primary proton energy.

b. Distribution of Beam Loss and Calculation of a_1 and a_3

We shall consider a target or extraction septum as a single loss region, and assume that no clean-up collimator or clipper is present. For multiple targets the procedure can be extended. Our analytic form for the beam loss distribution around the accelerator is

$$S(z) = 1 + a_1 e^{-a3z} \tag{8}$$

and

$$\oint S(z) = 2\pi R + \frac{a_1}{a_3}, \tag{9}$$

where R is the accelerator radius. For the CPS we have

$$a_3 \approx 15.4/\lambda_{\text{betatron}}, \tag{10}$$

where the betatron wavelength is

$$\lambda_{\text{betatron}} = \frac{2\pi R}{\upsilon} \tag{11}$$

υ being the number of betatron wavelengths around the accelerator. Assume that Eqs. (10) and (11) hold for higher-energy machines. Then the fraction of beam lost downstream from the target is

$$X = \frac{a_1/a_3}{2\pi R + a_1/a_3} = \frac{2\pi R \frac{a_1}{15.4\upsilon}}{2\pi R\left(1+\frac{a_1}{15.4\upsilon}\right)} = \frac{a_1}{15.4\upsilon + a_1}. \tag{12}$$

Solving for a_1 we have

$$a_1 = 15.4\upsilon \frac{X}{(1-X)} \tag{13}$$

From Eq. (10) we obtain

$$a_3 = \frac{2.45\upsilon}{R}. \tag{14}$$

6. Values of a_4, a_5, a_6

As discussed in chapter VIII and section C of this chapter, some of the parameters are more tightly constrained by the analytic fitting process than others. The results from these same sets of data have been used in arriving at the following parameters:

a. a_4.

The orbit-hole data is best fitted with a_4 in the range 2.1 to 2.2.

b. a_5.

There is little dependence of the orbit-hole data on the actual value chosen for the mean free path in the iron magnets (a_5). Excellent fits are obtained with $a_5 = 0.2$ (meters of iron), and this value is used in most problems.

c. a_6.

The mean free path in earth (a_6) is tightly constrained by the orbit-hole data with most of the values lying in the range $a_6 = 117 \pm 2$ g-cm^{-2}. In the specific examples that follow, a_6 is 116.5 g-cm^{-2}.

D. United States 200-GeV and European 300-GeV Synchrotrons

1. 200-GeV Accelerator

a. Machine Parameters

The accelerator specifications, loss assumptions, and maximum radiation fields developed in the Lawrence Radiation Laboratory (LRL) 200-BeV design study (UCRL-16000) are used in this shielding calculation example. Although it is now known that the 200-GeV accelerator, under design at Weston, will have a larger radius and a different type of extraction system that promises extremely high extraction

efficiencies, specific details are still in the process of change. For this reason we decided to repeat the shielding calculations for the LRL design-study accelerator. The pertinent parameters are:

Maximum machine energy E	200 GeV
Ultimate beam current I	5.0×10^{13} protons-sec^{-1}
Radius R	690 m
No. of betatron cycles υ	16.75
Total internal beam loss	
L_{target}	15% of circulating beam
L_{quiet}	2% of circulating beam
Safety factor F	2
Maximum radiation fields	
DE_{target}	2.5 mrem-h^{-1}
$DE_{quiet, general}$	1.25 mrem-h^{-1}
$DE_{quiet, buildings}$	0.25 mrem-h^{-1}

The safety factor reduces all maximum radiation fields by a factor of two. For consistency, we use these reduced numbers in the following calculation.

b. FLUXFT parameters

Parameters used in the FLUXFT program are:

from Eq. (13),	$a_1 = 1932$
from Eq. (14),	$a_3 = 0.0594$ m^{-1}
also:	$a_4 = 2.1$
	$a_5 = 0.2$
	$a_6 = 116.5$
	$a_7 = a_8 = 0$
	$a_2 a_9 = 2.68 \times 10^6$.

For Al detectors and for the neutron spectrum existing in the CPS earth, the flux is 0.80 n-cm^{-2}-sec^{-1} = 1 mrem-h^{-1}.

c. Results

The shielding thicknesses required, as computed by the FLUXFT program with the above constants, are listed in Table XE below. The 200-GeV magnets in the design study are some 120 g-cm^{-2} thinner than the CPS magnets, and this difference has been added to the shield thicknesses as calculated by the FLUXFT program.

Table XE. 200-GeV Shield thicknesses

Calculation	Target region	Quiet region near buildings	Quiet region, general area
This report	1855 g-cm^{-2}	1320 g-cm^{-2}	1160 g-cm^{-2}
200-BeV design study	2345 g-cm^{-2}	1515 g-cm^{-2}	1240 g-cm^{-2}
$t_{FLUXFT}/t_{design\ study}$	0.79	0.87	0.94

2. European 300-GeV Accelerator

a. Machine Parameters

The parameters used are those developed in the 1964 CERN design study for the 300-GeV synchrotron:

Maximum machine energy E	300 GeV
Ultimate beam current I	3×10^{13} protons sec^{-1}
Radius R	1200 m
No.of betatron cycles υ	28.25

Total internal beam loss

L_{target}	20% of circulating beam
L_{quiet}	20% of circulating beam

Maximum radiation field

$DE_{surface}$	0.8 mrem h^{-1}

b. FLUXFT Parameters

Parameters used in the FLUXFT program are:

from Eq. (13),	$a_1 = 435$
from Eq. (14),	$a_3 = 0.0575$
also:	$a_4 = 2.1$
	$a_5 = 0.2$
	$a_6 = 116.5$
	$a_7 = a_8 = 0$
	$a_2 a_9 = 1.39 \times 10^7$

For Al detectors, the flux is 0.80 n-cm^{-2}-sec^{-1} = mrem-h^{-1}.

c. Results

The shielding thicknesses required, as computed by the FLUXFT program with the above constants, are listed in Table XF below. The 300-GeV magnets in the design study are assumed to be 100-g-cm^{-2} thinner than the CPS magnets, and this difference has been added to the shield thicknesses calculated by the FLUXFT program.

Table XF. 300-GeV Shield thicknesses

Calculation	Target region	Quiet region
This report	1900	1285
300-GeV design study	1940	1480
$t_{FLUXFT}/t_{design\ study}$	0.98	0.87

3. Discussion

The shield-thickness calculations above give results quite close to those for the original 200- and 300-GeV design study reports, as can be seen from Tables XE and XF. Some reductions in shield thickness appear reasonable, and the resultant cost savings will, of course, be most welcome. What is not so apparent from the above comparisons is the increased confidence with which we can now make our design recommendations.

New higher-energy synchrotrons will be designed to have smaller extraction losses than those assumed in the 200- and 300-GeV design studies, which are now several years old. These smaller losses will allow thinner and less expensive shields and will correspondingly ease the construction and servicing problems. The same procedures used here-in fact, the same FLUXFT program and relevant parameters—will enable anyone to calculate the required shield geometry, once the loss parameters are specified. The shielding of the experimental areas, where most of the accelerated beam interacts, will then be a major design problem. The data taken in this experiment and the attenuation length of the penetrating neutron component derived from this data will also prove useful in solving that problem.

References

RanJ 67 J. Ranft, Nucl. Instr. Methods *48,* 133 (1967).

RanJ J. Ranft, private communications.

RouJ J. Routti and R. H. Thomas, Angular Distribution of Secondary Neutrons and protons from High-Energy Interactions, unpublished work.

RouJ 69 J. Routti, and R. H. Thomas, The Numerical Evaluation of Moyer Integrals, Stanford University internal report SUHP-69-1, 1969.

XI. RADIATION TRANSMISSION STUDIES ALONG LARGE TUNNELS AT THE CERN PS

A. Introduction

The major theoretical and experimental studies of the transmission of radiation by tunnels have concentrated on neutron fluxes produced by reactors. An excellent, although now somewhat out-of-date, summary is given by Price, Horton, and Spinney.[PriB 57] The transmission of thermal neutrons along ducts and the effects of bends in these ducts have been measured down to relative transmissions of approximately 10^{-4}. We are, of course, concerned around high-energy accelerators with the dose transmitted by neutrons of considerably higher energy than found around a nuclear reactor. Furthermore, transmissions of only approximately 10^{-5} or less are necessary for tunnels penetrating future high-energy accelerator shields. No experimental information existed for such low transmissions for high-energy neutrons prior to the series of experiments reported here.

De Staebler has reported gamma-ray dose level and fast-neutron flux as a function of position in a labyrinth at the Cambridge Electron Accelerator.[DeSH 63] He concludes that the measurements compare fairly well with calculations, although the dose transmission was only approximately 10^{-2}. Doty has made a duct transmission measurement using d-D and d-T neutrons as the source,[DotD 64] and obtained results not incompatible with theoretical calculations for similar transmissions.

Shaw[ShaK 66] has reported transmission measurements for gamma rays and neutrons along a curved tunnel leaving the Nimrod accelerator room. He finds that at a sufficient depth in the tunnel, where there was no direct contribution from the accelerator, intermediate and thermal neutrons were the major components of flux. The larger weighting of fast neutrons in dose-rate assessments, however, made the fast-neutron contribution to the dose roughly equivalent to that due to intermediate and thermal neutrons. The transmission of the tunnel for low-energy neutrons may be estimated using the semi-empirical relationship described by Price, Horton, and Spinney.[PriB 57]

B. Experimental Details

1. Description of the Tunnels used in the Transmission Measurements

As shown in Fig. XI-1, eight straight service survey tunnels radiate from a central building, providing convenient access to the accelerator room. The four larger tunnels have a rectangular cross section 2.8 m high by 1.8 m wide. They are constructed of 0.2-m-thick reinforced concrete and are covered with earth to a depth of at least 2.5 m over their entire length (although the thickness of earth covering becomes substantially greater close to the CPS). The inner walls of these tunnels are partially covered with cable trays, and close to the roof of each tunnel is a metal air-conditioning duct approximately 50 cm deep. Two of these tunnels were used in the transmission studies—those situated opposite straight sections 52 and 77. In these there was a minimum of wall covering and only minor obstructions along their length. Figure XI-2 indicates typical experimental conditions. Adjacent to the mouth of each tunnel is an equipment-storage room separated from the tunnel by a 20-cm-thick concrete wall. The presence of this large void at the mouth of the tunnel can give rise to uncertainties in the effective position of the tunnel mouth under certain conditions.

The four smaller tunnels are of roughly egg-shaped cross section. The entrance of these smaller tunnels is via a rectangular room 2.5 m high by 1.8 m wide by 6 m long, alongside which is an equipment storage room similar to those of the rectangular tunnels. The smaller tunnels are also constructed of reinforced concrete. Transmission studies were made along the small tunnel opposite straight section 89.

Opposite straight section 16 a curved tunnel was used. This tunnel is rectangular in cross section and about 3.6 m high and 3.2 m wide. It has a wide mouth and is straight for the first 10 m of its length, then curves on an arc of a circle of radius 25 m. Its overall length is 40 m.

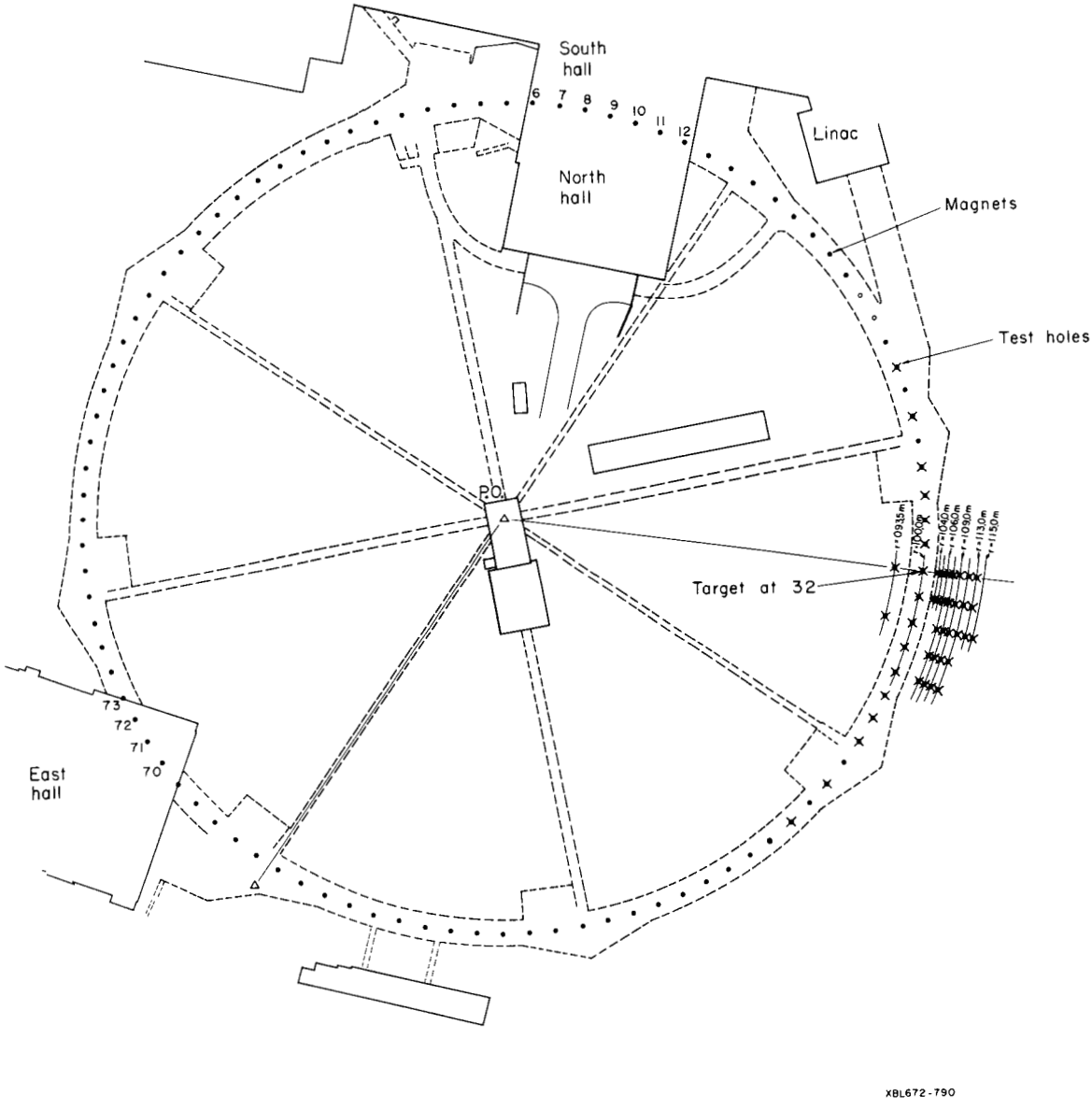

Fig. XI-1. General layout of the CERN proton synchrotron.

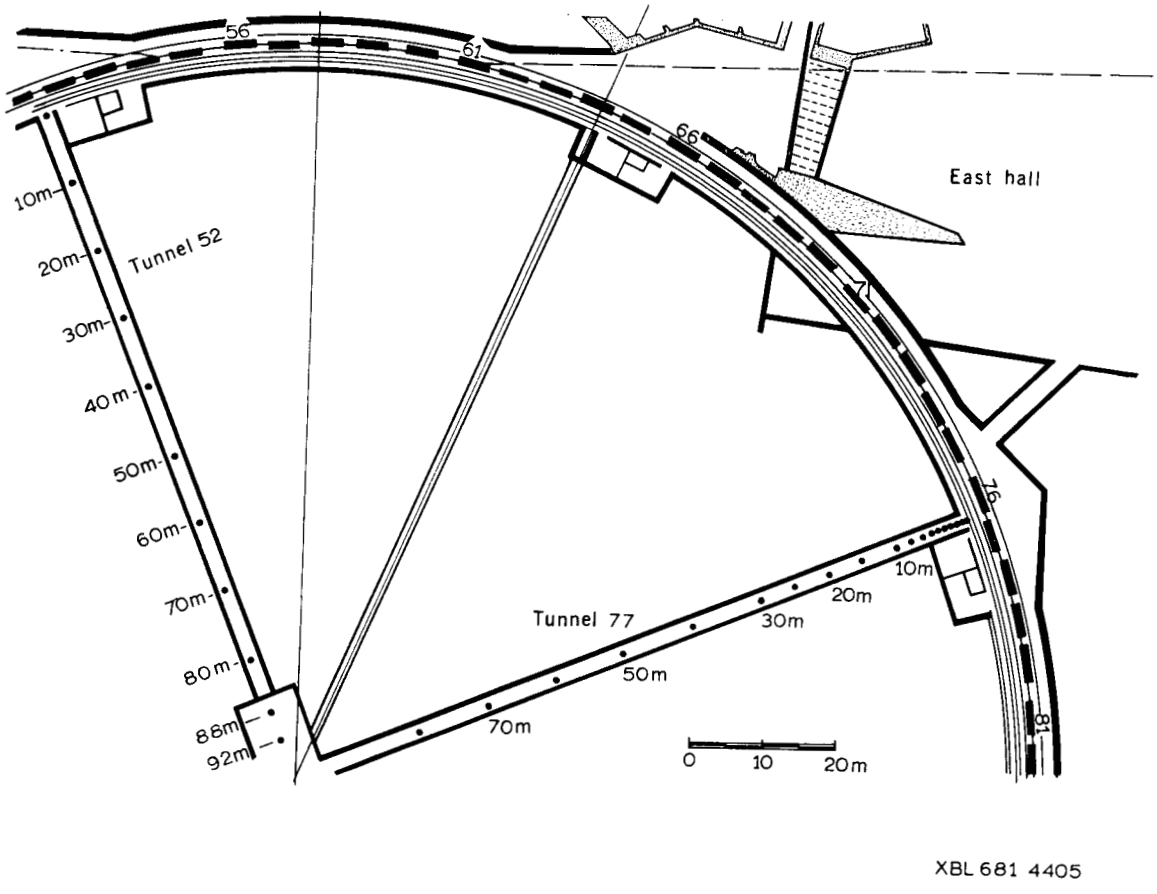

Fig. XI-2. Plan view of tunnels 52 and 77.

2. Radiation Detectors Used

Several different radiation detectors were used in this experiment to provide some information on the dose spectrum. Table XIA lists the detectors used (described in detail in Chapter III) and their important characteristics. The measurements were limited somewhat by detector sensitivity and the available source strength at the tunnel mouth.

Table XIA. Detectors and their characteristics.

Detector	Reaction	Energy range (MeV)
bare gold foils	$Au^{197}(n,\gamma)\ Au^{198}$	thermal
large bare indium foil	$In^{115}(n,\gamma)\ In^{116m}$	thermal
moderated gold foils	$Au^{197}(n,\gamma)\ Au^{198}$	0.02 to 20
Kodak Type-B neutron film	proton recoil	0.5 to 25
sulfur	$S^{32}(n,p)\ P^{32}$	>3
aluminum	$Al^{27}(n,\alpha)\ Na^{24}$	>6
plastic scintillator	$C^{12}(n,2n)\ C^{11}$	>20
$\beta\gamma$ film LiF TLD	gamma + charged particles	

3. PS Operating Conditions During Transmission Measurements

The transmission measurements were made under a variety of conditions, shown in Table XIB. Data were obtained along tunnel 52 with a clipper target in operation at 52 (Condition A). This provided an intense, well-located radiation source some meters from the actual tunnel mouth. Measurements of particle flux along the vacuum pipe and downstream of a similar target indicated a substantially uniform source for some two meters. Flux measurements at the tunnel mouth with gold foils and aluminum disks indicated a constant radiation field to better than 20%. Under these conditions, then, the source at the tunnel mouth is essentially uniform over the entire neutron energy spectrum measured.

Table XIB. PS operating conditions during transmission measurements.

Machine condition	Tunnel No.	Source type
A	52	Intense, localized. Clipper opposite tunnel mouth
B	77	High local beam loss
C	77	Diffuse, low local beam loss. High adjacent beam loss
D	<89	Diffuse
E	16	Diffuse

In tunnel 77 data were obtained under two entirely different conditions. One set of data was obtained with high local beam loss at straight section 77 relative to adjacent straight sections (Condition B). The transmission measurements were in excellent agreement with those made in tunnel 52. In Condition C a beam clipper was in operation in straight section 79. Under these conditions the source strength of section 79 was some three orders of magnitude higher than that of straight section 77. High-energy particles emitted in the backward direction could then enter the tunnel through the void described in Section B.2. Interactions

in, and scattering from, the tunnel walls then produced an effective source inside the actual tunnel mouth. (See Fig. XI-2). This effective source could be located some 4 m inside the tunnel mouth (See Section D 1a).

A gradient magnet was immediately opposite the mouth of the egg-shaped tunnel (89), producing a diffuse radiation source into the large entrance.

C. Experimental Data

1. Large Straight Tunnels

Measurements were made with all the detectors listed in Table XIA. Detectors were suspended at the approximate geometrical center of the tunnels and their spacing varied from 1 m near the tunnel entrance to 10 m at greater depth along the tunnel. Three different accelerator operating conditions were used for these measurements as discussed above.

Figures XI-3 and XI-4 summarize the transmission data obtained using the different detectors, and Appendix B gives the actual experimental data. Because of the varied accelerator operating conditions during which these data were obtained, absolute flux values are of no significance in this series of measurements. It is not possible to normalize the data in terms of circulating beam intensities. For convenience, therefore, the data are presented graphically by normalizing all the transmission curves to unity at a depth of 0 m. A systematic trend is immediately obvious in that the higher the threshold of the neutron detector, the larger the flux transmission. Thus the difference in overall transmission for thermal and C^{11} neutrons is more than a factor of ten at 80 m.

2. Small Straight Tunnels

Bare gold, moderated gold, neutron-track films, plastic scintillator, thermoluminescent dosimeter (TLD), and beta-gamma film badges were exposed up to distances of 50 m in the small tunnel. The experimental data, given in Appendix C and shown graphically in Fig. XI-5 are uncorrected for effective source position. Distances are measured from the start of the small tunnel mouth. Three measurements of flux were also made in the entrance leading into the small tunnel, and these data are also given.

3. Curved Tunnel

Bare and moderated gold or indium foils, fast-neutron plates, aluminum, and beta gamma films were exposed at a height of 1 m above the floor along the center line of the tunnel at approximately 5-m intervals. Figure XI-6 indicates the position of measurements. Appendix D gives the experimental data, and Figs. XI-7 and XI-8 show the results for bare indium and aluminum detectors. For convenience in presentation, the data have been normalized to unity at a distance of 10 m.

D. Interpretation of Experimental Data

1. Flux Transmission Along Straight Tunnels

a. Location of Effective Tunnel Mouth.

The nature of the source may influence the effective position of the tunnel mouth. The transmission curves in the first 10 m of tunnel 77 depend on the proximity of the beam clipper to the tunnel mouth. However, transmission at large depths should be independent of the particular accelerator operating conditions. Adjustment of the data taken under Condition C of Table XIB by assuming a virtual source some 4 m inside the tunnel mouth produces excellent agreement among all the comparable data taken under Conditions A, B, and C. Figure XI-9 indicates the improvement obtained by this small correction.

b. General Expression for Straight Tunnel Transmission.

The flux transmission T of a tunnel expressed as a function of length z along the tunnel, the effective tunnel radius a, and the energy response E of the detector is

$$T(z,a,E) = \Gamma\left(\frac{z}{a}, E\right) e^{-z/\lambda(E)} ,$$

where $T(z,a,E)$ is the overall transmission, $\Gamma\left(\frac{z}{a},E\right)$ is the transmission of the tunnel uncorrected for neutron-absorption processes, and $e^{-z/\lambda(E)}$ is a correction factor which takes account of neutron interactions in the air along the tunnel. The mean free path $\lambda(E)$ is determined by the neutron total cross

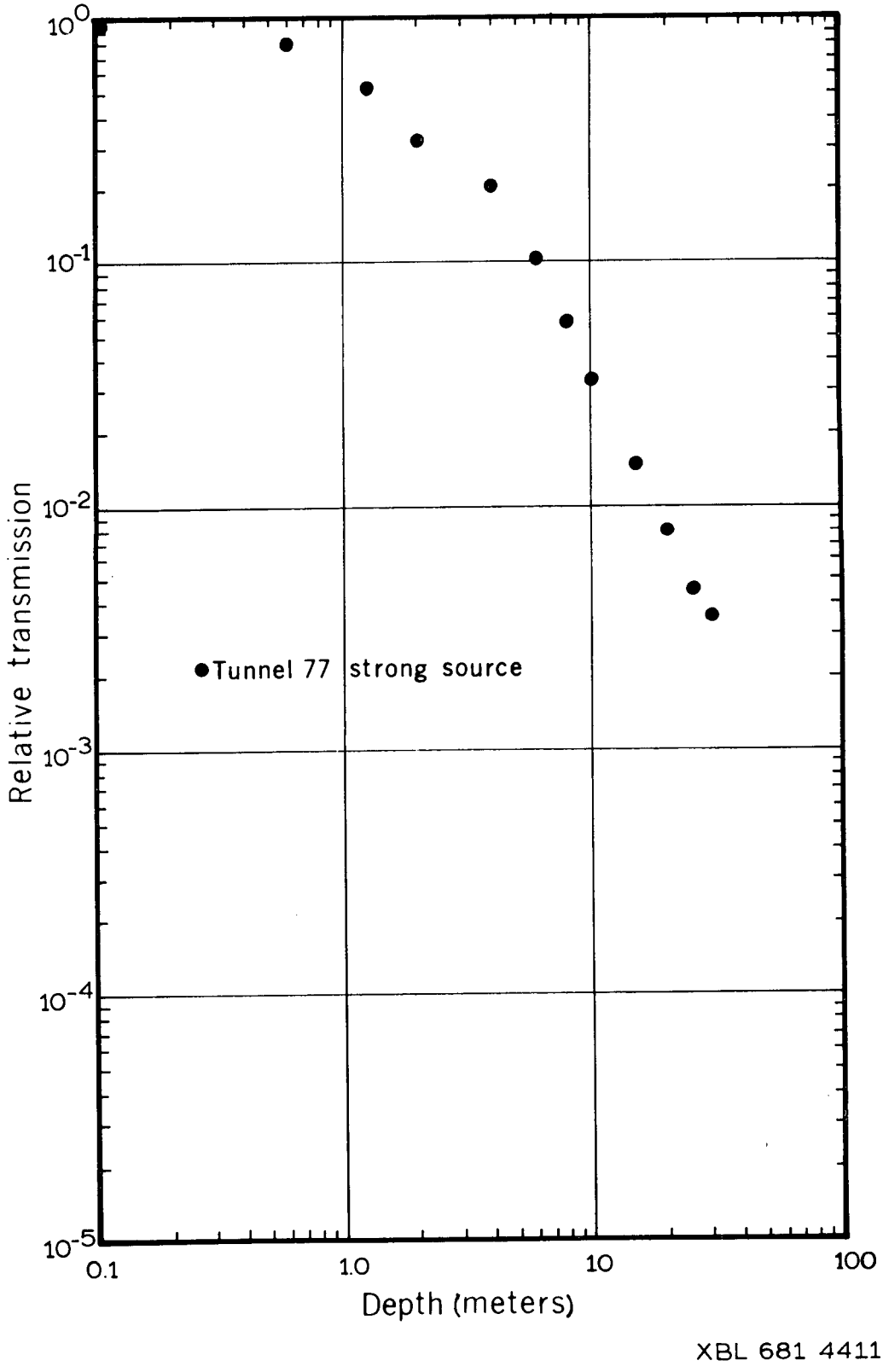

Fig. XI-3. Sulfur activation results in large tunnels.

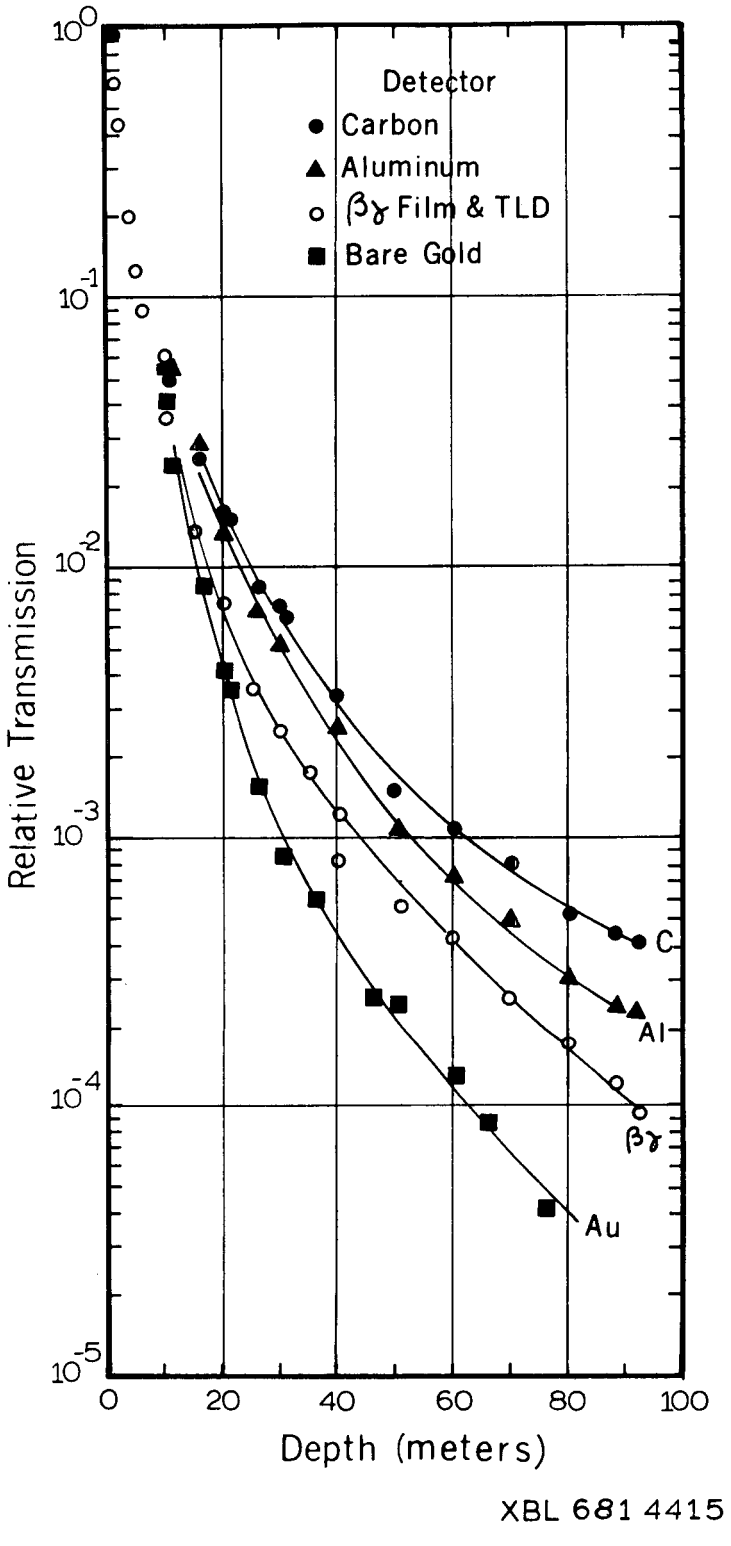

Fig. XI-4. Flux attenuation in large tunnels.

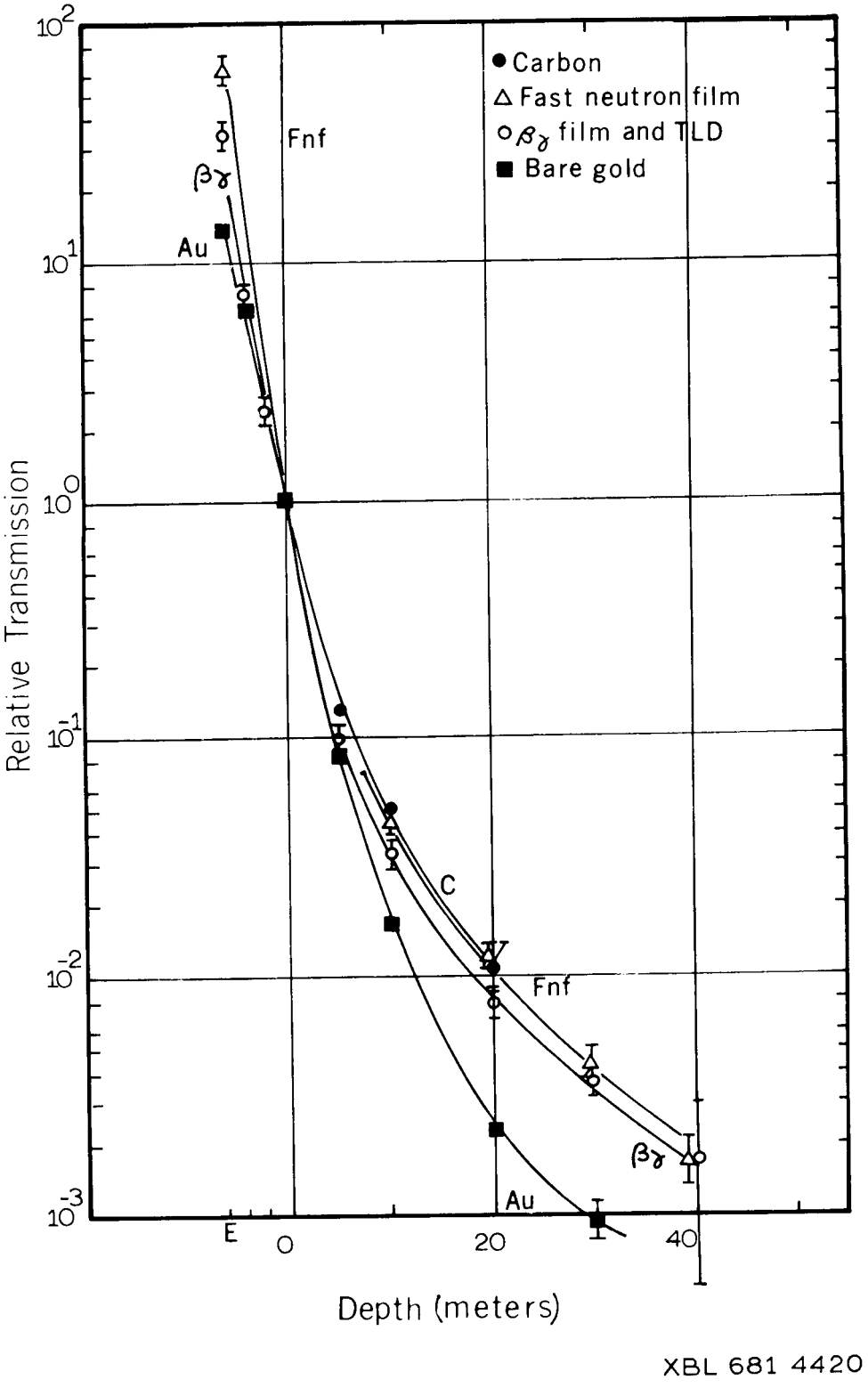

Fig. XI-5. Flux attenuation in small tunnel.

section in air. At large values of (z/a) we expect

$$\Gamma(\frac{z}{a}, E) \rightarrow (\frac{a}{z})^2$$

for $z/a \geqslant 10$, and thus a semilog plot of $z^2\, T(z, a, E)$ should give a straight line with negative slope λ (E).

Figure XI-10 shows semilog plots of $z^2\phi$ [proportional to $z^2 T$ (z, a, E)] against z (in meters) for badges and TLD, aluminum, and carbon. For penetrations greater than 20 m in the large tunnels, the attenuations are nearly exponential. Table XIC lists the estimated removal mean free paths (attenuation length) and the corresponding removal cross sections, assuming an atmosphere of nitrogen. At neutron energies between 1 and 20 MeV, the inelastic cross section for nitrogen is 200 mb, and the total cross section 2b.

We have not derived an analytic expression for neutron tunnel transmission that yields the correct dependence upon neutron energy. Therefore we suggest that for straight tunnels the experimental transmission curves be used, and that z/a be used to scale for tunnels of different dimensions.

2. Curved Tunnel Attenuation

The measurements show that the higher energy component of the neutron flux (as measured by aluminum detectors and fast-neutron films) is attenuated more rapidly than the thermal-neutron flux. The decrease of the flux measured by the moderated indium foils is approximately exponential, with an e-folding length of 3.9 m. This length is comparable to the value of 3.5 m found by Shaw[ShaK 66] from measurements in an equivalent tunnel on Nimrod at the Rutherford Laboratory.

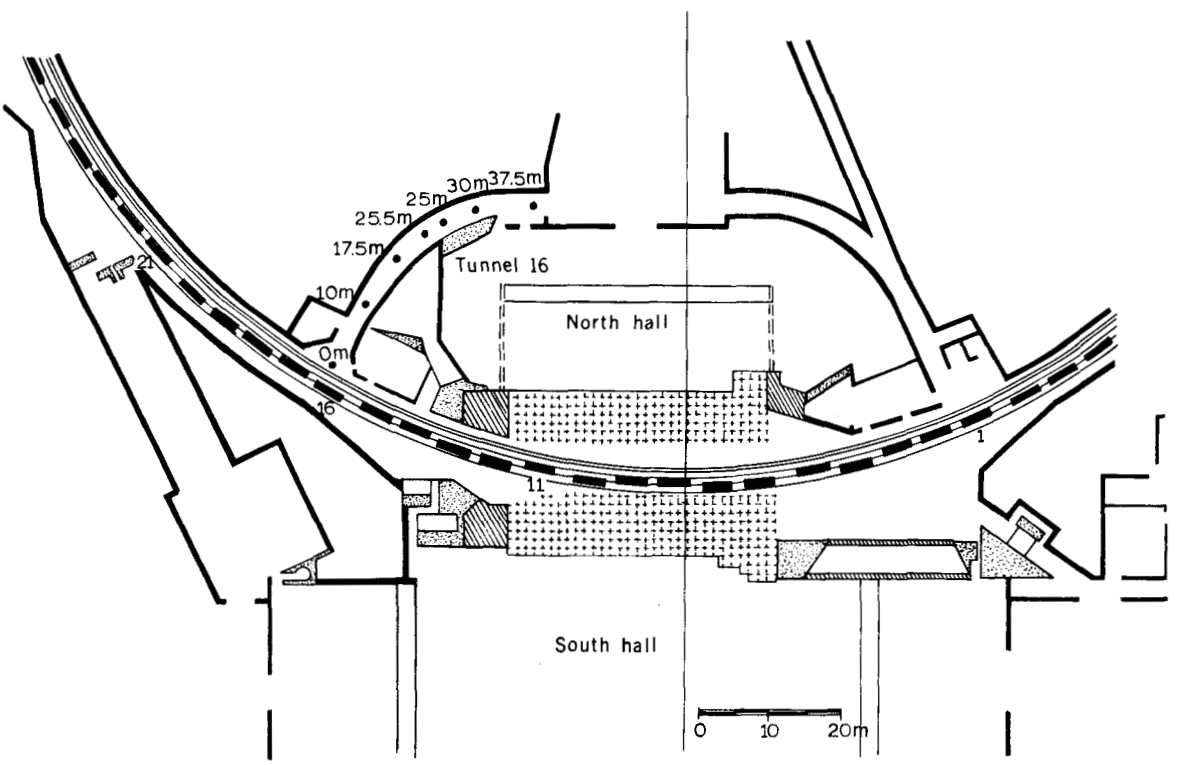

Fig. XI-6. Plan view of tunnel 16 showing detector locations.

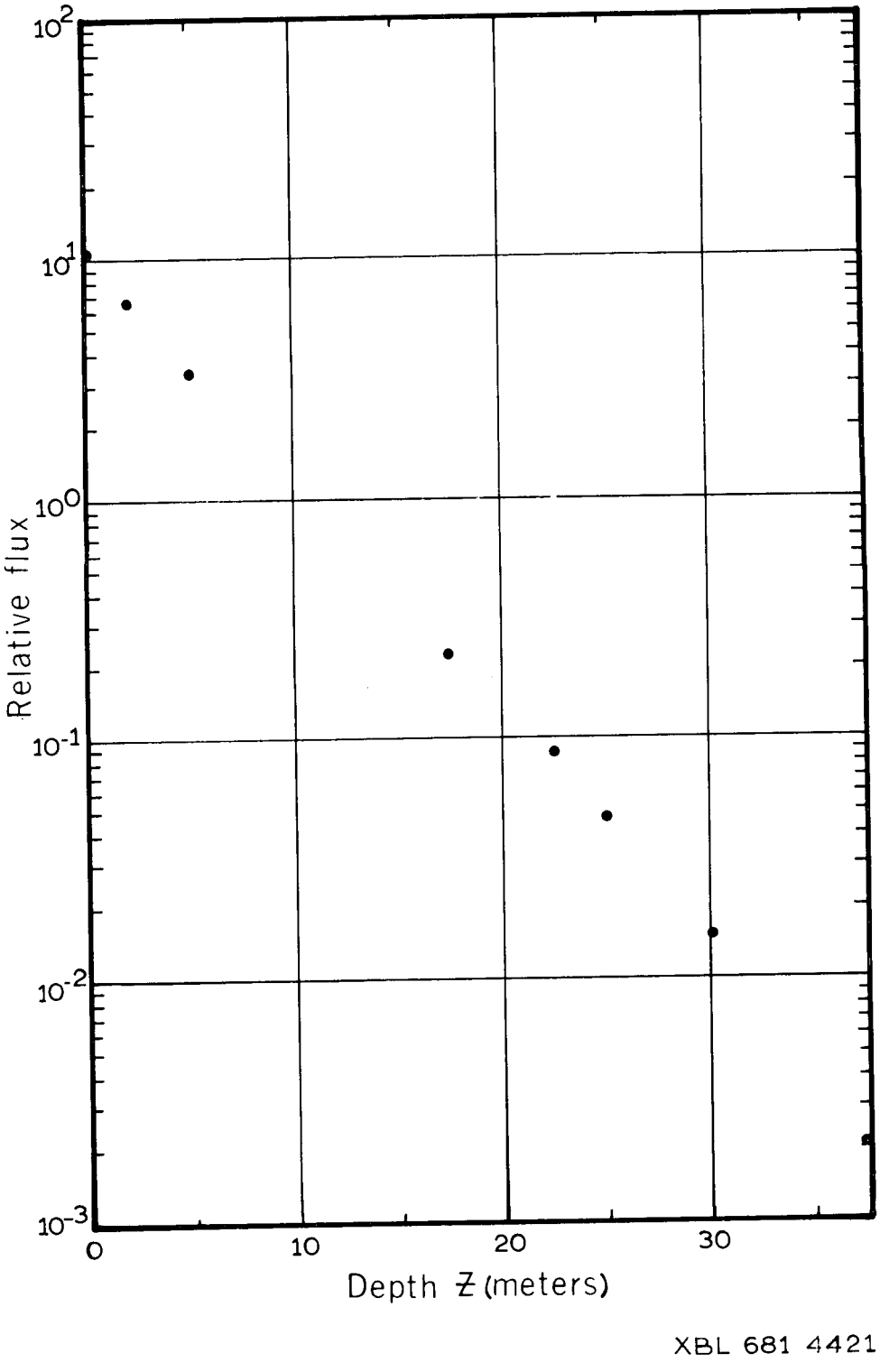

Fig. XI-7. Relative response of bare indium in a curved tunnel.

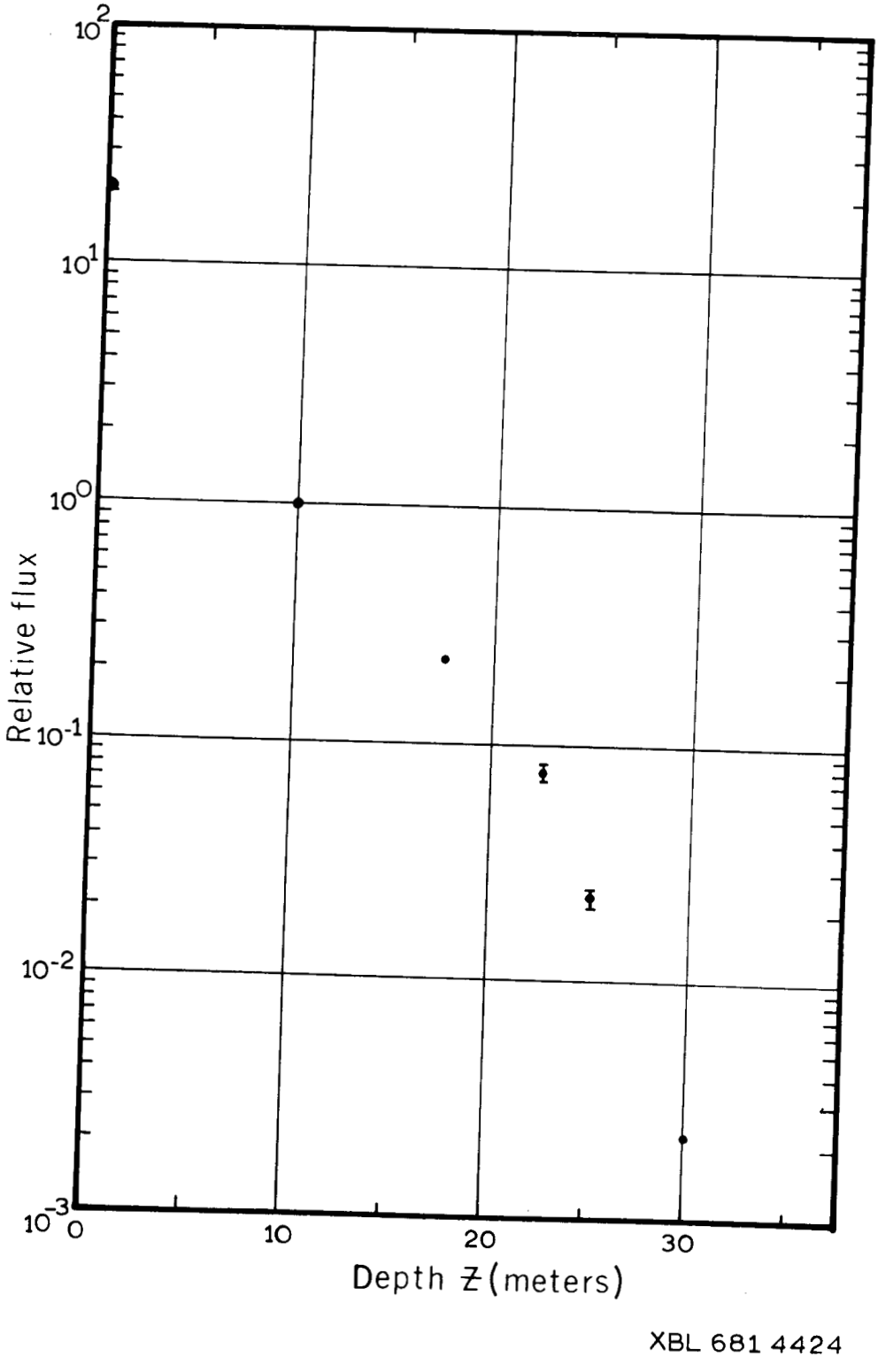

Fig. XI-8. Relative response of aluminum in a curved tunnel.

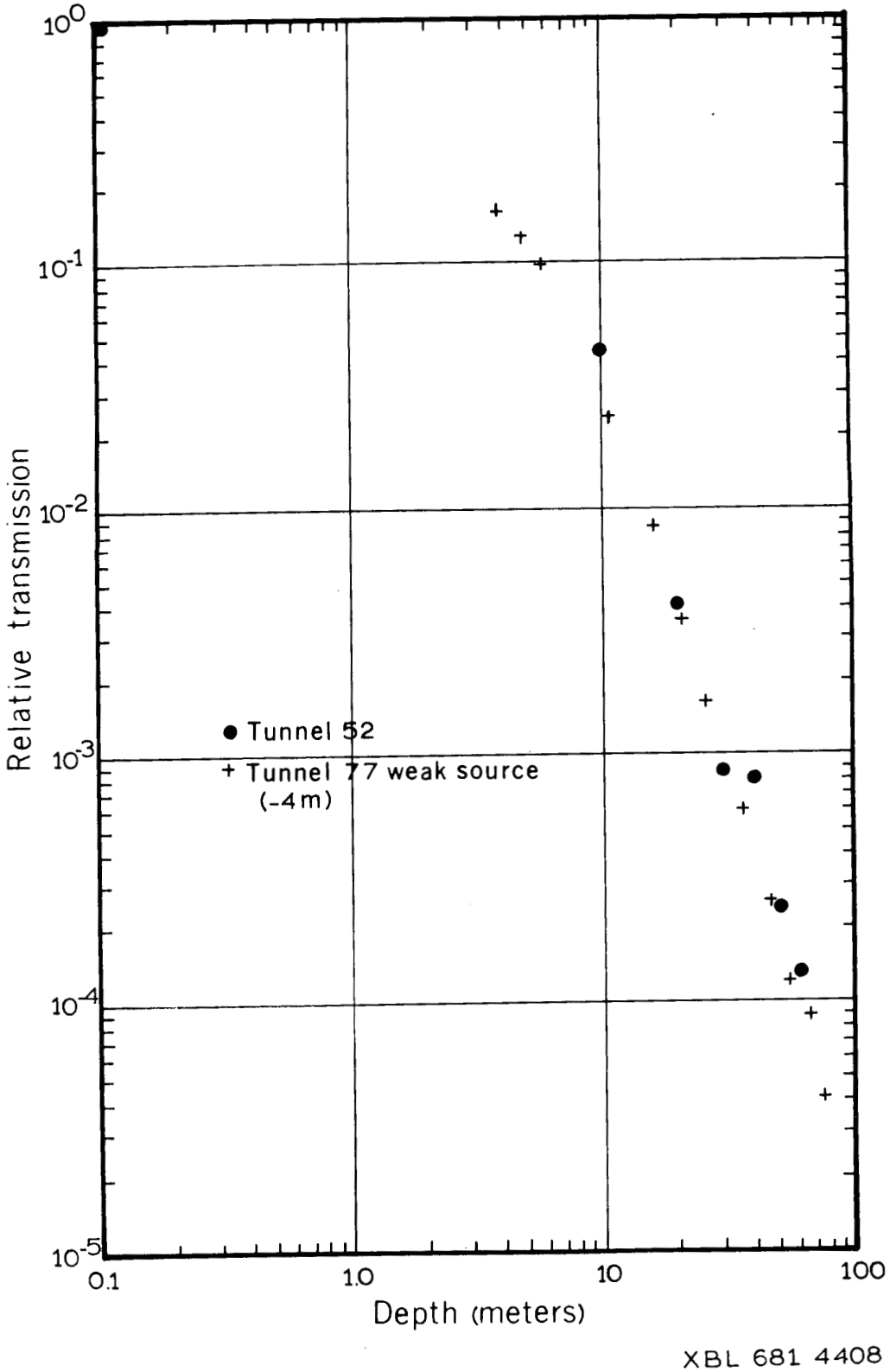

Fig. XI-9. Relative response of bare gold in large tunnels.

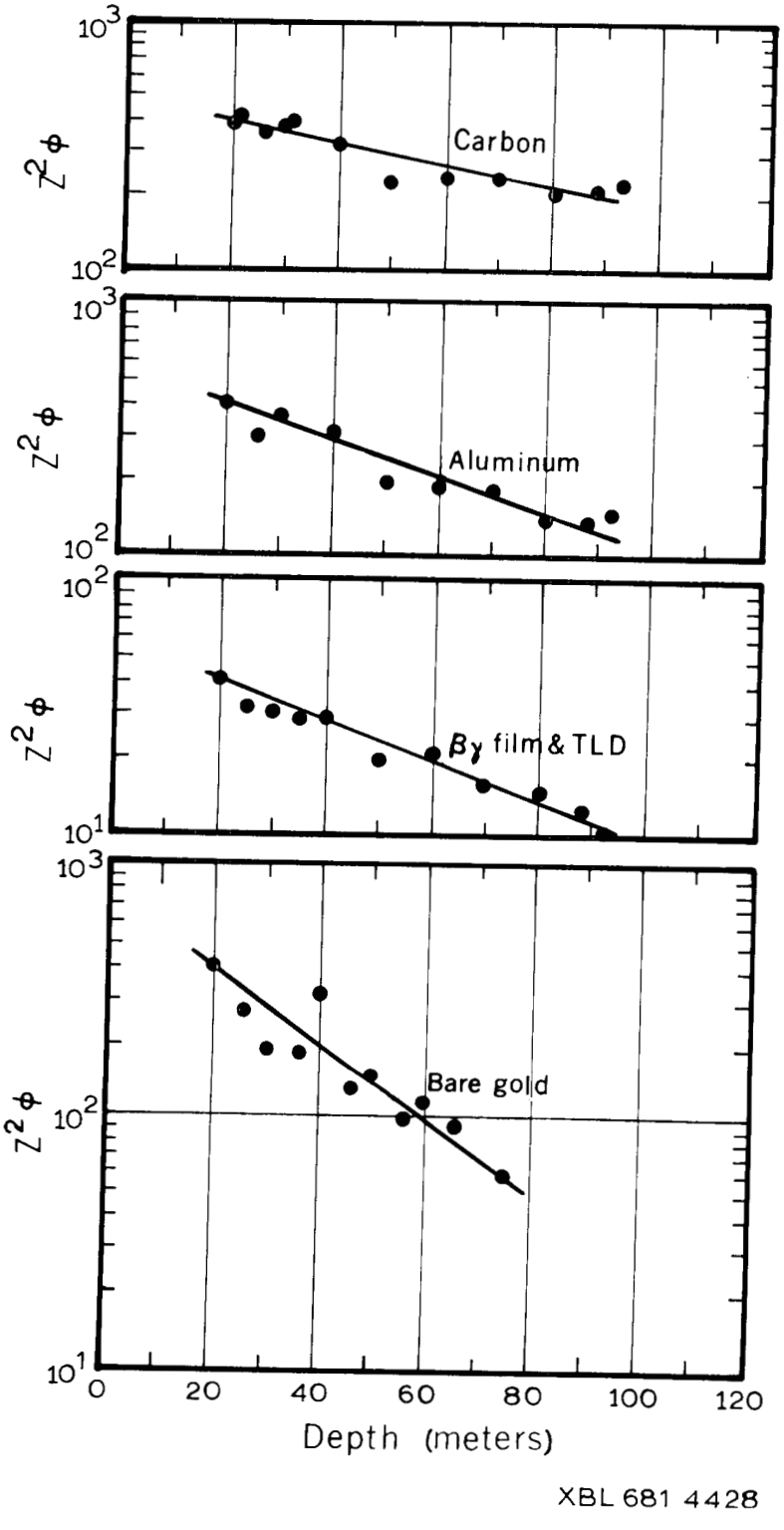

Fig. XI-10. Exponential absorption in the large tunnels for several detectors.

Table XIC. Attenuation lengths and removal cross sections for tunnel transmission.

Detectors	Attenuation length (meters)	Removal cross section (barns)
Plastic scintillator	100	1.9
Aluminum	60	3.2
Film and TLD	55	3.3
Bare gold	30	6.2

References

DeSH 63. H. DeStaebler, Radiation Measurements in the CEA Labyrinth, Stanford Linear Accelerator Report SLAC. TN-63-62, 1963.

DotD 64. D. R. Doty, Dose Measurements for Neutron Streaming in Ducts, U.S. Navy, Port Hueneme, California report R 282, March 1964.

PriB 57. B. T. Price, C. C. Horton, and K. T. Spinney, *Radiation Shielding* (Pergamon Press, New York, 1957).

ShaK 66. K. B. Shaw, Neutron Studies in Shields and Tunnels of the 7-GeV Proton Synchrotron Nimrod; *Proceedings of the Conference on Radiation Measurements in Nuclear Power, Berkeley, Gloustershire, England, 1966* (Institute of Physics and the Physical Society, London, England, 1966).

ACKNOWLEDGMENTS

An experiment of this duration and magnitude taking place so far from the home laboratories of some of its participants necessarily involves a contribution of cooperation and support from many people. The authors are anxious to recognize these contributions individually, but unfortunately, in so doing there is always the possibility that a particular individual will be overlooked or have his contribution in some way misinterpreted. The authors sincerely hope that this is not the case, and rely on the good will of the many persons who supported us to forgive any such inadvertent oversight.

To begin with, we wish to recognize those people who gave their generous assistance and help in having the experiment agreed to when it was first proposed. In this connection, we are extremely grateful to those on the European Committee on Future Accelerators, ECFA, for their sanction of the first proposal of this experiment and for their active interest during it. In addition, and in this same connection, we wish to thank Drs. M. Hine and K. Johnson of CERN. At the Lawrence Radiation Laboratory, Berkeley, we wish to thank Dr. H. Fidler for his efforts in arranging USAEC financial support for travel and equipment expenses for the Berkeley contingent, and Dr. E. Lofgren who, as leader of the Accelerator Study Group, gave his active and enthusiastic encouragement. During the experiment, we were attached to the ISR Division at CERN. We thank the members of this division who participated in the planning and execution of the experiment, particularly Drs. W. Middlekoop and B. de Raad.

Also, we are indebted to many at CERN in the PS group who operated the accelerator, helped us with problems of targeting and beam monitoring, and maintained close control over the myriad of operating parameters. In this relation we thank Dr. P. Standley, in charge of PS Operations; Mr. J. Freeman, for helping us with problems involving radiation control; and Dr. D. Dekkers, Mr. J. Madsen, and Dr. W. Richter for valuable discussions and advice on target and clipper problems. For important adjustments of various PS parameters at critical times we thank Mr. A. Colombo and Mr. C. Serre. We are indebted to Miss W. Riezler of NP division for the determination of the number of protons interacting in the target, and we also thank Dr. J. Ranft, then of the PS group and now of the Rutherford Laboratory, for many helpful theoretical discussions during the course of the experiment.

We specially thank the entire CERN Health Physics Group for their generosity and cooperation in acting as hosts and for providing space and accomodations for our counting equipment. In particular we wish to thank Dr. J. Baarli, Head of Health Physics, for his complete cooperation during the experiment and for his generosity in providing every assistance. Thanks are also due to many individuals in the CERN Health Physics Group. In particular we are grateful to Messrs. E. Barbe, J. Hanon, M. Nielsen, C. Raffnsøe, and C. Renaud who assisted in placing aluminum foils on the vacuum chamber to measure beam-loss distribution, the measurement of these foils, the intercomparison of neutron sources, and the health physics measurements mentioned in Chapter IX. We also thank Dr. A. Rindi for his advice and consultation on various technical aspects of the measurements.

The authors of this paper who travelled to CERN were also ably supported by home-based groups who provided assistance in many of the radiation measurements during the experiment and continued this after the experiment was over. In some cases, they accepted additional responsibilities and work which devolved upon them due to our absence. We also acknowledge their contribution to analysis and interpretation of the data we took.

At the Rutherford Laboratory Mr. M. Snowden, Mr. D. Perry, and the whole of the Radiation Protection Group were responsible for providing sulfur and other samples during the experiment and for subsequently counting them and assisting in the analysis. We thank Mr. H. Preston, AEE, Winfrith, Dorset, England, who was responsible for supplying and reading the LiF dosimeters used in the experiment. We also thank Mr. W. Seymour, AERE, Harwell, Berkshire, England, for developing, reading, and interpreting the beta-gamma films we used, and for providing meaningful calibration for these. We thank the Radiological Protection Service, Sutton, Surrey, England, who supplied their fast-neutron dosimeter films and some thermoluminescent dosimeters. They were also responsible for the reading and interpretation of the dosimeters; Mrs. J. Bishop and Mrs. W. Sheppard of Rutherford Laboratory read the fast-neutron films.

At the Lawrence Radiation Laboratory we are particularly grateful for the active and continued aid in computer programming of Mr. E. Close and Miss M. Simmons. Without the FLUXFT and TELLY programs which they developed, much of the data would not be interpreted. We also thank Mr. J. Routti in this regard, and in addition we are indebted to him for the penetrating mathematical insight which he brought to bear on the data-analysis problems which confronted us. Finally, we thank Mrs. N. Little for her continued assistance in the gathering together of all our data and for seeing that it was promptly processed by the computers.

Other noteworthy contributions were made by individuals not connected with any of our laboratories but who nevertheless helped with the experiment. We thank Mr. L. Kleppe, of Wayzata, Minnesota, and Sister Mary Roger, of Omaha, Nebraska, for quickly and accurately reading the fission-track plates we used and for reporting the results to us during the experiment. The most outstanding contribution of this nature was made by Dr. W. Moore of the Alternating Gradient Synchrotron Group, Brookhaven National Laboratory, who worked with us in CERN during part of the experiment. It was due to his effort in mathematical data analysis and statistical testing that we were able to avoid unnecessary duplication of measurements during the experiment and to realize a high degree of confidence in these measurements.

This work was done under the auspices of the U.S. Atomic Energy Commission.

APPENDICES

A. Principal Experimental Data
B. Flux Measurements in Large Tunnels
C. Flux Measurements in Small Tunnels
D. Flux Measurements in Curved Tunnels

Appendix A. Principal Experimental Data

Introduction

The tables in this section list all activation-detector data upon which results of this experiment are based, as well as almost all other data collected during the experiment. The information is presented in sufficient detail that the reader has at his disposal the same basic data available to the authors; thus he can perform his own analysis should he so desire.

Table A lists the Z-coordinates of the 100 standard monitor positions for aluminum foils that were placed on the accelerator vacuum vessel each running period. These Z-coordinates apply to all tables listing aluminum foils at the 100 standard positions, and no coordinate values appear on those tables.

Data tables are organized within the following system. The basic division is the accelerator running period – Runs I through VIII, comprising 10 major divisions. Each running period is subdivided into categories based on detector location, and each location category is (usually) ordered according to detector threshold energy.

The first table for each running period contains a brief summary of the experimental program, along with relevant machine operation parameters. All subsequent tables list detector data, including counting results, conversion into neutron flux intensities, and spatial coordinates of detector locations.

The coordinate system provided distances measured in meters for all three spatial coordinates (X, Y,Z). The X-coordinate measured distance radially from the machine center, referenced to *zero* at the machine center. (The mean radius of the beam orbit was 100.0 m.) The Y-coordinate measured distance above the plane of the circulating proton beam, referenced to *zero* at the beam plane. The Z-coordinate measured distance *along* the beam orbit, referenced to *zero* at the downstream edge of magnet 21. (The target was mounted 0.12 m beyond the downstream edge of magnet 31.) Complete sets of coordinates for detector locations are provided in this appendix, but only coordinate values that change within a table are listed on that table. Coordinates remaining constant throughout a table do not appear on that table, but are given below in the list of detector-location categories.

1. *Vacuum vessel:* detectors placed directly on the CPS vacuum pipe, usually on the top of this structure; results arranged in the order aluminum, sulfur, and TLD. The 100 aluminum foils at standard locations, listed for all runs, have constant coordinates X = 100.0 m, Y = 0.04 m.
2. *Roof buckets:* detectors placed in plastic buckets hung from roof of accelerator ring tunnel; results arranged in order of increasing energy threshold. Constant coordinates are X = 100.0 m, Y = 1.74 m.
3. *Orbit holes:* detectors placed in light-weight holders and lowered to exposure positions from ring top; results arranged in order of increasing energy threshold. Constant coordinate is X = 100.0 m.
4. *Radial holes:* detectors placed in small buckets and lowered to exposure positions from ring top; results arranged in order of increasing energy threshold. Constant coordinate is Y = 0.0 m.
5. *Surface, or ring top:* detectors placed on earth surface at exposure positions; results arranged in order of increasing energy threshold. Constant coordinate is X = 100.0 m.
6. *Miscellaneous:* detectors were frequently exposed at various other locations; such results are collected within this category. The most important type of locations are: angular-distribution studies around the target, with a constant coordinate X = 100.0 m; vertical profile arrays in the target vicinity, with a constant coordinate X = 100.0 m; and, radical-tunnel studies, with a constant coordinate Y = 0.0 m.

Table A. Standard Z-values for aluminum foils on the vacuum vessel.

Magnet No.	Z (meters)	Magnet No.	Z (meters)	Magnet No.	Z (meters)	Magnet No.	Z (meters)
22	0.12	47	157.12	72	314.12	97	471.12
23	6.12	48	163.12	73	320.12	98	477.12
24	12.12	49	169.12	74	326.12	99	483.12
25	18.12	50	175.12	75	332.12	100	489.12
26	24.12	51	181.12	76	338.12	1	495.12
27	31.52	52	188.52	77	345.52	2	502.52
28	37.52	53	194.52	78	351.52	3	508.52
29	43.52	54	200.52	79	357.52	4	514.52
30	49.52	55	206.52	80	363.52	5	520.52
31	55.52	56	212.51	81	369.52	6	526.52
32	62.92	57	219;92	82	376.92	7	533.92
33	68.92	58	225.92	83	382.92	8	539.92
34	74.92	59	231.92	84	388.92	9	545.92
35	80.92	60	237.92	85	394.92	10	551.92
36	86.92	61	243.92	86	400.92	11	557.92
37	94.32	62	251.32	87	408.32	12	565.32
38	100.32	63	257.32	88	414.32	13	571.32
39	106.32	64	263.32	89	420.32	14	577.32
40	112.32	65	269.32	90	426.32	15	583.32
41	118.32	66	275.32	91	432.32	16	589.32
42	125.72	67	282.72	92	439.72	17	596.72
43	131.72	68	288.72	93	445.72	18	602.72
44	137.72	69	294.72	94	451.72	19	608.72
45	143.72	70	300.72	95	457.72	20	614.72
46	149.72	71	306.72	96	463.72	21	620.72
							+ 7.40
							628.12

Data table headings always include accelerator running period, proton beam energy, detector type, and general category of detector locations. The heading may also include the following items, provided they remain constant for all entries in a particular table: detector size (or weight), installation number, exposure length, and average proton beam intensity.

The item "Detector type" also denotes the type of reaction observed. When listed without an indicated reaction product, we mean the following reactions:

$$Au^{197}\,(n,\gamma)\,Au^{198}$$

$$S^{32}\,(n,p)\,P^{32}$$

$$Al^{27}\,(n,\alpha)\,Na^{27}$$

$$C^{12}\,(n,2n)\,C^{11}.$$

Otherwise, the observed reaction product is indicated.

All values for count rates, neutron fluxes, and proton beam intensities are listed in the E-format of digital computer parlance. For example, 5.20 E+6 is 5.20×10^6.

A data table may contain as many as eight columns of information. As an introduction to these tables, the meanings of all columns are described here.

Installation number. Each running period was usually subdivided into a number of sequential exposures for the short half-life activities, e.g. carbon. Details of all exposures (installations) are given on the run summary sheet that appears as the first entry for each running period, and installation numbers are listed with all data on the following tables.

Location. These alphanumeric entries are the notations used throughout the experiment to denote detector positions during exposure. In most (but not all) cases, these notations are also descriptive of actual detector positions; i.e., 32—R means roof bucket at station 32.

Coordinates. Here we list the true spatial coordinates that *vary* for the locations of this particular set of detectors; the coordinates which remain constant for the set are usually *not* listed: i.e., X-values for orbit holes (100 meters) are not listed.

Exposure time. These entries denote the exposure time in minutes for a particular set of detectors, measured from *beam on* until *beam off.* For detectors exposed in a single installation this time is the entire exposure interval from start to finish, and in general is the actual *beam on* time. For detectors exposed throughout several installations, this time is the entire interval between the start of the first exposure and the end of the last exposure; it includes *beam off* times between successive installations.

Detector size. The size (or weight) of the detector used for each measurement is indicated in this column.

Net count rate. These entries represent actual counting data that have been processed to the following extent: Background has been subtracted to obtain the net sample activity count rates, and these net rates have been decay-corrected to a common point in time - the end of the exposure (t_0).

Error percent. The errors, in terms of statistical standard deviation of counting data, are expressed as percent, and are listed *only* if their magnitude is greater than 5% of the reported values, except that *no* errors are given for ionization chamber, sulfur, $\beta\gamma$ film, and TLD.

Average beam intensity ($\bar{I}$). The average proton-beam intensity is taken to be the pulse-by-pulse summation of the proton beam accelerated during an exposure (or exposures) divided by the total exposure time.

Flux intensity at $\bar{I}$. The neutron flux intensities listed here are obtained from the net count rates by applying the calibration constants discussed in Chapter III and, where applicable, corrections to saturation activation. These values are appropriate to the actual experimental conditions.

Flux intensity at 10^{12} *p/sec.* These neutron flux values are obtained from the actual fluxes calculated in the previous column and are normalized to a fictitious 10^{12}-p/sec beam intensity by direct scaling from average beam intensity values.

Run I Data

Run I exposure summary.*

Exposure number	Beam energy (GeV/c)	Average beam current (p/sec)	Exposure duration (min)	Exposure time
1	26.4	1.34 E+11	45	1450 – 1535
2	26.4	1.41 E+11	56	1604 – 1700
3	26.4	1.06 E+11	104	1716 – 1900
entire run	26.4	1.00 E+11	250	1450 – 1900

*Target location: straight section 32;
clipper location: straight section 79.

Run I. Activities for aluminum foils on the vacuum vessel.*

Standard position	Foil activity (pCi/g)	Standard position	Foil activity (pCi/g)	Standard position	Foil activity (pCi/g)	Standard position	Foil activity (pCi/g)
1	8.73 E+3	26	7.75 E+4	51	1.98 E+4	76	6.76 E+3
2	1.85 E+5	27	5.86 E+3	52	9.82 E+4	77	6.23 E+3
3	7.22 E+4	28	2.79 E+5	53	6.74 E+4	78	7.01 E+3
4	5.37 E+4	29	8.66 E+4	54	1.73 E+4	79	5.04 E+7
5	1.39 E+5	30	1.38 E+5	55	1.86 E+4	80	1.57 E+6
6	2.80 E+4	31	4.72 E+4	56	3.43 E+4	81	7.41 E+5
7	2.11 E+4	32	5.64 E+7	57	9.94 E+3	82	8.94 E+5
8	9.51 E+4	33	8.96 E+6	58	8.00 E+4	83	6.86 E+5
9	1.93 E+5	34	3.34 E+6	59	3.29 E+4	84	6.11 E+5
10	8.51 E+5	35	9.82 E+5	60	8.25 E+5	85	2.42 E+5
11	1.33 E+5	36	7.16 E+5	61	1.55 E+5	86	1.24 E+5
12	7.79 E+5	37	2.31 E+5	62	1.10 E+5	87	7.07 E+5
13	8.53 E+4	38	4.29 E+4	63	3.01 E+4	88	4.28 E+5
14	1.79 E+5	39	1.42 E+5	64	2.25 E+5	89	6.48 E+5
15	1.19 E+5	40	3.05 E+4	65	1.20 E+5	90	1.35 E+5
16	5.82 E+4	41	2.68 E+4	66	1.22 E+5	91	2.34 E+5
17	7.53 E+4	42	5.58 E+5	67	1.05 E+5	92	4.40 E+5
18	1.55 E+5	43	1.36 E+5	68	6.33 E+4	93	4.83 E+4
19	3.71 E+5	44	1.87 E+5	69	2.77 E+5	94	2.01 E+5
20	3.59 E+4	45	3.73 E+4	70	4.13 E+4	95	3.65 E+4
21	4.20 E+4	46	1.61 E+4	71	5.28 E+5	96	2.61 E+4
22	9.53 E+4	47	2.26 E+4	72	4.05 E+4	97	2.91 E+4
23	3.12 E+4	48	2.40 E+4	73	3.50 E+4	98	2.84 E+4
24	1.97 E+4	49	7.17 E+4	74	6.76 E+4	99	8.84 E+4
25	3.40 E+4	50	5.87 E+4	75	2.08 E+4	100	8.89 E+4

*One-hundred foils listed here.

Run I. 26.4 GeV/c
Sulfur All installations
Vacuum vessel 250-min exposure
4-g samples 1.00 E + 11 p/sec

Location	Coordinates	ϕ at $\bar{I}$ (n/cm^2-sec)	ϕ at I = 10^{12} p/sec (n/cm^2-sec)
1		1.43 E+4	1.43 E+5
2		2.40 E+5	2.40 E+6
3		8.18 E+4	8.18 E+5
4		7.19 E+4	7.19 E+5
5		2.78 E+5	2.78 E+6
6		7.93 E+4	7.93 E+5
7		2.11 E+4	2.11 E+5
8		1.29 E+5	1.29 E+6
9		3.07 E+5	3.07 E+6
10		1.17 E+6	1.17 E+7
11		1.87 E+5	1.87 E+6
12		1.13 E+6	1.13 E+7
13		9.92 E+4	9.92 E+5
14		2.58 E+5	2.58 E+6
15		2.15 E+5	2.15 E+6
16		9.00 E+4	9.00 E+5
17		9.68 E+4	9.68 E+5
18		2.11 E+5	2.11 E+6
19		8.98 E+5	8.98 E+6
20		6.36 E+4	6.36 E+5
21		6.70 E+4	6.70 E+5
22		1.02 E+5	1.02 E+6
23		3.49 E+4	3.49 E+5
24	Z = 12.7	4.43 E+4	4.43 E+5
25	Z = 19.0	5.20 E+4	5.20 E+5
26	Z = 25.24	1.56 E+5	1.56 E+6
27	Z = 31.52	7.44 E+3	7.44 E+4
28	Z = 37.80	4.48 E+4	4.48 E+5
29	Z = 44.09	1.83 E+5	1.83 E+6
30	Z = 50.36	3.79 E+5	3.79 E+6
31	Z = 56.64	9.41 E+4	9.41 E+5
32	Z = 62.92	6.61 E+7	6.61 E+8
33	Z = 69.20	1.09 E+7	1.09 E+8
34	Z = 75.48	4.57 E+6	4.57 E+7
35	Z = 81.76	1.57 E+6	1.57 E+7
36	Z = 88.08	8.92 E+5	8.92 E+6
37	Z = 94.32	2.71 E+5	2.71 E+6
38	Z = 100.60	5.94 E+4	5.94 E+5
39	Z = 106.88	1.71 E+5	1.71 E+6
40	Z = 113.16	5.60 E+4	5.60 E+5
41	Z = 119.44	2.98 E+4	2.98 E+5
42	Z = 125.72	6.90 E+5	6.90 E+6
43	Z = 132.00	2.42 E+5	2.42 E+6
44	Z = 138.28	3.05 E+5	3.05 E+6
45		5.44 E+4	5.44 E+5
46		1.68 E+4	1.68 E+5
47		3.54 E+4	3.54 E+5
48		3.79 E+4	3.79 E+5
49		1.11 E+5	1.11 E+6
50		1.11 E+5	1.11 E+6

Location	Coordinates	ϕ at $\bar{I}$ (n/cm^2-sec)	ϕ at I = 10^{12} p/sec (n/cm^2-sec)
51		2.33 E+11	2.33 E+5
52		1.34 E+5	1.34 E+6
53		8.42 E+4	8.42 E+5
54		2.98 E+4	2.98 E+5
55		3.96 E+4	3.96 E+5
56		7.66 E+4	7.66 E+5
57		9.16 E+3	9.16 E+4
58		1.91 E+5	1.91 E+6
59		2.33 E+4	2.33 E+5
60		8.36 E+5	8.36 E+6
61		2.15 E+5	2.15 E+6
62		7.19 E+4	7.19 E+5
63		4.66 E+4	4.66 E+5
64		3.65 E+5	3.65 E+6
65		1.81 E+5	1.81 E+6
66		3.99 E+5	3.99 E+6
67		1.63 E+5	1.63 E+6
68		7.01 E+4	7.01 E+5
69		6.92 E+5	6.92 E+6
70		4.59 E+4	4.59 E+5
71		8.33 E+5	8.33 E+6
72		6.05 E+4	6.05 E+5
73		3.85 E+4	3.83 E+5
74		9.59 E+4	9.59 E+5
75		3.72 E+4	3.72 E+5
76		5.20 E+3	5.20 E+4
77		2.73 E+3	2.73 E+4
78		5.94 E+3	5.94 E+4
79		6.94 E+7	6.94 E+8
80		2.69 E+6	2.69 E+7
81		8.58 E+5	8.58 E+6
82		1.18 E+6	1.18 E+7
83		8.96 E+5	8.96 E+6
84		7.91 E+5	7.91 E+6
85		3.01 E+5	3.02 E+6
86		1.16 E+5	1.16 E+6
87		8.09 E+5	8.09 E+6
88		4.77 E+5	4.77 E+6
89		1.13 E+6	1.13 E+7
90		1.59 E+5	1.59 E+6
91		3.61 E+5	3.61 E+6
92		5.82 E+5	5.82 E+6
93		5.44 E+4	5.44 E+5
94		2.89 E+5	2.89 E+6
95		5.69 E+4	5.69 E+5
96		3.47 E+4	3.47 E+5
97		4.48 E+4	4.48 E+5
98		2.73 E+4	2.73 E+5
99		9.92 E+4	9.92 E+5
100		2.26 E+5	2.26 E+6

Run I
Gold foils in moderators
Roof buckets
1-in. diam

26.4 GeV/c
All installations
250-min exposure
1.00 E+11 p/sec

Location	Coordinates	Net count rate (bkg subtracted) at t_0 (cpm/g)	ϕ at $\bar{I}$ (n/cm^2-sec)	ϕ at I = 10^{12} p/sec (n/cm^2-sec)
24−R	Z = 12.7	2.44 E+3	1.52 E+4	1.52 E+5
28−R	Z = 37.80	8.44 E+3	5.26 E+4	5.26 E+5
29−R	Z = 44.08	1.28 E+4	7.92 E+4	7.92 E+5
30−R	Z = 50.36	3.49 E+4	2.16 E+5	2.16 E+6
31−R	Z = 56.64	1.24 E+5	7.70 E+5	7.70 E+6
32−R	Z = 62.92	1.20 E+6	7.45 E+6	7.45 E+7
33−R	Z = 69.20	8.19 E+5	5.08 E+6	5.08 E+7
34−R	Z = 75.48	4.34 E+5	2.69 E+6	2.69 E+7
35−R	Z = 81.76	1.62 E+5	1.01 E+6	1.01 E+7
36−R	Z = 88.08	9.66 E+4	5.99 E+5	5.99 E+6
37−R	Z = 94.32	3.68 E+4	2.28 E+5	2.28 E+6
38−R	Z = 100.60	1.75 E+4	1.09 E+5	1.09 E+6
39−R	Z = 106.88	1.37 E+4	8.48 E+4	8.48 E+5
41−R	Z = 119.44	6.71 E+3	4.16 E+4	4.16 E+5
43−R	Z = 132.00	1.41 E+4	8.77 E+4	8.77 E+5

Run I
Sulfur
Roof buckets
4-g samples

26.4 GeV/c
All installations
250-min exposure
1.00 E+11 p/sec

Location	Coordinates	$\bar{\phi}$ at I (n/cm^2-sec)	$\bar{\phi}$ at I = 10^{12} p/sec (n/cm^2-sec)
1–R		5.20 E+3	5.20 E+4
2–R		8.58 E+3	8.58 E+4
3–R		3.49 E+3	3.49 E+4
4–R		1.77 E+3	1.77 E+4
5–R		1.04 E+4	1.04 E+5
6–R		5.29 E+3	5.29 E+4
7–R		1.13 E+3	1.13 E+4
8–R		4.64 E+4	4.64 E+5
9–R		1.98 E+4	1.98 E+5
10–R		4.61 E+4	4.61 E+5
11–R		2.14 E+4	2.14 E+5
12–R		2.16 E+4	2.16 E+5
13–R		1.08 E+4	1.08 E+5
14–R		8.42 E+3	8.42 E+4
15–R		9.09 E+3	9.09 E+4
16–R		4.23 E+3	4.23 E+4
17–R		4.44 E+3	4.44 E+4
18–R			
19–R		1.59 E+4	1.59 E+5
20–R		2.93 E+3	2.93 E+4
21–R		2.60 E+3	2.60 E+4
22–R		5.94 E+3	5.94 E+4
23–R		8.27 E+2	8.27 E+3
24–R	Z = 12.7	4.44 E+3	4.44 E+4
25–R	Z = 19.0	3.32 E+3	3.33 E+4
26–R	Z = 25.24	7.44 E+3	7.44 E+4
27–R	Z = 31.52	1.30 E+3	1.30 E+4
28–R	Z = 37.80	8.74 E+3	8.74 E+4
29–R	Z = 44.08	8.83 E+3	8.83 E+4
30–R	Z = 50.36	1.53 E+4	1.53 E+5
31–R	Z = 56.64	3.09 E+4	3.09 E+5
32–R	Z = 62.92	7.93 E+5	7.93 E+6
33–R	Z = 69.20	2.98 E+5	2.98 E+6
34–R	Z = 75.48	2.07 E+5	2.07 E+6
35–R	Z = 81.76	8.02 E+4	8.02 E+5
36–R	Z = 88.08	4.75 E+4	4.75 E+5
37–R	Z = 94.32	1.96 E+4	1.96 E+5
38–R	Z = 100.60	1.03 E+4	1.03 E+5
39–R	Z = 106.88	1.23 E+4	1.23 E+5
40–R	Z = 113.16	7.91 E+3	7.91 E+4
41–R	Z = 119.44	3.96 E+3	3.96 E+4
42–R	Z = 125.72	1.31 E+4	1.31 E+5
43–R	Z = 132.00	3.32 E+3	3.32 E+4
44–R	Z = 138.28	8.53 E+3	8.53 E+4
45–R		4.55 E+3	4.55 E+4
46–R		5.42 E+3	5.42 E+4
47–R		4.66 E+2	4.66 E+3
48–R			
49–R			
50–R		5.98 E+3	5.98 E+4

Location	Coordinates	ϕ at $\bar{I}$ (n/cm^2-sec)	ϕ at I = 10^{12} p/sec (n/cm^2-sec)
51–R		7.77 E+2	7.77 E+3
52–R		5.94 E+3	5.94 E+4
53–R			
54–R		5.24 E+3	5.24 E+4
55–R			
56–R		3.20 E+3	3.20 E+4
57–R			
58–R		5.22 E+3	5.22 E+4
59–R		7.82 E+2	7.82 E+3
60–R		1.70 E+4	1.70 E+5
61–R		9.12 E+3	9.12 E+4
62–R		5.24 E+3	5.24 E+4
63–R		3.07 E+3	3.07 E+4
64–R		6.23 E+3	6.23 E+4
65–R		9.08 E+3	9.08 E+4
66–R		9.72 E+3	9.72 E+4
67–R		4.55 E+3	4.55 E+4
68–R		1.20 E+4	1.20 E+5
69–R		4.91 E+3	4.91 E+4
70–R		1.03 E+4	1.03 E+5
71–R		1.64 E+4	1.64 E+5
72–R		1.01 E+4	1.01 E+5
73–R		5.56 E+3	5.56 E+4
74–R		4.05 E+3	4.05 E+4
75–R		6.20 E+2	6.20 E+3
76–R	Z = 44.1	2.89 E+2	2.89 E+3
77–R	Z = 50.4	2.17 E+3	2.17 E+4
78–R	Z = 56.6	3.72 E+3	3.72 E+4
79–R	Z = 62.9	5.33 E+5	5.33 E+6
80–R	Z = 69.2	9.68 E+4	9.68 E+5
81–R	Z = 75.5	5.58 E+4	5.58 E+5
82–R	Z = 81.8	3.72 E+4	3.72 E+5
83–R	Z = 88.1	1.06 E+4	1.06 E+5
84–R	Z = 94.3	3.07 E+4	3.07 E+5
85–R		1.66 E+4	1.66 E+5
86–R		8.60 E+3	8.60 E+4
87–R		2.44 E+4	2.44 E+5
88–R		1.82 E+4	1.82 E+5
89–R		2.11 E+4	2.11 E+5
90–R		8.58 E+3	8.58 E+4
91–R		1.98 E+4	1.98 E+5
92–R		1.91 E+4	1.91 E+5
93–R		3.70 E+3	3.70 E+4
94–R		1.08 E+4	1.08 E+5
95–R		3.74 E+3	3.74 E+4
96–R		4.28 E+3	4.28 E+4
97–R		6.41 E+3	6.41 E+4
98–R		1.33 E+4	1.33 E+5
99–R		3.90 E+3	3.90 E+4
100–R		1.59 E+3	1.59 E+4

Run I
Aluminum
Roof buckets
100-g samples

26.4 GeV/c
All installations
250-min. exposure
1.00 E+11 p/sec

Location	Coordinates	Net count rate (bkg subtracted) at t_0 (cpm/g)	Error (%)	ϕ at $\bar{I}$ (n/cm^2-sec)	ϕ at I=10^{12} p/sec (n/cm^2-sec)
1–R		4.71 E+2		6.11 E+2	6.11 E+3
2–R		1.93 E+3		2.50 E+3	2.50 E+4
3–R		8.54 E+2		1.11 E+3	1.11 E+4
4–R		7.86 E+2		1.02 E+3	1.02 E+4
5–R		2.55 E+3		3.31 E+3	3.31 E+4
6–R		8.73 E+2		1.13 E+3	1.13 E+4
7–R		6.84 E+2		8.88 E+2	8.88 E+3
8–R		1.55 E+4		2.01 E+4	2.01 E+5
9–R		4.55 E+3		5.91 E+3	5.91 E+4
10–R		1.72 E+4		2.24 E+4	2.24 E+5
11–R		4.63 E+3		6.03 E+3	6.03 E+4
12–R		6.11 E+3		7.96 E+3	7.96 E+4
13–R		2.09 E+3		2.72 E+3	2.72 E+4
14–R		3.20 E+3		4.17 E+3	4.17 E+4
15–R		2.43 E+3		3.17 E+3	3.17 E+4
16–R		1.27 E+3		1.64 E+3	1.64 E+4
17–R		8.63 E+2		1.12 E+3	1.12 E+4
18–R		Lost Sample			
19–R		3.72 E+3		4.83 E+3	4.83 E+4
20–R		1.01 E+3		1.31 E+3	1.31 E+4
21–R		6.89 E+2		8.94 E+2	8.94 E+3
22–R		1.15 E+3		1.50 E+3	1.50 E+4
23–R		5.17 E+2		6.71 E+2	6.71 E+3
24–R		4.17 E+2	5.1	5.41 E+2	5.41 E+3
25–R	Z = 19.0	7.62 E+2		9.88 E+2	9.88 E+3
26–R	Z = 25.24	7.86 E+2		1.02 E+2	1.02 E+4
27–R	Z = 31.52	4.25 E+2	5.1	5.52 E+2	5.52 E+3
28–R	Z = 37.80	1.78 E+3		2.30 E+3	2.30 E+4
29–R	Z = 44.08	1.01 E+3		1.30 E+3	1.30 E+4
30–R	Z = 50.36	4.03 E+3		5.23 E+3	5.23 E+4
31–R	Z = 56.64	7.44 E+3		9.66 E+3	9.66 E+4
32–R	Z = 62.92	2.78 E+5		3.60 E+5	3.60 E+6
33–R	Z = 69.20	1.38 E+5		1.80 E+5	1.80 E+6
34–R	Z = 75.48	8.03 E+4		1.04 E+5	1.04 E+6
35–R	Z = 81.76	3.14 E+4		4.08 E+4	4.08 E+5
36–R	Z = 88.08	1.96 E+4		2.54 E+4	2.54 E+5
37–R	Z = 94.32	1.09 E+4		1.31 E+4	1.41 E+5
38–R	Z = 100.60	7.00 E+3		9.09 E+3	9.09 E+4
39–R	Z = 106.88	6.37 E+3		8.27 E+3	8.27 E+4
40–R	Z = 113.16	3.15 E+3		4.09 E+3	4.09 E+4
41–R	Z = 119.44	1.63 E+3		2.12 E+3	2.12 E+4
42–R	Z = 125.72	4.77 E+3		6.19 E+3	6.19 E+4
43–R	Z = 132.00	2.10 E+3		2.73 E+3	2.73 E+4
44–R	Z = 138.28	3.85 E+3		4.99 E+3	4.99 E+4
45–R		1.20 E+3		1.56 E+3	1.56 E+4
46–R		5.80 E+2		7.53 E+2	7.53 E+3
47–R		4.33 E+2	5.2	5.62 E+2	5.62 E+3
48–R		3.84 E+2	5.6	4.99 E+2	4.99 E+3
49–R		6.03 E+2		7.83 E+2	7.83 E+3
50–R		1.20 E+3		1.56 E+3	1.56 E+4

Location	Coordinates	Net count rate (bkg subtracted) at t_0 (cpm/g)	Error (%)	ϕ at $\bar{I}$ (n/cm^2-sec)	ϕ at I=10^{12} p/sec (n/cm^2-sec)
51–R		4.02 E+2	5.5	5.22 E+2	5.22 E+3
52–R		9.23 E+2		1.20 E+3	1.20 E+4
53–R		4.33 E+2	5.4	5.62 E+2	5.62 E+3
54–R		2.71 E+2	7.6	3.52 E+2	3.52 E+3
55–R		2.63 E+2	6.7	3.42 E+2	3.42 E+3
56–R		2.53 E+2	8.0	3.29 E+3	3.29 E+3
57 –R		2.55 E+2	8.0	3.31 E+2	3.31 E+3
58–R		8.05 E+2		1.05 E+3	1.05 E+4
59–R		5.08 E+2		6.60 E+2	6.60 E+3
60–R		5.23 E+3		6.79 E+3	6.79 E+4
61–R		2.19 E+3		2.84 E+3	2.84 E+4
62–R		1.58 E+3		2.05 E+3	2.05 E+4
63–R		8.49 E+2		1.10 E+3	1.10 E+4
64–R		3.55 E+3		4.61 E+3	4.61 E+4
65–R		1.97 E+3		2.55 E+3	2.55 E+4
66–R		1.10 E+3		1.43 E+3	1.43 E+4
67–R		1.32 E+3		1.71 E+3	1.71 E+4
68–R		8.08 E+2		1.05 E+3	1.05 E+4
69–R		1.77 E+3		2.30 E+3	2.30 E+4
70–R		8.02 E+2		1.04 E+3	1.04 E+4
71–R		6.16 E+3		8.00 E+3	8.00 E+4
72–R		1.30 E+3		1.69 E+3	1.69 E+4
73–R		6.20 E+2	5.4	8.04 E+2	8.04 E+3
74–R		1.36 E+3		1.77 E+3	1.77 E+4
75–R		5.96 E+2	5.6	7.73 E+2	7.73 E+3
76–R	Z = 44.1	4.33 E+2	5.9	5.61 E+2	5.61 E+3
77–R	Z = 50.4	8.13 E+2		1.05 E+3	1.05 E+4
78–R	Z = 56.6	2.73 E+3		3.56 E+3	3.56 E+4
79–R	Z = 62.9	1.86 E+5		2.42 E+5	2.42 E+6
80–R	Z = 69.2	3.58 E+4		4.64 E+4	4.64 E+5
81–R	Z = 75.5	1.82 E+4		2.36 E+4	2.36 E+5
82–R	Z = 81.8	1.31 E+4		1.70 E+4	1.70 E+5
83–R	Z = 88.1	8.21 E+3		1.07 E+4	1.07 E+5
84–R	Z = 94.3	1.09 E+4		1.41 E+4	1.41 E+5
85–R		5.77 E+3		7.50 E+3	7.50 E+4
86–R		2.96 E+3		3.84 E+3	3.84 E+4
87–R		3.78 E+3		4.90 E+3	4.90 E+4
88–R		4.08 E+3		5.30 E+3	5.30 E+4
89–R		5.73 E+3		7.44 E+3	7.44 E+4
90–R		2.06 E+3		2.68 E+3	2.68 E+4
91–R		4.83 E+3		6.26 E+3	6.26 E+4
92–R		4.84 E+3		6.28 E+3	6.28 E+4
93–R		1.43 E+3		1.86 E+3	1.86 E+4
94–R		2.85 E+3		3.70 E+3	3.70 E+4
95–R		1.10 E+3		1.43 E+3	1.43 E+4
96–R		7.38 E+2		9.58 E+2	9.58 E+3
97–R		5.23 E+2	5.0	6.78 E+2	6.78 E+3
98–R		4.58 E+2	5.5	5.94 E+2	5.94 E+3
99–R		1.12 E+3		1.45 E+3	1.45 E+4
100–R		1.34 E+3		1.74 E+3	1.74 E+4

Run I
Carbon
Roof buckets

26.4 GeV/c
Installation 1
45-min exposure

1.34 E+1 p/sec

Location	Coordinates	Detector size (in.)	Net count rate (bkg subtracted) at t_0 (cpm)	$\phi = \bar{I}$ (n/cm^2-sec)	ϕ at I=10^{12} p/sec (n/cm^2-sec)
24–R	Z = 12.7	2	1.93 E+5	2.37 E+3	1.80 E+4
26–R	Z = 25.24	2	4.38 E35	5.37 E+3	4.08 E+4
28–R	Z = 37.80	2	4.08 E+5	5.0 E+3	3.80 E+4
29–R	Z = 44.08	2	6.54 E+5	8.03 E+3	6.10 E+4
30–R	Z = 50.36	2	1.23 E+6	1.51 E+4	1.15 E+5
31–R	Z = 56.64	1	1.44 E+6	1.76 E+4	1.34 E+5
32–R	Z = 62.92	1	6.59 E+7	8.09 E+5	6.15 E+6
33–R	Z = 69.20	1	4.02 E+7	4.93 E+5	3.75 E+6
34–R	Z = 75.48	1	3.06 E+7	3.76 E+5	2.86 E+6
35–R	Z = 81.76	2	1.36 E+7	1.67 E+5	1.27 E+6
36–R	Z = 88.08	2	2.05 E+7	2.52 E+5	1.91 E+6
37–R	Z = 94.32	2	6.57 E+6	8.07 E+4	6.13 E+5
38–R	Z = 100.60	2	1.04 E+7	1.27 E+5	9.65 E+5
39–R	Z = 106.88	2	5.68 E+6	6.97 E+4	5.30 E+5
41–R	Z = 119.44	2	1.95 E+6	2.39 E+4	1.82 E+5
43–R	Z = 132.00	2	1.47 E+6	1.80 E+4	1.37 E+5

Run I
Carbon
Roof buckets
1-in. detector

26.4 GeV/c
Installation 2
45-min exposure
1.41 E+11 p/sec

Location	Coordinates	Net count rate (bkg subtracted) at t_0 (cpm)	ϕ at $\bar{I}$ (n/cm^2-sec)	ϕ at I=10^{12} p/sec (n/cm^2-sec)
31–R	Z = 56.64	1.04 E+6	1.17 E+4	8.29 E+4
32–R	Z = 62.92	1.22 E+8	1.38 E+6	9.78 E+6
33–R	Z = 69.20	5.00 E+7	5.65 E+5	4.00 E+6
34–R	Z = 75.48	3.10 E+7	3.5 E+5	2.48 E+6

Run I
Carbon
Vent shaft
Coordinates: X = 103.2, Z = 70.6

26.4 GeV/c
45-min exposure
4-in. detector

Installation	Net count rate (bkg subtracted)	$\bar{I}$ (p/sec)	ϕ at $\bar{I}$ (n/cm^2-sec)	ϕ at I=10^{12} p/sec (n/cm^2-sec)
1	4.83 E+6	1.34 E+11	6.08 E+4	4.62 E+5
2	6.16 E+6	1.41 E+11	6.97 E+4	4.94 E+5

Run I
TLD
Roof buckets
22-mg samples

26.4 GeV/c
All installations
250-min. exposure
1.00 E+11 p/sec

Location	Coordinates	Indicated dose (rads)
1–R		1.3 E+0
2–R		9.0 E-1
3–R		1.8 E+0
4–R		1.5 E+0
5–R		4.1 E+0
6–R		1.5 E+0
7–R		1.6 E+0
8–R		3.32 E+1
9–R		6.0 E+0
10–R		1.67 E+1
11–R		7.3 E+0
12–R		1.28 E+1
13–R		4.2 E+0
14–R		5.5 E+0
15–R		4.5 E+0
16–R		3.5 E+0
17–R		3.0 E+0
18–R		—
19–R		6.1 E+0
20–R		2.1 E+0
21–R		1.6 E+0
22–R		2.8 E+0
23–R		1.5 E+0
24–R	Z = 12.7	1.1 E+0
25–R	Z = 19.0	1.9 E+0
26–R	Z = 25.24	1.6 E+0
27–R	Z = 31.52	2.0 E+0
28–R	Z = 37.80	3.1 E+0
29–R	Z = 44.08	2.5 E+0
30–R	Z = 50.36	1.0 E+1
31–R	Z = 56.64	2.02 E+1
32–R	Z = 62.92	3.55 E+2
33–R	Z = 69.20	2.19 E+2
34–R	Z = 75.48	1.97 E+2
35–R	Z = 81.76	8.12 E+1
36–R	Z = 88.08	6.61 E+1
37–R	Z = 94.32	4.63 E+1
38–R	Z = 100.60	3.89 E+1
39–R	Z = 106.88	3.61 E+1
40–R	Z = 113.16	1.92 E+1
41–R	Z = 119.44	6.8 E+0
42–R	Z = 125.72	1.18 E+1
43–R	Z = 132.00	5.8 E+0
44–R	Z = 138.28	7.2 E+0
45–R		2.5 E+0
46–R		1.6 E+0
47–R		1.5 E+0
48–R		1.2 E+0
49–R		1.1 E+0
50–R		1.9 E+0

Location	Coordinates	Indicated dose (rads)
51–R		8.0 E-1
52–R		2.4 E+0
53–R		1.2 E+0
54–R		1.0 E+0
55–R		6.0 E-1
56–R		6.0 E-1
57–R		8.0 E-1
58–R		1.8 E+0
59–R		1.0 E+0
60–R		8.0 E+0
61–R		4.6 E+0
62–R		3.7 E+0
63–R		1.9 E+0
64–R		7.1 E+0
65–R		3.4 E+0
66–R		3.6 E+0
67–R		3.0 E+0
68–R		2.1 E+0
69–R		3.3 E+0
70–R		1.5 E+0
71–R		1.27 E+1
72–R		3.9 E+0
73–R		1.9 E+0
74–R		2.6 E+0
75–R		2.3 E+0
76–R	Z = 44.1	1.4 E+0
77–R	Z = 50.4	2.3 E+0
78–R	Z = 56.6	5.8 E+0
79–R	Z = 62.9	3.03 E+2
80–R	Z = 69.2	5.87 E+1
81–R	Z = 75.5	2.28 E+1
82–R	Z = 81.8	2.55 E+1
83–R	Z = 88.1	2.15 E+1
84–R	Z = 94.3	2.08 E+1
85–R		1.37 E+1
86–R		7.6 E+0
87–R		1.03 E+1
88–R		9.5 E+0
89–R		1.15 E+1
90–R		4.9 E+0
91–R		8.6 E+0
92–R		8.3 E+0
93–R		3.5 E+0
94–R		4.7 E+0
95–R		2.2 E+0
96–R		1.6 E+0
97–R		1.3 E+0
98–R		1.1 E+0
99–R		1.8 E+0
100–R		2.0 E+0

Run I
Aluminum
Ring top

26.4 GeV/c
All installations
250-min. exposure

1.00 E+11 p/sec

Location	Coordinates	Detector size (g)	Net count rate (bkg subtracted) at t_0 (cpm)	Error (%)	ϕ at $\bar{I}$ (n/cm^2-sec)	ϕ at I=10^{12} p/sec (n/cm^2-sec)
26/0	Y = 6.38 Z = 25.24	3300	5.01 E+0	13.9	3.9 E-1	3.9 E+0
30/0	Y = 6.42 Z = 50.36	2200	3.23 E+0	69.9	3.2 E-1	3.2 E+0
31/0	Y = 6.40 Z = 62.92	1100	7.36 E+0	30.	1.28 E+0	1.28 E+1
32/0	Y = 6.42 Z = 69.92	1100	8.5 E+1	7.9	1.48 E+1	1.48 E+2
33/0	Y = 6.39 Z = 69.20	1100	9.5 E+1	7.25	1.65 E+1	1.65 E+2
34/0	Y = 6.29 Z = 75.48	1100	6.11 E+1	9.4	1.06 E+1	1.06 E+2
35/0	Y = 6.30 Z = 81.76	1100	2.64 E+1	12.3	4.6 E+0	4.6 E+1
36/0	Y = 6.26 Z = 88.08	1100	1.46 E+1	18.1	2.54 E+0	2.54 E+1
37/0	Y = 6.26 Z = 94.32	1100	6.94 E+0	32.5	1.21 E+0	1.21 E+1
41/0	Y = 6.39 Z = 119.4	3300	6.33 E+0	22	4.9 E-1	4.9 E+0
78/0	Z = 56.6	1100	2.45 E+0	120.	4.3 E-1	4.3 E+0
79/0	Z = 62.9	1100	7.04 E+1	7.1	1.23 E+1	1.23 E+2
80/0	Z = 69.2	1100	3.4 E+1	13.1	5.96 E+0	5.96 E+1
81/0	Z = 70.5	1100	1.03 E+1	41.	1.8 E+0	1.8 E+1

Run I
Carbon
Ring top

26.4 GeV/c
Installation 2
5-in. detector

1.41 E+11 p/sec

Location	Coordinates	Exposure time (min)	Net count rate (bkg subtracted) at t_0 (cpm)	Error (%)	ϕ at $\bar{l}$ (n/cm^2-sec)	ϕ at l=10^{12} p/sec (n/cm^2-sec)
24	Y = 6.35 Z = 12.7	64 min	7.73 E+0	424	8.7 E-2	6.17 E-1
26	Y = 6.38 Z = 25.24		3.27 E+2	15	3.70 E+0	2.62 E+1
28	Y = 6.38 Z = 37,80		2.09 E+2	17	2.36 E+0	1.67 E+1
29	Y = 6.35 Z = 44.08		9.72 E+1	34	1.10 E+0	7.80 E+0
30	Y = 6.42 Z = 50.36		1.58 E+2	16	1.79 E+0	1.27 E+1
31	Y = 6.40 Z = 62.92		1.31 E+2	18.6	1.49 E+0	1.06 E+1
32	Y = 6.42 Z = 62.92		4.28 E+3		4.83 E+1	3.42 E+2
33	Y = 6.39 Z = 69.20		5.71 E+3		6.46 E+1	4.58 E+2
34	Y = 6.29 Z = 75.48		3.97 E+3		4.49 E+1	3.18 E+2
35	Y = 6.30 Z = 81.76		1.47 E+3		1.66 E+1	1.18 E+2
36	Y = 6.26 Z = 88.08		8.00 E+2	6.1	9.04 E+0	6.41 E+1
37	Y = 6.26 Z = 94.32		9.87 E+2	6.8	1.11 E+1	7.9 E+1
38	Y = 6.27 Z = 100.60		4.59 E+2	14.5	5.18 E+0	3.67 E+1
39	Y = 6.32 Z = 106.88	45	3.48 E+2	26	3.94 E+0	2.79 E+1
41	Y = 6.39 Z = 119.44		5.83 E+2	12	6.59 E+0	4.67 E+a
43	Y = 6.40 Z = 132.00		5.86 E+2	18.5	6.62 E+0	4.69 E+1

Run II Data

Run II exposure summary.*

Exposure number	Beam energy (GeV/c)	Average beam current (p/sec)	Exposure duration (min)	Exposure time
1	26.4	1.99 E+11	63	2357 – 0100
2	26.4	2.01 E+11	191	0109 – 0420
1,2	26.4	1.93 E+11	263	2357 – 0420
3	26.4	1.98 E+11	62	0458 – 0600

*Target location: straight section 32;
clipper location: straight section 79.

Run II. Activities for aluminum foils on vacuum vessel.*

Standard position	Foil activity (pCi/g)	Standard position	Foil activity (pCi/g)	Standard position	Foil activity (pCi/g)	Standard position	Foil activity (pCi/g)
1	9.45 E+3	26	6.29 E+4	51	2.30 E+4	76	7.15 E+3
2	2.02 E+5	27	3.63 E+3	52	8.28 E+4	77	7.16 E+3
3	6.86 E+4	28	5.15 E+5	53	6.58 E+4	78	9.94 E+3
4	5.61 E+4	29	1.12 E+5	54	2.27 E+4	79	3.79 E+7
5	1.41 E+5	30	1.48 E+5	55	1.72 E+4	80	1.49 E+6
6	2.92 E+4	31	3.42 E+4	56	2.46 E+4	81	5.88 E+5
7	2.00 E+4	32	2.72 E+7	57	1.36 E+4	82	6.66 E+5
8	9.67 E+4	33	7.41 E+6	58	6.07 E+4	83	5.59 E+5
9	2.75 E+5	34	2.74 E+6	59	5.91 E+4	84	4.67 E+5
10	1.69 E+6	35	8.50 E+5	60	1.48 E+6	85	1.66 E+5
11	1.86 E+5	36	6.36 E+5	61	1.29 E+5	86	1.10 E+5
12	1.18 E+6	37	2.08 E+5	62	1.71 E+5	87	5.63 E+5
13	1.24 E+5	38	4.60 E+4	63	4.14 E+4	88	3.84 E+5
14	2.51 E+5	39	1.28 E+5	64	2.72 E+5	89	6.01 E+5
15	1.32 E+5	40	2.98 E+4	65	6.22 E+4	90	1.15 E+5
16	6.72 E+4	41	3.94 E+4	66	9.52 E+4	91	2.21 E+5
17	8.21 E+4	42	1.09 E+6	67	1.10 E+5	92	5.60 E+5
18	2.38 E+5	43	1.22 E+5	68	6.58 E+4	93	4.72 E+4
19	3.93 E+5	44	2.29 E+5	69	2.74 E+5	94	2.76 E+5
20	3.61 E+4	45	4.99 E+4	70	4.81 E+4	95	3.11 E+4
21	4.82 E+4	46	2.27 E+4	71	5.85 E+5	96	2.16 E+4
22	1.40 E+5	47	3.32 E+4	72	6.10 E+4	97	2.33 E+4
23	5.14 E+4	48	5.28 E+4	73	3.90 E+4	98	4.02 E+4
24	2.73 E+4	49	8.42 E+4	74	1.43 E+5	99	6.99 E+4
25	2.82 E+4	50	6.34 E+4	75	2.29 E+4	100	1.65 E+5

*One-hundred foils listed here.

Run II
Sulfur
Roof buckets
4-g samples

26.4 GeV/c
Installations 1 and 2
2.63-min exposure
1.93 E+11 p/sec

Location	Coordinates	$\phi = \overline{I}$ (n/cm^2-sec)	ϕ at I = 10^{12} p/sec (n/cm^2-sec)
27–R	Z = 31.52	2.34 E+3	1.21 E+4
28–R	Z = 37.80	1.82 E+4	9.41 E+4
29–R	Z = 44.1	8.16 E+3	4.23 E+4
30–R	Z = 50.4	3.18 E+4	1.65 E+5
31–R	Z = 56.6	5.15 E+4	2.67 E+5
31–1R	Z = 57.9	7.70 E+4	3.99 E+5
31–2R	Z = 58.9	1.26 E+5	6.54 E+5
31–3R	Z = 59.9	2.01 E+5	1.04 E+6
31–4R	Z = 60.9	3.71 E+5	1.92 E+6
31–5R	Z = 61.9	6.83 E+5	3.54 E+6
32–R	Z = 62.9	1.56 E+6	8.11 E+6
32–1R	Z = 63.9	2.08 E+6	1.08 E+7
32–2R	Z = 65.4	1.24 E+6	6.43 E+6
32–3R	Z = 66.4	8.05 E+5	4.17 E+6
32–4R	Z = 67.3	6.31 E+5	3.27 E+6
32–5R	Z = 68.2	6.18 E+5	3.20 E+6
33–R	Z = 69.2	7.60 E+5	3.94 E+6
33–1R	Z = 70.5	7.57 E+5	3.92 E+6
33–2R	Z = 71.5	5.54 E+5	2.87 E+6
33–3R	Z = 72.5	4.09 E+5	2.12 E+6
33–4R	Z = 73.5	3.82 E+5	1.98 E+6
33–5R	Z = 74.5	3.57 E+5	1.85 E+6
34–R	Z = 75.5	3.98 E+5	2.06 E+6
35–R	Z = 81.8	1.61 E+5	8.36 E+5
36–R	Z = 88.1	1.12 E+5	5.80 E+5
37–R	Z = 94.3	3.74 E+5	1.94 E+6
38–R	Z = 100.6	1.95 E+4	1.01 E+5
39–R	Z = 106.9	1.80 E+4	9.32 E+4
40–R	Z = 113.2	1.06 E+4	5.47 E+4
41–R	Z = 119.4	9.34 E+3	4.84 E+4
42–R	Z = 125.7	5.36 E+4	2.78 E+5

Location	Coordinates	$\phi = \bar{I}$ (n/cm^2-sec)	ϕ at I = 10^{12} p/sec (n/cm^2-sec)
43–R	Z = 132.0	1.59 E+4	8.22 E+4
44–R	Z = 138.3	5.36 E+4	2.78 E+5
45–R		8.86 E+3	4.59 E+4
46–R		4.21 E+3	2.18 E+4
47–R		2.57 E+3	1.33 E+4
48–R		2.10 E+3	1.09 E+4
76–R	Z = 44.1	4.88 E+3	2.53 E+4
77–R	Z = 50.4	7.22 E+3	3.74 E+4
78–R	Z = 56.6	2.03 E+4	1.05 E+5
78–1R	Z = 57.9	2.76 E+4	1.43 E+5
78–2R	Z = 58.9	4.71 E+4	2.44 E+5
78–3R	Z = 59.9	8.65 E+4	4.48 E+5
78–4R	Z = 60.9	1.62 E+5	8.42 E+5
78–5R	Z = 61.9	4.84 E+5	2.51 E+6
79–R	Z = 62.9	8.12 E+5	4.21 E+6
79–1R	Z = 63.9	6.14 E+5	3.18 E+6
79–2R	Z = 64.9	3.57 E+5	1.85 E+6
79–3R	Z = 65.9	2.01 E+5	1.04 E+6
79–4R	Z = 66.9	1.78 E+5	9.21 E+5
79-5R	Z = 67.9	1.91 E+5	9.88 E+5
80–R	Z = 69.2	1.85 E+5	9.59 E+5
80–1R	Z = 70.5	1.36 E+5	7.06 E+5
80–2R	Z = 71.5	8.68 E+4	4.50 E+5
80–3R	Z = 72.5	7.22 E+4	3.74 E+5
80–4R	Z = 73.5	7.43 E+4	3.85 E+5
80–5R	Z = 74.5	7.53 E+4	3.90 E+5
81–R	Z = 75.5	8.65 E+4	4.48 E+5
82–R	Z = 81.8	6.18 E+4	3.20 E+5
83–R	Z = 88.1	3.76 E+4	1.95 E+5
84–R	Z = 94.3	4.88 E+4	2.53 E+5

Run II
Aluminum
Roof buckets
100-g samples

26.4 GeV/c
Installations 1 and 2
263-min. exposure
1.93 E+11

Location	Coordinates	Net count rate (bkg. subtracted) at t_0 (cpm/g)	ϕ at $\bar{l}$ (n/cm^2-sec)	ϕ at $l = 10^{12}$ p/sec (n/cm^2/sec)
29–R	Z = 44.1	3.42 E+3	4.24 E+3	2.20 E+4
30–R	Z = 50.4	9.41 E+3	1.17 E+4	6.06 E+4
31–R	Z = 56.6	1.31 E+4	1.62 E+4	8.39 E+4
31–1R	Z = 57.9	2.0 E+4	2.48 E+4	1.28 E+5
31–2R	Z = 58.9	2.88 E+4	3.57 E+4	1.85 E+5
31–3R	Z = 59.9	4.76 E+4	5.91 E+4	3.06 E+5
31–4R	Z = 60.9	9.27 E+4	1.15 E+5	5.96 E+5
31–5R	Z = 61.9	1.96 E+5	2.43 E+5	1.26 E+6
32–1R	Z = 62.9	5.15 E+5	6.38 E+5	3.31 E+6
31–1R	Z = 63.9	7.43 E+5	9.22 E+5	4.78 E+6
32–2R	Z = 65.4	5.77 E+5	7.16 E+5	3.71 E+6
32–3R	Z = 66.4	3.43 E+5	4.25 E+5	2.20 E+6
32–4R	Z = 67.3	2.58 E+5	3.2 E+5	1.66 E+6
32–5R	Z = 68.2	2.14 E+5	2.65 E+5	1.37 E+6
33–R	Z = 69.2	2.67 E+5	3.31 E+5	1.71 E+6
33–1R	Z = 70.5	2.9 E+5	3.59 E+5	1.86 E+6
33–2R	Z = 71.5	2.36 E+5	2.9 E+5	1.50 E+6
33–3R	Z = 72.5	1.70 E+5	2.11 E+5	1.09 E+6
33–4R	Z = 73.5	1.4 E+5	1.73 E+5	8.96 E+5
33–5R	Z = 74.5	1.32 E+5	1.64 E+5	8.50 E+5
34–R	Z = 75.5	1.39 E+5	1.72 E+5	8.91 E+5
35–R	Z = 81.8	6.36 E+4	7.88 E+4	4.08 E+5
36–R	Z = 88.1	4.39 E+4	5.44 E+4	2.82 E+5
37–R	Z = 94.3	1.93 E+4	2.4 E+4	1.24 E+5
38–R	Z = 100.6	1.27 E+4	1.58 E+4	8.19 E+4
39–R	Z = 106.9	1.19 E+4	1.48 E+4	7.67 E+4
41–R	Z = 119.4	3.66 E+3	4.54 E+3	2.35 E+4
43–R	Z = 132.0	6.55 E+3	8.12 E+3	4.21 E+4

Run II
Carbon
Roof buckets

26.4 GeV/c
Installation 3
62-min. exposure

1.98 E+11 p/sec

Location	Coordinates	Detector size (in.)	Net count rate (bkg subtracted) at t_0 (cpm/g)	ϕ at $\bar{I}$ (n/cm^2-sec)	ϕ at I=10^{12} p/sec (n/cm^2-sec)
31–0 R	Z = 56.64	1	2.01 E+6	2.20 E+4	1.10 E+5
31–1 R	Z = 57.92	1	3.00 E+6	3.28 E+4	1.64 E+5
31–2 R	Z = 58.92	1	3.93 E+6	4.30 E+4	2.15 E+5
31–3 R	Z = 59.92	1	6.61 E+6	7.23 E+4	3.62 E+5
31–4 R	Z = 60.92	1	1.30 E+7	1.42 E+5	7.10 E+5
31–5 R	Z = 61.92	1	2.92 E+7	3.19 E+5	1.60 E+6
32–0 R	Z = 62.92	1	9.34 E+7	1.02 E+6	5.10 E+6
32–1 R	Z = 63.92	1	1.90 E+8	2.08 E+6	1.04 E+7
32–2 R	Z = 65.42	1	2.38 E+8	2.63 E+6	1.32 E+7
32–3 R	Z = 66.40	1	1.69 E+8	1.85 E+6	9.25 E+6
32–4 R	Z = 67.30	1	1.19 E+8	1.30 E+6	6.50 E+6
32–5 R	Z = 68.20	1	5.95 E+7	6.52 E+5	3.26 E+6
33–0 R	Z = 69.20	1	6.78 E+7	7.43 E+5	3.72 E+6
33–1 R	Z = 70.48	1	9.14 E+7	1.00 E+6	5.00 E+6
33–2 R	Z = 71.48	1	8.92 E+7	9.81 E+5	4.01 E+6
33–3 R	Z = 72.48	1	6.54 E+7	7.16 E+5	3.58 E+6
33–4 R	Z = 73.48	1	4.75 E+7	5.20 E+5	2.60 E+6
33–5 R	Z = 74.48	1	3.88 E+7	4.25 E+5	2.13 E+6
34–0 R	Z = 75.48	1	4.09 E+7	4.48 E+5	2.24 E+6
35–0 R	Z = 81.76	2	2.19 E+7	2.40 E+5	1.20 E+6
36–0 R	Z = 88.08	2	1.64 E+7	1.83 E+5	9.15 E+5
37–0 R	Z = 94.32	2	1.02 E+7	1.13 E+5	5.65 E+5

Run II
TLD
Roof buckets
22-mg samples

26.4 GeV/c
Installations 1 and 2
263-min. exposure
1.93 E+11 p/sec

Location	Coordinates	Indicated dose (rads/hour)
27–R	Z = 31.5	2.6 E+0
28–R	Z = 37.8	1.45 E+1
29–R	Z = 44.1	7.7 E+0
30–R	Z = 50.4	3.84 E+1
31–0R	Z = 56.6	4.0 E+1
31–1R	Z = 57.9	5.7 E+1
31–2R	Z = 58.9	7.5 E+1
31–3R	Z = 59.9	5.3 E+0
31–4R	Z = 60.9	1.76 E+2
31–5R	Z = 61.9	3.63 E+2
32–0R	Z = 62.9	1.12 E+3
32–1R	Z = 63.9	1.26 E+3
32–2R	Z = 65.4	1.86 E+3
32–3R	Z = 66.4	1.50 E+3
32–4R	Z = 67.3	1.15 E+3
32–5R	Z = 68.2	1.80 E+2
33–0R	Z = 69.2	8.23 E+2
33–1R	Z = 70.5	1.48 E+2
33–2R	Z = 71.5	9.53 E+2
33–3R	Z = 72.5	7.15 E+2
33–4R	Z = 73.5	5.02 E+2
33–5R	Z = 74.5	3.61 E+2
34–R	Z = 75.5	4.34 E+2
35–R	Z = 81.8	1.91 E+2
36–R	Z = 88.1	1.53 E+2
37–R	Z = 94.3	1.05 E+2
38–R	Z = 100.6	9.1 E+1
39–R	Z = 106.9	8.7 E+1
40–R	Z = 113.2	4.15 E+1
41–R	Z = 119.4	1.72 E+1
42–R	Z = 125.7	5.5 E+0
43–R	Z = 132.	1.87 E+1
44–R	Z = 138.3	2.45 E+1
45–R		9.8 E+0
46–R		5.5 E+0
47–R		4.5 E+0
48–R		5.1 E+0

Run II
Aluminum
Orbit holes
1.93 E+11 p/sec

26.4 GeV/c
Installations 7 and 2
263-min. exposure

Location	Coordinates	Detector size (g)	Net count rate (bkg subtracted) at t_0 (cpm)	Error (%)	ϕ at $\bar{I}$ (n/cm^2-sec)	ϕ at I=10^{12} p/sec (n/cm^2-sec)
24–330	Y = 3.62 Z = 12.7	500	1.60 E+2	5.0	5.3 E+1	2.75 E+2
24–370	Y = 4.11 Z = 12.7	500	1.21 E+2	5.5	2.0 E+1	1.04 E+2
24–430	Y = 4.70 Z = 12.7	1100	2.63 E+1	21.	4.4 E+0	2.28 E+1
24–48/49	Y = 5.25 Z = 12.7	2200	1.56 E+1	25.	1.5 E+0	7.77 E+0
24–60/61	Y = 6.43 Z = 12.7	2200		39.		
26–330	Y = 3.47 Z = 7.224	500	2.08 E+2		6.9 E+1	3.57 E+2
26–370	Y = 3.96 Z = 7.224	1100	1.27 E+2		2.1 E+1	1.09 E+2
26–430	Y = 4.55 Z = 7.224	1100	3.53 E+1	15.8	5.87 E+0	3.04 E+1
26–48/49	Y = 5.10 Z = 7.224	2200	2.8 E+1	14.8	2.67 E+0	1.38 E+1
28–330	Y = 3.63 Z = 19.790	500	5.25 E+2		1.75 E+2	9.07 E+2
28–390	Y = 4.22 Z = 19.790	500	1.55 E+2	5.2	5.15 E+1	2.67 E+2
28–430	Y = 4.71 Z = 19.790	1100	1.05 E+2	5.9	1.74 E+1	9.01 E+1
28–48/49	Y = 5.26 Z = 19.790	2200	5.09 E+1	10.	4.85 E+0	2.51 E+1
28–54/55	Y = 5.84 Z = 19.790	2200	1.09 E+1	43.	1.04 E+0	5.39 E+0
29–330	Y = 3.46 Z = 26.073	500	5.85 E+2		1.95 E+2	1.01 E+3
29–390	Y = 4.05 Z = 26.073	500	1.36 E+2	5.8	4.52 E+1	2.34 E+2
29–430	Y = 4.54 Z = 26.073	1100	1.13 E+2	6.5	1.88 E+1	9.74 E+1
29–48/49	Y = 5.09 Z = 26.073	2200	5.28 E+1	9.8	5.04 E+0	2.61 E+1
29–54/55	Y = 5.68 Z = 26.073	2200	1.70 E+1	27.8	1.62 E+0	8.39 E+0
30–330	Y = 3.49 Z = 32.356	500	9.19 E+2		3.05 E+2	1.58 E+3
30–390	Y = 4.08 Z = 32.356	500	2.28 E+2		7.58 E+1	3.92 E+2
30–430	Y = 4.57 Z = 32.356	1100	1.67 E+2		2.78 E+1	1.44 E+2
30–48/49	Y = 5.12 Z = 32.356	2200	7.4 E+1	8.2	7.08 E+0	3.67 E+1
30–54/55	Y = 5.71 Z = 32.356	2200	2.26 E+1	20.5	2.15 E+0	1.11 E+1
31–330	Y = 3.49 Z = 38.639	100	2.53 E+2	6.9	3.14 E+2	1.63 E+3
31–390	Y = 4.12 Z = 38.639	500	1.81 E+2	7.0	6.0 E+1	3.11 E+2

Location	Coordinates	Detector size (g)	Net count rate (bkg subtracted) at t_0 (cpm)	Error (%)	ϕ at $\bar{I}$ (n/cm^2-sec)	ϕ at I=10^{12} p/sec (n/cm^2-sec)
31–490	Y = 5.20 Z = 38.639	1100	3.46 E+1		5.75 E+0	2.98 E+1
31–450	Y = 4.71 Z = 38.639	500	5.4 E+1	12.1	1.8 E+1	9.3 E+1
31–54/55	Y = 5.75 Z = 38.639	2200	2.07 E+1	20.7	1.98 E+0	1.03 E+1
32–330	Y = 3.67 Z = 44.922	100	1.23 E+4		1.52 E+4	7.88 E+4
32–390	Y = 4.26 Z = 44.922	500	1.28 E+4		4.24 E+3	2.20 E+4
32–450	Y = 4.85 Z = 44.922	500	3.62 E+3		1.20 E+3	6.22 E+3
32–510	Y = 5.44 Z = 44.922	500	9.42 E+2		3.13 E+2	1.62 E+3
32–550	Y = 5.93 Z = 44.922	1100	5.82 E+2		9.68 E+1	5.02 E+2
32–610	Y = 6.35 Z = 44.922	1100	1.68 E+2	5.5	2.8 E+1	1.45 E+2
33–330	Y = 3.42 Z = 51.382	100	2.04 E+4		2.53 E+4	1.31 E+5
33–390	Y = 4.01 Z = 51.382	500	2.03 E+4		6.74 E+3	3.49 E+4
33–450	Y = 4.60 Z = 51.382	500	5.05 E+3		1.68 E+3	8.70 E+3
33–510	Y = 5.19 Z = 51.382	500	1.39 E+3		4.64 E+2	2.40 E+3
33–570	Y = 5.78 Z = 51.382	500	4.04 E+2		1.34 E+2	6.94 E+2
33–610	Y = 6.27 Z = 51.382	1100	2.85 E+3		4.7 E+1	2.44 E+2
34–330	Y = 3.63 Z = 57.372	100	5.15 E+3		6.39 E+3	3.31 E+4
34–390	Y = 4.22 Z = 57.372	500	5.73 E+3		1.91 E+3	9.90 E+3
34–450	Y = 4.81 Z = 57.372	500	1.51 E+3		5.01 E+2	2.60 E+3
34–510	Y = 5.40 Z = 57.372	500	4.30 E+2		1.43 E+2	7.41 E+2
34–550	Y = 5.89 Z = 57.372	1100	3.28 E+2		5.46 E+1	2.83 E+2
34–610	Y = 6.48 Z = 57.372	1100	1.11 E+2	5.4	1.84 E+1	9.53 E+1
35–330	Y = 3.45 Z = 63.655	500	1.33 E+4		4.44 E+3	2.30 E+4
35–390	Y = 4.04 Z = 63.655	500	3.08 E+3		1.02 E+3	5.28 E+3
35–450	Y = 4.63 Z = 63.655	500	7.80 E+2		2.59 E+2	1.34 E+3
35–510	Y = 5.22 Z = 63.655	500	2.26 E+2		7.5 E+1	3.89 E+2
35–550	Y = 5.71 Z = 63.655	1100	1.78 E+2		2.96 E+1	1.53 E+2
35–610	Y = 6.30 Z = 63.655	1100	3.95 E+1	14.5	6.57 E+0	3.40 E+1
36–330	Y = 3.31 Z = 69.938	500	1.30 E+4		4.34 E+3	2.25 E+4
36–390	Y = 3.90 Z = 69.938	500	2.75 E+3		9.16 E+2	4.75 E+3

Location	Coordinates	Detector size (g)	Net count rate (bkg subtracted) at t_0 (cpm)	Error (%)	ϕ at $\bar{I}$ (n/cm^2-sec)	ϕ at I=10^{12} p/sec)n/cm^2-sec)
36–450	Y = 4.49 Z = 69.938	500	6.36 E+2		2.11 E+2	1.09 E+3
36–490	Y = 4.98 Z = 69.938	1100	4.96 E+2		8.25 E+1	4.27 E+2
36–550	Y = 5.57 Z = 69.938	1100	1.46 E+2		2.4 E+1	1.24 E+2
36–610	Y = 6.16 Z = 69.938	1100	4.7 E+1	12.6	7.82 E+0	4.05 E+1
37–330	Y = 3.59 Z = 76.221	500	2.63 E+3		8.75 E+2	4.53 E+3
37–390	Y = 4.18 Z = 76.221	500	5.87 E+2		1.95 E+2	1.01 E+3
37–450	Y = 4.77 Z = 76.221	500	1.55 E+2	5.4	5.15 E+1	2.69 E+2
37–490	Y = 5.26 Z = 76.221	1100	1.06 E+2	6.54	1.76 E+1	9.12 E+1
37–550	Y = 5.85 Z = 76.221	1100	3.66 E+1	14.4	6.1 E+0	3.16 E+1
37–60/61	Y = 6.40 Z = 76.221	2200	2.4 E+1	18.	2.3 E+0	1.19 E+1
38–330	Y = 3.48 Z = 82.504		1.63 E+3		5.41 E+2	2.80 E+3
38–390	Y = 4.07 Z = 82.504	500	3.72 E+2		1.24 E+2	6.42 E+2
38–450	Y = 4.66 Z = 82.504	500	9.03 E+1	8.2	3.0 E+1	1.55 E+2
38–490	Y = 5.15 Z = 82.504	1100	7.2 E+1	7.5	1.2 E+1	6.22 E+1
38–550	Y = 5.74 Z = 82.504	1100	1.32 E+1	27.9	2.19 E+0	1.13 E+1
38–60/61	Y = 6.29 Z = 82.504	2200	1.24 E+1	35.	1.18 E+0	6.11 E+0
39–330	Y = 3.57 Z = 88.787	500	1.11 E+3		3.68 E+2	1.91 E+3
39–390	Y = 4.16 Z = 88.787	500	2.83 E+2		9.4 E+1	4.87 E+2
39–430	Y = 4.65 Z = 88.787	1100	1.79 E+2	5.24	2.98 E+1	1.54 E+2
39–490	Y = 5.24 Z = 88.787	1100	4.95 E+1	11.3	8.23 E+0	4.26 E+1
39–54/55	Y = 5.78 Z = 88.787	2200	2.94 E+1	16.2	2.80 E+0	1.45 E+1
41–330	Y = 3.57 Z = 101.351	500	3.36 E+2		1.12 E+2	5.80 E+2
41–370	Y = 4.06 Z = 101.351	1100	2.16 E+2		3.58 E+1	1.85 E+2
41–430	Y = 4.65 Z = 101.351	1100	6.07 E+1	10.1	1.01 E+1	5.23 E+1
41–490	Y = 5.24 Z = 101.351	1100	1.21 E+1	29.5	2.02 E+0	1.05 E+1
43–330	Y = 3.40 Z = 113.919	500	1.99 E+3		6.62 E+2	3.43 E+3
43–370	Y = 3.89 Z = 113.919	1100	1.23 E+3		2.05 E+2	1.06 E+3
43–430	Y = 4.48 Z = 113.919	1100	3.38 E+2		5.6 E+1	2.90 E+2
43–490	Y = 5.07 Z = 113.919	1100	8.52 E+1	7.98	1.42 E+1	7.36 E+1

Run II
Carbon
Orbit holes
1.99 E+11 p/sec

26.4 GeV/c
Installation 1
63-min. exposure

Location	Coordinates	Detector size (in.)	Net count rate (bkg subtracted) at t_0 (cpm)	Error (%)	ϕ at $\bar{I}$ (n/cm^2-sec)	ϕ at I=10^{12} p/sec (n/cm^2-sec)
31–33	Y = 3.53 Z = 56.64	4	7.91 E+4		8.62 E+2	4.33 E+3
31–45	Y = 4.65 Z = 56.64	5	5.92 E+3		6.45 E+1	3.21 E+2
31–57	Y = 5.83 Z = 56.64	5	3.86 E+2		4.2 E+0	2.11 E+1
32–33	Y = 3.67 Z = 62.92	4	3.97 E+6		4.33 E+4	2.18 E+5
32–45	Y = 4.85 Z = 62.92	4	3.02 E+5		3.288 E+3	1.65 E+4
32–57	Y = 5.97 Z = 62.92	5	2.71 E+4	7.7	2.95 E+2	1.48 E+3
33–33	Y = 3.42 Z = 69.20	4	6.92 E+6		7.54 E+4	3.79 E+5
33–45	Y = 4.60 Z = 69.20	4	4.21 E+5		4.591 E+3	2.31 E+4
33–57	Y = 5.78 Z = 69.20	4	2.35 E+4	8.8	2.57 E+2	1.29 E+3
34–33	Y = 3.63 Z = 75.48	4	1.78 E+6		1.95 E+4	9.80 E+4
34–45	Y = 4.81 Z = 75.48	4	1.19 E+5		1.292 E+3	6.49 E+3
34–57	Y = 5.99	4	1.01 E+4	10.4	1.10 E+2	5.53 E+2

Run II
Carbon
Ring top
5-in. detector

26.4 GeV/c
Installation 1
63-min. exposure
1.99 E+11 p/sec

Location	Coordinates	Net count rate (bkg subtracted) at t_0 (cpm)	Error (%)	ϕ at $\bar{I}$ (n/cm^2-sec)	ϕ at I=10^{12} p/sec (n/cm^2-sec)
31–T	Y = 6.40 Z = 56.64	1.2 E+2	7.4	1.3 E+0	6.5 E+0
32–T	Y = 6.42 Z = 62.92	8.145 E+3		8.87 E+1	4.46 E+2
33–T	Y = 6.39 Z = 69.20	8.545 E+3		9.31 E+1	4.68 E+2
34–T	Y = 6.29 Z = 75.48	5.574 E+3		6.07 E+1	3.05 E+2

Run II
Aluminum
Ring top
3300-g detector

26.4 GeV/c
Installations 1 and 2
263-min. exposure
1.93 E+11 p/sec

Location	Coordinates	Net count rate (bkg subtracted) at t_0 (cpm)	ϕ at $\bar{I}$ (n/cm^2-sec)	ϕ at I=10^{12} p/sec (n/cm^2-sec)
32-top	Y = 6.42 Z = 62.9	3.48 E+2	2.8 E+1	1.45 E+2
32-top	Y = 6.42 Z = 62.9	3.86 E+2	3.1 E+1	1.61 E+2

Run II
Aluminum
Vent shaft
500-g detector

26.4 GeV/c
Installations 1 and 2
263-min. exposure
1.93 E+11 p/sec

Location	Coordinates	Net count rate (bkg subtracted) at t_0 (cpm)	ϕ at $\bar{I}$ (n/cm^2-sec)	ϕ at I=10^{12} p/sec (n/cm^2-sec)
33-vent	X = 103.2 Z = 70.6	5.53 E+4	1.84 E+4	9.53 E+4

Run III Data

Run III exposure summary.*

Exposure number	Beam energy (GeV/c)	Average beam current (p/sec)	Exposure duration (min)	Exposure time
1	26.4	1.83 E+11	82	0038 – 0200
2	26.4	1.82 E+11	80	0214 – 0334
3	26.4	1.81 E+11	80	0344 – 0504
4	26.4	1.64 E+11	80	0511 – 0631
5	26.4	1.67 E+11	121	0637 – 0838
entire run	26.4	1.61 E+11	480	0038 – 0838

* Target location: straight section 32;
clipper location: straight section 79.

Run III. Aluminum foils on vacuum vessel.*

Standard position	Foil activity (pCi/g)	Standard position	Foil activity (pCi/g)	Standard position	Foil activity (pCi/g)	Standard position	Foil activity (pCi/g)
1	6.75 E+3	26	1.54 E+4	51	1.77 E+4	76	7.31 E+3
2	9.27 E+4	27	1.56 E+4	52	9.31 E+4	77	6.50 E+3
3	6.91 E+4	28	1.77 E+5	53	7.62 E+4	78	7.46 E+3
4	3.05 E+4	29	7.94 E+4	54	9.44 E+3	79	3.71 E+7
5	1.17 E+5	30	8.74 E+4	55	1.42 E+4	80	9.96 E+5
6	1.36 E+4	31	4.16 E+4	56	1.65 E+4	81	6.47 E+5
7	1.39 E+4	32	5.98 E+7	57	4.17 E+3	82	7.11 E+5
8	1.10 E+5	33	8.96 E+6	58	2.07 E+4	83	5.30 E+5
9	1.82 E+5	34	3.18 E+6	59	7.07 E+3	84	3.96 E+5
10	1.07 E+6	35	1.10 E+6	60	3.82 E+5	85	1.48 E+5
11	1.46 E+5	36	6.87 E+5	61	2.80 E+5	86	7.96 E+4
12	4.02 E+5	37	2.57 E+5	62	7.05 E+4	87	5.35 E+5
13	8.28 E+4	38	4.64 E+4	63	2.55 E+4	88	1.77 E+5
14	1.71 E+5	39	1.52 E+5	64	1.36 E+5	89	4.51 E+5
15	1.21 E+5	40	3.76 E+4	65	2.49 E+5	90	1.65 E+5
16	5.74 E+4	41	3.65 E+4	66	5.86 E+4	91	2.43 E+5
17	9.65 E+4	42	1.22 E+5	67	5.86 E+4	92	2.66 E+5
18	9.53 E+4	43	1.63 E+5	68	5.59 E+4	93	3.89 E+4
19	5.69 E+5	44	1.70 E+5	69	3.08 E+5	94	1.69 E+5
20	4.92 E+4	45	3.41 E+4	70	3.17 E+4	95	3.74 E+4
21	7.10 E+4	46	9.80 E+3	71	4.14 E+5	96	1.79 E+4
22	8.96 E+4	47	1.65 E+4	72	2.76 E+4	97	5.03 E+4
23	3.10 E+4	48	1.25 E+4	73	2.17 E+4	98	2.40 E+4
24	1.21 E+4	49	1.46 E+5	74	5.33 E+4	99	9.05 E+4
25	3.10 E+4	50	2.61 E+4	75	2.35 E+4	100	8.55 E+4

*One-hundred foils listed here.

Run III
Aluminum
Roof buckets
100-g samples

26.4 GeV/c
All installations
480-min. exposure
1.61 E+11

Location	Coordinates	Net count rate (bkg. subtracted) at t_0 (cpm/g)	ϕ at $\bar{I}$ (n/cm^2-sec)	ϕ at I = 10^{12} p/sec (n/cm^2-sec)
31–R	Z = 56.64	2.11 E+4	1.55 E+4	9.63 E+4
32–R	Z = 62.92	8.19 E+4	6.02 E+4	3.74 E+5
33–R	Z = 69.20	4.47 E+5	3.29 E+5	2.04 E+6
34–R	Z = 75.48	2.19 E+5	1.61 E+5	1.00 E+6
35–R	Z = 81.76	1.00 E+5	7.37 E+4	4.58 E+5
36–R	Z = 88.08	6.74 E+4	4.96 E+4	3.08 E+5
78–R	Z = 56.6	5.85 E+3	4.30 E+3	2.67 E+4
79–R	Z = 62.9	4.29 E+5	3.15 E+5	1.96 E+6
80–R	Z = 69.2	7.58 E+4	5.57 E+4	3.46 E+5

Run III
Aluminum
Orbit holes
500-g samples

26.4 GeV/c
All installations
480-min. exposure
1.61 E + 11 p/sec

Location	Coordinates	Net count rate (bkg. subtracted) at t_0 (cpm/g)	ϕ at I (n/cm^2-sec)	ϕ at I = 10^{12} p/sec (n/cm^2-sec)
32–390	Y = 4.26, Z = 62.92	2.04 E+4	4.02 E+3	2.50 E+4
33–390	Y = 4.01, Z = 69.20	3.14 E+4	6.19 E+3	3.84 E+4
33–510	Y = 5.19, Z = 69.20	2.25 E+3	4.44 E+2	2.76 E+3
34–390	Y = 4.22, Z = 75.48	7.87 E+3	1.55 E+3	9.63 E+3
34–510	Y = 5.40, Z = 75.48	6.19 E+2	1.22 E+2	7.58 E+2
35–390	Y = 4.04, Z = 81.76	5.16 E+3	1.02 E+3	6.34 E+3
36–390	Y = 3.90, Z = 88.08	4.33 E+3	8.54 E+2	5.30 E+3

Run III
Aluminum
Radial holes

26.4 GeV/c
All installations
480-min exposure

1.61 E+11 p/sec

Location	Coordinates	Detector size (g)	Net count rate (bkg subtracted) at t_0 (cpm)	Error (%)	ϕ at $\bar{T}$ (n/cm^2-sec)	ϕ at I=10^{12} p/sec (n/cm^2-sec)
32–935	X = 93.5 Z = 62.92	2200	1.32 E+3		7.46 E+2	4.63 E+3
32–1040	X = 104.0 Z = 62.92	500	3.28 E+4		6.47 E+3	4.02 E+4
32–1050	X = 105.0 Z = 62.92	500	2.11 E+3		4.17 E+2	2.59 E+3
32–1060	X = 106.0 Z = 62.92	2200	7.31 E+2		4.14 E+1	2.57 E+2
32–1075	X = 107.5 Z = 62.92	6600	3.55 E+1	12.3	1.14 E+0	7.1 E+0
33–1040	X = 104.0 Z = 69.20	500	2.05 E+4		4.04 E+3	2.51 E+4
33–1050	X = 105.0 Z = 69.20	500	2.19 E+3		4.31 E+2	2.68 E+3
33–1060	X = 106.0 Z = 69.20	2200	9.75 E+2		5.52 E+1	3.43 E+2
33–1075	X = 107.5 Z = 69.20	6600	7.39 E+1	5.4	2.37 E+0	1.47 E+1
33–1090	X = 109.0 Z = 69.20	6600				
34–935	X = 93.5 Z = 73.48	2200	1.68 E+3		9.49 E+1	5.10 E+2
34–1060	X = 106.0 Z = 73.48	2200	4.83 E+2		2.73 E+1	1.70 E+2
34–1075	X = 107.5 Z = 73.48	6600	2.45 E+1	12.6	7.8 E-1	4.8 E+0
35–1060	X = 106.0 Z = 81.76	2200	3.38 E+2		1.91 E+1	1.19 E+2
35–1075	X = 107.5 Z = 81.76	6600	1.56 E+1	11	5.0 E-1	3.1 E+0
36–1060	X = 106.0 Z = 88.08	2200	2.50 E+2		1.42 E+1	8.72 E+1
36–1075	X = 107.5 Z = 88.08	6600	3.12 E+1	8.1	1.0 E+0	6.2 E+0

Run III
Carbon
Radial holes

26.4 GeV/c
Installation 1
82-min. exposure

1.83 E+11 p/sec

Location	Coordinates	Detector size (in.)	Net count rate (bkg subtracted) at t_0 (cpm)	ϕ at $\bar{I}$ (n/cm^2-sec)	ϕ at I=10^{12} p/sec (n/cm^2-sec)
32–104	X = 104.0 Z = 62.92	4	2.16 E+6	2.22 E+4	1.21 E+5
32–105	X = 105.0 Z = 62.92	5	1.33 E+5	1.37 E+3	7.47 E+3
32–106	X = 106.0 Z = 62.92	5	1.26 E+4	1.30 E+2	7.09 E+2
32–107.5	X = 107.5 Z = 62.92	8	3.35 E+2	3.43 E+0	1.87 E+1
33–51	Y = 5.30 Z = 69.20	4	1.32 E+5	1.35 E+3	7.36 E+3
33–T	Y = 6.39 Z = 69.20	5	1.05 E+4	1.07 E+2	5.83 E+2
33–104	X = 104.0 Z = 69.20	4	1.40 E+6	1.43 E+4	7.79 E+4
33–105	X = 105.0 Z = 69.20	5	1;51 E+5	1.54 E+3	8.39 E+3
33–106	X = 106.0 Z = 69.20	5	2.07 E+4	2.12 E+2	1.16 E+3
33–107.5	X = 107.5 Z = 69.20	8	4.97 E+2	5.10 E+0	2.78 E+1

Run III
Carbon
Radial holes

26.4 GeV/c
Installation 2
80-min. exposure

1.82 E+11 p/sec

Location	Coordinates	Detector size (in.)	Net count rate (bkg subtracted) at t_0 (cpm)	ϕ at $\bar{I}$ (n/cm^2-sec)	ϕ at I=10^{12} p/sec (n/cm^2-sec)
33–104	X = 104.0 Z = 69.20	4	1.38 E+6	1.42 E+4	7.80 E+4
34–106	X = 106.0 Z = 75.48	5	8.93 E+3	9.2 E+1	5.05 E+2
34–1075	X = 107.5 Z = 75.48	8	2.02 E+2	2.08 E+0	1.14 E+1
35–106	X = 106.0 Z = 81.76	5	8.41 E+3	8.66 E+1	4.75 E+2
35–107.5	X = 107.5 Z = 81.76	8	2.23 E+2	2.29 E+0	1.26 E+1

Run III 26.4 GeV/c
Carbon Installation 3
Radial holes 80-min. exposure
1.81 E+11 p/sec

Location	Coordinates	Detector size (in.)	Net count rate (bkg subtracted) at t_0 (cpm)	Error (%)	ϕ at $\bar{I}$ (n/cm^2-sec)	ϕ at I=10^{12} p/sec (n/cm^2-sec)
33–104	X = 104.0 Z = 69.20	4	1.22 E+6		1.25 E+4	6.90 E+4
33–109	X = 109.0 Z = 69.20	8	1.30 E+2	7.3	1.56 E+0	8.62 E+0
36–106	X = 106.0 Z = 88.08	5	5.45 E+3		5.61 E+1	3.10 E+2
36–107.5	X = 107.5 Z = 88.08	5	2.48 E+2		2.55 E+0	1.41 E+1

Run III 26.4 GeV/c
Carbon Installation 4
Radial holes 80-min. exposure
4-in. detector 1.64 E+11 p/sec

Location	Coordinates	Net count rate (bkg subtracted) at t_0 (cpm)	ϕ at $\bar{I}$ (n/cm^2-sec)	ϕ at I=10^{12} p/sec (n/cm^2-sec)
33–104	X = 104.0 Z = 69.20	1.16 E+6	1.14 E+4	6.95 E+4

Run III — 26.4 GeV/c
Aluminum — All installations
Ring top — 480-min. exposure
3300=g detector — 1.61 E+11 p/sec

Location	Coordinates	Net count rate (bkg subtracted) at t_0 (cpm)	ϕ at $\bar{I}$ (n/cm^2-sec)	ϕ at I=10^{12} p/sec (n/cm^2-sec)
32/0	Y = 6.42 Z = 62.92	5.82 E+2	2.55 E+1	1.58 E+2
33/0	Y = 6.39 Z = 69.20	6.10 E+2	2.67 E+1	1.66 E+2

Run III — 26.4 GeV/c
Aluminum — All installations
Vent shaft — 480-min. exposure
500-g detector — 1.61 E+11 p/sec

Location	Coordinates	Net count rate (bkg subtracted) at t_0 (cpm)	ϕ at $\bar{I}$ (n/cm^2-sec)	ϕ at I=10^{12} p/sec (n/cm^2-sec)
33–V	Y = 103.2 Z = 70.6	8.92 E+4	1.76 E+4	1.09 E+5

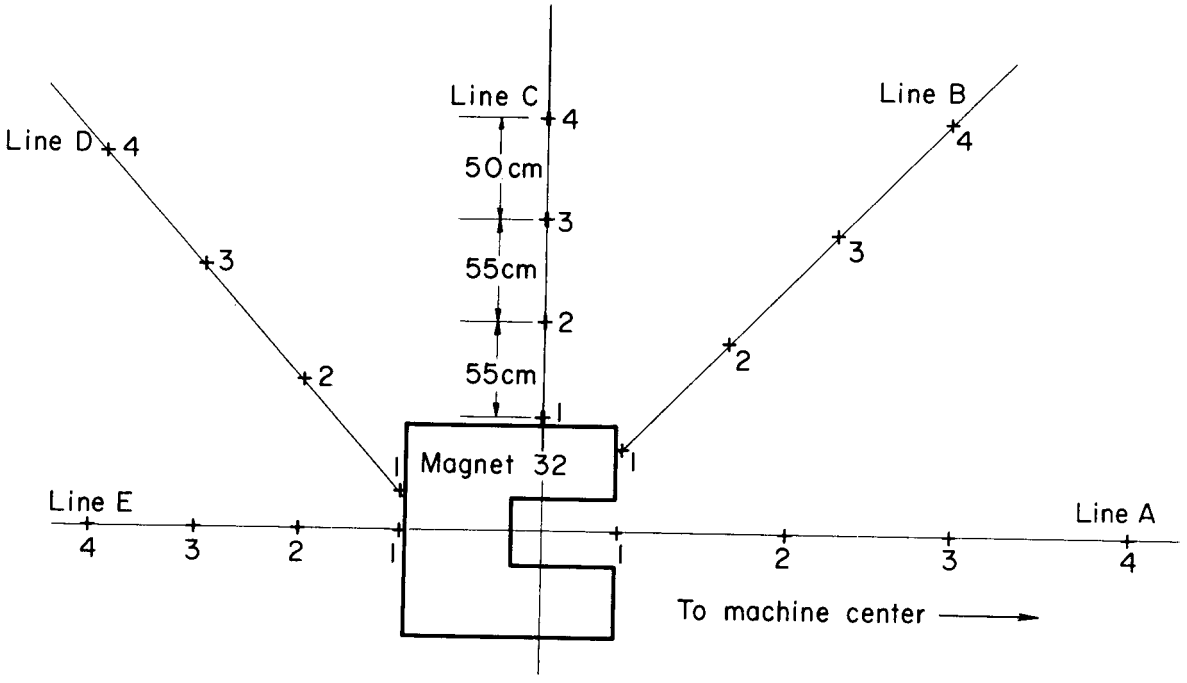

XBL693-2219

Vertical elevation to scale showing sample locations for Run III, Magnet-32 profiles looking downstream.

Run III
Sulfur
Magnet-32 profile
4-g detector

26.4 GeV/c
All installations
480-min. exposure
1.61 E+11 p/sec

Location	Coordinates	ϕ at $\bar{I}$ (n/cm^2-sec)	ϕ at I=10^{12} p/sec (n/cm^2-sec)
I/A/ 1	Z = 62.92	7.62 E+6	4.73 E+7
2	Z = 62.92	2.44 E+6	1.52 E+7
3	Z = 62.92	1.66 E+6	1.03 E+7
4	Z = 62.92	1.06 E+6	6.58 E+6
I/B/ 1	Z = 62.92	5.53 E+6	3.43 E+7
2	Z = 62.92	2.37 E+6	1.47 E+7
3	Z = 62.92	1.42 E+6	8.82 E+6
4	Z = 62.92	9.03 E+5	5.61 E+6
I/C/ 1	Z = 62.92	5.31 E+6	3.30 E+7
2	Z = 62.92	2.46 E+6	1.53 E+7
3	Z = 62.92	1.52 E+6	9.44 E+6
4	Z = 62.92	1.40 E+6	8.70 E+6
I/D/ 1	Z = 62.92	2.89 E+6	1.80 E+7
2	Z = 62.92	1.41 E+6	8.76 E+6
3	Z = 62.92	1.14 E+6	7.08 E+6
4	Z = 62.92	7.77 E+5	4.83 E+6
I/E/ 1	Z = 62.92	3.40 E+6	2.11 E+7
2	Z = 62.92	2.42 E+6	1.50 E+7
3	Z = 62.92	1.36 E+6	8.45 E+6
4	Z = 62.92	9.88 E+5	6.14 E+6
II/A/ 1	Z = 64.02	1.88 E+7	1.17 E+8
2	Z = 64.02	3.81 E+6	2.37 E+7
3	Z = 64.02	1.66 E+6	1.03 E+7
4	Z = 64.02	1.47 E+6	9.13 E+6
II/B/ 1	Z = 64.02	9.97 E+6	6.19 E+7
2	Z = 64.02	2.93 E+6	1.82 E+7
3	Z = 64.02	1.73 E+6	1.07 E+7
4	Z = 64.02	1.11 E+6	6.89 E+6
II/C/ 1	Z = 64.02	7.22 E+6	4.48 E+7
2	Z = 64.02	4.10 E+6	2.55 E+7
3	Z = 64.02	2.29 E+6	1.42 E+7
4	Z = 64.02	1.39 E+6	8.63 E+6
II/D/ 1	Z = 64.02	5.17 E+6	3.21 E+7
2	Z = 64.02	2.11 E+6	1.31 E+7
3	Z = 64.02	9.95 E+5	6.18 E+6
4	Z = 64.02	9.10 E+5	5.65 E+6
II/E/ 1	Z = 64.02	6.25 E+6	3.88 E+7
2	Z = 64.02	2.53 E+6	1.57 E+7
3	Z = 64.02	1.79 E+6	1.11 E+7
4	Z = 64.02	1.21 E+6	7.52 E+6

Location	Coordinates	ϕ at $\overline{I}$ (n/cm^2-sec)	ϕ at I=10^{12} p/sec (n/cm^2-sec)
III/A/1	Z = 65.52	1.05 E+7	6.52 E+7
2	Z = 65.52	4.84 E+6	3.01 E+7
3	Z = 65.52	2.20 E+6	1.37 E+7
4	Z = 65.52	1.45 E+6	9.01 E+6
III/B/1	Z = 65.52	4.77 E+6	2.97 E+7
2	Z = 65.52	2.67 E+6	1.66 E+7
3	Z = 65.52	1.46 E+6	9.07 E+6
4	Z = 65.52	1.24 E+6	7.70 E+6
III/C/1	Z = 65.52	1.30 E+6	8.07 E+6
2	Z = 65.52	1.05 E+6	6.52 E+6
3	Z = 65.52	1.36 E+6	8.45 E+6
4	Z = 65.52	1.12 E+6	6.96 E+6
III/D/1	Z = 65.52	9.06 E+5	5.63 E+6
2	Z = 65.52	8.04 E+5	4.99 E+6
3	Z = 65.52	7.14 E+5	4.43 E+6
4	Z = 65.52	6.13 E+5	3.81 E+6
III/E/1	Z = 65.52	1.40 E+6	8.70 E+6
2	Z = 65.52	9.78 E+5	6.07 E+6
3	Z = 65.52	8.02 E+5	4.98 E+6
4	Z = 65.52	8.78 E+5	5.45 E+6
IV/A/1	Z = 67.52	6.33 E+6	3.93 E+7
2	Z = 67.52	2.22 E+6	1.38 E+7
3	Z = 67.52	1.79 E+6	1.11 E+7
4	Z = 67.52	1.43 E+6	8.88 E+6
IV/B/1	Z = 67.52	1.34 E+6	8.32 E+6
2	Z = 67.52	1.38 E+6	8.57 E+6
3	Z = 67.52	1.02 E+6	6.33 E+6
4	Z = 67.52	7.86 E+5	4.88 E+6
IV/C/1	Z = 67.52	5.28 E+5	3.28 E+6
2	Z = 67.52	5.51 E+5	3.42 E+6
3	Z = 67.52	5.42 E+5	3.37 E+6
4	Z = 67.52	6.80 E+5	4.22 E+6
IV/D/1	Z = 67.52	3.96 E+5	2.46 E+6
2	Z = 67.52	3.56 E+5	2.21 E+6
3	Z = 67.52	4.52 E+5	2.81 E+6
4	Z = 67.52	4.38 E+5	2.72 E+6
IV/E/1	Z = 67.52	6.21 E+5	3.86 E+6
2	Z = 67.52	4.68 E+5	2.91 E+6
3	Z = 67.52	4.27 E+5	2.65 E+6
4	Z = 67.52		
V/A/ 1	Z = 69.52	3.88 E+6	2.41 E+7
2	Z = 69.52	1.98 E+6	1.23 E+7
3	Z = 69.52	1.30 E+6	8.07 E+6
4	Z = 69.52	1.06 E+6	6.58 E+6

Location	Coordinates	ϕ at $\bar{I}$ (n/cm^2-sec)	ϕ at I=10^{12} p/sec (n/cm^2-sec)
V/B/ 1	Z = 69.52	2.24 E+6	1.39 E+7
2	Z = 69.52	1.21 E+6	7.52 E+6
3	Z = 69.52	7.66 E+5	4.76 E+6
4	Z = 69.52	8.53 E+5	5.30 E+6
V/C/ 1	Z = 69.52	1.79 E+6	1.11 E+7
2	Z = 69.52	6.61 E+5	4.11 E+6
3	Z = 69.52	1.13 E+6	7.02 E+6
4	Z = 69.52	6.31 E+5	3.92 E+6
V/D/ 1	Z = 69.52	1.06 E+6	6.58 E+6
2	Z = 69.52	8.15 E+5	5.06 E+6
3	Z = 69.52	4.48 E+5	2.78 E+6
4	Z = 69.52	3.18 E+5	1.98 E+6
V/E/ 1	Z = 69.52	1.73 E+6	1.07 E+7
2	Z = 69.52	8.24 E+5	5.12 E+6
3	Z = 69.52	4.72 E+5	2.93 E+6
4	Z = 69.52	5.38 E+5	3.34 E+6

Run III
Aluminum
Magnet 32 profile
16.9-g detector

26.4 GeV/c
All installations
480-min. exposure
1.61 E+11 p/sec

Location	Coordinates	Net count rate (bkg subtracted) at t_0 (cpm)	ϕ at $\bar{l}$ (n/cm^2-sec)	ϕ at l=10^{12} p/sec (n/cm^2-sec)
I/A/1	Z = 62.92			
2	Z = 62.92			
3	Z = 62.92			
4	Z = 62.92	9.34 E+4	3.59 E+5	2.23 E+6
I/B/1	Z = 62.92			
2	Z = 62.92			
3	Z = 62.92			
4	Z = 62.92			
I/C/1	Z = 62.92			
2	Z = 62.92			
3	Z = 62.92			
4	Z = 62.92			
I/D/1	Z = 62.92			
2	Z = 62.92			
3	Z = 62.92			
4	Z = 62.92			
I/E/1	Z = 62.92			
2	Z = 62.92			
3	Z = 62.92			
4	Z = 62.92	1.00 E+5	3.85 E+5	2.39 E+6
I/A/1	Z = 64.02			
2	Z = 64.02			
3	Z = 64.02			
4	Z = 64.02	1.23 E+5	4.74 E+5	2.94 E+6
I/B/1	Z = 64.02			
2	Z = 64.02			
3	Z = 64.02			
4	Z = 64.02			
I/C/1	Z = 64.02			
2	Z = 64.02			
3	Z = 64.02			
4	Z = 64.02			
II/D/1	Z = 64.02			
2	Z = 64.02			
3	Z = 64.02			
4	Z = 64.02			
II/E/1	Z = 64.02			
2	Z = 64.02			
3	Z = 64.02			
4	Z = 64.02	1.18 E+5	4.55 E+5	2.82 E+6

Location	Coordinates	Net count rate (bkg subtracted) at t_0 (cpm)	ϕ at $\bar{I}$ (n/cm^2-sec)	ϕ at $I=10^{12}$ p/sec (n/cm^2-sec)
III/A/ 1	Z = 65.52			
2	Z = 65.52			
3	Z = 65.52			
4	Z = 65.52	1.58 E+5	6.06 E+5	3.76 E+6
III/B/ 1	Z = 65.52			
2	Z = 65.52			
3	Z = 65.52			
4	Z = 65.52			
III/C/ 1	Z = 65.52			
2	Z = 65.52			
3	Z = 65.52			
4	Z = 65.52			
III/D/ 1	Z - 65.52			
2	Z = 65.52			
3	Z = 65.52			
4	Z = 65.52			
III/E/ 1	Z = 65.52			
2	Z = 65.52			
3	Z = 65.52			
4	Z = 65.52	9.75 E+4	3.75 E+5	2.33 E+6
IV/A/ 1	Z = 67.52			
2	Z = 67.52			
3	Z = 67.52			
4	Z = 67.52	1.54 E+5	5.92 E+5	3.67 E+6
IV/B/ 1	Z = 67.52			
2	Z = 67.52			
3	Z = 67.52			
4	Z = 67.52			
IV/C/ 1	Z = 67.52			
2	Z = 67.52			
3	Z = 67.52			
4	Z = 67.52			
IV/D/ 1	Z = 67.52			
2	Z = 67.52			
3	Z = 67.52			
4	Z - 67.52			
IV/E/ 1	Z = 67.52			
2	Z = 67.52			
3	Z = 67.52			
4	Z = 67.52	5.45 E+4	2.09 E+5	1.30 E+6
V/A/ 1	Z = 69.52			
2	Z = 69.52			
3	Z = 69.52			
4	Z = 69.52	1.36 E+5	5.23 E+5	3.23 E+6

Location	Coordinates	Net count rate (bkg subtracted) at t_0 (cpm)	ϕ at $\bar{I}$ (n/cm^2-sec)	ϕ at I=10^{12} p/sec (n/cm^2-sec)
V/B/ 1	Z = 69.52			
2	Z = 69.52			
3	Z = 69.52			
4	Z = 69.52			
V/C/ 1	Z = 69.52			
2	Z = 69.52			
3	Z = 69.52			
4	Z = 69.52			
V/D/ 1	Z = 69.52			
2	Z = 69.52			
3	Z = 69.52			
4	Z = 69.52			
V/E/ 1	Z = 69.52			
2	Z = 69.52			
3	Z = 69.52			
4	Z = 69.52	4.78 E+4	!.84 E+5	!.14 E+6

Run III
TLD
Magnet 32 profile
22-mg detector

26.4 GeV/c
All installations
480-min. exposure
161 E+11 p/sec

Location	Coordinates	Dose (rads)
I/A/ 1	Z = 62.92	----
2	Z = 62.92	1.38 E+3
3	Z = 62.92	1.15 E+3
4	Z = 62.92	7.16 E+2
I/B/ 1	Z = 62.92	1.52 E+3
2	Z = 62.92	9.20 E+2
3	Z = 62.92	7.13 E+2
4	Z = 62.92	---
I/C/ 1	Z = 62.92	1.64 E+3
2	Z = 62.92	1.07 E+3
3	Z = 62.92	7.65 E+2
4	Z = 62.92	6.43 E+2
I/D/ 1	Z = 62.92	1.16 E+3
2	Z = 62.92	3.80 E+2
3	Z = 62.92	4.12 E+2
4	Z = 62.92	4.02 E+2
I/E/ 1	Z = 62.92	----
2	Z = 62.92	1.01 E+3
3	Z = 62.92	6.17 E+2
4	Z = 62.92	5.53 E+2
II/A/ 1	Z = 64.02	3.03 E+3
2	Z = 64.02	2.04 E+3
3	Z = 64.02	9.44 E+2
4	Z = 64.02	1.02 E+3
II/B/ 1	Z = 64.02	2.76 E+3
2	Z = 64.02	1.75 E+3
3	Z = 64.02	9.76 E+2
4	Z = 64.02	4.76 E+2
II/C/ 1	Z = 64.02	2.78 E+3
2	Z = 64.02	2.66 E+3
3	Z = 64.02	1.88 E+3
4	Z = 64.02	1.21 E+3
II/D/ 1	Z = 64.02	2.59 E+3
2	Z = 64.02	1.20 E+3
3	Z = 64.02	5.78 E+2
4	Z = 64.02	5.36 E+2
II/E/ 1	Z = 64.02	3.17 E+3
2	Z = 64.02	2.63 E+3
3	Z = 64.02	1.12 E+3
4	Z = 64.02	9.22 E+2

Location	Coordinates	Dose (rads)
III/A/1	Z = 65.52	3.85 E+3
2	Z = 65.52	3.32 E+3
3	Z = 65.52	2.39 E+3
4	Z = 65.52	----
III/B/1	Z = 65.52	3.49 E+3
2	Z = 65.52	2.27 E+3
3	Z = 65.52	1.36 E+3
4	Z = 65.52	7.48 E+2
III/C/1	Z = 65.52	6.40 E+2
2	Z = 65.52	2.02 E+3
3	Z = 65.52	1.61 E+3
4	Z = 65.52	1.13 E+3
III/D/1	Z = 65.52	4.35 E+2
2	Z = 65.52	9.35 E+2
3	Z = 65.52	7.85 E+2
4	Z = 65.52	4.80 E+2
III/E/1	Z = 65.52	5.13 E+2
2	Z = 65.52	1.26 E+3
3	Z = 65.52	9.73 E+2
4	Z = 65.52	7.57 E+2
IV/A/1	Z = 67.52	3.59 E+3
2	Z = 67.52	3.06 E+3
3	Z = 67.52	2.43 E+3
4	Z = 67.52	1.76 E+3
IV/B/1	Z = 67.52	8.00 E+2
2	Z = 67.52	----
3	Z = 67.52	1.11 E+3
4	Z = 67.52	8.43 E+2
IV/C/1	Z = 67.52	1.84 E+2
2	Z = 67.52	2.90 E+2
3	Z = 67.52	4.94 E+2
4	Z = 67.52	----
IV/D/1	Z = 67.52	1.40 E+2
2	Z = 67.52	2.07 E+2
3	Z = 67.52	2.71 E+2
4	Z = 67.52	3.91 E+2
IV/E/1	Z = 67.52	1.71 E+2
2	Z = 67.52	1.79 E+2
3	Z = 67.52	2.31 E+2
4	Z = 67.52	----

Location	Coordinates	Dose (rads)
V/A/ 1	Z = 69.52	3.35 E+2
2	Z = 69.52	2.69 E+3
3	Z = 69.52	1.90 E+3
4	Z = 69.52	1.32 E+3
V/B/ 1	Z = 69.52	----
2	Z = 69.52	1.43 E+3
3	Z = 69.52	8.13 E+2
4	Z = 69.52	6.50 E+2
V/C/ 1	Z = 69.52	----
2	Z = 69.52	4.64 E+2
3	Z = 69.52	----
4	Z = 69.52	4.99 E+2
V/D/ 1	Z = 69.52	9.76 E+2
2	Z = 69.52	3.50 E+2
3	Z = 69.52	2.11 E+2
4	Z = 69.52	1.47 E+2
V/E/ 1	Z = 69.52	2.02 E+3
2	Z = 69.52	5.66 E+2
3	Z = 69.52	----
4	Z = 69.52	3.17 E+2

Run III — 26.4 GeV/c
Carbon — 4-in. detector
Vent shaft — Coordinates: y = 103.2, z = 70.6

Installation	Exposure time (min.)	Net count rate (bkg subtracted) at t_0 (cpm)	$\bar{I}$ (p/sec)	ϕ at $\bar{I}$ (n/cm^2-sec)	ϕ at I=10^{12} p/sec (n/cm^2-sec)
1	82	4.67 E+6	1.83 E+11	4.84 E+4	2.64 E+5
2	80	4.72 E+6	1.82 E+11	4.92 E+4	2.70 E+5
4	80	4.02 E+6	1.64 E+11	3.96 E+4	2.41 E+5

Run III	26.4 GeV/c
Bare gold foils	All installations
Radial holes-vertical gradient	480-min. exposure
2-in. detector	1.61 E+11 p/sec

Location	Coordinates	Net count rate (bkg subtracted) at t_0 (cpm)	Error (%)	ϕ at $\bar{I}$ (n/cm^2-sec)	ϕ at I = 10^{12} p/sec (n/cm^2-sec)
33–1040	Y = 6.40 Z = 69.20	2.2 E+0	87.	1.97 E+0	1.22 E+1
33–1040	Y = 5.50 Z = 69.20	5.4 E+1	6.5	4.94 E+1	3.07 E+2
33–1040	Y = 4.40 Z = 69.20	3.62 E+2		3.30 E+2	2.05 E+3
33–1040	Y = 3.40 Z = 69.20	1.54 E+3		1.40 E+3	8.69 E+3
33–1040	Y = 2.30 Z = 69.20	3.77 E+3		3.43 E+3	2.13 E+4
33–1040	Y = 1.40 Z = 69.20	5.65 E+3		5.14 E+3	3.19 E+4

Run III	26.4 GeV/c
Moderated gold foils	All installations
Ring top	480-min. exposure
2-in. detector	1.61 E+11 p/sec

Location	Coordinates	Net count rate (bkg subtracted) at t_0 (cpm)	Error (%)	ϕ at $\bar{I}$ (n/cm^2-sec)	ϕ at I=10^{12} p/sec (n/cm^2-sec)
32/0	Y = 6.42 Z = 62.92	3.07 E+1	8.5	3.71 E+1	2.30 E+2
32/1	Y = 6.41 Z = 63.9	4.78 E+1	6.0	5.77 E+1	3.58 E+2
32/2	Y = 6.41 Z = 65.0	5.57 E+1	5.3	6.72 E+1	4.17 E+2
32/3	Y = 6.40 Z = 66.1	5.74 E+1	5.2	6.92 E+1	4.30 E+2
32/4	Y = 6.40 Z = 67.1	4.68 E+1	6.2	5.65 E+1	3.51 E+2
32/5	Y = 6.39 Z = 68.2	3.84 E+1	5.9	4.63 E+1	2.87 E+2
33/0	Y = 6.39 Z = 69.20	3.85 E+1	5.9	4.64 E+1	2.88 E+2
33/3	Y = 6.34 Z = 72.40	2.92 E+1	6.2	3.53 E+1	2.19 E+2

Run IV Data

Run IV exposure summary.*

Exposure number	Beam energy (GeV/c)	Average beam current (p/sec)	Exposure duration (min)	Exposure time
1	26.4	1.30 E+11	83	1707 – 1830
2	26.4	1.31 E+11	80	1840 – 2000
3	26.4	1.16 E+11	101	2009 – 2130
entire run	26.4	1.16 E+11	283	1707 – 2150

*Target location: straight section 32;
clipper location: straight section 79.

Run IV. Activities for aluminum foils on vacuum vessel.*

Standard position	Foil activity (pCi/g)	Standard position	Foil activity (pCi/g)	Standard position	Foil activity (pCi/g)	Standard position	Foil activity (pCi/g)
1		26	1.22 E+5	51	1.44 E+4	76	7.98 E+3
2	9.27 E+4	27	2.65 E+3	52	9.33 E+4	77	7.78 E+3
3	6.39 E+4	28	1.83 E+5	53	6.31 E+4	78	6.48 E+3
4	2.97 E+4	29	8.75 E+4	54	7.70 E+3	79	3.70 E+7
5	1.21 E+5	30	8.43 E+4	55	1.26 E+4	80	1.15 E+6
6	2.77 E+4	31	3.14 E+4	56	1.26 E+4	81	6.84 E+5
7	1.40 E+4	32	5.29 E+7	57	1.12 E+4	82	7.39 E+5
8	1.16 E+5	33	6.07 E+6	58	6.32 E+4	83	5.69 E+5
9	1.73 E+5	34	2.97 E+6	59	1.14 E+5	84	3.94 E+5
10	7.56 E+5	35	9.98 E+5	60	4.49 E+5	85	1.54 E+5
11	1.32 E+5	36	6.63 E+5	61	2.17 E+5	86	8.52 E+4
12	3.74 E+5	37	2.42 E+5	62	1.05 E+5	87	5.44 E+5
13	8.49 E+4	38	3.96 E+4	63	3.15 E+4	88	1.93 E+5
14	1.61 E+5	39	1.35 E+5	64	1.70 E+5	89	4.57 E+5
15	1.05 E+5	40	2.14 E+4	65	1.93 E+5	90	1.75 E+5
16	5.61 E+4	41	2.07 E+5	66	7.95 E+4	91	2.40 E+5
17	9.84 E+4	42	1.42 E+5	67	6.92 E+4	92	2.98 E+5
18	9.55 E+4	43	1.11 E+5	68	5.14 E+4	93	3.72 E+4
19	4.16 E+5	44	1.64 E+5	69	2.33 E+5	94	1.79 E+5
20	4.11 E+4	45	3.55 E+4	70	3.20 E+4	95	4.34 E+4
21	2.71 E+4	46	7.85 E+3	71	4.89 E+5	96	1.83 E+4
22	5.42 E+4	47	1.52 E+4	72	3.09 E+4	97	4.98 E+4
23	2.45 E+4	48	7.40 E+3	83	1.91 E+4	98	2.14 E+4
24	1.08 E+4	49	9.40 E+4	74	5.21 E+4	99	8.89 E+4
25	2.74 E+4	50	2.62 E+4	75	1.90 E+4	100	8.56 E+4

*One-hundred foils listed here.

Run IV
Sulfur
Roof buckets
4-g samples

26.4 GeV/c
All installations
283-min exposure
1.16 E+11 p/sec

Location	Coordinates	ϕ at $\bar{I}$ (n/cm^2-sec)	ϕ at I = 10^{12} p/sec (n/cm^2-sec)
31–R	Z = 56.64	3.34 E+4	2.87 E+5
32–R	Z = 62.92	9.83 E+5	8.44 E+6
32–1R	Z = 63.92	1.36 E+6	1.17 E+7
32–2R	Z = 65.42	9.83 E+5	8.44 E+6
32–3R	Z = 66.40	6.02 E+5	5.17 E+6
32–4R	Z = 67.30	4.38 E+5	3.76 E+6
32–5R	Z = 68.20	3.55 E+5	3.05 E+6
33–R	Z = 69.20	5.09 E+5	4.37 E+6
34–R	Z = 75.48	2.49 E+5	2.14 E+6
35–R	Z = 81.76	9.34 E+4	8.02 E+5
36–R	Z = 88.08	7.05 E+4	6.05 E+5
78–R	Z = 56.6	1.53 E+4	1.31 E+5
79–R	Z = 62.9	4.75 E+5	4.08 E+6
80–R	Z = 69.2	8.84 E+5	7.59 E+6

Run IV
Aluminum
Roof buckets
100-g samples

26.4 GeV/c
All installations
283-min. exposure
1.00 E+11 p/sec

Location	Coordinates	Net count rate (bkg. subtracted) at t_0 (cpm/g)	ϕ at $\bar{I}$ (n/cm^2-sec)	ϕ at I=10^{12} p/sec (n/cm^2-sec)
31–R	Z = 56.64	8.99 E+3	1.04 E+4	8.93 E+4
32–R	Z = 62.92	3.33 E+5	3.86 E+5	3.31 E+6
32–1R	Z = 63.92	4.97 E+5	5.77 E+5	4.95 E+6
32–2R	Z = 65.42	4.82 E+5	5.60 E+5	4.81 E+6
32–3R	Z = 66.40	2.81 E+5	3.27 E+5	2.81 E+6
32–4R	Z = 67.30	1.95 E+5	2.27 E+5	1.95 E+6
32–5R	Z = 68.20	1.47 E+5	1.70 E+5	1.46 E+6
33–R	Z = 69.20	1.88 E+5	2.18 E+5	1.87 E+6
34–R	Z = 75.48	9.81 E+4	1.14 E+5	9.79 E+5
35–R	Z = 81.76	4.48 E+4	5.20 E+4	4.46 E+5
36–R	Z = 88.08	3.06 E+4	3.55 E+4	3.05 E+5
78–R	Z = 56.6	2.70 E+3	3.13 E+3	2.69 E+4
79–R	Z = 62.9	2.08 E+5	2.42 E+5	2.08 E+6
80–R	Z = 69.2	3.74 E+4	4.34 E+4	3.73 E+5

Run IV — 26.4 GeV/c
Carbon — Installation 1
Roof buckets — 83-min exposure
1-in. detector — 1.30 E+11 p/sec

Location	Coordinates	Net count rate (bkg subtracted) at t_0 (cpm/g)	ϕ at $\bar{I}$ (n/cm^2-sec)	ϕ at I = 10^{12} p/sec (n/cm^2-sec)
32–0R	Z = 62.92	6.54 E+7	6.69 E+5	5.37 E+6
32–1R	Z = 63.92	1.45 E+8	1.49 E+6	1.20 E+7
32–2R	Z = 65.42	2.09 E+8	2.18 E+6	1.75 E+7
32–3R	Z = 66.40	1.48 E+8	1.54 E+6	1.24 E+7
32–4R	Z = 67.30	9.83 E+7	1.01 E+6	8.11 E+6

Run IV — 26.4 GeV/c
Bismuth-mica — All installations
Roof buckets — 283-min. exposure
~ 5-cm^2 detector — 1.16 E+11 p/sec

Location	Coordinates	Track-counting error (%)	ϕ at $\bar{I}$ (n/cm^2-sec)	ϕ at I=10^{12} p/sec (n/cm^2-sec)
32–R	Y = 1.74 Z = 62.92	7.6	7.74 E+5	6.64 E+6
32–1R	Y = 1.74 Z = 63.92	6.4	1.78 E+6	1.53 E+7
32–2R	Y = 1.74 Z = 65.42		3.43 E+6	2.94 E+7
32–3R	Y = 1.74 Z = 66.40		3.93 E+6	3.37 E+7
32–4R	Y = 1.74 Z = 67.30		3.54 E+6	3.04 E+7
32–5R	Y = 1.74 Z = 68.20	6.9	1.39 E+6	1.19 E+7
33–R	Y = 1.74 Z = 69.20	10.7	6.2 E+5	5.3 E+6

Run IV — 26.4 GeV/c
Gold-mica — All installations
Roof buckets — 283-min. exposure
~ 5-cm^2 detector — 1.16 E+11 p/sec

Location	Coordinates	Track-counting error (%)	ϕ at $\bar{I}$ (n/cm^2-sec)	ϕ at I=10^{12} p/sec (n/cm^2-sec)
32–R	Z = 62.92	21.	4.4 E+5	3.8 E+6
32–1R	Z = 63.92	9.6	1.6 E+6	1.4 E+7
32–2R	Z = 65.42	8.6	3.6 E+6	3.1 E+7
32–3R	Z = 66.40	7.6	4.3 E+6	3.7 E+7
32–4R	Z = 67.30	7.7	3.8 E+6	3.3 E+7
32–5R	Z = 68.20	9.1	1.3 E+6	1.1 E+7
33–R	Z = 69.20	16.	5.0 E+5	4.3 E+6

Run IV — 26.4 GeV/c
Lead-mica — All installations
Roof buckets — 283-min. exposure
~ 5-cm^2 detector — 1.16 E+11 p/sec

Location	Coordinates	Track-counting error (%)	ϕ at $\bar{I}$ (n/cm^2-sec)	ϕ at I=10^{12} p/sec (n/cm^2-sec)
32–R	Z = 62.92	10	6.4 E+5	5.5 E+6
32–1R	Z = 63.92	8.5	1.7 E+6	1.5 E+7
32–2R	Z = 65.42	6.6	2.9 E+6	2.5 E+7
32–3R	Z = 66.40	5.1	4.1 E+6	3.6 E+7
32–4R	Z = 67.30	5.4	3.8 E+6	3.3 E+7
32–5R	Z = 68.20	7.5	2.0 E+6	1.7 E+7
33–R	Z = 69.20	9.9	6.4 E+5	5.5 E+6

Run IV — 26.4 GeV/c
TLD — All installations
Roof buckets — 283-min. exposure
22-mg samples — 1.16 E+11 p/sec

Location	Coordinates	Indicated dose (rads/hour)
31–R	Z = 56.6	1.57 E+3
32–0R	Z = 62.9	1.29 E+3
32–1R	Z = 63.9	2.88 E+3
32–2R	Z = 65.4	3.06 E+3
32–3R	Z = 66.4	1.93 E+3
32–4R	Z = 67.3	1.35 E+3
32–5R	Z = 68.2	6.10 E+2
33–R	Z = 69.2	8.50 E+2
34–R	Z = 75.5	4.34 E+2
35–R	Z = 81.8	2.08 E+2
36–R	Z = 88.1	1.46 E+2
78–R	Z = 64.9	1.53 E+1
79–R	Z = 65.9	5.10 E+2
80–R	Z = 66.9	7.75 E+1

Run IV — 26.4 GeV/c
Aluminum — All installations
Orbit holes — 283-min. exposure
1.16 E+11 p/sec

Location	Coordinates	Detector size (g)	Net count rate (bkg subtracted) at t_0 (cpm)	Error (%)	ϕ at $\bar{I}$ (n/cm^2-sec)	ϕ at I=10^{12} p/sec (n/cm^2-sec)
34–330	Y = 3.63 Z = 75.48	16.9	7.11 E+2	1.5	4.32 E+3	3.71 E+4
34–330	Y = 3.63 Z = 75.48	100	3.77 E+3	0.9	4.38 E+3	3.76 E+4
34–390	Y = 4.22 Z = 75.48	500	3.89 E+3		1.21 E+3	1.04 E+4
34–510	Y = 5.40 Z = 75.48	500	3.10 E+2		9.42 E+1	8.08 E+2
35–390	Y = 4.04 Z = 81.76	500	1.78 E+3		5.55 E+2	4.76 E+3
36–390	Y = 3.90 Z = 88.08	500	2.05 E+3		6.36 E+2	5.46 E+3
33–V	Y = 103.2 Z = 70.6	500	4.00 E+4		1.24 E+4	1.07 E+5

Run IV
Aluminum
Orbit holes; streaming

26.4 GeV/c
All installations
283-min. exposure
1.16 E+11 p/sec

Location	Coordinates	Detector size (g)	Net count rate (bkg subtracted) at t_0 (cpm)	Error (%)	ϕ at $\bar{I}$ (n/cm^2-sec)	ϕ at I = 10^{12} p/sec (n/cm^2-sec)
32–330	Y = 3.67 Z = 62.92	16.9	1.62 E+3	1.3	9.81 E+3	8.42 E+4
32–330	Y = 3.67 Z = 62.92	100	8.48 E+3	1.2	9.84 E+3	8.45 E+4
32–390	Y = 4.26 Z = 62.92	500	1.17 E+4		3.64 E+3	3.12 E+4
32–450	Y = 4.85 Z = 62.92	500	3.60 E+3		1.12 E+3	9.61 E+4
32–510	Y = 5.44 Z = 62.92	500	1.16 E+3		3.60 E+2	3.09 E+3
32–570	Y = 6.03 Z = 62.92	500	4.31 E+2		1.32 E+2	1.31 E+3
33–330	Y = 3.42 Z = 69.20	100	1.38 E+4		1.61 E+4	1.38 E+5
33–390	Y = 4.01 Z = 69.20	500	1.64 E+4		5.09 E+3	4.37 E+4
33–450	Y = 4.60 Z = 69.20	500	3.77 E+3		1.17 E+3	1.00 E+4
33–510	Y = 5.19 Z = 69.20	500	1.10 E+3		3.41 E+2	2.93 E+3
33–570	Y = 5.78 Z = 69.20	500	3.49 E+2		1.07 E+2	9.18 E+3

Run IV
Carbon
Orbit holes
80-min. exposure

26.4 GeV/c
Installation 2
4-in. detector
1.31 E+11 p/sec

Location	Coordinates	Net count rate (bkg subtracted) at t_0 (cpm)	ϕ at $\bar{I}$ (n/cm^2-sec)	ϕ at I=10^{12} p/sec (n/cm^2-sec)
32–33	Y = 3.67 Z = 62.92	3.22 E+6	3.33 E+4	2.54 E+5
32–45	Y = 4.85 Z = 62.92	3.64 E+5	3.74 E+3	2.86 E+4
32–57	Y = 6.03 Z = 62.92	4.97 E+4	5.12 E+2	3.91 E+3
33–33	Y = 3.42 Z = 69.20	5.55 E+6	5.82 E+4	4.44 E+5
33–45	Y = 4.60 Z = 69.20	3.50 E+5	3.60 E+3	2.75 E+4
33–57	Y = 5.78 Z = 69.20	3.41 E+4	3.51 E+2	2.68 E+3

Run IV
Carbon
Ring top
83-min. exposure

26.4 GeV/c
Installation 1
5-in. detector
1.30 E+11

Location	Coordinates	Net count rate (bkg subtracted) at t_0 (cpm)	ϕ at $\bar{I}$ (n/cm^2-sec)	ϕ at I=10^{12} p/sec (n/cm^2-sec)
32–0	Y = 6.42 Z = 62.92	6.077 E+3	6.21 E+1	4.99 E+2
32–1	Y = 6.41 Z = 63.92	7.617 E+3	7.79 E+1	6.26 E+2
32–2	Y = 6.41 Z = 65.42	8.589 E+3	8.78 E+1	7.05 E+2
32–3	Y = 6.40 Z = 66.40	5.919 E+3	9.73 E+1	7.81 E+2
32–4	Y = 6.40 Z = 67.30	8.163 E+3	8.35 E+1	6.71 E+2
32–5	Y = 6.39 Z = 68.20	7.739 E+3	7.91 E+1	6.35 E+2
33–0	Y = 6.39 Z = 69.20	6.087 E+3	6.22 E+1	4.99 E+2

Run IV — 26.4 GeV/c
TLD — All installations
Orbit holes — 283-min. exposure
22-mg detector — 1.16 E+11 p/sec

Location	Coordinates	Dose (rads/h)
32–330	Y = 3.67 Z = 62.9	1.67 E+1
32–390	Y = 4.26 Z = 62.9	7.8 E+0
32–450	Y = 4.85 Z = 62.9	4.0 E+0
32–510	Y = 5.44 Z = 62.9	2.5 E+0
32–570	Y = 6.03 Z = 62.9	2.5 E+0
33–330	Y = 3.42 Z = 69.2	2.9 E+1
33–390	Y = 4.01 Z = 69.2	7.6 E+0
33–450	Y = 4.60 Z = 69.2	4.1 E+0
33–510	Y = 5.19 Z = 69.2	2.8 E+0
33–570	Y = 5.78 Z = 69.2	2.4 E+0
34–330	Y = 3.63 Z = 75.48	8.7 E+0
34–390	Y = 4.22 Z = 75.48	4.2 E+0
34–450	Y = 4.81 Z = 75.48	2.7 E+0
34–510	Y = 5.40 Z = 75.48	2.7 E+0
34–570	Y = 5.99 Z = 75.48	2.4 E+0
35–330	Y = 3.45 Z = 81.76	6.5 E+0
35–390	Y = 4.04 Z = 81.76	3.0 E+0
35–450	Y = 4.63 Z = 81.76	2.6 E+0
35–510	Y = 5.22 Z = 81.76	3.5 E+0
35–570	Y = 5.81 Z = 81.76	2.2 E+0
36–330	Y = 3.31 Z = 88.08	7.9 E+0
36–390	Y = 3.90 Z = 88.08	3.7 E+0
36–450	Y = 4.49 Z = 88.08	3.5 E+0
36–510	Y = 5.08 Z = 88.08	3.8 E+0
36–570	Y = 5.67 Z = 88.08	

Run IV — 26.4 GeV/c
Aluminum — All installations
Radial holes — 283-min. exposure
1.16 E+11 p/sec

Location	Coordinates	Detector size (g)	Net count rate (bkg subtracted) at t_0 (cpm)	Error (%)	ϕ at $\bar{I}$ (n/cm^2-sec)	ϕ at I=10^{12} p/sec (n/cm^2-sec)
32–1050	X = 105.0 Z = 62.92	500	1.08 E+3		3.35 E+2	2.88 E+3
32–1060	X = 106.0 Z = 62.92	2200	3.32 E+2		2.95 E+1	2.53 E+2
33–1060	X = 106.0 Z = 69.20	2200	4.89 E+2	1.7	4.35 E+1	3.73 E+2
33–1060	X = 106.0 Z = 69.20	2200	5.11 E+2	1.7	4.55 E+1	3.91 E+2
33–1060	X = 106.0 Z = 69.20	2200	5.04 E+2	1.7	4.49 E+1	3.86 E+2

Run IV — 26.4 GeV/c
Aluminum — All installations
Ring top — 283-min. exposure
3300-g detector — 1.16 E+11 p/sec

Location	Coordinates	Net count rate (bkg subtracted) at t_0 (cpm)	Error (%)	ϕ at $\bar{I}$ (n/cm^2-sec)	ϕ at I=10^{12} p/sec (n/cm^2-sec)
32/0	Y = 6.42 Z = 62.92	2.85 E+2		1.96 E+1	1.68 E+2
32/1	Y = 6.41 Z = 63.9	3.38 E+2		2.34 E+1	2.01 E+2
32/2	Y = 6.41 Z = 64.9	3.80 E+2		2.62 E+1	2.25 E+2
32/3	Y = 6.40 Z = 65.9	4.07 E+2	1.9	2.81 E+1	2.41 E+2
32/3	Y = 6.40 Z = 65.9	3.62 E+2	2.0	2.84 E+1	2.44 E+2
*32/3–IN	Y = 6.40 Z = 65.9	3.47 E+2		2.40 E+1	2.06 E+2
*32/3-OUT	Y = 6.40 Z = 65.9	2.50 E+2		1.72 E+1	1.48 E+2
32/4	Y = 6.40 Z = 66.9	3.83 E+2		2.65 E+1	2.08 E+2
32/5	Y = 6.40 Z = 67.9	3.17 E+2		2.19 E+1	1.88 E+2
33/0	Y = 6.39 Z = 69.20	2.91 E+2		2.01 E+1	1.73 E+2

*X = 98m for 32/3–IN location; X = 102 m for 32/3–OUT location.

Run IV
Aluminum → Na^{24}
Angular distribution
16.9-g detector

26.4 GeV/c
All installations
283-min. exposure
1.16 E+11 p/sec

Location (deg)	Coordinates	Net count rate (bkg subtracted) at t_0 (cpm)	ϕ at $\bar{I}$ (n/cm^2-sec)	ϕ at I=10^{12} p/sec (n/cm^2-sec)
3	Y = 0.05 Z = 63.92	5.63 E+5	4.03 E+7	3.46 E+8
20	Y = 0.35 Z = 63.86	8.62 E+4	6.17 E+6	5.30 E+7
30	Y = 0.50 Z = 63.78	4.66 E+4	3.34 E+6	2.87 E+7
40	Y = 0.64 Z = 63.68	3.09 E+4	2.22 E+6	1.91 E+7
50	Y = 0.76 Z = 63.56	2.36 E+4	1.69 E+6	1.45 E+7
60	Y = 0.87 Z = 63.42	1.72 E+4	1.23 E+6	1.06 E+7
70	Y = 0.94 Z = 63.26	1.35 E+4	9.66 E+5	8.29 E+6
80	Y = 0.98 Z = 63.10	1.18 E+4	8.47 E+5	7.27 E+6
90–V	Y = 1.00 Z = 62.92	8.99 E+3	6.44 E+5	5.53 E+6
90–H	Y = 0.00 Z = 62.92	1.28 E+4	9.17 E+5	7.87 E+6

Run IV
Carbon
Angular distribution
283-min. exposure

26.4 GeV/c
All installations
1-in. detector
1.16 E+11 p/sec

Location (deg)	Coordinates	Net count rate (bkg subtracted) at t_0 (cpm)	ϕ at $\bar{I}$ (n/cm^2-sec)	ϕ at I=10^{12} p/sec (n/cm^2-sec)
3	Y = 0.05 Z = 63.92	2.11 E+10	1.76 E+8	1.51 E+9
20	Y = 0.35 Z = 63.86	2.50 E+9	2.33 E+7	2.0 E+8
30	Y = 0.50 Z = 63.78	1.02 E+9	9.56 E+6	8.20 E+7
40	Y = 0.64 Z = 63.68	5.98 E+8	5.63 E+6	4.83 E+7
50	Y = 0.76 Z = 63.56	4.69 E+8	4.43 E+6	3.80 E+7
60	Y = 0.87 Z = 63.42	2.92 E+8	2.88 E+6	2.47 E+7
70	Y = 0.94 Z = 63.26	2.00 E+8	1.96 E+6	1.68 E+7
80	Y = 0.98 Z = 63.10	1.65 E+8	1.58 E+6	1.36 E+7
90	Y = 1.00 Z = 62.92	1.12 E+8	1.07 E+6	9.18 E+6
90–H	Y = 0.00 Z = 62.92	1.47 E+8	1.40 E+6	1.20 E+7
100–3	Y = 0.05 Z = 63.92		1.28 E+8	1.10 E+9
100–20	Y = 0.35 Z = 63.86		1.50 E+7	1.29 E+8
100–30	Y = 0.50 Z = 63.78		6.07 E+6	5.21 E+7
100–40	Y = 0.64 Z = 63.68		3.63 E+6	3.12 E+7
100–50	Y = 0.76 Z = 63.56		2.67 E+6	2.29 E+7
100–60	Y = 0.87 Z = 63.42		1.88 E+6	1.61 E+7
100–70	Y = 0.94 Z = 63.26		1.35 E+6	1.16 E+7
100–80	Y = 0.98 Z = 63.10		1.16 E+6	9.96 E+6
100–90V	Y = 1.00 Z = 62.92		7.08 E+5	6.08 E+6
100–90H	Y = 0.00 Z = 62.92			

Run IV
Aluminum → Na^{22}
Angular distribution
16.9-g detector

26.4 GeV/c
All installations
283-min. exposure
1.16 E+11 p/sec

Location (deg)	Coordinates	ϕ at $\bar{I}$ (n/cm^2-sec)	ϕ at $I=10^{12}$ p/sec (n/cm^2-sec)
100–3	Y = 0.05 Z = 63.92	1.05 E+8	9.01 E+8
100–20	Y = 0.35 Z = 63.86	1.30 E+7	1.12 E+8
100–30	Y = 0.50 Z = 63.18	6.06 E+6	5.20 E+7
100–40	Y = 0.64 Z = 63.68	3.75 E+6	3.22 E+7
100–50	Y = 0.76 Z = 63.56	2.98 E+6	2.56 E+7
100–60	Y = 0.87 Z = 63.42	1.96 E+6	1.68 E+7
100–70	Y = 0.94 Z = 63.26	1.48 E+6	1.27 E+7
100–80	Y = 0.98 Z = 63.10	1.24 E+6	1.06 E+7
100–90V	Y = 1.00 Z = 62.92	6.84 E+5	5.87 E+6
100–90H	Y 0.00 Z = 62.92	1.08 E+6	9.27 E+6

Run IV
Bismuth-mica
Angular distribution
~ 5-cm^2 detector

26.4 GeV/c
All installations
283-min-exposure
1.16 E+11 p/sec

Location	Coordinates	Track-counting error (%)	ϕ at $\bar{I}$ (n/cm^2-sec)	ϕ at $I=10^{12}$ p/sec (n/cm^2-sec)
100–3°	Y = 0.05 Z = 63.92			
100–20°	Y = 0.35 Z = 63.86		1.37 E+7	1.18 E+8
100–30°	Y = 0.50 Z = 63.78		5.95 E+6	5.11 E+7
100–40°	Y = 0.64 Z = 63.68		2.70 E+6	2.32 E+7
100–50°	Y = 0.76 Z = 63.56	5.4	2.34 E+6	2.01 E+7
100–60°	Y = 0.87 Z = 63.42	5.5	1.16 E+6	9.96 E+6
100–70°	Y = 0.94 Z = 63.26	6.7	7.6 E+5	6.5 E+6
100–80°	Y = 0.98 Z = 63.10	5.5	5.2 E+5	4.5 E+6
100–90°V	Y = 1.00 Z = 62.92	9.6	3.4 E+5	2.9 E+6
100–90°H	Y = 0.00 Z = 62.92	9.6	3.5 E+5	3.0 E+6

Run IV	26.4 GeV/c
Mercury	All installations
Angular distribution	283-min. exposure
432-g detector	1.16 E+11 p/sec

Location	Coordinates	Net count rate (bkg subtracted) at t_0 (cpm)	Error (%)	ϕ at I=10^{12} p/sec (n/cm^2-sec)
3°–100 cm	Y = 0.05 Z = 63.92	3.038 E+5		2.21 E+8
20°–100 cm	Y = 0.35 Z = 63.86	1.252 E+4		8.69 E+6
30°–100 cm	Y = 0.50 Z = 63.78	1.573 E+3		1.09 E+6
40°–100 cm	Y = 0.64 Z = 63.68	9.428 E+2		6.54 E+5
50°–100 cm	Y = 0.76 Z = 63.56	1.336 E+2		9.27 E+4
60°–100 cm	Y = 0.87 Z = 63.42	2.50 E+1	6.7	1.74 E+4
70°–100 cm	Y = 0.94 Z = 63.26	4.89 E+1		3.39 E+4
80°–100 cm	Y = 0.98 Z = 63.10	1.65 E+1	7.0	8.09 E+3
90°–100 cm	Y = 1.00 Z = 62.92	3.94 E+0	10.0	2.73 E+3
90°H–100 cm	Y = 0.00 Z = 62.92	2.212 E+1		1.54 E+4

Run IV-½ Data

Run IV-½ exposure summary.*

Exposure number	Beam energy (GeV/c)	Average beam current (p/sec)	Exposure duration (min)	Exposure time
entire run	19.2	4.54 E+11	5850	28–31 Oct. 1966

* Target locations: straight section 1, about 30% of beam
straight section 6, about 15% of beam
straight section 58, about 25% of beam
straight section 64, about 30% of beam;
clipper location: no clipper.

NOTE: No beam control by our experimental team during this period; above target-beam distribution is typical for these conditions.

Run IV-½. Activities for aluminum foils on vacuum vessel*

Standard position	Foil activity (pCi/g)	Standard position	Foil activity (pCi/g)	Standard position	Foil activity (pCi/g)	Standard position	Foil activity (pCi/g)
1	1.02 E+7	26	4.12 E+5	51	2.12 E+5	76	3.22 E+5
2	9.19 E+5	27	2.64 E+4	52	2.90 E+4	77	1.04 E+6
3	5.82 E+5	28	1.27 E+6	53	1.03 E+5	78	1.06 E+5
4	2.70 E+5	29	3.68 E+5	54	2.35 E+4	79	5.54 E+4
5	8.41 E+5	30	1.89 E+5	55	4.61 E+4	80	4.22 E+4
6	5.12 E+6	31	3.49 E+5	56	8.22 E+4	81	2.71 E+4
7	1.08 E+6	32	5.83 E+4	57	7.91 E+4	82	1.02 E+4
8	3.57 E+5	33	† 2.82 E+4	58	1.86 E+6	83	5.06 E+4
9	4.04 E+5	34	7.53 E+4	59	1.94 E+5	84	1.79 E+4
10	1.05 E+6	35	1.26 E+5	60	1.97 E+5	85	8.26 E+4
11	3.15 E+5	36	2.08 E+4	61	1.44 E+4	86	5.56 E+4
12	4.92 E+5	37	6.24 E+4	62	4.64 E+5	87	2.96 E+5
13	1.88 E+5	38	7.57 E+3	63	9.15 E+4	88	1.30 E+5
14	9.14 E+4	39	4.69 E+4	64	5.31 E+6	89	4.40 E+5
15	6.21 E+5	40	1.34 E+4	65	3.34 E+6	90	2.79 E+4
16	9.42 E+4	41	1.12 E+5	66	3.92 E+5	91	7.09 E+4
17	2.23 E+5	42	3.06 E+5	67	3.74 E+5	92	3.99 E+5
18	1.64 E+5	43	1.89 E+5	68	1.01 E+5	93	1.01 E+6
19	1.49 E+6	44	7.17 E+4	69	1.97 E+5	94	2.61 E+5
20	8.73 E+4	45	3.89 E+6	70	2.61 E+4	95	1.38 E+5
21	2.40 E+5	46	1.48 E+5	71	1.31 E+5	96	7.54 E+4
22	2.25 E+5	47	2.64 E+5	72	4.08 E+4	97	3.27 E+4
23	3.65 E+4	48	3.69 E+4	73	7.30 E+5	98	4.87 E+4
24	3.86 E+4	49	2.15 E+6	74	2.19 E+5	99	2.88 E+4
25	2.79 E+4	50	1.07 E+5	75	1.81 E+6	100	1.44 E+4

*One-hundred foils listed here.

†No good.

Run IV½ | 19.2 GeV/c
Sulfur | All installations
Roof buckets | 5850-min exposure
4-g samples | 4.54 E+11 p/sec

Location	Coordinates	ϕ at $\bar{I}$ (n/cm^2-sec)	ϕ at I = 10^{12} p/sec (n/cm^2-sec)
29–R	Z = 44.08	4.82 E+4	1.06 E+5
30–R	Z = 50.36	3.66 E+4	8.06 E+4
31–R	Z = 56.64	4.91 E+4	1.08 E+5
31–1R	Z = 57.92	5.92 E+4	1.30 E+5
31–2R	Z = 58.92	3.91 E+4	8.61 E+4
31–3R	Z = 59.92	2.31 E+4	5.09 E+4
31–4R	Z = 60.92	1.74 E+4	3.83 E+4
31–5R	Z = 61.92	1.49 E+4	3.28 E+4
32–R	Z = 62.92	1.70 E+4	3.74 E+4
32–1R	Z = 63.93	1.84 E+4	4.05 E+4
32–2R	Z = 65.42	1.60 E+4	3.52 E+4
32–3R	Z = 66.40	1.47 E+4	3.23 E+4
32–4R	Z = 67.30	1.68 E+4	3.70 E+4
32–5R	Z = 68.20	2.48 E+4	5.46 E+4
33–R	Z = 69.20	5.05 E+4	1.11 E+5
33–1R	Z = 70.48	5.15 E+4	1.13 E+5
33–2R	Z = 71.48	3.42 E+4	7.53 E+4
33–3R	Z = 72.48	2.28 E+4	5.02 E+4
33–4R	Z = 73.48	1.75 E+4	3.85 E+4
33–5R	Z = 74.48	1.78 E+4	3.92 E+4
34–R	Z = 75.48	–	–
35–R	Z = 81.76	2.55 E+4	5.61 E+4
36–R	Z = 88.08	8.13 E+3	1.79 E+4
37–R	Z = 94.32	6.61 E+3	1.46 E+4
38–R	Z = 100.60	2.84 E+3	6.26 E+3
39–R	Z = 106.88	5.46 E+3	1.20 E+4
40–R	Z = 113.16	–	–
41–R	Z = 119.44	1.81 E+4	3.99 E+4

Run IV½
Aluminum
Roof buckets
100-g samples

19.2 GeV/c
All installations
5850-min. exposure
4.54 E+11 p/sec

Location	Coordinates	Net count rate (bkg. subtracted) at t_0 (cpm/g)	ϕ at $\bar{I}$ (n/cm^2-sec)	ϕ at I = 10^{12} p/sec (n/cm^2-sec)
29–R	Z = 44.08	8.98 E+4	2.06 E+4	4.54 E+5
30–R	Z = 50.36	7.11 E+4	1.63 E+4	3.59 E+4
31–0R	Z = 56.64	8.30 E+4	1.91 E+4	4.21 E+4
31–1R	Z = 57.92	1.03 E+5	2.38 E+4	5.24 E+4
31–2R	Z = 58.92	8.12 E+4	1.87 E+4	4.12 E+4
31–3R	Z = 59.92	4.50 E+4	1.04 E+4	2.29 E+4
31–4R	Z = 60.92	3.24 E+4	7.45 E+3	1.64 E+4
31–5R	Z = 61.92	2.70 E+4	6.21 E+3	1.39 E+4
32–0R	Z = 62.92	2.90 E+4	6.66 E+3	1.47 E+4
32–1R	Z = 63.93	3.07 E+4	7.06 E+3	1.56 E+4
32–2R	Z = 65.42	2.92 E+4	6.71 E+3	1.48 E+4
32–3R	Z = 66.40	2.40 E+4	5.52 E+3	1.22 E+4
32–4R	Z = 67.30	2.53 E+4	5.81 E+3	1.28 E+4
32–5R	Z = 68.20	3.89 E+4	8.95 E+3	1.97 E+4
33–0R	Z = 69.20	9.23 E+4	2.12 E+4	4.67 E+4
33–1R	Z = 70.48	1.07 E+5	2.45 E+4	5.40 E+4
33–2R	Z = 71.48	8.10 E+4	1.86 E+4	4.10 E+4
33–3R	Z = 72.48	5.20 E+4	1.20 E+4	2.64 E+4
33–4R	Z = 73.48	3.71 E+4	8.53 E+3	1.88 E+4
33–5R	Z = 74.48	3.10 E+4	7.13 E+3	1.57 E+4
34–R	Z = 75.48	3.58 E+4	8.23 E+3	1.81 E+4
35–R	Z = 81.76	3.94 E+4	9.06 E+3	2.00 E+4
36–R	Z = 88.08	1.50 E+4	3.44 E+3	7.58 E+3
37–R	Z = 94.32	1.33 E+4	3.06 E+3	6.74 E+3
38–R	Z = 100.60	5.85 E+3	1.34 E+3	2.95 E+3
39–R	Z = 106.88	8.89 E+3	2.04 E+3	4.49 E+3
40–R	Z = 113.16	5.51 E+3	1.27 E+3	2.80 E+3
41–R	Z = 119.44	3.07 E+4	7.05 E+3	1.55 E+4

Run IV½	19.2 GeV/c
TLD	All installations
Roof buckets	5850-min. exposure
22-mg samples	4.54 E+11 p/sec

Location	Coordinates	Indicated dose (rads/hour)
29–R	Z = 44.1	5.13 E+2
30–R	Z = 50.4	1.08 E+3
31–0R	Z = 56.6	7.33 E+2
31–1R	Z = 57.9	1.04 E+3
31–2R	Z = 58.9	7.72 E+2
31–3R	Z = 59.9	5.75 E+2
31–4R	Z = 60.9	3.87 E+2
31–5R	Z = 61.9	3.28 E+2
32–0R	Z = 62.9	2.69 E+2
32–1R	Z = 63.9	3.54 E+2
32–2R	Z = 65.4	3.30 E+2
32–3R	Z = 66.4	2.90 E+2
32–4R	Z = 67.3	2.50 E+2
32–5R	Z = 68.2	3.74 E+2
33–0R	Z = 69.2	1.11 E+3
33–1R	Z = 70.5	1.34 E+3
33–2R	Z = 71.5	1.21 E+3
33–3R	Z = 72.5	9.65 E+2
33–4R	Z = 73.5	5.25 E+2
33–5R	Z = 74.5	3.21 E+2
34–R	Z = 75.5	4.12 E+2
35–R	Z = 81.8	4.20 E+2
36–R	Z = 88.1	1.68 E+2
37–R	Z = 94.3	1.43 E+2
38–R	Z = 100.6	9.24 E+1
39–R	Z = 106.9	9.24 E+1
40–R	Z = 113.2	6.05 E+1
41–R	Z = 119.4	3.16 E+2

Run IV½
Aluminum
Orbit holes

19.2 GeV/c
All installations
5850-min. exposure

4.54 E+11 p/sec

Location	Coordinates	Detector size (g)	Net count rate (bkg subtracted) at t_0 (cpm)	Error (%)	ϕ at $\bar{I}$ (n/cm^2-sec)	ϕ at I=10^{12} p/sec (n/cm^2-sec)
30–330T	Y = 3.65 Z = 50.36	1100	1.60 E+4		4.92 E+2	1.08 E+3
30–390T	Y = 4.24 Z = 50.36	1100	3.83 E+3		1.18 E+2	2.60 E+2
31–330T	Y = 3.69 Z = 56.64	1100	2.00 E+4		6.15 E+2	1.35 E+3
31–390T	Y = 4.28 Z = 56.64	1100	5.21 E+3		1.61 E+2	3.55 E+2
31–390L	Y = 4.20 Z = 56.64	1100	6.28 E+3		1.93 E+2	4.25 E+2
31–450T	Y = 4.87 Z = 56.64	1100	1.38 E+3		4.25 E+1	9.36 E+1
31–510	Y = 5.42 Z = 56.64	2200	7.52 E+2		1.33 E+1	2.93 E+1
32–330T	Y = 3.83 Z = 62.92	1100	5.24 E+3		1.61 E+2	3.55 E+2
32–390T	Y = 4.42 Z = 62.92	1100	1.36 E+3		4.19 E+1	9.23 E+1
32–450T	Y = 5.01 Z = 62.92	1100	3.89 E+2		1.2 E+1	2.64 E+1
32–510	Y = 5.56 Z = 62.92	2200	2.18 E+2		3.83 E+0	8.43 E+0
32–570	Y = 6.15 Z = 62.92	2200	6.5 E+1	5.0	1.12 E+0	2.47 E+0
33–330T	Y = 3.58 Z = 69.20	1100	2.47 E+4		7.62 E+2	1.68 E+3
33–390T	Y = 4.17 Z = 69.20	1100	6.03 E+3		1.86 E+2	4.10 E+2
33–450T	Y = 4.76 Z = 69.20	1100	1.58 E+3		4.87 E+1	1.07 E+2
33–510	Y = 5.31 Z = 69.20	2200	7.89 E+2		1.39 E+1	3.06 E+1
33–570	Y = 5.90 Z = 69.20	2200	2.37 E+2		4.16 E+0	9.15 E+0
34–330T	Y = 3.79 Z = 75.48	1100	8.96 E+3		2.76 E+2	6.08 E+2
34–390T	Y = 4.38 Z = 75.48	1100	2.38 E+3		7.32 E+1	1.61 E+2
36–330T	Y = 3.47 Z = 88.08	1100	6.90 E+3		2.13 E+2	4.69 E+2
36–330T	Y = 3.47 Z = 88.08	1100	6.88 E+3		2.12 E+2	4.67 E+2
38–330T	Y = 3.64 Z = 100.60	1100	1.55 E+3		4.77 E+1	1.05 E+2
38–390T	Y = 4.23 Z = 100.60	1100	3.92 E+2		1.19 E+1	2.62 E+2
41–330T	Y = 3.73 Z = 119.44	1100	6.42 E+3		1.98 E+2	4.36 E+2
41–390T	Y = 4.32 Z = 119.44	1100	1.62 E+3		4.97 E+1	1.10 E+2

Run IV½
TLD
Orbit holes
22-mg detector

19.2 GeV/c
All locations
5850-min. exposure
4.54 E+11 p/sec

Location	Coordinates	Dose (rads)
30–330	Y = 3.49 Z = 50.4	7.14 E+0
30–390	Y = 4.08 Z = 50.4	1.43 E+0
32–330	Y = 3.67 Z = 62.9	2.23 E+0
32–390	Y = 4.26 Z = 62.9	5.9 E-1
34–330	Y = 3.63 Z = 75.5	4.17 E+0
34–390	Y = 4.22 Z = 75.5	8.5 E-1
36–330	Y = 3.31 Z = 88.1	4.40 E+0
36–390	Y = 3.90 Z = 88.1	5.9 E-1
38–330	Y = 3.48 Z = 100.6	6.7 E-1
38–390	Y = 4.07 Z = 100.6	1.6 E-1
41–330	Y = 3.57 Z = 113.2	1.45 E+1
41–390	Y = 4.16 Z = 113.2	5.8 E-1

Run IV½
Aluminum
Vent shaft

19.2 GeV/c
All installations
5850-min. exposure

4.54 E+11 p/sec

Location	Coordinates	Detector size (g)	Net count rate (bkg subtracted) at t_0 (cpm)	ϕ at $\bar{I}$ (n/cm^2-sec)	ϕ at I = 1-^{12} p/sec (n/cm^2-sec)
33–vent	X = 103.2 Z = 70.6	500	2.05 E+4	1.26 E+3	2.78 E+3

Run V Data

Run V exposure summary.*

Exposure number	Beam energy (GeV/c)	Average beam current (p/sec)	Exposure duration (min)	Exposure time
1	26.4	1.44 E+11	90	2029 – 2159
2	26.4	1.46 E+11	76	2214 – 2330
3	26.4	1.52 E+11	158	0052 – 0330
entire run	26.4	1.14 E+11	421	2029 – 0330

*Target location: straight section 32;

clipper location: straight section 79.

Run V. Activities for aluminum foils on vacuum vessel.*

Standard position	Foil activity (pCi/g)	Standard position	Foil activity (pCi/g)	Standard position	Foil activity (pCi/g)	Standard position	Foil activity (pCi/g)
1	3.52 E+4	26	1.70 E+5	51	1.44 E+4	76	1.73 E+4
2	1.12 E+5	27	1.29 E+4	52	1.85 E+5	77	9.77 E+3
3	7.43 E+4	28	8.57 E+4	53	5.06 E+4	78	9.30 E+3
4	2.68 E+4	29	4.86 E+4	54	1.18 E+4	79	4.41 E+7
5	1.41 E+5	30	1.02 E+5	55	1.55 E+4	80	1.18 E+6
6	2.48 E+4	31	4.27 E+4	56	2.65 E+4	81	8.94 E+5
7	1.84 E+4	32	5.49 E+7	57	8.60 E+3	82	1.10 E+6
8	7.80 E+4	33	8.37 E+6	58	2.64 E+4	83	8.23 E+5
9	1.85 E+5	34	3.00 E+6	59	2.09 E+4	84	3.02 E+5
10	9.70 E+5	35	9.74 E+5	60	2.80 E+5	85	1.81 E+5
11	1.61 E+5	36	6.93 E+5	61	4.75 E+5	86	7.52 E+4
12	2.35 E+5	37	2.26 E+5	62	1.36 E+5	87	1.04 E+6
13	5.35 E+4	38	4.62 E+4	63	7.28 E+4	88	1.11 E+5
14	1.62 E+5	39	2.11 E+5	64	2.05 E+5	89	7.67 E+5
15	1.42 E+5	40	2.73 E+4	65	1.16 E+5	90	2.83 E+5
16	5.78 E+4	41	4.42 E+4	66	7.00 E+4	91	3.19 E+5
17	9.38 E+4	41	1.78 E+5	67	1.33 E+5	92	1.11 E+5
18	1.22 E+5	43	1.34 E+5	68	8.02 E+4	93	3.56 E+4
19	6.51 E+5	44	1.70 E+5	69	2.91 E+5	94	1.86 E+5
20	3.58 E+4	45	2.87 E+4	70	5.77 E+4	95	6.71 E+4
21	4.24 E+4	46	8.85 E+3	71	7.68 E+5	96	1.82 E+4
22	6.43 E+4	47	1.95 E+4	72	4.48 E+4	97	2.18 E+4
23	3.90 E+4	48	1.42 E+4	73	3.29 E+4	98	2.10 E+4
24	2.38 E+4	49	8.07 E+4	74	1.37 E+5	99	1.17 E+5
25	1.03 E+5	50	2.97 E+4	75	3.10 E+4	100	1.36 E+5

* One-hundred foils listed here.

Run V	26.4 GeV/c
TLD	All installations
Vacuum vessel	421-min. exposure
22-mg sample	1.14 E+11 p/sec

Location	Dose (rads/h)
1	----
4	2.41 E+2
7	1.73 E+2
10	1.45 E+4
13	5.69 E+2
16	6.19 E+2
19	4.59 E+3
22	4.74 E+2
25	7.03 E+2
28	3.24 E+2
31	3.62 E+2
32	1.09 E+4
33	1.03 E+4
34	5.58 E+4
37	3.39 E+3
40	1.77 E+2
43	1.38 E+3
46	9.65 E+1
49	3.60 E+2
52	1.83 E+3
55	1.20 E+2
58	1.92 E+2
61	2.54 E+3
64	2.87 E+3
67	1.10 E+3
70	4.61 E+2
73	2.30 E+2
76	1.45 E+2
79	1.13 E+4
82	2.22 E+4
85	2.46 E+3
88	7.48 E+2
91	5.05 E+3
94	1.81 E+2
97	1.67 E+2
100	5.07 E+2

Run V	26.4 GeV/c
Sulfur	All installations
Roof buckets	421-min exposure
4.0-g samples	1.14 E+11 p/sec

Location	Coordinates	ϕ at $\bar{I}$ (n/cm^2-sec)	ϕ at I = 10^{12} p/sec (n/cm^2-sec)
29–R	Z = 44.08	–	–
30–R	Z = 50.36	–	–
31–R	Z = 56.64	3.48 E+4	3.05 E+5
32–R	Z = 62.92	9.47 E+5	8.29 E+6
32–1R	Z = 63.92	1.26 E+6	1.10 E+7
32–2R	Z = 64.92	1.04 E+6	9.12 E+6
32–3R	Z = 65.92	6.45 E+5	5.64 E+6
32–4R	Z = 66.92	4.91 E+5	4.30 E+6
32–5R	Z = 67.92	3.76 E+5	3.29 E+6
33–R	Z = 69.20	5.25 E+5	4.59 E+6
33–1R	Z = 70.48	5.25 E+5	4.59 E+6
33–2R	Z = 71.48	3.66 E+5	3.20 E+6
33–3R	Z = 72.48	2.69 E+5	2.35 E+6
33–4R	Z = 73.48	2.30 E+5	2.01 E+6
33–5R	Z = 74.48	2.30 E+5	2.01 E+6
34–R	Z = 75.48	2.71 E+5	2.37 E+6
35–R	Z = 81.76	1.09 E+5	9.54 E+5
36–R	Z = 88.08	6.63 E+4	5.80 E+5
78–R	Z = 56.6	1.14 E+4	9.94 E+4
79–R	Z = 62.9	6.96 E+5	6.09 E+6
80–R	Z = 69.2	1.06 E+5	9.25 E+5

Run V
Aluminum
Roof buckets
100-g samples

26.4 GeV/c
All installations
421-min. exposure
1.14 E+11 p/sec

Location	Coordinates	Net count rate (bkg. subtracted) at t_0 (cpm/g)	ϕ at $\bar{I}$ (n/cm^2-sec)	ϕ at I=10^{12} p/sec (n/cm^2-sec)
29–R	Z = 44.08	2.05 E+3	1.69 E+3	1.48 E+4
30–R	Z = 50.36	9.76 E+3	8.01 E+3	7.02 E+4
31–R	Z = 56.64	1.31 E+4	1.07 E+4	9.36 E+4
32–R	Z = 62.92	4.69 E+5	3.85 E+5	3.37 E+6
32–1R	Z = 63.92	6.97 E+5	5.73 E+5	5.02 E+6
32–2R	Z = 64.92	6.77 E+5	5.56 E+5	4.86 E+6
32–3R	Z = 65.92	4.24 E+5	3.48 E+5	3.04 E+6
32–4R	Z = 66.92	3.35 E+5	2.75 E+5	2.41 E+6
32–5R	Z = 67.92	2.24 E+5	1.84 E+5	1.61 E+6
33–R	Z = 69.20	2.63 E+5	2.16 E+5	1.89 E+6
33–1R	Z = 70.48	2.90 E+5	2.38 E+5	2.08 E+6
33–2R	Z = 71.48	2.31 E+5	1.89 E+5	1.65 E+6
33–3R	Z = 72.48	1.69 E+5	1.38 E+5	1.21 E+6
33–4R	Z = 73.48	1.27 E+5	1.04 E+5	9.10 E+5
33–5R	Z = 74.48	1.28 E+5	1.05 E+5	9.19 E+5
34–R	Z = 75.48	1.42 E+5	1.16 E+5	1.01 E+6
35–R	Z = 81.76	6.03 E+4	4.95 E+4	4.33 E+5
36–R	Z = 88.08	4.12 E+4	3.38 E+4	2.96 E+5
78–R	Z = 56.6	4.82 E+3	3.96 E+3	3.46 E+4
79–R	Z = 62.9	3.72 E+5	3.05 E+5	2.67 E+6
80–R	Z = 69.2	5.77 E+4	4.73 E+4	4.14 E+5

Run V
Carbon → Be^7
Roof buckets
90-min. exposure

26.4 GeV/c
Installation 1
1-in. detector
1.44 E+11 p/sec

Location	Coordinates	Net count rate (bkg subtracted) at t_0 (cpm)	Error (%)	ϕ at $\bar{I}$ (n/cm^2-sec)	ϕ at $I=10^{12}$ p/sec (n/cm^2-sec)
32–1R	Z = 63.92	1.15 E+1	10.4	1.31 E+6	9.12 E+6
32–2R	Z = 64.92	1.36 E+1		1.55 E+6	1.08 E+7
32–3R	Z = 65.92	2.26 E+1		2.58 E+6	1.80 E+7
32–4R	Z = 66.92	1.42 E+1		1.62 E+6	1.13 E+7
32–5R	Z = 67.92	1.21 E+1		1.38 E+6	9.60 E+6
33–R	Z = 69.20	4.1 E+0	27	4.7 E+5	3.3 E+6

Run V
Bismuth-mica
Roof buckets
~ 5-cm^2 detector

26.4 GeV/c
All installations
421-min. exposure
1.14 E+11 p/sec

Location	Coordinates	Track-counting error (%)	ϕ at $\bar{I}$ (n/cm^2-sec)	ϕ at $I=10^{12}$ p/sec (n/cm^2-sec)
32–R	Y = 1.74 Z = 62.92			
32–1R	Y = 1.74 Z = 63.92	8.	3.84 E+5	3.36 E+6
32–2R	Y = 1.74 Z = 64.92		7.88 E+5	6.89 E+6
32–3R	Y = 1.74 Z = 65.92	7.	7.77 E+5	6.80 E+6
32–4R	Y = 1.74 Z = 66.92	7.8	7.37 E+5	6.45 E+6
32–5R	Y = 1.74 Z = 67.92	8.1	3.29 E+5	2.88 E+6
33–R	Y = 1.74 Z = 69.20			
33–1R	Y= 1.74 Z = 70.48	11.7	2.03 E+5	1.78 E+6

Run V	26.4 GeV/c
Mercury	All installations
Roof buckets	421-min. exposure
432-g detector	1.14 E+11 p/sec

Location	Coordinates	Net count rate (bkg subtracted) at t_0 (cpm)	ϕ at I=10^{12} p/sec (n/cm^2-sec)
32–2	Y = 1.74 Z = 65.42	3.258 E+2	1.84 E+5
32–3	Y = 1.74 Z = 66.40	1.427 E+3	8.08 E+5
32–4	Y = 1.74 Z = 67.30	1.164 E+3	6.60 E+5
32–5	Y = 1.74 Z = 68.20	7.622 E+2	4.32 E+5
33–0	Y = 1.74 Z = 69.20	8.82 E+1	5.00 E+4

Run V	26.4 GeV/c
TLD	All installations
Roof buckets	421-min. exposure
22-mg samples	1.14 E+11 p/sec

Location	Coordinates	Indicated dose (rads/hour)
31–R	Z = 57.9	4.95 E+1
32–0R	Z = 62.9	1.89 E+3
32–1R	Z = 63.9	4.09 E+3
32–2R	Z = 64.9	4.51 E+3
32–3R	Z = 65.9	2.47 E+3
32–4R	Z = 66.9	1.31 E+3
32–5R	Z = 67.9	7.92 E+2
33–0R	Z = 69.2	9.71 E+2
33–1R	Z = 70.5	1.20 E+3
33–2R	Z = 71.5	1.05 E+3
33–3R	Z = 72.5	6.44 E+2
33–4R	Z = 73.5	5.30 E+2
33–5R	Z = 74.5	4.11 E+2
34–R	Z = 75.5	4.55 E+2
35–R	Z = 81.8	2.23 E+2
36–R	Z = 88.1	1.62 E+2
78–R	Z = 56.6	1.54 E+1
79–R	Z = 62.9	8.65 E+2
80–R	Z = 69.2	1.51 E+2

Run V — 26.4 GeV/c
Aluminum — All installations
Orbit holes — 421-min. exposure
Detector size: 500 g — 1.14 E+11 p/sec

Location	Coordinates	Detector size (g)	Net count rate (bkg subtracted) at t_0 (cpm)	ϕ at $\bar{I}$ (n/cm^2-sec)	ϕ at I=10^{12} p/sec (n/cm^2-sec)
31–330	Y = 3.53 Z = 56.64	500	9.28 E+2	2.04 E+2	1.78 E+3
31–390	Y = 4.12 Z = 56.64		1.96 E+2	4.32 E+1	3.78 E+2
34–330	Y = 3.63 Z = 75.48		1.91 E+4	4.20 E+3	3.67 E+4
34–390	Y = 4.22 Z = 75.48		5.08 E+3	1.12 E+3	9.80 E+3
35–330	Y = 3.45 Z = 81.76		1.32 E+4	2.92 E+3	2.55 E+4
35–390	Y = 4.04 Z = 81.76		2.99 E+3	6.58 E+2	5.76 E+3
36–330	Y = 3.31 Z = 88.08		1.20 E+4	2.64 E+3	2.31 E+4
36–390	Y = 3.90 Z = 88.08		2.66 E+3	5.85 E+2	5.12 E+3
33–V	Y = 103.2 Z = 70.6		6.11 E+4	1.34 E+4	1.17 E+5

Run V — 26.4 GeV/c
Aluminum — All installations, except installation 1
Orbit holes; streaming — only at location 32–330
Detector size: 555g

Location	Coordinates	Exposure time (min)	Net count rate (bkg subtracted) at t_0 (cpm)	$\bar{I}$ p/sec	ϕ at I (n/cm^2-sec)	ϕ at I=10^{12} p/sec (n/cm^2-sec)
32–330	Y = 3.67 Z = 62.92	90	1.59 E+4	1.44 E+11	1.12 E+4	7.79 E+4
32–390	Y = 4.26 Z = 62.92	421	1.34 E+4	1.14 E+11	2.28 E+3	1.99 E+4
32–450	Y = 4.85 Z = 62.92	421	3.39 E+3	1.14 E+11	5.78 E+2	5.06 E+3
32–510	Y = 5.44 Z = 62.92	421	9.30 E+2	1.14 E+11	1.59 E+2	1.39 E+3
32–570	Y = 6.03 Z = 62.92	421	2.41 E+2	1.14 E+11	4.11 E+1	3.60 E+2
33–330	Y = 3.42 Z = 69.20	421	1.08 E+5	1.14 E+11	1.85 E+4	1.62 E+5
33–390	Y = 4.01 Z = 69.20	421	2.52 E+4	1.14 E+11	4.30 E+3	3.76 E+4
33–450	Y = 4.60 Z = 69.20	421	6.22 E+3	1.14 E+11	1.06 E+3	9.27 E+3
33–510	Y = 5.19 Z = 69.20	421	1.60 E+3	1.14 E+11	2.73 E+2	2.39 E+3
33–570	Y = 5.78 Z = 69.20	421	4.39 E+2	1.14 E+11	7.48 E+1	6.54 E+2

Run V
Aluminum
Ring top
3300-g detector

26.4 GeV/c
All installations
421-min. exposure
1.14 E+11 p/sec

Location	Coordinates	Net count rate (bkg subtracted) at t_0 (cpm)	ϕ at $\bar{I}$ (n/cm^2-sec)	ϕ at I=10^{12} p/sec (n/cm^2-sec)
32/0	Y = 6.42 Z = 62.92	3.11 E+2	1.51 E+1	1.32 E+2

Run V — 26.4 GeV/c
Carbon — Installation 2
Ring top — 5-in. detector
76-min. exposure — 1.46 E+11 p/sec

Location	Coordinates	Net count rate (bkg subtracted) at t_0 (cpm)	Error (%)	ϕ at $\bar{I}$ (n/cm^2-sec)	ϕ at I=10^{12} p/sec (n/cm^2-sec)
24	Y = 6.35 Z = 12.7	3.77 E+1	34.8	3.9 E-1	2.67 E-0
26	Y = 6.38 Z = 25.24	1.94 E+1	63.	2.0 E-2	1.37 E-1
28	Y = 6.38 Z = 37.80	6.34 E+1	22.5	6.6 E-1	4.51 E-0
30	Y = 6.42 Z = 50.36	5.66 E+1	32.5	5.9 E-1	4.04 E-0
31	Y = 6.40 Z = 56.64	9.63 E+1	18.6	1.00 E+0	6.84 E+0
32	Y = 6.42 Z = 62.92	5.137 E+3		5.34 E+1	3.65 E+2
33	Y = 6.39 Z = 69.20	7.509 E+3		7.81 E+1	5.34 E+2
34	Y = 6.29 Z = 75.48	3.900 E+3		4.06 E+1	2.78 E+2
35	Y = 6.30 Z = 81.76	1.385 E+3		1.44 E+1	9.85 E+1
39	Y = 6.32 Z = 106.88	9.86 E+1	22.9	1.03 E+0	7.05 E+0

Run V — 26.4 GeV/c
Carbon — Installation 1
Radial holes — 90-min. exposure
1.44 E+11 p/sec

Location	Coordinates	Detector size (in.)	Net count rate (bkg subtracted) at t_0 (cpm)	ϕ at $\bar{I}$ (n/cm^2-sec)	ϕ at I=10^{12} p/sec (n/cm^2-sec)
33–105	X = 105.0 Z = 69.20	5	1.35 E+5	1.367 E+3	9.51 E+3
33–109	X = 109.0 Z = 69.20	8	2.21 E+1	$<$ 2 E-1	

Run V
Gold foils
Vacuum vessel
~ 0.5-g detector

26.4 GeV/c
Installations 1 and 2
421-min. exposure

Location	Coordinates	Net count rate (bkg subtracted) at t_0 (cpm)	ϕ at $I = 10^{12}$ p/sec (n/cm^2-sec)
32/0	Z = 63.12	6.65 E+2	3.29 E+9
32/20	Z = 63.32	9.18 E+2	4.54 E+9
32/40	Z = 63.52	6.99 E+2	3.45 E+9
32/60	Z = 63.72	5.55 E+2	2.74 E+9
32/80	Z = 63.92	3.59 E+2	1.77 E+9

Run V
Sulfur
Vacuum vessel
4-g detector

26.4 GeV/c
All installations
421-min. exposure
1.14 E+11 p/sec

Location	Coordinates	ϕ at $\bar{I}$ (n/cm^2-sec)	ϕ at $I=10^{12}$ p/sec (n/cm^2-sec)
32/0	Z = 63.12	5.74 E+7	5.02 E+8
32/10	Z = 63.22	5.20 E+7	4.55 E+8
32/20	Z = 63.32	5.58 E+7	4.88 E+8
32/30	Z = 63.42	3.76 E+7	3.29 E+8
32/40	Z = 63.52	3.07 E+7	2.69 E+8
32/50	Z = 63.62	2.66 E+7	2.33 E+8
32/60	Z = 63.72	2.32 E+7	2.03 E+8
32/70	Z = 63.82	2.77 E+7	2.42 E+8
32/80	Z = 63.92	2.81 E+7	2.46 E+8
32/90	Z = 64.02	4.58 E+7	4.01 E+8
32/100	Z = 64.12	5.02 E+7	4.39 E+8
32/110	Z = 64.22	3.71 E+7	3.25 E+8

Run V
Mercury
Magnet 32 gap

26.4 GeV/c
432-g detector
X = -20 cm

Installation	Location	Coordinates	Exposure time (min.)	Net count rate (bkg subtracted) at t_0 (cpm)	Error (%)	$\bar{I}$ (p/sec)	ϕ at $I=10^{12}$ p/sec (n/cm^2-sec)
All	Segment C	Y = 99.80 Z = 65.46	421	1.199 E+2		1.14 E+11	6.97 E+4
1,2	Segment E	Y = 99.80 Z = 66.31	181	1.456 E+1	5.5	1.33 E+11	1.3 E+4
1,2	Segment G	Y = 99.80 Z = 67.18	181	7.352 E+0	9.2	1.33 E+11	6.4 E+3
1,2	Coil box behind Segment J	Y = 0.30 Z = 69.0	181	1.014 E+3		1.33 E+11	8.82 E+5

Run V
Carbon → Be^7
Magnet–32 gap
90-min. exposure

26.4 GeV/c
Installation 1
2-in. detector
1.44 E+11 p/sec

Location	Coordinates	Net count rate (bkg subtracted) at t_0 (cpm)	ϕ at $\bar{I}$ (n/cm^2-sec)	ϕ at $I=10^{12}$ p/sec (n/cm^2-sec)
C–A	Y = 99.80 Z = 64.64	2.06 E+3	5.87 E+7	4.08 E+8
C–C	Y = 99.80 Z = 65.46	1.03 E+3	2.93 E+7	2.04 E+8
C–E	Y = 99.80 Z = 66.31	6.12 E+2	1.74 E+7	1.21 E+8
C–G	Y = 99.80 Z = 67.18	5.28 E+2	1.50 E+7	1.04 E+8
C–I	Y = 99.80 Z = 68.00	5.72 E+2	1.63 E+7	1.13 E+8

Run V
Sulfur
Angular distribution
4-g detector

26.4 GeV/c
All installations
421 min. exposure
1.14 E+11 p/sec

Location (deg)	Coordinates	ϕ at $\bar{I}$ (n/cm^2-sec)	ϕ at I=10^{12} p/sec (n/cm^2-sec)
25–25	Y = 0.11 Z = 63.15	3.28 E+7	2.87 E+8
25–45	Y = 0.18 Z = 63.10	1.76 E+7	1.54 E+8
25–65	Y = 0.23 Z = 63.02	1.08 E+6	9.43 E+7
25–90	Y = 0.25 Z = 62.92	7.53 E+6	6.59 E+7
100–3	Y = 0.05 Z = 63.92	3.76 E+7	3.29 E+8
100–10	Y = 0.18 Z = 63.90	2.07 E+7	1.81 E+8
100–20	Y = 0.35 Z = 63.86	1.03 E+6	9.05 E+7
100–30	Y = 0.50 Z = 63.78	6.69 E+6	5.85 E+7
100–40	Y = 0.64 Z = 63.68	4.71 E+6	4.12 E+7
100–60	Y = 0.87 Z = 63.42	2.79 E+6	2.44 E+7
100–90	Y = 1.00 Z = 62.92	-----	-----

Run V
Aluminum → Na^{22}
Angular distribution
169-g detector

26.4 GeV/c
All installations
421-min. exposure
1.14 E+11 p/sec

Location (deg)	Coordinates	ϕ at $\bar{I}$ (n/cm^2-sec)	ϕ at $I = 10^{12}$ p/sec (n/cm^2-sec)
25–25	Y = 0.11 Z = 63.15	9.72 E+7	8.50 E+8
25–45	Y = 0.18 Z = 63.10	3.30 E+7	2.89 E+8
25–65	Y = 0.23 Z = 63.02	1.31 E+7	1.15 E+8
25–90	Y = 0.25 Z = 62.92	6.73 E+6	5.89 E+7
100–3	Y = 0.05 Z = 63.92	1.42 E+8	1.24 E+9
100–10	Y = 0.18 Z = 63.90	3.67 E+7	3.21 E+8
100–20	Y = 0.35 Z = 63.86	1.80 E+7	1.57 E+8
100–30	Y = 0.50 Z = 63.78	9.18 E+6	8.03 E+7
100–40	Y = 0.64 Z = 63.68	4.85 E+6	4.24 E+7
100–60	Y = 0.87 Z = 63.42	2.14 E+6	1.87 E+7
100–90	Y = 1.00 Z = 62.92		

Run V
Aluminum
Angular distribution
16.9-g detector

26.4 GeV/c
All installations
421-min. exposure
1.14 E+11 p/sec

Location (deg)	Coordinates	Net count rate (bkg subtracted) at t_0 (cpm)	ϕ at $\bar{I}$ (n/cm^2-sec)	ϕ at $I=10^{12}$ p/sec (n/cm^2-sec)
25–25	Y = 0.11 Z = 63.15	5.85 E+5	2.97 E+7	2.60 E+8
25–45	Y = 0.18 Z = 63.10	2.55 E+5	1.29 E+7	1.13 E+8
25–65	Y = 0.23 Z = 63.02	1.27 E+5	6.44 E+6	5.63 E+7
25–90	Y = 0.25 Z = 62.92	8.14 E+4	4.12 E+6	3.60 E+7
100–3	Y = 0.05 Z = 63.92	7.31 E+5	3.70 E+7	3.24 E+8
100–10	Y = 0.18 Z = 63.90	2.44 E+5	1.23 E+7	1.08 E+8
100–20	Y = 0.35 Z = 63.86	1.45 E+6	6.22 E+6	5.44 E+7
100–30	Y = 0.50 Z = 63.78	8.55 E+5	3.67 E+6	3.21 E+7
100–40	Y = 0.64 Z = 63.68	5.45 E+5	2.34 E+6	2.05 E+7
100–60	Y = 0.87 Z = 63.42	2.94 E+5	1.26 E+6	1.10 E+7

Run V
Carbon
Angular distribution
90-min. exposure

26.4 GeV/c
Installation 1
1-in. detector
1.44 E+11

Location	Coordinates	ϕ at $\bar{I}$ (n/cm^2-sec)	ϕ at I=10^{12} p/sec (n/cm^2-sec)
3 deg 100cm	Y = 0.05 Z = 63.92	2.46 E+8	1.71 E+9
10 deg 100cm	Y = 0.18 Z = 63.90	8.10 E+7	5.64 E+8
20 deg 100 cm	Y = 0.35 Z = 63.86	3.84 E+7	2.62 E+8
25 deg 25 cm	Y = 0.11 Z = 63.15	1.60 E+8	1.11 E+9
30 deg 100 cm	Y = 0.50 Z = 63.78	1.81 E+7	1.26 E+8
40 deg 100 cm	Y = 0.64 Z = 63.68	1.00 E+7	6.96 E+7
45 deg 25 cm	Y = 0.18 Z = 63.10	5.48 E+7	3.81 E+8
60 deg 100 cm	Y = 0.87 Z = 63.42	4.07 E+6	2.83 E+7
65 deg 25 cm	Y = 0.23 Z = 63.02	2.09 E+7	1.45 E+8
90 deg 25 cm	Y = 0.25 Z = 62.92	1.23 E+7	8.56 E+7

Run V
Carbon → Be^7
Angular distribution
90-min. exposure

26.4 GeV/c
Installation 1
1-in. detector
1.44 E+11 p/sec

Location (deg)	Coordinates	ϕ at $\bar{I}$ (n/cm^2-sec)	ϕ at I=10^{12} p/sec (n/cm^2-sec)
25–25	Y = 0.11 Z = 63.15	1.25 E+8	8.70 E+8
25–45	Y = 0.18 Z = 63.10	4.25 E+7	2.96 E+8
25–65	Y = 0.23 Z = 63.02	1.48 E+7	1.03 E+8
25–90	Y = 0.25 Z = 62.92	8.40 E+6	5.84 E+7
100–3	Y = 0.05 Z = 63.92	1.74 E+8	1.21 E+9
100–10	Y = 0.18 Z = 63.90	5.81 E+7	4.04 E+8
100–20	Y = 0.35 Z = 63.86	2.50 E+7	1.74 E+8
100–30	Y = 0.50 Z = 63.78	1.21 E+7	8.42 E+7
100–40	Y = 0.64 Z = 63.68	5.56 E+6	3.87 E+7
100–60	Y = 0.87 Z = 63.42	2.91 E+6	2.02 E+7

Run V
Bismuth-mica
Angular distribution
~ 5-cm^2 detector

26.4 GeV/c
All installations
421-min. exposure
1.14 E+11 p/sec

Location	Coordinates	Track-counting error (%)	ϕ at $\bar{I}$ (n/cm^2-sec)	ϕ at I=10^{12} p/sec (n/cm^2-sec)
25–25°	Y = 0.11 Z = 63.15		2.53 E+7	2.21 E+8
25–45°	Y = 0.18 Z = 63.10		9.43 E+6	8.25 E+7
25–65°	Y = 0.23 Z = 63.02		2.79 E+6	2.44 E+7
25–90°	Y = 0.25 Z = 62.92	7.	5.10 E+5	4.46 E+6
100–3°	Y = 0.05 Z = 63.92			
100–10°	Y = 0.18 Z = 63.90		1.70 E+7	1.49 E+8
100–20°	Y = 0.35 Z = 63.86		6.86 E+6	6.0 E+7
100–30°	Y = 0.50 Z = 63.78		2.61 E+6	2.28 E+7
100–40°	Y = 0.64 Z = 63.68		1.22 E+6	1.07 E+7
100–60°	Y = 0.87 Z = 63.42	8.4	3.57 E+5	3.12 E+6
100–90°	Y = 1.00 Z = 62.92			

Run V
Mercury

26.4 GeV/c
Angular distribution

Installation	Location	Coordinates	Exposure time (min.)	Detector size (g)	Net count rate (bkg subtracted) at t_0 (cpm)	$\bar{I}$ (p/sec)	ϕ at $I=10^{12}$ p/sec (n/cm^2-sec)
All	3°–100 cm	Y = 0.05 Z = 63.92	421	152	1.597 E+5	1.14 E+11	2.57 E+8
All	10°–100 cm	Y = 0.18 Z = 63.90	421	152	4.153 E+4	1.14 E+11	6.69 E+7
All	20°–100 cm	Y = 0.35 Z = 63.86	421	152	1.425 E+4	1.14 E+11	2.30 E+7
All	25°–25 cm	Y = 0.11 Z = 63.15	421	152	3.065 E+4	1.14 E+11	4.94 E+7
All	30°–100 cm	Y = 0.50 Z = 63.78	421	152	1.8509 E+3	1.14 E+11	2.98 E+6
All	40°–100 cm	Y = 0.64 Z = 63.68	421	152	3.065 E+2	1.14 E+11	4.94 E+5
All	45°–25 cm	Y = 0.18 Z = 63.10	421	152	2.397 E+3	1.14 E+11	3.77 E+6
All	60°–100 cm	Y = 0.87 Z = 63.42	421	432	6.011 E+1	1.14 E+11	3.42 E+4
All	65°–25 cm	Y = 0.23 Z = 63.02	421	152	1.580 E+2	1.14 E+11	2.55 E+5
1,2	90°–25 cm	Y = 0.25 Z = 62.92	181	152	1.001 E+1	1.33 E+11	2.43 E+4

Run V
Bismuth-mica
Magnet top
~ 5-cm^2 detector

26.4 GeV/c
All installations
421-min. exposure
1.14 E+11 p/sec

Location	Coordinates	Track-counting error (%)	ϕ at $\bar{I}$ (n/cm^2-sec)	ϕ at I=10^{12} p/sec (n/cm^2-sec)
m 32 a o	Y = 0.60 Z = 64.66		8.17 E+6	7.15 E+7
m 32 a	Y = 0.60 Z = 65.09		2.10 E+6	1.84 E+7
m 32 b	Y = 0.60 Z = 65.30	5.5	8.23 E+5	7.20 E+6
m 32 c	Y = 0.60 Z = 65.73	11.6	2.07 E+5	1.81 E+6
m 32 d	Y = 0.60 Z = 66.15	14.	1.29 E+5	1.13 E+6
m 32 e	Y = 0.60 Z = 66.58	15.	1.09 E+5	9.54 E+5
m 32 f	Y = 0.60 Z = 67.00	15.	1.13 E+5	9.89 E+5
m 32 g	Y = 0.60 Z = 67.43	16.5	1.05 E+5	9.19 E+5
m 32 h	Y = 0.60 Z = 67.86	21.	6.06 E+4	5.30 E+5
m 32 j l		5.1	1.81 E+6	1.58 E+7

Run V
Carbon → Be^7
Magnet-32 top
90-min. exposure

26.4 GeV/c
Installation 1
2-in. detector
1.44 E+11 p/sec

Location	Coordinates	Net count rate (bkg subtracted) at t_0 (cpm)	Error (%)	ϕ at $\bar{I}$ (n/cm^2-sec)	ϕ at I=10^{12} p/sec (n/cm^2-sec)
B	Y = 0.60 Z = 65.08	6.19 E+1		1.77 E+6	1.23 E+7
C	Y = 0.60 Z = 65.46	2.17 E+1	6.5	6.2 E+5	4.3 E+6
D	Y = 0.60 Z = 65.88	1.26 E+1	8.7	3.6 E+5	2.5 E+6
E	Y = 0.60 Z = 66.31	8.0 E+0	10.2	2.3 E+5	1.6 E+6
G	Y = 0.60 Z = 67.18	8.6 E+0	10.3	2.4 E+5	1.7 E+6
J–1	Y = 0.30 Z = 69.0	9.01 E+1		2.56 E+6	1.78 E+7

Run V
Sulfur
Vertical profile array
4-g detector

26.4 GeV/c
All installations
421-min. exposure
1.14 E+11 p/sec

Location	Coordinates	ϕ at $\bar{I}$ (n/cm^2-sec)	ϕ at I=10^{12} p/sec (n/cm^2-sec)
32/0/100	Y = 0.74 Z = 62.92	2.32 E+6	2.03 E+7
32/0/50	Y = 1.24 Z = 62.92	1.37 E+5	1.24 E+6
32/0/B	Y = 1.74 Z = 62.92	9.48 E+5	8.29 E+6
32/0/H	Y = 2.14 Z = 62.92	7.84 E+5	6.86 E+6
32/1/100	Y = 0.74 Z = 63.92	4.62 E+6	4.04 E+7
32/1/50	Y = 1.24 Z = 63.92	2.21 E+6	1.93 E+7
32/1/B	Y = 1.74 Z = 63.92	1.26 E+6	1.10 E+7
32/1/H	Y = 2.14 Z = 63.92	9.33 E+5	8.16 E+6
m 32 o a	Y = 0.60 Z = 64.66	5.38 E+6	4.71 E+7
m 32 a	Y = 0.60 Z = 65.09	2.83 E+6	2.48 E+7
32/2/100	Y = 0.74 Z = 64.92	2.17 E+6	1.90 E+7
32/2/50	Y = 1.24 Z = 64.92	1.50 E+6	1.31 E+7
32/2/B	Y = 1.74 Z = 64.92	1.04 E+6	9.12 E+6
32/2/H	Y = 2.14 Z = 64.92	9.38 E+5	8.21 E+6
m 32 b	Y = 0.60 Z = 65.30	1.42 E+6	1.24 E+7
m 32 c	Y = 0.60 Z = 65.73	5.59 E+5	4.89 E+6
32/3/100	Y = 0.74 Z = 65.92	4.64 E+5	4.06 E+6
32/3/50	Y = 1.24 Z = 65.92	6.20 E+5	5.42 E+6
32/3/B	Y = 1.74 Z = 65.92	6.46 E+5	5.65 E+6
32/3/H	Y = 2.14 Z = 65.92	6.39 E+5	5.59 E+6
m 32 d	Y = 0.60 Z = 66.15	4.08 E+5	3.57 E+6
m 32 e	Y = 0.60 Z = 66.58	3.39 E+5	2.97 E+6
m 32 f	Y = 0.60 Z = 67.00	3.18 E+5	2.78 E+6
32/4/100	Y = 0.74 Z = 66.92	3.85 E+5	3.37 E+6
32/4/50	Y = 1.24 Z = 66.92	4.53 E+5	3.96 E+6

Location	Coordinates	ϕ at $\bar{I}$ (n/cm^2-sec)	ϕ at I=10^{12} p/sec (n/cm^2-sec)
32/4/B	Y = 1.74 Z = 66.92	4.90 E+5	4.29 E+6
32/4/H	Y = 2.14 Z = 66.92	4.75 E+5	4.16 E+6
m 32 g	Y = 0.60 Z = 67.43	3.31 E+5	2.90 E+6
m 32 h	Y = 0.60 Z = 67.86	2.83 E+5	2.48 E+6
32/5/100	Y = 0.74 Z = 67.92	3.90 E+5	3.41 E+6
32/5/50	Y = 1.24 Z = 67.92	3.76 E+5	3.29 E+6
32/5/B	Y = 1.74 Z = 67.92	4.18 E+5	3.66 E+6
32/5/H	Y = 2.14 Z = 67.92	4.59 E+5	4.02 E+6
m 32 i	Y = 0.60 Z = 68.28	2.77 E+5	2.42 E+6
m 32 j	Y = 0.60 Z = 68.50	2.46 E+5	2.15 E+6
m 32 j o	Y = 0.60 Z = 68.92	5.13 E+5	4.49 E+6
m 32 j l	Y = 0.30 Z = 69.0		
s 32 a	Y = 0.60 Z = 69.36	2.08 E+6	1.82 E+7
33/0/100	Y = 0.74 Z = 69.48	1.23 E+6	1.08 E+7
33/0/50	Y = 1.24 Z = 69.48	7.48 E+5	6.54 E+6
33/0/B	Y = 1.74 Z = 69.48	5.25 E+5	4.59 E+6
33/0/H	Y = 2.14 Z = 69.48	4.55 E+5	3.98 E+6
s 33 b	Y = 0.60 Z = 69.79	2.57 E+6	2.25 E+7
s 33 c	Y = 0.60 Z = 70.23	1.55 E+6	1.36 E+7
33/1/100	Y = 0.74 Z = 70.48	1.41 E+6	1.23 E+7
33/1/50	Y = 1.24 Z = 70.48	7.70 E+5	6.74 E+6
33/1/B	Y = 1.14 Z = 70.48	5.25 E+5	4.59 E+6
33/1/H	Y = 2.14 Z = 70.48	4.10 E+5	3.59 E+6
m 33 o a	Y = 0.60 Z = 70.66	1.23 E+6	1.08 E+7
m 33 a	Y = 0.60 Z = 71.09	5.65 E+5	4.94 E+6
m 33 b	Y = 0.60 Z = 71.30	3.15 E+5	2.76 E+6
33/2/100	Y = 0.74 Z = 71.48	2.88 E+5	2.52 E+6
33/2/50	Y = 1.24 Z = 71.48	3.94 E+5	3.45 E+6

Location	Coordinates	ϕ at $\bar{I}$ (n/cm^2-sec)	ϕ at I=10^{12} p/sec (n/cm^2-sec)
33/2/B	Y = 1.74 Z = 71.48	3.67 E+5	3.21 E+6
33/2/H	Y = 2.14 Z = 71.48	3.49 E+5	3.05 E+6
m 33 c	Y = 0.60 Z = 71.73	2.25 E+5	1.97 E+6
m 33 d	Y = 0.60 Z = 72.15	2.16 E+5	1.89 E+6
33/3/100	Y = 0.74 Z = 72.48	2.30 E+5	2.01 E+6
33/3/50	Y = 1.24 Z = 72.48	2.86 E+5	2.50 E+6
33/3/B	Y = 1.74 Z = 72.48	2.67 E+5	2.34 E+6
33/3/H	Y = 2.14 Z = 72.48	2.88 E+5	2.52 E+6
m 33 e	Y = 0.60 Z = 72.58	2.02 E+5	1.77 E+6
m 33 f	Y = 0.60 Z = 73.00	2.07 E+5	1.81 E+6
m 33 g	Y = 0.60 Z = 73.43	2.10 E+5	1.84 E+6
33/4/100	Y = 0.74 Z = 73.48	2.23 E+5	1.95 E+6
33/4/50	Y = 1.24 Z = 73.48	2.37 E+5	2.07 E+6
33/4/B	Y = 1.74 Z = 73.48	2.30 E+5	2.01 E+6
33/4/H	Y = 2.14 Z = 73.48		2.03 E+6
m 33 h	Y = 0.60 Z = 73.86	2.00 E+5	1.75 E+6
m 33 i	Y = 0.60 Z = 74.28	1.62 E+5	1.42 E+6
33/5/100	Y = 0.74 Z = 74.48	2.02 E+5	1.77 E+6
33/5/50	Y = 1.24 Z = 74.48	2.50 E+5	2.19 E+6
33/5/B	Y = 1.74 Z = 74.48	2.30 E+5	2.01 E+6
33/5/H	Y = 2.14 Z = 74.48	2.34 E+5	2.05 E+6
m 33 j	Y = 0.60 Z = 74.50	1.52 E+5	1.33 E+6
m 33 j o	Y = 0.60 Z = 74.92	2.30 E+5	2.01 E+6
34/0/100	Y = 0.74 Z = 75.48	5.04 E+5	4.41 E+6
34/0/50	Y = 1.24 Z = 75.48	3.18 E+5	2.78 E+6
34/0/B	Y = 1.74 Z = 75.48	2.72 E+5	2.38 E+6
34/0/H	Y = 2.14 Z = 75.48	2.23 E+5	1.95 E+6

Run V
Aluminum
Vertical-profile array

26.4 GeV/c
All installations
421-min. exposure
1.14 E+11 p/sec

Location	Coordinates	Detector size (g)	Net count rate (bkg subtracted) at t_0 (cpm)	Error (%)	ϕ at $\bar{I}$ (n/cm^2-sec)	ϕ at I=10^{12} p/sec (n/cm^2-sec)
32/0/100	Y = 0.74 Z = 62.92	16.9	2.47 E+5		1.06 E+6	9.27 E+6
32/0/50	Y = 1.24 Z = 62.92	16.9	1.31 E+5		5.62 E+5	4.92 E+6
32/0/B	Y = 1.74 Z = 62.92	100	4.69 E+5		3.85 E+5	3.37 E+6
32/0/H	Y = 2.14 Z = 62.92					
32/1/100	Y = 0.74 Z = 63.92	16.9	5.48 E+5		2.35 E+6	2.06 E+7
32/1/50	Y = 1.24 Z = 63.92	16.9	2.27 E+5		9.74 E+5	8.52 E+6
32/1/B	Y = 1.74 Z = 63.92	100	6.97 E+5		5.73 E+5	5.01 E+6
32/1/H	Y = 2.14 Z = 63.92					
m 32 o a	Y = 0.60 Z = 64.66	16.9	7.93 E+5		3.40 E+6	2.97 E+7
m 32 a	Y = 0.60 Z = 65.09	16.9	3.79 E+5		1.63 E+6	1.43 E+7
32/2/100	Y = 0.74 Z = 64.92	16.9	3.38 E+5		1.45 E+6	1.27 E+7
32/2/50	Y = 1.24 Z = 64.92	16.9	2.07 E+5		8.88 E+5	7.77 E+6
32/2/B	Y = 1.74 Z = 64.92	100	6.77 E+5		5.66 E+5	4.86 E+6
32/2/H	Y = 2.14 Z = 64.92					
m 32 b	Y = 0.60 Z = 65.30	16.9	1.71 E+5		7.33 E+5	6.41 E+6
m 32 c	Y = 0.60 Z = 65.73	16.9	6.53 E+4		2.80 E+5	2.45 E+6
32/3/100	Y = 0.74 Z = 65.92	16.9	5.11 E+4		2.19 E+5	1.92 E+6
32/3/50	Y = 1.24 Z = 65.92	16.9	9.95 E+4		4.27 E+5	3.74 E+6
32/3/B	Y = 1.74 Z = 65.92	100	4.24 E+5		3.48 E+5	3.04 E+6
32/3/H	Y = 2.14 Z = 65.92					
m 32 d	Y = 0.60 Z = 66.15	16.9	4.44 E+4		1.91 E+5	1.67 E+6
m 32 e	Y = 0.60 Z = 66.58	16.9	3.62 E+4		1.55 E+5	1.36 E+6
m 32 f	Y = 0.60 Z = 67.00	16.9	3.40 E+4		1.46 E+5	1.28 E+6
32/4/100	Y = 0.74 Z = 66.92	16.9	3.60 E+4		1.55 E+5	1.36 E+6
32/4/50	Y = 1.24 Z = 66.92	16.9	4.39 E+4		1.88 E+5	1.64 E+6

Location	Coordinates	Detector size (g)	Net count rate (bkg subtracted) at t_0 (cpm)	Error (%)	ϕ at $\bar{I}$ (n/cm^2-sec)	ϕ at I=10^{12} p/sec (n/cm^2-sec)
32/4/B	Y = 1.74 Z = 66.92	100	3.35 E+5		2.75 E+5	2.41 E+6
32/4/H	Y = 2.14 Z = 66.92					
m 32 g	Y = 0.60 Z = 67.43	16.9	3.04 E+4		1.32 E+5	1.15 E+6
m 32 h	Y = 0.60 Z = 67.86	16.9	2.68 E+4		1.15 E+5	1.01 E+6
32/5/100	Y = 0.74 Z = 67.92	16.9	2.62 E+4		1.13 E+5	9.89 E+6
32/5/50	Y = 1.24 Z = 67.92	16.9	3.75 E+4		1.61 E+5	1.41 E+6
32/5/B	Y = 1.74 Z = 67.92	100	2.24 E+5		1.84 E+5	1.61 E+6
32/5/H	Y = 2.14 Z = 67.92					
m 32 i	Y = 0.60 Z = 68.28	16.9	2.39 E+4		1.03 E+5	9.01 E+5
m 32 j	Y = 0.60 Z = 68.50	16.9	2.35 E+4		1.01 E+5	8.84 E+5
m 32 j o	Y = 0.60 Z = 68.92	16.9	4.81 E+4		2.06 E+5	1.80 E+6
m 32 j l	Y = 0.30 Z = 69.0	16.9	3.41 E+5		1.46 E+6	1.28 E+7
s 32 a	Y = 0.60 Z = 69.36	16.9	2.71 E+5		1.17 E+6	1.02 E+7
33/0/100	Y = 0.74 Z = 69.48	16.9	1.29 E+5		5.55 E+5	4.86 E+6
33/0/50	Y = 1.24 Z = 69.48	16.9	7.07 E+4		3.03 E+5	2.65 E+6
33/0/B	Y = 1.74 Z = 69.48	100	2.63 E+5		2.16 E+5	1.89 E+6
33/0/H	Y = 2.14 Z = 69.48					
s 33 b	Y = 0.60 Z = 69.79	16.9	3.11 E+5		1.34 E+6	1.17 E+7
s 33 c	Y = 0.60 Z = 70.23	16.9	1.86 E+5		8.00 E+5	7.00 E+6
33/1/100	Y = 0.74 Z = 70.48	16.9	1.65 E+5		7.09 E+5	6.20 E+6
33/1/50	Y = 1.24 Z = 70.48	16.9	7.77 E+4		3.34 E+5	2.92 E+6
33/1/B	Y = 1.74 Z = 70.48	100	2.90 E+5		2.38 E+5	2.08 E+6
33/1/H	Y = 2.14 Z = 70.48					
m 33 o a	Y = 0.60 Z = 70.66	16.9	1.70 E+5		7.31 E+5	6.40 E+6
m 33 a	Y = 0.60 Z = 71.09	16.9	6.49 E+4		2.79 E+5	2.44 E+6
m 33 b	Y = 0.60 Z = 71.30	16.9	3.63 E+4		1.56 E+5	1.36 E+6
33/2/100	Y = 0.74 Z = 71.48	16.9	3.16 E+4		1.35 E+5	1.18 E+6
33/2/50	Y = 1.24 Z = 71.48	16.9	4.81 E+4		2.06 E+5	1.80 E+6

Location	Coordinates	Detector size (g)	Net count rate (bkg subtracted) at t_0 (cpm)	Error (%)	ϕ at $\bar{I}$ (n/cm^2-sec)	ϕ at I=10^{12} p/sec (n/cm^2-sec)
33/2/B	Y = 1.74 Z = 71.48	100	2.31 E+5		1.89 E+5	1.65 E+6
33/2/H	Y = 2.14 Z = 71.48					
m 33 c	Y = 0.60 Z = 71.73	16.9	2.32 E+4		9.96 E+4	8.71 E+5
m 33 d	Y = 0.60 Z = 72.15	16.9	2.03 E+4		8.72 E+4	7.63 E+5
33/3/100	Y = 0.74 Z = 72.48	16.9	2.13 E+4		9.16 E+4	8.01 E+5
33/3/50	Y = 1.24 Z = 72.48	16.9	2.91 E+4		1.25 E+5	1.09 E+6
33/3/B	Y = 1.74 Z = 72.48	100	1.69 E+5		1.38 E+5	1.21 E+6
33/3/H	Y = 2.14 Z = 72.48					
m 33 e	Y = 0.60 Z = 72.58	16.9	2.07 E+4		8.87 E+4	7.76 E+5
m 33 f	Y = 0.60 Z = 73.00	16.9	2.16 E+4		9.29 E+4	8.13 E+5
m 33 g	Y = 0.60 Z = 73.43	16.9	2.17 E+4		9.34 E+4	8.17 E+5
33/4/100	Y = 0.74 Z = 73.48	16.9	2.17 E+4		9.30 E+4	8.14 E+5
33/4/50	Y = 1.24 Z = 73.48	16.9	2.37 E+4		1.02 E+5	8.92 E+5
33/4/B	Y = 1.74 Z = 73.48	100	1.27 E+5		1.04 E+5	9.10 E+5
33/4/H	Y = 2.14 Z = 73.48					
m 33 h	Y = 0.60 Z = 73.86	16.9	1.88 E+4		8.07 E+4	7.06 E+5
m 33 i	Y = 0.60 Z = 74.28	16.9	1.69 E+4		7.27 E+4	6.36 E+5
33/5/100	Y = 0.74 Z = 74.48	16.9	1.92 E+4		8.24 E+4	7.21 E+5
33/5/50	Y = 1.24 Z = 74.48	16.9	2.41 E+4		1.03 E+5	9.01 E+5
33/5/B	Y = 1.74 Z = 74.48	100	1.28 E+5		1.05 E+5	9.19 E+5
33/5/H	Y = 2.14 Z = 74.48					
m 33 j	Y = 0.60 Z = 74.50	16.9	1.52 E+4		6.52 E+4	5.70 E+5
m 33 j o	Y = 0.60 Z = 74.92	16.9	2.34 E+4		1.00 E+5	8.75 E+5
34/0/100	Y = 0.74 Z = 75.48	16.9	5.55 E+4		2.38 E+5	2.08 E+6
34/0/50	Y = 1.24 Z = 75.48	16.9	3.44 E+4		1.48 E+5	1.29 E+6
34/0/B	Y = 1.74 Z = 75.48	100	1.42 E+5		1.16 E+5	1.01 E+6
34/0/H	Y = 2.14 Z = 75.48					

Run V
Aluminum → Na^{22}
Vertical-profile array

26.4 GeV/c
All installations
421-min. exposure
1.14 E+11 p/sec

Location	Coordinates	Detector size (g)	Net count rate (bkg subtracted) at t_0 (cpm)	Error (%)	ϕ at $\bar{I}$ (n/cm^2-sec)	ϕ at I=10^{12} p/sec (n/cm^2-sec)
32/0/100	Y = 0.74 Z = 62.92	16.9	6.33 E+1		1.38 E+6	1.21 E+7
32/0/50	Y = 1.24 Z = 62.92		3.14 E+1	7.9	6.83 E+5	5.98 E+6
32/0/B	Y = 1.74 Z = 62.92					
32/0/H	Y = 2.14 Z = 62.92					
32/1/100	Y = 0.74 Z = 63.92	16.9	2.06 E+2		4.48 E+6	3.92 E+7
32/1/50	Y = 1.24 Z = 63.92	16.9	7.58 E+1		1.65 E+6	1.44 E+7
32/1/B	Y = 1.74 Z = 63.92					
32/1/H	Y = 2.14 Z = 63.92					
m 32 o a	Y = 0.60 Z = 64.66	16.9	3.91 E+2		8.52 E+6	7.45 E+7
m 32 a	Y = 0.60 Z = 65.09	16.9	1.58 E+2		3.44 E+6	3.01 E+7
32/2/100	Y = 0.74 Z = 64.92	16.9	1.97 E+2		4.29 E+6	3.75 E+7
32/2/50	Y = 1.24 Z = 64.92	16.9	1.02 E+2		2.22 E+6	1.94 E+7
32/2/B	Y = 1.74 Z = 64.92					
32/2/H	Y = 2.14 Z = 64.92					
m 32 b	Y = 0.60 Z = 65.30	16.9	6.56 E+1		1.43 E+6	1.25 E+7
m 32 c	Y = 0.60 Z = 65.73	16.9	2.41 E+1	5.1	5.24 E+5	4.58 E+6
32/3/100	Y = 0.74 Z = 65.92	16.9	1.89 E+1	6.9	4.11 E+5	3.60 E+6
32/3/50	Y = 1.24 Z = 65.92	16.9	6.01 E+1		1.32 E+6	1.15 E+7
32/3/B	Y = 1.74 Z = 65.92					
32/3/H	Y = 2.14 Z = 65.92					
m 32 d	Y = 0.60 Z = 66.15	16.9	1.64 E+1		3.56 E+5	3.11 E+6
m 32 e	Y = 0.60 Z = 66.58	16.9	1.05 E+1	5.1	2.29 E+5	2.00 E+6
m 32 f	Y = 0.60 Z = 67.00	16.9	9.47 E+0		2.06 E+5	1.80 E+6
32/4/100	Y = 0.74 Z = 66.92	16.9	1.1 E+1	5.7	2.39 E+5	2.09 E+6

Location	Coordinates	Detector size (g)	Net count rate (bkg subtracted) at t_0 (cpm)	Error (%)	ϕ at $\bar{I}$ (n/cm^2-sec)	ϕ at I=10^{12} p/sec (n/cm^2-sec)
32/4/50	Y = 1.24 Z = 66.92	16.9	1.55 E+1	6.6	3.36 E+5	2.94 E+6
32/4/B	Y = 1.74 Z = 66.92					
32/4/H	Y = 2.14 Z = 66.92					
m 32 g	Y = 0.60 Z = 67.43	16.9	1.01 E+1		2.19 E+5	1.92 E+6
m 32 h	Y = 0.60 Z = 67.86	16.9	6.84 E+0		1.49 E+5	1.30 E+6
32/5/100	Y = 0.74 Z = 67.92	16.9	7.52 E+0		1.63 E+5	1.43 E+6
32/5/50	Y = 1.24 Z = 67.92	16.9	9.80 E+0		2.13 E+5	1.86 E+6
32/5/B	Y = 1.74 Z = 67.92					
32/5/H	Y = 2.14 Z = 67.92					
m 32 i	Y = 0.60 Z = 68.28	16.9	7.20 E+0		1.57 E+5	1.37 E+6
m 32 j	Y = 0.60 Z = 68.50	16.9	5.95 E+0		1.30 E+5	1.14 E+6
m 32 j o	Y = 0.60 Z = 68.92	16.9	1.1 E+1	7.8	2.39 E+5	2.09 E+6
m 32 j l	Y = 0.30 Z = 68.67	16.9	1.31 E+2		2.85 E+6	2.49 E+7
s 32 a	Y = 0.60 Z = 69.36	16.9	1.19 E+2		2.58 E+6	2.26 E+7
33/0/100	Y = 0.74 Z = 69.48	16.9	4.2 E+1	5.0	9.17 E+5	8.02 E+6
33/0/50	Y = 1.24 Z = 69.48	16.9	2.03 E+1		4.40 E+5	3.85 E+6
33/0/B	Y = 1.74 Z = 69.48					
33/0/H	Y = 2.14 Z = 69.48					
s 33 b	Y = 0.60 Z = 69.79	16.9	1.13 E+2		2.46 E+6	2.15 E+7
s 33 c	Y = 0.60 Z = 70.23	16.9	6.41 E+1		1.39 E+6	1.22 E+7
33/1/100	Y = 0.74 Z = 70.48	16.9	6.59 E+1		1.43 E+6	1.25 E+7
33/1/50	Y = 1.24 Z = 70.48	16.9	2.99 E+1	6.7	6.50 E+5	5.69 E+6
33/1/B	Y = 1.74 Z = 70.48					
33/1/H	Y = 2.14 Z = 70.48					
m 33 o a	Y = 0.60 Z = 70.66	16.9	7.21 E+1		1.57 E+6	1.37 E+7
m 33 a	Y = 0.60 Z = 71.09	16.9	2.32 E+1	6.5	5.05 E+5	4.42 E+6
m 33 b	Y = 0.60 Z = 71.30	16.9	1.40 E+1		3.05 E+5	2.67 E+6
33/2/100	Y = 0.74 Z = 71.48	16.9	1.2 E+1		2.61 E+5	2.28 E+6

Location	Coordinates	Detector size (g)	Net count rate (bkg subtracted) at t_0 (cpm)	Error (%)	ϕ at $\bar{I}$ (n/cm^2-sec)	ϕ at I=10^{12} p/sec n/cm^2-sec)
33/2/50	Y = 1.24 Z = 71.48	16.9	2.2 E+1		4.77 E+5	4.17 E+6
33/2/B	Y = 1.74 Z = 71.48					
33/2/H	Y = 2.14 Z = 71.48					
m 33 c	Y = 0.60 Z = 71.73	16.9	6.57 E+0		1.43 E+5	1.25 E+6
m 33 d	Y = 0.60 Z = 72.15	16.9	6.25 E+0	5.5	1.36 E+5	1.19 E+6
33/3/100	Y = 0.74 Z = 72.48	16.9	6.15 E+0		1.34 E+5	1.17 E+6
33/3/50	Y = 1.24 Z = 72.48	16.9	1.03 E+1		2.23 E+5	1.95 E+6
33/3/B	Y = 1.74 Z = 72.48					
33/3/H	Y = 2.14 Z = 72.48					
m 33 e	Y = 0.60 Z = 72.58	16.9	5.28 E+0		1.15 E+5	1.01 E+6
m 33 f	Y = 0.60 Z = 73.00	16.9	5.71 E+0	5.6	1.24 E+5	1.08 E+6
m 33 g	Y = 0.60 Z = 73.43	16.9	6.07 E+0		1.32 E+5	1.15 E+6
33/4/100	Y = 0.74 Z = 73.48	16.9	6.78 E+0		1.47 E+5	1.29 E+6
33/4/50	Y = 1.24 Z = 73.48	16.9	6.45 E+0		1.40 E+5	1.22 E+6
33/4/B	Y = 1.74 Z = 73.48					
33/4/H	Y = 2.14 Z = 73.48					
m 33 h	Y = 0.60 Z = 73.86	16.9	5.30 E+0		1.15 E+5	1.01 E+6
m 33 i	Y = 0.60 Z = 74.28	16.9	4.97 E+0		1.08 E+5	9.45 E+5
33/5/100	Y = 0.74 Z = 74.48	16.9	5.49 E+0		1.19 E+5	1.04 E+6
33/5/50	Y = 1.24 Z = 74.48	16.9	6.80 E+0		1.48 E+5	1.29 E+6
33/5/B	Y = 1.74 Z = 74.48					
33/5/H	Y = 2.14 Z = 74.48					
m 33 j	Y = 0.60 Z = 74.50	16.9	4.52 E+0		9.83 E+4	8.60 E+5
m 33 j o	Y = 0.60 Z = 74.92	16.9	6.33 E+0	5.4	1.38 E+5	1.21 E+6
34/0/100	Y = 0.79 Z = 75.48	16.9	1.68 E+1		3.66 E+5	3.20 E+6
34/0/50	Y = 1.24 Z = 75.48	16.9	1.01 E+1	5.7	2.20 E+5	1.92 E+6
34/0/B	Y = 1.74 Z = 75.48					
34/0/H	Y = 2.14 Z = 75.48					

Run V
TLD
Vertical profile array
22-mg detector

26.4 GeV/c
All installations
421-min. exposure
1.14 E+11 p/sec

Location	Coordinates	Dose (rads/h)
32/0/100	Y = 0.74 Z = 62.92	5.27 E+3
32/0/50	Y = 1.24 Z = 62.92	3.29 E+3
32/0/B	Y = 1.74 Z = 62.92	1.89 E+3
32/0/H	Y = 2.14 Z = 62.92	1.34 E+3
32/1/100	Y = 0.74 Z = 63.92	2.08 E+4
32/1/50	Y = 1.24 Z = 63.92	1.15 E+4
32/1/B	Y = 1.74 Z = 63.92	4.08 E+3
32/1/H	Y = 2.14 Z = 63.92	2.23 E+3
m 32 o a	Y = 0.60 Z = 64.66	
m 32 a	Y = 0.60 Z = 65.09	
32/2/100	Y = 0.74 Z = 64.92	1.86 E+4
32/2/50	Y = 1.24 Z = 64.92	1.03 E+4
32/2/B	Y = 1.74 Z = 64.92	4.51 E+3
32/2/H	Y = 2.14 Z = 64.92	2.96 E+3
m 32 b	Y = 0.60 Z = 65.30	
m 32 c	Y = 0.60 Z = 65.73	
32/3/100	Y = 0.74 Z = 65.92	5.12 E+2
32/3/50	Y = 1.24 Z = 65.92	3.23 E+3
32/3/B	Y = 1.74 Z = 65.92	2.46 E+3
32/3/H	Y = 2.14 Z = 65.92	2.50 E+3
m 32 d	Y = 0.60 Z = 66.15	
m 32 e	Y = 0.60 Z = 66.58	
m 32 f	Y = 0.60 Z = 67.00	
32/4/100	Y = 0.74 Z = 66.92	3.95 E+2
32/4/50	Y = 1.24 Z = 66.92	8.18 E+2

Location	Coordinates	Dose (rads/h)
32/4/B	Y = 1.74 Z = 66.92	1.30 E+3
32/4/H	Y = 2.14 Z = 66.92	1.70 E+3
m 32 g	Y = 0.60 Z = 67.43	
m 32 h	Y = 0.60 Z = 67.86	
32/5/100	Y = 0.74 Z = 67.92	2.72 E+2
32/5/50	Y 1.24 Z = 67.92	5.26 E+2
32/5/B	Y = 1.74 Z = 67.92	7.90 E+2
32/5/H	Y = 2.14 Z = 67.92	1.47 E+3
m 32 i	Y = 0.60 Z = 68.28	
m 32 j	Y = 0.60 Z = 68.50	
m 32 j o	Y = 0.60 Z = 68.92	
m 32 j l		
s 32 a	Y = 0.60 Z = 69.36	
33/0/100	Y = 0.74 Z = 69.48	2.98 E+3
33/0/50	Y = 1.24 Z = 69.48	1.46 E+3
33/0/B	Y = 1.74 Z = 69.48	9.70 E+2
33/0/H	Y = 2.14 Z = 69.48	8.39 E+2
s 33 b	Y = 0.60 Z = 69.79	
s 33 c	Y = 0.60 Z = 70.23	
33/1/100	Y = 0.74 Z = 70.48	5.79 E+3
33/1/50	Y = 1.24 Z = 70.48	1.84 E+3
33/1/B	Y = 1.74 Z = 70.48	1.19 E+3
33/1/H	Y = 2.14 Z = 70.48	9.35 E+3
m 33 o a	Y = 0.60 Z = 70.66	
m 33 a	Y = 0.60 Z = 71.09	
m 33 b	Y = 0.60 Z = 71.30	
33/2/100	Y = 0.74 Z = 71.48	3.68 E+2
33/2/50	Y = 1.24 Z = 71.48	1.24 E+3
33/2/B	Y = 1.74 Z = 71.48	1.05 E+3

Location	Coordinates	Dose (rads/h)
33/2/H	Y = 2.14 Z = 71.48	9.76 E+2
m 33 c	Y = 0.60 Z = 71.73	
m 33 d	Y = 0.60 Z = 72.15	
33/3/100	Y = 0.74 Z = 72.48	3.23 E+2
33/3/50	Y = 1.24 Z = 72.48	5.74 E+2
33/3/B	Y = 1.74 Z = 72.48	6.43 E+2
33/3/H	Y = 2.14 Z = 72.48	6.20 E+2
m 33 e	Y = 0.60 Z = 72.58	
m 33 f	Y = 0.60 Z = 73.00	
m 33 g	Y = 0.60 Z = 73.43	
33/4/100	Y = 0.74 Z = 73.48	2.64 E+2
33/4/50	Y = 1.24 Z = 73.48	4.05 E+2
33/4/B	Y = 1.74 Z = 73.48	5.30 E+2
33/4/H	Y = 2.14 Z = 73.48	5.06 E+2
m 33 h	Y = 0.60 Z = 73.86	
m 33 i	Y = 0.60 Z = 74.28	
33/5/100	Y = 0.74 Z = 74.48	2.61 E+1
33/5/50	Y = 1.24 Z = 74.48	3.51 E+1
33/5/B	Y = 1.74 Z = 74.48	4.10 E+2
33/5/H	Y = 2.14 Z = 74.48	4.25 E+2
m 33 j	Y = 0.60 Z = 74.50	
m 33 j o	Y = 0.60 Z = 74.92	
34/0/100	Y = 0.74 Z = 75.48	9.48 E+2
34/0/50	Y = 1.24 Z = 75.48	5.79 E+2
34/0/B	Y = 1.74 Z = 75.48	4.54 E+2
34/0/H	Y = 2.14 Z = 75.48	4.05 E+2

Run V
Aluminum
Tunnel 77
1.14 E+11 p/sec

26.4 GeV/c
All installations
421-min. exposure

Location	Detector size (g)	Net count rate (bkg subtracted) at t_0 (cpm)	Error (%)	ϕ at $\bar{I}$ (n/cm^2-sec)	ϕ at I=10^{12} p/sec (n/cm^2-sec)
77/0–A	500	1.82 E+4		4.01 E+3	3.51 E+4
77/0–B	500	1.59 E+4		3.51 E+3	3.07 E+4
77/0–C	500	1.67 E+4		3.67 E+3	3.21 E+4
77/0–D	500	1.77 E+4		3.89 E+3	3.40 E+4
77/0–E	500	1.73 E+4		3.81 E+3	3.33 E+4
77/0–F	500	1.70 E+4		3.75 E+3	3.28 E+4
77/1.25	500	3.25 E+3		7.16 E+2	6.26 E+3
77/4	500	8.60 E+2		1.89 E+2	1.65 E+3
77/6	500	7.06 E+2		1.56 E+2	1.36 E+3
77/10	500	4.77 E+1	9.6	1.05 E+1	9.2 E+
77/15	2200	4.11 E+1	11.2	2.6 E+0	2.27 E+1
77/20	2200	2.2 E+1	11.5	1.39 E+0	1.22 E+1
77/30	6600	8.64 E+0	14.1	3.1 E-1	2.71 E+0

Run V
Aluminum
Tunnel 77-roof bucket
500-g detector

26.4 GeV/c
All installations
421-min. exposure
1.14 E+11 p/sec

Location	Coordinates	Net count rate (bkg subtracted) at t_0 (cpm)	ϕ at $\bar{I}$ (n/cm^2-sec)	ϕ at I=10^{12} p/sec (n/cm^2-sec)
77–R	Z = 50.4	1.73 E+4	3.82 E+3	3.34 E+4

Run VI Data

Run VI exposure summary.*

Exposure number	Beam energy (GeV/c)	Average beam current (p/sec)	Exposure duration (min)	Exposure time
1	14.64	6.38 E+11	10	2107 – 2117
2	14.64	6.44 E+11	42	2126 – 2208
entire run	14.64	5.48 E+11	61	2107 – 2208

*Target location: straight section 32;
clipper location: straight section 79.

Run VI | 14.6 GeV/c
Sulfur | All installations
Vacuum vessel | 61-min. exposure
4-g detector | 5.48 E+11 p/sec

Location	Coordinates	ϕ at $\bar{I}$ (n/cm^2-sec)	ϕ at I=10^{12} p/sec (n/cm^2-sec)
1		1.64 E+5	3.00 E+5
2		5.81 E+5	1.06 E+6
3		2.11 E+5	3.85 E+5
4		1.30 E+5	2.37 E+5
5		6.14 E+5	1.12 E+6
6		3.65 E+5	6.65 E+5
7		7.90 E+5	1.44 E+6
8		5.20 E+5	9.48 E+5
9		2.14 E+6	3.90 E+6
10		1.01 E+7	1.84 E+7
11		1.66 E+6	3.02 E+6
12		3.62 E+6	6.61 E+6
13		1.13 E+6	2.07 E+6
14		3.46 E+6	6.32 E+6
15		9.43 E+5	1.72 E+6
16		4.70 E+5	8.58 E+5
17		4.73 E+5	8.62 E+5
18		7.07 E+5	1.29 E+6
19		5.65 E+6	1.03 E+7
20		3.71 E+6	6.76 E+5
21		5.02 E+5	9.16 E+5
22		2.92 E+6	5.33 E+6
23		6.14 E+5	1.12 E+6
24	Z = 12.7	3.97 E+5	7.24 E+5
25	Z = 19.0	3.17 E+5	5.78 E+5
26	Z = 25.24	1.91 E+6	3.49 E+6
27	Z = 31.51	4.84 E+4	8.83 E+4
28	Z = 37.80	3.71 E+6	6.76 E+6
29	Z = 44.08	2.30 E+6	4.19 E+6
30	Z = 50.36	1.99 E+6	3.63 E+6
31	Z = 56.64	5.24 E+6	9.56 E+6
32	Z = 62.92	2.63 E+8	4.79 E+8
33	Z = 69.20	3.44 E+7	6.27 E+7
34	Z = 75.48	1.13 E+7	2.07 E+7
35	Z = 81.76	4.35 E+6	7.93 E+6
36	Z = 88.08	2.54 E+6	4.64 E+6
37	Z = 94.32	1.16 E+6	2.12 E+6
38	Z = 100.60	2.92 E+5	5.33 E+5
39	Z = 106.88	1.25 E+6	2.28 E+6
40	Z = 113.16	1.91 E+5	3.49 E+5

Location	Coordinates	ϕ at $\bar{I}$ (n/cm^2-sec)	ϕ at I=10^{12} p/sec (n/cm^2-sec)
41	Z = 119.44	5.47 E+5	9.97 E+5
42	Z = 125.72	3.70 E+6	6.74 E+6
43	Z = 132.00	9.27 E+5	1.69 E+6
44	Z = 138.28	1.58 E+6	2.89 E+6
45		5.20 E+5	9.48 E+5
46		1.84 E+5	3.36 E+5
47		8.88 E+4	1.62 E+5
48		1.50 E+5	2.73 E+5
49		1.05 E+6	1.91 E+6
50		3.13 E+5	5.71 E+5
51		1.00 E+5	1.83 E+5
52		8.66 E+5	1.58 E+6
53		5.00 E+5	9.12 E+5
54		1.43 E+5	2.60 E+5
55		2.19 E+5	3.99 E+5
56		3.94 E+5	7.19 E+5
57		1.30 E+5	2.37 E+5
58		2.75 E+6	5.02 E+6
59		1.89 E+6	3.45 E+6
60		9.49 E+6	1.73 E+7
61		5.70 E+5	1.04 E+6
62		1.88 E+6	3.43 E+6
63		6.14 E+5	1.12 E+6
64		1.94 E+6	3.54 E+6
65		4.14 E+5	7.56 E+5
66		6.74 E+5	1.23 E+6
67		4.84 E+4	8.83 E+4
68		4.54 E+5	8.29 E+5
69		1.20 E+6	2.19 E+6
70		3.44 E+5	6.27 E+5
71		6.63 E+5	1.21 E+6
72		1.13 E+6	2.07 E+6
73		2.62 E+5	4.79 E+5
74		5.47 E+6	9.97 E+6
75		2.30 E+5	4.19 E+5
76		2.83 E+5	5.17 E+5
77		6.09 E+4	1.11 E+5
78		1.02 E+5	1.87 E+5
79		1.35 E+8	2.46 E+8
80		7.68 E+6	1.40 E+7
81		8.06 E+6	1.47 E+7
82		3.71 E+6	6.76 E+6
83		1.30 E+6	2.37 E+6
84		6.58 E+5	1.20 E+6
85		4.95 E+5	9.03 E+5

Location	Coordinates	ϕ at $\bar{I}$ (n/cm^2-sec)	ϕ at I=10^{12} p/sec (n/cm^2-sec)
86		4.84 E+5	8.83 E+5
87		1.44 E+6	2.62 E+6
88		5.11 E+5	9.32 E+5
89		3.11 E+6	5.67 E+6
90		1.23 E+7	2.24 E+7
91		2.09 E+6	3.81 E+6
92		1.13 E+6	2.07 E+6
93		8.06 E+5	1.47 E+6
94		1.95 E+6	3.56 E+6
95		6.14 E+5	1.12 E+6
96		3.06 E+5	5.58 E+5
97		3.06 E+5	5.58 E+5
98		4.78 E+5	8.71 E+5
99		3.62 E+5	6.61 E+5
100		1.22 E+6	2.22 E+6

Run VI
Sulfur
Vacuum vessel
4-g detector

14.6 GeV/c
All installations
61-min. exposure
5.48 E+11 p/sec

Location	Coordinates	ϕ at $\bar{I}$ (n/cm^2-sec)	ϕ at I=10^{12} p/sec (n/cm^2-sec)
32/0	Z = 63.12	2.06 E+8	3.76 E+8
32/10	Z = 63.22	1.86 E+8	3.40 E+8
32/20	Z = 63.32	1.35 E+8	2.46 E+8
32/30	Z = 63.42	1.13 E+8	2.07 E+8
32/40	Z = 63.52	7.46 E+7	1.36 E+8
32/50	Z = 63.62	6.03 E+7	1.10 E+8
32/60	Z = 63.72	5.59 E+7	1.02 E+8
32/70	Z = 63.82	6.03 E+7	1.10 E+8
32/80	Z = 63.92	8.33 E+7	1.52 E+8
32/90	Z = 64.02	1.14 E+8	2.08 E+8
32/100	Z = 64.12	1.45 E+8	2.64 E+8
32/110	Z = 64.22	8.94 E+7	1.63 E+8

Run VI. Activities for aluminum foils on vacuum vessel.*

Standard position	Foil activity (pCi/g)	Standard position	Foil activity (pCi/g)	Standard position	Foil activity (pCi/g)	Standard position	Foil activity (pCi/g)
1	7.75 E+4	26	1.31 E+5	51	1.23 E+4	76	3.19 E+4
2	6.74 E+4	27	2.97 E+3	52	1.59 E+5	77	7.13 E+3
3	4.10 E+4	28	3.35 E+5	53	5.60 E+4	78	7.98 E+3
4	2.07 E+4	29	2.08 E+5	54	1.51 E+4	79	2.17 E+7
5	5.50 E+4	30	2.00 E+5	55	1.92 E+4	80	1.01 E+6
6	2.37 E+4	31	7.27 E+4	56	5.81 E+4	81	1.37 E+6
7	1.40 E+4	32	4.11 E+7	57	1.75 E+4	82	4.10 E+5
8	4.95 E+4	33	4.65 E+6	58	4.32 E+5	83	1.99 E+5
9	2.50 E+5	34	1.35 E+6	59	2.41 E+5	84	9.38 E+4
10	1.02 E+6	35	4.40 E+5	60	9.07 E+5	85	5.78 E+4
11	2.19 E+5	36	3.61 E+5	61	4.91 E+4	86	9.18 E+4
12	7.49 E+5	37	1.44 E+5	62	2.25 E+5	87	2.16 E+5
13	2.27 E+5	38	3.81 E+4	63	9.39 E+4	88	7.34 E+4
14	4.44 E+5	39	1.24 E+5	64	1.99 E+5	89	4.27 E+5
15	1.21 E+5	40	3.31 E+4	65	7.28 E+4	90	1.66 E+5
16	6.58 E+4	41	7.30 E+4	66	8.30 E+4	91	2.93 E+5
17	7.91 E+4	42	4.43 E+5	67	7.05 E+3	92	1.68 E+5
18	1.00 E+5	43	1.33 E+5	68	6.63 E+4	93	1.14 E+5
19	5.13 E+5	44	1.76 E+5	69	1.28 E+5	94	2.44 E+5
20	4.20 E+4	45	3.52 E+4	70	3.77 E+4	95	6.41 E+4
21	6.70 E+4	46	1.25 E+4	71	8.77 E+4	96	4.81 E+4
22	7.60 E+5	47	9.47 E+3	72	1.38 E+5	97	3.10 E+4
23	9.66 E+4	48	1.39 E+4	73	3.88 E+4	98	7.42 E+4
24	4.80 E+4	49	1.18 E+5	74	7.34 E+5	99	4.52 E+4
25	3.72 E+4	50	2.25 E+4	75	4.70 E+4	100	6.71 E+4

*One-hundred foils listed here.

Run VI	14.6 GeV/c
TLD	All installations
Vacuum vessel	61-min. exposure
22-mg sample	5.48 E+11 p/sec

Location	Dose (rads/h)
1	2.24 E+2
4	-----
7	1.32 E+2
10	3.73 E+3
13	1.86 E+3
16	6.81 E+2
19	4.02 E+2
22	2.68 E+3
25	3.05 E+2
28	1.23 E+3
31	5.35 E+2
32	6.03 E+3
33	2.22 E+3
34	4.81 E+3
37	2.00 E+3
40	1.81 E+2
43	1.15 E+3
46	1.58 E+2
49	1.02 E+3
52	1.28 E+3
55	2.08 E+2
58	4.71 E+3
61	5.50 E+2
64	1.17 E+3
67	3.46 E+1
70	5.13 E+2
73	2.83 E+2
76	3.95 E+2
79	6.16 E+3
82	3.75 E+3
85	3.79 E+2
88	1.17 E+3
91	2.30 E+3
94	2.21 E+3
97	4.27 E+2
100	3.76 E+2

Run VI
Sulfur
Roof buckets
4-g sample

14.6 GeV/c
All installations
61-min exposure
5.48 E+11

Location	Coordinates	ϕ at $\bar{I}$ (n/cm^2-sec)	ϕ at I = 10^{12} p/sec (n/cm^2-sec)
29–R	Z = 44.08	2.24 E+4	4.08 E+4
30–R	Z = 50.36	2.78 E+4	5.08 E+4
31–R	Z = 56.64	1.08 E+5	1.97 E+5
31–1R	Z = 57.92	1.98 E+4	3.61 E+4
31–2R	Z = 58.92	2.38 E+5	4.35 E+5
31–3R	Z = 59.92	3.65 E+5	6.65 E+5
31–4R	Z = 60.92	7.18 E+5	1.31 E+6
31–5R	Z = 61.92	1.29 E+6	2.35 E+6
32–R	Z = 62.92	2.54 E+6	4.64 E+6
32–1R	Z = 63.92	3.24 E+6	5.91 E+6
32–2R	Z = 64.92	2.92 E+6	5.33 E+6
32–3R	Z = 65.92	1.74 E+6	3.18 E+6
32–4R	Z = 66.92	1.29 E+6	2.35 E+6
32–5R	Z = 67.92	1.12 E+6	2.04 E+6
33–R	Z = 69.20	1.33 E+6	2.42 E+6
33–1R	Z = 70.48	1.33 E+6	2.42 E+6
33–2R	Z = 71.48	9.92 E+5	1.81 E+6
33–3R	Z = 72.48	5.98 E+5	1.09 E+6
33–4R	Z = 73.48	5.54 E+5	1.01 E+6
33–5R	Z = 74.48	5.27 E+5	9.61 E+5
34–R	Z = 75.48	5.76 E+5	1.05 E+6
35–R	Z = 81.76	2.09 E+5	3.81 E+5
36–R	Z = 88.08	1.04 E+5	1.89 E+5
76–R	Z = 44.1	–	–
77–R	Z = 50.4	–	–
78–R	Z = 56.6	9.76 E+3	1.78 E+4
78–1R	Z = 57.9	1.95 E+4	3.56 E+4
78–2R	Z = 58.9	8.22 E+4	1.50 E+5
78–3R	Z = 59.9	1.07 E+5	1.96 E+5
78–4R	Z = 60.9	2.14 E+5	3.90 E+5
78–5R	Z = 61.9	6.14 E+5	1.12 E+6
79–R	Z = 62.9	1.14 E+6	2.08 E+6
79–1R	Z = 63.9	8.00 E+5	1.46 E+6
79–2R	Z = 64.9	4.24 E+5	7.73 E+5
79–3R	Z = 65.9	2.30 E+5	4.19 E+5
79–4R	Z = 66.9	2.01 E+5	3.67 E+5
79–5R	Z = 67.9	2.11 E+5	3.85 E+5
80–R	Z = 69.2	2.52 E+5	4.59 E+5
80–1R	Z = 70.5	2.36 E+5	4.30 E+5
80–2R	Z = 71.5	1.34 E+5	2.44 E+5
80–3R	Z = 72.5	6.69 E+4	1.22 E+5
80–4R	Z = 73.5	1.91 E+5	3.49 E+5
80–5R	Z = 74.5	2.46 E+5	4.48 E+5

Run VI
Aluminum
Roof buckets
100-g samples

14.6 GeV/c
All installations
61-min. exposure
5.48 E+11

Location	Coordinates	Net count rate (bkg. subtracted) at t_0 (cpm/g)	ϕ at $\bar{I}$ (n/cm^2-sec)	ϕ at I = 10^{12} p/sec (n/cm^2-sec)
29–R	Z = 44.1	2.98 E+3	1.48 E+4	2.70 E+4
30–R	Z = 50.4	6.85 E+3	3.39 E+4	6.18 E+4
31–R	Z = 56.6	7.10 E+3	3.52 E+4	6.42 E+4
31–1R	Z = 57.9	1.04 E+4	5.14 E+4	9.38 E+4
31–2R	Z = 58.9	1.42 E+4	7.01 E+4	1.28 E+5
31–3R	Z = 59.9	2.26 E+4	1.12 E+5	2.04 E+5
31–4R	Z = 60.9	4.53 E+4	2.24 E+5	4.09 E+5
31–5R	Z = 61.9	8.89 E+4	4.40 E+5	8.03 E+5
32–0R	Z = 62.9	1.83 E+5	9.06 E+5	1.65 E+6
32–1R	Z = 63.9	3.04 E+5	1.50 E+6	2.74 E+6
32–2R	Z = 64.9	3.00 E+5	1.49 E+6	2.72 E+6
32–3R	Z = 65.9	2.03 E+5	1.00 E+6	1.82 E+6
32–4R	Z = 66.9	1.52 E+5	7.51 E+5	1.37 E+6
32–5R	Z = 67.9	1.07 E+5	5.31 E+5	9.69 E+5
33–0R	Z = 69.2	1.16 E+5	5.76 E+5	1.05 E+6
33–1R	Z = 70.5	1.22 E+5	6.06 E+5	1.11 E+6
33–2R	Z = 71.5	9.26 E+4	4.59 E+5	8.37 E+5
33–3R	Z = 72.5	6.93 E+4	3.43 E+5	6.26 E+5
33–4R	Z = 73.5	5.26 E+4	2.61 E+5	4.76 E+5
33–5R	Z = 74.5	5.19 E+4	2.57 E+5	4.69 E+5
34–R	Z = 75.5	5.02 E+4	2.49 E+5	4.54 E+5
35–R	Z = 81.8	2.26 E+4	1.12 E+5	2.04 E+5
36–R	Z = 88.1	1.48 E+4	7.35 E+4	1.34 E+5
37–R	Z = 94.3	6.87 E+3	3.40 E+4	6.20 E+4
38–R	Z = 100.6	4.26 E+3	2.11 E+4	3.85 E+4
78–R	Z = 56.6	1.60 E+3	7.88 E+3	1.44 E+4
78–1R	Z = 57.9	2.29 E+3	1.14 E+4	2.08 E+4
78–2R	Z = 58.9	3.59 E+3	1.78 E+4	3.25 E+4
78–3R	Z = 59.9	6.54 E+3	3.24 E+4	5.91 E+4
78–4R	Z = 60.9	1.38 E+4	6.84 E+4	1.25 E+5
78–5R	Z = 61.9	5.18 E+4	2.56 E+5	4.67 E+5
79–0R	Z = 62.9	1.06 E+5	5.23 E+5	9.54 E+5
79–1R	Z = 63.9	8.90 E+4	4.41 E+5	8.04 E+5
79–2R	Z = 64.9	4.67 E+4	2.31 E+5	4.21 E+5
79–3R	Z = 65.9	2.01 E+4	9.97 E+4	1.82 E+5
79–4R	Z = 66.9	1.72 E+4	8.52 E+4	1.55 E+5
79–5R	Z = 67.9	2.00 E+4	9.92 E+4	1.81 E+5
80–0R	Z = 69.2	2.46 E+4	1.22 E+5	2.23 E+5
80–1R	Z = 70.5	1.87 E+4	9.24 E+4	1.69 E+5
80–2R	Z = 71.5	1.21 E+4	5.98 E+4	1.09 E+5
80–3R	Z = 72.5	1.08 E+4	5.34 E+4	9.74 E+4
80–4R	Z = 73.5	1.33 E+4	6.58 E+4	1.20 E+5
80–5R	Z = 74.5	1.95 E+4	9.65 E+4	1.76 E+5

Run VI
Carbon
Roof buckets
1-in. diam detector

14.6 GeV/c
Installation 1
10-min. exposure
6.38 E+11 p/sec

Location	Coordinates	Net count rate (bkg.subtracted) at t_0 (cpm/g)	ϕ at $\bar{T}$ (n/cm^2-sec)	ϕ at I=10^{12} p/sec (n/cm^2-sec)
32–0R	Z = 62.92	6.15 E+7	2.05 E+6	3.21 E+6
32–1R	Z = 63.92	1.35 E+8	4.51 E+6	7.06 E+6
32–2R	Z = 65.42	1.87 E+8	6.25 E+6	9.79 E+6
32–3R	Z = 66.40	1.39 E+8	4.63 E+6	7.25 E+6
32–4R	Z = 67.30	1.22 E+8	4.09 E+6	6.40 E+6
32–5R	Z = 68.20	4.29 E+7	1.40 E+6	2.19 E+6
33–0R	Z = 69.20	4.11 E+7	1.37 E+6	2.15 E+6

Run VI
Mercury
Roof buckets
432-g detector

14.6 GeV/c
Installations 1 and 2
61-min. exposure
5.48 E+11 p/sec

Location	Coordinates	Net count rate (bkg subtracted) at t_o (cpm)	ϕ at I=10^{12} p/sec (n/cm^2-sec)
32–0	Y = 1.74 Z = 62.92	4.570 E+0	2.37 E+3
32–1	Y = 1.74 Z = 63.92	3.540 E+1	1.83 E+4
32–2	Y = 1.74 Z = 65.42	3.071 E+2	1.59 E+5
32–3	Y = 1.74 Z = 66.40	6.295 E+2	3.25 E+5
32–4	Y = 1.74 Z = 67.30	1.702 E+3	8.80 E+5
32–5	Y = 1.74 Z = 68.20	9.308 E+2	4.81 E+5
33–0	Y = 1.74 Z = 69.20	1.319 E+2	6.82 E+4

Run VI
TLD
Roof buckets
22-mg samples

14.6 GeV/c
All installations
61-min. exposure
5.48 E+11 p/sec

Location	Coordinates	Indicated dose (rads/hour)
29–R	Z = 44.1	3.6 E+0
30–R	Z = 50.4	1.81 E+1
31–0R	Z = 56.6	1.15 E+1
31–1R	Z = 57.9	3.36 E+1
31–2R	Z = 58.9	3.7 E+1
31–3R	Z = 59.9	5.7 E+1
31–4R	Z = 60.9	1.03 E+2
31–5R	Z = 61.9	2.33 E+2
32–0R	Z = 62.9	3.21 E+2
32–1R	Z = 63.9	7.04 E+2
32–2R	Z = 64.9	9.18 E+2
32–3R	Z = 65.9	7.55 E+2
32–4R	Z = 66.9	2.03 E+2
32–5R	Z = 67.9	3.26 E+2
33–0R	Z = 69.2	4.16 E+2
33–1R	Z = 70.5	5.05 E+2
33–2R	Z = 71.5	4.23 E+2
33–3R	Z = 72.5	2.70 E+2
33–4R	Z = 73.5	1.94 E+2
33–5R	Z = 74.5	3.75 E+2
34–R	Z = 75.5	1.77 E+2
35–R	Z = 81.8	8.65 E+1
36–R	Z = 88.1	6.71 E+1
78–R		5.2 E+0
79–R		3.23 E+2
80–R		1.05 E+1

Run VI
Aluminum
Orbit holes
500-g detector

14.6 GeV/c
All installations
61-min. exposure
5.48 E+11 p/sec

Location	Coordinates	Net count rate (bkg subtracted) at t_0 (cpm)	Error (%)	ϕ at $\bar{I}$ (n/cm^2-sec)	ϕ at I = 10^{12} p/sec (n/cm^2-sec)
31–330	Y = 3.53 Z = 56.6	6.50 E+2		8.63 E+2	1.57 E+3
31–390	Y = 4.12 Z = 56.6	1.33 E+2	6.5	1.76 E+2	3.21 E+2
31–390	Y = 4.12 Z = 56.6	1.36 E+2	5.1	1.81 E+2	3.30 E+2
34–330	Y = 3.63 Z = 75.5	7.29 E+3		9.68 E+3	1.77 E+4
34–390	Y = 4.22 Z = 75.5	1.90 E+3		2.53 E+3	4.61 E+3
34–450	Y = 4.81 Z = 75.5	5.13 E+2		6.82 E+2	1.24 E+3
34–510	Y = 5.40 Z = 75.5	1.51 E+2		2.01 E+2	3.67 E+2
34–570	Y = 5.99 Z = 75.5	4.18 E+1	8.1	5.55 E+1	1.01 E+2
35–330	Y = 3.45 Z = 81.8	4.94 E+3		6.57 E+3	1.20 E+4
35–390	Y = 4.04 Z = 81.8	1.12 E+3		1.49 E+3	2.72 E+3
36–330	Y = 3.31 Z = 88.1	4.48 E+3		5.96 E+3	1.09 E+4
36–390	Y = 3.90 Z = 88.1	9.74 E+2		1.30 E+3	2.37 E+3

Run VI
Aluminum
Orbit holes
555-g detector

14.6 GeV/c
Installation 2
42-min. exposure
6.44 E+11 p/sec

Location	Coordinates	Net count rate (bkg subtracted) at t_0 (cpm)	ϕ at $\bar{I}$ (n/cm^2-sec)	ϕ at I=10^{12} p/sec (n/cm^2-sec)
33–330	Y = 3.42 Z = 69.2	3.95 E+4	5.85 E+4	9.08 E+4
33–390	Y = 4.01 Z = 69.2	9.55 E+3	1.42 E+4	2.20 E+4
33–450	Y = 4.60 Z = 69.2	2.49 E+3	3.69 E+3	5.73 E+3
33–510	Y = 5.19 Z = 69.2	6.79 E+2	1.01 E+3	1.57 E+3
33–510	Y = 5.19 Z = 69.2	6.49 E+2	9.63 E+2	1.50 E+3
33–570	Y = 5.78 Z = 69.2	1.86 E+2	2.76 E+2	4.29 E+2
33–570	Y = 5.78 Z = 69.2	1.82 E+2	2.70 E+2	4.19 E+2

Run VI
Carbon
Orbit holes
4-in. detector

14.6 GeV/c
Installation 2
42-min. exposure
6.44 E+11 p/sec

Location	Coordinates	Net count rate (bkg subtracted) at t_0 (cpm)	ϕ at $\bar{I}$ (n/cm^2-sec)	ϕ at I=10^{12} p/sec (n/cm^2-sec)
32–33	Y = 3.67 Z = 62.92	6.87 E+6	8.82 E+4	1.37 E+5
32–39	Y = 4.26 Z = 62.92	2.74 E+6	3.64 E+4	5.65 E+4
32–45	Y = 4.85 Z = 62.92	8.46 E+5	1.07 E+4	1.66 E+4
32–51	Y = 5.44 Z = 62.92	2.93 E+5	3.705 E+3	5.75 E+3
32–57	Y = 6.03 Z = 62.92	1.14 E+5	1.444 E+3	2.24 E+3
33–33	Y = 3.42 Z = 69.20	1.49 E+7	2.02 E+5	3.14 E+3
33–39	Y = 4.01 Z = 69.20	3.74 E+6	4.76 E+4	7.39 E+4
33–45	Y = 4.60 Z = 69.20	9.13 E+5	1.16 E+4	1.80 E+4
33–51	Y = 5.19 Z = 69.20	2.43 E+5	3.079 E+9	4.78 E+9
33–57	Y = 5.78 Z = 69.20	6.77 E+4	8.57 E+2	1.33 E+3

Run VI
Aluminum
Vent shaft
500-g detector

14.6 GeV/c
All locations
61-min. exposure
2.26 E+4 p/sec

Location	Coordinates	Net count rate (bkg subtracted) at t_0 (cpm)	ϕ at $\bar{I}$ (n/cm^2-sec)	ϕ at I=10^{12} p/sec (n/cm^2-sec)
33–Vent	X = 103.2 Z = 70.6	2.26 E+4	3.01 E+4	5.49 E+4

Run VI
Aluminum
Radial holes
500-g detector

14.6 GeV/c
All installations
61-min. exposure
5.48 E+11 p/sec

Location	Coordinates	Detector size (g)	Net count rate (bkg subtracted) at t_0 (cpm)	Error (%)	ϕ at $\bar{I}$ (n/cm^2-sec)	ϕ at $I=10^{12}$ p/sec (n/cm^2-sec)
32–1040	X = 104.0 Z = 62.9	500	9.68 E+3		1.29 E+4	2.35 E+4
32–1050	X = 105.0 Z = 62.9	500	5.84 E+2		7.76 E+2	1.42 E+3
32–1060	X = 106.0 Z = 62.9	2200	1.93 E+2		7.35 E+1	1.34 E+2
32–1075	X = 107.5 Z = 62.9	6600	1.37 E+1	11.8	2.96 E+0	5.40 E+0
33–1040	X = 104.0 Z = 69.2	500	6.90 E+3		9.18 E+3	1.67 E+4
33–1050	X = 105.0 Z = 69.2	500	7.62 E+2		1.01 E+3	1.84 E+3
33–1060	X = 106.0 Z = 69.2	2200	1.30 E+2		4.97 E+1	9.07 E+1
33–1075	X = 107.5 Z = 69.2	6600	2.74 E+1	8.29	5.92 E+0	1.08 E+1
34–1060	X = 106.0 Z = 75.5	2200	9.8 E+1	5.2	3.7 E+1	6.75 E+1
34–1075	X = 107.5 Z = 75.5	6600	6.29 E+0	18.7	1.36 E+0	2.48 E+0
35–1060	X = 106.0 Z = 81.8	2200	9.2 E+1	5.5	3.51 E+1	6.40 E+1
35–1075	X = 107.5 Z = 81.8	6600	6.82 E+0	14.8	1.47 E+0	2.68 E+0
36–1060	X = 106.0 Z = 88.1	2200	8.15 E+1	6.1	3.1 E+1	5.65 E+1
36–1075	X = 107.5 Z = 88.1	6600	2.58 E+0	67.	5.5 E-1	1.00 E+0

Run VI
Aluminum
Ring top
3300-g detector

14.6 GeV/c
All installations
61-min. exposure
5.48 E+11 p/sec

Location	Coordinates	Net count rate (bkg subtracted) at t_0 (cpm)	ϕ at $\bar{I}$ (n/cm^2-sec)	ϕ at I=10^{12} p/sec (n/cm^2-sec)
32–top	Z = 62.9	1.72 E+2	5.06 E+1	9.23 E+1
33–top	Z = 62.9	1.77 E+2	5.2 E+1	9.48 E+1

Run VI
Gold foils
Vacuum vessel
~ 0.5-g detector

14.6 GeV/c
Installations 1 and 2
61-min. exposure

Location	Coordinates	Net count rate (bkg subtracted) at t_0 (cpm)	ϕ at I = 10^{12} p/sec (n/cm^2-sec)
32/0	Z = 63.12	6.23 E+2	2.80 E+9
32/20	Z = 63.32	7.23 E+2	3.26 E+9
32/40	Z = 63.52	4.98 E+2	2.24 E+9
32/60	Z = 63.72	3.77 E+2	1.70 E+9
32/80	Z = 63.92	3.00 E+2	1.35 E+9

Run VI
Sulfur
Angular distribution
4-g detector

14.6 GeV/c
All installations
61-min. exposure
5.48 E+11 p/sec

Location (deg)	Coordinates	ϕ at $\bar{I}$ (n/cm^2-sec)	ϕ at I=10^{12} p/sec (n/cm^2-sec)
25–25	Y = 0.11 Z = 63.15	1.05 E+8	1.92 E+8
25–45	Y = 0.18 Z = 63.10	6.52 E+7	1.19 E+8
25–65	Y = 0.23 Z = 63.02	3.49 E+7	6.37 E+7
25–90	Y = 0.25 Z = 62.92	2.55 E+7	4.65 E+7
100–3	Y = 0.05 Z = 63.92	9.09 E+7	1.66 E+8
100–10	Y = 0.18 Z = 63.90	5.02 E+7	9.16 E+7
100–20	Y = 0.35 Z = 63.86	2.69 E+7	4.91 E+7
100–30	Y = 0.50 Z = 63.68	1.65 E+7	3.01 E+7
100–40	Y = 0.64 Z = 63.68	1.27 E+7	2.32 E+7
100–60	Y = 0.87 Z = 63.42	7.39 E+6	1.35 E+7
100–90	Y = 1.00 Z = 62.92	4.35 E+6	7.93 E+6

Run VI
Aluminum → Na^{22}
Angular distribution
16.9-g detector

14.6 GeV/c
All installations
61-min. exposure
5.48 E+11 p/sec

Location (deg)	Coordinates	ϕ at $\bar{I}$ (n/cm^2-sec)	ϕ at I=10^{12} p/sec (n/cm^2-sec)
25–25	Y = 0.11 Z = 63.15	2.88 E+8	5.25 E+8
25–45	Y = 0.18 Z = 63.10	1.19 E+8	2.17 E+8
25–65	Y = 0.23 Z = 63.02	4.55 E+7	8.30 E+7
25–90	Y = 0.25 Z = 62.92	2.51 E+7	4.58 E+7
100–3	Y = 0.05 Z = 63.92	3.32 E+8	6.06 E+8
100–10	Y = 0.18 Z = 63.90	1.13 E+8	2.06 E+8
100–20	Y = 0.35 Z = 63.86	5.08 E+7	9.26 E+7
100–30	Y = 0.50 Z = 63.78	2.49 E+7	4.54 E+7
100–40	Y = 0.64 Z = 63.68	1.48 E+7	2.70 E+7
100–60	Y = 0.37 Z = 63.42	6.30 E+6	1.49 E+7
100–90	Y = 1.00 Z = 62.92	3.43 E+6	6.26 E+6

Run VI — 14.6 GeV/c
Carbon — Installation 1
Angular distribution — 10-min. exposure
1-in. detector — 6.38 E+11 p/sec

Location	Coordinates	Net count rate (bkg subtracted) at t_0 (cpm)	ϕ at $\bar{l}$ (n/cm^2-sec)	ϕ at $l=10^{12}$ p/sec (n/cm^2-sec)
3 deg 100 cm	Y = 0.05 Z = 63.92	2.06 E+10	6.87 E+8	1.08 E+10
10 deg 100 cm	Y = 0.18 Z = 63.90	6.79 E+9	2.27 E+8	3.56 E+9
20 deg 100 cm	Y = 0.35 Z = 63.86	3.40 E+9	1.13 E+8	1.77 E+9
25 deg 25 cm	Y = 0.11 Z = 63.15	1.62 E+10	5.40 E+8	8.46 E+9
30 deg 100 cm	Y = 0.50 Z = 63.78	1.63 E+9	5.44 E+7	8.52 E+8
40 deg 100 cm	Y = 0.64 Z = 63.68	8.90 E+8	2.87 E+7	4.49 E+8
45 deg 25 cm	Y = 0.18 Z = 63.10	6.03 E+9	2.05 E+8	3.21 E+9
60 deg 100 cm	Y = 0.87 Z = 63.42	3.60 E+8	1.20 E+7	1.88 E+8
65 deg 25 cm	Y = 0.23 Z = 63.02	2.37 E+9	7.89 E+7	1.24 E+10
90 deg 100 cm	Y = 1.00 Z = 62.92	1.37 E+8	4.56 E+6	7.14 E+7
90 deg 25 cm	Y = 0.25 Z = 62.92	1.19 E+9	3.76 E+7	5.89 E+8

Run VI
Mercury
Angular distribution

14.6 GeV/c
Installations 1 and 2
61-min. exposure
5.48 E+11 p/sec

Location	Coordinates	Detector size (g)	Net count rate (bkg subtracted) at t_0 (cpm)	ϕ at $I=10^{12}$ p/sec (n/cm^2-sec)
3°–100 cm	Y = 0.05 Z = 63.92	152	4.98 E+5	7.32 E+8
10°–100 cm	Y = 0.18 Z = 63.90	152	8.27 E+4	1.22 E+8
20°–100 cm	Y = 0.35 Z = 63.86	152	1.38 E+4	2.03 E+7
25°–25 cm	Y = 0.11 Z = 63.15	152	5.91 E+4	8.64 E+7
30°–100 cm	Y= 0.50 Z = 63.78	152	3.04 E+3	4.48 E+6
40°–100 cm	Y = 0.64 Z = 63.68	152	5.88 E+2	8.65 E+5
45°–25 cm	Y = 0.18 Z = 63.10	152	5.02 E+3	7.38 E+6
60°–100 cm	Y = 0.87 Z = 63.42	432	8.73 E+1	4.53 E+4
65°–25 cm	Y = 0.23 Z = 63.02	152	3.06 E+2	4.49 E+5
90°–100 cm	Y = 1.00 Z = 62.92	432	4.74 E+0	2.45 E+3
90°–25 cm	Y = 0.25 Z = 62.92	152	2.03 E+1	3.00 E+4

Run VI	14.6 GeV/c
TLD	All installations
Angular distribution	61-min. exposure
22-mg detector	5.48 E+11 p/sec

Location	Coordinates	Dose (rads)
25–25°	Y = 0.11 Z = 63.15	1.05 E+3
25–45°	Y = 0.18 Z = 63.10	2.01 E+3
25–65°	Y = 0.23 Z = 63.02	2.84 E+3
25–90°	Y = 0.25 Z = 62.92	2.18 E+3
100–2°	Y = 0.05 Z = 63.92	3.00 E+3
100–10°	Y = 0.18 Z = 63.90	----
100–20°	Y = 0.35 Z = 63.86	3.25 E+3
100–30°	Y = 0.50 Z = 63.78	2.87 E+3
100–40°	Y = 0.64 Z = 63.68	2.38 E+3
100–60°	Y = 0.87 Z = 63.42	1.28 E+3
100–90°	Y = 1.00 Z = 62.92	4.73 E+2

Run VI
Sulfur
Vertical profile array
4-g detector

14.6 GeV/c
All installations
61-min. exposure
5.48 E+11 p/sec

Location	Coordinates	ϕ at $\bar{I}$ (n/cm^2-sec)	ϕ at I=10^{12} p/sec (n/cm^2-sec)
32/0/100	Y = 0.74 Z = 62.92	7.15 E+6	1.30 E+7
32/0/50	Y = 1.24 Z = 62.92	3.63 E+6	6.62 E+6
32/0/B	Y = 1.74 Z = 62.92	2.53 E+6	4.61 E+6
32/0/H	Y = 2.14 Z = 62.92	2.06 E+6	3.76 E+6
32/1/100	Y = 0.74 Z = 63.92	1.19 E+7	2.17 E+7
32/1/50	Y = 1.24 Z = 63.92	5.53 E+6	8.68 E+6
32/1/B	Y = 1.74 Z = 63.92	3.23 E+6	5.89 E+6
32/1/H	Y = 2.14 Z = 63.92	2.35 E+6	4.29 E+6
m 32 o a	Y = 0.60 Z = 64.66	1.68 E+7	3.06 E+7
m 32 a	Y = 0.60 Z = 65.09	7.59 E+6	1.38 E+7
32/2/100	Y = 0.74 Z = 64.92	5.72 E+6	1.04 E+7
32/2/50	Y = 1.24 Z = 64.92	4.10 E+6	7.48 E+6
32/2/B	Y = 1.74 Z = 64.92	2.91 E+6	5.31 E+6
32/2/H	Y = 2.14 Z = 64.92	2.40 E+6	4.38 E+6
m 32 b	Y = 0.60 Z = 65.30	2.96 E+6	5.40 E+6
m 32 c	Y = 0.60 Z = 65.73	1.59 E+6	2.90 E+6
32/3/100	Y = 0.74 Z = 65.92	1.18 E+6	2.15 E+6
32/3/50	Y = 1.24 Z = 65.92	1.66 E+6	3.03 E+6
32/3/B	Y = 1.74 Z = 65.92	1.74 E+6	3.17 E+6
32/3/H	Y = 2.14 Z = 65.92	1.72 E+6	3.14 E+6
m 32 d	Y = 0.60 Z = 66.15	1.07 E+6	1.95 E+6
m 32 e	Y = 0.60 Z = 66.58	8.58 E+5	1.56 E+6
m 32 f	Y = 0.60 Z = 67.00	8.04 E+5	1.47 E+6
32/4/100	Y = 0.74 Z = 66.92	9.83 E+5	1.79 E+6
32/4/50	Y = 1.24 Z = 66.92	1.18 E+6	2.15 E+6

Location	Coordinates	ϕ at $\bar{I}$ (n/cm^2-sec)	ϕ at I=10^{12} p/sec (n/cm^2-sec)
32/4/B	Y = 1.74 Z = 66.92	1.29 E+6	2.35 E+6
32/4/H	Y = 2.14 Z = 66.92	1.35 E+6	2.46 E+6
m 32 g	Y = 0.60 Z = 67.43	8.15 E+5	1.49 E+6
m 32 h	Y = 0.60 Z = 67.86	6.92 E+5	1.26 E+6
32/5/100	Y = 0.74 Z = 67.92	8.87 E+5	1.62 E+6
32/5/50	Y = 1.24 Z = 67.92	1.06 E+6	1.93 E+6
32/5/B	Y = 1.74 Z = 67.92	1.11 E+6	2.02 E+6
32/5/H	Y = 2.14 Z = 67.92	1.18 E+6	2.15 E+6
m 32 i	Y = 0.60 Z = 68.28	5.98 E+5	1.09 E+6
m 32 j	Y = 0.60 Z = 68.50	5.78 E+5	1.05 E+6
m 32 j o	Y = 0.60 Z = 68.92	1.15 E+6	2.10 E+6
m 32 j l	Y = 0.30 Z = 69.0	6.50 E+6	1.19 E+7
s 33 a	Y = 0.60 Z = 69.36	3.38 E+6	6.16 E+6
33/0/100	Y = 0.74 Z = 69.48	2.94 E+6	5.36 E+6
33/0/50	Y = 1.24 Z = 69.48	1.69 E+6	3.08 E+6
33/0/B	Y = 1.74 Z = 69.48	1.32 E+6	2.41 E+6
33/0/H	Y = 2.14 Z = 69.48	1.03 E+6	1.88 E+6
s 33 b	Y = 0.60 Z = 69.79	4.99 E+6	9.10 E+6
s 33 c	Y = 0.60 Z = 70.23	4.75 E+6	8.66 E+6
33/1/100	Y = 0.74 Z = 70.48	3.38 E+6	6.16 E+6
33/1/50	Y = 1.24 Z = 70.48	1.79 E+6	3.26 E+6
33/1/B	Y = 1.74 Z = 70.48	1.32 E+6	2.41 E+6
33/1/H	Y = 2.74 Z = 70.48	1.10 E+6	2.01 E+6
m 32 o a	Y = 0.60 Z = 70.66	3.27 E+6	5.96 E+6
m 33 a	Y = 0.60 Z = 71.09	1.33 E+6	2.43 E+6
m 33 b	Y = 0.60 Z = 71.30	8.42 E+5	1.54 E+6
33/2/100	Y = 0.74 Z = 71.48	7.06 E+5	1.29 E+6
33/2/50	Y = 1.24 Z = 71.48	9.37 E+5	1.71 E+6

Location	Coordinates	ϕ at $\bar{I}$ (n/cm^2-sec)	ϕ at I=10^{12} p/sec (n/cm^2-sec)
33/2/B	Y = 1.74 Z = 71.48	9.86 E+5	1.80 E+6
33/2/H	Y = 2.14 Z = 71.48	8.31 E+5	1.52 E+6
m 33 c	Y = 0.60 Z = 71.73	5.40 E+5	9.85 E+5
m 33 d	Y = 0.60 Z = 72.15	5.02 E+5	9.16 E+5
33/3/100	Y = 0.74 Z = 72.48	5.40 E+5	9.85 E+5
33/3/50	Y = 1.24 Z = 72.48	5.68 E+5	1.04 E+6
33/3/B	Y = 1.74 Z = 72.48	5.96 E+5	1.09 E+6
33/3/H	Y = 2.14 Z = 72.48	7.17 E+5	1.31 E+6
m 33 e	Y = 0.60 Z = 72.58	4.06 E+5	7.40 E+5
m 33 f	Y = 0.60 Z = 73.00	4.34 E+5	7.92 E+5
m 33 g	Y = 0.60 Z = 73.43	4.03 E+5	7.35 E+5
33/4/100	Y = 0.74 Z = 73.48	4.68 E+5	8.54 E+5
33/4/50	Y = 1.24 Z = 73.48	5.28 E+5	9.63 E+5
33/4/B	Y = 1.74 Z = 73.48	5.53 E+5	1.01 E+6
33/4/H	Y = 2.14 Z = 73.48	5.13 E+5	9.36 E+5
m 33 h	Y = 0.60 Z = 73.86	3.63 E+5	6.62 E+5
m 33 i	Y = 0.60 Z = 74.48	3.49 E+5	6.37 E+5
33/5/100	Y = 0.74 Z = 74.48	4.38 E+5	7.99 E+5
33/5/50	Y = 1.24 Z = 74.48	5.27 E+5	9.61 E+5
33/5/B	Y = 1.74 Z = 74.48	5.24 E+5	9.56 E+5
33/5/H	Y = 2.14 Z = 74.48	5.33 E+5	9.72 E+5
m 33 j	Y = 0.60 Z = 74.50	3.41 E+5	6.22 E+5
m 33 j o	Y = 0.60 Z = 74.92	5.53 E+5	1.01 E+6
34/0/100	Y = 0.74 Z = 75.48	1.06 E+6	1.93 E+6
34/0/50	Y = 1.24 Z = 75.48	6.27 E+5	1.44 E+6
34/0/B	Y = 1.74 Z = 75.48	5.72 E+5	1.04 E+6
34/0/H	Y = 2.14 Z = 75.48	4.72 E+5	8.61 E+5

Run VI — 14.6 GeV/c
Aluminum — All installations
Vertical profile array — 61-min. exposure
5.48 E+11 p/sec

Location	Coordinates	Detector size (g)	Net count rate (bkg subtracted) at t_0 (cpm)	ϕ at $\bar{I}$ (n/cm^2-sec)	ϕ at I=10^{12} p/sec (n/cm^2-sec)
32/0/100	Y = 0.74 Z = 62.92	16.9	1.21 E+5	3.13 E+6	5.71 E+6
32/0/50	Y = 1.24 Z = 62.92	16.9	6.11 E+4	1.58 E+6	2.88 E+6
32/0/B	Y = 1.74 Z = 62.92	100	1.83 E+5	9.06 E+5	1.65 E+6
32/0/H	Y = 2.14 Z = 62.92	16.9	3.15 E+4	8.17 E+5	1.49 E+6
32/1/100	Y = 0.74 Z = 63.92	16.9	2.45 E+5	6.34 E+6	1.16 E+7
32/1/50	Y = 1.24 Z = 63.92	16.9	1.10 E+5	2.85 E+6	5.20 E+6
32/1/B	Y = 1.74 Z = 63.92	100	3.04 E+5	1.50 E+6	2.74 E+6
32/1/H	Y = 2.14 Z = 63.92	16.9	4.21 E+4	1.09 E+6	1.99 E+6
m 32 o a	Y = 0.60 Z = 64.66	16.9	3.97 E+5	1.03 E+7	1.88 E+7
m 32 a	Y = 0.60 Z = 65.09	16.9	1.73 E+5	4.49 E+6	8.19 E+6
32/2/100	Y = 0.74 Z = 64.92	16.9	1.60 E+5	4.14 E+6	7.55 E+6
32/2/50	Y = 1.24 Z = 64.92	16.9	9.14 E+4	2.37 E+6	4.32 E+6
32/2/B	Y = 1.74 Z = 64.92	100	3.00 E+5	1.49 E+6	2.72 E+6
32/2/H	Y = 2.14 Z = 64.92	16.9	4.31 E+4	1.12 E+6	2.04 E+6
m 32 b	Y = 0.60 Z = 65.30	16.9	6.33 E+4	1.64 E+6	2.99 E+6
m 32 c	Y = 0.60 Z = 65.73	16.9	3.05 E+4	7.90 E+5	1.44 E+6
32/3/100	Y = 0.74 Z = 65.92	16.9	2.43 E+4	6.30 E+5	1.15 E+6
32/3/50	Y = 1.24 Z = 65.92	16.9	4.71 E+4	1.22 E+6	2.23 E+6
32/3/B	Y = 1.74 Z = 65.92	100	2.03 E+5	1.00 E+6	1.82 E+6
32/3/H	Y = 2.14 Z = 65.92	16.9	3.29 E+4	8.52 E+5	1.55 E+6
m 32 d	Y = 0.60 Z = 66.15	16.9	1.79 E+4	4.64 E+5	8.46 E+5
m 32 e	Y = 0.60 Z = 66.58	16.9	1.46 E+4	3.78 E+5	6.89 E+5
m 32 f	Y = 0.60 Z = 67.00	16.9	1.41 E+4	3.66 E+5	6.68 E+5
32/4/100	Y = 0.74 Z = 66.92	16.9	1.61 E+4	4.17 E+5	7.61 E+5
32/4/50	Y = 1.24 Z = 66.92	16.9	2.04 E+4	5.29 E+5	9.65 E+5

Location	Coordinates	Detector size (g)	Net count rate (bkg subtracted) at t_0 (cpm)	ϕ at $\bar{I}$ (n/cm^2-sec)	ϕ at I=10^{12} p/sec (n/cm^2-sec)
32/4/B	Y = 1.74 Z = 66.92	100	1.52 E+5	7.51 E+5	1.37 E+6
32/4/H	Y = 2.14 Z = 66.92	16.9	2.60 E+4	6.73 E+5	1.23 E+6
m 32 g	Y = 0.60 Z = 67.43	16.9	1.26 E+4	3.25 E+5	5.93 E+5
m 32 h	Y = 0.60 Z = 67.86	16.9	1.10 E+4	2.85 E+5	5.20 E+5
32/5/100	Y = 0.74 Z = 67.92	16.9	1.29 E+4	3.34 E+5	6.09 E+5
32/5/50	Y = 1.24 Z = 67.92	16.9	1.65 E+4	4.28 E+5	7.81 E+5
32/5/B	Y = 1.74 Z = 67.92	100	1.07 E+5	5.31 E+5	9.69 E+5
32/5/H	Y = 2.14 Z = 67.92	16.9	2.30 E+4	5.96 E+5	1.09 E+6
m 32 i	Y = 0.60 Z = 68.28	16.9	9.99 E+3	2.59 E+5	4.72 E+5
m 32 j	Y = 0.60 Z = 68.50	16.9	1.00 E+4	2.60 E+5	4.74 E+5
m 32 j o	Y = 0.60 Z = 68.92	16.9	1.86 E+4	4.81 E+5	8.77 E+5
m 32 j l	Y = 0.30 Z = 69.0	16.9	1.52 E+5	3.95 E+6	7.20 E+6
s 32 a	Y = 0.60 Z = 69.36	16.9	6.60 E+4	1.71 E+6	3.12 E+6
33/0/100	Y = 0.74 Z = 69.48	16.9	5.25 E+4	1.36 E+6	2.48 E+6
33/0/50	Y = 1.24 Z = 69.48	16.9	3.08 E+4	7.98 E+5	1.46 E+6
33/0/B	Y = 1.74 Z = 69.48	100	1.16 E+5	5.76 E+5	1.05 E+6
33/0/H	Y = 2.14 Z = 69.48	16.9	1.87 E+4	4.84 E+5	8.83 E+5
s 33 b	Y = 0.60 Z = 69.79	16.9	9.34 E+4	2.42 E+6	4.41 E+6
s 33 c	Y = 0.60 Z = 70.23	16.9	9.71 E+4	2.52 E+6	4.60 E+6
33/1/100	Y = 0.74 Z = 70.48	16.9	6.86 E+4	1.78 E+6	3.25 E+6
33/1/50	Y = 1.24 Z = 70.48	16.9	3.50 E+4	9.08 E+5	1.66 E+6
33/1/B	Y = 1.74 Z = 70.48	100	1.22 E+5	6.06 E+5	1.11 E+6
33/1/H	Y = 2.14 Z = 70.48	16.9	1.89 E+4	4.89 E+5	8.92 E+5
m 33 o a	Y = 0.60 Z = 70.66	16.9	7.63 E+4	1.98 E+6	3.61 E+6
m 33 a	Y = 0.60 Z = 71.09	16.9	2.85 E+4	7.39 E+5	1.35 E+6
m 33 b	Y = 0.60 Z = 71.30	16.9	1.44 E+4	3.72 E+5	6.79 E+5
33/2/100	Y = 0.74 Z = 71.48	16.9	1.34 E+4	3.47 E+5	6.33 E+5
33/2/50	Y = 1.24 Z = 71.48	16.9	2.05 E+4	5.30 E+5	9.67 E+5

Location	Coordinates	Detector size (g)	Net count rate (bkg subtracted) at t_0 (cpm)	ϕ at $\bar{I}$ (n/cm^2-sec)	ϕ at I=10^{12} p/sec (n/cm^2-sec)
33/2/B	Y = 1.74 Z = 71.48	100	9.26 E+4	4.59 E+5	8.37 E+5
33/2/H	Y = 2.14 Z = 71.48	16.9	1.52 E+4	3.92 E+5	7.15 E+5
m 33 c	Y = 0.60 Z = 71.73	16.9	9.06 E+3	2.35 E+5	4.29 E+5
m 33 d	Y = 0.60 Z = 72.15	16.9	8.29 E+3	2.15 E+5	3.92 E+5
33/3/100	Y = 0.74 Z = 72.48	16.9	8.35 E+3	2.16 E+5	3.94 E+5
33/3/50	Y = 1.24 Z = 72.48	16.9	1.13 E+4	2.92 E+5	5.33 E+5
33/3/B	Y = 1.74 Z = 72.48	100	6.93 E+4	3.43 E+5	6.26 E+5
33/3/H	Y = 2.14 Z = 72.48	16.9	1.23 E+4	3.19 E+5	5.82 E+5
m 33 e	Y = 0.60 Z = 72.58	16.9	7.84 E+3	2.03 E+5	3.70 E+5
m 33 f	Y = 0.60 Z = 73.00	16.9	7.74 E+3	2.00 E+5	3.65 E+5
m 33 g	Y = 0.60 Z = 73.43	16.9	7.40 E+3	1.92 E+5	3.50 E+5
33/4/100	Y = 0.74 Z = 73.48	16.9	7.75 E+3	2.01 E+5	3.67 E+5
33/4/50	Y = 1.24 Z = 73.48	16.9	9.00 E+3	2.33 E+5	4.25 E+5
33/4/B	Y = 1.74 Z = 73.48	100	5.26 E+4	2.61 E+5	4.76 E+5
33/4/H	Y = 2.14 Z = 73.48	16.9	9.95 E+3	2.58 E+5	4.71 E+5
m 33 h	Y = 0.60 Z = 73.86	16.9	6.73 E+3	1.74 E+5	3.17 E+5
m 33 i	Y = 0.60 Z = 74.28	16.9	5.97 E+3	1.55 E+5	2.83 E+5
33/5/100	Y = 0.74 Z = 74.48	16.9	7.88 E+3	2.04 E+5	3.72 E+5
33/5/50	Y = 1.24 Z = 74.48	16.9	9.90 E+3	2.57 E+5	4.69 E+5
33/5/B	Y = 1.74 Z = 74.48	100	5.19 E+4	2.57 E+5	4.69 E+5
33/5/H	Y = 2.14 Z = 74.48	16.9	9.36 E+3	2.43 E+5	4.43 E+5
m 33 j	Y = 0.60 Z = 74.50	16.9	5.48 E+3	1.42 E+5	2.59 E+5
m 33 j o	Y = 0.60 Z = 74.92	16.9	8.68 E+3	2.25 E+5	4.10 E+5
34/0/100	Y = 0.71 Z = 75.48	16.9	1.92 E+4	4.98 E+5	9.08 E+5
34/0/50	Y = 1.24 Z = 75.48	16.9	1.20 E+4	3.09 E+5	5.64 E+5
34/0/B	Y = 1.74 Z = 75.48	100	5.02 E+4	2.49 E+5	4.54 E+5
34/0/H	Y = 2.14 Z = 75.48	16.9	8.32 E+3	2.15 E+5	3.92 E+5

Run VI
Aluminum → Na^{22}
Vertical profile array
16.9-g detector

14.6 GeV/c
All installations
61-min. exposure
5.48 E+11

Location	Coordinates	Net count rate (bkg subtracted) at t_0 (cpm)	Error (%)	ϕ at $\bar{I}$ (n/cm^2-sec)	ϕ at I=10^{12} p/sec (n/cm^2-sec)
32/0/100	Y = 0.74 Z = 62.92	2.62 E+1		3.94 E+6	7.19 E+6
32/0/50	Y = 1.24 Z = 62.92	1.27 E+1		1.90 E+6	3.47 E+6
32/0/B	Y = 1.74 Z = 62.92				
32/0/H	Y = 2.14 Z = 62.92	4.79 E+0	8.3	7.21 E+5	1.32 E+6
32/1/100	Y = 0.74 Z = 63.92	8.73 E+1		1.31 E+7	2.39 E+7
32/1/50	Y = 1.24 Z = 63.92	3.19 E+1		4.77 E+6	8.70 E+6
32/1/B	Y = 1.74 Z = 63.92				
32/1/H	Y = 2.14 Z = 63.92	9.66 E+0		1.45 E+6	2.64 E+6
m 32 o a	Y = 0.60 Z = 64.66	1.42 E+2		3.07 E+7	5.60 E+7
m 32 a	Y = 0.60 Z = 65.09	5.47 E+1		8.19 E+6	1.49 E+7
32/2/100	Y = 0.74 Z = 64.92	7.64 E+1		1.15 E+7	2.10 E+7
32/2/50	Y = 1.24 Z = 64.92	3.58 E+1		5.38 E+6	9.81 E+6
32/2/B	Y = 1.74 Z= 64.92				
32/2/H	Y = 2.14 Z = 64.92	1.22 E+1		1.83 E+6	3.34 E+6
m 32 b	Y = 0.60 Z = 65.30	1.82 E+1		2.73 E+6	4.98 E+6
m 32 c	Y = 0.60 Z = 65.73	6.08 E+0		9.13 E+5	1.67 E+6
32/3/100	Y = 0.74 Z = 65.92	5.72 E+0	5.7	8.56 E+5	1.56 E+6
32/3/50	Y = 1.24 Z = 65.92	2.10 E+1		3.16 E+6	5.76 E+6
32/3/B	Y = 1.74 Z = 65.92				
32/3/H	Y = 2.14 Z = 65.92	1.29 E+1		1.94 E+6	3.54 E+6
m 32 d	Y = 0.60 Z = 66.15	4.34 E+0	7.2	6.50 E+5	1.19 E+6
m 32 e	Y = 0.60 Z = 66.58	3.25 E+0	9.8	4.87 E+5	8.88 E+5
m 32 f	Y = 0.60 Z = 67.00	3.28 E+0	9.1	4.91 E+5	8.96 E+5
32/4/100	Y = 0.74 Z = 66.92	2.35 E+0	11.3	3.52 E+5	6.42 E+5
32/4/50	Y = 1.24 Z = 66.92	3.66 E+0	9.1	5.48 E+5	1.00 E+6

Location	Coordinates	Net count rate (bkg subtracted) at t_0 (cpm)	Error (%)	ϕ at $\bar{I}$ (n/cm^2-sec)	ϕ at I=10^{12} p/sec (n/cm^2-sec)
32/4/B	Y = 1.74 Z = 66.92				
32/4/H	Y = 2.14 Z = 66.92	7.75 E+0		1.16 E+6	2.12 E+6
m 32 g	Y = 0.60 Z = 67.43	2.25 E+0	13.9	3.38 E+5	6.17 E+5
m 32 h	Y = 0.60 Z = 67.86	2.12 E+0	14.9	3.18 E+5	5.80 E+5
32/5/100	Y = 0.74 Z = 67.92	1.14 E+0	18.1	1.71 E+5	3.12 E+5
32/5/50	Y = 1.24 Z = 67.92	2.18 E+0	8.6	3.27 E+5	5.96 E+5
32/5/B	Y = 1.74 Z = 67.92				
32/5/H	Y = 2.14 Z = 67.92	6.52 E+0	5.2	9.78 E+5	1.78 E+5
m 32 i	Y = 0.60 Z = 68.28	2.76 E+0	11.2	4.14 E+5	7.55 E+5
m 32 j	Y = 0.60 Z = 68.50	1.60 E+0	14.5	2.40 E+5	4.38 E+5
m 32 j o	Y = 0.60 Z = 68.92	3.49 E+0	8.9	5.24 E+5	9.56 E+5
m 32 j l	Y = 0.30 Z = 68.67	4.76 E+1		7.16 E+6	1.31 E+7
s 32 a	Y = 0.60 Z = 69.36	1.68 E+1		2.53 E+6	4.61 E+6
33/0/100	Y = 0.74 Z = 69.48	1.14 E+1	5.3	1.71 E+6	3.12 E+6
33/0/50	Y = 1.24 Z = 69.48	5.83 E+0		8.75 E+5	1.60 E+6
33/0/B	Y = 1.74 Z = 69.48				
33/0/H	Y = 2.14 Z = 69.48	3.13 E+0	8.8	4.73 E+5	8.63 E+5
s 33 b	Y = 0.60 Z = 69.79	2.72 E+1		4.09 E+6	7.46 E+6
s 33 c	Y = 0.60 Z = 70.23	3.15 E+1		4.73 E+6	8.63 E+6
33/1/100	Y = 0.74 Z = 70.48	2.12 E+1	5.3	3.19 E+6	5.82 E+6
33/1/50	Y = 1.24 Z = 70.48	9.42 E+0		1.41 E+6	2.57 E+6
33/1/B	Y = 1.74 Z = 70.48				
33/1/H	Y = 2.14 Z = 70.48	3.87 E+0	6.9	5.80 E+5	1.06 E+6
m 33 o a	Y = 0.60 Z = 70.66	2.69 E+1		4.04 E+6	7.37 E+6
m 33 a	Y = 0.60 Z = 71.09	7.06 E+0		1.06 E+6	1.93 E+6
m 33 b	Y = 0.60 Z = 71.30	2.97 E+0	10.3	4.46 E+5	8.14 E+5
33/2/100	Y = 0.74 Z = 71.48	5.09 E+0	6.3	7.63 E+5	1.39 E+6

Location	Coordinates	Net count rate (bkg subtracted) at t_0 (cpm)	Error (%)	ϕ at $\bar{I}$ (n/cm^2-sec)	ϕ at I=10^{12} p/sec (n/cm^2-sec)
33/2/50	Y = 1.24 Z = 71.48	5.96 E+0	5.4	8.94 E+5	1.63 E+6
33/2/B	Y = 1.74 Z = 71.48				
33/2/H	Y = 2.14 Z = 71.48	4.87 E+0	6.7	7.30 E+5	1.33 E+6
m 33 c	Y = 0.60 Z = 71.73	2.59 E+0	12.3	3.88 E+5	7.08 E+5
m 33 d	Y = 0.60 Z = 72.15	2.22 E+0	14.1	3.34 E+5	6.09 E+5
33/3/100	Y = 0.74 Z = 72.48	1.90 E+0	16.4	2.86 E+5	5.22 E+5
33/3/50	Y = 1.24 Z = 72.48	3.81 E+0	8.2	5.71 E+5	1.04 E+6
33/3/B	Y = 1.74 Z = 72.48				
33/3/H	Y = 2.14 Z = 72.48	3.15 E+0	10.1	4.73 E+5	8.63 E+5
m 33 e	Y = 0.60 Z = 72.58				
m 33 f	Y = 0.60 Z = 73.00				
m 33 g	Y = 0.60 Z = 73.43				
33/4/100	Y = 0.74 Z = 73.48				
33/4/50	Y = 1.24 Z = 73.48				
33/4/B	Y = 1.74 Z = 73.48				
33/4/H	Y = 2.14 Z = 73.48	2.36 E+0	15.1	3.54 E+5	6.46 E+5
m 33 h	Y = 0.60 Z = 73.86				
m 33 i	Y = 0.60 Z = 74.28				
33/5/100	Y = 0.74 Z = 74.48				
33/5/50	Y = 1.24 Z = 74.48				
33/5/B	Y = 1.74 Z = 74.48				
33/5/H	Y = 2.14 Z = 74.48				
m 33 j	Y = 0.60 Z = 74.50				
m 33 j o	Y = 0.60 Z = 74.92	2.04 E+0	15.7	3.06 E+5	5.58 E+5
34/0/100	Y = 0.74 Z = 75.48	3.24 E+0		4.87 E+5	8.88 E+5
34/0/50	Y = 1.24 Z = 75.48				
34/0/B	Y = 1.74 Z = 75.48				
34/0/H	Y = 2.14 Z = 75.48				

Run VI — 14.6 GeV/c
TLD — All installations
Vertical profile array — 61-min. exposure
22-mg detector — 5.48 E+11 p/sec

Location	Coordinates	Dose (rads)
32/0/100	Y = 0.74 Z = 62.92	6.15 E+2
32/0/50	Y = 1.24 Z = 62.92	2.57 E+2
32/0/B	Y = 1.74 Z = 62.92	1.79 E+2
32/0/H	Y = 2.14 Z = 62.92	1.33 E+2
32/1/100	Y = 0.74 Z = 63.92	2.06 E+3
32/1/50	Y = 1.24 Z = 63.92	9.20 E+2
32/1/B	Y = 1.74 Z = 63.92	3.92 E+2
32/1/H	Y = 2.14 Z = 63.92	2.45 E+2
m 32 o a	Y = 0.60 Z = 64.66	2.03 E+3
m 32 a	Y = 0.60 Z = 65.09	9.70 E+2
32/2/100	Y = 0.74 Z = 64.92	1.50 E+3
32/2/50	Y = 1.24 Z = 64.92	1.02 E+3
32/2/B	Y = 1.74 Z = 64.92	5.11 E+2
32/2/H	Y = 2.14 Z = 64.92	3.67 E+2
m 32 b	Y = 0.60 Z = 65.30	2.71 E+2
m 32 c	Y = 0.60 Z = 65.73	1.44 E+2
32/3/100	Y = 0.74 Z = 65.92	7.6 E+1
32/3/50	Y = 1.24 Z = 65.92	5.37 E+2
32/3/B	Y = 1.74 Z = 65.92	4.21 E+2
32/3/H	Y = 2.14 Z = 65.92	3.38 E+2
32/2/100	Y = 0.74 Z = 64.92	1.50 E+3
32/2/50	Y = 1.24 Z = 64.92	1.02 E+3
32/2/B	Y = 1.74 Z = 64.92	5.11 E+2
32/2/H	Y = 2.14 Z = 64.92	3.67 E+2
m 32 b	Y = 0.60 Z = 65.30	2.71 E+2

Location	Coordinates	Dose (rads)
m 32 c	Y = 0.60 Z = 65.73	1.44 E+2
32/3/100	Y = 0.74 Z = 65.92	7.6 E+1
32/3/50	Y = 1.24 Z = 65.92	5.37 E+2
32/3/B	Y = 1.74 Z = 65.92	4.21 E+2
32/3/H	Y = 2.14 Z = 65.92	3.38 E+2
m 32 d	Y = 0.60 Z = 66.15	8.39 E+1
m 32 e	Y = 0.60 Z = 66.58	7.99 E+1
m 32 f	Y = 0.60 Z = 67.00	9.31 E+1
32/4/100	Y = 0.74 Z = 66.92	1.31 E+2
32/4/50	Y = 1.24 Z = 66.92	2.30 E+2
32/4/B	Y = 1.74 Z = 66.92	1.13 E+2
32/4/H	Y = 2.14 Z = 66.92	2.21 E+2
m 32 g	Y = 0.60 Z = 67.43	6.6 E+1
m 32 h	Y = 0.60 Z = 67.86	6.62 E+1
32/5/100	Y = 0.74 Z = 67.92	9.28 E+1
32/5/50	Y = 1.24 Z = 67.92	1.64 E+2
32/5/B	Y = 1.74 Z = 67.92	1.82 E+2
32/5/H	Y = 2.14 Z = 67.92	3.66 E+2
m 32 i	Y = 0.60 Z = 68.28	5.88 E+1
m 32 j	Y = 0.60 Z = 68.50	5.33 E+1
m 32 j o	Y = 0.60 Z = 68.92	5.60 E+1
m 32 j i	Y = 0.30 Z = 69.0	1.02 E+3
s 32 a	Y = 0.60 Z = 69.36	6.88 E+2
33/0/100	Y = 0.74 Z = 69.48	6.30 E+2
33/0/50	Y = 1.24 Z = 69.48	3.15 E+2
33/0/B	Y = 1.74 Z = 69.48	2.32 E+2
33/0/H	Y = 2.14 Z = 69.48	2.07 E+2
s 33 b	Y = 0.60 Z = 69.79	1.15 E+3
s 33 c	Y = 0.60 Z = 70.23	1.24 E+3

Location	Coordinates	Dose (rads)
33/1/100	Y = 0.74 Z = 70.48	8.90 E+2
33/1/50	Y = 1.24 Z = 70.48	4.26 E+2
33/1/B	Y = 1.74 Z = 70.48	2.81 E+2
33/1/H	Y = 2.14 Z = 70.48	1.96 E+2
m 33 o a	Y = 0.60 Z = 70.66	7.80 E+2
m 33 a	Y = 0.60 Z = 71.09	1.58 E+2
m 33 b	Y = 0.60 Z = 71.30	8.31 E+1
33/2/100	Y = 0.74 Z = 71.48	9.30 E+1
32/2/50	Y = 1.24 Z = 71.48	2.74 E+2
33/2/B	Y = 1.74 Z = 71.48	2.36 E+2
33/2/H	Y = 2.14 Z = 71.48	2.00 E+2
m 33 c	Y = 0.60 Z = 71.73	5.34 E+1
m 33 d	Y = 0.60 Z = 72.15	4.79 E+1
33/3/100	Y = 0.74 Z = 72.48	6.29 E+1
33/3/50	Y = 1.24 Z = 72.48	1.30 E+2
33/3/B	Y = 1.74 Z = 72.48	1.52 E+2
33/3/H	Y = 2.14 Z = 72.48	2.05 E+2
m 33 e	Y = 0.60 Z = 72.58	5.42 E+1
m 33 f	Y = 0.60 Z = 73.00	4.51 E+1
m 33 g	Y = 0.60 Z = 73.43	3.95 E+1
33/4/100	Y = 0.74 Z = 73.48	5.94 E+1
33/4/50	Y = 1.24 Z = 73.48	1.46 E+2
33/4/B	Y = 1.74 Z = 73.48	1.08 E+2
33/4/H	Y = 2.14 Z = 73.48	1.18 E+2
m 33 h	Y = 0.60 Z = 73.86	4.05 E+1
m 33 i	Y = 0.60 Z = 74.28	3.81 E+1
33/5/100	Y = 0.74 Z = 74.48	6.07 E+1
33/5/50	Y = 1.24 Z = 74.48	8.82 E+1
33/5/B	Y = 1.74 Z = 74.48	2.09 E+2
33/5/H	Y = 2.14 Z = 74.48	1.20 E+2

Location	Coordinates	Dose (rads)
M 33 j	Y = 0.60 Z = 74.50	4.31 E+1
m 33 j o	Y = 0.60 Z = 74.92	3.96 E+1
34/0/100	Y = 0.74 Z = 75.48	1.58 E+2
34/0/50	Y = 1.24 Z = 75.48	1.12 E+2
34/0/B	Y = 1.74 Z = 75.48	9.86 E+1
34/0/H	Y = 2.14 Z = 75.48	9.40 E+1

Run VI-½ Data

Run VI-½ exposure summary.*

Exposure Number	Beam energy (GeV/c)	Average beam current (p/sec)	Exposure duration (min)	Exposure time
1	14.64	2.17 E+11	40	0237 – 0317
2	14.64	4.49 E+11	50	0328 – 0418
3	14.64	4.45 E+11	40	0436 – 0516
4	14.64	4.16 E+11	40	0530 – 0610
5	14.64	4.40 E+11	41	0623 – 0704
entire run	14.64	3.13 E+11	267	0237 – 0704

*Target location: straight section 32;
clipper location: straight section 79.

Run VI½. Activities for aluminum foils on vacuum vessel.*

Standard position	Foil activity (pCi/g)	Standard position	Foil activity (pCi/g)	Standard position	Foil activity (pCi/g)	Standard position	Foil activity (pCi/g)
1	2.28 E+4	26	5.66 E+4	51	1.21 E+4	76	2.48 E+4
2	8.29 E+4	27	2.82 E+3	52	3.67 E+4	77	8.39 E+3
3	5.62 E+4	28	1.95 E+5	53	5.36 E+4	78	8.90 E+3
4	3.07 E+4	29	1.32 E+5	54	1.19 E+4	79	3.13 E+7
5	7.58 E+4	30	8.23 E+4	55	1.97 E+4	80	1.81 E+6
6	2.26 E+4	31	4.73 E+4	56	3.57 E+4	81	1.88 E+6
7	1.22 E+4	32	4.06 E+7	57	8.90 E+3	82	5.97 E+5
8	4.67 E+4	33	4.81 E+6	58	2.74 E+5	83	5.70 E+5
9	1.54 E+5	34	1.35 E+6	59	3.24 E+5	84	3.76 E+5
10	1.04 E+6	35	4.53 E+5	60	1.11 E+5	85	8.33 E+4
11	1.33 E+5	36	3.45 E+5	61	4.40 E+4	86	8.00 E+4
12	5.99 E+5	37	1.39 E+5	62	2.78 E+5	87	2.56 E+5
13	1.34 E+5	38	3.37 E+4	63	1.12 E+5	88	3.72 E+5
14	2.51 E+5	39	1.25 E+5	64	1.59 E+5	89	6.03 E+5
15	9.36 E+4	40	2.53 E+4	65	4.30 E+4	90	1.27 E+5
16	5.39 E+4	41	7.17 E+4	66	7.77 E+4	91	4.38 E+5
17	7.04 E+4	42	3.01 E+5	67	5.78 E+4	92	1.56 E+5
18	1.32 E+5	43	1.28 E+5	68	7.31 E+4	93	8.83 E+4
19	7.21 E+5	44	1.45 E+5	69	8.93 E+4	94	1.66 E+5
20	4.81 E+4	45	3.72 E+4	70	3.07 E+4	95	5.34 E+4
21	5.29 E+4	46	1.20 E+4	71	6.85 E+4	96	3.83 E+4
22	2.93 E+5	47	1.09 E+4	72	9.05 E+4	97	4.20 E+4
23	5.94 E+4	48	1.04 E+4	73	3.17 E+4	98	5.44 E+4
24	3.47 E+4	49	8.16 E+4	74	6.88 E+5	99	5.86 E+4
25	1.92 E+4	50	2.40 E+4	75	4.40 E+4	100	2.02 E+5

*One-hundred foils listed here.

Run VI½
Aluminum
Roof buckets
100-g samples

14.6 GeV/c
All installations
267-min. exposure
3.13 E+11 p/sec

Location	Coordinates	Net count rate (bkg. subtracted) at t_0 (cpm/g)	ϕ at $\bar{I}$ (n/cm^2-sec)	ϕ at $I = 10^{12}$ p/sec (n/cm^2-sec)
31–R	Z = 56.6	1.52 E+4	1.86 E+4	5.94 E+4
32–R	Z = 62.9	5.19 E+5	6.34 E+5	2.03 E+6
33–R	Z = 69.2	2.68 E+5	3.27 E+5	1.04 E+6
34–R	Z = 75.5	1.18 E+5	1.45 E+5	4.63 E+5

Run VI½
Aluminum
Orbit holes
555-g detector

14.6 GeV/c
All installations
267-min exposure
3.13 E+11 p/sec

Location	Coordinates	Net count rate (bkg subtracted) at t_0 (cpm)	ϕ at $\bar{I}$ (n/cm^2-sec)	ϕ at I=10^{12} p/sec (n/cm^2-sec)
33–330	Y = 3.42 Z = 69.2	2.46 E+4	6.25 E+3	2.00 E+4
33–390	Y = 4.01 Z = 69.2	6.15 E+3	1.56 E+3	4.98 E+3
33–450	Y = 4.60 Z = 69.2	1.46 E+3	3.70 E+2	1.18 E+3
33–510	Y = 5.19 Z = 69.2	3.91 E+2	9.92 E+1	3.17 E+2
33–570	Y = 5.78 Z = 69.2	1.11 E+2	5.96 E+1	1.90 E+2

Run VI½ — 14.6 GeV/c
Carbon — Installation 1
Orbit holes; streaming — 40-min. exposure
Hole 32-earth; hole 33-empty — 4-in. detector
2.17 E+11 p/sec

Location	Coordinates	Net count rate (bkg subtracted) at t_0 (cpm)	ϕ at I=10^{12} p/sec (n/cm^2-sec)
32–33	Y = 3.67 Z = 62.92	2.63 E+6	1.33 E+5
32–39	Y = 4.26 Z = 62.92	7.43 E+5	3.76 E+4
32–45	Y = 4.55 Z = 62.92	1.89 E+5	9.54 E+3
32–51	Y = 5.44 Z = 62.92	5.33 E+4	2.70 E+3
32–57	Y = 6.03 Z = 62.92	1.39 E+4	7.09 E+2
33–33	Y = 3.42 Z = 69.20	6.07 E+6	3.14 E+5
33–39	Y = 4.01 Z = 69.20	1.85 E+6	9.37 E+4
33–45	Y = 4.60 Z = 69.20	5.10 E+5	2.58 E+4
33–51	Y = 5.19 Z = 69.20	1.57 E+5	7.93 E+3
33–57	Y = 5.78 Z = 69.20	5.42 E+4	2.74 E+3

Run VI½ 14.6 GeV/c
Carbon Installation 2
Orbit holes; streaming 50-min. exposure
Hole 32-earth; hole 33-empty 4-in. detector
4.49 E+11 p/sec

Location	Coordinates	Net count rate (bkg subtracted) at t_0 (cpm)	ϕ at $\bar{I}$ (n/cm^2-sec)	ϕ at I=10^{12} p/sec (n/cm^2-sec)
32–33	Y = 3.67 Z = 62.92	5.37 E+6	6.36 E+4	1.42 E+5
32–39	Y = 4.26 Z = 62.92	2.13 E+6	2.51 E+4	5.60 E+4
32–45	Y = 4.85 Z = 62.92	6.61 E+5	7.77 E+3	1.73 E+4
32–51	Y = 5.44 Z = 62.92	2.30 E+5	2.71 E+3	6.04 E+3
32–57	Y = 6.03 Z = 62.92	9.02 E+4	1.06 E+3	2.36 E+3
33–33	Y = 3.42 Z = 69.20	1.12 E+7	1.33 E+5	2.97 E+5
33–39	Y = 4.01 Z = 69.20	2.78 E+6	3.30 E+4	7.36 E+4
33–45	Y = 4.60 Z = 69.20	6.83 E+5	8.04 E+3	1.79 E+4
33–51	Y = 5.19 E Z = 69.20	1.75 E+5	2.06 E+3	4.59 E+3
33–57	Y = 5.78 Z = 69.20	5.10 E+4	6.00 E+2	1.34 E+3

Run VI½ — 14.6 GeV/c
Carbon — Installation 3
Orbit holes; streaming — 40-min. exposure
Hole 32: earth + H_2O — 4-in. detector
Hole 33: Al + H_2O — 4.45 E+11 p/sec

Location	Coordinates	Net count rate (bkg subtracted) at t_0 (cpm)	ϕ at $\bar{I}$ (n/cm^2-sec)	ϕ at I=10^{12} p/sec (n/cm^2-sec)
32–33	Y = 3.67 Z = 62.92	4.31 E+6	5.62 E+4	1.26 E+5
32–39	Y = 4.26 Z = 62.92	1.07 E+6	1.39 E+4	3.13 E+4
32–45	Y = 4.85 Z = 62.92	2.65 E+5	3.43 E+3	7.72 E+3
32–51	Y = 5.44 Z = 62.92	7.18 E+4	9.29 E+2	2.09 E+3
32–57	Y = 6.03 Z = 62.92	1.89 E+4	2.45 E+2	5.51 E+2
33–33	Y = 3.42 Z = 69.20	1.07 E+7	1.42 E+5	3.20 E+5
33–39	Y = 4.01 Z = 69.20	2.11 E+6	2.73 E+4	6.14 E+4
33–45	Y = 4.60 Z = 69.20	5.16 E+5	6.68 E+3	1.50 E+4
33–51	Y = 5.12 Z = 69.20	1.33 E+5	1.72 E+3	3.87 E+3
33–57	Y = 5.78 Z = 69.20	3.71 E+4	4.80 E+2	1.08 E+3

Run VI½ — 14.6 GeV/c
Carbon — Installation 4
Orbit holes; streaming — 40-min. exposure
Hole 32: Al+H_2O — 4-in. detector
Hole 33: Earth + H_2O — 4.16 E+11 p/sec

Location	Coordinates	Net count rate (bkg subtracted) at t_0 (cpm)	ϕ at I = 10^{12} p/sec (n/cm^2-sec)
32–33	Y = 3.67 Z = 62.92	3.94 E+6	1.24 E+5
32–39	Y = 4.26 Z = 62.92	9.29 E+5	2.91 E+4
32–45	Y = 4.85 Z = 62.92	2.37 E+5	7.35 E+4
32–51	Y = 5.44 Z = 62.92	6.18 E+4	1.02 E+3
32–57	Y = 6.03 Z = 62.92	1.58 E+4	4.92 E+2
33–33	Y = 3.42 Z = 69.20	9.27 E+6	2.91 E+5
33–39	Y = 4.01 Z = 69.20	2.13 E+6	6.63 E+4
33–45	Y = 4.60 Z = 69.20	5.09 E+5	1.58 E+4
33–51	Y = 5.19 Z = 69.20	1.35 E+5	4.20 E+3
33–57	Y = 5.78 Z = 69.20	3.70 E+4	1.15 E+3

Run VI½ — 14.6 GeV/c
Aluminum — All installations
Vent shaft — 267-min. exposure
500-g detector — 3.13 E+11 p/sec

Location	Coordinates	Net count rate (bkg subtracted) at t_0 (cpm)	ϕ at $\bar{I}$ (n/cm^2-sec)	ϕ at I=10^{12} p/sec (n/cm^2-sec)
33—vent	X = 103.2 Z = 70.6	5.50 E+4	1.80 E+4	5.75 E+4

Run VI½
Aluminum
Radial holes

14.6 GeV/c
All installations
267-min. exposure

3.13 E+11

Location	Coordinates	Detector size (g)	Net count rate (bkg subtracted) at t_0 (cpm/g)	ϕ at $\bar{I}$ (n/cm^2-sec)	ϕ at I=10^{12} p/sec (n/cm^2-sec)
32–1060	X = 106.0 Z = 62.9	2200	4.42 E+2	4.16 E+1	1.33 E+2
32–1075	X = 107.5 Z = 62.9	2200	4.3 E+1	2.3 E+0	7.35 E+0
33–1075	X = 107.5 Z = 69.2	6600	9.01 E+1	4.8 E+0	1.53 E+1
33–1060	X = 106.0 Z = 69.2	2200	3.18 E+2	3.0 E+1	9.58 E+1

Run VI½ 14.6 GeV/c
Carbon Installation 5
Tunnel 77 41-min. exposure
4.40 E+11 p/sec

Location (m)	Detector size (g)	Net count rate (bkg subtracted) at t_0 (cpm)	Error (%)	ϕ at I=10^{12} p/sec (n/cm^2-sec)
0	5	3.72 E+5		1.08 E+4
1.25	5	2.49 E+5		7.27 E+3
4	5	7.39 E+4		2.15 E+3
6	5	7.96 E+4		2.32 E+3
10	5	3.33 E+3		9.70 E+2
15	5	1.175 E+3		3.41 E+1
20	8	6.27 E+2		1.82 E+1
25	8	3.55 E+2		1.03 E+1
30	8	2.05 E+2	7.2	5.91 E+0
35	8	1.635 E+2	5.3	4.77 E+0

Run VII Data

Run VII exposure summary.*

Exposure number	Beam energy (GeV/c)	Average beam current (p/sec)	Exposure duration (min)	Exposure time
1	14.64	5.43 E+11	10	2044 – 2054
2	14.64	5.75 E+11	80	2109 – 2229
3	14.64	6.33 E+11	60	2243 – 2343
4	14.64	6.40 E+11	60	0005 – 0105
5	14.64	5.56 E+11	60	0116 – 0216
6	14.64	6.33 E+11	60	0228 – 0328
7	14.64	6.26 E+11	60	0338 – 0438
entire run	14.64	4.99 E+11	474	2044 – 0438

*Target location: straight section 32;
clipper location: straight section 52.

Run VII. Activities for aluminum foils on the vacuum vessel; standard positions.*

Standard position	Z	Foil activity (pCi/g)	Standard position	Z	Foil activity (pCi/g)
1		1.46 E+4	26	24.12	2.75 E+5
2		5.00 E+4	27	31.52	1.08 E+4
3		2.97 E+4	28	37.52	3.47 E+5
4		2.42 E+4	29	43.52	1.88 E+5
5		6.79 E+4	30	49.52	1.40 E+5
6		1.85 E+4	31	55.52	6.36 E+4
7		8.50 E+3	32	62.92	3.96 E+7
8		4.60 E+4	33	68.92	4.75 E+6
9		2.17 E+5	34	74.92	1.32 E+6
10		1.16 E+6	35	80.92	4.31 E+5
11		2.09 E+5	36	86.92	3.38 E+5
12		1.01 E+6	37	94.32	1.38 E+5
13		2.02 E+5	38	100.32	4.21 E+4
14		3.57 E+5	39	106.32	1.41 E+5
15		1.09 E+5	40	112.32	7.21 E+4
16		6.01 E+4	41	118.32	1.58 E+5
17		6.44 E+4	42	125.72	5.54 E+5
18		9.70 E+4	43	131.72	1.08 E+5
19		4.98 E+5	44	137.72	1.79 E+5
20		4.38 E+4	45	143.72	3.96 E+4
21		1.12 E+5	46	149.72	1.57 E+4
22		5.01 E+5	47	157.12	1.30 E+4
23		9.93 E+4	48	163.12	1.79 E+4
24	12.12	4.66 E+4	49	169.12	1.26 E+5
25	18.12	1.26 E+5	50	175.12	2.27 E+4

Standard position	Z	Foil activity (pCi/g)	Standard position	Z	Foil activity (pCi/g)
51	181.12	1.46 E+4	76		3.00 E+4
52	188.52	2.04 E+7	77		1.35 E+4
53	194.52	1.92 E+6	78		1.07 E+4
54		1.30 E+6	79		1.16 E+4
55		4.58 E+5	80	376.92	1.21 E+4
56		8.78 E+5	81		1.06 E+4
57		8.69 E+4	82		5.04 E+3
58		2.64 E+5	83		1.23 E+4
59		5.61 E+5	84		8.55 E+3
60		1.19 E+6	85	408.32	9.26 E+3
61		8.00 E+4	86		6.16 E+4
62		2.91 E+5	87		1.23 E+5
63		2.80 E+5	88		1.65 E+4
64		3.06 E+5	89		1.34 E+5
65		2.45 E+5	90	439.72	2.58 E+4
66		1.59 E+5	91		5.82 E+3
67		9.37 E+4	92		8.10 E+4
68		8.60 E+4	93		6.92 E+4
69		1.22 E+5	94		2.43 E+5
70		4.64 E+4	95	471.12	4.26 E+4
71		1.28 E+5	96		3.28 E+4
72		1.48 E+5	97		1.79 E+4
73		5.36 E+4	98		5.86 E+4
74		7.75 E+5	99		2.21 E+4
75	345.52	5.64 E+4	100	502.52	7.19 E+4

*One hundred foils listed here.

Run VII	14.6 GeV/c
Bare gold foils	All installations
Roof buckets	474-min. exposure
2-in. detector	4.99 E+11 p/sec

Location	Coordinates	net count rate (bkg subtracted) at t_0 (cpm)	ϕ at $\bar{I}$ (n/cm^2-sec)	ϕ at I=10^{12} p/sec (n/cm^2-sec)
29–R	Z = 44.08	1.23 E+4	1.51 E+5	3.03 E+5
31–R	Z = 56.64	7.04 E+4	8.61 E+5	1.73 E+6
31–2R	Z = 58.92	1.40 E+5	1.71 E+6	3.43 E+6
32–R	Z = 62.92	3.97 E+5	4.85 E+6	9.72 E+6
35–R	Z = 81.76	6.54 E+4	8.00 E+5	1.60 E+6

Run VII	14.6 GeV/c
Moderated gold foils	All installations
Roof buckets	474-min exposure
2-in. detector	4.99 E+11 p/sec

Location	Coordinates	Net count rate (bkg subtracted) at t_0 (cpm)	ϕ at $\bar{I}$ (n/cm^2-sec)	ϕ at I=10^{12} p/sec (n/cm^2-sec)
29–R	Z = 44.08	2.49 E+4	4.05 E+5	8.12 E+5
31–R	Z = 56.64	1.07 E+5	1.75 E+6	3.51 E+6
31–2R	Z = 58.92	3.43 E+5	5.56 E+6	1.11 E+7
32–R	Z = 62.92	1.17 E+6	1.91 E+7	3.83 E+7
35–R	Z = 81.76	1.55 E+5	2.51 E+6	5.03 E+6

Run VII
Sulfur
Roof buckets
4-g samples

14.6 GeV/c
All installations
474-min exposure
4.99 E+11 p/sec

Location	Coordinates	ϕ at $\overline{I}$ (n/cm^2-sec)	ϕ at I = 10^{12} p/sec (n/cm^2-sec)
29–R	Z = 44.08	3.35 E+4	6.72 E+4
30–R	Z = 50.36	6.03 E+4	1.21 E+5
31–R	Z = 56.64	1.01 E+5	2.03 E+5
31–1R	Z = 57.92	1.55 E+5	3.11 E+5
31–2R	Z = 58.92	2.06 E+5	4.12 E+5
31–3R	Z = 59.92	3.80 E+5	7.62 E+5
31–4R	Z = 60.92	6.29 E+5	1.26 E+6
31–5R	Z = 61.92	1.13 E+6	2.26 E+6
32–R	Z = 62.92	2.27 E+6	4.55 E+6
32–1R	Z = 63.93	3.13 E+6	6.27 E+6
32–2R	Z = 64.92	2.77 E+6	5.56 E+6
32–3R	Z = 65.92	1.58 E+6	3.16 E+6
32–4R	Z = 66.92	1.16 E+6	2.33 E+6
32–5R	Z = 67.92	1.02 E+6	2.05 E+6
33–R	Z = 69.20	1.21 E+6	2.42 E+6
33–1R	Z = 70.48	1.15 E+6	2.31 E+6
33–2R	Z = 71.48	8.33 E+5	1.67 E+6
33–3R	Z = 72.48	6.24 E+5	1.25 E+6
33–4R	Z = 73.48	4.71 E+5	9.43 E+5
33–5R	Z = 74.48	4.75 E+5	9.52 E+5
34–R	Z = 75.48	5.49 E+5	1.10 E+6
35–R	Z = 81.76	2.05 E+5	4.10 E+5
36–R	Z = 88.08	1.32 E+5	2.64 E+5
37–R	Z = 94.32	5.29 E+5	1.06 E+6
38–R	Z = 100.60	2.75 E+4	5.51 E+4

Run VII
Aluminum
Roof buckets
100-g samples

14.6 GeV/c
All installations
474-min. exposure
4.99 E+11 p/sec

Location	Coordinates	Net count rate (bkg. subtracted) at t_0 (cpm/g)	ϕ at $\bar{I}$ (n/cm^2-sec)	ϕ at $I=10^{12}$ P/sec (n/cm^2-sec)
29–R	Z = 44.08	1.56 E+4	1.16 E+4	2.32 E+4
30–R	Z = 50.36	3.49 E+4	2.60 E+4	5.21 E+4
31–R	Z = 56.64	4.42 E+4	3.28 E+4	6.57 E+4
31–1R	Z = 57.92	6.34 E+4	4.70 E+4	9.42 E+4
31–2R	Z = 58.92	8.32 E+4	6.18 E+4	1.24 E+5
31–3R	Z = 59.92	1.41 E+5	1.05 E+5	2.10 E+5
31–4R	Z = 60.92	2.71 E+5	2.02 E+5	4.05 E+5
31–5R	Z = 61.92	5.11 E+4	4.48 E+5	8.98 E+5
32–R	Z = 62.92	1.09 E+5	9.53 E+5	1.91 E+6
32–1R	Z = 63.92	1.74 E+5	1.52 E+6	3.05 E+6
32–2R	Z = 64.92	1.70 E+5	1.49 E+6	2.99 E+6
32–3R	Z = 65.92	1.14 E+5	9.98 E+5	2.00 E+6
32–4R	Z = 66.92	7.61 E+4	6.67 E+4	1.34 E+5
32–5R	Z = 67.92	5.37 E+4	4.71 E+5	9.44 E+5
33–R	Z = 69.20	6.07 E+4	5.32 E+5	1.07 E+6
33–1R	Z = 70.48	6.41 E+4	5.62 E+5	1.13 E+6
33–2R	Z = 71.48	5.16 E+4	4.52 E+5	9.06 E+5
33–3R	Z = 72.48	4.17 E+5	3.10 E+5	6.21 E+5
33–4R	Z = 73.48	3.18 E+5	2.37 E+5	4.75 E+5
33–5R	Z = 74.48	3.00 E+5	2.23 E+5	4.47 E+5
34–R	Z = 75.48	3.14 E+5	2.33 E+5	4.67 E+5
35–R	Z = 81.76	1.40 E+5	1.04 E+5	2.08 E+5
36–R	Z = 88.08	9.23 E+4	6.86 E+4	1.37 E+5
37–R	Z = 94.32	4.13 E+4	3.07 E+4	6.15 E+4
38–R	Z = 100.60	2.72 E+4	2.02 E+4	4.05 E+4
50–R		6.22 E+3	4.62 E+3	9.26 E+3
51–R				
52–R		4.20 E+5	3.12 E+5	6.25 E+5
53–R		1.47 E+5	1.09 E+5	2.18 E+5
54–R		1.49 E+5	1.11 E+5	2.22 E+5
55–R		7.68 E+4	5.71 E+4	1.14 E+5
56–R		7.66 E+4	5.70 E+4	1.14 E+5
57–R		2.87 E+4	2.13 E+4	4.27 E+4
58–R		7.91 E+4	5.88 E+4	1.18 E+5
59–R		4.42 E+4	3.29 E+4	6.59 E+4
60–R		1.14 E+5	8.49 E+4	1.70 E+5

Run VII
Carbon
Roof buckets
1-in.-diam detector

14.6 GeV/c
Installation 1
10-min. exposure
5.43 E+11 p/sec

Location	Coordinates	Net count rate (bkg subtracted) at t_0 (cpm/g)	ϕ at $\bar{I}$ (n/cm^2-sec)	ϕ at I = 10^{12} p/sec (n/cm^2-sec)
29–0R	Z = 44.08	4.38 E+5	1.46 E+4	2.69 E+4
31–0R	Z = 56.64	1.01 E+6	3.38 E+4	6.23 E+4
31–2R	Z = 58.92	2.03 E+6	6.76 E+4	1.25 E+4
32–0R	Z = 62.92	5.67 E+7	1.89 E+6	3.48 E+6
35–0R	Z = 81.76	9.58 E+6	3.20 E+5	5.89 E+5

Run VII
TLD
Roof buckets
22-mg samples

26.4 GeV/c
All installations
474-min exposure
4.99 E+11 p/sec

Location	Coordinates	Indicated dose (rads/hour)
31–2R	Z = 57.9	1.92 E+2
31–2R	Z = 57.9	1.88 E+2
31–2R	Z = 57.9	1.96 E+2
31–2R	Z = 57.9	2.04 E+2
31–2R	Z = 57.9	2.02 E+2
31–2R	Z = 57.9	2.00 E+2
31–2R	Z = 57.9	2.09 E+2
32–0R	Z = 62.9	3.20 E+3
32–0R	Z = 62.9	3.36 E+3
32–0R	Z = 62.9	3.22 E+3
32–0R	Z = 62.9	3.15 E+3
32–0R	Z = 62.9	3.33 E+3
32–0R	Z = 62.9	3.32 E+3
32–0R	Z = 62.9	3.32 E+3

Run VII
Aluminum
Orbit holes
500-g detector*

14.6 GeV/c
All installations
474-min. exposure
4.99 E+11 p/sec

Location	Coordinates	Net count rate (bkg subtracted) at t_0 (cpm)	Error (%)	ϕ at $\bar{I}$ (n/cm^2-sec)	ϕ at I = 10^{12} p/sec (n/cm^2-sec)
31–330	Y = 3.53 Z = 56.64	3.59 E+3		5.54 E+2	1.11 E+3
31–390	Y = 4.12 Z = 56.64	7.27 E+2		1.45 E+2	2.91 E+2
31–450	Y = 4.71 Z = 56.64	1.87 E+2		3.73 E+1	7.47 E+1
31–510	Y = 5.30 Z = 56.64	5.21 E+1	10.	1.04 E+1	2.08 E+1
31–570	Y = 5.89 Z = 56.64	1.44 E+1	19.	2.8 E+0	5.6 E+0
32–330	Y = 3.42 Z = 62.92	1.22 E+5		2.44 E+4	4.88 E+4
32–390	Y = 4.26 Z = 62.92	3.59 E+4		7.16 E+3	1.43 E+4
32–450	Y = 4.71 Z = 62.92	9.41 E+3		1.88 E+3	3.77 E+3
32–510	Y = 5.44 Z = 62.92	2.37 E+3		4.73 E+2	9.48 E+2
32–570	Y = 6.03 Z = 62.92	6.46 E+2		1.29 E+2	2.58 E+2
33–330	Y = 3.67 Z = 69.20	2.58 E+5		5.14 E+4	1.03 E+5
33–390	Y = 4.01 Z = 69.20	6.91 E+4		1.38 E+4	2.76 E+4
33–450	Y = 4.60 Z = 69.20	1.72 E+4		3.44 E+3	6.89 E+3
33–510	Y = 5.19 Z = 69.20	4.42 E+3		8.82 E+2	1.77 E+3
33–570	Y = 5.78 Z = 69.20	1.28 E+3		2.55 E+2	5.11 E+2
34–330	Y = 3.63 Z = 75.48	5.36 E+4		8.26 E+3	1.66 E+4
34–390	Y = 4.22 Z = 75.48	1.30 E+4		2.59 E+3	5.19 E+3
34–450	Y = 4.81 Z = 75.48	3.51 E+3		7.00 E+2	1.40 E+3
34–510	Y = 5.40 Z = 75.48	1.03 E+3		2.06 E+2	4.13 E+2
34–570	Y = 5.90 Z = 75.48	2.92 E+2		5.8 E+1	1.16 E+2
35–330	Y = 3.45 Z = 81.76	3.72 E+4		5.74 E+3	1.15 E+4
35–390	Y = 4.04 Z = 81.76	7.54 E+3		1.50 E+3	3.01 E+3
35–450	Y = 4.63 Z = 81.76	1.88 E+3		3.75 E+2	7.52 E+2
35–510	Y = 5.22 Z = 81.76	5.48 E+2		1.09 E+2	2.18 E+2
35–570	Y = 5.81 Z = 81.76	1.51 E+2		3.0 E+1	6.0 E+1
36–330	Y = 3.31 Z = 88.08	2.68 E+4		5.35 E+3	1.07 E+4

Location	Coordinates	Net count rate (bkg subtracted) at t_0 (cpm)	Error (%)	ϕ at $\bar{I}$ (n/cm^2-sec)	ϕ at $I = 10^{12}$ p/sec (n/cm^2-sec)
36–390	Y = 3.90 Z = 88.08	6.45 E+3		1.29 E+3	2.58 E+3
36–450	Y = 4.49 Z = 88.08	1.48 E+3		2.94 E+2	5.89 E+2
36–510	Y = 5.08 Z = 88.08	4.15 E+2		8.3 E+1	1.66 E+2
36–570	Y = 5.67 Z = 88.08	1.07 E+2	5.8	2.1 E+1	4.2 E+1
37–330	Y = 3.59 Z = 94.32	5.18 E+3		1.03 E+3	2.06 E+3
37–390	Y = 4.18 Z = 94.32	1.28 E+3		2.55 E+2	5.11 E+2
37–450	Y = 4.77 Z = 94.32	3.31 E+2		6.6 E+1	1.32 E+2
37–510	Y = 5.36 Z = 94.32	1.03 E+2	5.6	2.0 E+1	4.0 E+1
37–570	Y = 5.95 Z = 94.32	2.4 E+1	13.	4.7 E+0	9.4 E+0
38–330	Y = 3.48 Z = 100.60	3.37 E+3		6.72 E+2	1.35 E+3
38–390	Y = 4.07 Z = 100.60	8.22 E+2		1.64 E+2	3.29 E+2
38–450	Y = 4.66 Z = 100.60	2.07 E+2		4.1 E+1	8.2 E+1
38–510	Y = 5.30 Z = 100.60	5.6 E+1	6.4	1.1 E+1	2.2 E+1
38–570	Y = 5.84 Z = 100.60	1.6 E+1	14.	3.1 E+0	6.2 E+0

*All detectors were 500 g except those at locations 31–330, 34–330, and 35–330, which were 555 g.

Run VII
Carbon
Orbit holes
4-in. detector

14.6 GeV/c
Installation 4
60-min. exposure
6.40 E+11 p/sec

Location	Coordinates	Net count rate (bkg subtracted) at t_0 (cpm)	ϕ at $\bar{I}$ (n/cm^2-sec)	ϕ at I=10^{12} p/sec (n/cm^2-sec)
31–33	Y = 3.53 Z = 56.64	1.27 E+5	1.400 E+3	2.18 E+3
31–39	Y = 4.12 Z = 56.64	3.02 E+4	3.34 E+2	5.21 E+2
31–45	Y = 4.71 Z = 56.64	7.456 E+3	8.24 E+1	1.29 E+2
31–51	Y = 5.30 Z = 56.64	1.905 E+3	2.10 E+1	3.27 E+1
31–57	Y = 5.89 Z = 56.64	6.88 E+2	7.6 E+0	1.10 E+1
34–33	Y = 3.63 Z = 75.48	2.76 E+6	3.05 E+4	4.76 E+4
34–39	Y = 4.22 Z = 75.48	7.90 E+5	8.732 E+3	1.36 E+4
34–45	Y = 4.81 Z = 75.48	2.19 E+5	2.417 E+3	3.77 E+3
34–51	Y = 5.40 Z = 75.48	6.10 E+4	6.75 E+2	1.05 E+3
34–57	Y = 5.99 Z = 75.58	1.73 E+4	1.94 E+2	3.03 E+2
35–33	Y = 3.45 Z = 81.76	1.87 E+6	2.07 E+4	3.23 E+4
35–39	Y = 4.04 Z = 81.76	4.50 E+5	4.975 E+3	7.76 E+3
35–45	Y = 4.63 Z = 81.76	1.16 E+5	1.284 E+3	2.00 E+3
35–51	Y = 5.22 Z = 81.76	3.13 E+4	3.46 E+2	5.40 E+2
35–57	Y = 5.81 Z = 81.76	9.089 E+3	1.00 E+2	1.56 E+2

Run VII 14.6 GeV/c
Moderated gold foils All installations
Ring top 474-min. exposure
4.99 E+11 p/sec

Location	Coordinates	Detector size (in.)	Net count rate (bkg subtracted) at t_0 (cpm)	Error (%)	ϕ at $\bar{I}$ (n/cm^2-sec)	ϕ at $I=10^{12}$ p/sec (n/cm^2-sec)
31/3.6	Y = 6.41 Z = 60.24	2 (2)	1.2 E+1	5.3	8.5 E+0	1.70 E+1
31/4.8	Y = 6.42 Z = 61.44	2 (2)	3.65 E+1	6.6	2.59 E+1	5.19 E+1
32/0	Y = 6.42 Z = 62.92	2 (2)	9.7 E+1		6.9 E+1	1.38 E+2
32/1.2	Y = 6.41 Z = 64.15	2 (2)	1.19 E+2		8.47 E+1	1.70 E+2
32/2.4	Y = 6.41 Z = 65.32	2 (2)	1.35 E+2		9.6 E+1	1.92 E+2
32/3.6	Y = 6.40 Z = 66.52	2 (2)	1.44 E+2		1.02 E+2	2.04 E+2
32/4.8	Y = 6.40 Z = 67.72	2 (2)	1.83 E+2		1.30 E+2	2.61 E+2
33/0	Y = 6.39 Z = 69.20	2	6.79 E+1		8.3 E+1	1.66 E+2
34/0	Y = 6.29 Z = 75.48	2 (2)	5.85 E+1		4.15 E+1	8.32 E+1
35/0	Y = 6.30 Z = 81.76	2 (2)	1.90 E+1	5.8	1.35 E+1	2.71 E+1
36/0	Y = 6.26 Z = 88.08	2 (2)	1.43 E+1	9.0	1.01 E+1	2.02 E+1
37/0	Y = 6.26 Z = 94.32	2 (2)	7.57 E+0		5.37 E+0	1.08 E+1

Run VII
Aluminum
Ring top
4.99 E+11 p/sec

14.6 GeV/c
All installations
474-min. exposure

Location	Coordinates	Detector size (g)	Net count rate (bkg subtracted) at t_0 (cpm)	Error (%)	ϕ at $\bar{I}$ (n/cm^2-sec)	ϕ at I = 10^{12} p/sec (n/cm^2-sec)
31/0	Y = 6.40 Z = 56.64	6600	2.5 E+1	11.	8.0 E-1	1.6 E+0
31/4.8	Y = 6.42 Z = 61.44	6600	4.41 E+2		1.43 E+1	2.87 E+1
32/0	Y = 6.42 Z = 62.92	2250	8.16 E+2		4.1 E+1	8.22 E+1
32/1.2	Y = 6.41 Z = 64.15	2250	1.09 E+3		5.48 E+1	1.10 E+2
32/2.4	Y = 6.41 Z = 65.32	2250	1.32 E+3		6.63 E+1	1.33 E+2
32/3.6	Y = 6.40 Z = 66.52	2250	1.27 E+3		6.4 E+1	1.28 E+2
32/4.8	Y = 6.40 Z = 67.72	2250	1.28 E+3		6.44 E+1	1.29 E+2
33/0	Y = 6.39 Z = 69.20	2250	9.38 E+2		4.7 E+1	9.42 E+1
33/3.2	Y = 6.34 Z = 72.40	2250	6.83 E+2		3.43 E+1	6.87 E+1
34/0	Y = 6.29 Z = 75.48	2250	4.11 E+2		2.07 E+1	4.15 E+1
35/0	Y = 6.30 Z = 81.76	6600	2.43 E+2		7.86 E+0	1.58 E+1

Run VII — 14.6 GeV/c
Carbon — Installation 6
Ring top — 60-min. exposure
5-in. detector — 6.33 E+11 p/sec

Location (m)	Coordinates	Net count rate (bkg subtracted) at t_0 (cpm)	ϕ at $\bar{I}$ (n/cm^2-sec)	ϕ at I=10^{12} p/sec (n/cm^2-sec)
31–3.6	Y = 6.40 Z = 60.24	1.60 E+3	1.77 E+1	2.79 E+1
31–4.8	Y = 6.40 Z = 61.44	5.66 E+3	6.26 E+1	0.88 E+1
32–0	Y = 6.42 Z = 62.92	1.49 E+4	1.65 E+2	2.61 E+2
32–1.2	Y = 6.42 Z = 64.12	1.88 E+4	2.08 E+2	3.28 E+2
32–2.4	Y = 6.42 Z = 65.32	2.41 E+4	2.67 E+2	4.22 E+2
32–3.6	Y = 6.42 Z = 66.52	2.31 E+4	2.55 E+2	4.03 E+2
32–4.8	Y = 6.42 Z = 67.72	2.43 E+4	2.68 E+2	4.23 E+2
33–0	Y = 6.39 Z = 69.20	2.00 E+4	2.22 E+2	3.51 E+2

Run VII — 14.6 GeV/c
Carbon — Installation 7
Ring top — 60-min. exposure
6.26 E+11 p/sec

Location	Coordinates	Detector size (in.)	Net count rate (bkg subtracted) at t_0 (cpm)	ϕ at $\bar{I}$ (n/cm^2-sec)	ϕ at I=10^{12} p/sec (n/cm^2-sec)
33–0	Y = 6.39 Z = 69.20	5	1.64 E+4	1.81 E+2	2.89 E+2
34–0	Y = 6.29 Z = 75.48	8	7.26 E+3	8.03 E+1	1.28 E+2
35–0	Y = 6.30 Z = 81.76	8	2.42 E+3	2.68 E+1	4.28 E+1
36–0	Y = 6.26 Z = 88.08	8	1.23 E+3	1.36 E+1	2.17 E+1
37–0	Y = 6.26 Z = 94.32	8	6.41 E+2	7.1 E+0	1.13 E+1

Run VII
Ion chamber
Ring top

14.6 GeV/c
Installation 5
5.6 E+11 p/sec

Location	Coordinates	Measurement time (sec)	$\bar{I}$ (μR/h)
31	Z = 56.64	38.4	9.36 E+1
31	Z = 56.64	35.6	1.01 E+2
31.5	Z = 59.78	9.0	4.0 E+2
31.5	Z = 59.78	43.	4.18 E+2
32	Z = 62.92	9.0	4.00 E+3
32	Z = 62.92	Pulse 1.5	9.60 E+3
32.5	Z = 66.06	5.2	6.90 E+3
32.5	Z = 66.06	Pulse 1.5	1.68 E+4
33	Z = 69.20	7	5.14 E+3
33	Z = 69.20	Pulse 1.5	1.20 E+4
33.5	Z = 72.34	8.4	4.28 E+3
33.5	Z = 72.34	9.5	3.78 E+3
33.5	Z = 72.34	10.5	3.43 E+3
33.5	Z = 72.34	12.4	2.90 E+3
33.5	Z = 72.34	Pulse 1.5	9.60 E+3
33.5	Z = 72.34	Pulse 1.5	7.20 E+3
34	Z = 75.48	21.0	1.72 E+3
34	Z = 75.48	20.8	1.73 E+3
34.5	Z = 78.62	15.	1.20 E+3
34.5	Z = 78.62	27.8	1.30 E+3
35	Z = 81.76	40.8	8.82 E+2
35.5	Z = 84.92	54.	6.67 E+2
35.5	Z = 84.92	5.2	6.92 E+2
36	Z = 88.08	7.0	5.14 E+2
36	Z = 88.08	7.5	4.80 E+2
37	Z = 94.32	15.8	2.28 E+2
38	Z = 100.6	26.8	1.34 E+2
39	Z = 106.88	31.0	1.16 E+2
40	Z = 113.16	64.2	5.6 E+1
41	Z = 119.44	68.4	5.3 E+1
42	Z = 125.72	30.	1.20 E+2
43	Z = 132.00	21.5	1.67 E+2
51	Z = 181.12	94.	3.8 E+1
51.5	Z = 184.82	34.2	1.05 E+2
52	Z = 188.52	59.6	6.04 E+2
52.5	Z = 191.52	38.0	9.47 E+2
53	Z = 194.52	40.0	9.00 E+2

Location	Coordinates	Measurement time (sec)	$\bar{I}$ (μ R/h)
53.5	Z = 197.52	55.8	6.45 E+2
54	Z = 200.52	63.0	5.71 E+2
54.5	Z = 203.52	8.3	4.34 E+2
55	Z = 206.52	11.2	3.21 E+2
55.5	Z = 209.52	13.2	2.73 E+2
56	Z = 212.52	13.8	2.61 E+2

Values from these tables were used to construct Figs. IV-3 and IV-4. Single-pulse and short-measurement-time readings were not used.

Run VII
Ion chamber
Ring top

14.6 GeV/c
Installation 6
5.6 E+11 p/sec

Location	Coordinates	Measurement time (sec)	$\bar{I}$ (μR/h)
32.5	X = 102.5 Z = 66.06	10.0	3.60 E+3
32.5	X = 101.5 Z = 66.06	6.0	6.00 E+3
32.5	X = 100. Z = 66.06	4.8	7.50 E+3
32.5	X = 98.5 Z = 66.06	5.0	7.20 E+3
32.5	X = 97.5 Z = 66.06	6.0	6.00 E+3
33	X = 102.5 Z = 69.20	12.0	3.00 E+3
33	X = 101.5 Z = 69.20	8.4	4.28 E+3
33	X = 100. Z = 69.20	6.6	5.45 E+3
33	X = 98.5 Z = 69.20	6.2	5.80 E+3
33	X = 97.5 Z = 69.20	6.8	5.29 E+3
33.5	X = 102.5 Z = 72.34	15.2	2.37 E+3
33.5	X = 101.5 Z = 72.34	8.5	4.24 E+3
33.5	X = 100. Z = 72.34	8.0	4.50 E+3
33.5	X = 98.5 Z = 72.34	5.8	6.21 E+3
33.5	X = 97.5 Z = 72.34	7.0	5.14 E+3
33.5	X = 98. Z = 72.34	6.0	6.00 E+3
33.5	X = 99. Z = 72.34	7.2	5.00 E+3
34	X = 102.5 Z = 75.48	31.5	1.14 E+3
34	X = 101.5 Z = 75.48	21.4	1.68 E+3
34	X = 100. Z = 75.48	13.8	2.61 E+3
34	X = 98.5 Z = 75.48	9.8	3.67 E+3
34	X = 97.5 Z = 75.48	12.	3.00 E+3
34.5	X = 102.5 Z = 78.62	45.8	7.86 E+2
34.5	X = 101.5 Z = 78.62	28.6	1.26 E+3
34.5	X = 100. Z = 78.62	20.8	1.73 E+3
34.5	X = 98.5 Z = 78.62	15.0	2.40 E+3

Location	Coordinates	Measurement time (sec)	$\bar{I}$ (μR/h)
34.5	X = 97.5 Z = 78.62	15.0	2.40 E+3
53.	X = 101.5 Z = 194.52	39.8	9.05 E+2
53.	X = 100. Z = 194.52	29.2	1.23 E+3
53.	X = 98.5 Z = 194.52	27.4	1.32 E+3
53.	X = 97.5 Z = 194.52	29.6	1.22 E+3
54.	X = 101.5 Z = 200.52	9	4.00 E+2
54.	X = 100. Z = 200.52	7.4	4.85 E+2
54.	X = 98.5 Z = 200.52	5.6	6.45 E+2
55.5	X = 100. Z = 209.52	12.2	2.95 E+2
55	X = 100. Z = 206.52	95.6	3.8 E+1
55	X = 100. Z = 206.52	10.4	3.46 E+2
55	X = 100. Z = 206.52	11.4	3.16 E+2
57	X = 100. Z = 219.92	25.	1.44 E+2
58	X = 100. Z = 225.92	24.	1.50 E+2
59	X = 100. Z = 231.92	25.5	1.41 E+2
60	X = 100. Z = 237.92	14.	2.57 E+2

Values from these tables were used to construct Figs. IV-3 and IV-4. Single-pulse and short-measurement-time readings were not used.

Run VII
Aluminum
Vent shaft
500-g detector

14.6 GeV/c
All installations
474-min. exposure
4.99 E+11 p/sec

Location	Coordinates	Net count rate (bkg subtracted) at t_0 (cpm)	ϕ at $\bar{I}$ (n/cm^2-sec)	ϕ at I=10^{12} p/sec (n/cm^2-sec)
33–V	X = 103.2 Z = 70.6	1.55 E+5	3.09 E+4	6.19 E+4

Run VII
Aluminum
Radial holes
500-g detector

14.6 GeV/c
All installations
474-min. exposure
4.99 E+11 p/sec

Location	Coordinates	Net count rate (bkg subtracted) at t_0 (cpm)	Error (%)	ϕ at $\bar{I}$ (n/cm^2-sec)	ϕ at I = 10^{12} p/sec (n/cm^2-sec)
32–935	Z = 62.92	6.49 E+2		1.29 E+2	2.58 E+2
34–935	Z = 75.48	9.7 E+1	8.4	1.9 E+1	3.8 E+1
32–1040	Z = 62.92	5.85 E+4		1.17 E+4	2.34 E+4

Run VII
Carbon
Radial holes
6.33 E+11 p/sec

14.6 GeV/c
Installation 3
60-min. exposure

Location	Coordinates	Detector size (in.)	Net count rate (bkg subtracted) at t_0 (cpm)	Error (%)	ϕ at $\bar{I}$ (n/cm^2-sec)	ϕ at I=10^{12} p/sec (n/cm^2-sec)
32–935	X = 93.5 Z = 62.92	4	3.92 E+4		4.34 E+2	6.86 E+2
34–935	X = 93.5 Z = 75.48	4	6.639 E+3		7.34 E+1	1.16 E+2
34–106	X = 106.0 Z = 75.48	5	8.847 E+3		9.78 E+1	1.55 E+2
34–107.5	X = 107.5 Z = 75.48	8	1.79 E+2		1.97 E+0	3.11 E+0
35–106	X = 106.0 Z = 81.76	5	1.03 E+4		1.14 E+2	1.80 E+2
35–107.5	X = 107.5 Z = 81.76	8	3.15 E+2		3.5 E+0	5.53 E+0
36–106	X = 106.0 Z = 88.08	5	9.534 E+3		1.05 E+2	1.66 E+2
36–107.5	X = 107.5 Z = 88.08	5	1.84 E+2	6.6	2.0 E+0	3.16 E+0

Run VII. Activities for close-spaced aluminum foils on the vacuum vessel. Data for foils at the standard positions are listed in the preceding table.

Magnet No.	Station	Z	Foil activity (pCi/g)	Magnet No.	Station	Z	Foil activity (pCi/g)
24	1	13.34	4.86 E+4	30	37	50.74	1.38 E+5
	2	13.68	4.76 E+4		38	51.08	2.69 E+5
	3	14.48	2.55 E+4		39	51.88	9.68 E+4
	4	15.28	2.26 E+4		40	52.68	7.41 E+4
	5	16.08	1.74 E+4		41	53.48	5.22 E+4
	6	16.88	5.47 E+4		42	54.28	4.35 E+4
25	7	19.34	7.19 E+4	31	43	58.14	1.45 E+5
	8	19.68	1.76 E+5		44	58.48	1.33 E+5
	9	20.48	8.20 E+4		45	59.28	8.23 E+4
	10	21.28	6.31 E+4		46	60.08	7.17 E+4
	11	22.08	7.03 E+4		47	60.88	1.19 E+5
	12	22.88	9.81 E+4		48	62.82	2.05 E+5
26	13	26.74	2.00 E+5	32	49	64.14	2.06 E+7
	14	27.08	1.81 E+5		50	64.48	2.34 E+7
	15	27.88	9.76 E+4		51	65.28	1.09 E+7
	16	28.68	6.20 E+4		52	66.08	8.64 E+6
	17	29.48	6.82 E+4		53	66.88	8.47 E+6
	18	31.42	5.08 E+4		54	67.68	6.31 E+6
27	19	32.74	2.16 E+4	33	55	70.14	4.77 E+6
	20	33.08	8.15 E+4		56	70.48	8.30 E+6
	21	33.88	4.85 E+4		57	71.28	6.98 E+6
	22	34.68	4.91 E+4		58	72.08	6.22 E+6
	23	35.48	4.59 E+4		59	72.88	5.73 E+6
	24	36.28	4.04 E+4		60	73.68	3.57 E+6
28	25	38.74	1.70 E+5	34	61	76.14	1.42 E+6
	26	39.08	3.67 E+5		62	76.48	2.18 E+6
	27	39.88	4.38 E+5		63	77.28	1.36 E+6
	28	40.68	1.36 E+5		64	78.08	7.53 E+5
	29	41.48	1.51 E+5		65	78.88	9.74 E+5
	30	42.28	1.53 E+5		66	79.68	7.24 E+5
29	31	44.74	1.25 E+5	35	67	82.14	3.25 E+5
	32	45.08	9.07 E+4		68	82.48	6.08 E+5
	33	45.88	6.20 E+4		69	83.28	5.72 E+5
	34	46.68	4.63 E+4		70	84.08	6.83 E+5
	35	47.48	1.41 E+5		71	84.88	1.43 E+6
	36	48.28	1.74 E+5		72	85.68	1.65 E+6

Magnet No.	Station	Z	Foil activity (pCi/g)	Magnet No.	Station	Z	Foil activity (pCi/g)
36	73	89.54	2.00 E+5	43	115	132.94	5.05 E+4
	74	89.88	5.24 E+5		116	133.28	9.64 E+4
	75	90.68	3.11 E+5		117	134.08	9.68 E+4
	76	91.48	1.74 E+5		118	134.88	8.35 E+4
	77	94.22	1.47 E+5		119	135.68	2.23 E+5
	78	94.22	1.43 E+5		120	136.48	5.57 E+5
37	79	95.54	1.05 E+5	44	121	138.04	1.95 E+5
	80	95.88	1.46 E+5		122	139.28	1.28 E+5
	81	96.68	1.20 E+5		123	140.08	5.16 E+4
	82	97.48	1.17 E+5		124	140.88	3.82 E+4
	83	98.28	2.05 E+5		125	141.68	3.26 E+4
	84	99.08	4.60 E+5		126	142.48	2.81 E+4
38	85	101.54	3.90 E+4	45	127	144.94	3.09 E+4
	86	101.88	7.29 E+4		128	145.28	3.56 E+4
	87	102.68	6.17 E+4		129	146.08	3.82 E+4
	88	103.48	7.37 E+4		130	146.88	3.45 E+4
	89	104.28	9.22 E+4		131	147.68	4.01 E+4
	90	105.08	1.31 E+5		132	148.48	3.42 E+4
39	91	107.54	6.38 E+4	46	133	152.34	1.43 E+4
	92	107.88	7.54 E+4		134	152.68	2.57 E+4
	93	108.68	5.93 E+4		135	153.48	1.62 E+4
	94	109.48	5.17 E+4		136	154.28	1.56 E+4
	95	110.28	6.90 E+4		137	155.08	1.09 E+4
	96	111.08	5.61 E+4		138	157.02	1.03 E+4
40	97	113.54	2.04 E+4	47	139	158.34	8.31 E+3
	98	113.88	2.32 E+4		140	158.68	2.13 E+4
	99	114.68	2.54 E+4		141	159.48	3.51 E+4
	100	115.48	3.01 E+4		142	160.28	3.56 E+4
	101	116.28	2.10 E+4		143	161.08	6.37 E+4
	102	117.08	3.72 E+4		144	161.88	5.74 E+4
41	103	120.94	3.27 E+4	48	145	164.34	1.22 E+4
	104	121.28	3.18 E+4		146	164.68	2.30 E+4
	105	122.08	2.47 E+4		147	165.48	1.27 E+4
	106	122.88	4.05 E+4		148	166.28	7.54 E+3
	107	123.68	1.07 E+5		149	167.08	8.33 E+3
	108	125.62	1.55 E+6		150	167.88	7.17 E+3
42	109	126.94	5.15 E+5	49	151	170.34	3.21 E+4
	110	127.28	2.74 E+5		152	170.68	3.88 E+4
	111	128.08	1.24 E+5		153	171.48	2.47 E+4
	112	128.88	8.27 E+4		154	172.28	1.50 E+4
	113	129.68	7.83 E+4		155	173.08	1.49 E+4
	114	130.48	8.71 E+4		156	173.88	1.99 E+4

Magnet No.	Station	Z	Foil activity (pCi/g)
50	157	176.34	3.41 E+4
	158	176.88	3.66 E+4
	159	177.68	2.29 E+4
	160	178.48	2.34 E+4
	161	179.28	1.89 E+4
	162	180.08	2.05 E+4
51	163	183.74	8.09 E+3
	164	184.08	1.22 E+4
	165	184.88	8.91 E+3
	166	185.68	1.29 E+4
	167	186.48	2.81 E+4
	168	188.42	1.49 E+5
52	169	189.74	3.33 E+6
	170	190.08	5.06 E+6
	171	190.88	2.70 E+6
	172	191.68	2.29 E+6
	173	192.48	1.17 E+6
	174	193.28	1.36 E+6
53	175	195.74	1.06 E+6
	176	196.08	3.48 E+6
	177	196.88	3.85 E+6
	178	197.68	4.03 E+6
	179	198.48	4.29 E+6
	180	199.28	3.79 E+6
54	181	201.74	1.03 E+6
78	182	352.74	1.95 E+4
	183	353.08	2.77 E+4
	184	353.88	1.64 E+4
	185	354.68	1.04 E+4
	186	355.48	8.75 E+3
	187	356.28	1.15 E+4
79	188	358.74	1.03 E+4
	189	359.08	1.26 E+4
	190	359.88	1.16 E+4
	191	360.68	1.36 E+4
	192	361.48	2.50 E+4
	193	362.28	3.24 E+4
80	194	364.74	1.26 E+4
	195	365.08	3.33 E+4
	196	365.88	5.51 E+4
	197	366.68	2.19 E+4
	198	367.48	1.15 E+4
	199	368.28	1.01 E+4
81	200	370.74	7.06 E+3

Run VII — 14.6 GeV/c
Bare gold foils — All installations
Tunnel 52 — 474-min. exposure
4.99 E+11 p/sec

Location	Coordinates	Detector size (in.)	Net count rate (bkg subtracted) at t_0 (cpm/g)	Error (%)	ϕ at $\bar{I}$ (n/cm^2-sec)	ϕ at I=10^{12} p/sec (n/cm^2-sec)
52/0	X = 0.0	1	4.78 E+4		1.02 E+6	2.04 E+6
52/10	X = 10.0	1	2.80 E+4		4.93 E+4	9.88 E+4
52/20	X = 20.0	1	2.61 E+3		4.61 E+3	9.24 E+3
52/30	X = 30.0	1	5.37 E+2		9.48 E+2	1.90 E+3
52/40	X = 40.0	2	2.53 E+2		2.33 E+2	4.67 E+2
52/50	X = 50.0	2	7.6 E+1	5.1	7.02 E+1	1.41 E+2
52/60	X = 60.0	2	4.2 E+1	7.1	3.85 E+1	7.72 E+1
52/70	X = 70.0	2	2.43 E+1	8.3	2.24 E+1	4.49 E+1
52/80	X = 80.0	2	1.51 E+1	9.3	1.4 E+1	2.81 E+1
52/90	X = 88.0	2	9.93 E+0	15.7	9.15 E+0	1.83 E+1

Run VII — 14.6 GeV/c
Bare gold foils — All installations
Tunnel 77 — 474-min. exposure
4.99 E+11 p/sec

Location	Coordinates	Detector size (in.)	Net count rate (bkg subtracted) at t_0 (cpm)	Error (%)	ϕ at $\bar{I}$ (n/cm^2-sec)	ϕ at I=10^{12} p/sec (n/cm^2-sec)
77/0	0.0	1	7.39 E+3		1.30 E+4	2.61 E+4
77/100		2	7.3 E+0	6.1	6.72 E+0	1.35 E+1

Run VII — 14.6 GeV/c
Moderated gold foils — All installations
Tunnel 77 — 474-min. exposure
4.99 E+11 p/sec

Location	Coordinates	Detector size (in.)	Net count rate (bkg subtracted) at t_0 (cpm/g)	Error (%)	ϕ at $\bar{I}$ (n/cm^2-sec)	ϕ at I=10^{12} p/sec (n/cm^2-sec)
77/0	Z = 0.0	1	1.50 E+4		3.11 E+4	6.23 E+4
77/100	Z = 2	2	1.85 E+1	11.7	2.26 E+1	4.53 E+1

Run VII
Moderated gold foils
Tunnel 52

14.6 GeV/c
All installations
474-min. exposure

4.99 E+11 p/sec

Location	Coordinates	Detector size (in.)	Net count rate (bkg subtracted) at t_0 (cpm)	ϕ at $\bar{I}$ (n/cm^2-sec)	ϕ at I=10^{12} p/sec (n/cm^2-sec)
52/0	X = 0.0	1	1.36 E+5	3.75 E+6	7.52 E+6
52/10	X = 10.0	1	5.22 E+4	1.08 E+5	2.16 E+5
52/20	X = 20.0	1	7.73 E+3	1.60 E+4	3.21 E+4
52/30	X = 30.0	1	2.14 E+3	4.44 E+3	8.90 E+3
52/40	X = 40.0	2	1.43 E+3	1.75 E+3	3.51 E+3
52/50	X = 50.0	2	4.59 E+2	5.60 E+2	1.12 E+3
52/60	X = 60.0	2	4.00 E+2	4.89 E+2	9.80 E+2
52/70	X = 70.0	2	1.70 E+2	2.08 E+2	4.17 E+2
52/80	X = 80.0	2	1.17 E+2	1.43 E+2	2.87 E+2
52/90	X = 88.0	2	7.1 E+1	8.7 E+1	1.74 E+2
52/100	X = 92.0	2	1.21 E+2	1.47 E+2	2.95 E+2

Run VII
Aluminum
Tunnel 52

14.6 GeV/c
All installations
4.99 E+11 p/sec

Location	Coordinates	Detector size (g)	Net count rate (bkg subtracted) at t_0 (cpm)	ϕ at $\bar{I}$ (n/cm^2-sec)	ϕ at I=10^{12} p/sec (n/cm^2-sec)
52/0	X = 0.0	500	5.87 E+5	8.58 E+4	1.72 E+5
52/10	X = 10.0	500	3.06 E+4	4.48 E+3	8.98 E+3
52/20	X = 20.0	500	7.70 E+3	1.13 E+3	2.26 E+3
52/30	X = 30.0	500	3.00 E+3	4.39 E+2	8.80 E+2
52/40	X = 40.0	500	1.48 E+3	2.17 E+2	4.35 E+2
52/50	X = 50.0	2200	2.07 E+3	8.66 E+1	1.74 E+2
52/60	X = 60.0	2200	1.46 E+3	6.13 E+1	1.23 E+2
52/70	X = 70.0	6600	1.74 E+3	4.14 E+1	8.30 E+1
52/80	X = 80.0	6600	1.04 E+3	2.46 E+1	4.93 E+1
52/90	X = 88.0	6600	8.83 E+2	2.10 E+1	4.21 E+1
52/100	X = 92.0	6600	8.03 E+2	1.91 E+1	3.83 E+1
*52/10	X = 10.0	500	2.24 E+4	4.48 E+3	8.98 E+3

*This detector was exposed for 474 min; all other detectors were also exposed during beam tune-up, but flux values are normalized to the 474-min exposure.

Run VII
Carbon
Tunnel 52

14.6 GeV/c
Installation 5
60-min. exposure

5.56 E+11 p/sec

Location (m)	Coordinates	Detector size (in.)	Net count rate (bkg subtracted) at t_0 (cpm)	ϕ at I=10^{12} p/sec (n/cm^2-sec)
0	X = 0.0	1	1.26 E+7	2.50 E+5
10	X = 10.0	1	7.64 E+5	1.52 E+4
20	X = 20.0	4	2.01 E+5	4.00 E+3
30	X = 30.0	4	8.85 E+4	1.76 E+3
40	X = 40.0	4	4.25 E+4	8.45 E+2
50	X = 50.0	5	1.83 E+4	3.63 E+2
60	X = 60.0	5	1.01 E+4	2.74 E+2
70	X = 70.0	5	1.38 E+4	1.09 E+2
80	X = 80.0	5	6.61 E+3	1.31 E+2
88	X = 88.0	5	5.65 E+3	1.12 E+2
92	X = 92.0	5	5.21 E+3	1.04 E+2

Run VIII Data

Run VIII exposure summary.*

Exposure number	Beam energy (GeV/c)	Average beam current (p/sec)	Exposure duration (min)	Exposure time
1	26.43	9.03 E+11	0.05	0944
2	26.43	6.50 E+11	60	1002 – 1102
3	26.43	6.52 E+11	90	1113 – 1243
4	26.43	6.58 E+11	60	1254 – 1354
5	26.43	6.67 E+11	90	1406 – 1536
6	26.43	6.76 E+11	90	1545 – 1715
exposures 2-6	26.43	5,97 E+11	433	1002 – 1715

*Target location: straight section 32;
clipper location: straight section 79.

Run VIII. Activities for aluminum foils on vacuum vessel.*

Standard position	Foil activity (pCi/g)	Standard position	Foil activity (pCi/g)	Standard position	Foil activity (pCi/g)	Standard position	Foil activity (pCi/g)
1	2.86 E+4	26	5.76 E+4	57	7.56 E+3	76	1.22 E+5
2	3.19 E+4	27	5.33 E+3	52	3.64 E+4	77	8.46 E+4
3	5.24 E+4	28	6.51 E+5	53	5.26 E+4	78	3.12 E+4
4	2.82 E+4	29	6.45 E+5	54	1.24 E+4	79	3.75 E+7
5	1.76 E+5	30	1.35 E+5	55	3.82 E+4	80	1.99 E+6
6	2.63 E+4	31	7.64 E+4	56	5.99 E+4	81	1.69 E+6
7	2.23 E+4	32	3.05 E+7	57	2.97 E+4	82	7.66 E+5
8	1.52 E+4	33	3.54 E+6	58	2.46 E+5	83	6.18 E+5
9	1.05 E+5	34	1.03 E+6	59	3.31 E+5	84	4.93 E+5
10	9.83 E+5	35	3.76 E+5	60	5.74 E+5	85	1.29 E+5
11	1.07 E+5	36	2.71 E+5	61	4.14 E+4	86	9.06 E+4
12	4.45 E+5	37	1.11 E+5	62	1.60 E+5	87	2.87 E+5
13	9.89 E+4	38	2.76 E+4	63	1.55 E+5	88	6.71 E+5
14	1.01 E+5	39	1.39 E+5	64	1.27 E+5	89	1.19 E+6
15	1.66 E+5	40	2.57 E+4	65	9.21 E+4	90	2.09 E+5
16	3.57 E+4	41	1.91 E+5	66	4.76 E+4	91	1.05 E+6
17	2.51 E+4	42	6.20 E+5	67	4.05 E+4	92	2.47 E+5
18	4.55 E+4	43	2.62 E+5	68	3.92 E+4	93	3.68 E+5
19	1.89 E+5	44	2.13 E+5	69	6.31 E+4	94	2.19 E+5
20	1.75 E+4	45	8.90 E+5	70	2.00 E+4	95	1.18 E+5
21	5.19 E+4	46	4.54 E+4	71	5.70 E+4	96	9.09 E+4
22	2.73 E+5	47	1.02 E+5	72	1.17 E+5	97	2.48 E+5
23	4.02 E+4	48	1.99 E+4	73	8.40 E+4	98	9.18 E+4
24	2.01 E+4	49	1.98 E+4	74	7.71 E+5	99	9.71 E+4
25	1.37 E+4	50	1.56 E+4	75	5.32 E+5	100	3.74 E+5

*One-hundred foils listed here.

Run VIII
Sulfur
Roof buckets
4-g samples

14.6 GeV/c
All installations
433-min exposure
5.97 E+11 p/sec

Location	Coordinates	ϕ at $\bar{I}$ (n/cm^2-sec)	ϕ at I = 10^{12} p/sec (n/cm^2-sec)
29–R	Z = 44.1	1.52 E+5	2.55 E+5
30–R	Z = 50.4	9.25 E+4	1.55 E+5
31–R	Z = 56.6	1.42 E+5	2.37 E+5
31–1R	Z = 57.9	2.50 E+5	4.19 E+5
31–2R	Z = 58.9	3.61 E+5	6.05 E+5
31–3R	Z = 59.9	5.18 E+5	8.67 E+5
31–4R	Z = 60.9	9.13 E+5	1.53 E+6
31–5R	Z = 61.9	1.77 E+6	2.96 E+6
32–R	Z = 62.9	3.65 E+6	6.12 E+6
32–1R	Z = 63.9	4.70 E+6	7.88 E+6
32–2R	Z = 64.9	4.27 E+6	7.15 E+6
32–3R	Z = 65.9	2.23 E+6	3.74 E+6
32–4R	Z = 66.9	1.72 E+6	2.89 E+6
32–5R	Z = 67.9	1.36 E+6	2.28 E+6
33–R	Z = 69.2	1.87 E+6	3.14 E+6
33–1R	Z = 70.5	1.66 E+6	2.78 E+6
33–2R	Z = 71.5	1.21 E+6	2.02 E+6
33–3R	Z = 72.5	9.37 E+5	1.57 E+6
33–4R	Z = 73.5	7.70 E+5	1.29 E+6
33–5R	Z = 74.5	7.22 E+5	1.21 E+6
34–R	Z = 75.5	7.70 E+5	1.29 E+6
35–R	Z = 81.8	2.85 E+5	4.77 E+5
36–R	Z = 88.1	1.80 E+5	3.02 E+5
76–R	Z = 44.1	7.76 E+4	1.30 E+5
77–R	Z = 50.4	6.21 E+4	1.04 E+5
78–R	Z = 56.6	1.10 E+5	1.84 E+5
78–1R	Z = 57.9	1.71 E+5	2.87 E+5
78–2R	Z = 58.9	2.27 E+5	3.81 E+5
78–3R	Z = 59.9	3.83 E+5	6.41 E+5
78–4R	Z = 60.9	7.58 E+5	1.27 E+6
78–5R	Z = 61.9	2.06 E+6	3.45 E+6
79–R	Z = 62.9	3.46 E+6	5.80 E+6
79–1R	Z = 63.9	2.72 E+6	4.55 E+6
79–2R	Z = 64.9	1.44 E+6	2.42 E+6
79–3R	Z = 65.9	8.48 E+5	1.42 E+6
79–4R	Z = 66.9	8.42 E+5	1.41 E+6
79–5R	Z = 67.9	8.60 E+5	1.44 E+6
80–R	Z = 69.2	9.08 E+5	1.52 E+6
80–1R	Z = 70.5	7.22 E+5	1.21 E+6
80–2R	Z = 71.5	5.22 E+5	8.74 E+5
80–3R	Z = 72.5	4.23 E+5	7.08 E+5
80–4R	Z = 73.5	4.67 E+5	7.82 E+5
80–5R	Z = 74.5	5.76 E+5	9.65 E+5

Run VIII
Aluminum
Roof buckets
100-g samples

14.6 GeV/c
All installations
433-min. exposure
5.97 E+11 p/sec

Location	Coordinates	Net count rate (bkg. subtracted) at t_0 (cpm/g)	ϕ at $\bar{I}$ (n/cm^2-sec)	ϕ at $I=10^{12}$ p/sec (n/cm^2-sec)
29–R	Z = 44.1	6.11 E+4	7.09 E+4	1.19 E+5
30–R	Z = 50.4	2.95 E+4	3.42 E+4	5.73 E+4
31–R	Z = 56.6	4.05 E+4	4.7 E+4	7.87 E+4
32–0R	Z = 62.9	1.03 E+5	9.70 E+5	1.62 E+6
32–1R	Z = 63.9	1.51 E+5	1.43 E+6	2.40 E+6
32–2R	Z = 64.9	1.51 E+5	1.43 E+6	2.40 E+6
32–3R	Z = 65.9	1.02 E+5	9.6 E+5	1.61 E+6
32–4R	Z = 66.9	7.80 E+4	7.38 E+5	1.24 E+6
32–5R	Z = 67.9	4.85 E+4	4.58 E+5	7.67 E+5
33–0R	Z = 69.2	5.34 E+4	5.05 E+5	8.46 E+5
34–R	Z = 70.5	2.75 E+5	3.19 E+5	5.34 E+5
35–R	Z = 81.8	1.23 E+5	1.43 E+5	2.40 E+5
36–R	Z = 88.1	8.08 E+4	9.37 E+4	1.60 E+5
78–R	Z = 56.6	2.29 E+4	2.66 E+4	4.46 E+4
79–R	Z = 62.9	1.19 E+5	1.13 E+6	1.89 E+6
80–R	Z = 69.2	3.25 E+5	3.77 E+5	6.31 E+5

Run VIII
Aluminum
Surface
2250-g detector

14.6 GeV/c
All installations
433-min. exposure
5.97 E+11 p/sec

Location	Coordinates	Net count rate (bkg subtracted) at t_0 (cpm)	ϕ at $\bar{\bar{I}}$ (n/cm^2-sec)	ϕ at I=10^{12} p/sec (n/cm^2-sec)
32—top	Y = 6.42 Z = 62.9	7.57 E+2	4.11 E+1	6.88 E+1
33—top	Y = 6.39 Z = 69.2	8.59 E+2	4.66 E+1	7.80 E+1

Run VIII
Aluminum
Tunnel 16

14.6 GeV/c
All installations
433-min. exposure

5.97 E+11 p/sec

Location	Detector size (g)	Net count rate (bkg subtracted) at t_0 (cpm)	Error (%)	ϕ at $\bar{I}$ (n/cm^2-sec)	ϕ at $I = 10^{12}$ p/sec (n/cm^2-sec)
16/0m	500	1.01 E+4		2.18 E+3	3.65 E+3
16/10m	500	4.90 E+2		1.05 E+2	1.76 E+2
16/20m	2200	4.02 E+2		2.48 E+1	4.15 E+1
16/30m	3300	1.63 E+2		7.8 E+0	1.30 E+1
16/40m	6600	7.51 E+1	6.5	2.62 E+0	4.39 E+0

Appendix B. Flux Measurements in Large Tunnels

Detector: carbon

Tunnel 52		Tunnel 77†	
Depth (meters)	Flux* (n/cm^2-sec)	Depth (meters)	Flux (n/cm^2-sec)
0	1.34×10^5	0	4.7×10^3
10	8.16×10^3	1.25	3.1×10^3
20	2.15×10^3	4.0	9.40×10^2
30	9.45×10^2	6.0	1.01×10^3
40	4.54×10^2	10	43
50	1.95×10^2	15	15
60	1.47×10^2	20	8.0
70	1.07×10^2	25	4.5
80	70.6	30	2.6
88	60.3	35	2.1
92	55.7		

Detector: aluminum

Tunnel 52		Tunnel 77†		
Depth (meters)	Flux (n/cm^2-sec)	Depth (meters)	Flux (n/cm^2-sec)	Error (%)
0	1.17×10^5	0	3.82×10^3	
10	6.11×10^3	1.25	7.16×10^2	
20	1.54×10^3	4	1.91×10^2	
30	5.99×10^2	6	1.57×10^2	
40	2.97×10^2	10	12.0	8.4
50	1.19×10^2	15	2.7	10.7
60	84	20	1.5	10.7
70	57	30	0.33	13
80	33.6			
88	28.6			
92	26.0			

*Corrected for beam variations during exposure.
†Weak source at mouth.

Detector: fast-neutron film

Tunnel 52		Tunnel 77*	
Depth (meters)	Tracks per field	Depth (meters)	Tracks per field
20	117±6	0.5	12.7±1.1
30	59±3	1.25	15.5±1.2
40	32±2	4	4.2±0.2
50	11.8±0.3	6	4.0±0.1
60	7.1±0.3	8	4.8±0.2
70	4.7±0.1	10	0.39±0.02
80	2.94±0.06	15	0.065±0.005
88	1.96±0.08	20	0.025±0.005
92	1.83±0.06	25	0.005±0.005

Detector: sulfur

Tunnel 52			Tunnel 77†		
Depth (meters)	Relative flux (n/cm^2-sec)	Error (%)	Depth (meters)	Relative flux (n/cm^2-sec)	Error (%)
0	1.35×10^5	3.7	0	4505	
10	7.5×10^3	10	0.5	3660	
20	1.9×10^3	60	1.25	2345	
			2	1480	
			4	903	
			6	463	5.0
			8	266	6.0
			10	150	6.0
			15	66.3	8.0
			20	35.6	10
			25	20.3	15
			30	16.1	17

*Weak source at mouth.

†Strong source at mouth.

Detector: bare gold

(i) Tunnel 52, Run VII

Depth (meters)	Flux (n/cm^2-sec)	Error (%)
0	3.9×10^6	
10	1.75×10^5	
20	1.6×10^4	
30	3.35×10^3	
40	3.15×10^3	
50	9.4×10^2	5.1
60	5.2×10^2	7.1

(ii) Tunnel 77, composite*

Depth (meters)	Relative flux (n/cm^2-sec)
0	1.00
0.5	7.6×10^{-1}
1.25	5.0×10^{-1}
2	3.8×10^{-1}
3	2.15×10^{-1}
4	1.58×10^{-1}
5	8.6×10^{-2}
6	6.4×10^{-2}
7	5.5×10^{-2}
8	3.1×10^{-2}
9	2.6×10^{-2}
10	2.0×10^{-2}
15	4.7×10^{-3}
20	1.72×10^{-3}
25	6.8×10^{-4}
30	3.7×10^{-4}
40	1.16×10^{-4}
50	4.9×10^{-5}
60	2.35×10^{-5}
70	1.65×10^{-5}
80	7.7×10^{-6}

*Weak source at mouth.

Detector: moderated gold

Tunnel 52

Depth (meters)	Flux (n/cm^2-sec)
0	1.02×10^7
10	3.2×10^5
20	4.8×10^4
30	1.3×10^4
40	1.75×10^4
50	5.7×10^3
60	4.9×10^3
70	2.1×10^3
92	1.45×10^3

Detector: $\beta\gamma$ film

Composite data-Tunnels 52 and 77*		Tunnel 77†	
Depth (meters)	Relative dose‡ (rads)	Depth (meters)	dose (rads)
0	1370	0	5.6 ±0.3
1.25	866	0.5	2.24±0.05
2	595	1.25	1.83±0.05
4	272	2.0	1.34±0.05
5	170	4.0	0.45±0.02
6	125	6.0	0.24±0.02
8	81	8.0	0.06±0.01
10	50	10	0.06±0.01
15	19.5	15	0.02±0.01
20	10.2	20	0.03±0.01
25	5.01		
30	3.38		
35	2.34		
40	1.65		
50	0.78		
60	0.58		
70	0.34		
80	0.23		
88	0.16		
92	0.12		

*Strong source at mouth.

†Weak source at mouth.

‡Errors $\lesssim$ 3%.

Detector: carbon

Position	Flux (n/cm^2-sec)
0	55.7
5	7.3
10	2.6
20	0.6±20%

Detector: fast-neutron film

Position	Tracks per field	
	Run VIII	Run IX
E 1		91.0 ±5.5
0	23.0 ±1.5	1.44±0.07
10	1.25±0.03	0.07±0.01
20	0.29±0.02	
30	0.10±0.01	
40	0.04±0.01	

Detector: moderated gold

Position	Flux (n/cm^2-sec)
E1	*
0	*
10	2.70×10^2
20	49
30	19.2±5%

* Results omitted because of high counting loss.

Detector: bare gold

Position	Run VIII		Run IX, 1-in gold		Run IX, 2-in. gold		Run IX. 5, 1-in gold	
	Relative flux (n/cm^2-sec)	Error (%)	flux (n/cm^2-sec)	Error (%)	C_{sat}	Error (%)	Relative flux (n/cm^2-sec)	Error (%)
E1			1.67×10^4		1.09×10^5		6.16×10^4	
E2			8.45×10^3		5.60×10^4		2.60×10^4	
E3			3.47×10^3		2.25×10^4		1.08×10^4	
0			1.38×10^3		9.08×10^3		3.93×10^3	
5			1.17×10^2	7	7.20×10^2	7	3.20×10^3	
10	1.56×10^2		26.1	17	1.5×10^2	30	61.9	5
20	17.6	6	4.6	100			7.2	15
30	9.6	10						

Detector: $\beta\gamma$ film and TLD

Position	Dose (rads)			
	$\beta\gamma$ film			
	Run VIII	Run IX	Run IX-5	TLD, Run IX-5
E1	70	4.4	270	190 360
E2		0.59	48	0.27 85
E3		0.22	19	12 30
0	2.2	0.11	6.7	5.3 13
5		0.01	0.70	0.42 1.4
10	0.085		0.20	0.19 0.33
20	0.02		0.05	0.04 0.09
30	0.02		0.02	0.02 0.05
40	0.01		0.01	0.00 0.02

Appendix D. Flux Measurements in Curved Tunnels

Detector: aluminum

Depth (m)	Flux (n/cm^2-sec) Run IX	Run VIII	Error (%)
0	1.87×10^3	2181	
2	7.15×10^2		
5	2.9×10^2		
10	61	107	24
17.5	5.1	24.8	
22.5		8.6	
25		2.6	6.5
30		0.6	

Detector: fast-neutron films

Depth (m)	Tracks per Field Run VIII
0	127 ±1.7
2	
5	
10	26 ±1.5
17.5	5.4 ±0.2
22.5	1.06±0.06
25	0.22±0.02
30	0.04±0.01

Detector: moderated indium

Depth (m)	Relative flux (n/cm^2-sec)
0	1.33×10^6
10	8.85×10^4
17.5	1.66×10^4
22.5	5.14×10^3
25	2.61×10^3
30	620
37.5	100

Detector: bare indium and gold

Depth (m)	Run VIII Indium relative flux (n/cm^2-sec)	Run IX 1-in. gold flux (n/cm^2-sec)	Run IX 2-in. gold C_{sat}	Run IX.5 1-in. gold relative flux (n/cm^2-sec)
0	9.36×10^5	7.35×10^3	5.03×10^4	6.81×10^4
2		4.93×10^3	3.08×10^4	
5		2.54×10^3	1.58×10^4	2.14×10^4
10	8.95×10^4	7.43×10^2	4.54×10^3	6.67×10^3
17.5	1.91×10^4	1.73×10^2	1.07×10^3	1.48×10^3
22.5	7.20×10^3	70.2	4.50×10^2	4.80×10^2
25	4.10×10^3			
30	1.12×10^3	16.3	1.00×10^2	84.1
37.5	1.61×10^2			15.6

Detector: $\beta\gamma$ film and TLD

	Dose (rads)				
	$\beta\gamma$ film				
Depth (m)	Run VIII	Run IX	Run IX.5	Run IX.5 TLD	
0		2.8	580	550	600
2		1.07			
5		0.44	104	70	110
10	0.38	0.16	30	13	32
17.5	0.14	0.04	6.1	7.3	9.5
22.5	0.04	0.01	1.76	1.5	2.4
30			0.18	0.11	0.25
37.5			0.03	0.01	0.05